

Lecture Notes in Physics

Editorial Board

- R. Beig, Wien, Austria
W. Beiglböck, Heidelberg, Germany
W. Domcke, Garching, Germany
B.-G. Englert, Singapore
U. Frisch, Nice, France
P. Hänggi, Augsburg, Germany
G. Hasinger, Garching, Germany
K. Hepp, Zürich, Switzerland
W. Hillebrandt, Garching, Germany
D. Imboden, Zürich, Switzerland
R. L. Jaffe, Cambridge, MA, USA
R. Lipowsky, Golm, Germany
H. v. Löhneysen, Karlsruhe, Germany
I. Ojima, Kyoto, Japan
D. Sornette, Nice, France, and Los Angeles, CA, USA
S. Theisen, Golm, Germany
W. Weise, Garching, Germany
J. Wess, München, Germany
J. Zittartz, Köln, Germany

The Lecture Notes in Physics

The series Lecture Notes in Physics (LNP), founded in 1969, reports new developments in physics research and teaching – quickly and informally, but with a high quality and the explicit aim to summarize and communicate current knowledge in an accessible way. Books published in this series are conceived as bridging material between advanced graduate textbooks and the forefront of research to serve the following purposes:

- to be a compact and modern up-to-date source of reference on a well-defined topic;
- to serve as an accessible introduction to the field to postgraduate students and non-specialist researchers from related areas;
- to be a source of advanced teaching material for specialized seminars, courses and schools.

Both monographs and multi-author volumes will be considered for publication. Edited volumes should, however, consist of a very limited number of contributions only. Proceedings will not be considered for LNP.

Volumes published in LNP are disseminated both in print and in electronic formats, the electronic archive is available at springerlink.com. The series content is indexed, abstracted and referenced by many abstracting and information services, bibliographic networks, subscription agencies, library networks, and consortia.

Proposals should be sent to a member of the Editorial Board, or directly to the managing editor at Springer:

Dr. Christian Caron
Springer Heidelberg
Physics Editorial Department I
Tiergartenstrasse 17
69121 Heidelberg/Germany
christian.caron@springer-sbm.com

G. Cuniberti G. Fagas K. Richter (Eds.)

Introducing Molecular Electronics

Editors

Gianaurelio Cuniberti

Klaus Richter

Institut für Theoretische Physik

Universität Regensburg

Universitätsstr. 31

93053 Regensburg, Germany

E-mail: g.cuniberti@physik.uni-regensburg.de

klaus.richter@physik.uni-regensburg.de

Giorgos Fagas

National Microelectronics

Research Center (NMRC)

Nanotechnology Group

Lee Maltings, Cork, Ireland

E-mail: gfagas@nmrc.ie

Gianaurelio Cuniberti, Giorgos Fagas, Klaus Richter, *Introducing Molecular Electronics*,
Lect. Notes Phys. 680 (Springer, Berlin Heidelberg 2005), DOI 10.1007/b101525

Library of Congress Control Number: 2005930443

ISSN 0075-8450

ISBN-10 3-540-27994-6 Springer Berlin Heidelberg New York

ISBN-13 978-3-540-27994-5 Springer Berlin Heidelberg New York

This work is subject to copyright. All rights are reserved, whether the whole or part of the material is concerned, specifically the rights of translation, reprinting, reuse of illustrations, recitation, broadcasting, reproduction on microfilm or in any other way, and storage in data banks. Duplication of this publication or parts thereof is permitted only under the provisions of the German Copyright Law of September 9, 1965, in its current version, and permission for use must always be obtained from Springer. Violations are liable for prosecution under the German Copyright Law.

Springer is a part of Springer Science+Business Media

springeronline.com

© Springer-Verlag Berlin Heidelberg 2005

Printed in The Netherlands

The use of general descriptive names, registered names, trademarks, etc. in this publication does not imply, even in the absence of a specific statement, that such names are exempt from the relevant protective laws and regulations and therefore free for general use.

Typesetting: by the author using a Springer L^AT_EX macro package

Printed on acid-free paper SPIN: 11332886 57/TechBooks 543210

Foreword

Klaus von Klitzing

Max-Planck-Institut für Festkörperforschung, Heisenbergstraße 1, 70569 Stuttgart, Germany

Already many Cassandras have prematurely announced the end of the silicon roadmap and yet, conventional semiconductor-based transistors have been continuously shrinking at a pace which has brought us to nowadays cheap and powerful microelectronics. However it is clear that the traditional scaling laws cannot be applied if unwanted tunnel phenomena or ballistic transport dominate the device properties. It is generally expected, that a combination of silicon CMOS devices with molecular structure will dominate the field of nanoelectronics in 20 years.

The visionary ideas of atomic- or molecular-scale electronics already date back thirty years but only recently advanced nanotechnology, including e.g. scanning tunneling methods and mechanically controllable break junctions, have enabled to make distinct progress in this direction. On the level of fundamental research, state of the art techniques allow to manipulate, image and probe charge transport through uni-molecular systems in an increasingly controlled way. Hence, molecular electronics is reaching a stage of trustable and reproducible experiments. This has lead to a variety of physical and chemical phenomena recently observed for charge currents owing through molecular junctions, posing new challenges to theory. As a result a still increasing number of open questions determines the future agenda in this field.

Both, related pioneering experiments and corresponding new theoretical approaches are featured in the present volume of the Springer Series of Lecture Notes in Physics. The contributions to this volume, written by many of the international leaders in the field, span the whole range from single molecules to molecular materials, from carbon nanotube-based devices to organic molecular bridges and proposals for future architectures. The theoretical chapters cover elaborate ab initio calculations as well as novel complementary model-based approaches.

The chapters of the present volume start from an introductory, tutorial level, ideal for graduate students, but also cover many timely aspects of quantum transport at the molecular scale and thereby represent the state of the art in the field, relevant for experts and researchers attracted to this discipline.

The complementary view of authors from chemistry and physics reflects the need for a strong transdisciplinary effort to make clear advances in molecular electronics. This book constitutes a coherent and balanced account of

this rapidly progressing field. It will serve as an important reference volume filling the existing gap between specialized research papers and proceedings, and closed- disciplinary research reviews. I consider this book as a valuable addition to the Springer Series of Lecture Notes in Physics.

Preface

In recent years molecular electronics, particularly the investigation of charge transport processes at molecular scales, has become an immensely vivid field of cross-disciplinary blend encompassing more traditional condensed-matter, mesoscopic, molecular and chemical physics, as well as chemistry. The aim of this book is to provide, on the one hand, an introduction into the mature experimental and theoretical foundations, techniques, and ideas which have been driving this subject. On the other hand, it is to present a balanced overview over the state-of-the-art research in this rapidly progressing discipline.

The present Lecture Notes in Physics volume is addressed to young scientists with a basic background in condensed-matter or chemical physics, and it may serve as an orientation for scientists who are interested in or are planning to enter the exciting field of molecular electronics. Moreover, many of the presented results and viewpoints are certainly also new and of interest to specialists in the field. In order to cover a broad range of both experimental and theoretical topics the book has been written by several authors. Each chapter of the volume is aimed at an own introduction and at a reasonably self-contained account of the respective subtopic. A more general introduction to the contents of each chapter and survey of the field, as well as a compilation of further related introductory and review literature, is given in the first chapter.

This book grew out of the very stimulating international workshop *Advances in Molecular Electronics: From Molecular Materials to Single-Molecule Devices* held in February 2004 in Dresden (Germany) at the *Max Planck Institute for the Physics of Complex Systems*, which also sponsored the event. Most of the volume contributions arose from lectures presented there. We thank all the speakers and participants who contributed to the great success of that meeting and particularly Katrin Lantsch for the superb organization. We greatly thank all authors of the chapters of the present Lecture Notes for their enthusiasm, efforts, and, finally, patience during the different stages of this project. Furthermore, the comments by the referees and the valuable advice from the scientific editors of the Springer Lecture Notes, which contributed significantly towards the coherence and readability of the volume, are greatly acknowledged.

We are grateful to *Max Planck Institute for the Physics of Complex Systems* and the *German Research Foundation* through the “University Graduate Training Programme DFG-GRK-638: Nonlinearity and Nonequilibrium in Condensed Matter” for additional financial support. We also thank Markus Gaa’s who helped us to prepare the final version of this volume.

Finally we would like to thank Drs. Claus Ascheron, Angela Lahee and Christian Caron at Springer Verlag for their valuable help and cooperation.

Regensburg and Cork
March 2005

G. Cuniberti
G. Fagas
K. Richter

Contents

Introducing Molecular Electronics: A Brief Overview

<i>Gianaurelio Cuniberti, Giorgos Fagas, and Klaus Richter</i>	1
1 A Passage Through Time: Past, Present and Future Challenges	1
2 What You Find in the Book – a Passage Through Its Contents	4
3 What is not Included in the Book – Literature Hints	6
References	8

Part I Theory

Foundations of Molecular Electronics – Charge Transport in Molecular Conduction Junctions

<i>Joshua Jortner, Abraham Nitzan and Mark A. Ratner</i>	13
1 Prologue	13
2 Theoretical Approaches to Conductance	18
3 The Relationship Between Electron Transfer Rates and Molecular Conduction	21
4 Interaction with Nuclear Degrees of Freedom	22
5 Remarks and Generalities	33
References	45

AC-Driven Transport Through Molecular Wires

<i>Peter Hänggi, Sigmund Kohler, Jörg Lehmann, Michael Strass</i>	55
1 Introduction	55
2 Basic Concepts	56
3 Floquet Approach to the Driven Transport Problem	59
4 Weak-Coupling Approximations	65
5 Photon-Assisted Transport Across a Molecular Bridge	70
6 Conclusions	72
References	73

Electronic Structure Calculations for Nanomolecular Systems

<i>Rosa Di Felice, Arrigo Calzolari, Daniele Varsano, Angel Rubio</i>	77
1 Electronic Structure of Nanomolecular Systems	77

2	Selected Applications of Ground-State Electronic Structure Calculations by DFT	79
3	Linear Response by TDDFT	88
4	Wannier Functions for Electronic Structure Calculations	97
	References	107

Ab-initio Non-Equilibrium Green's Function Formalism for Calculating Electron Transport in Molecular Devices

K.	<i>Stokbro, J. Taylor, M. Brandbyge, H. Guo</i>	117
1	Introduction	117
2	Mean Field Electronic Structure Theory	118
3	Application of DFT to Modeling Molecular Electronics Devices ..	120
4	Implementation: McDCAL, TranSIESTA, and Atomistix Virtual NanoLab	134
5	Resistance of Molecular Wires	135
6	Non-Equilibrium Forces	141
7	Conclusion	147
	References	147

Tight-Binding DFT for Molecular Electronics (gDFTB)

A.	<i>Di Carlo, A. Pecchia, L. Latessa, Th. Frauenheim and G. Seifert</i> ..	153
1	Introduction	153
2	The Self-Consistent Density-Functional Tight-Binding	155
3	Setup of the Transport Problem	157
4	The Green's Function Technique	159
5	The Relationship with the Keldysh Green's Functions	160
6	The Terminal Currents	163
7	The Poisson Equation	164
8	Atomic Forces	165
9	gDFTB Example Applications	167
10	Incoherent Electron-Phonon Scattering	169
11	Comments on DFT Applied to Transport	179
12	Conclusions	180
	References	181

Current-Induced Effects in Nanoscale Conductors

Neil	<i>Bushong, Massimiliano Di Ventra</i>	185
1	Current Through a Nanoscale Junction	185
2	Current-Induced Forces	188
3	Shot Noise	190
4	Local Heating	194
5	Inelastic Conductance	200
6	Conclusions	202
	References	202

Single Electron Tunneling in Small Molecules

<i>Maarten R. Wegewijs, Matthias H. Hettler, Christian Romeike, Axel Thielmann, Katja Nowack, Jürgen König</i>	207
1 Introduction	207
2 Tunneling Transport	208
3 Electronic Excitations of a Benzene Ring	213
4 Spin Excitations of a [2 × 2] Grid Molecule	215
5 Vibrational Excitations and Multiple Orbitals	219
6 Current Noise (Shot Noise)	222
7 Conclusions	225
References	226

Transport through Intrinsic Quantum Dots in Interacting Carbon Nanotubes

<i>M. Thorwart, R. Egger, M. Grifoni</i>	229
1 Introduction	229
2 Electrical Transport in Individual SWNTs	230
3 Markovian Master Equation Approach	236
4 Quantum Monte Carlo Simulations	242
5 Conclusions	246
References	247

Part II Experiment

Contacting Individual Molecules Using Mechanically Controllable Break Junctions

<i>Jan van Ruitenbeek, Elke Scheer and Heiko B. Weber</i>	253
1 Introduction	253
2 Experimental Techniques	255
3 Simple Molecules	259
4 Molecules Bonded by Thiol Groups to Gold	266
5 Conclusions and Prospects	271
References	271

Intrinsic Electronic Conduction Mechanisms in Self-Assembled Monolayers

<i>Wenyong Wang, Takhee Lee, Mark A. Reed</i>	275
1 Introduction	275
2 Experiment	277
3 Theoretical Basis	279
4 Results	282
5 Conclusions	295
References	296

Making Contacts to Single Molecules: Are We There Yet?

<i>J. Tomfohr, G.K. Ramachandran, O.F. Sankey and S.M. Lindsay</i>	301
1 Introduction	301
2 Contact Resistance in NP Contact Experiments	303
3 Changing the NP Size	307
4 Status of Single Molecule Measurements	309
References	310

Six Unimolecular Rectifiers and What Lies Ahead

<i>Robert M. Metzger</i>	313
1 Introduction	313
2 Metal Contacts	318
3 The Aviram-Ratner Ansatz	318
4 Three Processes for Rectification by Organic Monolayers	320
5 Current and Resistance Across a Metal-Molecule-Metal System ..	321
6 Assembly Techniques: Physisorption Versus Chemisorption	322
7 The “Organic Rectifier Project”	323
8 Electrical Properties of Monolayers and Multilayers	325
9 Rectification of $C_{16}H_{33}Q-3CNQ$	325
10 Molecular Properties of $C_{16}H_{33}Q-3CNQ$	326
11 Film Properties of $C_{16}H_{33}Q-3CNQ$	327
12 Metal – LB Film – Metal Sandwiches of $C_{16}H_{33}Q-3CNQ$	328
13 Unimolecular Rectification by $C_{16}H_{33}Q-3CNQ$	329
14 Chemisorbed Monolayer Rectifiers	332
15 Three More Rectifiers	335
16 Direction of “Forward Current” in Rectifiers	338
17 Challenges for the Near Future	339
18 Conclusion	343
19 End-Notes	343
References	344

Quantum Transport in Carbon Nanotubes

<i>Elsa Thune and Christoph Strunk</i>	351
1 Introduction	351
2 Synthesis	352
3 The Structure of Carbon Nanotubes	354
4 Electronic Structure of Nanotubes	358
5 Electron Transport Experiments	361
6 Conclusions	375
References	375

Carbon Nanotube Electronics and Optoelectronics

<i>S. Heinze, J. Tersoff,, Ph. Avouris</i>	381
1 Introduction	381
2 Schottky Barrier Carbon Nanotube Transistors	382

3 Conclusions and Outlook	406
References	407

Charge Transport in DNA-based Devices

<i>Danny Porath, Noa Lapidot and Julio Gomez-Herrero</i>	411
1 Introduction	411
2 Direct Electrical Transport Measurements in DNA	415
3 Conclusions and Perspectives	436
References	438

Part III Outlook

CMOL: Devices, Circuits, and Architectures

<i>Konstantin K. Likharev and Dmitri B. Strukov</i>	447
1 Introduction	447
2 Devices	449
3 Circuits	452
4 CMOL Memories	455
5 CMOL FPGA: Boolean Logic Circuits	460
6 CMOL CrossNets: Neuromorphic Networks	467
7 Conclusions	474
References	474

Architectures and Simulations for Nanoprocessor Systems Integrated on the Molecular Scale

<i>Shamik Das, Garrett Rose, Matthew M. Ziegler, Carl A. Picconatto, James C. Ellenbogen</i>	479
1 Introduction	479
2 Starting at the Bottom: Molecular Scale Devices in Device-Driven Architectures for Nanoprocessors	482
3 Challenges for Nanoelectronics in Developing Nanoprocessors	485
4 A Brief Survey of Nanoprocessor System Architectures	490
5 Principles of Nanoprocessor Architectures Based on FPGAs and PLAs	496
6 Sample Simulation of a Circuit Architecture for a Nanowire-Based Programmable Logic Array	499
7 Conclusion	505
References	506

Index	513
--------------------	------------

List of Contributors

Gianaurelio Cuniberti

Institute for Theoretical Physics
University of Regensburg, 93040
Regensburg, Germany

Giorgos Fagas

Tyndall National Institute
Lee Maltings, Prospect Row
Ireland

Klaus Richter

Institute for Theoretical Physics
University of Regensburg, 93040
Regensburg, Germany

Joshua Jortner

School of Chemistry
Tel Aviv University
Tel Aviv, 69978, Israel

Abraham Nitzan

School of Chemistry
Tel Aviv University
Tel Aviv, 69978, Israel

Mark A. Ratner

Department of Chemistry
and Institute
for Nanotechnology Northwestern
University, Evanston
Illinois 60208, U.S.A.

Peter Hänggi

Institut für Physik
Universität Augsburg
Universitätsstraße 1
86135 Augsburg, Germany

Sigmund Kohler

Institut für Physik, Universität
Augsburg Universitätsstraße 1
86135 Augsburg, Germany

Jörg Lehmann

Institut für Physik, Universität
Augsburg Universitätsstraße 1
86135 Augsburg, Germany

Michael Strass

Institut für Physik, Universität
Augsburg Universitätsstraße 1
86135 Augsburg, Germany

Rosa Di Felice

INFM National Center on
nanoStructures and bioSystems
at Surfaces (S3), Modena, Italy
rosa@unimore.it

Arrigo Calzolari

INFM National Center on
nanoStructures and bioSystems
at Surfaces (S3), Modena
Italy

Daniele Varsano

Departamento de Fisica de
Materiales, Facultad de Quimicas
Universidad del Pais Vasco
Centro Mixto CSIC-UPV/EHU and
Donostia
International Physics Center (DIPC)
San Sebastian, Spain
arubio@sc.ehu.es

Angel Rubio

Departamento de Fisica de
Materiales Facultad de Quimicas
Universidad del Pais Vasco
Centro Mixto CSIC-UPV/EHU and
Donostia
International Physics Center (DIPC)
San Sebastian, Spain
arubio@sc.ehu.es

K. Stokbro

Nanoscience Center
Universitetsparken 5d, 2100
Copenhagen East Denmark
ks@nano.ku.dk

J. Taylor

Atomistix Inc, Juliane Maries Vej 30
DK-2100 Copenhagen East
Denmark
jt@atomistix.com

M. Brandbyge

Department of Micro and
Nanotechnology (MIC)
Technical University of Denmark
Building 345 East
DK-2800 Kongens Lyngby, Denmark
mbr@mic.dtu.dk

H. Guo

Department of Physics McGill
University Montreal (Quebec)
PQ H3A 2T8, Canada
guo@phys.mcgill.ca

A. Di Carlo

Dept. Elect. Eng., University of
Rome “Tor Vergata”, Via del
Politecnico 1, I-00133 Roma, Italy
dicarlo@ing.uniroma2.it

A. Pecchia

Dept. Elect. Eng., University of
Rome “Tor Vergata”, Via del
Politecnico 1, I-00133 Roma
Italy

Th. Frauenheim

Dept. of Theoretical Physics
University of Paderborn
33098 Paderborn, Germany

G. Seifert

Institut f. Physikalische Chemie
Technische Universität Dresden
01062 Dresden
Germany

Neil Bushong

Department of Physics
University of California
San Diego La Jolla
CA 92093-0319, USA
bushong@physics.ucsd.edu

Massimiliano Di Ventra

Department of Physics
University of California
San Diego, La Jolla
CA 92093-0319, USA
diventra@physics.ucsd.edu

Maarten R. Wegewijs

Institut für Theoretische Physik A
RWTH Aachen, 52056 Aachen
Germany

R. Egger

Institut für Theoretische Physik
Heinrich-Heine-Universität
Universitätsstr. 1
40225 Düsseldorf, Germany

Matthias H. Hettler

Forschungszentrum Karlsruhe,
Institut für Nanotechnologie
76021 Karlsruhe, Germany

M. Grifoni

Institut für Theoretische Physik
Universität Regensburg
Universitätsstr. 31
93035 Regensburg, Germany

Christian Romeike

Institut für Theoretische Physik A
RWTH Aachen, 52056 Aachen
Germany

Jan van Ruitenbeek

Kamerlingh Onnes Laboratorium
Universiteit Leiden
Postbus 9504, 2300 RA Leiden
The Netherlands
Ruitenbeek@physics.leidenuniv.nl

Axel Thielmann

Forschungszentrum Karlsruhe
Institut für Nanotechnologie
76021 Karlsruhe, Germany

Elke Scheer

Universität Konstanz
Fachbereich Physik
Universitätsstr. 10
78464 Konstanz, Germany
Elke.Scheer@uni-konstanz.de

Katja Nowack

Institut für Theoretische Physik A
RWTH Aachen, 52056 Aachen
Germany

Heiko B. Weber

Institut für Angewandte Physik
Universität
Erlangen-Nürnberg
91058 Erlangen, Germany
Forschungszentrum Karlsruhe
Institut für Nanotechnologie
76021 Karlsruhe, Germany
Heiko.Weber@physik.uni-erlangen.de

Jürgen König

Institut für Theoretische Physik III
Ruhr-Universität Bochum
44780 Bochum, Germany

Wenyong Wang

Semiconductor Electronics Division
National Institute of
Standards and Technology
M.S. 8120, Gaithersburg
MD 20899-8120, USA

M. Thorwart

Institut für Theoretische Physik
Heinrich-Heine-Universität
Universitätsstr. 1
40225 Düsseldorf, Germany

Takhee Lee

Department of Materials Science
and Engineering, Gwangju
Institute of Science and
Technology, Gwangju 500-712
Korea

Mark A. Reed

Departments of Electrical
Engineering and Applied
Physics, Yale University
P.O. Box 208284, New Haven
CT 06520, USA
mark.reed@yale.edu

J. Tomfohr

Department of Physics and
Astronomy

G.K. Ramachandran

Department of Physics and
Astronomy

O.F. Sankey

Department of Physics and
Astronomy

S.M. Lindsay

Department of Physics and
Astronomy
The Biodesign Institute Arizona
State University, Tempe
AZ 85287, USA

Robert M. Metzger

Department of Chemistry
Box 870336, University of Alabama
Tuscaloosa, AL 35487-0336
USA

**Elsa Thune and Christoph
Strunk**

Institute of Experimental and
Applied Physics, University of
Regensburg
Universitätsstr. 31
93040 Regensburg, Germany
elsa.thune@physik.uni-regensburg.de
christoph.strunk@physik.uni-regensburg.de

S. Heinze

Institute of Applied Physics
University of Hamburg
Jungiusstrasse 9a, 20355 Hamburg
Germany
heinze@physnet.uni-hamburg.de

J. Tersoff

IBM Research Division,
T. J. Watson Research Center
Yorktown Heights, New York 10598
USA
tersoff@us.ibm.com

Ph. Avouris

T. J. Watson Research Center
Yorktown Heights, New York 10598
USA
avouris@us.ibm.com

Danny Porath

Department of Physical Chemistry
The Hebrew University
Jerusalem 91904, Israel
porath@chem.ch.huji.ac.il

Noa Lapidot

Department of Physical Chemistry
The Hebrew University
Jerusalem 91904, Israel

Julio Gomez-Herrero

Departamento Física
de la Materia Condensada
Universidad Autónoma de
Madrid, Madrid 28049, Spain

Konstantin. K. Likharev

Stony Brook University, Stony
Brook
NY 11794, USA

Dmitri. B. Strukov

Stony Brook University
Stony Brook, NY 11794, USA

Shamik Das

The MITRE Corporation, M/S
H619
7525 Colshire Drive
McLean, VA 22102
{sdas,grose,picconatto,ellenbgn}
@mitre.org

Garrett Rose

The MITRE Corporation, M/S
H619
7525 Colshire Drive
McLean, VA 22102

Matthew M. Ziegler

IBM T. J. Watson Research Center
1101 Kitchawan Road
P. O. Box 218
Yorktown Heights, NY 10598
zieglerm@us.ibm.com

Carl A. Picconatto

The MITRE Corporation, M/S
H619
7525 Colshire Drive
McLean, VA 22102

James C. Ellenbogen

The MITRE Corporation, M/S
H619
7525 Colshire Drive
McLean, VA 22102

Introducing Molecular Electronics: A Brief Overview

Gianaurelio Cuniberti¹, Giorgos Fagas², and Klaus Richter¹

¹ Institute for Theoretical Physics, University of Regensburg, 93040 Regensburg, Germany

² Tyndall National Institute, Lee Maltings, Prospect Row, Ireland

Abstract. We give a brief account of the foundations, state-of-the-art, major topics, and challenges of charge transport at the molecular scale. This summary is not aiming at completeness, but rather gives an overview of what follows in the different chapters of this volume.

1 A Passage Through Time: Past, Present and Future Challenges

In this and subsequent chapters we mostly view molecular electronics as defined via the concept of single molecules being either the active elements in hybrid electronics or integrating a range of elementary functions necessary in computation. This working definition should be contrasted with that relating the condensed-phase properties of a material with the molecular nature of its building blocks like for example in molecular crystals. Despite being relatively loose, such a picture allows to draw a rough boundary line between the modern applications of organic (opto)-electronics based on bulk materials and those envisaged by the seminal idea of Ari Aviram and Mark Ratner (Fig. 1). Considering the lack of any experiments that could be immediately realized at that time, they published back in 1974 a paper entitled “Molecular Rectifiers” [1], where with an extreme dose of visionary content they discuss theoretically the possibility to construct a “very simple electronic device, a rectifier, based on the use of a single organic molecule”. It has turned out that observing true molecular rectification is highly nontrivial as discussed in detail later in the volume (Chap. 12). However, their proposal formed a brave attempt that would strengthen the foundations of the field with hopes of electronic applications truly at the molecular scale. And with most recent advances thirty years later, we are very close to witnessing a challenging theoretical prediction being regularly realized as it often happens for excellent theories where new concepts out-trace the bare interpretation of experiments.

The Aviram-Ratner model is probably the first concrete example involving unimolecular *quantum transport* and its applications. As such however, it is intimately connected with the *electron transfer* theories and related experiments which were being fruitfully developed in parallel. These have explored the electron dynamics in molecules and unveiled possible path mechanisms

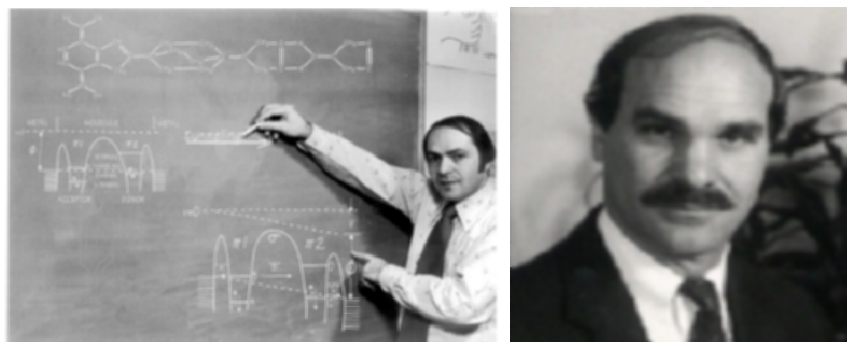


Fig. 1. *Left:* Ari Aviram explains the principles of the Aviram-Ratner theory on molecular rectification to a group of American journalists. This picture was published in the Gannet Westchester Newspaper on Thursday, January 4, 1979. *Right:* Mark Ratner

leading to the Nobel Prize for Chemistry to Rudolf Marcus in 1992. If one wishes to uncover roots even earlier in time, it is worth noting that first charge and energy transfer studies in molecules started in the 1940s by Robert Mulliken and Albert Szent-Gyorgyi in relation to the so-called donor-acceptor systems.

With interest remaining steady through time, rapid progress in molecular electronics has eventually been made in the last decade (Fig. 2) owing to successes on the experimental front. Sophisticated tools have allowed single molecules to be contacted and current-voltage characteristics to be measured by utilizing molecular functionality and recognition in order to assemble an electronic device, as well as advents in scanning probe microscopy and nano-lithography -patterning techniques. Therefore, molecular electronics nowadays has been driving one of the most exciting interdisciplinary efforts in nanosciences. Under its “umbrella” it embraces many traditional disciplines, such as: (i) self-assembly and supramolecular chemistry, a domain rightly lying between the analytical chemistry and biology boundaries and (ii) electronic device characterization, a common strength of physical and electrical engineering research. But why do we need to consider molecular electronics and what makes quantum transport at these length-scales so challenging? The answer to the first question is motivated by the technological needs imposed by the exponential miniaturization trend of conventional semiconductor-based electronics. The latter has been experienced since the sixties and early recognized in the so-called Moore’s law [2]. Despite the momentum provided by the technology thrive, molecular electronics also flourishes due to the series of fundamental issues it poses and which have been receiving sound answers only recently. Most important are the manifestations of quantum transport when electrons transverse a single molecule

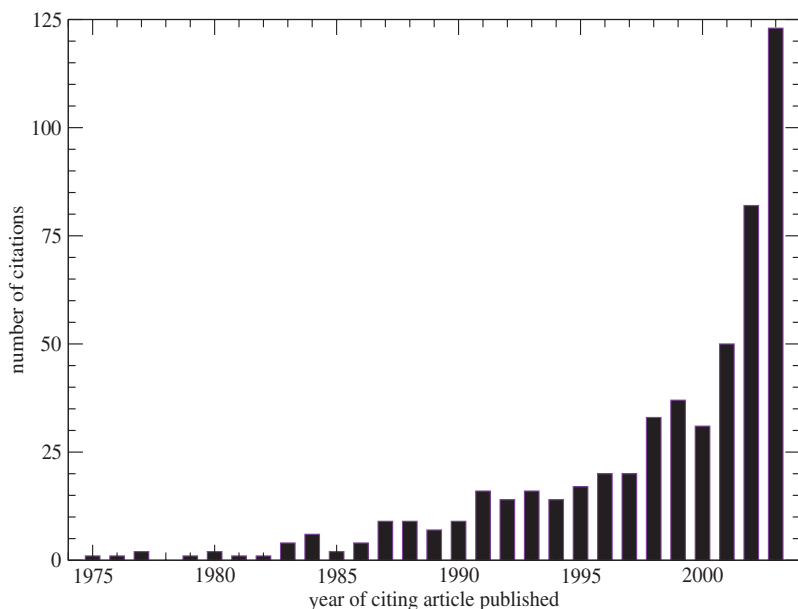


Fig. 2. An indicator of the evolution of molecular electronics is provided by the number of citations per year to the seminal Aviram-Ratner study [1] during the last three decades. Data taken from the ISI Web of Knowledge

at a constant rate and the influence of the interactions with the external environment when the truly small joins smoothly to the relatively large.

Studies of charge-transport in reduced dimensions preceded with setups of artificially tailored semiconductors leading to the discovery of a wealth of mesoscopic quantum phenomena. For example, the quantum Hall effect, the conductance quantization, and the Coulomb blockade all intrinsically rely on the confinement of electrons in two, one or zero dimensions. Nevertheless, in usual mesoscopic systems the electric current flows through relatively smooth potential landscapes on the atomic scale. This allows for simple descriptions of the electronic structure via the effective mass approximation but contrasts the need to accommodate the precise atomic scale roughness and chemical synthesis in molecular devices. In addition, characteristic electronic energy (time) scales are such that the overall dynamics of charge carriers becomes increasingly complex since they may move in a correlated manner in the field of both the atomic nuclei and the other electrons.

The route to molecular electronics sketched above allows to conclude that the field has matured and grown so to define immediate challenges and new directions [3–5]. Some of these such as the reproducibility and the characterization of the contacts in the experiments, or the improvement of the computational schemes both depending on the transport regime and the underlying

mechanisms, are discussed in this book. Others are growing in fertile labs around the world. In the next two sections we shall present several of the accomplishments and complementary perspectives in more detail.

2 What You Find in the Book – a Passage Through Its Contents

Molecular electronics gains momentum from bridging (nano)physics and chemistry and, as all scientific disciplines, it receives input from theory and experiment providing a mutual influence and challenge. Hence, the topics of the different chapters have been chosen to complement each other with regard to techniques presented or phenomena addressed and angle of perspective. The volume consists of a (nearly) balanced number of theoretical (Theoretical Part: Chaps. 1 to 8) and experimental (Experimental Part: Chaps. 9 to 15) contributions and two further more visionary parts on integration on the molecular scale (Outlook Part: Chaps. 16 and 17), thereby covering a broad, though certainly not the entire (see Sec. 3), spectrum of nowadays molecular-scale electronics.

The content of each chapter is rather self-contained, and hence in reading the book one need not follow the order of the chapters as given. The format is such that the volume could be used as a “crash course” for students interested in broadening their knowledge as well as for prospective newcomers in this exciting arena. For researchers already active in the field, the volume covers enough areas in detail so that it may be beneficial as a reference.

Serving as an entry for the reader, the first theory chapter starts from the foundations of molecular electronics. It subsequently develops into a complete survey that includes the latest advances in the theoretical understanding of charge-transport processes in molecules. In Chap. 2 the authors move one step further and present a comprehensive elaboration on effects and control of charge transport in molecular wires driven through external time-dependent fields. The latter fundamental interaction is an essential feature that needs to be investigated for potential applications. Chaps. 1 and 2 introduce the conceptual and mathematical framework including Green functions and the density matrix representation, which are commonly employed in the studies of quantum kinetics. These chapters represent to a large extend model-driven developments where a tight-binding description used for molecular wires. As such, they allow a qualitative understanding of the involved processes and their detailed mechanisms, discussed in a whole body of further literature.

Complementary in spirit, the following three chapters are devoted to different numerical methods designed so that the precise electronic structure properties of the molecular junction components are calculated from first-principles. In Chap. 3, the state-of-the-art in ab-initio methods is presented with more emphasis given to the density functional theory (DFT) based formulation of the many-body problem. Although there is much criticism at

present concerning current applications at the non-equilibrium conditions of a molecular device and the overall performance when comparing with experiments (much of which is triggered from the authors themselves; also in following chapters), this method is most efficient when it comes to calculating quantum transport properties. It also allows for relatively transparent qualitative conclusions to be drawn via its inherent mapping to a single-particle picture.

Therefore, while there is a vivid parallel activity that works out the DFT-shortcomings, Chaps. 4 and 5 elaborate further on how such obtained electronic structures combine with the quantum transport Green function methods within two different numerical implementations. The first scheme is built from the DFT-package SIESTA [6]; the second simulator has been developed from an approximate DFT-scheme featuring the strengths of a subsequent tight-binding implementation (DFTB) [7]. Several examples are illustrated for electron transport across realistic molecular junctions. Both approaches cope with the non-equilibrium charge distributions present under finite bias conditions and can in principle include inelastic effects, e.g., induced by the energy exchange of the electronic subsystem with the nuclei (electron-phonon interaction).

Presenting an alternative DFT method based on the Lippmann-Schwinger formulation of scattering, Chap. 6 deals with the interesting problem of how current flow itself influences the properties of the underlying conductor. An approach in order to treat the combined electron-ion dynamics underlying the technologically very important issue of heating is also developed.

The remaining two theory chapters address particular aspects of electron-electron interactions. In Chap. 7, complementary to the strong-coupling regime studied, e.g. in Chaps. 4 and 5, the limit of weak coupling of a nanoscale conductor to the leads is discussed. This regime commonly implies charging and Coulomb blockade effects and correspondingly, at the level of the indicated method, a description in terms of master equations for the sequential charge flow through the junction. In the last theory part, Chap. 8, the physics of carbon nanotube (CNT) molecular systems moves into focus and the effect of strong many-electron correlations in low-dimensional systems is presented. Focusing on the possibility to induce new kind of excitations described by the Luttinger liquid framework, the predictions of such advanced techniques is discussed in relation to the experimental observations (following also in Chap. 13).

The experimental contributions cover different prominent experimental techniques for measuring charge transport through molecular-scale conductors. Chap. 9 comprises experiments from three leading groups in the field, all employing molecular break junction techniques for single-molecule measurements. The hitherto successes and new possibilities of such setups are presented. In Chap. 10, Mark Reed and coworkers give a complementary account by describing the transport mechanisms in self-assembled molecular

monolayers between metallic electrodes. The discussion includes most recent experimental results on the inelastic electron spectroscopy of molecular junctions formed by alkanethiols. In Chap. 11, a further method is presented, namely, contacting a self-assembled monolayer via a scanning probe operating in the conductive mode. The case of intervening nanoparticles is discussed in relation with an overall critical review on making single-molecule contacts.

Chapter 12 gives a very detailed account on the issue of molecular rectification as envisaged by Ari Aviram and Mark Ratner, from a chemist's perspective. The technical challenges and possible processes leading to the effect that stands the molecular electronics hallmark are analyzed through the presentation of different devices that have so far exhibited rectifying properties.

Chapters 13 and 14 are devoted to the electronics and optoelectronics of CNTs spanning the whole range from basic concepts to most recent measurements of phase-coherent transport (Chap. 13) and contact effects (Chap. 14). Particularly for non-experts, the very pedagogical introductory part of Chap. 13, starting from the basics, is recommended to be read before its theoretical counterpart Chap. 8. Issues underlying the nature of the transport mechanisms in single- and multi-wall CNTs are clearly presented. Chapter 14 discusses the fundamental problem of electrically characterizing the interface formed between a CNT and a metal which is of key-technological importance to the operation of CNT-based transistors.

The experimental part closes with Chap. 15, where the challenging field of DNA-based devices is jointly reviewed from the broad perspective of two research groups very active in this direction. The controversial conduction properties of DNA oligomers together with its phenomenal self-recognition properties trigger here a critical discussion.

Although the potential application of molecular electronics has already attracted the interest of some large corporates [8] and features predominantly in the emergent devices of the International Technology Roadmap for Semiconductors, one should acknowledge the fact that the scaling down of silicon technologies will continue far beyond the nowadays 90 nm technology node. However, molecular electronics may provide in the long term building blocks for alternative technologies most probably not in the way we think of to date. To this end, the most prevalent idea consists in merging the semiconductor macro-devices with the extreme miniaturization of molecular-based elements. The final part of this volume, i.e., Chaps. 16 and 17, takes a glimpse at the future and deals with possible strategies in assembling molecular devices and integrate them within current running technologies.

3 What is not Included in the Book – Literature Hints

As already mentioned, charge carrier dynamics in molecular electronics shares many similarities with the current flow in mesoscopic and nanoscale mat-

ter as, e.g., has been realized in low-dimensional semiconductors. Hence, the foundations of quantum transport, which stem from the kinetic theory in statistical mechanics and the theoretical approaches to molecular-scale charge transport have been further elaborated from earlier studies in mesoscopic physics. Textbooks covering the basics of the subject from different aspects as well as key experiments comprise the monographs by Datta [9,10], Imry [11] and Ferry and Goodnick [12], to mention only a few. Advanced quantum transport theories are presented, e.g., in the books by Bruus and Flensberg [13], Haug and Jauho [14], and Rammer [15]. See also particularly the volume edited by Grabert and Devoret [16] for a selection of reviews on charge and transport phenomena in the Coulomb blockade regime. On the other hand, the second major root of nowadays theoretical molecular electronics, electron and energy transfer theory, is addressed in the books by May and Kühn [17], Kuznetsov and Ulstrup [18] and Nitzan [19].

Specific advances in both theoretical and experimental molecular electronics throughout the last decade have been documented in several conference proceedings, special issues, and edited books. Here, we again include a non-exhaustive selection [20–27]. We also wish to point out a few recent excellent theory reviews covering complementary methods and aspects of molecular-scale transport [28–32]. Monographs on molecular electronics are still rare [33].

With the selection of the contents of this volume, we tried to cover major branches in the field of molecular electronics through representative chapters arising from both experimental and theoretical cutting-edge research. However, this recently established field eventually proliferates in such a way that it appears impossible to comprise adequately all emergent research lines within a single volume. Hence, here follows a list of adjacent topics and sub-fields which are not covered but may play an increasing role in opposing the new challenges:

1. Setups based on scanning probe microscopy (SPM) of molecules on surfaces definitely represent another prominent experimental approach for accessing single-molecule conductance features leading to a spectroscopic analysis. These particular SPM techniques are certainly under-represented in the present book, and we refer the interested reader to [34] for an overview of the wide spectrum of the state-of-the-art experiments.
2. Quantum electron transport through atomic chains and point contacts has much in common with that through single-molecule bridges with regard to experimental challenges and techniques used, numerical methods employed as well as observed phenomena (e.g., conductance quantisation, contact characterization, phonon spectroscopy, shot noise). For a recent review on the physics of metallic atomic contacts see, e.g., [35].
3. Though carbon nanotube-based molecular-scale electronics is featured in Chap. 8 and in Chaps. 13 and 14 from the theoretical and experimental viewpoint, respectively, many aspects of this broad and rapidly develop-

ing pillar of molecular electronics could not be covered. Hence, as further entries to the physics of CNTs and more specialized literature we mention the excellent books in Refs. [36–38].

4. As indicated in the introduction, the focus of the present book is on effects regarding “unimolecular” systems. Molecular Electronics from a broader perspective would include a discussion on the conduction and optical properties of materials such as molecular solids, polymer films and liquid crystals. This branch is far more developed and technological applications are decades ahead, for instance in organic light emitting diodes devices.

The works represented in this volume reflect to a large extend fairly established knowledge bridging the gap to the most recent developments. Further research topics that are currently pursued such as molecular spintronics [39] and the interplay between molecular conduction and vibrations, to cite few of them, are only briefly touched. The same holds true for the important efforts in treating correlated transport [40] as well as for quantum chemical calculations (beyond DFT) and their implementation into quantum transport methods. Nevertheless, we believe that the material adequately furnishes creative thought, and it is our hope that it will also resonate with the non-expert. Finally, owing to the personal background of the editors, the reader may recognize a slight imbalance between physics, chemical physics and chemistry, with respect to the choice of topics of this truly transdisciplinary field, towards physics-oriented issues, techniques, and viewpoints. We are ready to bear this responsibility and express our trust to the reader’s patience in finding a way to feed her/his scientific interests and curiosity through the accompanying literature.

Acknowledgements

We acknowledge support from the *Volkswagen Stiftung*, the *Deutsche Forschungsgemeinschaft* (GRK 638), and the *Science Foundation Ireland*. Particularly, we would like to thank the *Max Planck Institute for the Physics of Complex Systems* in Dresden and its founding director, Peter Fulde, first for providing an optimal environment for their fruitful collaboration among the members of the institute and second for supporting the two meetings *trans-mol 2001* and *admol 2004* [41] on molecular-scale transport that constituted the fertile soil for the steady growth of the present volume.

References

1. A. Aviram, M.A. Ratner: Molecular rectifiers, *Chem. Phy. Lett.* **29**, 277–283 (1974)
2. G.E. Moore: Cramming more components onto integrated circuits, *Electronics* **38**, 114–116 (1965)

3. A. Nitzan, M.A. Ratner: Electron transport in molecular wire junctions, *Science* **300**, 1384–1389 (2003)
4. J.R. Heath, M.A. Ratner: Molecular electronics, *Physics Today May issue*, 43–49 (2003)
5. C. Joachim, J.K. Gimzewski, A. Aviram: Electronics using hybrid-molecular and mono-molecular devices, *Nature* **408**, 541–548 (2000)
6. J.M. Soler, E. Artacho, J.D. Gale, A. García, J. Junquera, P. Ordejón, D. Sánchez-Portal: The SIESTA method for ab initio order-*N* materials simulation, *J. Phys.-Condens. Matter* **14**, 2745–2779 (2002)
7. T. Frauenheim, G. Seifert, M. Elstner, T. Niehaus, C. Köhler, M. Amkreutz, M. Sternberg, Z. Hajnal, A. Di Carlo, S. Suhai: Atomistic simulations of complex materials: ground-state and excited-state properties, *J. Phys.-Condens. Matter* **14**, 3015–3047 (2002)
8. R. Overton: Molecular electronics will change everything. The next big thing is very, very small, *Wired* **8** (2000)
9. S. Datta: *Quantum Transport: Atom to Transistor* (Cambridge University Press, 2005)
10. S. Datta: *Electronic Transport in Mesoscopic Systems* (Cambridge University Press, Cambridge, 1999)
11. Y. Imry: *Introduction to Mesoscopic Physics* (Oxford University Press, 2002)
12. D.K. Ferry, S.M. Goodnick: *Transport in Nanostructures*, Vol. 6 of Cambridge Studies in Semiconductor Physics & Microelectronic Engineering (Cambridge University Press, 1999)
13. H. Bruus, K. Flensberg: *Many-Body Quantum Theory in Condensed Matter Physics: An Introduction*, Oxford Graduate Texts (Oxford University Press, New York, 2004)
14. H. Haug, A.P. Jauho: *Quantum Kinetics in Transport and Optics of Semiconductors*, Solid State Sciences (Springer, 1996)
15. J. Rammer: *Quantum Transport Theory* (HarperCollins Publishers, 1998)
16. H. Grabert, M.H. Devoret (Eds.): *Single Charge Tunneling* (Plenum Press, 1992)
17. V. May, O. Kühn: *Charge and Energy Transfer Dynamics in Molecular Systems* (Wiley-VCH, 2004)
18. A.M. Kuznetsov, J. Ulstrup: *Electron Transfer in Chemistry and Biology: An Introduction to the Theory* (John Wiley & Sons, Inc., 1999)
19. A. Nitzan: *Chemical Dynamics in Condensed Phases* (Oxford University Press, 2006), to appear
20. R. Friend, M. Reed (Eds.): Physics of electronic transport in single atoms, molecules and related nanostructures (Special Section), *Nanotechnology* **15**, S433–S867 (2004)
21. R. Waser (Ed.): *Nanoelectronics and Information Technology: Advanced Electronic Materials and Novel Devices* (Wiley-VCH, 2003)
22. M.A. Reed, T. Lee (Eds.): *Molecular Nanoelectronics* (American Scientific Publishers, 2003)
23. P. Hänggi, M. Ratner, S. Yaliraki (Eds.): Processes in molecular wires (Special Issue), *Chemical Physics* **281**, 111–502 (2002)
24. J.R. Reimers, C.A. Picconatto, J.C. Ellenbogen, R. Shashidar (Eds.): *Molecular Electronics III*, Vol. 1006 of Annals of the New York Academy of Sciences (New York Academy of Sciences, 2003)

25. A. Aviram, M.A. Ratner, V. Mujica (Eds.): *Molecular Electronics II*, Vol. 852 of Annals of the New York Academy of Sciences (New York Academy of Sciences, 2002)
26. A. Aviram, M.A. Ratner (Eds.): *Molecular Electronics I*, Vol. 852 of Annals of the New York Academy of Sciences (New York Academy of Sciences, 1998)
27. J. Jortner, M.A. Ratner: *Molecular Electronics* (Blackwell Science, 1997)
28. S. Kohler, J. Lehmann, P. Hänggi: Driven quantum transport on the nanoscale, *Physics Reports* **406**, 379–443 (2005)
29. S. Sanvito: *Ab-initio methods for spin-transport at the nanoscale level* (American Scientific Publishers, 2005), [cond-mat/0503445](#)
30. A. Pecchia, A. Di Carlo: Atomistic theory of transport in organic and inorganic nanostructures, *Reports on Progress in Physics* **67**, 1497–1561 (2004)
31. T. Seideman: Current-driven dynamics in molecular-scale devices, *J. Phys.-Condens. Matter* **15**, R521–R549 (2003)
32. A. Nitzan: Electron transmission through molecules and molecular interfaces, *Ann. Rev. Phys. Chem.* **52**, 681–750 (2001)
33. J.M. Tour: *Molecular Electronics: Commercial Insights, Chemistry, Devices, Architecture and Programming* (World Scientific Publishing Co. Pte. Ltd., 2003)
34. F. Moresco: (2003), “Manipulation of large molecules by low temperature stm: model systems for molecular electronics”, Habilitation thesis, Freie Universität Berlin, Berlin
35. N. Agrait, A. Levy Yeyati, J.M. van Ruitenbeek: Quantum properties of atomic-sized conductors, *Physics Reports* **377**, 81–279 (2003)
36. R. Saito, G. Dresselhaus, M.S. Dresselhaus: *Physical Properties of Carbon Nanotubes* (World Scientific Publishing Co. Pte. Ltd., London, 1998)
37. S. Reich, C. Thomsen, J. Maultzsch: *Carbon Nanotubes: Basic Concepts and Physical Properties* (Wiley-VCH, 2004)
38. S. Roth, D. Carroll: *One-Dimensional Metals: Conjugated Polymers, Organic Crystals, Carbon Nanotubes* (Wiley-VCH, 2004)
39. A.R. Rocha, V. García Suárez, S. Bailey, C. Lambert, J. Ferrer, S. Sanvito: Towards molecular spintronics, *Nature Materials* **4**, 335–339 (2005). Related software Smeagol available at <http://www.tcd.ie/Physics/Smeagol/>.
40. A. Ferretti, A. Calzolari, R. Di Felice, F. Manghi, M.J. Caldas, M. Buongiorno Nardelli, E. Molinari: First-principles theory of correlated transport through nanojunctions, *Phys. Rev. Lett.* **94**, 116 802 (2005). Related software WanT available at <http://www.wannier-transport.org>.
41. “transmol and admol symposia”,
<http://www.mpiipks-dresden.mpg.de/~admol/>
<http://www.mpiipks-dresden.mpg.de/~transmol/>

Foundations of Molecular Electronics – Charge Transport in Molecular Conduction Junctions

Joshua Jortner¹, Abraham Nitzan¹ and Mark A. Ratner²

¹ School of Chemistry, Tel Aviv University, Tel Aviv, 69978, Israel

² Department of Chemistry and Institute for Nanotechnology, Northwestern University, Evanston, Illinois 60208, U.S.A.

Abstract. The most fundamental structure involved in molecular electronics is a molecular transport junction, consisting of one (ideally) or more molecules extending between two electrodes. These junctions combine the fundamental process of intramolecular electron transfer with the mixing of molecular and continuum levels at the electrodes and the nonequilibrium process of voltage-driven currents. Much of this book is devoted to the complicated but significant behaviors that arise from this conjunction. This introductory chapter attempts to sketch some of the principles and also some of the unresolved issues that characterize molecular transport junctions.

Sections 2–4 deal with fundamental ideas. These include an appropriate theoretical formulation of the conductance calculation in terms of non-equilibrium Green's functions, the relationship between junction conductance and nonadiabatic electron transfer rates in the same molecular entities, and the role and magnitude of interactions between the dynamics of the transferring electronic charges and the nuclear degrees of freedom. Section 5 addresses some of the outstanding and difficult issues in understanding junction transport, including geometry and its change with voltage, the electrostatic profile under applied voltage, electronic structure models and their limitations, and fluctuations and switching phenomena in junctions.

Molecular electronics is an area of very rapidly growing scientific and applied interest and activity. While the technological drivers, including materials, electrochemical, biological, sensing, memory and logic applications are all important, the fundamental issues involved in the nonequilibrium responses of molecule-based hybrid materials to applied electromagnetic fields is the fundamental driver for this science. In this sense, molecular electronics is a sort of spectroscopy. Due to the intensity and quality of the research being done in the area, the community may soon be able to understand molecular transport spectroscopy at a level of depth and sophistication almost comparable to other, more traditional spectroscopies. Contemporary research in the area, as exemplified in this book and at the Dresden conference that initiated the book, is driving in that direction.

1 Prologue

Molecular electronics, one of the major fields of current efforts in nanoscience, involves the exploration of the electronic level structure, response and transport, together with the development of electronic devices and applications that depend on the properties of matter at the molecular scale. This includes

single molecules, molecular arrays and molecular networks connected to other electronic components. Its major application areas include sensors, displays, smart materials, molecular motors, logic and memory devices, molecular scale transistors and energy transduction devices. Often molecular electronics is envisioned as the next step in device miniaturization. The importance of molecules in device applications stems not only from their electronic properties, but also from their ability to bind to one another, recognize each other, assemble into larger structures, and exhibit dynamical stereochemistry [1–11].

While the promise of new technological breakthroughs has been a major driving force in this field, consideration of molecular systems as components of electronic devices raises important fundamental questions. In particular, while traditional quantum chemistry deals with molecules as electronically closed systems, practitioners of molecular electronics face problems involving molecular systems that are open to their electronic environment and, moreover, function in situations far from equilibrium. Informed design of such devices requires an understanding of the interplay among molecular structure, dynamics and function. In addition, for particular applications such as switching, rectification and memory storage/reading on the molecular level, we need to understand the non-linear response of such systems. Possible heating in such junctions should be considered as well, implying the need to understand relaxation and heat conduction in such molecular structures. Finally, the vision to adjust and to monitor the operation of these devices brings out the need to understand different control modes, ranging from structural design to interaction with external forces such as a radiation field or other molecular entities.

During the past half century remarkable progress was made in establishing the conceptual framework for electron transfer (ET) processes [11] in molecular, supermolecular, and biophysical systems. ET provides a central conceptual and technical basis for molecular electronics, pertaining both to molecular devices and to molecular materials. ET in supermolecules falls into two general categories: (1) Bridged species, often consisting of an electron donor (D) and an electron acceptor (A), linked by a non-rigid or a rigid molecular bridge (B); and (2) biophysical systems such as the photosynthetic reaction centers (RC) of bacteria and plants, where the primary process (the conversion of solar energy into chemical energy) proceeds via a sequence of well-organized, highly efficient, directional and specific ET processes between prosthetic groups embedded in the protein medium.

The control of ET in donor/bridge/acceptor (DBA) or donor/acceptor (DA) systems in solution [12], in a solid [13], in a protein [14], in DNA [15] or within an “isolated” solvent-free supermolecule [16] can be accomplished by: (1) Structural control. ‘Molecular engineering’ of the D, A and B subunits determines the molecular energetics and the direct D–A or superexchange D–B–A electronic coupling. (2) Intramolecular dynamic control of the nuclear equilibrium configurational changes (i.e. nuclear distortions) that accompany

ET [17]. (3) Medium control of ‘conventional’ ET in a solvent or in a cluster. The functions of the medium on $\text{DBA} \rightarrow \text{D}^+ \text{BA}^-$ ET include: (i) the energetic stabilization of the ionic states; (ii) and the coupling of the electronic states with the medium nuclear motion, which originates from short-range and long-range interactions in polar solvents, with short-range interactions with C–H group dipoles in non-polar hydrocarbons and with polar amino acid residues in protein. (4) Dynamic medium control of ET [18] involving either the medium acting as a heat bath, solvent-controlled ET, specific dynamic control of pathways by solvent motions (‘gating’), or very slow solvent relaxations such as in glassy matrices, that lead to reduced solvent reorganization energies.

The structural, intramolecular, solvent, and dynamic control of ET allows for the design of molecular systems where ET is: (i) ultrafast (on the time scale of ~ 1 ps to ~ 100 fs), overwhelming any energy waste processes; (ii) highly efficient, eliminating any back reactions; (iii) stable with respect to the predictable variation of molecular and medium properties; (iv) practically invariant with respect to temperature changes.

ET theory for donor–acceptor charge transfer represents the non-adiabatic ET rate $k_{\text{D} \rightarrow \text{A}}$ in the basic form

$$k_{\text{D} \rightarrow \text{A}} = (2\pi/\hbar)V^2 \mathcal{F} \quad (1)$$

where V is the effective electronic coupling and \mathcal{F} is the thermally averaged nuclear vibrational Franck–Condon factor. This microscopic description rests on several ingredients: (1). ET is described as a radiationless transition. (2). The Born–Oppenheimer separability of electronic and nuclear motion applies, enabling the description of the system in terms of diabatic potential surfaces Fig. 1 (3). The electronic coupling is sufficiently weak to warrant the description of the radiationless transition in the non-adiabatic limit. (4). Microscopic ET rates are insensitive to medium dynamics. This state of affairs is realized for the common situation of clear separation of time scales between electronic and nuclear processes. (5). Incoherent charge transfer between the donor–acceptor sites, involving dephasing at each ET step. This state of affairs is analogous to Holstein’s small polaron [19] in the incoherent limit.

The electronic coupling in the DBA system $V = V_{\text{DA}} + V_{\text{super}}$ consists of a sum of a direct D–A exchange contribution V_{DA} between the electronic states of DA and $D^+ A^-$, and a superexchange off-resonance interaction [20] V_{super} . The accumulated information concerning the distance dependence of both direct and superexchange interactions is that both interactions are expected to exhibit an exponential distance dependence [21]

$$V = \alpha \exp(-\beta R_{\text{DA}}), \quad (2)$$

where R_{DA} is the (either edge-to-edge or center-to-center) D–A distance. The distance dependence of intramolecular superexchange interactions in man-made synthetic systems and nature-made biological photosynthetic systems

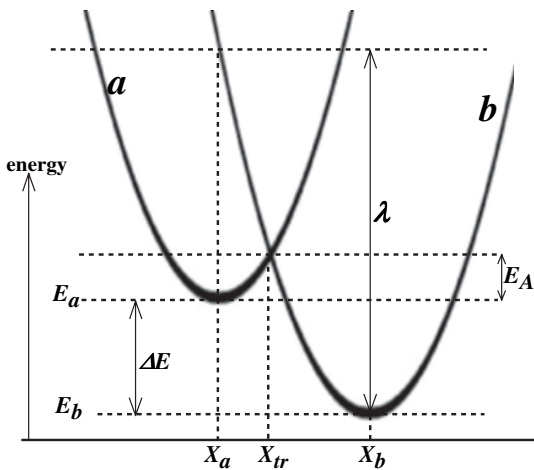


Fig. 1. A schematic diagram showing the energetics of an electron transfer reaction in terms of two diabatic surfaces, characterized by their curvature, the gap energy ΔE and the reorganization energy λ

and in DNA provides a dynamic ruler for the interrogation of the distance dependence of incoherent charge transfer between molecular sites, which are driven by the electronic coupling with $k_{D \rightarrow A}$ constrained by the nuclear Franck-Condon factor.

In direct comparison with the ET picture in Fig. 1, the simplest energy representation for a molecular transport junction (MJ) is given in Fig. 2. The two electrodes are assumed made of the same material, which is taken to be simple metal with a Fermi level denoted E_f . The discrete levels shown for the molecule represent (just as the continuum levels in the metal do) one-electron energies. In particular, the highest-occupied and lowest empty molecular orbitals (HOMO and LUMO respectively) define a gap, and E_f must lie within this gap. Under conditions where these metals are thermally equilibrated, the Landauer formula for the coherent conductance of the junction is given by (1)

$$g(\Phi) = \frac{e}{\pi \hbar} \frac{\partial}{\partial \Phi} \int_0^\infty dE T(E) (f(E) - f(E + e\Phi)) \quad (3)$$

(here g , Φ , T , f , E , are respectively the conductance, the voltage, the transmission through the molecular junction, the Fermi functions describing the populations on the two metal leads and the energy variable). When the derivative on the rhs of (3) is removed, one obtains a formula for the current, I , in terms of the populations and the elastically-scattered transmission. Equation (3) is the simplest useful result for transport, and has the same role there that (1) has in the ET processes. It is actually reminiscent of the ET result of (1): the rate (ET) or the current (molecular junctions) is given by the product of a population term and a scattering probability.

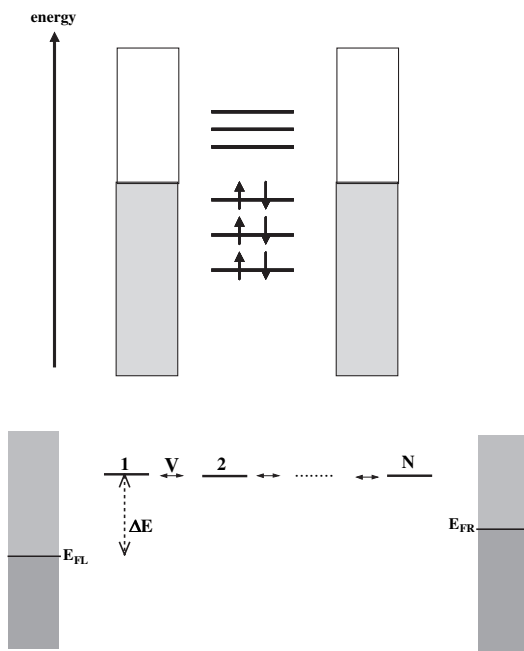


Fig. 2. (a) A schematic diagram of a molecular junction, comprising two electrodes with Fermi energies E_{FL} and E_{FR} ($E_{FR} - E_{FL} = e\Phi$) connected by a molecular species. The latter is characterized by its HOMO-LUMO gap, as shown. (b) Same as (a), except that the molecule is represented in a local (e.g. atomic orbital) basis set

As a voltage is applied to the junction, the two Fermi levels differ by Φe , the voltage times the elementary charge. Whenever one of the Fermi levels crosses a molecular level, there is a possibility for resonant transfer, and one expects a local maximum in the $g(\Phi)$ measurement.

The similarity of the rate measurement in nonadiabatic intramolecular ET and the transport in molecular junctions is striking. The comparison is made explicit in Table 1.

Table 1. Comparison of Rate and Transport Processes

Intramolecular Nonadiabatic Rates	Molecular Junction Transport
rate constant $k(\text{sec}^{-1})$	conductance $g(\Omega^{-1})$
electron tunneling	electron tunneling
vibronic bath	electronic bath (electrodes)
(1)	(3)

Since both processes are determined by electron tunneling, they are closely related to one another, as will be discussed in Sect. 3, after a brief description of conductance formulations in Sect. 2. The bath medium, into which the energy is dissipated, differs from the vibrations and solvent polarization in ET to the electrode Fermi sea for simple coherent transport in junctions; this leads to quite different temperature dependences for the two phenomena.

Section 3 discusses the magnitudes expected for the conductance and for the rate constants, and presents an analysis of the relationship between these two important observable properties. Section 4 is devoted to behaviors arising from the interactions of the electronic and vibrational degrees of freedom, including inelastic tunneling spectroscopy and the transition from coherent to activated behavior. Section 5 presents a very brief overview of some of the outstanding issues involved in modeling transport junctions.

Over the past half century the properties of non-molecular electronic materials, i.e., metals, semiconductors and dielectrics, and their interfaces, have been investigated extensively and are well understood. Only relatively recently was a similar effort directed towards systems involving molecular, mostly organic, materials. During the past decade a new focus on the electronic transport properties of single molecule junctions, as well as molecular and biomolecular DNA chains, is emerging. This research is motivated not only by envisioned single molecule devices, but also by the conceptual simplicity of such systems that offer convenient platforms for correlating theory and experiment, and by the intrinsic challenge involved in understanding thermodynamic response, both electronic and structural, of molecular species in a transport junction.

This book is devoted to the area of molecular electronics, and to explicating and demonstrating some of its crucial understandings, accomplishments and challenges. This introductory overview chapter addresses the interrelationship among charge transfer, transmission and transport in molecular systems, providing the conceptual framework for molecular electronics. It should be regarded as a sketchy introduction to the field, not a survey. The authors apologize for the many omissions, and the deeply incomplete literature citations, in this chapter. These should be remedied by the wide scope and depth of this book as an entirety.

2 Theoretical Approaches to Conductance

In this section, we give a brief outline of the standard approaches for modeling and understanding transport in MJ. Carbon nanotubes, because of their stiffness and aspect ratio, constitute a special case, and we focus rather on organic molecules.

The simplest interpretation of Scanning Tunneling Microscope images was developed by Tersoff and Hamann [22], and states that the current is proportional to the total density of states at the position of the terminal atom of the

tip and at the Fermi energy. For molecular junctions, this picture is invalid, because the two molecular ends are both in contact with an electrode.

When a molecular structure, acting as a wire, is functionalized to two electrodes, a molecular transport junction is formed. The simplest discussion of transport is then to assume that incoming electrons are scattered both at the interfaces between the metal and the molecule and along the wire itself. Under these conditions, the conductance will depend on the net probability of scattering. An important point first noticed by Landauer [23, 24] is that such scattering does not have to be inelastic – even elastic scattering will prevent electrons making it through the junction. Dissipation of energy will eventually occur, but that can happen in the (macroscopic) leads leading to the molecular junction.

This fundamental realization suggests that the junction resistance in this case arises from its behavior as a scatterer, and its conductance can therefore be calculated simply from scattering theory. This *coherent conductance* is expected to characterize most short molecular wires, particularly those in which transport occurs far from resonance between the metal Fermi energy and the molecular eigenstates,¹ and at low temperature for short wires. Under those conditions, the conductance $g(E, V)$ is given by

$$g(E, V) = \frac{2e^2}{h} \sum_{ij} t_{ij}(E, V) \quad (4)$$

Here the prefactor is the quantum of conductance, and t_{ij} is the probability that a carrier coming from the left lead in transverse mode i will be transmitted to the right lead in transverse mode j .

A more general approach includes not only elastic scattering, but also such issues as interaction between the molecule and the electrodes and the coupling to vibrations and to external fields such as light or thermal gradients. The most common formulation is the Keldysh-Kadanoff-Baym [25–28] one in terms of non-equilibrium Green's functions (NEGF). Reference [29–35] The use of molecular electronic structure theory for the molecule, combined with models for the interface and appropriate treatments (NEGF formulations [29–36], Lippman/Schwinger scattering approaches [37–40]) of the scattering process lead to actual calculations of molecular transport.

In the limit of small applied voltage V , the coherent conductance can be written as

$$g(\Phi) = \frac{e^2}{\pi\hbar} Tr_M \{ G^M(\Phi) \Gamma^R(\Phi) G^{M+}(\Phi) \Gamma^L(\Phi) \} \quad (5)$$

Here the Green's function G^M describes propagation through the molecule, and Γ^R and Γ^L are respectively the spectral densities coupling the molecule to the electrodes on the left and the right. The Tr_M denotes a

¹Near resonance the possibility for dephasing and relaxation may limit the validity of (4)

trace over the states of the molecule, and G^M is modified from the bare molecule propagator by including the broadening and shifting effects of the molecule/electrode interactions.

The dependence of the conductance on the molecular species arises mostly from the Green's function G in (5). In a very simple single-determinant description, if we use i, j to denote atomic orbitals and μ for molecular orbitals, the matrix elements of G are

$$G_{i,j}(E) = \sum_{\mu} \langle i|\mu \rangle \langle \mu|j \rangle / (E - E_{\mu} - \Sigma_{\mu}) \quad (6)$$

with E, E_{μ} and Σ_{μ} respectively the energy variable, the molecular orbital energy and the self-energy. The self energy is a complex function – its real part describes the shift of the resonance due to interaction with the external partners, while the imaginary part, Γ , characterizes the lifetime of the state. Note that (as is intuitive) the G will maximize when the injection energy E is close to a molecular orbital resonance energy E_{μ} and when the molecular orbital involved has substantial components from the atomic orbitals i, j on the two ends of the molecule.

A particularly simple junction contains only one homonuclear diatomic (such as H_2), with one basis function on each atom. References [3, 41] ignoring electron repulsion and orbital overlap, the two degenerate sites of energy E_0 mix by a tunneling energy t_0 . Then the conductance becomes $g(E_F)$ where

$$g(E) = \frac{e^2}{\pi \hbar} \frac{\Gamma |t_0|^2}{|(E - E_0 + (1/2)i\Gamma)^2 - t_0|^2} \quad (7)$$

When injection occurs exactly on resonance ($E_F = E_0 \pm t_0$) and $t_0^2 \gg \Gamma^2$, this behaves as a pure Landauer channel.

$$g = g_0 = 2e^2/h \quad (8)$$

Note that this holds independent of the spectral density Γ , so long as the energy $E - E_0 - t_0$ overlaps with any nonvanishing value of Γ . The elastic current for resonance injection is g_0 , independent of the (nonvanishing) binding between molecule and electrodes. Experimental reports of near-unit conductance for dihydrogen on platinum at low temperatures [42] may reflect such injection.

One way to produce resonance injection is to move the molecular eigenstate energies by a gating field. Recent work with a molecular transistor injection has indeed observed resonant injection, and $g \cong g_0$, for such molecules as ferrocene [43].

Note that if $\Gamma^2 \ll t_0^2$ but injection is not on resonance (but, say, at midgap), we find [41]

$$g = g_0 \frac{4t_0^2 \Gamma^2}{(t_0^2 + \Gamma)^2} \rightarrow 0 \quad (9)$$

The conductance then exhibits turnover behavior, vanishing at $t_0 = 0$ (as seen from (7)) because no mixing of the two molecular sites occurs, and at $t_0 \gg \Gamma$, because there is no available spectral density at the orbital resonance energy.

3 The Relationship Between Electron Transfer Rates and Molecular Conduction

We have already noted that electron transfer and molecular conduction are two facets of electron transmission through a molecular environment, and as such should be interrelated. Still this relationship is not a trivial one for several reasons. First, as discussed in Sect. 1 there are fundamental differences between the two processes that arise from different physical boundary conditions. One is driven by nuclear relaxation at the donor and acceptor sites while the other is made possible by absorption of the transmitted electron in the continuum of metal electronic states. Secondly, even though the core process in both situations is electron transmission through a molecular layer or bridge, the fact that in the conduction process one puts a potential across the junction may change the electronic structure of the bridge; at the simplest level this gives rise to a potential gradient on the bridge itself, implying change in local energies. Finally, the two quantities observed, transfer rate in one case and conductance in the other, are different physical observables of different dimensionalities.

Still, the conduction property of a given molecular system and the electron transfer properties of the same system should be closely related at least for low bias potentials and once the different boundary processes have been sorted out. Expression relating the two were recently derived both for the coherent transport regime and for the incoherent hopping regime. Here we limit ourselves to demonstrating the physical issues involved using simple limiting forms. For the coherent transport regime and symmetric electron transfer one finds [3, 44]

$$g \approx \frac{8e^2}{\pi^2 \Gamma_D^{(L)} \Gamma_A^{(R)} \mathcal{F}} k_{D \rightarrow A} \quad (10)$$

where g is the zero bias conduction, $k_{D \rightarrow A}$ is the donor-to-acceptor electron transfer rate, \mathcal{F} is the Franck-Condon weighted density of states thermal environment (see (1)) and $\Gamma_D^{(L)}$ and $\Gamma_A^{(R)}$ represent the inverse escape time of an electron on the donor molecule when next to (say) the left metal electrode, into that electrode, and similarly for the acceptor next to the right metal electrode. Equation (10) is a limiting form obtained when these rates are comparable to, or larger than the inverse energy difference between the metal's Fermi energy and the energy of molecular orbital that is active in the transport process. Another limiting form is obtained for incoherent hopping transfer through a long molecular bridge, provided that energy shifts caused

by the molecule-metal coupling are small relative to $k_B T$. It reads (again for symmetric electron transfer) [45]

$$g \approx \frac{e^2}{k_B T} k_{D \rightarrow A} \quad (11)$$

The simple form of the latter result stems from the fact that for incoherent hopping transmission through a long chain is dominated by dynamics on the chain itself and not at the molecule-lead contacts. Interestingly, and quite accidentally, both (10) and (11) yield at room temperature similar numerical estimates

$$g \sim (e^2/\pi\hbar)(10^{-13}k_{D \rightarrow A}(S^{(s^{-1})})) \cong [10^{-17}k_{D \rightarrow A}(s^{-1})]\Omega^{-1} \quad (12)$$

when the semiclassical Marcus expression [46] for \mathcal{F} in a symmetric donor-acceptor problem, $\mathcal{F} \approx (\sqrt{4\pi\lambda k_B T})^{-1} \exp(-\lambda/4k_B T)$ is used in (10) together with the value $\lambda = 0.5$ eV for the reorganization energy and the values $\Gamma_D^{(L)} = \Gamma_A^{(R)} \sim 0.5$ eV for the electron escape rates into the electrodes. Actual values of these parameters can of course differ, but these representative values provide an order-of-magnitude criterion for observing conduction in the small voltage-bias regime of molecular conduction junctions. For example, with a current detector sensitive to pico-amperes, $k_{D \rightarrow A}$ has to exceed $\sim 10^6$ s $^{-1}$ (for the estimates of \mathcal{F} and Γ given above) before measurable current can be observed at 0.1 V across such a junction. Such estimates should be exercised with caution, both because the above expressions are approximate limiting forms of more complex relationships within the corresponding models and because the models themselves are highly simplified. Still, they may be useful as rough order of magnitude estimates as was indeed found in a recent comparison of electron transfer and conduction through alkane bridges [47].

4 Interaction with Nuclear Degrees of Freedom

Electron transfer processes, as described in Sect. 1 involve electron-phonon coupling in an essential way: this coupling causes the relaxation process that affects electron localization on the donor and acceptor species and thereby drives the transfer process. As discussed in Sect. 2, molecular conduction is driven by a potential difference between two infinite electrodes and phonon induced localization does not play any essential role in affecting this driving. Still, also in molecular conduction, the coupling between electronic and nuclear degrees of freedom is of great interest on several counts. First, it underlines the interplay between coherent transport by carrier tunneling and/or band motion, polaronic conduction and incoherent, thermally assisted hopping transport [3]. Indeed, the importance of the full hopping regime, in which charges are definitely localized on the molecular bridge, has been demonstrated both in the Coulomb blockade limit [48] and in a polaron-type localization situation [49]. Secondly, it is directly relevant to the issue of junction

heating [50–52]. Also, vibronic interactions accompanying electron transport may lead to specific nuclear motions such as rotations [53, 54], lateral hopping of molecules on the surface [55], atomic rearrangements [56] and chemical reactions [57]. Finally, nuclear motions can directly manifest themselves as inelastic signals in the current-voltage spectra. Inelastic electron tunneling spectroscopy (IETS) has been an important tool for identifying molecular species in tunnel junctions for a long time [58]. With the development and advances in scanning tunneling microscopy (STM) and spectroscopy (STS) it has proven invaluable as a tool for identifying and characterizing molecular species within the conduction region [54, 59–62]. Indeed, this is the only direct way to ascertain that a molecular species indeed participates in the conduction process, and at the same time to provide important spectroscopic and structural data on the conducting molecule, in particular information on the strength of the vibronic coupling itself [63].

4.1 Timescale Issues

The relative importance of vibronic (or electron-phonon) interactions in electron transmission processes is an issue of relative timescales. If the transmission event is fast on the timescale of nuclear motion the latter may be taken static, and we only need to average the resulting elastic transmission probability over the relevant ensemble of nuclear configurations. The other extreme limit, where the nuclear motion is fast relative to the electronic process is usually not relevant in our system. Dynamic electron-phonon effects may potentially play a significant role when the electronic and nuclear timescale are similar. In order to make an assessment of this possibility an estimate of the relevant electronic timescale is needed. For resonance electron transfer this timescale is associated with the electronic coupling, e.g. for band motion – by the inverse bandwidth. For off resonance tunneling transmission a useful estimate is provided by the tunneling traversal time, τ_{trav} , essentially a (non-rigorous) estimate of the time available for a tunneling electron to interact with degrees of freedom localized in the barrier region. For example, for a particle of mass m and energy E that tunnel through a rectangular barrier of height U and width D , the traversal time is given by

$$\tau_{\text{trav}} = \sqrt{\frac{m}{2(U-E)}} D \quad (13)$$

while for transmission in the model of Fig. 2b, involving N bridge levels and an energy gap ΔE we obtain [64]

$$\tau_{\text{trav}} = \frac{\hbar N}{\Delta E} \quad (14)$$

It may in fact be shown [64] that both (13) and (14) are limiting cases of a more general expression. For typical molecular parameters, say $D = 1 \text{ nm}$,

$N \cong 2 - 4$ and $\Delta E = U - E = 1$ V (13) and (14) yield τ_{trav} in the range $0.1 - 1$ fs. On this short timescale one may disregard nuclear motion and inelastic effects on electron transmission. We see however that for smaller ΔE inelastic effects may become relevant. In particular this is often the case in resonance tunneling situations. For example, a recent computational study of electron tunneling through water films [65] has revealed the existence of water structures that support resonance tunneling in the energy range of up to 1 eV below the vacuum barrier and with traversal timescales of the order of ~ 10 fs, similar to the period of the OH stretch vibrations in water.

4.2 Transition from Coherent to Incoherent Motion

In most treatments of electron transmission and conduction through insulating barriers one assumes that the barrier nuclear configuration is static. (This should be distinguished from nuclear relaxation at the donor and acceptor sites in the electron transfer process which is the driving force for this process). The breakdown of this assumption can potentially have far reaching consequences. In the extreme case, energy transfer into nuclear motions from the transmitting electrons may lead to conformation changes and eventually to disintegration of the junction. Indeed, an important factor in designing molecular conductors is their structural stability and understanding processes that can undermine this stability is of utmost importance [66]. A single molecule junction that carries 1 nA of current over a voltage drop of 1 volt passes $\sim 10^{10}$ eV of energy per second, many orders of magnitude more than is needed to atomize its components. This implies the need for understanding heat generation and dissipation in molecular conductors. In the other limit of very weak electron-nuclear interaction, electron transfer and transmission remain essentially the same, still the signature of electron-phonon coupling may be observed as vibrational features in the voltage dependence of the current observed in inelastic tunneling spectroscopy.

In very common intermediate cases, energy does not accumulate excessively in the junction, still interactions with the thermal environments can lead to a fundamental change in the transmission mechanism: Coherent transfer is replaced by incoherent hopping. This can be simply demonstrated [29], for a one dimensional wire problem where, in the linear transport regime, the Landauer formula [29] for the conduction reads

$$g(E) = \frac{e^2}{\pi \hbar} \mathcal{T} \quad (15)$$

where \mathcal{T} is the transmission coefficient and e the electron charge. Consider now a conductor of length L as a series of N macroscopic scatterers. At each scatterer the electron can be transmitted with probability \mathcal{T} , or reflected with probability $\mathcal{P} = 1 - \mathcal{T}$. Let the total transmission through N such objects be \mathcal{T}_N , so that $\mathcal{T} = \mathcal{T}_1$. *Provided that the phase of the wavefunction is destroyed after each transmission-reflection event*, so that we can add

probabilities, the transmission through an N scatterers system is obtained by considering a connection in series of an $N - 1$ scatterer system with an additional scatterer, and summing over all multiple scattering paths

$$\mathcal{T}_N = \mathcal{T}_{N-1}(1 + \mathcal{R}\mathcal{R}_{N-1} + (\mathcal{R}\mathcal{R}_{N-1})^2 + \dots)\mathcal{T} = \frac{\mathcal{T}\mathcal{T}_{N-1}}{1 - \mathcal{R}\mathcal{R}_{N-1}} \quad (16)$$

with $\mathcal{R} = 1 - \mathcal{T}$ and $\mathcal{R}_N = 1 - \mathcal{T}_N$. This implies

$$\frac{1 - \mathcal{T}_N}{\mathcal{T}_N} = \frac{1 - \mathcal{T}_{N-1}}{\mathcal{T}_{N-1}} + \frac{1 - \mathcal{T}}{\mathcal{T}} = N \frac{1 - \mathcal{T}}{\mathcal{T}} \quad (17)$$

so that

$$\mathcal{T}_N = \frac{\mathcal{T}}{N(1 - \mathcal{T}) + \mathcal{T}} = \frac{L_0}{L + L_0} \quad (18)$$

where $L_0 = \mathcal{T}/V(1 - \mathcal{T})$ and $v = N/L$ is the scatterer density. Using this transmission coefficient in (15) yields

$$g(E) = \frac{e^2}{\pi\hbar} \frac{L_0}{L + L_0} \quad (19)$$

that gives the inverse length dependence characteristic of Ohm's law as $L \rightarrow \infty$.

More detailed treatments can handle situations where dephasing is not complete at each scatterer. Büttiker [67] has introduced phase destruction processes by conceptually attaching an electron reservoir onto the constriction under the condition that, while charge carriers are exchanged between the current-carrying system and the reservoir, no net averaged current is flowing into this reservoir. Such a contact, essentially a voltage probe, acts as a phase breaking scatterer, and the dephasing efficiency is controlled by adjusting the coupling strength between this device and the system. A very different approach to dephasing was considered by Bixon and Jortner [68, 69] who pointed out that the irregular nature of Franck Condon overlaps between intramolecular vibrational states associated with different electronic centers can lead to phase erosion in resonant electron transfer. Yet another approach uses the machinery of non-equilibrium statistical mechanics, starting from a Hamiltonian that includes the junction and its thermal environment and deriving reduced equations of motion for the electron dynamics. This leads to a dynamical description that includes the effect of dephasing and energy relaxation that are characterized by properties of the thermal bath and the system-bath coupling.

Figures 3–8 show some theoretical results based on the latter approach and recent experimental results that show the effect of dephasing and activation [70, 72]. While the transition from tunneling to activation dominated rate processes has been known in other rate phenomena, the manifestation of this transition in the length dependence of tunneling conduction or electron transfer rate is a relatively recent development. Table 2 [73] summarizes these results for the Markovian limit of the thermal relaxation process.

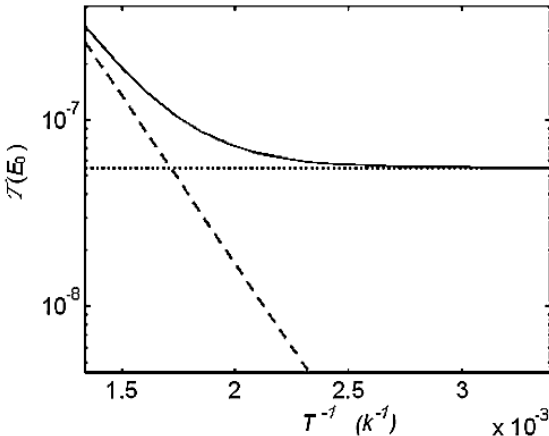


Fig. 3. The integrated elastic (*dotted line*) and activated (*dashed line*) components of the transmission (zero bias conduction), and the total transmission probability (*full line*) displayed as function of inverse temperature (from [50])

Table 2. Bridge length dependence of the transmission rate [73]

Physical Process	Bride Lengthh (N) Dependence	
Super exchange (small N , large $\Delta E_B/V_B$, large $\Delta E_B/k_B T$)	$e^{\beta N}$	$-\beta' = 2 \ln(V_B/\Delta E_B)$
Steady state hopping (large N , small $\Delta E_B/V_B$, small $\Delta E_B/k_B T$)	N^{-1}	
Non-directional hopping (large N , small $\Delta E_B/V_B$, small $\Delta E_B/k_B T$)	N^{-2}	
Intermediate range intermediate N , small $\Delta E_B/V_B$	$(k_{up}^{-1} + k_{diff}^{-1}N)^{-1}$	$k_{up} \sim (V_B^2 k / \Delta E^2) e^{-\Delta E_B/k_B T}$ $k_{diff} \sim (4V_B^2/k) e^{-\Delta E_B/k_B T}$
Steady state hopping + competing loss at every bridge site	$-e^{\alpha N}$	$\alpha = \sqrt{\Gamma_B(\Gamma_B + k)/2V_B}$

Notation: N -site bridge, with intersite electronic tunneling matrix element V_B , injection energy barrier E_B , temperature T , friction coefficient (inverse dephasing time) κ .

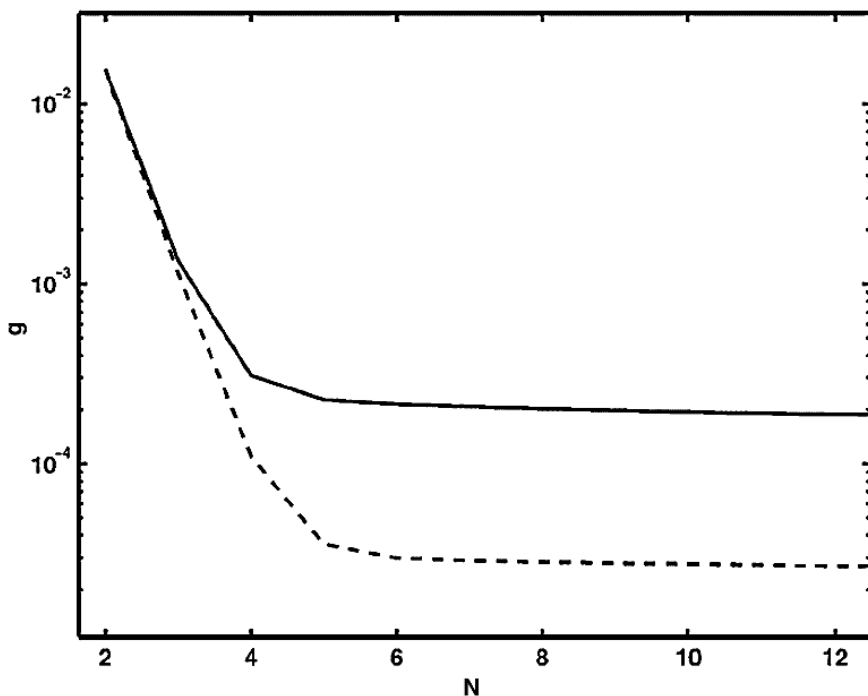


Fig. 4. Bridge length dependence of molecular conduction (or electron transfer rate), showing the transition from exponential decrease with chain length for short chains to a weak $(k_1 + k_2 N)^{-1}$ dependence at long length. The parameters used in this calculation are $\Delta E = E_B - E_F = 0.2 \text{ eV}$, $V = 0.05 \text{ eV}$, $\Gamma_L = \Gamma_R = 0.1 \text{ eV}$ and the rate of thermal relaxation 0.01 eV , and the results shown are obtained using temperatures of 300 K (*lower curve*) and 500 K (From [50])

4.3 Heating and Heat Conduction

As already noted, a molecule that carries 1nA of electronic current across a potential bias of 1 V is passing $\sim 10^{10} \text{ eV}$ of energy per second. A tiny fraction of this energy, if it remains on the molecule for more than a few ps, will cause molecular ionization or dissociation and disintegration of the junction. With the objective of achieving a stable conducting operation (as opposed to, say, inducing a chemical reaction by passing a current) two questions are in order. First, what is the rate of electronic energy dissipation (heat generation, i.e. increased nuclear kinetic energy) on the molecular bridge and, second, how fast is the heat transfer out of the molecule, into the surrounding environment. The most challenging situation is that where heat can flow from the molecule only onto the electrodes with which it is in contact.

For a molecule that carries a current I under a potential bias Φ in a steady state operation, the answer [74] to the first question is $\kappa I \Phi$, where

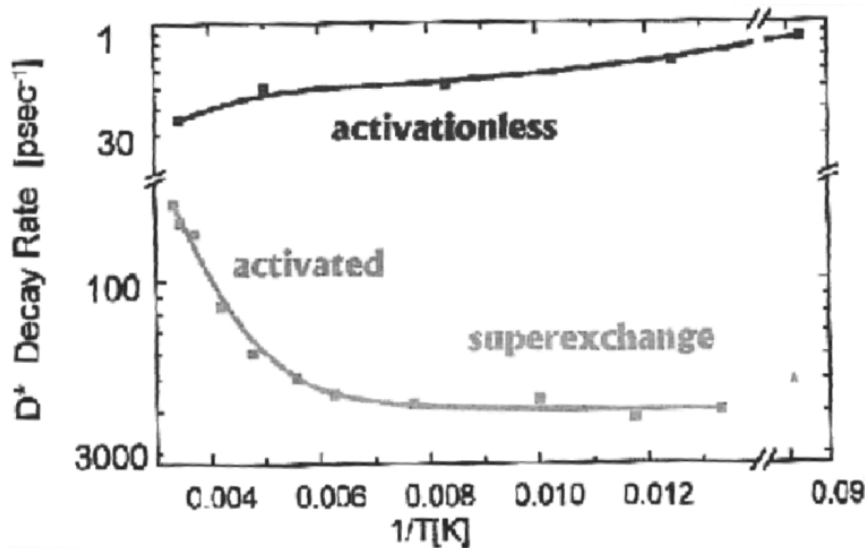


Fig. 5. Temperature dependence of the electron transfer rate in the photoreaction center (G. Hartwich, G. Bieser, T. L. Angenbachen, P. Müller, M. Richter, A. Ogronik, H. Scheer and M.E. Michel-Beyerle, Biophys. J. 71, A8 (1997); see also M. Bixon and J. Jortner, [11]). The activationless behavior (upper curve) corresponds to the wild-type reaction center while crossing from super-exchange at low temperature to activated behavior at higher T is exhibited in a chemically engineered reaction center in which the bacteriochlorophyll is replaced by vinyl bacteriochlorophyl

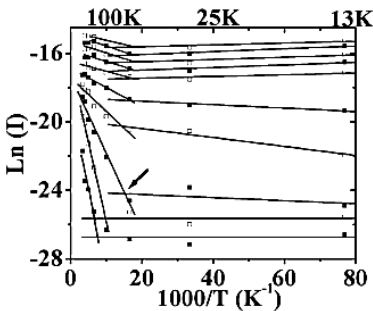


Fig. 6. Temperature dependence of the current through 1-nitro-2,5-di(phenylethyynyl- 4'-mercapto) benzene molecules between gold electrodes, showing transition from non-activated to activated behavior with a bias-dependent activation energy (After [70])

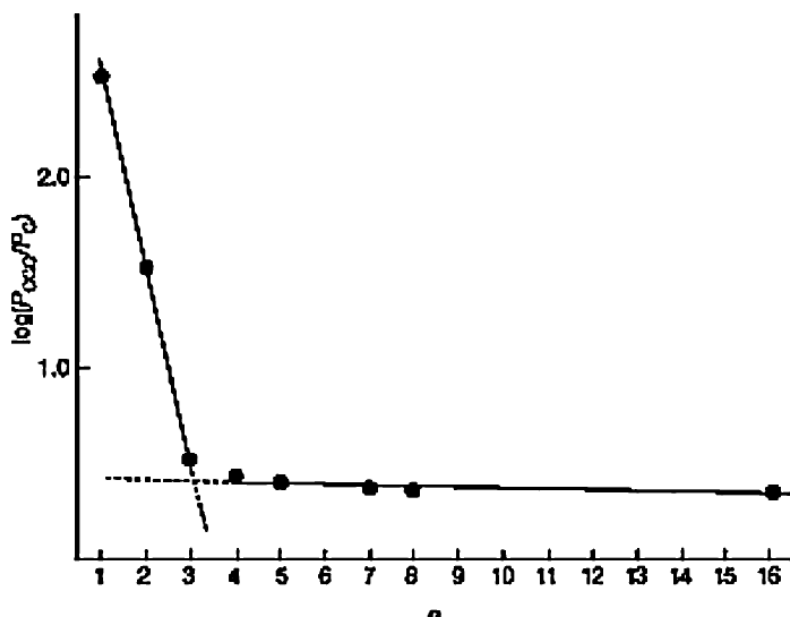


Fig. 7. Measured length dependence of electron transfer yields in DNA (from [71])

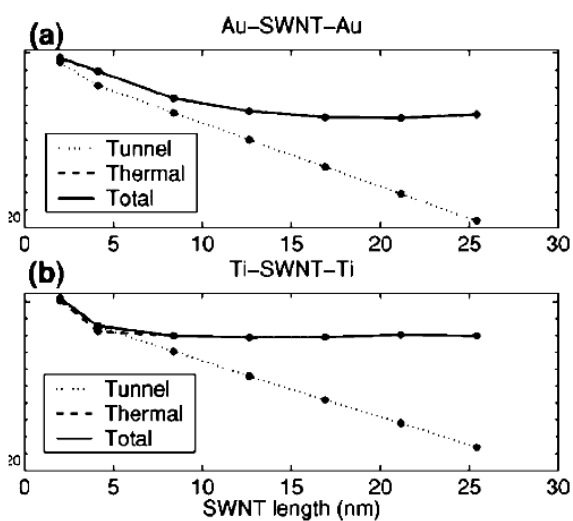


Fig. 8. Room temperature calculated conductance of a single-walled nanotube between gold electrodes, as a function of nanotube length. (from [35])

$0 \geq \kappa \geq 1$. A calculation based on a tight-binding model [74] with electron-phonon coupling estimated from molecular reorganization energies yields κ of order 0.1. Thus the heat conduction problem in molecular junctions becomes crucial. As a zero-order approximation one may try to represent the molecular wire as a cylinder characterized by the classical heat conduction coefficient of saturated organic materials. This yields the results [74] of Fig. 9 that may lead us to conclude that the temperature rise expected under reasonable operating conditions is not significant. It appears though that using classical heat conduction for such estimates fails for two reasons. First, the size of molecular conduction bridges is often small enough to make phonon motion essentially ballistic and classical heat conduction concepts largely invalid. This actually enhances heat transfer out of the molecule relative to what is expected in macroscopic, diffusive, conduction. On the other hand, small molecular systems are restricted environments, limited in the number and spectrum of available phonon modes. This reduces the efficiency of heat dissipation out of the molecule and the net outcome [51], as we know from experiment, is that junction stability may be compromised by passing current through its molecular component.

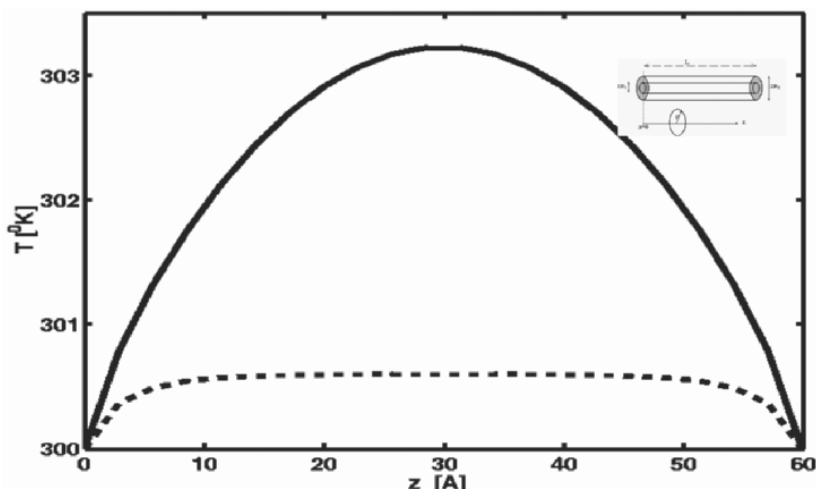


Fig. 9. A model estimate of the temperature rise of a current carrying molecular junction (model as a cylinder (see inset) connecting the electrodes). Heat is assumed to be deposited at the center of the cylinder at a rate of 10^{10} eV/s (an estimate from a theory based on the Redfield formalism for a current of 10 nA at voltage 1 eV) and the classical heat equation. With heat conduction $\sigma_h = 3.5 \cdot 10^{-4}$ cal/(s · cm · K) typical of organic solids is used to estimate the cooling. (from [73]). The length of the cylinder is 60 Å. The *upper curve* is obtained from a calculation that assumes that heat flows out of the molecule only at the contacts with the leads. The *lower curve* is from a calculation that assumes cooling through the entire molecular surface

4.4 Inelastic Electron Tunneling Spectroscopy (IETS)

Inelastic tunneling spectroscopy, an increasingly important tool for studies of molecular conduction junctions, provides the possibility to view directly the consequence of electron-phonon interaction in the tunneling current. Experimentally one looks for vibrational signatures in the current/voltage response of the junction. An important technical difference between IETS and electronic optical spectroscopy is that in the latter case the energy of the observable (light) is easily resolved, while a current is an integral over energy (see (3)) that needs to be differentiated to get energy resolved information.

Vibrational signatures in the current-voltage relationships of molecular junctions can stem from two origins (see Fig. 10a). At the threshold where the potential bias between the left and right electrodes exceeds $\hbar\omega_0$, where ω_0 is the frequency of a nuclear vibrational mode on the bridge, the tunneling electron can exchange energy with this mode and the additional inelastic signal is observed as a conduction step, i.e. a peak in the second derivative $d^2I/d\Phi^2$ of the current with respect to the voltage. If the potential bias is such that an electronic level of the bridge just enters the window between the Fermi-energy of the two electrodes, resonance tunneling takes place and the corresponding peak in the conductance $dI/d\Phi$ may be accompanied by satellite vibrational peaks similar to those observed in resonance Raman scattering. An example of the resulting spectroscopy is shown in Fig. 12 of Chap. 30. References [61, 75] discuss recent observations of vibrational structures dressing resonance tunneling currents.

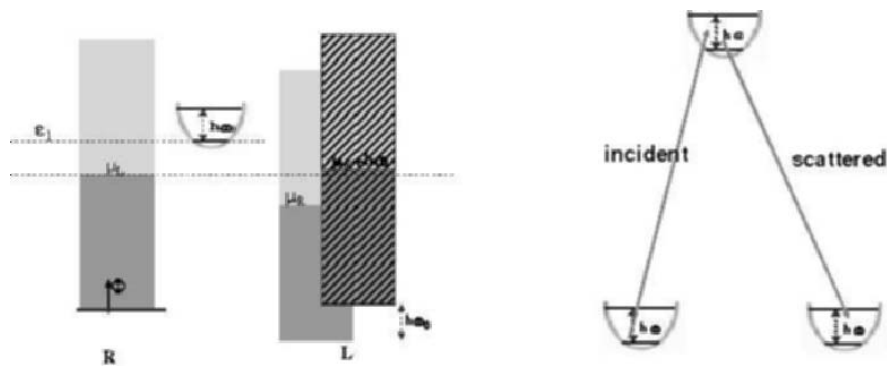
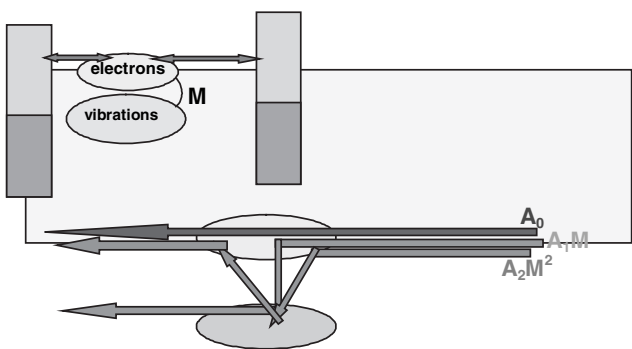


Fig. 10. A schematic view of the level structure for inelastic electron tunneling (left) and for Raman scattering (right). The shaded areas in left figure denote the continuous manifolds of states of the two leads where the lines separating the occupied and unoccupied states are the corresponding Fermi energies. For the right lead two manifolds are shown: one where the corresponding molecular state is the ground vibrational state of the molecule, and the other (diagonally shaded) where the molecule is in the first excited vibrational state. The horizontal dotted lines at heights μ_L and ε_1 are added to guide the eye

At the threshold $|e\Phi| = \hbar\omega_0$ of the inelastic tunneling channel both the elastic and the inelastic fluxes change, with the latter obviously increasing from its zero value below threshold. In contrast, as first noted by Persson and Baratoff [76], depending on the energetic parameters of the system, the correction to the elastic current may be negative. Furthermore, this negative change in the elastic tunneling component may outweigh the positive contribution of the inelastic current, leading to a negative peak in the second derivative of the current/voltage relationship. Such negative features have indeed been observed in recent single-molecule IETS studies [60, 71]. It should be noted that not only the sign but also the shape of these peaks depend on the energetic parameters of the system [77], and recent results [62] (see also Chap. 30) that show relatively strong derivative-like features in the low temperature IETS spectrum of C8 alkane thiols may be another manifestation of the same effect. The origin of this rich range of behaviors is the interference between different orders (in the electron-phonon coupling M) of the elastic contribution to the tunneling current, as explained by Fig. 11. This figure refers to a simple model [77] with a single bridge electronic state (1) and a single phonon mode, described by the Hamiltonian

$$\hat{H}_0 = \varepsilon_1 \hat{c}_1^\dagger \hat{c}_1 + \sum_{k \in L, R} \varepsilon_k \hat{d}_k^\dagger \hat{d}_k + \omega_0 \hat{a}^\dagger \hat{a} + \sum_{k \in L, R} (V_{k1} \hat{d}_k^\dagger \hat{c}_1 + h.c.) + M(\hat{a}^\dagger + \hat{a}) \hat{c}_1^\dagger \hat{c}_1 \quad (20)$$

where \hat{c}_1^\dagger and \hat{c}_1 are creation and annihilation operators for electrons on the bridging level of energy ε_1 , $\{k\} = \{l\}, \{r\}$ are sets of electronic states representing the left (L) and the right (R) electrodes with the corresponding



$$(A_0 + A_1 M + A_2 M^2)^2 = A_0^2 + M^2 (A_1^2 + A_0 A_2) \quad \downarrow \text{elastic} \quad \downarrow \text{inelastic} \quad \downarrow \text{elastic}$$

Fig. 11. A scheme used to explain the low order elastic and inelastic components of the IETS signal. See text for details

creation and annihilation operators \hat{d}_k^\dagger and \hat{d}_k and \hat{a}_k^\dagger and \hat{a} are creation and annihilation operator for the phonon mode of frequency ω_0 . The tunneling amplitude may be written, to second order in the electron-phonon coupling M as $A = A_0 + A_1 M + A_2 M^2$ where A_0 is the amplitude of a zero order process that involves no phonons, A_1 is a 1-phonon inelastic tunneling amplitude and A_2 is a 2-phonon elastic amplitude that describes a second order process where one phonon was created then destroyed. Clearly, the intensity A^2 contains in second order contributions of inelastic process, and interfering elastic processes as seen in Fig. 11.

5 Remarks and Generalities

Since junction transport is in some senses an extension of non-adiabatic molecular electron transfer, conductances and rate constants are closely related (Sect. 3), and both undergo characteristic changes between coherent and incoherent motion mechanisms (Sect. 4). Because of these similarities, there are a number of common issues that will arise in the measurement of either conductance or electron transfer rates. These are discussed in Sect. 5.1 of this chapter. There are, however, some special aspects of junction transport, that arise from the nature of the states and the dynamical processes involved. These aspects are discussed in Sect. 5.2.

5.1 Electron Transfer and Conductance: Common Issues

Electronic States

Because charge transfer or transport is the defining process, both ET and JC (electron transfer and junction conductance) deal with initial and final electronic states. In junctions, the electronic states in question lie within the continuum of the leads. For ET, both the initial and final states are isolated molecule electronic eigenstates. Nevertheless, the transport coefficients (k_{ET} and g) will vary with varying initial or final electronic state. While this has been extensively investigated in the ET field [1, 78, 79] (in particular using photoelectrochemistry), it is also expected to be present in junctions: indeed, photoexcited junction transport has been discussed in the theoretical literature [80], and some initial experimental aspects are beginning to appear [81].

Electron Correlation

The electron correlation problem enters into both processes. This term refers to the fact that interelectron repulsion both makes the electronic structure of molecules or solids a problem that is impossible to solve exactly, and substantially modifies energy levels. In most treatments of ET or MJ, a major simplification is made in that only the single electron terms of a model Hamiltonian

are used: these models are sometimes called tight binding [82], or extended Huckel or one electron. Electron repulsions cause major changes in the properties of individual molecules (for example, they change the optical spectra qualitatively, they are responsible for bond formation and taking them into account is the dominant reason why electronic structure calculations in 2004 are better than they were in 1946).

Calculations employing electronic correlation, often using density functional theory, are now becoming standard both in transport [29–41, 83] and in transfer, but nevertheless major problems still inhere in dealing correctly with the effects of correlation. A specific instance involving junction behavior will be discussed in Sect. 5.2.

Spin Effects

Because of the Exclusion Principle, interactions between same spin and opposite spin electrons are different. In ET, these spin effects are strongly marked in situations involving particular open shell transition metal ions, notably cobalt. In junction transport, there have been a number of theoretical analyses of possible spin effects [84]: one idea is that the spins are polarized in the metallic electrode, and the amplitude for scattering through the junction for same spin and differing spin electrons will differ. The opposite limit involves non-singlet states on the molecule itself. No experimental observations of such phenomena are yet reported. There is also an interesting issue of spin quantization axis, since the two electrodes and the molecule might have quite differing spin axes.

Geometry

It has already been stressed that to obtain useful structure/function relationships, one needs to know structure. Electronic structure calculation for individual molecules can give bond lengths and bond angles, for stable organics, that are essentially as exact as experiment. For ET reactions, then, the geometry problem is to some extent computationally solved. In stark contrast, with the possible exception of nanotubes, nearly nothing is known experimentally about the actual geometry of molecules in transport junctions: this is a non-equilibrium situation, and non-equilibrium methods are required to calculate such geometries. There have been some attempts in this direction [85], but since experimental determination of the geometries is so very difficult, it is not known how accurate such calculations are.

5.2 Junction Conductance

Because ET is one of the most important reactions in chemistry, the issues discussed in Sect. 5.1 of this chapter have been investigated there both theoretically and experimentally. Since studies of JC are essentially only a decade

old, and since the metrical problems are so serious, much of this territory has been unexplored. But other effects can dominate in junction transport, and these differentiate the ET and JC situations.

Geometric Behavior

Modifications in structure lead to modifications in molecular properties; such structure/function relationships are at the heart of modern chemistry. In JC, as already stated several times, the geometries are effectively unknown, and indeed there does not seem any direct scattering method that can be used experimentally to find accurately the geometry of a molecule made of first row atoms in the presence of a large number of metal or semiconductor atoms constituting the electrode. Indirect structural analysis, using vibrational spectroscopy and scanning probe information, is becoming available [62, 86]. Until such geometric information permits comparison with computations both of the structure and of transport with different structures, this will comprise a very serious difficulty for accurate comparison between modeling and experiments. Beautiful experiments have demonstrated that electronic currents in junctions can actually break chemical bonds, excite vibrations, and otherwise alter the structural chemistry of the molecules of these junctions [53, 54, 57, 59–61, 74]. Understanding that variation remains a major task.

Voltage Profiles

The issue of voltage profiles, effectively the electrochemical potential across a junction in a non-equilibrium state, can be crucial in determining behaviors. This has been studied beginning with a clarification by Datta and his collaborators of the importance of the voltage drop structure [87]. Figure 12 shows some calculations of the local electrostatic field across a model wire system in the Huckel description [88]: notice the change in shape from the simple ramp (which is correct in the absence of any charge within the junctions) to a highly screened interaction in which most of the field drops at the electrode/molecule interface. The extent to which a voltage drop occurs at any given spot can only be determined by a self consistent calculation that takes into account carrier-carrier interactions, because it is necessary to solve simultaneously the Poisson equation for the electrostatics and the Schrödinger equation for the wave function. The smooth curves in Fig. 12 come from solving these equations simultaneously for a simple junction model of a wire. In more extensive calculations on the molecules, there have been attempts to describe the electrostatics. Figure 13 shows the calculated electrostatics for a junction consisting of an organic between gold electrodes [89]. There are substantial changes in the potential due to the presence of electrical charge

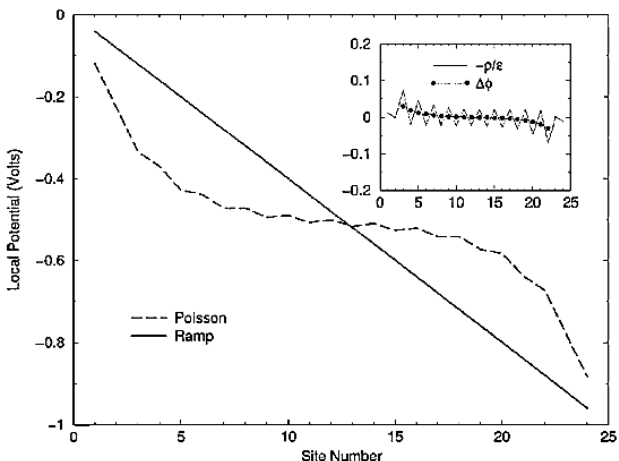


Fig. 12. The effective electrostatic potential acting across a Huckel-level molecular wire contacting two metallic electrodes. The potential indicated as Poisson is a self-consistent solution to the Poisson and Schrodinger equations, while the ramp is simply the applied electrostatic potential. The inset shows the second derivative of the potential (*solid*) and the density divided by the local dielectric constant (*broken*). After [88]

distributions, as is to be expected. Note also that although some of the potential drops at the interfacial regime, substantial amounts do drop across the molecular structure itself.

Understanding the generalities of the voltage profile is crucial, because different voltage profiles will give different solutions to the Schrödinger equation, and therefore different transport predictions. Self consistent field calculations using density functional methods are becoming the standard here [89–91], and can be used to approximate the charge distributions, and therefore the voltage profiles, once self consistency is obtained.

Heuristically, if current is to be continuous throughout the junction, and if Ohm's law were to be obeyed, then the local drop in potential should be proportional to the local resistance. It follows from this argument that if the mixing at the interface is weak, much of the voltage will drop at the interface, and this seems to be borne out by calculations.

Creative work by the McEuen and his collaborators in carbon nanotubes has measured [92] the electrostatic potential, essentially by scanning a voltage probe across the molecule at a functional junction. They observe specific drops along the tube, which are attributed to defects. The actual drop at the interface cannot be measured, because the interface geometry is simply too tight. Measurements of energy dissipation suggest major drops in the field at the interface, as is to be expected. While such measurements would be very

helpful for small molecule circuits, the short length (~ 1 nm) makes them very difficult.

The simplest way to think about such effects is to consider that molecules act like polarizable capacitors in junctions, and that the molecular charge distribution polarizes itself to offset the applied field. In this sense, the interface looks slightly like an electrochemical double layer.

The superexchange mechanisms, as detailed above, suggest that whichever effectively coupled frontier level is closer in energy to the injection energy in the junction case, or closer in energy to the donor in the ET case, should dominate the rate constant. Analysis is more difficult with the junctions, only because so many levels of the “extended molecules” enter. For example, very recent calculations by the Bredas Group [93] and by Basch and collaborators [93] have demonstrated that the effective levels of the extended molecule are not the HOMO and the LUMO, because of the importance of metal-induced gap states [94]. Important, strongly coupled levels can be found by population analysis, and for the simple benzenedithiol case there are of the order of a dozen intervening in the extended molecule [93].

Classically, one expects that the presence of a charge distribution near a metal will result in polarization of the metal, and that this polarization can be well described in terms of an image potential picture. Computationally, using electronic structure methods to calculate this image is difficult [96], essentially because of the interelectronic repulsions in the metal. It is not clear how well any of the “extended molecule” schemes currently in vogue for calculating junction transport deal with the very important image problem, nor is it really clear how to include the image heuristically (double counting of image effects must be avoided). Very recent work by the Purdue group [95] has used a self consistent solution to the Poisson equation with an image correction, within a semiempirical CNDO model Hamiltonian. They calculate both the effective voltage profile and the I/V characteristics. The results show rectification behavior, agreeing very well with break junction transport measurements [99].

Electron Correlation

An important set of phenomena directly related to electron correlation effects is characteristic of mesoscopic physics, and is beginning to be observed in molecular junctions. One of these is the so called Kondo effect [48], in which there is actually a maximum in the conductance at zero voltage, if there is an odd spin on the molecular bridge. Effectively, this comes because of exchange interactions creating a very small peak in the density of the states at the metallic Fermi level. The strength of these interactions is characteristically weak, and (Fig. 14) the Kondo maximum disappears at higher temperature. The possible engineering of molecules to give a larger Kondo-like peak constitutes a significant challenge both for experiment and for theory.

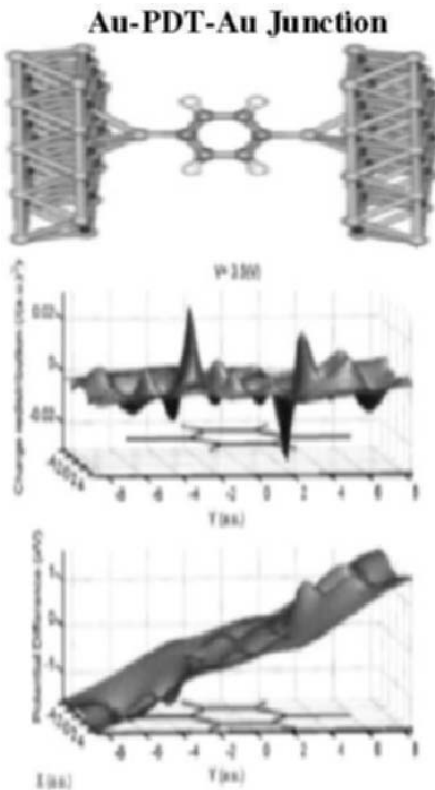


Fig. 13. The difference in electrostatic potentials between the molecule plus electrode and the junction under voltage. The center frame shows the calculated charge transfer, using a very reduced basis set. After [89]

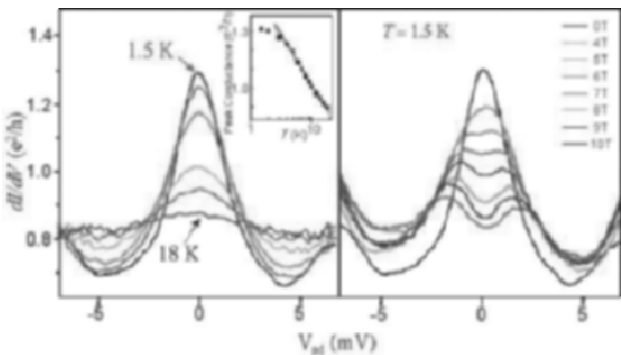


Fig. 14. The observed Kondo-type resonance in the transport through a dithiolated odd-spin Co complex between gold electrodes. Note the disappearance of the resonance peak with increase of temperature. After [48]

When the interfacial mixing (the spectral densities) of the two electrodes become weak, the molecule can act as, effectively, a perfect extended quantum dot structure. Figure 15 shows the observation of the so called “coulomb blockade” structure for a bridge consisting of a gold dot linked to the electrode by duplex DNA strands. The characteristic blockade steps correspond to the charging of the dot, and are seen because of weak effective spectral densities of the two electrodes. Such coulomb blockade structures have been observed in many other molecules [48], and in particular an actual coulombic staircase structure has been reported for a long oligomer of paraphenylenevinylen [49], where a combination of multielectron effects and vibronic interactions is responsible for the multiple charging of the bridge.

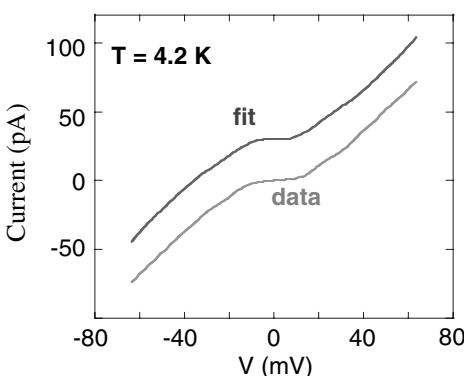


Fig. 15. The coulomb blockade spectrum of a DNA-functionalized Au dot between Au electrodes. The fit is to the standard two-resistor, two capacitor equivalent circuit. After S-W. Chung et al., submitted to Small

Computational Approaches

While use of simple models such as the Newns/Anderson form for the electrode spectral density (based on a one-dimensional tight binding metal) [97] or a Huckel [95] or tight-binding form [82] for the molecular Hamiltonian are extremely useful for understanding general behaviors, there is extensive current activity in actual electronic structure calculations of junction conductance. One approach uses a jellium model for the electrodes and a scattering picture in terms of the Lippman-Schwinger equation for the molecule. This has been extensively applied [37–40], and has a particularly attractive aspect in using a generalized Ehrenfest approach to allow actual geometry optimization under current-flow conditions [85].

More commonly, the junction is broken into two parts, an “extended molecule” consisting of the actual molecule and a few electrode atoms at each end, and the reminder of the electrodes. The latter are represented in terms of their

surface Green's functions, and act as source and drain. The extended molecule is treated using a chosen electronic structure model [29–36]. The choice of method and the basis set determines the quality of the calculation, and self-consistent solution of transport and electronic structure allows prediction of the voltage-dependent conductance. Usually, some form of static Density Functional Theory (DFT) is used for the electronic structure problem.

There are substantive difficulties here, including the fact that static DFT does a very poor job of representing electron injection or ionization processes (essentially the content of the G in (5)), and the balance problem between the basis sets on the molecule and the metal atoms [83,98]. Several contributions both in this book and elsewhere [98] describe alternate, sometimes more sophisticated electronic structure approaches. Since ab-initio methods using correlation corrections of the coupled cluster or Moller-Plesset type do a quite good job in describing ionization and electron capture, their use for conductance seems promising. Basis set issues might be simplified by going to plane-wave formulations.

Reliability, Reproducibility, Experimental Conditions and Switching

Because junction transport is such a new measurement, the community continues to seek the most effective ways to make voltage spectroscopic measurements of transport. Several of the important schemes for doing so will be outlined in the following chapters of this book. In general, however, the measurements break down into two major categories. First, there are break junction measurements [42,99,100], fabrication schemes [101], particular limits of crossed-wire, STM and nanodot collection measurements [102–104], in which one is presumably measuring a small number (ideally 1) of molecules. Second are measurements on adlayers, in which many thousands of molecules can contribute to the transport [105,106]. There is no necessary reason why these two sorts of measurement should give the same current/voltage signatures, even if the molecules are identical, and the electrodes are identical [107]. There are several reasons why such disparities might exist:

First, the spectral densities (effective inverse contact resistance) could vary between adlayers and single molecules. Indeed, calculations indicate [108] (and measurements of adlayer stability and motion also suggest [109] that there are several stable sites for the most common geometries, such as thiol/gold or siloxy linkages [110]. These different geometries are also calculated to have different spectral densities, and therefore different conductance signatures [108]. This is almost certainly the reason for the often-observed striking switching in time dependent measurements of transport. Figure 16 shows an important contribution from the Weiss laboratory [104], with switching on and switching off of transport through a conjugated molecule in a mixed adlayer film. Figure 17 shows the histograms observed by Tao's group [111], found by an electrochemical break-junction scheme. This

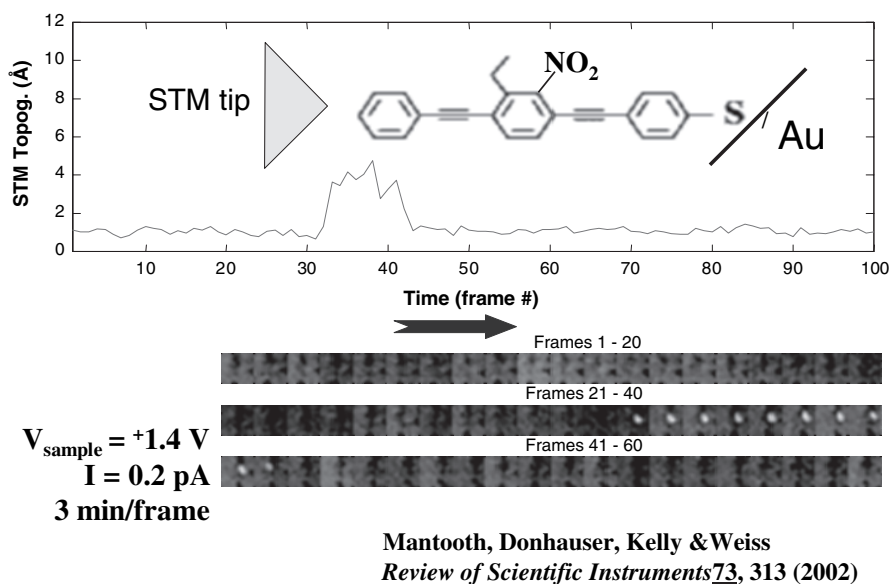


Fig. 16. The observed fluctuations in the transport current to an STM tip probing a pi-type thiol in an adsorbed self-assembled monolayer. Note the strong fluctuations in the current with time. After [104]

is an important measurement, demonstrating clearly the differing conductance values expected for differing geometries. Reed's Group [112] has reported significant conductance fluctuations in disordered SAM structures, but far better reproducibility for ordered ones. For stable organics bound to Si electrodes, fluctuations are very small [100, 101]. The simplest and most persuasive argument for observed conductance switching is indeed geometric change of the environment, just as it is for single molecule spectroscopy and spectral diffusion. Given these different possible geometries and resulting different conductances, it is not surprising that any individual measurement of transport could differ from another.

Second, the presence of self-assembled monolayers on surfaces changes both the work function and the Fermi energy of the metal [113]. Since the Fermi energy enters into the voltage profile, and into the injection gap, it is clear that a given molecule may have a different conductance signature in the presence of an adlayer film than it would on a bare metal, independent of any geometric change.

Given these realizations, it is clear that extensive comparative measurements will have to be made before actual current/voltage/Fermi level behavior is clarified.

Probably the simplest multiple-molecule situation involves alkane thiol adlayers: these are very regular and relatively stable. Moreover, the very

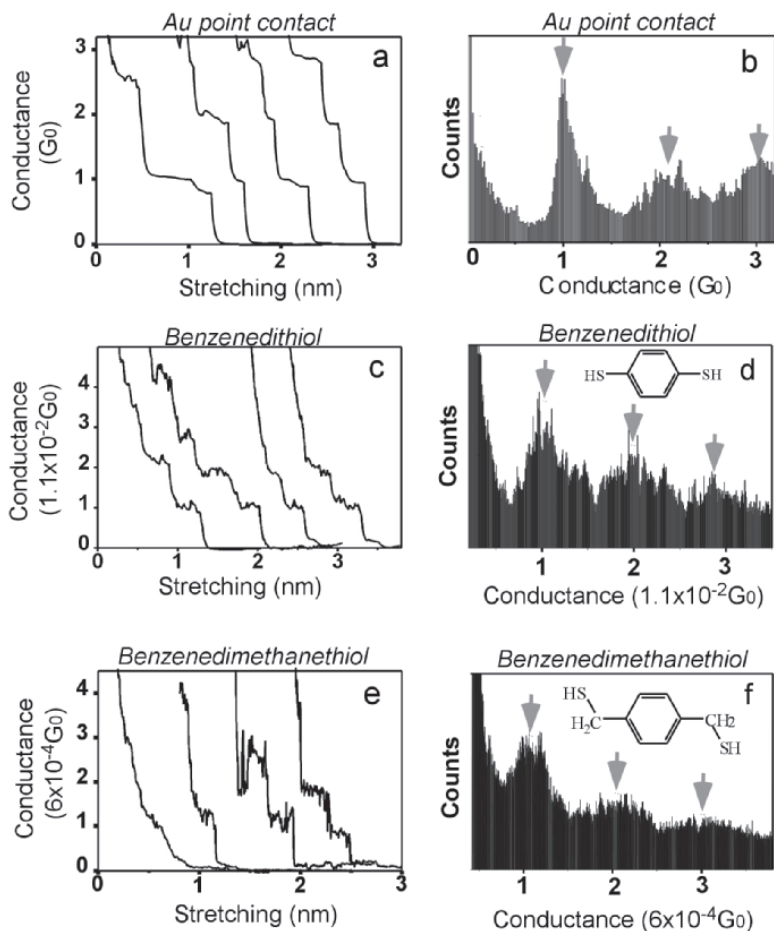


Fig. 17. Histograms for molecular junction conductance observed in an electrochemical environment. The histograms are based on multiple samples, obtained in an electrochemical break-junction measurement. Note the breadth of the observed conductance, the near-quantized transport in the metal wires, and the higher transport in the benzene dithiol than in the xylene dithiol. After [111]

large gap expected due to the saturated electronic structure of the alkane suggests (for example using the Buttiker–Landauer time scale) that here transport will occur by simple quantum mechanical barrier tunneling, expected to follow roughly the Simmons equation [114] and to exhibit no temperature dependence. Precisely these characteristics have been observed in several laboratories [105, 115] – the transport is indeed temperature independent, and indeed decays exponentially with length as would be expected for alkanes. Calculations from several laboratories on such systems agree very well with the experiment for the slope of the exponential decay [116, 117]. Nevertheless,

interface effects, electrode instabilities and fabrication problems continue to haunt transport measurements [118].

While stochastic switching arising from thermal or voltage-driven geometry changes can complicate the interpretation of conductance, using controlled molecular geometric changes to modify transport may be a very significant aspect of molecular electronics. Several theoretical papers address the idea of using a stereochemical change [119–121], driven by the applied field, to switch a molecular geometry and therefore to use the molecule as a dynamic circuit element, producing a switch or rectifier. It was pointed out by Datta and collaborators that the use of a standard FET geometry is difficult for molecular species, because the short molecular lengths (of order 1nm) would require a very thin oxide layer (less than the molecular length) for effective switching [122]. Using a stereochemical switch in a two-electrode (source/drain) rather than the three-electrode (source/gate/drain) structure of the traditional FET would constitute a particularly neat form of true molecular electronics (Fig. 18) [119–122].

Other switching phenomena, and indeed a very different set of conductance behaviors, occur when semiconducting electrodes replace metallic ones [101, 102]. It has been demonstrated [100] that reproducible negative differential conductance spectra can occur in transport through a chemisorbed

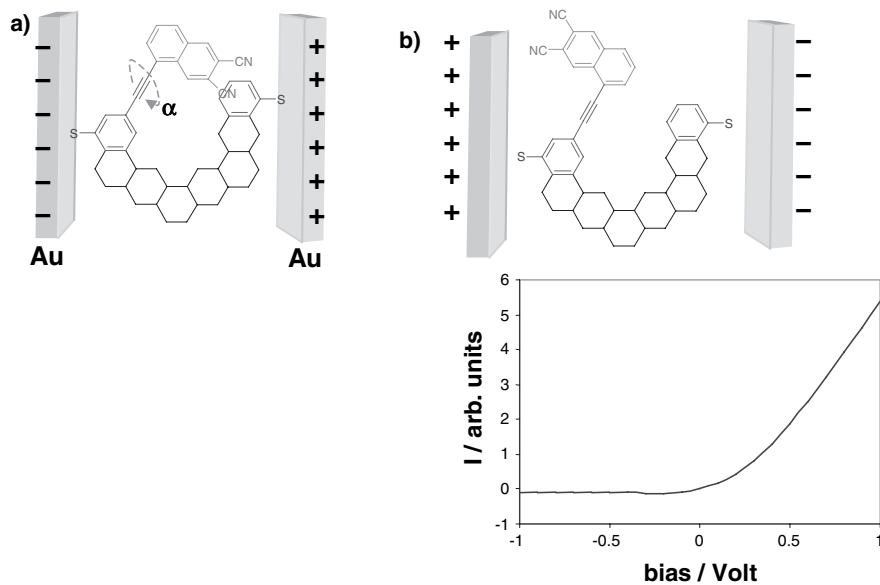


Fig. 18. A proposed molecular junction switch based on rotation about an intramolecular triple bond. Upon changing bias direction, the isomerization substantially changes pi overlap, changing the ambient predicted conductance by more than a factor of 100. After [121]

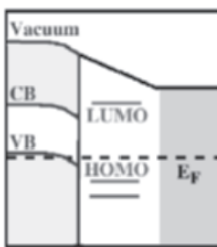
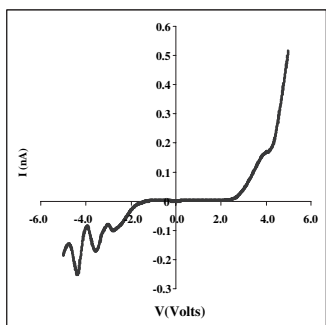
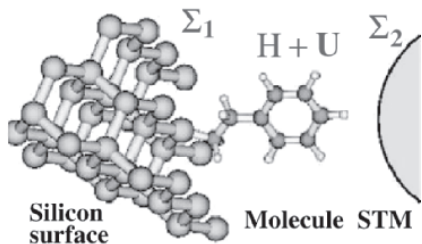
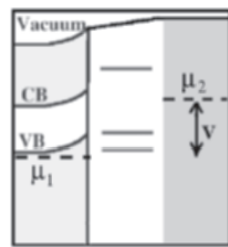
(a) $V = 0$ (b) $V > 0$

Fig. 19. Observed negative differential conductance in a Si-based molecular junction. The structure is made by adding a free-radical molecule, called tempo, to a single surface dangling bond on a heavily-doped Si single crystal. The conductance fluctuations arise from the bandgaps in Si. After [100]

molecular species on a Si electrode (Fig. 19). Such switching behavior in a stable geometry, which might be very valuable in actual computational circuitry, can be understood in terms of the bandgaps in the semiconductor electrode [122].

For most interesting molecules, convergence between experiment and theory has been more difficult to obtain. As discussed both in this section and in the following papers, such convergence is not expected until we have much more information on the geometry, the environment, the electronic structure and the binding in the given molecular junction. These issues of reliability are now being seriously addressed, and the field is making great progress toward turning molecular junction transport into a reliable model science.

Acknowledgements

Mark Ratner is grateful to the DoD MURI/DURINT program, the DARPA Moletronics/MOLEAPPS Program, the NSF-NCN program at Purdue University and the NASA URETI program for support of his work. AN thanks the Israel Science Foundation, the U.S. – Israel Binational Science Foundation and the Volkswagen Foundation for financial support of his research.

References

1. C. Joachim, J.K. Gimzewski, and A. Aviram: Electronics using hybrid-molecular and mono-molecular devices, *Nature* **408**, 541 (2000).
2. A. Nitzan and M. Ratner: Electron transport in molecular wire junctions, *Science* **300**, 1384 (2003).
3. A. Nitzan: Electron transmission through molecules and molecular interfaces, *Ann. Rev. Phys. Chem.* **52**, 681 (2001).
4. P. Hanggi, M. Ratner, and S. Yaliraki, eds., *Chemical Physics* **281**, 111 (2002).
5. J.R. Heath and M.A. Ratner: Molecular electronics, *Physics Today* **56**, 43 (2003); C.R. Kagan and M.A. Ratner, eds., *MRS Bulletin*, **29**, #6 (2004)
6. D.M. Adams, L. Brus, C.E.D. Chidsey, et al.: Charge transfer on the nanoscale: Current status, *J. Phys. Chem. B* **107**, 6668 (2003).
7. M.C. Petty, M.R. Bryce, and D. Bloor, *Introduction to Molecular Electronics* (Oxford University Press, Oxford, 1995); C.A. Mirkin, and M.A. Ratner: Molecular electronics, *Annu. Rev. Phys. Chem.*, **43**, 719 (1992); A. Aviram, ed., *Molecular Electronics – Science and Technology* (American Institute of Physics, College Park, MD, 1992); A. Aviram, M.A. Ratner, and V. Mujica: Molecular electronics – science and technology, eds., *Ann. N.Y. Acad. Sci.*, **852**, (1998); J. Jortner, and M.A. Ratner, eds. *Molecular Electronics* (Blackwell Science, Cambridge, MA, 1997); M.A. Ratner, and M.A. Reed, *Encyclopedia of Science and Technology*, 3rd ed., (Academic Press, New York, 2002); V. Mujica, and M.A. Ratner, in *Handbook of Nanoscience, Engineering and Technology*, W.A. Goddard III, D.W. Brenner, S.E. Lyshevshi, and G.J. Iafrate, eds. (CRC Press, Boca Raton, FL, 2002); M.A. Reed, and T. Lee, eds., *Molecular Nanoelectronics* (American Scientific Publishers, Stevenson Ranch, CA, 2003).
8. Jeffrey R. Reimers, et al.: Molecular Electronics III, eds., *Ann. N.Y. Acad. Sci.*, **1006**, (2003).
9. Thomas Tsakalakos, Ilya A. Ovid'ko and Asuri K. Vasudevan, eds., *Nanostructures: Synthesis, Functional Properties and Applications*, (Kluwer, Dordrecht, 2003).
10. A. Aviram, M. Ratner, and V. Mujica, eds., *Molecular electronics II*, *Ann. N.Y. Acad. Sci.*, **960**, (2002).
11. J. Jortner, and M. Bixon, in *Advances in Chemical Physics*, I. Prigogine, and S. Rice, eds. 106 (Wiley, New York, 1999); A.M. Kuznetsov, *Charge Transfer in Physics, Chemistry and Biology* (Gordon & Breach, New York, 1995); A.M. Kuznetsov, J. Ulstrup, A.M.K., et al., *Electron Transfer in Chemistry and Biology: An Introduction to the Theory* (Wiley, New York, 1998).
12. R.A. Marcus: Chemical and electrochemical electron-transfer theory, *Ann. Rev. Phys. Chem.* **15**, 155 (1964).
13. J.R. Miller, J.V. Beitz, and R. Huddleston: Effect of free energy on rates of electron transfer between molecules, *J. Am. Chem. Soc.* **106**, 5057 (1984).
14. J. Jortner and B. Pullman, eds., *Perspectives in Photosynthesis*. Dordrecht: Kluwer, 1990.
15. J. Jortner, M. Bixon, T. Langenbacher, and M.E. Michel-Beyerle: Charge transfer and transport in DNA, Proceed. *Natl. Acad. Sci. USA* **95**, 12759 (1998).
16. M. Bixon and J. Jortner, [1], p. 35.

17. J. Ulstrup and J. Jortner: The effect of intramolecular quantum modes on free energy relationships for electron transfer reaction, *J. Chem. Phys.* **63**, 4358 (1975).
18. M. Bixon and J. Jortner: Solvent relaxation dynamics and electron transfer, *Chem. Phys.* **176**, 467 (1993).
19. T. Holstein: Polaron motion. I. Molecular crystal model, *Ann. Phys. (N.Y.)* **8**, 325, 343 (1959).
20. H. McConnell: Intramolecular charge transfer in aromatic free radicals, *J. Chem. Phys.* **35**, 508 (1961).
21. J. Jortner: Temperature dependent activation energy for electron transfer between biological molecules, *J. Chem. Phys.* **64**, 4860 (1976); V. Mujca, M. Kemp, M. Roitberg, and M.A. Ratner: Electron conduction in molecular wires. I. A scattering formalism and II. Application to scanning tunneling microscopy, *J. Chem. Phys.* **101**, 6849, 6856 (1994).
22. J. Tersoff, and D.R. Hamann: Theory of the scanning tunneling microscope, *Phys. Rev. B*, **31**, 805 (1985).
23. R. Landauer: Spatial variation of currents and field due to localized scatterers in metallic conduction, *IBM J. Res. Dev.* **1**, 223, (1957); R. Landauer: Electrical resistance of disordered one-dimensional lattices, *Phil. Mag.*, **21**, 863 (1970).
24. C.W.J. Beenakker, and H. van Houten: Advances in research and applications. Quantum transport in semiconductor nanostructures, *Solid State Physics*, **44**, 1 (Academic Press, New York, 1991).
25. L.V. Keldysh, *Sov. Phys. JETP*, **20**, 1018 (1965).
26. L. P. Kadanoff, and G. Baym, *Quantum Statistical Mechanics; Green's function Methods in Equilibrium and Nonequilibrium* (W.A. Benjamin, New York, 1962).
27. Y. Meir and N.S. Wingreen: Landauer formula for the current through an interacting electron region, *Phys. Rev. Lett.* **68**, 2512 (1992)
28. T. Seideman, and W.H. Miller: Quantum mechanical reaction probabilities via a discrete variable representation-absorbing boundary condition Green's function, *J. Chem. Phys.*, **97**, 2499 (1992); T. Seideman, and W.H. Miller: Calculation of the cumulative reaction probability via a discrete variable representation with absorbing boundary conditions, *J. Chem. Phys.*, **96**, 4412 (1992).
29. S. Datta, *Electric transport in Mesoscopic Systems* (Cambridge University Press, Cambridge, 1995); S. Datta, to be published.
30. Y. Xue, S. Datta, and M.A. Ratner: Charge transfer and "band lineup" in molecular electronic devices: A chemical and numerical interpretation, *J. Chem. Phys.*, **115**, 4292 (2001).
31. L.E. Hall, J.R. Reimers, N.S. Hush, et al.: Formalism, analytical model, and a priori Green's-function-based calculations of the current-voltage characteristics of molecular wires, *J. Chem. Phys.*, **112**, 1510 (2000).
32. S. Datta, W.D. Tian, S.H. Hong, et al.: Current-voltage characteristics of self-assembled monolayers by scanning tunneling microscopy, *Phys. Rev. Lett.*, **79**, 2530 (1997).
33. H. Ness, and A.J. Fisher: Quantum inelastic conductance through molecular wires, *Phys. Rev. Lett.*, **83**, 452 (1999); E.G. Petrov, I.S. Tolokh, and V. May: The magnetic-field influence on the inelastic electron tunnel current mediated

by a molecular wire, *J. Chem. Phys.*, **109**, 9561 (1998); E.G. Emberly, and G. Kirczenow: Electron standing-wave formation in atomic wires, *Phys. Rev. B*, **60**, 6028 (1999); E.G. Emberly, and G. Kirczenow: Models of electron transport through organic molecular monolayers self-assembled on nanoscale metallic contacts, *Phys. Rev. B*, **64**, 235412 (2001); M. Brandbyge et al.: Density-functional method for nonequilibrium electron transport, *Phys. Rev. B*, **65**, 165401 (2002); B. Larade, et al.: Conductance, *I-V* curves, and negative differential resistance of carbon atomic wires, *Phys. Rev. B*, **64**, 075420 (2001); J. Taylor, H. Guo, J. Wang: Ab initio modeling of open systems: Charge transfer, electron conduction, and molecular switching of a C₆₀ device, *Phys. Rev. B*, **63**, 121104(R) (2001); M. Magoga, and C. Joachim: Minimal attenuation for tunneling through a molecular wire, *Phys. Rev. B*, **57**, 1820 (1998); M. Magoga, and C. Joachim: Conductance of molecular wires connected or bonded in parallel, *Phys. Rev. B*, **59**, 16011 (1999); P. Stampfus, et al., in *Proceedings NIC Symposium*; D. Wolf, G. Munster, M. Kremer, eds., **20**, 101 (2003); R. Baer and D. Neuhauser: Ab initio electrical conductance of a molecular wire, *Int. J. Quant. Chem.*, **91**, 524 (2003); R. Baer, et al: Ab initio study of the alternating current impedance of a molecular junction, *J. Chem. Phys.* **120**, 3387 (2004).

34. J.K. Tomfohr, and O. Sankey: Complex band structure, decay lengthg, and Fermi level alignment in simple molecular electronic systems, *Phys. Rev. B*, **65**, 245105 (2002); B. Larade, J. Taylor, H. Mehrez, and H. Guo: Conductance, *I-V* curves, and negative differential resistance of carbon atomic wires, *Phys Rev. B*, **64**, 075420 (2001); J. Taylor, H. Guo, and J. Wang: Ab initio modeling of open systems; Charge transfer, electron conduction, and molecular switching of a C₆₀ device, *Phys. Rev. B*, **63**, 121104(R) (2001); H. Mehrez, G. Hong, J. Wang, and C. Roland: Carbon nanotubes in the Coulomb blockade regime, *Phys. Rev. B*, **63**, 245410/1 (2001); A. di Carlo et al.: Theoretical tools for transport in molecular nanostructures, *Physica B*, **314**, 86 (2002); J.C. Cuevas et al.: theoretical description of the electrical conduction in atomic and molecular junctions, *Nanotechnology*, **14**, R29 (2003); J.J. Palacios et al.: First-principal approach to electrical transport in atomic-scale nanostructures, *Phys. Rev. B*, **66**, 035322 (2002).
35. Y.Q. Xue and M.A. Ratner: Microscopic study of electrical transport through individual molecules with metallic contacts. (2). Effect fo the interface structure, *Phys. Rev. B*, **68**, 115407 (2003); and: Schottky barrier at metal-finite semiconduction carbon nanotube interfaces, *Appl. Phys. Lett.* **83**, 2429 (2003).
36. T. Seideman, and H. Guo: Quantum transport and current-triggered dynamics in molecular tunnel junctions, *J. Theor. Comp. Chem.*, **2**, 439 (2004).
37. N.D. Lang: Resistance of atomic wires, *Phys. Rev. B*, **52**, 5335 (1995).
38. N.D. Lang, and P. Avouris: Carbon-atom wires: Charge-transfer doping, voltage drop, and the effect of distortions, *Phys. Rev. Lett.*, **84**, 358 (2000).
39. M. diVentra, S. Pantelides, and N. Lang: Erratum: Current-induced forces in molecular wires [Phys. Rev. Lett., **88**, 046801 (2002)], *Phys. Rev. Lett.*, **89**, 139902 (2002); M. Di Ventra, and S.T. Pantelides: Scanning tunneling microscopy images: A full ab initio approach, *Phys. Rev. B*, **59**, R5320 (1999).
40. S.N. Rashkeev, M. Di Ventra, and S.T. Pantelides: Transport in molecular transistors: Symmetry effects and nonlinearities, *Phys. Rev. B*, **66**, 033301/1 (2002); Y. Zhongqin, N.D. Lang, and M. Di Ventra: Effects of geometry and

- doping on the operation of molecular transistors, *App. Phys. Lett.*, **82**, 1938 (2003); S.T. Pantelides, M. Di Ventra, and N.D. Lang: First-principles simulations of molecular electronics, *Ann. N.Y. Acad. Sci.*, **960**, 177 (2002); S.T. Pantelides, M. Di Ventra, N.D. Lang, and S.N. Rashkeev: Molecular electronics by the numbers, *IEEE Transactions on Nanotechnology*, **1**, 86 (2002); M. Di Ventra, N.D. Lang, and S.T. Pantelides: Electronic transport in single molecules, *Chem. Phys.*, **281**, 189 (2002); M. Di Ventra, S.T. Pantelides, and N.D. Lang: Current-induced forces in molecular wires, *Phys. Rev. Lett.*, **88**, 046801 (2002); M. Di Ventra, and N.D. Lang: Transport in nanoscale conductors from first principles, *Phys. Rev. B*, **65**, 045402 (2002).
41. A. Troisi, and M.A. Ratner: Molecular wires conductance: Some theoretical and computational aspects, *Molecular Nanoelectronics*, M.A. Reed, and T. Lee, eds., 1 (American Scientific Publishers, Stevenson Ranch, CA, 2003).
 42. R.H.M. Smit, Y. Noat, C. Untiedt, N.D. Lang, M.C.V. Hemert, and J.M. van Ruitenbeek: Measurement of the conductance of a hydrogen molecule, *Nature*, **419**, 906 (2002).
 43. M. Fuhrer, S.A. Getty, L. Wang, C. Engtrakul, and L. R. Sita: Near-perfect conduction through a ferrocene-based molecular wire, unpublished.
 44. A. Nitzan: A relationship between electron-transfer rates and molecular conduction, *J. Phys. Chem. A*, **105**, 2677 (2001).
 45. A. Nitzan: The relationship between electron-transfer rate and molecular conduction. (2). The sequential hopping case, *Israel J. Chem.*, **42**, 163 (2002).
 46. R.A. Marcus: On the theory of electron-transfer reactions. (6). Unified treatment for homogeneous and electrode reactions, *J. Chem. Phys.*, **43**, 679 (1965); M.D. Newton: Quantum chemical probes of electron-transfer kinetics: The nature of donor acceptor interactions, *Chem. Rev.*, **91**, 767 (1991).
 47. D.M. Adams et al.: Charge transfer on the nanoscale: Current status, *J. Phys. Chem. B*, **107**, 6668 (2003)
 48. J. Park, A.N. Pasupathy, J.I. Goldsmith, C.C. Chang, Y. Yaish, J.R. Petta, M. Rinkoski, J.P. Sethna, H.D. Abruna, P.L. McEuen, and D.C. Ralph: Coulomb blockade and the Kondo effect in single-atom transistors, *Nature*, **417**, 722 (2002); W. Liang et al.: Kondo resonance in a single-molecule transistor, *Nature* **417**, 725 (2002)
 49. S. Kubatkin, A. Danilov, M. Hjort, J. Cornil, J.-L. Bredas, N. Stuhr-Hansen, P. Hedegard, and T. Bjornholm: Single-electron transistor of a single organic molecule with access to several redox states, *Nature*, **425**, 698 (2003).
 50. D. Segal and A. Nitzan: Steady-state quantum mechanics of thermally relaxing systems, *Chem. Phys.* 268, 315 (2001); D. Segal, and A. Nitzan: Heating in current carrying molecular junctions, *J. Chem. Phys.*, **117**, 3915 (2002).
 51. D. Segal, A. Nitzan, and P. Hanggi: Thermal conductance through molecular wires, *J. Chem. Phys.*, **119**, 6840 (2003).
 52. Y.-C. Chen, M. Zwolak, and M. DiVentra: Local heating in nanoscale conductors, *Nano Lett.*, **3**, 1691 (2003); T.N. Todorov: Local heating in ballistic atomic-scale contacts, *Philosoph. Mag. B*, **77**(4), 965 (1998); M.J. Montgomery, T.N. Todorov, and A.P. Sutton: Power dissipation in nanoscale conductors, *J. Phys.: Cond. Matt.*, **14**, 5377 (2002).
 53. B.C. Stipe, M.A. Rezaei, and W. Ho: Inducing and viewing the rotational motion of a single molecule, *Science*, **279**, 1907 (1998).

54. B.C. Stipe, M.A. Rezaei, and W. Ho: Localization of inelastic tunneling and the determination of atomic-scale structure with chemical specificity, *Phys. Rev. Lett.*, **82**, 1724 (1999).
55. T. Komeda, Y. Kim, M. Kawai, B.N.J. Persson, and H. Ueba: Lateral hopping of molecules induced by excitation of internal vibration mode, *Science*, **295**, 2055 (2002).
56. S. Alavi, B. Larade, J. Taylor, H. Guo, and T. Seideman: Current-triggered vibrational excitation in single-molecule transistors, *Chem. Phys.*, **281**, 293 (2002); T. Seideman: Current-triggered dynamics in molecular-scale devices, *J. Phys.: Cond. Matt.*, **15**, R521 (2003); B.N.J. Persson, and H. Ueba; Theory of inelastic tunneling induced motion of adsorbates on metal surfaces, *Surf. Sci.*, **12**, 502 (2002).
57. S.-W. Hla, L. Bartels, G. Meyer, and K.-H. Rieder: Inducing all steps of a chemical reaction with the scanning tunneling microscope tip: Towards single molecule engineering, *Phys. Rev. Lett.*, **85**, 2777 (2000); G.V. Nazin, X.H. Qiu, and W. Ho: Visualization and spectroscopy of a metal-molecule-metal bridge, *Science*, **302**, 77 (2003); J.R. Hahn, and W. Ho: Oxidation of a single carbon monoxide molecule manipulated and induced with a scanning tunneling microscope, *Phys. Rev. Lett.*, **87**, 166102 (2001).
58. E.L. Wolf, *Principles of electron tunneling spectroscopy* (Oxford University Press, New York, 1985); K.W. Hipps and U. Mazur: Inelastic electron tunneling: An alternative molecular spectroscopy, *J. Phys. Chem.*, **97**, 7803 (1993).
59. H.J. Lee and W. Ho: Single-bond formation and characterization with a scanning tunneling microscope, *Science*, **286**, 1719 (1999); N. Lorente, M. Persson, L.J. Lauhon, and W. Ho: Symmetry selection rules for vibrationally inelastic tunneling, *Phys. Rev. Lett.*, **86**, 2593 (2001); J.R. Hahn, and W. Ho: Single molecule imaging and vibrational spectroscopy with a chemical modified tip of a scanning tunneling microscope, *Phys. Rev. Lett.*, **87**, 196102 (2001); L.J. Lauhon and W. Ho: Direct observation of the quantum tunneling of single hydrogen atoms with a scanning tunneling microscope, *Phys. Rev. Lett.*, **85**, 4566 (2000); J. Gaudioso, J.L. Laudon, and W. Ho: vibrationally mediated negative differential resistance in a single molecule, *Phys. Rev. Lett.*, **85**, 1918 (2000); L.J. Lauhon and W. Ho: Single-electron vibrational spectroscopy and microscopy: CO on Cu(001) and Cu(110), *Phys. Rev. B*, **60**, R8525 (1999); H.J. Lee and W. Ho: Structural determination by single-molecule vibrational spectroscopy and microscopy: Contrast between copper and iron carbonyls, *Phys. Rev. B*, **61**, R16347 (2000).
60. J.R. Hahn, H.J. Lee, and W. Ho: Electronic resonance and symmetry in single-molecule inelastic electron tunneling, *Phys. Rev. Lett.*, **85**, 1914 (2000).
61. N.B. Zhitenev, H. Meng, and Z. Bao: Conductance of small molecular junctions, *Phys. Rev. Lett.*, **88**, 226801 (2002); H. Park, J. Park, A.K.L. Lim, E.H. Anderson, A.P. Alivisatos, and P.L. McEuen: Nanomechanical oscillations in a single-C₆₀ transistor, *Nature*, **407**, 57 (2000).
62. W. Wang, T. Lee, I. Kretzschmar, and M.A. Reed: Inelastic electron tunneling spectroscopy of alkanedithiol self-assembled monolayers, *Nano Lett.*, **4**, 643 (2004); J.G. Kushmerick, J. Lazorcik, C.H. Patterson, R. Shashidhar, D.S. Seferos, and G.C. Bazan: Vibronic contributions to charge transport across molecular junctions, *Nano Lett.*, **4**, 639 (2004).

63. A. Nitzan, M. Galperin, and M.A. Ratner: Inelastic electron tunneling spectroscopy in molecular junctions: Peaks and dips, submitted for publication (cond-mat/0405472).
64. A. Nitzan, J. Jortner, J. Wilkie, et al.: Tunneling time for electron transfer reactions, *J. Phys. Chem. B*, **104**, 5661-5665 (2000).
65. U. Peskin, A. Edlund, I. Bar-On, et al.: Transient resonance structures in electron tunneling through water, *J. Chem. Phys.*, **111**, 7558 (1999).
66. E. Yablonovitch: The chemistry of solid-state electronics, *Science*, **246**, 347 (1989).
67. R. Venugopal, M. Paulsson, S. Goasguen, S. Datta, and M. Lundstrom: A simple quantum mechanical treatment of scattering in nanoscale transistors, *J. App. Phys.*, **93**, 5613 (2003); M. Buttiker: Four-terminal phase-coherent conductance, *Phys. Rev. Lett.*, **57**, 1761 (1986).
68. M. Bixon, and J. Jortner: Vibrational coherence in nonadiabatical dynamics, *J. Chem. Phys.*, **107**, 1470 (1997).
69. M. Bixon, and J. Jortner: Electron transfer via bridges, *J. Chem. Phys.*, **107**, 5154 (1997).
70. Y. Selzer, et al.: Temperature effects on conduction through a molecular junction, *Nanotechnology* 15, S483 (2004); and: Thermally activated conduction in molecular junctions, *J. Am. Chem. Soc.* **126**, 4052 (2004).
71. B. Giese et al.: Direct observation of the hole transfer through DNA by hopping between adenine bases and by tunneling, *Nature* **412**, 318 (2001).
72. D. Segal, A. Nitzan, W.B. Davis, M.R. Wasilewski, and M.A. Ratner: Electron transfer rates in bridged molecular systems. 2. A steady-state analysis of coherent tunneling and thermal transitions, *J. Phys. Chem. B*, **104**, 3817 (2000); D. Segal, and A. Nitzan: Conduction in molecular junctions: Inelastic effects, *Chem. Phys.*, **281**, 235 (2002); D. Segal, and A. Nitzan: Steady-state quantum mechanics of thermally relaxing systems, *Chem. Phys.*, **268**, 315 (2001), and references therein.
73. D. Segal, and A. Nitzan: Heating in current carrying molecular junctions, *J. Chem. Phys.*, **117**, 3915 (2002).
74. X.H. Qiu, G.V. Nazin, and W. Ho: Vibronic states in single molecule electron transport, *Phys. Rev. Lett.*, **92**, 206102 (2004).
75. B.N.J. Persson, and A. Baratoff: Inelastic electron tunneling from a metal tip: The contribution from resonant processes, *Phys. Rev. Lett.*, **59**, 339 (1987).
76. A. Bayman, P. Hansma, and W.C. Kaska: Shifts and dips in inelastic-electron-tunneling spectra due to the tunnel-junction environment, *Phys. Rev. B*, **24**, 2449 (1981).
77. M. Galperin, M.A. Ratner, and A. Nitzan: Hysteresis, switching and negative differential resistance in molecular junctions: A polaron model, *Nano Letters*, **5**(1), 125 (2005).
78. M.R. Wasilewski: Photoinduced electron transfer in supramolecular systems for artificial photosynthesis, *Chem. Rev.*, **92**, 435 (1992).
79. G. Closs, J.R. Miller: Intramolecular long-distance electron transfer in organic molecules, *Science*, **240**, 440 (1988).
80. J. Lehmann, S. Kohler, P. Hanggi, and A. Nitzan: Molecular wires acting as coherent quantum ratchets, *Phys. Rev. Lett.*, **88**, 228305 (2002); J. Lehmann, S. Kohler, P. Hanggi, and A. Nitzan: Rectification of laser-induced electronic transport through molecules, *J. Chem. Phys.*, **118**, 3283 (2002); S. Kohler,

- S. Camalea, M. Strass, J. Lehmann, G.-L. Ingold, and P. Hanggi: Charge transport through a molecule driven by a high-frequency field, *Chem. Phys.*, **296**, 243 (2004); J. Lehmann, S. Camalea, S. Kohler, and P. Hanggi: Laser controlled molecular switches and transistors, *Chem. Phys. Lett.*, **368**, 282 (2003); A. Keller, O. Atabek, M. Ratner, and V. Mujica: Laser-assisted conductance of molecular wires, *J. Phys. B Atomic Molecular & Optical Physics*, **35**, 4981 (2002); A. Tikhonov, R.D. Coalson, and Y. Dahnovsky: Calculating electron transport in a tight-binding model of a field driven molecular wire: Floquet theory, *J. Chem. Phys.*, **116**, 10909 (2002); A. Tikhonov, R.D. Coalson, and Y. Dahnovsky: Calculating electron current in a tight-binding model of a field driven molecular wire: Application to xylyl-dithiol, *J. Chem. Phys.*, **117**, 567 (2002).
81. Y. Kamada, N. Naka, S. Saito, N. Nagasawa, Z.M. Li, and Z.K. Tang: Photo-irradiation effects on electrical conduction of single wall carbon nanotubes, *Solid State Communications*, **123**, 375 (2002); V. Gerstner, A. Knoll, W. Pfeiffer, A. Thon, and G. Gerber: Femtosecond laser assisted scanning tunneling microscopy, *J. Appl. Phys.*, **88**, 4851 (2000); R.J. Schoelkopf, A.A. Kozhevnikov, D.E. Prober, and M.J. Rooks: Observation of “photon-assisted” shot-noise in a phase-coherent conductor, *Phys. Rev. Lett.*, **80**, 2437 (1998); R.J. Schoelkopf, P.J.B., A.A. Kozhevnikov, D.E. Prober, and M.J. Rooks: Frequency dependence of shot noise in a diffusive mesoscopic conductor, *Phys. Rev. Lett.*, **78**, 3370 (1997); B.J. Keay, S.J. Allen, Jr., J. Galán, J.P. Kaminski, K.L. Campman, A.C. Gossard, U. Bhattacharya, and M.J.W. Rodwell: Photon-assisted electric field domains and multiphoton-assisted tunneling in semiconductor superlattices, *Phys. Rev. Lett.*, **75**, 4098 (1995); Dulic D, et al.: One-way optoelectronic switching of photochromic molecules on gold, *Phys. Rev. Lett.*, **91**, 207402 (2003).
82. T. Frauenheim, et al.: Atomistic simulations of complex materials: Ground state and excited-state properties, *J. Phys. Cond. Matt.*, **14**, 3015 (2002).
83. C.W. Bauschlicher, Jr., A. Ricca, Y. Xue, and M.A. Ratner: Current-voltage curves for molecular junctions: pyrene versus diphenylacetylene, *Chem. Phys. Lett.*, **390**, 246 (2004); J.M. Seminario, L.E. Cordova and P.A. Derosa: An ab initio approach to the calculation of current-voltage characteristics of programmable molecular devices, Proc. IEEE **91**, 1958 (2000); Y. Xue, S. Datta, and M.A. Ratner: Charge transfer and “band lineup” in molecular electronic devices: A chemical and numerical interpretation, *J. Chem. Phys.*, **115**, 4292 (2001).
84. K. Tagami, L. Wang, and M. Tsukada: Interface sensitivity in quantum transport through single molecules, *Nano Lett.*, **4**, 209 (2004); E. Emberly and G. Kirczenow: Molecular spintronics: Spin-dependent electron transport in molecular wires, *Chem. Phys.* **281**, 311(2002); E.G Petrov, I.S. Tolokh and V. May: Magnetic field control of an electron tunnel current through a molecular wire, *J. Chem. Phys.* **108**, 4386(1998).
85. Z.Q. Yang and M. Di Ventra: Nonlinear current-induced forces in Si atomic wires, *Phys. Rev. B* **67**, 161311 (2003).
86. X.-Y. Zhu: Charge transport at metal-molecule interfaces: A spectroscopic view, *J. Phys. Chem. B*, **108**, (2004).
87. S. Datta, W. Tian, S. Hong, R. Reifenberger, J.I. Henderson, C.P. Kubiak: Current-voltage characteristics of self-assembled monolayers by scanning tun-

- nelling microscopy, *Phys. Rev. Lett.*, **79**, 2530 (1997); W. Tian, S. Datta, S. Hong, R. Reifenberger, J.I. Henderson, and C.P. Kubiak: Conductance spectra of molecular wires, *J. Chem. Phys.*, **109**, 2874 (1998); Y. Xue, S. Datta, S. Hong, R. Reifenberger, J.I. Henderson, and C.P. Kubiak: Negative differential resistance in the scanning tunneling spectroscopy of organic molecules, *Phys. Rev. B*, **59**, R7852 (1999).
88. V. Mujica, A.E. Roitberg and M. Ratner: Molecular wire conductance: Electrostatic potential spatial profile, *J. Chem. Phys.*, **112**, 6834 (2000)
89. A. Xue, and M.A. Ratner: Microscopic study of electrical transport through individual molecules with metallic contacts. II. Effect of the interface structure, *Phys. Rev. B*, **68**, 115407 (2003).
90. C. Liang, A.W. Ghosh, M. Paulsson, S. Datta: Electrostatic potential profiles of molecular conductors, *Phys. Rev. B*, **69**, 115302 (2004).
91. M. Di Ventra, S.T. Pantelides, and N.D. Lang: The benzene molecule as a molecular resonant-tunneling transistor, *App. Phys. Lett.*, **76**, 3448 (2000).
92. A. Bachtold, et al.: Scanned probe microscopy of electronic transport in carbon nanotubes, *Phys. Rev. Lett.*, **84**, 6082 (2000).
93. Y. Karzazi, et al.: Influence of contact geometry and molecular derivatization on the interfacial interactions between gold and conjugated wires, *Chem. Phys. Lett.*, **387**, 502 (2004); H. Basch, and M.A. Ratner: Binding at molecule/gold transport interfaces. II. Orbitals and density of states, *J. Chem. Phys.*, **119**, 11943 (2003).
94. F. Zahid, M. Paulsson and S. Datta: Electrical conduction through molecules, in *Advanced Semiconductors and Organic Nanotechniques*, H. Morkoc, ed., (Academic Press, New York, 2003).
95. F. Zahid, M. Paulsson et al., to be published.
96. A. Rassolov, M.A. Ratner, and J.A. Pople: Semiempirical models for image electrostatics. I. Bare external charge, *J. Chem. Phys.*, **114**, 2062 (2001).
97. V. Mujica, M. Kemp, and M.A. Ratner: Electron conduction in molecular wires. I. A scattering formalism and II. Application to scanning tunneling microscopy, *J. Chem. Phys.*, **101**, 6849, 6856 (1994).
98. D.S. Kosov: Schrödinger equation for current carrying states, *J. Chem. Phys.*, **116**, 6368 (2002); J. Tomfohr, O. F. Sankey: Theoretical analysis of electron transport through organic molecules, *J. Chem. Phys.*, **120**, 1542 (2004); K. Thygesen et al., work in progress; R. Car, K. Burke, et al, work in progress.
99. J. Reichert, H.B. Weber, M. Mayor, H.V. Lohneysen: Low-temperature conductance measurements on single molecules, *Appl. Phys. Lett.*, **82**, 4137 (2003); J.O. Lee et al.: Electrical transport study of phenylene-based π -conjugated molecules in a three terminal geometry, *Annals Of The New York Academy Of Sciences*, **1006**, 122 (2003); D. Janes et al., to be published; M.A. Reed, et al.: Conductance of a molecular junction, *Science*, **278**, 252 (1997). The structure assumed here may be incorrect: e.g. P.L. Pugmire, M.J. Tarlov, R.D. van Zee: The structure of benzenedimethanethiol self-assembled monolayers on gold grown by solution and vapor techniques, *Langmuir*, **19**, 3720 (2003).
100. N.P. Guisinger, M.E. Greene, R. Basu, A.S. Baluch, M.C. Hersam: Room temperature negative differential resistance through individual organic molecules on silicon surfaces, *Nano Lett.*, **4**, 55 (2004).

101. X.P. Cao, R.J. Hamers: Silicon surfaces as electron acceptors: Dative bonding of amines with Si(001) and Si(111) surfaces, *J. Am. Chem. Soc.* **123**, 10988 (2001); S.N. Patitsas et al.: Current-induced organic-silicon bond breaking: Consequences for molecular devices, *Surf. Sci.* **457**, L425 (2000)
102. J.G. Kushmerick, et al.: Understanding charge transport in molecular electronics, *Ann. NY Acad. Sci.* **1006**, 277 (2003)
103. X.D. Cui, et al.: Reproducible measurement of single-molecule conductivity, *Science*, **294**, 571 (2001).
104. B. Mantooh, et al.: Cross-correlation image tracking for adsorbate analysis and drift correction, *Rev. Sci. Inst.*, **73**, 313 (2002).
105. R.P. Andres, et al.: “Coulomb staircase” at room temperature in a self-assembled molecular nanostructure, *Science* **272**, 1323 (1996); A. Dhirani, et al.: Self-assembled molecular rectifiers, *J. Chem. Phys.* **106**, 5249 (1997); R. McCreery, et al.: Molecular rectification and conductance switching in carbon-based molecular junctions by structural rearrangement accompanying electron injection, *J. Am. Chem. Soc.* **125**, 10748 (2003); D.J. Wold, et al.: Distance dependence of electron tunneling through self-assembled monolayers measured by conducting probe atomic force microscopy: Unsaturated versus saturated molecular junctions, *J. Phys. Chem. B*, **106**, 2813 (2002)
106. C. Lin, and C.R. Kagan: Layer-by-layer growth of metal-metal bonded supramolecular thin films and its use in the fabrication of lateral nanoscale devices, *J. Am. Chem. Soc.*, **125**, 336 (2003).
107. Y. Selzer, et al.: Temperature effects on conduction through a molecular junction, *Nanotechnology*, **15**, S483 (2004).
108. H. Basch, and M.A. Ratner, unpublished.
109. G. Poirier: Characterization of organosulfur molecular monolayers on Au(111) using scanning tunneling microscopy, *Chem. Revs.*, **97**, 1117 (1997).
110. S. Liu, R. Maoz, J. Sagiv: Planned nanostructures of colloidal gold via self-assembly on hierarchically assembled organic bilayer template patterns with in-situ generated terminal amino functionality, *Nano Lett.*, **4**, 845 (2004).
111. X.Y. Xiao, B.Q. Xu, N.J. Tao: Measurement of single molecule conductance: Benzenedithiol and benzenedimethanethiol; *Nano Lett.*, **4**, 267 (2004).
112. W. Wang, T. Lee, and M.A. Reed: Mechanism of electron conduction in self-assembled alkanethiol monolayer devices, *Phys. Rev. B*, **68**, 035416 (2003).
113. J.W. Gadzuk and E.W. Plummer: Field emission energy distribution (FEED), *Revs. Mod. Phys.*, **45**, 487 (1973).
114. G.G. Fagas, A. Kambili and M. Elstner: Complex band structure: A method to determine the off-resonant electron transport in oligomers, *Chem. Phys. Lett.*, **389**, 268 (2004); V. Mujica, and M.A. Ratner: Current-voltage characteristics of tunneling molecular junctions for off-resonance injection, *Chem. Phys.*, **264**, 395 (2002).
115. W. Wang, T. Lee, and M.A. Reed: Intrinsic molecular electronic transport: Mechanisms and methods, *J. Phys. Chem. B*, in press.
116. C.C. Kaun, H. Guo: Resistance of alkanethiol molecular wires, *Nano Lett.*, **3**, 1521 (2003).
117. H. Basch, and M.A. Ratner: Binding at molecule/gold transport interfaces. V. Comparison of different metals and molecular bridges, submitted to *J. Chem. Phys.*
118. A. Salomon, et al.: Comparison of electronic transport measurements on organic molecules, *Adv. Mat.* **15**, 1881 (2003)

119. P.E. Kornilovitch, A.M. Bratkovsky, and R. S. Williams: Bistable molecular conductors with a field-switchable dipole group, *Phys. Rev. B*, **66**, 245413 (2002).
120. E.G. Emberly, and G. Kirczenow: The smallest molecular switch, *Phys. Rev. Lett.*, **91**, 188301 (2003).
121. A. Troisi, M.A. Ratner: Conformational molecular rectifiers, *Nano Lett.*, **4**, 591 (2004).
122. T. Rakshit, G.C. Liang, A. Ghosh, S. Datta: Silicon based molecular electronics, cond-mat/0305695 (2003), submitted to *Phys. Rev. Lett.*

AC-Driven Transport Through Molecular Wires

Peter Hänggi, Sigmund Kohler, Jörg Lehmann, and Michael Strass

Institut für Physik, Universität Augsburg, Universitätsstraße 1, 86135 Augsburg, Germany

Abstract. We consider electrical transport properties of a molecular wire under the influence of time-dependent electromagnetic fields. A formalism based on Floquet theory is derived which allows to calculate both the dc current through the molecular wire and the associated noise power. Approximations for the case of a weak wire-lead coupling are studied in detail.

1 Introduction

Owing to the recent experimental progress in the fabrication and characterisation of nanostructures involving single or a few molecules, the research field of molecular electronics currently enjoys a vivid activity, as exemplified by the present volume. Thereby, the main focus has been put on contacting single molecules by nanoelectrodes. This allows to apply a transport voltage and to measure the resulting electrical current [1–8]. For the corresponding theoretical investigations, two lines of research are presently followed. The one is the *ab-initio* computation of the orbitals relevant for the motion of excess charges through the molecular wire [9–12], as described in Chaps. 3–6. The other line employs rather universal models to gain a qualitative understanding of the transport mechanisms involved [13–19]. Two particular problems addressed within model calculations are the conduction mechanism in the presence of electron-phonon coupling [14] and the length dependence of the current-voltage characteristics [13, 17]. The present work also employs rather general models: We describe the molecules by a linear arrangement of tight-binding levels with the terminating sites attached to leads.

Typical energy scales of molecules lie in the infrared regime where most of today's lasers work. Hence, lasers represent a natural possibility to excite the electrons of the molecular wire and, thus, to study the corresponding changes of the conduction properties [20]. One particular question in this context is the influence of excitations by electromagnetic fields and oscillatory gate voltages on the electron transport. Such excitations bear intriguing phenomena like photon-assisted electron tunnelling [21–23] and quantum ratchet effects [24, 25]. From a fundamental point of view, these effects are of interest because the external fields enable selective electron excitations and allow to study their interplay with the underlying transport mechanism. In practical

applications, time-dependent effects can be used to control and steer currents in coherent conductors. Such control schemes can be valuable, however, only if they operate at tolerable noise levels. Thus, the corresponding current noise is also of prominent interest.

An experimental starting point for the investigation of the influence of electromagnetic fields on molecular conduction is the laser excitation of electrons to higher orbitals of the contacted molecule. The resulting changes of the current through a contacted molecule due to the influence of a laser field are studied. In particular, we focus on the modification of the length dependence of the conductivity [26–28]. At present, the corresponding experiments are attempted, but still no clearcut effect has been reported. The molecule-lead contacts seem stable even against relatively intense laser fields, but a main problem is the exclusion and suppression of side effects like, e.g. heating of the break junction which otherwise might distort the molecule-tip setup and, thus, be responsible for the observed enhancement of the conductance.

2 Basic Concepts

2.1 Model for Driven Molecular Wire Coupled to Leads

The entire setup of the ac-driven molecular wire coupled to leads is described by the time-dependent Hamiltonian

$$H(t) = H_{\text{wire}}(t) + H_{\text{leads}} + H_{\text{contacts}} , \quad (1)$$

where the different terms correspond to the molecular wire, the leads, and the wire-lead couplings, respectively. We focus on the regime of coherent quantum transport where the main physics at work occurs on the wire itself. In doing so, we neglect other possible influences originating from driving induced hot electrons in the leads, dissipation on the wire and, as well, electron-electron interaction effects. Then, in a tight-binding (Hückel) approximation with N localised atomic orbitals $|n\rangle$, the wire Hamiltonian reads

$$H_{\text{wire}}(t) = \sum_{n,n'} H_{nn'}(t) c_n^\dagger c_{n'} . \quad (2)$$

The fermion operators c_n , c_n^\dagger annihilate and create, respectively, an electron in the orbital $|n\rangle$. The influence of an applied ac field with frequency $\Omega = 2\pi/T$ results in a periodic time-dependence of the wire Hamiltonian: $H_{nn'}(t+T) = H_{nn'}(t)$. The leads are modelled by ideal electron gases,

$$H_{\text{leads}} = \sum_q (\epsilon_{Lq} c_{Lq}^\dagger c_{Lq} + \epsilon_{Rq} c_{Rq}^\dagger c_{Rq}) , \quad (3)$$

where c_{Lq}^\dagger (c_{Rq}^\dagger) creates an electron in the state $|Lq\rangle$ ($|Rq\rangle$) with energy ϵ_{Lq} (ϵ_{Rq}) in the left (right) lead. The tunnelling Hamiltonian

$$H_{\text{contacts}} = \sum_q \left(V_{Lq} c_{Lq}^\dagger c_1 + V_{Rq} c_{Rq}^\dagger c_N \right) + \text{h.c.} \quad (4)$$

establishes the contact between the sites $|1\rangle$, $|N\rangle$ and the respective lead, as sketched in Fig. 1. This tunnelling coupling is described by the spectral density

$$\Gamma_\ell(\epsilon) = 2\pi \sum_q |V_{\ell q}|^2 \delta(\epsilon - \epsilon_{\ell q}) \quad (5)$$

of lead ℓ , with $\ell = L, R$. Assuming that the lead modes are dense $\Gamma_\ell(\epsilon)$ becomes a smooth function. Although we will derive expressions for arbitrary spectral density, we here remark that, often, one is interested mainly in the properties of the molecular wire itself and not in the details of the wire-lead coupling. Then it is convenient to assume in the relevant regime, the spectral density to be energy-independent and, thus, to employ the so-called wide-band limit $\Gamma_\ell(\epsilon) \rightarrow \Gamma_\ell = \text{const}$.

To fully specify the dynamics, we choose as an initial condition for the left/right lead a grand-canonical electron ensemble at temperature T and electro-chemical potential $\mu_{L/R}$, respectively. Then, at initial time t_0 , the only nontrivial expectation values of the lead operators read

$$\langle c_{\ell' q'}^\dagger c_{\ell q} \rangle = f_\ell(\epsilon_{\ell q}) \delta_{\ell \ell'} \delta_{qq'} \quad (6)$$

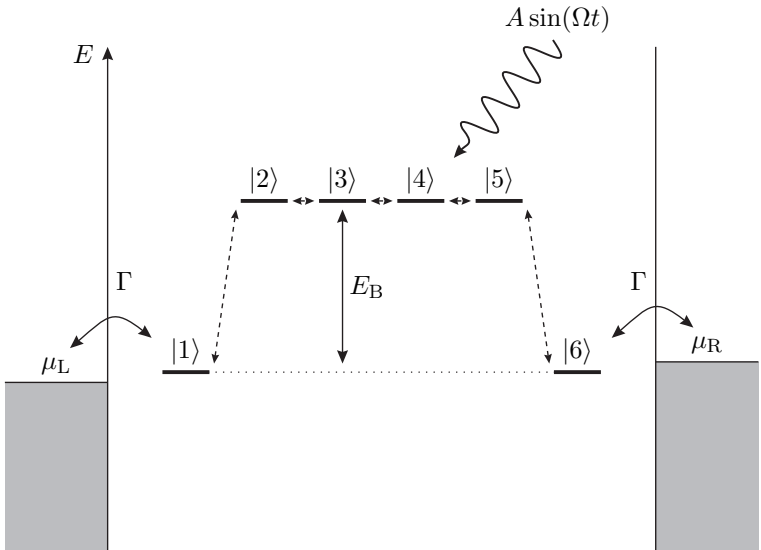


Fig. 1. Level structure of a molecular wire bridge consisting $N = 6$ orbitals. The two end sites are coupled to two leads with chemical potentials μ_L and $\mu_R = \mu_L + eV$ and are bridge by the $N - 2$ orbitals lying E_B above in energy. All adjacent orbitals are coupled by the tunnelling matrix elements Δ . A laser with frequency Ω and amplitude A acts on the molecular wire

where $f_\ell(\epsilon) = (1 + \exp[(\epsilon - \mu_\ell)/k_B T])^{-1}$ denotes the Fermi function in lead ℓ and k_B is the Boltzmann constant. An applied voltage V maps to a chemical potential difference $\mu_R - \mu_L = eV$ with $-e$ being the electron charge.

2.2 Current Through Static Molecular Wire

Before elucidating the influence of a driving field, let us first briefly review the scattering approach which applies to the corresponding static situation, i.e. without driving. In the absence of interactions, the current through a nanosystem like a molecular wire considered here, can be expressed in terms of the transmission $T(E)$, i.e., the probability for an electron of a given energy E being transmitted from one lead to the other. This allows to write the current as

$$I = \frac{e}{2\pi\hbar} \int dE [f_R(E) - f_L(E)] T(E). \quad (7)$$

For the evaluation of the transmission, one often uses the relation [29–31]

$$T(E) = \text{tr}[G^\dagger(E) \Sigma_R(E) G(E) \Sigma_L(E)], \quad (8)$$

which expresses the transmission in terms of the retarded Green function $G(E)$ of the system and the self-energies $\Sigma_{L/R}(E)$ resulting from the coupling to the leads. The trace in the last equation sums over all single-particle states of the wire.

Besides the mean value of the current, another quantity of interest is its fluctuation, i.e., the current noise which is described by the symmetrised correlation function

$$S_\ell(t, t') = \frac{1}{2} \langle \Delta I_\ell(t) \Delta I_\ell(t') + \Delta I_\ell(t') \Delta I_\ell(t) \rangle \quad (9)$$

of the current fluctuation operator $\Delta I_\ell(t) = I_\ell(t) - \langle I_\ell(t) \rangle$. For a stationary process, the correlation function $S(t, t') = S(t - t')$ is a function of only the time difference. The noise strength can be characterised by the zero-frequency component of $S_\ell(\tau)$,

$$\bar{S}_\ell = \int_{-\infty}^{\infty} d\tau S_\ell(\tau). \quad (10)$$

It can be shown that due to charge-conservation for two-terminal devices \bar{S}_ℓ is independent of the contact ℓ , i.e., $\bar{S}_L = \bar{S}_R \equiv \bar{S}$. The noise strength S may be expressed in terms of the transmission function $T(E)$ as [32]

$$S = \frac{e^2}{2\pi\hbar} \int dE \left\{ T(E) [f_L(E)[1 - f_L(E)] + f_R(E)[1 - f_R(E)]] + T(E)[1 - T(E)] [f_R(E) - f_L(E)]^2 \right\}. \quad (11)$$

As a dimensionless measure for the *relative* noise strength, we employ the so-called Fano factor [33]

$$F = \frac{\bar{S}}{e|\bar{I}|} , \quad (12)$$

where \bar{I} denotes the time-average of the current expectation value $\langle I_\ell(t) \rangle$. Note that in a two-terminal device, the absolute value of the average current is independent of the contact ℓ . The Fano factor is constructed such that for uncorrelated events $F = 1$, i.e., it describes the noise levels with respect to a Poisson process. Historically, the zero-frequency noise (10) contains a factor 2, i.e. $\bar{S}' = 2\bar{S}$, resulting from a different definition of the Fourier transform. Then, the Fano factor is defined as $F = \bar{S}'/2e|\bar{I}|$.

3 Floquet Approach to the Driven Transport Problem

We now derive from the model described in Sect. 2.1 expressions for both the current through the molecular wire and the associated noise by solving the corresponding Heisenberg equations of motions. To do so, we start from the equations of motion for the annihilation operators in lead ℓ ,

$$\dot{c}_{\ell q} = -\frac{i}{\hbar}\epsilon_{\ell q} c_{\ell q} - \frac{i}{\hbar}V_{\ell q} c_{n_\ell} , \quad (13)$$

which are straightforwardly integrated to read

$$c_{\ell q}(t) = c_{\ell q}(t_0)e^{-i\epsilon_{\ell q}(t-t_0)/\hbar} - \frac{i}{\hbar}V_{\ell q} \int_0^{t-t_0} d\tau e^{-i\epsilon_{\ell q}\tau/\hbar} c_{n_\ell}(t-\tau) , \quad (14)$$

where n_ℓ denotes the molecular wire site attached to lead ℓ , i.e., $n_L = 1$ and $n_R = N$. Inserting (14) into the Heisenberg equations for the wire operators yields in the asymptotic limit $t_0 \rightarrow -\infty$

$$\dot{c}_{n_\ell}(t) = -\frac{i}{\hbar} \sum_{n'} H_{n_\ell, n'}(t) c_{n'}(t) - \frac{1}{\hbar} \int_0^\infty d\tau \Gamma_\ell(\tau) c_{n_\ell}(t-\tau) + \xi_\ell(t) , \quad (15)$$

$$\dot{c}_n(t) = -\frac{i}{\hbar} \sum_{n'} H_{nn'}(t) c_{n'}(t) , \quad n = 2, \dots, N-1 . \quad (16)$$

where the lead response function $\Gamma_\ell(t)$ results from the Fourier transformation of the spectral density [5],

$$\Gamma_\ell(t) = \int_{-\infty}^{+\infty} \frac{d\epsilon}{2\pi\hbar} e^{-i\epsilon t/\hbar} \Gamma_\ell(\epsilon) . \quad (17)$$

In the wide-band limit $\Gamma_\ell(\epsilon) \rightarrow \Gamma_\ell$, one obtains $\Gamma_\ell(t) = \Gamma_\ell \delta(t)$ and in this case the equations of motion for the wire operators are memory-free. The influence of the operator-valued Gaussian noise

$$\xi_\ell(t) = -\frac{i}{\hbar} \sum_q V_{\ell q}^* e^{-i\epsilon_{\ell q}(t-t_0)/\hbar} c_{\ell q}(t_0) \quad (18)$$

is fully specified by the expectation values $\langle \xi_\ell(t) \rangle = 0$ and

$$\langle \xi_{\ell'}^\dagger(t') \xi_\ell(t) \rangle = \delta_{\ell\ell'} \frac{1}{2\pi\hbar^2} \int d\epsilon e^{-i\epsilon(t-t')/\hbar} \Gamma_\ell(\epsilon) f_\ell(\epsilon), \quad (19)$$

which follow directly from the definition (18) and the initial conditions (6). It is convenient to define the Fourier representation of the noise operator, $\xi_\ell(\epsilon) = \int dt \exp(i\epsilon t/\hbar) \xi_\ell(t)$ whose correlation function

$$\langle \xi_\ell^\dagger(\epsilon) \xi_{\ell'}(\epsilon') \rangle = 2\pi \Gamma_\ell(\epsilon) f_\ell(\epsilon) \delta(\epsilon - \epsilon') \delta_{\ell\ell'} \quad (20)$$

follows directly from (19).

3.1 Retarded Green Function

The equations of motion (15) and (16) represent a set of linear inhomogeneous equations and, thus, can be solved with the help of a retarded Green function $G(t, t') = -(i/\hbar) U(t, t') \theta(t - t')$ which obeys

$$\left(i\hbar \frac{d}{dt} - \mathcal{H}(t) \right) G(t, t') + i \int_0^\infty d\tau \Gamma(\tau) G(t - \tau, t') = \delta(t - t') \quad (21)$$

where $\Gamma(t) = |1\rangle \Gamma_L(t) \langle 1| + |N\rangle \Gamma_R(t) \langle N|$ and $\mathcal{H}(t)$ is the one-particle Hamiltonian corresponding to (2). At this stage, it is important to note upon inspection that the propagator of the homogeneous equations obeys $U(t, t') = U(t + T, t' + T)$ and, accordingly, the retarded Green function

$$G(t, \epsilon) = -\frac{i}{\hbar} \int_0^\infty d\tau e^{i\epsilon\tau/\hbar} U(t, t - \tau) = G(t + T, \epsilon) \quad (22)$$

is also T -periodic in the time argument. Thus, we can employ the Fourier decomposition $G(t, \epsilon) = \sum_k e^{-ik\Omega t} G^{(k)}(\epsilon)$, with the coefficients

$$G^{(k)}(\epsilon) = \frac{1}{T} \int_0^T dt e^{ik\Omega t} G(t, \epsilon). \quad (23)$$

Physically, $G^{(k)}(\epsilon)$ describes the propagation of an electron with initial energy ϵ under the absorption (emission) of $|k|$ photons for $k > 0$ ($k < 0$). In the limiting case of a time-independent situation, all sideband contributions with $k \neq 0$ vanish and $G(t, \epsilon)$ becomes time-independent and identical to $G^{(0)}(\epsilon)$.

From the definition (21) of the Green function and its Fourier representation (22), it can be shown that the solution of the Heisenberg equations (15), (16) reads

$$c_n(t) = \frac{i}{2\pi} \sum_\ell \int d\epsilon e^{-i\epsilon t/\hbar} G_{n,n_\ell}(t, \epsilon) \xi_\ell(\epsilon), \quad (24)$$

where we have defined $G_{n,n_\ell}(t,t') = \langle n|G(t,t')|n_\ell\rangle$.

Below, we need for the elimination of back-scattering terms the relation

$$\begin{aligned} G^\dagger(t, \epsilon') - G(t, \epsilon) &= \left(i\hbar \frac{d}{dt} - \epsilon' + \epsilon \right) G^\dagger(t, \epsilon') G(t, \epsilon) \\ &\quad + i \int_0^\infty d\tau e^{i\epsilon\tau/\hbar} G^\dagger(t, \epsilon') \Gamma(\tau) G(t - \tau, \epsilon) \\ &\quad + i \int_0^\infty d\tau e^{-i\epsilon'\tau/\hbar} G^\dagger(t - \tau, \epsilon') \Gamma^\dagger(\tau) G(t, \epsilon). \end{aligned} \quad (25)$$

A proof starts from the definition of the Green function, (21). By Fourier transformation with respect to t' , we obtain the relation

$$\left(i\hbar \frac{d}{dt} + \epsilon - \mathcal{H}(t) \right) G(t, \epsilon) + i \int_0^\infty d\tau e^{i\epsilon\tau/\hbar} \Gamma(\tau) G(t - \tau, \epsilon) = \mathbf{1} \quad (26)$$

which we multiply by $G^\dagger(t, \epsilon)$ from the left. The difference between the resulting expression and its hermitian adjoint with ϵ and ϵ' interchanged is relation (25).

3.2 Current Through the Driven Molecular Wire

Owing to charge conservation, the (net) current flowing from lead ℓ into the molecular wire is determined by the negative time derivative of the charge in lead ℓ . Thus, the current operator reads $I_\ell = ie[H(t), N_\ell]/\hbar$, where $N_\ell = \sum_q c_{\ell q}^\dagger c_{\ell q}$ denotes the corresponding electron number and $-e$ the electron charge. By using (14) and (18), we obtain

$$\begin{aligned} I_L(t) &= \frac{e}{\hbar} \int_0^\infty d\tau \{ \Gamma_L(\tau) c_1^\dagger(t) c_1(t - \tau) + \Gamma_L^*(\tau) c_1^\dagger(t - \tau) c_1(t) \} \\ &\quad - e \{ c_1^\dagger(t) \xi_L(t) + \xi_L^\dagger(t) c_1(t) \}. \end{aligned} \quad (27)$$

This operator-valued expression for the time-dependent current is a convenient starting point for the evaluation of expectation values like the dc and ac current and the current noise.

Time-Average Current

To obtain the current $\langle I_L(t) \rangle$, we insert the solution (24) of the Heisenberg equation into the current operator (27) and use the expectation values (20). The resulting expression

$$\begin{aligned} \langle I_L(t) \rangle &= \frac{2e}{\hbar} \sum_\ell \int d\epsilon \int_0^\infty d\tau \Gamma_\ell(\epsilon) f_\ell(\epsilon) \text{Im} e^{i\epsilon\tau/\hbar} G_{1\ell}^*(t, \epsilon) \Gamma_L(\tau) G_{1\ell}(t - \tau, \epsilon) \\ &\quad + 2e \int d\epsilon \Gamma_L(\epsilon) f_L(\epsilon) \text{Im} G_{11}(t, \epsilon) \end{aligned} \quad (28)$$

still contains back-scattering terms G_{11} and, thus, is not of a “scattering form”. Indeed, bringing (28) into a form that resembles the static current formula (7) requires some tedious algebra. Such a derivation has been presented for the linear conductance of time-independent systems [30], for tunnelling barriers [29] and mesoscopic conductors [31] in the static case for finite voltage, and for a wire consisting of levels that couple equally strong to both leads [34]. For the periodically time-dependent case in the absence of electron-electron interactions, such an expression has been *derived* only recently [35, 36].

Inserting the matrix element $\langle 1| \dots |1\rangle$ of (25) eliminates the back-scattering terms and yields for the time-dependent current the expression

$$\langle I_L(t) \rangle = \frac{e}{\hbar} \int d\epsilon \{ T_{LR}(t, \epsilon) f_R(\epsilon) - T_{RL}(t, \epsilon) f_L(\epsilon) \} - \frac{d}{dt} q_L(t) \quad (29)$$

where

$$q_L(t) = \frac{e}{2\pi} \int d\epsilon \Gamma_L(\epsilon) \sum_n |G_{n1}(t, \epsilon)|^2 f_L(\epsilon) \quad (30)$$

denotes the charge oscillating between the left lead and the wire. Obviously, since $q_L(t)$ is time-periodic and bounded, its time derivative cannot contribute to the average current. The corresponding charge arising from the right lead, $q_R(t)$, is *a priori* unrelated to $q_L(t)$; the actual charge on the wire reads $q_L(t) + q_R(t)$. The time-dependent current is determined by the time-dependent transmission

$$T_{LR}(t, \epsilon) = 2 \operatorname{Re} \int_0^\infty d\tau e^{i\epsilon\tau/\hbar} \Gamma_L(\tau) G_{1N}^*(t, \epsilon) G_{1N}(t - \tau, \epsilon) \Gamma_R(\epsilon). \quad (31)$$

The corresponding expression for $T_{RL}(t, \epsilon)$ follows from the replacement $(L, 1) \leftrightarrow (R, N)$. We emphasise that (29) obeys the form of the current formula (7) for a *static* conductor within a scattering formalism. In particular, consistent with [37, 38], no “Pauli blocking factors” $(1 - f_\ell)$ appear in our derivation. In contrast to a static situation, this is in the present context relevant since for a driven system generally $\bar{w}_{Lq, Rq'} \neq \bar{w}_{Rq', Lq}$, such that a contribution proportional to $f_L(\epsilon_{Lq'})f_R(\epsilon_{Rq})$ would not cancel [37, 39].

The dc current obtained from (29) by time-averaging can be written in an even more compact form if we insert for the Green function the Fourier representation (23). This results in

$$\bar{I} = \frac{e}{h} \sum_k \int d\epsilon \left\{ T_{LR}^{(k)}(\epsilon) f_R(\epsilon) - T_{RL}^{(k)}(\epsilon) f_L(\epsilon) \right\}, \quad (32)$$

where

$$T_{LR}^{(k)}(\epsilon) = \Gamma_L(\epsilon + k\hbar\Omega) \Gamma_R(\epsilon) |G_{1N}^{(k)}(\epsilon)|^2, \quad (33)$$

$$T_{RL}^{(k)}(\epsilon) = \Gamma_R(\epsilon + k\hbar\Omega) \Gamma_L(\epsilon) |G_{N1}^{(k)}(\epsilon)|^2, \quad (34)$$

denote the transmission probabilities for electrons from the right to the left lead and vice versa, respectively, with initial energy ϵ and final energy $\epsilon + k\hbar\Omega$, i.e., the probability for an scattering event under the absorption (emission) of $|k|$ photons if $k > 0$ ($k < 0$).

For a static situation, the transmissions $T_{LR}^{(k)}(\epsilon)$ and $T_{RL}^{(k)}(\epsilon)$ are identical and contributions with $k \neq 0$ vanish. Thus, it is possible to write the current (32) in the form (7) as a product of a *single* transmission $T(\epsilon)$, which is independent of the direction, and the difference of the Fermi functions, $f_R(\epsilon) - f_L(\epsilon)$. We emphasise that in the driven case this no longer holds true.

Noise Power

Like in the static case, we characterise the noise power by the zero-frequency component of the current-current correlation function (9). However, in the driven case, $S_\ell(t, t') = S_\ell(t + T, t' + T)$ is still time-dependent. Since it shares the time-periodicity of the driving, it is possible to characterise the noise level by the zero-frequency component of $S_\ell(t, t - \tau)$ averaged over the driving period,

$$\bar{S}_\ell = \frac{1}{T} \int_0^T dt \int_{-\infty}^{\infty} d\tau S_\ell(t, t - \tau) . \quad (35)$$

It can be shown [36] that for driven two-terminal devices, \bar{S}_ℓ is independent of the contact ℓ , i.e., $\bar{S}_L = \bar{S}_R \equiv \bar{S}$.

We start by writing $S_L(t, t - \tau)$ with the current operator (27) and insert the solution (24) of the Heisenberg equations of motion. Then, we again employ relation (25) and finally obtain the more symmetric expression

$$\begin{aligned} \bar{S} = & \frac{e^2}{\hbar} \sum_k \int d\epsilon \left\{ \Gamma_R(\epsilon_k) \Gamma_R(\epsilon) \left| \sum_{k'} \Gamma_L(\epsilon_{k'}) G_{1N}^{(k'-k)}(\epsilon_k) [G_{1N}^{(k')}(\epsilon)]^* \right|^2 f_R(\epsilon) \bar{f}_R(\epsilon_k) \right. \\ & \left. + \Gamma_R(\epsilon_k) \Gamma_L(\epsilon) \left| \sum_{k'} \Gamma_L(\epsilon_{k'}) G_{1N}^{(k'-k)}(\epsilon_k) [G_{11}^{(k')}(\epsilon)]^* - i G_{1N}^{(-k)}(\epsilon_k) \right|^2 f_L(\epsilon) \bar{f}_R(\epsilon_k) \right\} \\ & + \text{same terms with the replacement } (L, 1) \leftrightarrow (R, N) . \end{aligned} \quad (36)$$

We have defined $\epsilon_k = \epsilon + k\hbar\Omega$ and replaced the sums over the lead states by energy integrations using the spectral density (5).

Floquet Decomposition in the Wide-Band Limit

We now consider the wide-band limit $\Gamma_\ell(\epsilon) = \Gamma_\ell$ and, consequently, $\Gamma_\ell(t) = \Gamma_\ell \delta(\tau)$. Then, solving the equations of motion (21) for the Green function is equivalent to computing a complete set of solutions for the equation

$$i\hbar \frac{d}{dt} |\psi(t)\rangle = (\mathcal{H}_{\text{wire}}(t) - i\Sigma) |\psi(t)\rangle , \quad (37)$$

with the self-energy $\Sigma = |1\rangle\Gamma_L/2\langle 1| + |N\rangle\Gamma_R/2\langle N|$ resulting from the coupling to the leads. Equation (37) is linear and possesses time-dependent, \mathcal{T} -periodic coefficients. Thus, it is possible to construct a complete set of solutions with the Floquet ansatz

$$|\psi_\alpha(t)\rangle = \exp[(-i\epsilon_\alpha/\hbar - \gamma_\alpha)t] |u_\alpha(t)\rangle , \quad (38)$$

$$|u_\alpha(t)\rangle = \sum_k \exp(-ik\Omega t) |u_{\alpha,k}\rangle . \quad (39)$$

The so-called Floquet states $|u_\alpha(t)\rangle$ obey the time-periodicity of $\mathcal{H}_{\text{wire}}(t)$ and have been decomposed into a Fourier series. In a Hilbert space that is extended by a periodic time coordinate, the so-called Sambe space [40], they obey the Floquet eigenvalue equation [41, 42]

$$\left(\mathcal{H}_{\text{wire}}(t) - i\Sigma - i\hbar \frac{d}{dt}\right) |u_\alpha(t)\rangle = (\epsilon_\alpha - i\hbar\gamma_\alpha) |u_\alpha(t)\rangle . \quad (40)$$

Due to the Brillouin zone structure of the Floquet spectrum [40, 41, 43], it is sufficient to compute all eigenvalues of the first Brillouin zone, $-\hbar\Omega/2 < \epsilon_\alpha \leq \hbar\Omega/2$. Since the operator on the l.h.s. of (40) is non-Hermitian, the eigenvalues $\epsilon_\alpha - i\hbar\gamma_\alpha$ are generally complex valued and the (right) eigenvectors are not mutually orthogonal. Thus, to determine the propagator, we need to solve also the adjoint Floquet equation yielding again the same eigenvalues but providing the adjoint eigenvectors $|u_\alpha^+(t)\rangle$. It can be shown that the Floquet states $|u_\alpha(t)\rangle$ together with the adjoint states $|u_\alpha^+(t)\rangle$ form at equal times a complete bi-orthogonal basis: $\langle u_\alpha^+(t)|u_\beta(t)\rangle = \delta_{\alpha\beta}$ and $\sum_\alpha |u_\alpha(t)\rangle\langle u_\alpha^+(t)| = \mathbf{1}$. A proof requires to account for the time-periodicity of the Floquet states since the eigenvalue equation (40) holds in a Hilbert space extended by a periodic time coordinate [41, 44].

Using the Floquet equation (40), it is straightforward to show that the propagator can be written as

$$U(t, t') = \sum_\alpha e^{-i(\epsilon_\alpha/\hbar - i\gamma_\alpha)(t-t')} |u_\alpha(t)\rangle\langle u_\alpha^+(t')| , \quad (41)$$

where the sum runs over all Floquet states within one Brillouin zone. Consequently, the Fourier coefficients of the Green function read

$$G^{(k)}(\epsilon) = -\frac{i}{\hbar} \int_0^\mathcal{T} \frac{dt}{T} e^{ik\Omega t} \int_0^\infty d\tau e^{i\epsilon\tau/\hbar} U(t, t-\tau) \quad (42)$$

$$= \sum_{\alpha, k'} \frac{|u_{\alpha, k'+k}\rangle\langle u_{\alpha, k'}^+|}{\epsilon - (\epsilon_\alpha + k'\hbar\Omega - i\hbar\gamma_\alpha)} . \quad (43)$$

In general, the Floquet equation (40) has to be solved numerically. From the resulting Floquet states and quasienergies one directly obtains the Green

function (23). In the zero temperature limit considered here, the Fermi functions in the expressions for the average current (32) and the zero-frequency noise (36) become step functions. Therefore, the integrands are rational functions and the remaining energy integrals can be performed analytically.

4 Weak-Coupling Approximations

In the previous section, exact expression for the dc current and the zero-frequency noise for a periodic but otherwise arbitrary ac driving have been derived. Within the wide-band limit, both quantities can be expressed in terms of the solutions of the Floquet equation (40), i.e., the solution of a non-Hermitian eigenvalue problem in an extended Hilbert space. For the case of energy-dependent wire-lead coupling $\Gamma_\ell(\epsilon)$, the corresponding computation becomes rather cumbersome. Moreover, for finite temperatures, the energy integration in the expressions (32) and (36) have to be performed numerically. In the next two sections, we shall demonstrate how these problems can be overcome in the important special case of a weak wire-lead coupling.

4.1 Asymptotic Weak Coupling

In the limit of very weak wire-lead coupling, i.e., for coupling constants Γ_ℓ which are far lower than all other energy scales of the wire Hamiltonian, it is possible to treat the self-energy contribution $-i\Sigma$ in the non-Hermitian Floquet equation (40) as perturbation. Then, the zeroth order of the Floquet equation

$$\left(\mathcal{H}_{\text{wire}}(t) - i\hbar \frac{d}{dt} \right) |\phi_\alpha(t)\rangle = \epsilon_\alpha^0 |\phi_\alpha(t)\rangle, \quad (44)$$

describes the driven wire in the absence of the leads, where $|\phi_\alpha(t)\rangle = \sum_k \exp(-ik\Omega t) |\phi_{\alpha,k}\rangle$ are the “usual” Floquet states with quasienergies ϵ_α^0 . In the absence of degeneracies the first order correction to the quasienergies is $-i\hbar\gamma_\alpha^1$ where

$$\gamma_\alpha^1 = \frac{1}{\hbar} \int_0^T \frac{dt}{T} \langle \phi_\alpha(t) | \Sigma | \phi_\alpha(t) \rangle \quad (45)$$

$$= \frac{\Gamma_L}{2\hbar} \sum_k |\langle 1 | \phi_{\alpha,k} \rangle|^2 + \frac{\Gamma_R}{2\hbar} \sum_k |\langle N | \phi_{\alpha,k} \rangle|^2. \quad (46)$$

Since the first order correction to the Floquet states will contribute to neither the current nor the noise, the zeroth-order contribution $|u_\alpha(t)\rangle = |u_\alpha^+(t)\rangle = |\phi_\alpha(t)\rangle$ is already sufficient for the present purpose. Consequently, the transmission (33) assumes the form

$$T_{LR}^{(k)}(\epsilon) = \Gamma_L \Gamma_R \sum_{\alpha,\beta,k',k''} \frac{\langle N | \phi_{\alpha,k'} \rangle \langle \phi_{\alpha,k'+k} | 1 \rangle \langle 1 | \phi_{\beta,k''+k} \rangle \langle \phi_{\beta,k''} | N \rangle}{[\epsilon - (\epsilon_\alpha^0 + k' \hbar \Omega + i\hbar\gamma_\alpha^1)][\epsilon - (\epsilon_\beta^0 + k'' \hbar \Omega - i\hbar\gamma_\beta^1)]} \quad (47)$$

and $T_{\text{RL}}^{(k)}(\epsilon)$ accordingly. The transmission (49) exhibits for small values of Γ_ℓ sharp peaks at energies $\epsilon_\alpha^0 + k'\hbar\Omega$ and $\epsilon_\beta^0 + k''\hbar\Omega$ with widths $\hbar\gamma_\alpha^1$ and $\hbar\gamma_\beta^1$. Therefore, the relevant contributions to the sum come from terms for which the peaks of both factors coincide and, in the absence of degeneracies in the quasienergy spectrum, we keep only terms with

$$\alpha = \beta, \quad k' = k''. \quad (48)$$

Then provided that γ_α^1 is small, the fraction in (49) is a Lorentzian and can be approximated by $\pi\delta(\epsilon - \epsilon_\alpha^0 - k'\hbar\Omega)/\hbar\gamma_\alpha^1$ yielding the transmission

$$T_{\text{LR}}^{(k)}(\epsilon) = \Gamma_L \Gamma_R \sum_{\alpha, k'} \frac{\pi}{\hbar\gamma_\alpha^1} |\langle 1 | \phi_{\alpha, k'+k} \rangle \langle \phi_{\alpha, k'} | N \rangle|^2 \delta(\epsilon - \epsilon_\alpha^0 + k'\hbar\Omega). \quad (49)$$

The energy integration in (32) can now be performed even for finite temperature and we obtain for the dc current the expression

$$\bar{I} = \frac{e}{\hbar} \sum_{\alpha, k, k'} \frac{\Gamma_{L\alpha k} \Gamma_{R\alpha k'}}{\Gamma_{L\alpha} + \Gamma_{R\alpha}} [f_R(\epsilon_\alpha^0 + k'\hbar\Omega) - f_L(\epsilon_\alpha^0 + k\hbar\Omega)]. \quad (50)$$

The coefficients

$$\Gamma_{L\alpha k} = \Gamma_L |\langle 1 | \phi_{\alpha, k} \rangle|^2, \quad \Gamma_{L\alpha} = \sum_k \Gamma_{L\alpha k}, \quad (51)$$

$$\Gamma_{R\alpha k} = \Gamma_R |\langle N | \phi_{\alpha, k} \rangle|^2, \quad \Gamma_{R\alpha} = \sum_k \Gamma_{R\alpha k}, \quad (52)$$

denote the overlap of the k th sideband $|\phi_{\alpha, k}\rangle$ of the Floquet state $|\phi_\alpha(t)\rangle$ with the first site and the last site of the wire, respectively. We have used $2\hbar\gamma_\alpha^1 = \Gamma_{L\alpha} + \Gamma_{R\alpha}$ which follows from (46).

Within the same approximation, we expand the zero-frequency noise (36) to lowest-order in Γ_ℓ : After inserting the spectral representation (43) of the Green function, we again keep only terms with identical Floquet index α and identical sideband index k to obtain

$$\begin{aligned} \bar{S} = & \frac{e^2}{\hbar} \sum_{\alpha, k, k'} \frac{\Gamma_{R\alpha k'} \bar{f}_R(\epsilon_\alpha^0 + k'\hbar\Omega)}{(\Gamma_{L\alpha} + \Gamma_{R\alpha})^3} \{ 2\Gamma_{L\alpha}^2 \Gamma_{R\alpha k} f_R(\epsilon_\alpha^0 + k\hbar\Omega) \\ & + (\Gamma_{L\alpha}^2 + \Gamma_{R\alpha}^2) \Gamma_{L\alpha k} f_L(\epsilon_\alpha^0 + k\hbar\Omega) \} \\ & + \text{same terms with the replacement } L \leftrightarrow R. \end{aligned} \quad (53)$$

4.2 Master-Equation Approach

An essential step in the derivation of the weak-coupling approximation (49) was the assumption that only terms with $\alpha = \beta$ contribute significantly to the transmission (47). This condition is clearly violated in the presence of degeneracies on the quasienergy spectrum or intermediate wire-lead coupling strength. Then, one has to refine the discussion presented above.

Current Formula

We start again from unsymmetric expression (28) for the time-dependent current across the contact between the wire and the left lead. After performing the average over one driving period, it assumes the form

$$\begin{aligned} \bar{I} = & \frac{2e}{\hbar T} \sum_{\ell} \int d\epsilon \int_0^{\infty} d\tau \int_0^T dt \Gamma_{\ell}(\epsilon) f_{\ell}(\epsilon) \text{Im} e^{i\epsilon\tau/\hbar} G_{1\ell}^*(t, \epsilon) \Gamma_L(\tau) G_{1\ell}(t - \tau, \epsilon) \\ & + 2e \int d\epsilon \Gamma_L(\epsilon) f_L(\epsilon) \text{Im} G_{11}^{(0)}(\epsilon). \end{aligned} \quad (54)$$

Let us first consider the second term in this expression, which is linear in the retarded Green function $G_{11}^{(0)}(\epsilon)$ and, thus, its evaluation does not suffer from having two poles close to each other. Then, we can perform the energy integration in (54) the same way as in the last subsection to obtain the contribution

$$-\frac{e}{\hbar} \sum_{\alpha, k} |\langle 1 | \phi_{\alpha, k} \rangle|^2 \Gamma_L(\epsilon_{\alpha}^0 + k\hbar\Omega) f(\epsilon_{\alpha}^0 + k\hbar\Omega - \mu_L) \quad (55)$$

to the time-averaged current.

The first term in (54) has to be treated with more care since it is quadratic in the retarded Green function. Thus, in the case of degeneracies of the quasi-energy spectrum, the approximation scheme described in the previous paragraph breaks down (cf. also discussion in Sect. 4.1) and a more elaborate treatment is necessary. For this, it turns out to be advantageous to go one step back in the derivation of (54), namely to use the form given in (27), yielding for the first term in (54)

$$\frac{2e}{\hbar T} \int_0^{\infty} d\tau \int_0^T dt \text{Re} \left[\Gamma_L(\tau) \langle c_1^\dagger(t) c_1(t - \tau) \rangle \right]. \quad (56)$$

Assuming that $\Gamma_L(\epsilon)$ is a slowly varying function for all relevant energies ϵ , i.e., $\Delta\Gamma_L/\Gamma_L \ll 1$, we can replace the time-evolution of c_1 from the time t back to $t - \tau$ by the zeroth-order expression $c_1(t - \tau, t) = U_0^\dagger(t - \tau, t) c_1 U_0(t - \tau, t)$ with U_0 being the propagator (41) in the limit $\Gamma_{L/R} \rightarrow 0$. We have introduced the wire operators $c_{\alpha}(t)$ in the “Floquet picture” by means of the time-dependent transformation [24, 25]

$$c_{\alpha}(t) = \sum_n \langle \phi_{\alpha}(t) | n \rangle c_n. \quad (57)$$

Using the inverse transformation $c_n = \sum_{\alpha} \langle n | \phi_{\alpha}(t) \rangle c_{\alpha}(t)$, we obtain

$$c_1(t - \tau, t) \approx \sum_{\alpha k} e^{-ik\Omega t} e^{i(\epsilon_{\alpha}^0 + k\hbar\Omega)\tau/\hbar} \langle 1 | \phi_{\alpha, k} \rangle c_{\alpha}(t) \quad (58)$$

such that we can then rewrite the current (56) in terms of the expectation values $P_{\alpha\beta}(t) = \langle c_\beta^\dagger(t) c_\alpha(t) \rangle_t$ at time t . In order to determine the values of $P_{\alpha\beta}(t)$ at asymptotic times, we now derive for these expectation values a kinetic equation. Before doing so, however, we simplify (56) further by using of the fact, that the $P_{\alpha\beta}(t)$ are \mathcal{T} -periodic functions and can thus be decomposed into a Fourier series $P_{\alpha\beta}(t) = \sum_k \exp(-ik\Omega t) P_{\alpha\beta,k}$. This brings (56) into the form

$$\frac{2e}{\hbar} \sum_{\alpha,\beta,k,k'} \int_0^\infty d\tau \operatorname{Re} \left[\Gamma_L(\tau) e^{i(\epsilon_\alpha^0 + k\hbar\Omega)\tau/\hbar} \langle \phi_{\beta,k+k'} | 1 \rangle \langle 1 | \phi_{\alpha,k} \rangle P_{\alpha\beta,k'} \right]. \quad (59)$$

Using the definition (17) of the Fourier transform of the spectral density $\Gamma_L(\epsilon)$, we finally find for the time-averaged current through the molecular wire

$$\bar{I} = \frac{e}{\hbar} \sum_{\alpha,k} \Gamma_L(\epsilon_\alpha^0 + k\hbar\Omega) \left[\sum_{\beta,k'} \operatorname{Re} (\langle \phi_{\beta,k+k'} | 1 \rangle \langle 1 | \phi_{\alpha,k} \rangle P_{\alpha\beta,k'}) - |\langle 1 | \phi_{\alpha,k} \rangle|^2 f(\epsilon_\alpha^0 + k\hbar\Omega - \mu_L) \right]. \quad (60)$$

Note that we have disregarded principal value terms corresponding to an energy renormalisation due to the wire-lead coupling.

Floquet-Markov Master Equation

Having expressed the current in terms of the wire expectation values $P_{\alpha\beta}(t)$, we now derive their dynamics in the regime of a weak to moderately strong wire-lead coupling. We thus consider the time-derivative $\dot{P}_{\alpha\beta}(t)$, which with the help of the zeroth-order Floquet equation (44) can be written as

$$\dot{P}_{\alpha\beta}(t) = -\frac{i}{\hbar} (\epsilon_\alpha^0 - \epsilon_\beta^0) P_{\alpha\beta}(t) + \operatorname{Tr} \left[c_\beta^\dagger(t) c_\alpha(t) \dot{\rho}(t) \right]. \quad (61)$$

In order to focus on the wire-lead coupling, we switch for the further evaluation of the second term to the corresponding interaction picture $\tilde{O}(t, t_0) = U_0(t, t_0)^\dagger O(t) U_0(t, t_0)$, where the propagator of the isolated molecule and leads can be formally written as

$$U_0(t, t_0) = \tilde{T} \exp \left(-\frac{i}{\hbar} \int_{t_0}^t dt' [H_{\text{wire}}(t') + H_{\text{leads}}] \right). \quad (62)$$

The dynamics are then governed by the Liouville-von Neumann equation in the interaction picture

$$i\hbar \frac{d}{dt} \tilde{\rho}(t, t_0) = [\tilde{H}_{\text{contacts}}(t, t_0), \tilde{\rho}(t, t_0)], \quad (63)$$

which after integration reads

$$\tilde{\varrho}(t, t_0) = \tilde{\varrho}(t_0, t_0) - \frac{i}{\hbar} \int_{t_0}^t dt' [\tilde{H}_{\text{contacts}}(t', t_0), \tilde{\varrho}(t', t_0)] . \quad (64)$$

Upon re-insertion of this relation into the right-hand side of (63), we obtain an integro-differential equation for the time-derivative of the density matrix, namely

$$\begin{aligned} \dot{\tilde{\varrho}}(t, t_0) = & - \frac{i}{\hbar} [\tilde{H}_{\text{contacts}}(t, t_0), \tilde{\varrho}(t_0, t_0)] \\ & - \frac{1}{\hbar^2} \int_0^{t-t_0} d\tau [\tilde{H}_{\text{contacts}}(t, t_0), [\tilde{H}_{\text{contacts}}(t-\tau, t_0), \tilde{\varrho}(t-\tau, t_0)]] . \end{aligned} \quad (65)$$

At this point, we assume that the dynamics induced by transitions due to the weak coupling H_{contacts} is slow, so that $\tilde{\varrho}(t-\tau, t_0)$ can be approximated by $\tilde{\varrho}(t, t_0)$ in the integral. This so-called Born-Markov-approximation of course also requires $t \gg t_0$. After a back transformation into the Schrödinger picture, we therefore consider the asymptotic limit $t_0 \rightarrow -\infty$. Using the resulting expression, we can cast (61) into the form

$$\begin{aligned} \dot{P}_{\alpha\beta}(t) = & - \frac{i}{\hbar} (\epsilon_\alpha^0 - \epsilon_\beta^0) P_{\alpha\beta}(t) \\ & - \frac{1}{\hbar^2} \int_0^\infty d\tau \left\langle [[c_\beta^\dagger(t) c_\alpha(t), H_{\text{contacts}}], \tilde{H}_{\text{contacts}}(t-\tau, t)] \right\rangle_t . \end{aligned} \quad (66)$$

Here, we have used twice the relation $\text{Tr } A[B, C] = \text{Tr}[A, B]C$, which directly results from the cyclic invariance of the trace. For the further evaluation of the $H_{\text{contacts}}(t-\tau, t)$, we use that $\tilde{c}_n(t-\tau, t)$ is given by the right-hand side of (58). After some algebraic manipulations of the double commutator in the integrand, we eventually arrive at the Floquet-Markov master equation

$$\begin{aligned} \dot{P}_{\alpha\beta} = & - \frac{i}{\hbar} (\epsilon_\alpha^0 - \epsilon_\beta^0) P_{\alpha\beta} + \frac{1}{2} \sum_{\ell=L,R} \sum_{kk'} e^{i(k'-k)\Omega t} \\ & \times \left\{ \Gamma_\ell(\epsilon_\alpha^0 + k\hbar\Omega) \langle \phi_{\alpha,k'} | n_\ell \rangle \langle n_\ell | \phi_{\beta,k} \rangle f(\epsilon_\alpha^0 + k\hbar\Omega - \mu_\ell) \right. \\ & + \Gamma_\ell(\epsilon_\beta^0 + k\hbar\Omega) \langle \phi_{\alpha,k'} | n_\ell \rangle \langle n_\ell | \phi_{\beta,k} \rangle f(\epsilon_\beta^0 + k\hbar\Omega - \mu_\ell) \\ & - \sum_{\alpha'} \Gamma_\ell(\epsilon_{\alpha'}^0 + k\hbar\Omega) \langle \phi_{\alpha,k'} | n_\ell \rangle \langle n_\ell | \phi_{\alpha',k} \rangle P_{\alpha'\beta} \\ & \left. - \sum_{\beta'} \Gamma_\ell(\epsilon_{\beta'}^0 + k'\hbar\Omega) \langle \phi_{\beta',k'} | n_\ell \rangle \langle n_\ell | \phi_{\beta,k} \rangle P_{\alpha\beta'} \right\} . \end{aligned} \quad (67)$$

Here, we have assumed that the ideal leads always stay in thermal equilibrium and thus are described by the expectation values (6). Moreover, principal value terms stemming from an renormalisation of the wire energies due to the coupling to the leads have been neglected again.

The solution of the master equation together with the current expression (60) derived earlier, permits an efficient numerical calculation of the dc current through the molecular wire even for rather large systems or for energy dependent couplings. Furthermore, as we shall demonstrate later on the basis of a specific example that this approach still works well in the presence of degeneracies in the quasienergy spectrum. In fact, one can recover the weak-coupling expansion presented in Sect. 4.1 from the master equation formalism within a so-called rotating-wave approximation [25]. Finally, we note that the master equation (67) can be generalised to describe within a mean-field description also the influence of an additional electron-vibrational coupling on the molecular wire [45].

5 Photon-Assisted Transport Across a Molecular Bridge

As an application of our formalism, we now consider the photon-assisted transport through a molecular bridge as sketched in Fig. 1. In our numerical studies, we use the hopping matrix element Δ as the energy unit; in a realistic molecule, Δ is of the order 0.1 eV. We choose a rather small wire-lead hopping rate $\Gamma = 0.1\Delta/\hbar$, which corresponds to a current $e\Gamma = 2.56 \times 10^{-5}$ A, in order to ensure the applicability of our weak-coupling approximation. Laser frequencies $\Omega \approx \Delta/\hbar$ then lie in the infrared spectral range. For a typical distance of 5 Å between two neighbouring sites, a driving amplitude $A = \Delta$ is equivalent to an electrical field strength of 2×10^6 V/cm.

It is instructive to first consider the situation without laser driving. Then in the limit $E_B \gg \Delta$, transport through the donor-bridge-acceptor complex proceeds via the tunnel doublet $(|1\rangle \pm |N\rangle)/\sqrt{2}$ formed by the states $|1\rangle$ and $|N\rangle$. The tunnel coupling is mediated by the so-called super-exchange by way of the $N - 2$ bridge states. The corresponding tunnel splitting is approximatively given by $2\Delta(\Delta/E_B)^{N-2}$ and thus is exponentially small [46]. For details, see Chap. 1.

When a laser field with a frequency that matches the energy difference between the tunnel doublet and the bridge states whose energies range from $E_B - 2\Delta$ to $E_B + 2\Delta$ is turned on, a direct channel for the transport through the wire is opened. At the resonance peaks, the current no longer decays exponentially fast with increasing wire length, but scales as $\bar{I} \propto A^2/(N-1)\Gamma$ [28]. This photon-assisted tunnelling effect is shown in Fig. 2a, where the dc current is depicted as a function of the laser frequency Ω . Both the results from an exact numerical calculation based on the scattering formula (32) and from the master equation formalism are displayed. They agree very well over the whole range of driving frequencies Ω as can be expected for resonant transport through the donor-bridge-acceptor complex. Due to the quasi-degeneracy of the donor-acceptor doublet, the weak-coupling approximation (50) breaks down completely in the present case and incorrectly

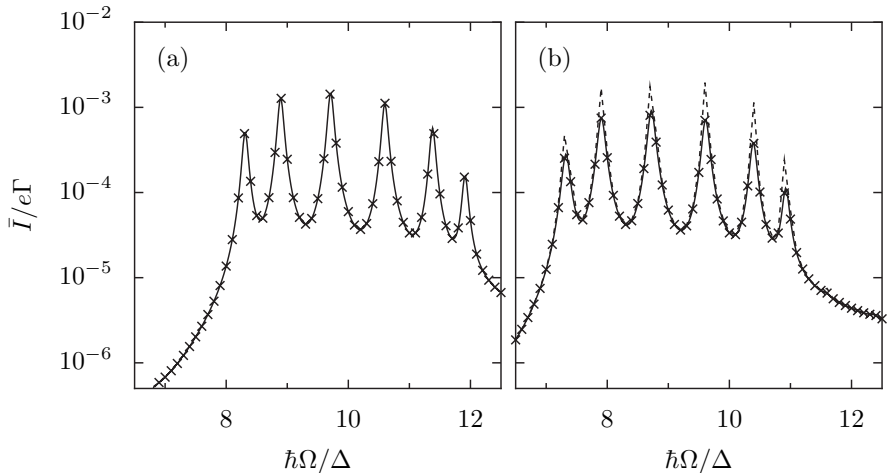


Fig. 2. Dc current \bar{I} through molecular wire bridge with $N = 8$ sites in the presence of a weak external driving with amplitude $A = 0.1\Delta$ as a function of the driving frequency Ω . The bridge height is $E_B = 10\Delta$ and the leftmost and the rightmost site lie at (a) $E_1 = E_8 = 0$ or (b) $E_1 = -\Delta$ and $E_8 = \Delta$. The external bias voltage is $V = 10\Delta/e$, and the temperature $T = 0$. The solid line shows the exact result (32) and the crosses correspond to the master equation result (60). The dashed line in panel (b) depicts the limit of very weak wire-lead coupling, (50)

predicts a current $\bar{I} = e\Gamma/2$ independent of the driving frequency Ω (not shown).

Due to possible asymmetries of the molecule itself or as a consequence of the applied dc bias voltage, the assumption that the donor and the acceptor levels are degenerate, might not be fulfilled. Thus, it is desirable to test the stability of the above results against shifts of the on-site energies of the donor and the acceptor. The dc current for this situation is shown in Fig. 2b. We again observe that the master equation result agrees very well with the numerically exact result from the scattering formalism. Moreover, now also the weak-coupling approximation (50) agrees qualitatively with the exact results. However, the weak-coupling approximation fails to quantitatively predict the peak heights.

Figure 3 demonstrates that at the resonances, the Fano factor assumes values considerably lower than one as expected for the transport through a resonant single level [32]. This reveals that at the resonant excitations, the transport mechanism is no longer dominated by tunnelling across a high barrier.

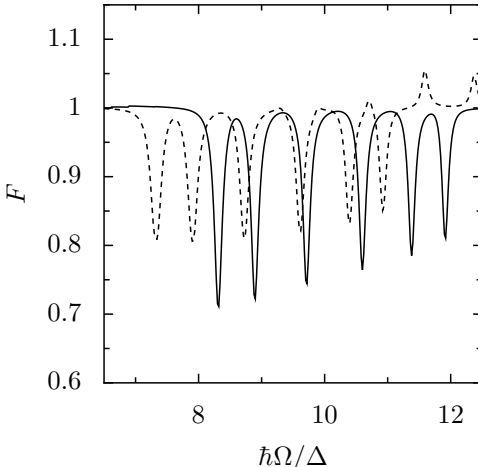


Fig. 3. Relative noise power characterised by the Fano factor $F = \bar{S}/e|\bar{I}|$ for unbiased (*solid line*) and biased (*broken*) donor and acceptor sites. All parameters are as in Fig. 2

6 Conclusions

We have put forward two theoretical approaches for the calculation of the dc current and its noise power through a molecular wire in the presence of a time-periodic external field, namely (i) a scattering approach and (ii) a master equation method. Both are based on the Floquet theorem and, thus, allow an exact treatment of the driven transport problem. The presented Floquet scattering formalism starts by integrating out the lead degrees of freedom. Then, the resulting equation of motion for the Green function of the wire electrons is mapped to a non-hermitian eigenvalue problem in a Hilbert space which is extended by a periodic time-coordinate. Finally, the expression for the dc current can be written in terms of generalised transmissions which describe electron transport under the absorption and emission of photons. The corresponding expression for the current noise, however, cannot be brought into such a convenient form: Indeed, in the presence of time-dependent driving, the noise not only depends on transmission probabilities but also on the phases of the transmission amplitudes.

Alternatively, for sufficiently weak wire-lead coupling, the transport can be described by a master equation which is decomposed into the Floquet states of the isolated driven molecule. While being perturbative, this approach has also its benefits: Since only the Floquet states in the absence of the leads are needed, one can employ many standard methods known from the Floquet treatment of atoms and molecules in laser fields. Moreover, the master equation formalism can be extended readily to the case of energy-dependent coupling $\Gamma_\ell(\epsilon)$ and also allows to include phonon-damping [45].

Finally, even for intermediately strong wire-lead coupling, the results obtained within the master equation approach agree very well with the exact results.

Of foremost interest in view of ongoing experiments, is the enhancement of molecular conduction by resonant excitations. The corresponding theoretical analysis has revealed that resonant excitations from the terminating atoms to the bridge levels yield peaks in the current as a function of the driving frequency. The laser irradiation induces a large current enhancement of several orders of magnitude and also can reduce the current noise level. The observation of these resonances could serve as an experimental starting point for the more challenging attempt of measuring quantum ratchet effects [24, 25] or current switching by laser fields [35, 36, 47, 48].

Acknowledgements

The authors would like to thank Sébastien Camalet, Gert-Ludwig Ingold, Heiko B. Weber, and Jan Würfel for useful discussions. This work has been supported by the Volkswagen-Stiftung under Grant No. I/77217 and the DFG Sonderforschungsbereich 486, project A10.

References

1. M.A. Reed, C. Zhou, C.J. Muller, T.P. Burgin, J.M. Tour: Conductance of a molecular junction, *Science* **278**, 252 (1997)
2. X.D. Cui, A. Primak, X. Zarate, J. Tomfohr, O.F. Sankey, A.L. Moore, T.A. Moore, D. Gust, G. Harris, S.M. Lindsay: Reproducible measurement of single-molecule conductivity, *Science* **294**, 571 (2001)
3. J. Reichert, R. Ochs, D. Beckmann, H.B. Weber, M. Mayor, H. von Löhneysen: Driving current through single organic molecules, *Phys. Rev. Lett.* **88**, 176 804 (2002)
4. H.B. Weber, J. Reichert, F. Weigend, R. Ochs, D. Beckmann, M. Mayor, R. Ahlrichs, H. von Löhneysen: Electronic transport through single conjugated molecules, *Chem. Phys.* **281**, 113 (2002)
5. P. Hänggi, M. Ratner, and S. Yaliraki, *Processes in Molecular Wires*, *Chem. Phys.* **281**, 111 (2002).
6. A. Nitzan, M.A. Ratner: Electron transport in molecular wire junctions, *Science* **300**, 1384 (2003)
7. J.R. Heath, M.A. Ratner: Molecular electronics, *Phys. Today* **56**(5), 43 (2003)
8. R.M. Metzger: Unimolecular electrical rectifiers, *Chem. Rev.* **103**, 3803 (2003)
9. M. Di Ventra, N.D. Lang: Transport in nanoscale conductors from first principles, *Phys. Rev. B* **65**, 045 402 (2002)
10. J. Heurich, J.C. Cuevas, W. Wenzel, G. Schön: Electrical transport through single-molecule junctions: From molecular orbitals to conduction channels, *Phys. Rev. Lett.* **88**, 256 803 (2002)

11. T. Seideman: Current-driven dynamics in molecular-scale devices, *J. Phys. C* **15**, R521 (2003)
12. T. Seideman, H. Guo: Quantum transport and current-triggered dynamics in molecular tunnel junctions, *J. Theo. Comp. Chem.* **2**, 439 (2003)
13. V. Mujica, M. Kemp, M.A. Ratner: Electron conduction in molecular wires. I. A scattering formalism, *J. Chem. Phys.* **101**, 6849 (1994)
14. D. Segal, A. Nitzan, W.B. Davis, M.R. Wasielewski, M.A. Ratner: Electron transfer rates in bridged molecular systems 2: A steady-state analysis of coherent tunneling and thermal relaxation, *J. Phys. Chem.* **104**, 3817 (2000)
15. D. Boese, H. Schoeller: Influence of nanomechanical properties on single-electron tunneling: A vibrating single-electron transistor, *Europhys. Lett.* **54**, 668 (2001)
16. E.G. Petrov, P. Hänggi: Nonlinear electron current through a short molecular wire, *Phys. Rev. Lett.* **86**, 2862 (2001)
17. A. Nitzan: Electron transmission through molecules and molecular interfaces, *Annu. Rev. Phys. Chem.* **52**, 681 (2001)
18. G. Cuniberti, G. Fagas, K. Richter: Fingerprints of mesoscopic leads in the conductance of a molecular wire, *Chem. Phys.* **281**, 465 (2002)
19. M.H. Hettler, W. Wenzel, M.R. Wegewijs, H. Schoeller: Current collapse in tunneling transport through benzene, *Phys. Rev. Lett.* **90**, 076 805 (2003)
20. S. Kohler, J. Lehmann, P. Hänggi: Driven transport on the nanoscale, *Phys. Rep.* **406**, 379 (2005)
21. C.A. Stafford, N.S. Wingreen: Resonant photon-assisted tunneling through a double quantum dot: An electron pump from spatial rabi oscillations, *Phys. Rev. Lett.* **76**, 1916 (1996)
22. T. Fujisawa, S. Tarucha: Photon assisted tunnelling in single and coupled quantum dot systems, *Superlatt. Microstruct.* **21**, 247 (1997)
23. T.H. Oosterkamp, T. Fujisawa, W.G. van der Wiel, K. Ishibashi, R.V. Hijman, S. Tarucha, L.P. Kouwenhoven: Microwave spectroscopy of a quantum-dot molecule, *Nature* **395**, 873 (1998)
24. J. Lehmann, S. Kohler, P. Hänggi, A. Nitzan: Molecular wires acting as coherent quantum ratchets, *Phys. Rev. Lett.* **88**, 228 305 (2002)
25. J. Lehmann, S. Kohler, P. Hänggi, A. Nitzan: Rectification of laser-induced electronic transport through molecules, *J. Chem. Phys.* **118**, 3283 (2003)
26. A. Keller, O. Atabek, M. Ratner, V. Mujica: Laser-assisted conductance of molecular wires, *J. Phys. B* **35**, 4981 (2002)
27. S. Kohler, J. Lehmann, S. Camaret, P. Hänggi: Resonant laser excitation of molecular wires, *Israel J. Chem.* **42**, 135 (2002)
28. S. Kohler, J. Lehmann, M. Strass, P. Hänggi: Molecular wires in electromagnetic fields, *Adv. Solid State Phys.* **44**, 151 (2004)
29. C. Caroli, R. Combescot, P. Nozieres, D. Saint-James: Direct calculation of the tunneling current, *J. Phys. C* **4**, 916 (1971)
30. D.S. Fisher, P.A. Lee: Relation between conductivity and transmission matrix, *Phys. Rev. B* **23**, 6851 (1981)
31. Y. Meir, N.S. Wingreen: Landauer formula for the current through an interacting electron region, *Phys. Rev. Lett.* **68**, 2512 (1992)
32. Ya. M. Blanter, M. Büttiker: Shot noise in mesoscopic conductors, *Phys. Rep.* **336**, 1 (2000)
33. U. Fano: Ionization yield of radiations. II. The fluctuations of the number of ions, *Phys. Rev.* **72**, 26 (1947)

34. A.P. Jauho, N.S. Wingreen, Y. Meir: Time-dependent transport in interacting and noninteracting resonant-tunneling systems, Phys. Rev. B **50**, 5528 (1994)
35. S. Camalet, J. Lehmann, S. Kohler, P. Hänggi: Current noise in ac-driven nanoscale conductors, Phys. Rev. Lett. **90**, 210602 (2003)
36. S. Camalet, S. Kohler, P. Hänggi: Shot-noise control in ac-driven nanoscale conductors, Phys. Rev. B **70**, 155326 (2004)
37. S. Datta, M.P. Anantram: Steady-state transport in mesoscopic systems illuminated by alternating fields, Phys. Rev. B **45**, 13761 (1992)
38. S. Datta: *Electronic Transport in Mesoscopic Systems* (Cambridge University Press, Cambridge, 1995)
39. M. Wagner: Probing Pauli blocking factors in quantum pumps with broken time-reversal symmetry, Phys. Rev. Lett. **85**, 174 (2000)
40. H. Sambe: Steady states and quasienergies of a quantum-mechanical system in an oscillating field, Phys. Rev. A **7**, 2203 (1973)
41. M. Grifoni, P. Hänggi: Driven quantum tunneling, Phys. Rep. **304**, 229 (1998)
42. A. Buchleitner, D. Delande, J. Zakrzewski: Non-dispersive wave packets in periodically driven quantum systems, Phys. Rep. **368**, 409 (2002)
43. J.H. Shirley: Solution of the Schrödinger equation with a Hamiltonian periodic in time, Phys. Rev. **138**, B979 (1965)
44. P. Jung, P. Hänggi: Resonantly driven Brownian motion: Basic concepts and exact results, Phys. Rev. A **41**, 2977 (1990)
45. J. Lehmann, S. Kohler, V. May, P. Hänggi: Vibational effects in laser-driven molecular wires, J. Chem. Phys. **121**, 2278 (2004)
46. M.A. Ratner: Bridge-assisted electron transfer: Effective electronic coupling, J. Phys. Chem. **94**, 4877 (1990)
47. J. Lehmann, S. Camalet, S. Kohler, P. Hänggi: Laser controlled molecular switches and transistors, Chem. Phys. Lett. **368**, 282 (2003)
48. S. Kohler, S. Camalet, M. Strass, J. Lehmann, G.L. Ingold, P. Hänggi: Charge transport through a molecule driven by a high-frequency field, Chem. Phys. **296**, 243 (2004)

Electronic Structure Calculations for Nanomolecular Systems

Rosa Di Felice¹, Arrigo Calzolari¹, Daniele Varsano², and Angel Rubio²

¹ INFM National Center on nanoStructures and bioSystems at Surfaces (S3), Modena, Italy
rosa@unimore.it

² Departamento de Fisica de Materiales, Facultad de Quimicas, Universidad del País Vasco, Centro Mixto CSIC-UPV/EHU and Donostia International Physics Center (DIPC), San Sebastian, Spain
arubio@sc.ehu.es

Abstract. The electronic structure constitutes the fundamentals on which a reliable quantitative knowledge of the electrical properties of materials should be based. Here, we first present an overview of the methods employed to elucidate the ground-state electronic properties, with an emphasis on the results of Density Functional Theory (DFT) calculations on selected cases of (bio)molecular nanostructures that are currently exploited as potential candidates for devices. In particular, we show applications to carbon nanotubes and assemblies of DNA-based homoguanine stacks. Then, to move ahead from the *electronic properties* to the computation of measurable features in the operation of nanodevices (e.g., *transport characteristics, optical yield*), we proceed along two different lines to address two non-negligible issues: the role of excitations and the role of contacts. On one hand, for an accurate simulation of charge transport, as well as of optoelectronic features, the ground state is not sufficient and one needs to take into account the excited states of the system: to this aim, we introduce Time-Dependent DFT (TDDFT), we describe the TDDFT frameworks and their relation to the optical properties of materials. We present the application of TDDFT to compute the optical absorption spectra of fluorescent proteins and of DNA bases. On the other hand, the details of the conductor-leads interfaces are of crucial importance to determine the current under applied voltage, and one should compute the transport properties for a device geometry that mimics the experimental setup: to this aim, we introduce a novel development based on Wannier functions. The method, which is a framework for both an in-depth analysis of the electronic states and the plug-in of tight-binding parameters into the Green's function, is described with the aid of examples on nanostructures potentially relevant for device applications.

1 Electronic Structure of Nanomolecular Systems

The methods commonly adopted for large scale calculations of the electronic properties of molecular nanostructures were mostly adapted from the theories available for materials at the macro- and mesoscopic scales. Such computational schemes are based on the solution of the many-body Schrödinger equation. While the problem is completely defined in terms of the total

number of particles N and the external potential $v(\mathbf{r})$, its solution depends on $3N$ coordinates. This makes the direct search for either exact or approximate solutions to the many-body problem a task of rapidly increasing complexity.

The non-relativistic time-independent Schrödinger equation for the system is

$$\hat{H}\Phi(\mathbf{r}_1, \dots, \mathbf{r}_N) = E\Phi(\mathbf{r}_1, \dots, \mathbf{r}_N) \quad (1)$$

where the Hamiltonian operator is (atomic units $\hbar = e = m_e = 4\pi\epsilon_0 = 1$ are used throughout, unless explicitly stated)

$$\hat{H} = \hat{T}_0 + \hat{V}_{e-i} + \hat{U}_{e-e} + \hat{U}_{i-i}. \quad (2)$$

\hat{T}_0 is the kinetic energy of the electrons, \hat{V}_{e-i} is the potential energy of the electrons in the field of the α nuclei of charge Z_α , \hat{U}_{e-e} (\hat{U}_{i-i}) is the electron-electron (ion-ion) electrostatic energy. Equation (1) is an eigenvalue equation for the N -electron many-body wave-function Φ , where \hat{H} is hermitian. In this time-independent formulation, the Schrödinger equation (1) for the Hamiltonian \hat{H} is equivalent to the variational principle $\delta E[\Phi] = 0$. The well-known Hartree and Hartree-Fock methods correspond to searching for solutions of $\delta E[\Phi] = 0$ in the subspace of the products of single-particle orbitals and in the subspace of antisymmetrized products of single-particle orbitals (Slater determinants).

The Hartree-Fock theory (HF) [1] is obtained by considering the wavefunction to be a single Slater determinant: thus, the N -body problem is reduced to N one-body problems with a self-consistent requirement due to the dependence of the HF effective potential on the wave-functions. By the variational theorem, the HF total energy is a variational upper bound of the ground-state energy for its particular symmetry. The HF eigenvalues are estimates of the true excitation energies: the assumption made in this statement is that the one-electron wave function of any electron in any energy level is the same in the N and $(N - 1)$ systems (Koopman's theorem), e.g., the relaxation of the system upon a change in the number of particles is neglected. A better procedure to estimate the excitation energies is to perform self-consistent calculations for the N and $(N - 1)$ states and subtract the total energies (this is called the “self-consistent method” for excitation energies, which has also been used in other theoretical frameworks, as DFT). Note that for extended systems this scheme gives the same result as the Koopman's theorem, and more refined methods should be implemented to address the problem of excitation energies (quasi-particles, QPs) in solids as well as in nanostructures. The HF theory is far from being exact, because the wavefunction of the system cannot be written as a single determinant: MBPT is then required to obtain reliable energies and electronic spectra [1, 2]. HF is often used in conjunction with perturbation theory in the Møller-Plesset (MP) formalism to solve nanomolecular problems. Šponer and coworkers extensively applied these combined methodologies (2nd order MP, also referred

to as MP2) to aggregates of DNA bases [3, 4]: a discussion of the theoretical framework and of its efficiency to deal with biomolecular systems where non-chemical bonding plays a strong role, can be found in their works and in the references therein. This kind of studies (HF+MP), based on the explicit knowledge of the many-body wave-function in (1), are still too computationally cumbersome for reasonable applications to molecular nanostructures. The alternative DFT formulation [5–11], based on the particle density rather than on the many-body wave-function, is instead feasible and has been rather successful [12].

Nanomolecular systems are interesting on one hand to study genuine fundamental quantum mechanical effects: Kondo and Coulomb blockade behaviors have been observed in aromatic molecules containing a redox center, as well as in carbon nanotubes [13–16]. On the other hand, they have a huge potential for applications in electronics and optoelectronics, in view of device miniaturization and intelligent fabrication [17, 18] based on recognition and self-assembly (supramolecular chemistry [19, 20]). In both respects, research efforts aim at unraveling their transport and optical excitation properties, which for a theoretical approach require the full accurate account of many-body electronic correlations to compute the electronic structure. However, it is possible to gain a deep knowledge of the system already at the ground-state level, and then use it as the starting point for many-body perturbation theory (MBPT). Thus, in the following we first exemplify the computation of ground-state electronic properties by Density Functional Theory (DFT) (Sect. 2). In the second part we describe selected approaches for the theoretical investigation of excited-state optical (Sect. 3) and transport (Sect. 4) features.

2 Selected Applications of Ground-State Electronic Structure Calculations by DFT

Within DFT, the ground-state energy of an interacting system of electrons in an external potential can be written as a functional of the ground-state electronic density [5–8]. When comparing to standard quantum chemistry methods, this approach is particularly appealing, because it does not rely on the complete knowledge of the N -electron wave-function, but only on the electronic density. However, although the theory is exact, the energy functional contains an unknown quantity called the exchange-correlation energy, $E_{xc}[n]$, that must be approximated in practical implementations. Although failures of DFT are known, its use continues to increase due to the better scaling with the number of atoms and the fact that failures are connected with a particular choice of the local-functional, with the possibility of improving the accuracy as more and more sophisticated exchange-correlation functionals are generated.

Since excellent presentations of DFT are available in the existing literature, in both the static and dynamical formulations, we completely skip here the formal treatment. The computer packages [21–26]³ employed for the different examples are explicitly cited below.

We present few illustrative examples based on the experience of the authors. (i) In carbon nanotubes (CNTs), where all the bonds imply reactive chemistry (e.g., the formation of orbitals filled with electrons shared by different atoms), the structure and relative energetics between different conformations are well reproduced at the DFT level. (ii) In DNA base assemblies instead, where interactions that do not imply making or breaking of bonds (e.g., H-bonding, Van der Waals) play a role, correlations beyond DFT are important already at the ground-state level to predict the structure, whereas their effect on the electronic spectrum has not yet been assessed. However, we show here what can be learnt at the ground-state level if one gives up predicting the structure and energetics.

2.1 Carbon Nanotubes

Nanotubes are of both fundamental and technological importance: being quasi-one-dimensional (1D) structures, they possess a number of exceptional properties. While the peculiar electronic structure – metallic versus semiconducting behavior – of CNTs depends sensitively on the diameter and the chirality [27, 28], boron nitride (BN) tubes display a more uniform behavior with a wide band-gap (larger than 4 eV), almost independent of diameter and chirality [29, 30]. The potential applications of nanotubes in nano-technology are numerous [31–33], ranging from (opto)electronic to mechanical devices.

Given their importance and their broad range of electronic characteristics, CNTs have been an ideal playground for DFT simulations to investigate a number of features. Scanning tunnelling microscopy (STM) and spectroscopy (STS) have been among the most powerful experimental techniques to study and manipulate nanotubes. STM is a local probe that allows to extract information about the spatial localization. First-principle DFT simulations enable the computation of STM images of nanostructures, starting from the knowledge of their ground-state electronic structure. In the following, we focus on the DFT-based simulation of STM images of selected CNTs, according to a basic formalism presented elsewhere [34]. We focus on the role of the local environment in the electronic properties of CNTs.

We do not discuss here the effect of tube-substrate coupling [35]. As a first issue, we show how tube-tube interactions modify the electronic structure. In Fig. 1 we present the calculated STM/STS image obtained for an external voltage of +0.5 eV for a bundle made of three (8,8) nanotubes, and compare the electronic structure to that of an isolated (8,8) tube. The STM image

³Several other DFT software packages, besides those cited here, are distributed. Most of them are publicly available on the world wide web for academic institutions.

is quite different from the typical patterns of isolated tubes [35]. The inter-tube coupling clearly modifies the spectral features (right panel of Fig. 1). There are two main effects. (i) The presence of tube-tube interaction opens a “pseudogap” close to the Fermi level (see the well at $E = 0$), as already predicted for randomly oriented nanotube ropes [36] (pseudogap of ~ 0.1 eV). The bundle remains metallic. We remark that such predictions found experimental demonstration in low-temperature STM measurements [37], for metallic tubes and ropes similar to that shown in Fig. 1. (ii) The interaction between different tubes in a bundle makes the electron-hole asymmetry in the DOS more accentuated. The spike structure of the van Hove singularities is smoothed out. The fact that the position in energy of the peaks is not strongly modified explains the success of using isolated single-wall nanotube (SWNT) spectra to describe the experimental data, even though most experiments are performed on bundles. However, Fig. 1 also shows that the shape of the spectra (relative intensities) is significantly different for bundles with respect to isolated tubes. Therefore, care must be adopted in quantitative comparisons.

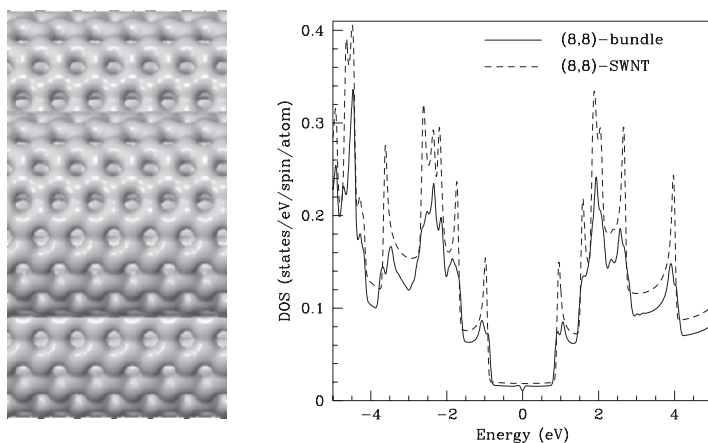


Fig. 1. STM image (*left*) and DOS (*right*) for a small carbon nanotube-rope formed by three (8,8) SWNTs (with 1.09 nm diameter) packed in a triangular lattice, with an inter-tube distance of 0.345 nm. The DOS plot clearly shows the opening of a “pseudogap” of about ~ 0.1 eV around the Fermi level. The DOS of the nanotube rope is compared in the same plot to the DOS of an isolated (8,8) SWNT [Adapted from [38] with permission; Copyright 1999 by Springer-Verlag]

As a second issue, we address the role of topological defects [39], focusing on Stone-Wales (SW) defects [40, 41]. STM images for an applied bias potential of ± 1.5 eV are presented in Fig. 2 for a (10,10) CNT (a) and for a zig-zag (6,0) BNT (b). Such images illustrate that the SW deformation creates a very localized modification of the STM pattern as compared to a perfect tube (the

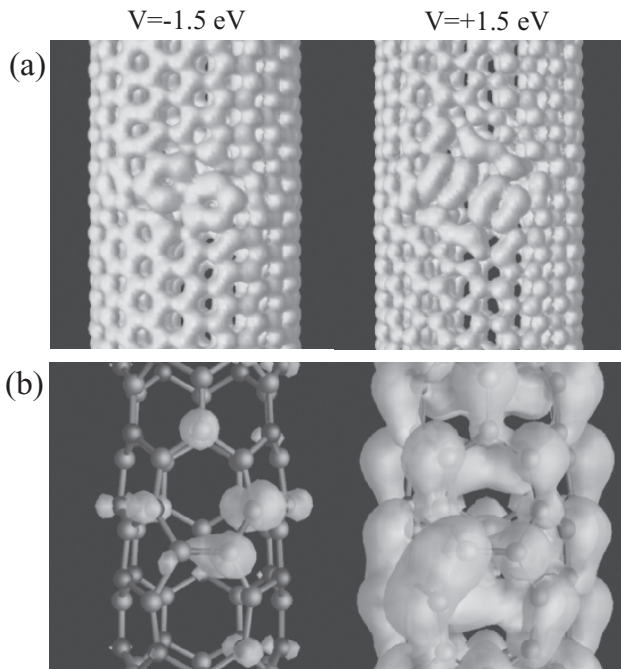


Fig. 2. Simulated constant current STM images for a C(10,10) (a) and a BN(6,0) (b) nanotube with a single SW defect for applied external tip-sample bias of $\pm 1.5 \text{ eV}$. The orientation of the centered bond joining the two pentagons of the SW defect is set to $\pi/4$ degrees to the tube axis in the case of the carbon nanotube and perpendicular to the tube axis in the case of the BN nanotube. SW-defect states in the BN band-gap are clearly seen (with N-N π and B-B π^* character for negative and positive bias, respectively) (From [39] with permission; Copyright 2004 by the American Physical Society)

decay length of the perturbation is very short, few unit cells). The symmetry of the image corresponding to occupied/unoccupied states is completely different. The calculations clearly indicate that the SW defect can be, indeed, experimentally accessible by STM measurements.

We conclude this brief section by highlighting again how the ground-state electronic structure computed by DFT may be exploited for advanced applications, such as the simulation of scanning probe experiments, both by advancing predictions that may later find experimental validation, and by interpreting already available data. In the field of nanotubes, the close synergy between theory and experiment has been extremely valuable in the latest years.

2.2 Model and Realistic DNA-Base Stacks

DNA is the very representative example of a molecular motif which has always been retained a big challenge for the performance of density functional theory. In fact, whereas the intra-base coupling is dictated by covalent bonds, the basic features of intrinsic self-assembly, which are hydrogen-bonding and inter-planar stacking, have a non-covalent origin founded on long-range tails of the Coulomb interaction. Such terms are well known to be lacking in the DFT treatment. Therefore, the ab-initio computation of both the structural [3, 4] and electronic [42]⁴ properties of various DNA molecules and fragments was traditionally the reign of quantum chemistry investigations that applied wave-function-based methods, mostly HF with accurate basis sets or HF+MP2. Such studies revealed that the energetics of π -stacked base pairs in a variety of conformations intimately depends on correlation forces and is therefore beyond the DFT range [3, 4]. Therefore, for a long time ab-initio DNA simulations remained limited to base pairs, whereas only classical molecular dynamics methods with parametrized force fields were applied to inquire about the overall helical assembly. Although the current situation, even with the most accurate exchange-correlation functionals does not allow for structural predictions, we will show here the great power of the DFT framework to learn the very deep features of the electronic structure of model systems or even of real complex systems [42–46] for which the structure is independently available.

The prompt for investigating the electronic properties of DNA rose from the evidence that DNA molecules in solution are able to propagate over long distances an oxidative charge (hole) injected at a controlled point along the sequence [42, 47, 48]. The early studies by Barton and coworkers stimulated several other scientists to investigate the solution chemistry of DNA charge migration [49–51]. Simultaneously, the measurement of high charge transfer rates also generated the question whether DNA molecules could support an electric current in a nanotechnology setup: therefore, physicists became interested in probing the electrical properties of DNA single molecules, bundles, and networks, by direct conductivity measurements [43, 52–55], which are reviewed in Chap. 15 of this volume [56]. Such a great wealth of experimental activity in turn stimulated theoretical efforts towards bandstructure analysis. For a long time the efficiency of charge migration in DNA was cast in terms of the charge transfer rate k_{da} between a donor d and an acceptor a , each with a discrete number of localized vibronic states. k_{da} is the main quantity in the Marcus-Hush-Jortner theory [57, 58]. The basic ingredients of the Marcus's formula, (3), are the electronic coupling V_{da} and the reorganization energy λ contained in the nuclear factor FC (the latter accounts for vibronic effects)

$$k_{da} = \frac{2\pi}{\hbar} |V_{da}|^2 (FC) . \quad (3)$$

⁴Contribution by N. Rösch and A. Voityuk in volume II.

With the advent of direct conductivity measurements, the quest for theorists was instead the computation and interpretation of the quantum conductance

$$\mathcal{G} = \frac{2e^2}{h}\mathcal{T}, \quad (4)$$

where \mathcal{T} is the transmission function (or *transmittance*). The quantum conductance \mathcal{G} is an index of the efficiency with which mobile charges are transmitted through a bridge connecting two metal pads. The similarity, differences, and quantitative mutual relations between charge transfer in a donor-acceptor system (applied to study DNA solution chemistry) and charge transport in a molecular nano-junction (applied to interpret conductivity measurements in DNA) were recently reported by Nitzan [59, 60] and are also summarized in Chap. 1 of this volume [61]. Here we simply show what can be learnt about the suitability of DNA molecules as conductive bridges by computing the electronic structure of guanine stacks [62].

Model guanine stacks. Justified by the good performance of plane-wave DFT on isolated guanines [62], model periodic stacked configurations of guanines were investigated with the particular aim to detect the geometrical conditions conducive to the establishment of strong inter-plane coupling and a dispersive bandstructure. The focus on guanine rather than on the other bases was motivated on one hand by its low oxidation potential, which makes it the most suitable among the nucleo-bases to mediate hole transfer [49, 63, 64], and on the other hand to the existence of G-rich structures in several different conformations including double [43, 44, 54] and quadruple [65, 66] helices. The bandstructure of the model stacks was computed [62] for the model assemblies of Fig. 3(a,b) along the periodicity axis. The amount of band dispersion for the HOMO- and LUMO-derived bands was characterized as a function of the rotation angle between G molecules in adjacent stacked planes. Figure 3(c,d) summarizes the results for the most relevant geometries: it shows that the dispersion of such bands is maximum for eclipsed stacks, whereas it is vanishing for guanines rotated by 36 degrees as in B-DNA. The eclipsed stack exhibits orbital delocalization through the stacking axis (Fig. 3c). Only when the angle Θ is very small the degree of overlap between neighboring π wave-functions is enough to guarantee orbital delocalization along the stacking. Instead, for angles typical of the natural DNA motifs (close to 36 degrees) the vanishing coupling is incompatible with band-like charge mobility. In the latter case, other mediating factors such as small polarons [67] may be invoked to explain charge propagation. Although the study reported here was limited to model configurations not representative of any real molecule employed in experiments, the results provide a useful framework to interpret the effects of geometry-dependent electronic structure on the efficiency for charge mobility.

DNA derivatives: the G4 quadruple helix. The ideas that stimulated the exploitation of G4-DNA [68] in DNA-based technology, as an alternative to the poorly conductive [42, 69] double helical DNA, are: (i) the sequence

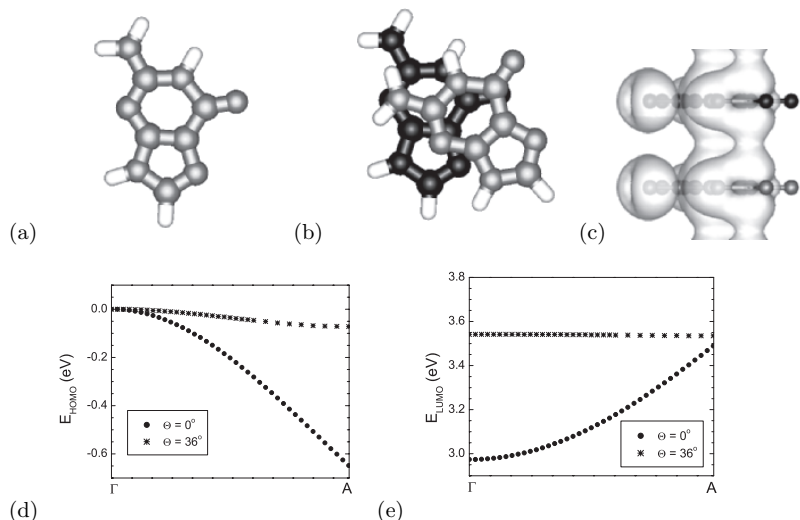


Fig. 3. (a,b) Top-view images of the periodic columnar guanine stacks in which the bases on adjacent planes are eclipsed (a) and rotated by 36° (b). The graphics show only the two G molecules in the unit supercell. Spheres of different gray intensity are used to identify atoms on two different planes. The white sticks represent H atoms protruding outside the rings. (c) Isosurface plot of the HOMO of the eclipsed stack. No nodal plane between consecutive guanines exist. (d) HOMO-band dispersion along the periodicity axis. The bending of the HOMO band for the eclipsed system from Γ to A is 0.65 eV downwards, equivalent to an effective mass for holes $m_h = 1.04$, m_0 (m_0 is the free electron mass). (e) LUMO-band dispersion along the periodicity axis. The bending of the LUMO band for the eclipsed system from Γ to A is 0.52 eV upwards, equivalent to an effective mass for electrons $m_e = 1.41m_0$. Such effective masses are typical of wide-bandgap semiconductors. The A point is the edge of the 1-dimensional BZ. The principal bandgap depends on the geometry: its DFT value (with typical DFT underestimation [8]) is 2.97 eV for $\Theta = 0^\circ$, 3.55 eV for $\Theta = 36^\circ$.

uniformity (G4 quadruple helices are made of the guanine base alone); (ii) the larger inter-planar overlap than in B-DNA; (iii) the stronger H-bonding coupling (8 instead of 2 or 3 H-bonds per plane) and consequent higher stiffness; (iv) the stability in the presence of metals (metal centers may hybridize electronically with guanine giving alternative channels for charge migration).

K(I)-G4 quadruple helices (containing potassium ions each with a formal charge 1+) from X-ray data [65] were simulated [46, 70] in the effort towards studying the electronic properties of *realistic* nucleotide-based structures, with particular emphasis on the role of electronic coupling and orbital hybridization between the different components (i.e., the metals and the nucleo-bases). Technical details of the simulations may be found in the original papers [46, 70]. Figure 4 defines the structure of short G4 molecules,

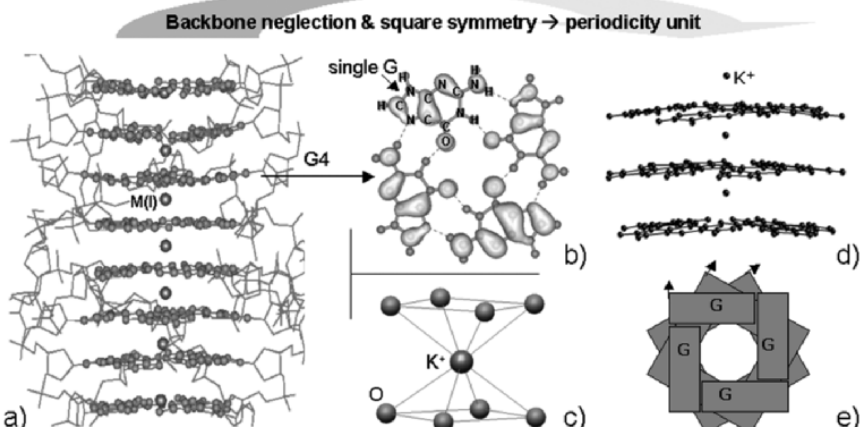


Fig. 4. (a) Ball-and-stick representation of the X-ray crystal structure for G4 quadruple helical molecules [65]. The crystals are formed by short molecules of 8 stacked tetrads. The crystallized molecules are stabilized with Na(I) ions (blue spheres). (b) The four guanine molecules in each plane, connected by 8 H-bonds forming two concentric rings in a square-like symmetry. (c) Scheme of the 8-fold coordination of each metal cation with the neighboring O atoms. (d) The relaxed atomic structure of the unit simulation supercell, constituted of only 3 planes and containing potassium instead of sodium ions. The simulated infinite wires were obtained by applying periodic boundary conditions along the stacking axis. The periodic unit was obtained by noting that the 30° inter-planar rotation makes the fourth plane equivalent to the first, and by neglecting the backbone. (e) Schematic representation of the square symmetry underlying the quadruplex motif. [(a-c) Adapted from [46] with permission; Copyright 2004 by the American Chemical Society]. (d-e) Adapted from [70] with permission; Copyright 2002 by the American Institute of Physics]

some geometrical details, and the construction of the periodic supercell for the PW-DFT calculations.

The bandstructure, the DOS, and a contour-plot of the system are shown in Fig. 5. For the G stacks presented in the previous example, $\pi-\pi$ coupling may give rise to delocalized Bloch orbitals, whose band dispersion depends on the relative rotation angle between nucleo-bases in adjacent planes. In the guanine quadruplexes, which are the object of this example, the C_4 square symmetry enhances the spatial $\pi-\pi$ overlap with respect to a segment of G-rich double helical DNA. Hence, one may expect an improvement of the band-like behavior. Instead, Fig. 5a shows that the G4 wires are characterized by multiplets of 12 flat bands⁵. This evidence implies that coherent band-like

⁵The modulo-12 multiplicity of such multiplets stems from the number of guanine molecules in the supercell [46, 70]. The highest occupied multiplet is due to the π -like guanine HOMO.

transport for quadruple helices that resemble the crystallized molecules is not predicted⁶. However, our results suggest a possible alternative mechanism for charge migration, by virtue of which *effective* dispersive bands are formed. By a combined inspection of the bandstructure (Fig. 5a) and the DOS (Fig. 5b), one may point out the following facts: (i) the energy levels in each multiplet are very close to each other, separated by an average energy difference of about 20 meV, which is less than room temperature; (ii) the DOS, obtained with gaussian spreading of the computed energy levels, shows that indeed the multiplet splitting and its total amplitude induce the formation of dispersive energy peaks. In practice, the Density of States resembles that of a wide-bandgap semiconductor, with a *valence* band (peaks a-e) separated from the *conduction* band by an energy gap (the DFT value is 3.5 eV). The small amplitude of peak a and the fact that another energy gap divides it from peak b make it not a very appealing semiconductor from the point of view of efficient charge migration through the guanine stack. A wide band in a continuous energy range would be desirable. Yet, the existence of DOS peaks with a non-vanishing amplitude means a high number of electron states in the same energy range, easily accessible to charge carriers. Moreover, the presence of several similar orbitals (the HOMO of guanine) in a restricted space, make electronic coupling between consecutive planes easy, justifying the interpretation of the HOMO-derived band (around the energy origin in Fig. 5) in terms of the convolution of the 12 electron states in the multiplet. A contour-plot of this convolution is shown in Fig. 5c: it highlights the presence of continuous channels available for mobile charges through the stacked bases. No effective metal-base hybridization is revealed.

Further studies on guanine quadruplexes are currently ongoing to elucidate several open issues, that ultimately may be solved through a synergy between PW-DFT simulations and experimental studies on the same molecules. (i) Are other metals, e.g. transition metals with different viable oxidation states, more suitable for chemical hybridization with guanine? Can they give alternative charge transport/transfer mechanisms? (ii) Which are the effects of structural deformations on the electronic properties? Axial and lateral conformational changes may occur when the molecules are coupled to the inorganic world, and the consequences on the electronic properties are still questioned. (iii) Which are the effects of the counter-ions present outside the helices in solution and probably remaining in the first hydration shell upon drying in the nano-technological setup?

⁶Unfortunately, so far there is no experimental demonstration of whether and how the structure of G4-DNA is modified when the molecules are employed in a device setup, deposited on and/or between inorganic materials and in a dry environment. If the structure is strongly compromised in nano-devices, the electronic properties may be also altered.

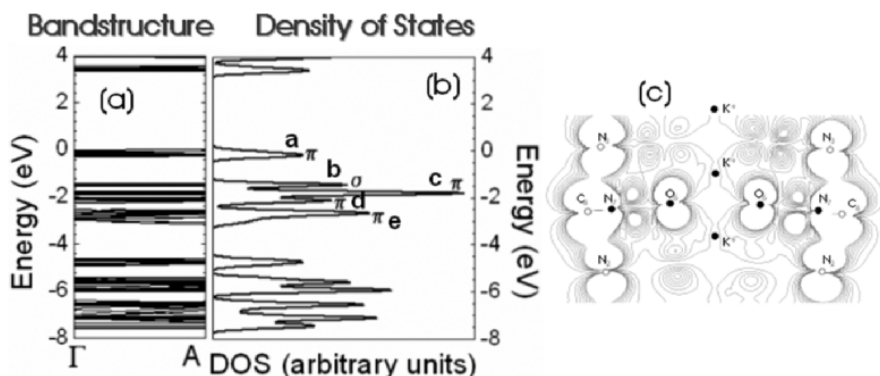


Fig. 5. (a) Bandstructure of the simulated periodic G4 wire shown in Fig. 4. The A point on the horizontal axis is the edge of the one-dimensional BZ along the stacking axis. (b) Total DOS of the G4 wire. The letters a-e label the highest occupied DOS peaks. Each peak is formed by 12 electron states with the same character of charge distribution. Peak a stems from the HOMO of guanine. The π -versus σ character is also reported in the figure. (c) Contour plot of the convolution of 12 highest occupied electron states: a continuous charge channels through the outer part of the helix is evidenced [Adapted from [70] with permission; Copyright 2004 by the American Institute of Physics]

3 Linear Response by TDDFT

The original formulation of the Hohenberg-Kohn-Sham DFT [6–8] is not, in general, applicable to excited states or to problems involving time-dependent external fields, thus excluding the calculation of optical response properties, electronic spectra, QPs, photochemistry. However, theorems have now been proved for time-dependent density functional theory (TDDFT) which extend the applicability of the original theory. In this section we briefly present the foundations of TDDFT and refer the reader to exhaustive reviews [71–73, 76] for a deeper discussion of TDDFT and its applications [77].

TDDFT is based on the Runge-Gross theorem [78]: given a system of electrons prepared in an initial state $|\Phi(t_0)\rangle$, there is a one-to-one correspondence between the external time-dependent potential v_{ext} and the time-dependent electron density $n(\mathbf{r}, t)$. This is a generalization to time-dependent potentials and densities of the stationary DFT one-to-one correspondence:

$$n(\mathbf{r}, t) \leftrightarrow v(\mathbf{r}, t) . \quad (5)$$

Note that in this case: (i) Two potentials are considered equivalent if they differ by any purely time-dependent function, instead of a constant as in ordinary DFT. In fact, two such potentials produce wave-functions which are equal up to a purely time-dependent phase, which is cancelled when any observable is calculated from them. (ii) There is a dependence on the

initial quantum state of the system [79]. (iii) Contrary to intuition, the v -representability problem (the problem of the existence of a potential that produces a given density) is milder in the time-dependent case, and has been solved by van Leeuwen [80], as an extension of the Runge-Gross theorem [78].

As in the static case, a time-dependent KS scheme can be introduced by considering a non-interacting system that reproduces the exact interacting density $n(\mathbf{r}, t)$. The time-dependent Kohn-Sham equations read

$$\left[-\frac{1}{2} \nabla^2 + v_{\text{eff}}(\mathbf{r}, t) \right] \varphi_i(\mathbf{r}, t) = i \frac{\partial}{\partial t} \varphi_i(\mathbf{r}, t), \quad (6)$$

where $v_{\text{eff}}(\mathbf{r}, t) = v_{\text{H}}(\mathbf{r}, t) + v_{\text{xc}}(\mathbf{r}, t) + v_{\text{ext}}(\mathbf{r}, t)$ is the effective time dependent potential felt by the electrons. It consists of the sum of the external time-dependent applied field, the time-dependent Hartree term, and the exchange-correlation potential. The time-dependent density can be easily evaluated from the Kohn-Sham eigenfunctions $n(\mathbf{r}, t) = \sum_{i=1}^N |\varphi_i(\mathbf{r}, t)|^2$. The initial state $|\Phi(t_0)\rangle$ should be representable by an initial Slater determinant built with the set of one-electron orbitals $\{\Phi_{j0}\}_{j=1}^N$.

3.1 Excitation Energies in TDDFT

The response of the system to an external perturbation is directly related to the excited states of the N -particle system. The linear response of the system can be determined from the density-density response function χ , that is defined by $\delta n(\mathbf{r}, \omega) = \int d^3 r' \chi(\mathbf{r}, \mathbf{r}'; \omega) \delta v_{\text{ext}}(\mathbf{r}', \omega)$, where δn is the density variation induced by the perturbing potential δv_{ext} . The same induced density can be calculated in the Kohn-Sham system $\delta n(\mathbf{r}, \omega) = \int d^3 r' \chi_0(\mathbf{r}, \mathbf{r}'; \omega) \delta v_{\text{eff}}(\mathbf{r}', \omega)$ where δv_{eff} includes the external field plus the induced Hartree and exchange-correlation potentials ($\delta v_{\text{eff}}(\mathbf{r}, \omega) = \delta v_{\text{ext}}(\mathbf{r}, \omega) + \int d^3 r' \frac{\delta n(\mathbf{r}')}{|\mathbf{r} - \mathbf{r}'|} + \int d^3 r' \frac{\delta V_{\text{xc}}(\mathbf{r})}{\delta n(\mathbf{r}')} \delta n(\mathbf{r}')$). The Kohn-Sham response function χ_0 describes the response of non-interacting electrons, and can be written in terms of the *ground-state* Kohn-Sham eigenvalues ϵ_i and eigenfunctions ψ_i

$$\chi_0(\mathbf{r}, \mathbf{r}'; \omega) = \sum_{ij} (f_i - f_j) \frac{\psi_i(\mathbf{r}) \psi_j^*(\mathbf{r}) \psi_j(\mathbf{r}') \psi_i^*(\mathbf{r}')}{\omega - \omega_{ij} + i\eta} \quad (7)$$

where $\omega_{ij} = (\epsilon_j - \epsilon_i)$ and f_i 's are Fermi occupation numbers. Now it is simple to derive a Dyson-like equation for the interacting response function. For a spin-unpolarized system it reads [82, 83]

$$\begin{aligned} \chi(\mathbf{r}, \mathbf{r}'; \omega) &= \chi_0(\mathbf{r}, \mathbf{r}'; \omega) + \int d^3 r_1 \int d^3 r_2 \chi_0(\mathbf{r}, \mathbf{r}_1; \omega) \\ &\times \left[\frac{1}{|\mathbf{r}_1 - \mathbf{r}_2|} + f_{\text{xc}}(\mathbf{r}_1, \mathbf{r}_2, \omega) \right] \chi(\mathbf{r}_2, \mathbf{r}'; \omega), \end{aligned} \quad (8)$$

where we have introduced the so-called time-dependent exchange-correlation kernel $f_{xc}(\mathbf{r}, \mathbf{r}', \omega) = \frac{\delta v_{xc}[n(\mathbf{r}, \omega)]}{\delta n(\mathbf{r}', \omega)} \Big|_{\delta v_{ext}=0}$. Looking at the analytical structure of the interacting linear response function for a finite system, it is easy to show that χ has poles at $\omega = \Omega$, where Ω are the excitation energies of the system [82,83]. On the other hand, χ_0 has poles at the Kohn-Sham eigenvalue differences $\epsilon_i - \epsilon_j$. By exploiting these facts, one can derive an eigenvalue equation for the exact eigenmodes and eigenfrequencies of the system [82,83]:

$$\int d^3 r' \Xi(\mathbf{r}, \mathbf{r}', \omega) \xi(\mathbf{r}', \omega) = \lambda(\omega) \xi(\mathbf{r}, \omega) , \quad (9)$$

where the function Ξ is defined by

$$\Xi(\mathbf{r}, \mathbf{r}', \omega) = \delta(\mathbf{r} - \mathbf{r}') - \int d^3 x \chi_0(\mathbf{r}, \mathbf{x}, \omega) \left[\frac{1}{|\mathbf{x} - \mathbf{r}'|} + f_{xc}(\mathbf{x}, \mathbf{r}', \omega) \right] . \quad (10)$$

This is a rigorous statement, that allows the determination of the excitation energies of the system from the knowledge of χ_0 and f_{xc} . To solve the eigenvalue equation one can expand $\xi(\mathbf{r}, \omega)$ in an appropriate basis and solve numerically the resulting matrix-eigenvalue equation. The matrix equation to be solved is (in a quadratic form more familiar in the quantum-chemistry community)

$$\sum_{a'i'\sigma'} [\delta_{\sigma\sigma'} \delta_{aa'} \delta_{ii'} (\epsilon_{j\sigma} - \epsilon_{k\sigma})^2 + 2\sqrt{\epsilon_{a\sigma} - \epsilon_{i\sigma}} K_{ai\sigma, a'i'\sigma'}(\Omega) \sqrt{\epsilon_{a'\sigma'} - \epsilon_{i'\sigma'}}] \times \beta_{a'i'\sigma'} = \Omega^2 \beta_{ai\sigma} , \quad (11)$$

with

$$K_{jk\sigma, j'k'\sigma'}(\omega) = \int d^3 r \int d^3 r' \psi_{j\sigma}^*(\mathbf{r}) \psi_{k\sigma}(\mathbf{r}) \times \left[\frac{1}{|\mathbf{r} - \mathbf{r}'|} + f_{xc}(\mathbf{r}, \mathbf{r}', \omega) \right] \psi_{j'\sigma'}(\mathbf{r}') \psi_{k'\sigma'}^*(\mathbf{r}') . \quad (12)$$

In (11) $\omega_{jk\sigma} = \epsilon_{j\sigma} - \epsilon_{k\sigma}$, and $f_{ij} = f_i - f_j$ is the difference of orbital occupation numbers. If the excitation is well described by one single-particle transition between an occupied and a virtual state, one can neglect the off-diagonal terms of $K_{jk\sigma, j'k'\sigma'}$ to obtain the single-pole approximation (SPA) to the excitation energies [82,83]. For a spin-unpolarized system this approximation is cast into the following equality:

$$\Omega = \omega_{12} + \text{Re} [K_{12\uparrow, 12\uparrow} \pm K_{12\uparrow, 12\downarrow}] , \quad (13)$$

where Re indicates the real part of the expression in parentheses. This approximation can be viewed as an attempt to correct the Kohn-Sham excitation energies individually, without including collective electronic effects. Note that, apart from the truncation of the expansions, two main

approximations are necessary to calculate the excitation energies: (i) the static Kohn-Sham orbitals have to be calculated with an approximate static exchange-correlation potential; (ii) the frequency-dependent exchange-correlation kernel $f_{xc\sigma\sigma'}(\mathbf{r}, \mathbf{r}', \omega)$ has to be approximated. Equation (13) describes properly the spin-multiplet structure of otherwise spin-unpolarized ground states through the spin-dependence of f_{xc} : by performing the transformation $f_{xc}^{(1)} = (f_{xc\uparrow\uparrow} + f_{xc\downarrow\downarrow})/2$ and $f_{xc}^{(2)} = (f_{xc\uparrow\uparrow} - f_{xc\downarrow\downarrow})/2$, one gets

$$\begin{aligned}\omega_{\text{singlet}} &= \omega_{12} + 2\mathcal{R} \int d^3r \int d^3r' \psi_1^*(\mathbf{r}) \psi_2(\mathbf{r}) \\ &\quad \times \left[\frac{1}{|\mathbf{r} - \mathbf{r}'|} + f_{xc}^{(1)}(\mathbf{r}, \mathbf{r}', \omega) \right] \psi_1(\mathbf{r}') \psi_2^*(\mathbf{r}') \\ \omega_{\text{triplet}} &= \omega_{12} + 2\mathcal{R} \int d^3r \int d^3r' \psi_1^*(\mathbf{r}) \psi_2(\mathbf{r}) \\ &\quad \times f_{xc}^{(2)}(\mathbf{r}, \mathbf{r}', \omega) \psi_1(\mathbf{r}') \psi_2^*(\mathbf{r}')\end{aligned}\quad (14)$$

Several calculations for the lowest excitation energies of atoms and molecules have been performed with these formulas with very promising results [71, 72, 82–86].

Full solution of the TDDFT-Kohn-Sham equations. Another very efficient method to calculate the optical spectrum of finite systems is based on solving directly the time-dependent Kohn-Sham equations in response to an external electromagnetic field. This method, originally used for the study of nuclear reactions [87], was later applied to clusters [88, 89] and biomolecules [90]. All those studies are now being performed under the **octopus** project [91] and can address not only linear-response for optical properties, but also non-linear response and nuclear dynamics. A time-evolution scheme has also been recently implemented to solve the spectral function of the Bethe-Salpeter equation (BSE) [92].

The starting point for the time-dependent simulations is the Kohn-Sham ground state of the electronic system in the nuclear equilibrium configuration. To obtain the linear optical absorption spectrum one excites all frequencies of the system by applying the electric field $\delta v_{\text{ext}}(\mathbf{r}, t) = -\kappa z \delta(t)$. This is equivalent to giving a small momentum κ to the electrons [87–89, 91]. The KS wave-functions at time δt are simply

$$\varphi_i(\mathbf{r}, \delta t) = e^{i\kappa z} \varphi_i(\mathbf{r}, 0). \quad (15)$$

These orbitals are then propagated in time

$$\varphi_i(\mathbf{r}, t + \Delta t) = \hat{T} \left(e^{-i \int_t^{t+\Delta t} dt \hat{H}_{\text{KS}}(t)} \right) \varphi_i(\mathbf{r}, t). \quad (16)$$

In this method, only occupied states need to be propagated. The spectrum can then be obtained from the induced dipole moments, and from the perturbation δv_{ext} .

One of the major advantages of this framework is that it can be trivially extended to handle non-linear response and nuclear dynamics. The possibility of performing combined electronic and nuclear optimizations within the TDDFT framework, practically brings this scheme to the same level of other methods that allow for simultaneous prediction of the atomic configuration and of the quantum mechanical electronic structure [21–23, 26, 74, 93, 94].

3.2 Comments

As discussed above, one of the main ingredients in TDDFT is the exchange-correlation kernel. This is a complex quantity that includes all the non-trivial many-body effects. Approximate kernels have been proposed over the past years and we only mention here some of the most widely used [71–73, 77].

The simplest approximation for $v_{xc}(\mathbf{r}, t)$ is the adiabatic LDA (ALDA) in which the static LDA exchange-correlation potential is used in the time-dependent Kohn-Sham equations, but evaluated with the time-dependent density. Following the same reasoning, it is straightforward to construct adiabatic generalized-gradient approximation (AGGA) potentials [75]. Unfortunately, the onset of absorption in optical spectra calculated either with the ALDA or with most AGGA functionals is typically below the observed ones (by several eV's in the case of atoms). This problem is caused by the wrong asymptotic behavior of the LDA and GGA potentials: as the exchange term does not cancel exactly the self-interaction part of the Hartree potential, the potentials go exponentially to zero instead of having the correct $-1/r$ behavior for neutral systems. To overcome some of the shortcomings of explicit density functionals, orbital-dependent xc-functionals can be used [95, 96].

In spite of its success in several cases, TDDFT has a number of commonly invoked failures that still undermine the confidence of the scientific community in its accuracy and validity. One is the severe underestimation of high-lying excitation energies in molecules when simple exchange and correlation functionals are employed. The most spectacular failure of the TDLDA is in the calculation of the photo-absorption spectrum of non-metallic solids, especially in systems like wide band-gap semiconductors. In fact, the LDA fails to give a significant correction to the simple RPA results. The reason is the following. For infinite systems, the Coulomb potential is $4\pi/q^2$. It is hence clear that, if f_{xc} must be able to correct the RPA response for $q \rightarrow 0$, it should behave asymptotically like $1/q^2$ when $q \rightarrow 0$. This is not the case for the local or gradient-corrected approximations.

Several attempts have been made to correct this problem within TDDFT.

(i) One path was started by Reining and collaborators [97], who derived the frequency-dependent kernel by imposing the TDDFT kernel to be static and equal, in the Bloch representation, to the screened Coulomb interaction [77, 97]. In this approach the KS wave-functions are assumed to coincide with the QP ones. Important excitonic effects for semiconductors are already obtained by using only the static long-range term $\Delta f_{xc}(q, G, G') =$

$-\delta_{G,G'}\alpha/|q+G|^2$, where α is a numerical constant [97] ($\alpha \approx 0.2$ for Si, and GaAs). On similar grounds, the work by Marini et al. [98] has developed a robust and efficient frequency dependent and non-local f_{xc} that takes into account local field effects, by imposing TDDFT to reproduce the many-body diagrammatic expansion of the BSE polarization function. The results are encouraging [98]. What remains to be characterized is the class of systems for which this successful approach is feasible and yields accurate results.

(ii) Kim and Görling extracted the photo-absorption spectrum of silicon from TDDFT simulations, by using the EXX approximation both in the calculation of the ground-state and for f_{xc} [100]. They found that the spectrum collapsed due to the long-range nature of the Coulomb interaction. However, by cutting off the interaction, they were able to recover agreement with experiments.

(iii) In any finite system subject to an electric field, there is accumulation of charge at the surface, which will induce a counter-field inside the sample. It is not possible for any local (or semi-local) functional of the density to describe the counter-field produced by the macroscopic polarization of the system [101, 102]. To circumvent this problem, it has been proposed to use as an extra dynamical variable the surface charge, or equivalently the macroscopic field produced by that charge [103]. Another way to take into account the macroscopic polarization is by the current response of the system within a time-dependent current-density functional formalism [104].

A general TDDFT is well suited to handle electron correlations and current-induced forces in molecular devices: Work along these lines is in progress. However, the non-adiabaticity is far from being solved. The Ehrenfest-path non-adiabatic TDDFT-based Molecular Dynamics is one possibility. In fact, it is difficult to believe that any method based on the full classical limit for the ions is able to describe intrinsically non-adiabatic phenomena, such as e.g. current-induced isomerization processes in molecular devices. Multi-component TDDFT may be a suitable extension for this purpose [105, 106].

3.3 Selected Applications of TDDFT

Biomolecular Photoreceptors

On one hand, spectacular advances were achieved over the last years in the characterization of the structural and dynamical properties of biomolecules, by a combination of quantum mechanical and classical molecular mechanics methods. On the other hand, the theoretical understanding of the interaction of those molecules with external time-dependent fields is still in its infancy, in spite of the large amount of experimental work on photoactive molecules. A photoactive molecule is usually constituted of a relatively small active center (chromophore) and of its surrounding medium (rest of the molecule plus

environment). Optical processes related, for instance, to vision and photosynthesis, rely on a subtle interplay between optical absorption in the photoactive center and its decaying mechanism through coupling to the vibrational modes of the molecule.

An appealing photoactive molecule is the green fluorescent protein (GFP). The measured optical absorption spectrum of the wild type (wt) GFP shows two main resonances at 2.63 and 3.05 eV [109, 110] (see Fig. 6), that are attributed to two different thermodynamically stable protonation states of the chromophore (neutral and negative chromophore, respectively). So far, ab-initio quantum chemistry has not been able to provide satisfactory agreement with the spectroscopic data, and thus has not contributed too much to confirm or rule out various possible scenarios of photodynamics in the GFP. A good description of the optical properties of the GFP photoreceptor has been achieved [90] by using an approach that combines a QM/MM method to obtain the structure with TDDFT to treat the electronic excitations. The structures were optimized using a hybrid QM/MM method [111–113] with a semiempirical hamiltonian [114] to describe the quantum subsystem. The QM region included a sequence of three amino-acids that form the chromophore: Ser65, Tyr66 and Gly67. The optimized structure of the chromophore, with the most important neighbor residues, is shown in Fig. 6. On the other hand, the anionic form of the chromophore was obtained by

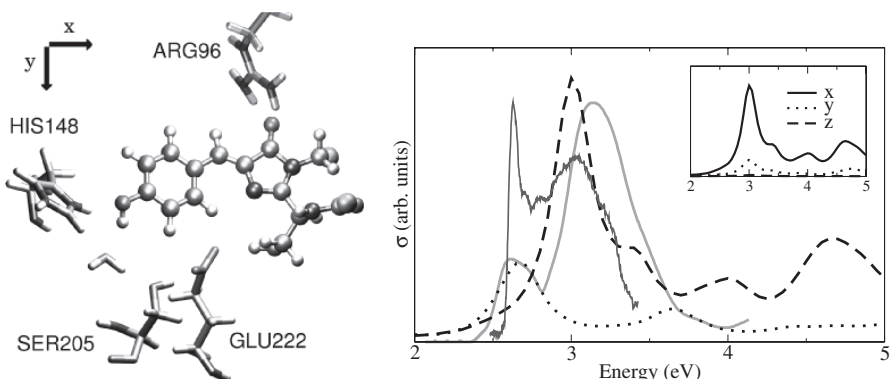


Fig. 6. *Left panel:* Optimized structure of the neutral chromophore and its closest charged residues inside the GFP: His148, Arg96 (positive) and Glu222 (negative). *Right panel:* Computed photoabsorption cross section of the neutral (dashed line) and anionic (dotted line) chromophores. For comparative purposes the anionic results have been divided by 4. Experimental results at 1.6 K (dark thin solid lines) [109] and room temperature (light thick solid line) [110] are also given. The inset shows a decomposition of the calculated spectrum of the neutral chromophore in the three directions, showing the inherent anisotropy of the green fluorescent protein molecule [Adapted from [90] with permission; Copyright 2003 by the American Physical Society]

deprotonation of Tyr66 and protonation of Glu222. The computed photoabsorption spectra of the GFP neutral and anionic chromophores, shown in Fig. 6, are in excellent agreement with experiment assuming the presence of the two forms of the photo-receptor, protonated and deprotonated respectively, in an approximately 4:1 ratio. Furthermore, it can be seen in the inset of Fig. 6 that light polarized along the x-direction is responsible for the lowest optical transition in the neutral chromophore. The molecule is nearly transparent to visible light polarized along the other two orthogonal directions. The GFP turns out to be a rather anisotropic molecule in the visible region, a property that could be used to enhance the photo-dynamical processes in well oriented GFP samples for opto-electronic devices.

The above example shows that the novel approach based on TDDFT, developed for the computation of optical spectra of finite systems, holds great promise for future applications in biochemistry and biophysics. It is able to handle not only the optical response but also ultrashort femtosecond electron-ion dynamics.

Optical Response of DNA Bases and Base Pairs

Another example of biological interest, that has been studied by searching for the full solution of the TDDFT-Kohn-Sham equations, is the calculation of the optical properties of the DNA bases [115]. Here we present the optical spectrum of adenine in the 9H-form, the only tautomer which is present in the adenine nucleotide, the molecular building block of DNA and RNA polymers. The calculation was performed for the isolated base in the gas phase, i.e. without taking into account solvent effects. From experiments [116, 117], it is clear that the absorption spectra of the individual nucleobases are quite complex: in the low energy region they are formed by several excitations of $\pi \rightarrow \pi^*$ character and a number of $n \rightarrow \pi^*$ transitions. The latter features are difficult to characterize, because of their extremely weak oscillation strengths. However, they are thought to play an important role for non-radiative decay of the excited states [118, 119]. These experiments are made in different solvent conditions, and for different adenine derivatives. Therefore, one should be extremely careful in comparing the results of gas-phase calculations with data from solution experiments.

The ground-state geometry was optimized without planar constraints, using the B3LYP potential [120]. The time-propagation of the KS equations was performed using the LDA and GGA time-dependent xc functionals. These different functionals yielded identical results. The geometry, the Kohn-Sham HOMO and LUMO, and the calculated photoabsorption cross section, are shown in Fig. 7.

The spectrum resolved in the three spatial directions clearly demonstrates the anisotropy of the molecule. From this calculation the most bright excitations are located at: 4.54, 4.88, 5.70, 6.21, 6.77, and 7.41 eV. Performing

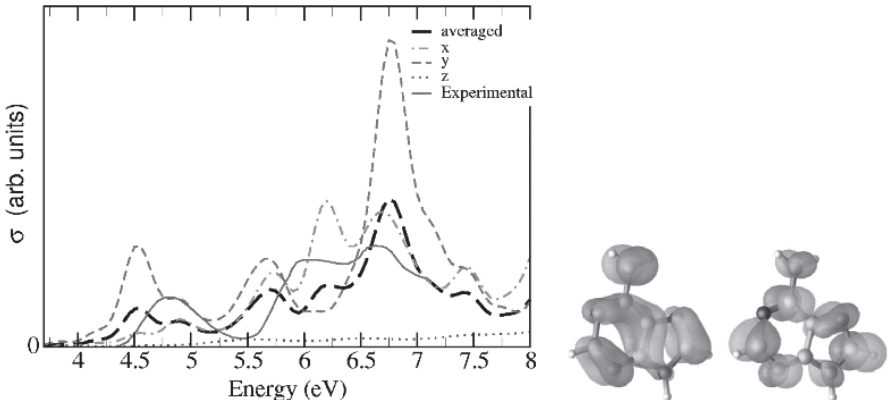


Fig. 7. Calculated photoabsorption cross section of adenine along the three directions and averaged (black line). In the inset, the HOMO (π) and LUMO (π^*) Kohn-Sham orbitals are shown: different colors indicate different sign of the wavefunctions. An experimental absorption spectra of deoxyadenosine 5'-phosphate in solution is also shown (thin solid line) from [116]

linear response calculations in the frequency domain (11) it is possible to unveil the character of such transitions [121], which turn out to be prevalently $\pi \rightarrow \pi^*$. From the experiments cited above, one can distinguish the following excitation energies: 4.9 (measured in vapor [117]), 5.7–6.1, 6.8, and 7.7 eV. Apart from the last excitation where the sugar and phosphate may play an important role, and the first one that is not measured in these experiments, we find a satisfactory agreement with an accuracy of 0.1 eV. A recent review presents a critical collection of the latest ab-initio calculations [122]. Early calculations are reviewed separately [123].

It is also possible within a time-evolution scheme to calculate circular dichroism (CD) [89], which is a very powerful tool used in the characterization of biomolecules. In particular, the complex rotatory strength function $R(\omega) = R_x(\omega) + R_y(\omega) + R_z(\omega)$ is given in terms of the Fourier transform of the time evolution of the angular momentum operator $L_z(t) = \sum_i^{\text{occ}} \langle \varphi_i | -i(r \times \nabla)_z | \varphi_i \rangle$. Early results for the CD spectra of DNA bases are encouraging [115]. Because the CD technique is routinely used along with chemical synthesis to characterize the obtained molecules, the successful ab-initio computation of CD spectra will represent in the near future a powerful tool for the interpretation of experimental data, as well as for the prediction of novel molecules suitably designed for a precise purpose.

4 Wannier Functions for Electronic Structure Calculations

The electronic structure in periodic solids is conventionally described in terms of extended Bloch functions (BFs) $\psi_{\mathbf{k}n}(\mathbf{r})$: n and \mathbf{k} label the band number and the wave vector respectively. In fact, by virtue of the Bloch theorem, the Hamiltonian \hat{H} commutes with the lattice-translation operator $\hat{T}_{\mathbf{R}}$ (\mathbf{R} is a vector of the crystal lattice), leading to a set of eigenstates (the Bloch states) for the Hilbert space. This property restricts the crystal problem to a single unit cell. The properties of the infinite solid are then recovered with an integral over the BZ, in the reciprocal space. An alternative description for the electronic ground state can be derived in terms of localized Wannier functions $w_n(\mathbf{r}-\mathbf{R})$ [124], that constitute a site(\mathbf{R})- and band(n)-dependent orthogonal basis set for the tight-binding form of the wave-function. Being related by a unitary transformation, the two representations (Bloch and Wannier) are mathematically equivalent. However, because of their localized character, the WFs are particularly suited to the treatment of localized phenomena. For instance, WFs yield a localized picture of chemical bonding (Lewis-like) [125, 126].

Recently, WFs have attracted an increasing interest for their possible application to a wide range of (i) physical problems (e.g., the modern theory of bulk polarization [102, 127], the development of linear scaling order- N and ab-initio molecular dynamics approaches [128–131], the calculation of quantum electronic transport [132], the study of magnetic properties and strongly-correlated electrons [133–135]) and of (ii) physical systems (e.g., crystal and amorphous semiconductors [136–138], ferroelectric perovskites [139], transition metals [140, 141], metal-oxides [142], photonic lattices [143–145], high-pressure hydrogen and liquid water [146–148], SWNTs and 1-dimensional nanostructures [132, 149], metallic interfaces [150]).

The major obstacle to the construction of the Wannier functions in practical calculations is their non-uniqueness: They are *gauge dependent*, namely infinite sets of WFs, with different properties, may be defined for the same physical system. This non-uniqueness arises from the freedom in the choice of the phase factor of the electronic wave-function, that is not assigned by the Schrödinger equation. Additional complications concern the difficulties in dealing with degeneracies among the energy bands in the Brillouin zone. This extends the arbitrariness related to freedom of the phase factor to a gauge transformation ($U^{(\mathbf{k})}$) that mixes bands among themselves at each \mathbf{k} -point of the BZ. A different gauge transformation does not translate into a simple change of the overall phases of the WFs, but affects their shape, analytic behavior and localization properties.

Among the different methods presented so far, we adopted a localization algorithm that allows to transform a set of BFs – calculated by means of ab-initio approaches [23, 26] – into a unique set of Maximally localized Wannier functions (MLWFs) [151, 152]. The formulation of the minimum-spread

criterion extends the concept of *localized molecular orbitals*, proposed by Boys [126] for molecules, to the solid-state case. We apply this algorithm to study the electronic properties of selected nanostructures, and to develop a novel implementation of quantum conductance calculations [153].

4.1 Selected Applications of Wannier Computationin Nanostructures

Analysis of the Chemical Bonding: C Chains

Traditional chemistry is based on local concepts. For instance, covalently bonded materials are described in terms of bonds and electron pairs, where the bonding properties are determined by the closest atomic neighborhood. Thus, the characteristics of a bond (distance, angles, strength, character, etc.) essentially depends on the coordination number of each atom, while the second-nearest neighbors and more distant atoms give only weaker contributions. This is the typical case of molecules or insulating materials. However, even in metallic systems where this simple bond concept is no longer valid, locality still exists and manifests fundamental aspects.

The standard electronic structure calculations typically do not bring a deep insight into the localization properties of matter: the Bloch states, for instance, describe the electronic states of the overall crystal and not the individual chemical bonds. On the contrary, a set of maximally localized orbitals may give an insightful picture of the bonding properties [154].

These issues are best illustrated by nano-sized Carbon systems [132]. We focus on an allotrope, known as *carbyne*, based on a linear chain of *sp*-hybridized carbon atoms in two possible forms: isomeric polyethynylene diylidene (polycumulene, or simply cumulene) and polyyne (polyyne). The cumulene form is characterized by an equidistant arrangement of C atoms with double *sp*-bonds ($=C=C=$)_{*n*}, while the polyyne form is a dimerized linear chain with alternating single-triple bonds ($-C\equiv C-$)_{*n*}.

The calculated MLWFs allow us to investigate the effects of structural relaxation on the electronic properties of infinite carbon chains [132]. To obtain the WFs, we first relaxed both the atomic and the electronic structure of the C-chain by employing a standard ab-initio DFT plane-wave pseudopotential code [23]. Then, by using the *WanT code* [153], we transformed the resulting Bloch eigenstates into a set of maximally localized WFs. Results are summarized in Fig. 8. Cumulene (Fig. 8, left) is characterized by symmetric *sp*-bonds, uniformly distributed along the chain. σ states (Fig. 8a) are localized in the middle of $C=C$ bonds, whereas π states (Fig. 8b) are centered around C atoms. In polyyne (Fig. 8, right), σ orbitals are localized both on single $C-C$ and on triple $C\equiv C$ bonds, with a σ state in the middle of each bond (Fig. 8a'). The π orbitals (Fig. 8b') are localized only on the $C\equiv C$ bonds: there are two of these π orbitals in the middle of each triple bond, but no one around the single bonds. The distribution of the WFs reproduces

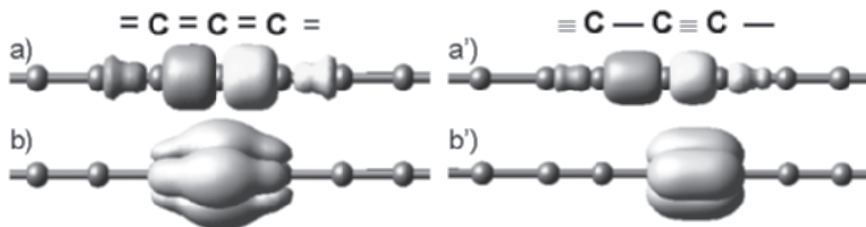


Fig. 8. Isosurfaceplots of (a,a') σ and (b,b') π WFs, for the cumulene (left) and polyyne (right) forms of carbyne [Adapted from [132] with permission; Copyright 2004 by the American Physical Society]

the alternation of single-triple bonds in polyyne, otherwise not accessible in the delocalized Bloch scheme.

Heuristically, we may relate the electrical properties of the chains to the geometrical properties of the WFs. The symmetric cumulene chain with all identical bonds presents a metallic behavior. On the contrary, polyyne is a semiconductor: the relaxation of the carbon-carbon distances into inequivalent alternating bonds induces a Peierls-type distortion, which stabilizes the structure and generates energy gaps at the edges of the BZ. The metallic behavior of cumulene is in qualitative agreement with the geometrical properties of the WF's. While the σ states (Fig. 8a,a') are centred in the middle of the $C - C$ bonds for both structures, the π orbitals (Fig. 8b,b'), which stem from the bands near the Fermi level, are centred in the middle of the bond in polyyne and on top of atoms in cumulene. The displacement of π Wannier functions from the center of the bonds to the atoms is the expression of the near-free character (delocalization) of the cumulene electrons, within a localized basis set picture. This result confirms the suitability of MLWFs for treating both localized and nearly-free electron systems, and for discriminating non uniform bonding patterns.

Spontaneous Polarization in Boron Nitride Nanotubes

The macroscopic polarization of a dielectric has a well known phenomenological definition in classical physics, but a microscopic description cannot be obtained in standard quantum mechanical treatments. The *longitudinal* polarization (\mathbf{P}_L) of a *finite* material is related to the dipole per unit volume, and manifests itself when the bulk periodicity is broken, e.g. as a screening field due to the charge accumulation at the sample surfaces. \mathbf{P}_L is experimentally accessible but its direct calculation is impractical. The problem lies in the attempt to calculate the dipole moment for a bulk *infinite* solid. Since Born-von-Karman boundary conditions are used to recover the thermodynamic limit, the dipole moment (i.e., the position operator), which depends on the truncation of the unitary cell, is ill defined. The so called *Modern*

theory of polarization [102, 127] gives a rigorous definition of the polarization in a periodic system: the term accessible from a theoretical point of view is the variation of the *transverse* polarization $\Delta\mathbf{P}^{(\lambda)}$, that is a gauge-invariant Berry's phase of the Bloch orbitals, with respect to two reference states, related by an adiabatic transformation λ . The transverse polarization has no relation with the charge density of the sample, and it is related to the measurable polarization through the relation $\Delta\mathbf{P} = \epsilon_0\mathbf{P}_L$, where ϵ_0 is the dielectric tensor.

$\mathbf{P}^{(\lambda)}$ can be split into an ionic $\mathbf{P}_{ion}^{(\lambda)}$ contribution and an electronic $\mathbf{P}_{el}^{(\lambda)}$ one [155]. The ionic part $\mathbf{P}_{ion}^{(\lambda)} = \frac{e}{V} \sum_I Z_I^{(\lambda)} R_I^{(\lambda)}$ is straightforwardly calculated from the spatial displacements of the ionic charges Z_I . The electronic part is given by

$$\mathbf{P}_{el}^{(\lambda)} = -\frac{2ie}{(2\pi)^3} \sum_n \int_{BZ} d^3k \langle u_{kn} | \nabla_{\mathbf{k}}^2 | u_{kn} \rangle , \quad (17)$$

where u_{kn} is the periodic part of the occupied Bloch states of the system. The Berry's phase (modulo 2π) is defined as

$$\phi_{\alpha}^{(\lambda)} = V \mathbf{G}_{\alpha} \cdot \mathbf{P}_{el}^{(\lambda)} / e , \quad (18)$$

where V is the volume of the unit cell and \mathbf{G}_{α} is the reciprocal lattice vector along the α direction. The integrand in (17) is the expectation value of the position operator \mathbf{r} , which in turn is related to the definition of the MLWFs [151]. It turns out that an alternative formulation of the electronic polarization may be expressed in terms of the center of charge of the Wannier functions of the occupied bands $\langle \mathbf{r} \rangle_n$ (a detailed formulation is given elsewhere [102, 127])

$$\mathbf{P}_{el}^{(\lambda)} = -\frac{2e}{V} \sum_n \langle \mathbf{r} \rangle_n . \quad (19)$$

The Wannier centers provide an intuitive correspondence with the classical concept of *electron localization*, that is used in the classical definition of the macroscopic polarization.

We illustrate the outlined framework by computing the spontaneous polarization in boron nitride nanotubes (BNNTs) [149], which are among the broad variety of candidates for nano-junctions. Unlike carbon nanotubes (CNTs), most BN structures are non-centrosymmetric and polar, which may suggest the existence of a non-zero spontaneous polarization. As mentioned before, although the transverse polarization \mathbf{P} itself is not a physical observable, the difference between two crystal states can indeed be measured and calculated. In this case we assume as reference states a polar BNNT and a non polar CNT with the same geometry. The adiabatic transformation is defined by a *virtual crystal* procedure that uniformly transforms the non polar CNT into the corresponding BNNT, substituting carbon atoms with boron and nitrogen atoms [149]. The electronic contribution to the polarization is given by

$$\Delta \mathbf{P}_{el}^{(BN)} = -\frac{2e}{V} \sum_i (\mathbf{r}_i^{(BN)} - \mathbf{r}_i^{(C)}) , \quad (20)$$

which is directly proportional to the shift of the Wannier centers. The results for C and BN zigzag nanotubes of arbitrary diameter are reported in Fig. 9. The σ WFs are centered in the middle of C-C bonds in CNTs, while they are shifted towards the more electronegative cations (N) in BNNTs. However, since the shifts of the centers from C to BN (black arrows in the Fig. 9) have the same magnitude along each bond, the effects compensate, giving a zero contribution to the electronic polarization. On the contrary, the π states are centered on the cations in BNNTs, while they show a characteristic V-shape in CNTs. The difference between the two states gives rise to a non vanishing electronic polarization along the axis of the BN nanotubes. Thus, this real-space description gives a simple but quantitative description of the electronic part of the spontaneous polarization.

Incidentally, note that the total spontaneous polarization is zero for BN-NTs, due to an exact cancellation of the ionic and electronic contributions. The results suggest that, in spite of the different electronegativity of the their constituents, BNNTs are non-polar nanostructures [149].

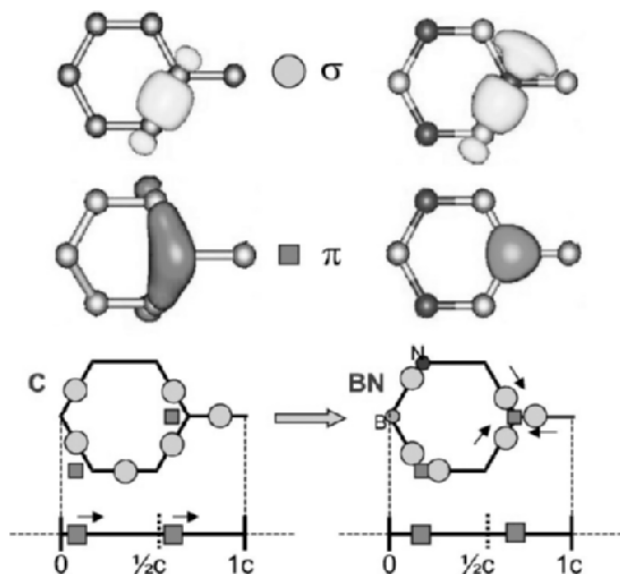


Fig. 9. *Upper panels:* Isosurfaces of the σ and π WFs for C (left) and BN (right) nanotubes. *Lower panel:* schematic position of the Wannier centers in C and BN hexagons, and the projections of the π states onto the nanotube axes. The centers of σ (π) states are represented with circles (squares). See text for further details [Adapted from [149] with permission; Copyright 2003 by the American Physical Society]

Electronic Transport in Nanostructures

We consider the exploitation of the MLWFs as a minimal basis set for the computation of the ballistic electronic transport in nanostructures [132, 150].

The standard approaches to electronic transport in semiconductors are based on the semiclassical Boltzmann's theory. The dynamics of the charge carriers and the response to external fields follow the classical equations of motion, whereas the scattering events are included in a perturbative approach, via the quantum mechanical *Fermi's Golden Rule*. However, this semiclassical description is unsuitable for nanodevices where the tiny size requires a fully quantum mechanical theory [156] for a reliable quantitative treatment.

The quantum description of the electronic conductance is a complicated non-equilibrium problem. Here we focus on the *ballistic transport regime*. In this case the electronic conduction is characterized by the scattering properties of the system, i.e. by the probability that a charge carrier might travel from one lead to the other through a conductor region. This approach neglects the non-equilibrium effects (e.g., external bias) and the incoherent scattering processes, such as the electron-phonon or the electron-electron interactions.

The Landauer formalism and some implementations of it are already reported in Chaps. 4–6 of this collection [157–159], and in several basic references cited therein. Here, we focus on few principles necessary to introduce our particular implementation through the MLWFs. Let us consider a system composed of a conductor, C , connected to two semi-infinite leads⁷, L and R , as in Fig. 10. The conductance through a region of interacting electrons (the C region in Fig. 10) is related to the scattering properties of the region itself via the Landauer formula [156], (4). The transmission function can be easily expressed as [160]

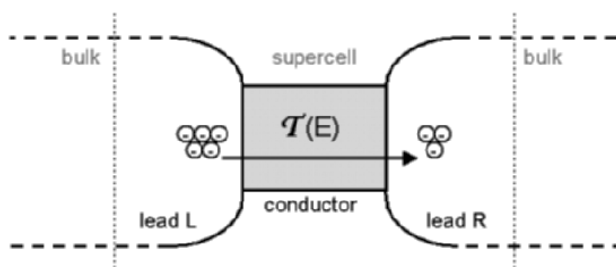


Fig. 10. Geometry of a typical conductance calculation. The nanodevice is modeled as a naniconductor (C) that bridges two metallic leads (L and R) (From [132] by permission; Copyright 2004 by the American Physical Society)

⁷In the application of the Landauer formula, it is customary to compute the transmission probability assuming that each lead is connected to a reflection-less contact whose electron energy distribution is known [156].

$$\mathcal{T} = \text{Tr}(\Gamma_L G_C^r \Gamma_R G_C^a), \quad (21)$$

where $G_C^{\{r,a\}}$ are the retarded and advanced lattice Green's functions of the conductor, and $\Gamma_{\{L,R\}}$ are functions that describe the coupling of the conductor to the leads.

The effect of the semi-infinite leads on the conductor can be described by means of finite-dimension operators known as the *self-energies* $\Sigma_{L,R}$. The self-energy terms can be viewed as effective Hamiltonians that account for the coupling of the conductor with the leads. The Green's function G_C and the coupling functions $\Gamma_{\{L,R\}}$ of (21) are explicitly obtained from the self-energies as

$$G_C = (\epsilon - H_C - \Sigma_L - \Sigma_R)^{-1}, \quad (22)$$

$$\Gamma_{\{L,R\}} = i[\Sigma_{\{L,R\}}^r - \Sigma_{\{L,R\}}^a]. \quad (23)$$

H_C is the Hamiltonian matrix of the conductor, calculated with respect to a localized real-space basis set.

The expressions for the self-energies can be deduced along the lines traced by Buongiorno Nardelli [161] using the formalism of *principal layers* [162] in the framework of the surface Green's function matching theory. We obtain

$$\begin{aligned} \Sigma_L &= H_{LC}^\dagger (\epsilon - H_{00}^L - (H_{01}^L)^\dagger \bar{T}_L)^{-1} H_{LC}, \\ \Sigma_R &= H_{CR} (\epsilon - H_{00}^R - H_{01}^R T_R)^{-1} H_{CR}^\dagger, \end{aligned} \quad (24)$$

where $H_{nm}^{L,R}$ are the matrix elements of the Hamiltonian between the layer orbitals of the left and the right leads, respectively, and $T_{L,R}$ and $\bar{T}_{L,R}$ are the appropriate transfer matrices, easily computable from the Hamiltonian matrix elements via an interactive procedure [163].

The only required inputs are the matrix elements of the Hamiltonian, (e.g. H_{00} and H_{01}), expanded within a localized-orbital basis. The accuracy of the results directly depends on two main features: (i) the accuracy in the description of the electronic structure of the system (an ab-initio scheme is desirable), and (ii) the condition that principal layers do not couple beyond nearest neighbors, which means that the basis for the computation of the Hamiltonian terms in (24) is well localized. By choosing the maximally-localized WFs representation, we devise a scheme that allows us to connect an accurate first principle description of the ground state through plane-wave pseudopotential DFT calculations, familiar to the electronic structure community active in condensed matter physics, to a local picture suitable to plug into (24), thus satisfying the two above requirements⁸.

⁸A solution which is alternative to our formulation, and was already implemented by other scientists, relies on computing the ground-state electronic properties of the system from first principles directly on a localized basis set, such as atomic orbitals [22, 164] or gaussians [165], instead of plane waves. See also Chaps. 4 and 5 in this book.

The matrix elements of the Hamiltonian in the MLWF basis may be easily calculated using the same unitary matrix $U^{(\mathbf{k})}$ obtained in the localization procedure [151]. By means of the ab-initio energy eigenvalues ($\tilde{\epsilon}_{m\mathbf{k}}$), we write down the Hamiltonian matrix $\tilde{H}_{mn}(\mathbf{k}) = \tilde{\epsilon}_{m\mathbf{k}}\delta_{m,n}$, which is diagonal in the basis of the Bloch eigenstates. We calculate the matrix for the rotated states,

$$H^{(rot)}(\mathbf{k}) = (U^{(\mathbf{k})})^\dagger \tilde{H}_{mn}(\mathbf{k}) U^{(\mathbf{k})}. \quad (25)$$

Next, we transform $H^{(rot)}(\mathbf{k})$ into a set of N Bravais lattice vectors \mathbf{R} within a Wigner-Seitz supercell centered around $\mathbf{R}=0$:

$$H_{mn}^{(rot)}(\mathbf{R}) = \frac{1}{N} \sum_{\mathbf{k}} e^{-i\mathbf{k}\cdot\mathbf{R}} H^{(rot)}(\mathbf{k}) = \langle w_{m\mathbf{0}} | \hat{H} | w_{n\mathbf{R}} \rangle, \quad (26)$$

where the factor $\frac{1}{N}$ stems from the folding of the uniform mesh of \mathbf{k} -points in the BZ. Thus, the term with $\mathbf{R} = 0$ gives the *on site* matrix elements $H_{00} = \langle w_{m\mathbf{0}} | \hat{H} | w_{n\mathbf{0}} \rangle$, and the term $\mathbf{R} = 1$ gives the *coupling* matrix elements $H_{01} = \langle w_{m\mathbf{0}} | \hat{H} | w_{n\mathbf{1}} \rangle$. These matrix elements are the necessary input for the computation of the quantum conductance. We refer the reader to the original paper [132] for the detailed description of the mathematical algorithms.

This multi-step method [153] operates as a postprocessing scheme after ab-initio electronic structure calculations, without introducing external parameters. For what concerns algorithms, our localized-basis method can be compared to a tight-binding approach: in both cases the elements of the Hamiltonian matrix are built up using a few orbitals per site and this drastically reduces the computational effort in the determination of transport properties. The employment of semi-empirical methods requires a careful choice of the parameters, which need to fit the characteristics of the simulated system. On the contrary, this approach based on the evaluation of MLWFs may exploit the transferability properties intrinsic in the ab-initio methods. To compute the two-terminal conductance one needs, in principle, three sets of calculations (two sets if the leads are of the same material): a bulk calculation to describe each of the two infinite leads, and a supercell calculation which includes the conductor and the interfaces with the leads (the central region between the two dotted vertical lines in Fig. 10). The Hamiltonian matrices $H_{0,0}^{L,R}$ and $H_{0,1}^{L,R}$ are obtained from the lead bulk calculations; the other Hamiltonian matrices of (24) come instead from the supercell calculation. The transfer matrix approach defined in (22–24) requires the matching between the bulk-like and the supercell sub-systems. To obtain this matching, it is necessary that the external part of the supercell exactly reproduces the bulk properties of the leads. Hence: the supercell must be sufficiently thick.

It is worth spending some words to clarify what is the meaning of Wannier functions for the conductor: as the WFs derive from Bloch states, they are well defined for periodically repeated systems; on the contrary, in the framework of Fig. 10, the conductor is finite. We can deal with the WFs of the

conductor, because we are treating it in a supercell approach, where periodic boundary conditions are applied. Indeed, from a mathematical point of view one can calculate the Bloch functions of the whole supercell and the corresponding Wannier functions are well defined. However, the supercell contains both the finite conductor and a portion of the connected leads: thus, in principle, one obtains the global WFs of the coupled system and not only for the very conductor. The key point of this scheme is related to the localization properties of the MLWFs: in fact, being the MLWFs strongly localized, it is possible to distinguish between those centered on the conductor and those centered on the leads. This feature allows us to define the WFs for the conductor and the leads, and to compute the corresponding elements of the Hamiltonian matrices.

This kind of approach brings two additional remarkable advantages. First, the fact that the conductor/lead interfaces are treated in the same supercell employed for the bridge, assures a detailed description of the contacts from a microscopic point of view. Second, since WFs are related to chemical bonding, one can unambiguously recognize a given lead WF from both the bulk lead and the supercell calculations: they must be identical.

As a prototypical example of a two terminal device, we computed the quantum conductance for a small zigzag (5,0) carbon nanotube in the presence of an isolated substitutional silicon defect. The *conductor* region is a finite segment of nanotube which contains the defect, while the *leads* are simulated by two semi-infinite ideal nanotubes. Figure 11a shows the iso-surfaces of two calculated Wannier functions with a σ character. Far away from the defect, the WF is symmetric and centered in the middle of the C-C bond. On the contrary, near the Si atom the electronic orbital is polarized and mainly localized around the nearest C atoms. The different electronegativity between silicon and carbon favors the localization of electronic states changing the conduction properties of the system.

Figure 11b displays the quantum conductance of the nanotube with (C(5,0)/Si, solid line) and without (C(5,0), dashed line) the presence of the defect. The conductance of the ideal (5,0) nanotube shows the typical step-like shape and a metallic behavior, which is the result of the high curvature of such a small radius nanotube [166]. Once a single Si defect is introduced, the system maintains its metallic character but the overall spectrum changes drastically. We observe a general reduction of the conductance across the whole energy range, and the distortion of the step-like shape of the pure nanotube. The appearance of dips, corresponding to the discontinuities in the original step function, is a characteristic feature of nanotubes with defects [167]: the backscattering of electrons reduces the quantum conductance.

The multi-step procedure [153] presented in this final section opens the way to selectively describe the quantum conductance in terms of the relevant one-electron states that contribute directly to the transport process [132,150]. Furthermore, by taking into account that the MLWFs constitute an analytical

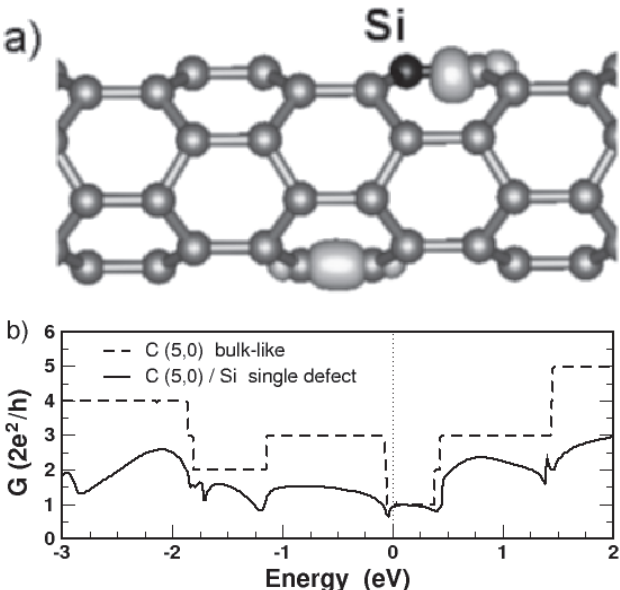


Fig. 11. (a) Isosurface of two σ WFs in a (5,0) carbon nanotube in the presence of a substitutional Si defect (blue sphere). The polarization of the σ states is due to the effect of the Si defect. (b) Quantum conductance plots for the (5,0) nanotube with (solid line) and without (dashed line) the Si defect. The vertical dotted line marks the Fermi Level [Adapted from [132] with permission; Copyright 2004 by the American Physical Society]

basis set for the Hilbert space, it is straightforward to extend the concepts of ballistic transport to more complex physical phenomena. For instance, the method is suitable for extensions that introduce the effects of short range electron-electron correlations [168], or for the inclusion of non-equilibrium effects related to the presence of an external applied bias.

Acknowledgements

The work on the DNA bases at both INFM-S3 and UPV/DIPC was partially funded by the EC through contract IST-2001-38951 (project “DNA-based Nanowires”).

AR and DV were supported by the European Community through the Network of Excellence NANOQUANTA (NOE 500198-2); by the Spanish MCyT (MAT2001-0946); by the University of the Basque Country (9/UPV 00206.215-13639/2001). The computer time was granted by DIPC and CEPBA (Barcelona). AR and DV benefited from stimulating discussions and collaborations with A. Castro, M.A.L. Marques, A. Marini, L. Wirtz, M. Gruneing, G. F. Bertsch, M. L. Cohen, R. Del Sole, P. M. Echenique, R. Godby,

E. K. U. Gross, X. López, E. San Sebastian, G. Onida, L. Reining, K. Yabana, Y. Miyamoto, D. Tomanek and Ph. Lambin.

RDF and AC were supported by INFM through the Parallel Computing Initiative. Additional funding was provided by MIUR-Italy through FIRB-NOMADE. Computations were done at CINECA, Bologna, Italy. Anna Garbesi, Elisa Molinari, Marco Buongiorno Nardelli, Carlo Cavazzoni, Nicola Marzari, and Andrea Ferretti are gratefully acknowledged for collaborations and discussions.

References

1. A. Szabo and N.S. Ostlund: *Modern Quantum Chemistry. Introduction to Advanced Electronic Structure Theory*, (Dover Publications, Mineola NY 1996)
2. T. Helgaker, P. Jørgensen, and J. Olsen: *Molecular Electronic-Structure Theory*, (Wiley, Chichester 2000)
3. J. Šponer, J. Leszczynski, and P. Hobza: Structures and Energies of Hydrogen-Bonded DNA Base Pairs. A Nonempirical Study with Inclusion of Electron Correlation, *J. Phys. Chem.* **100**, 1965 (1996)
4. J. Šponer, J. Leszczynski, and P. Hobza: Nature of Nucleic Acid-Base Stacking: Nonempirical ab Initio and Empirical Potential Characterization of 10 Stacked Base Dimers. Comparison of Stacked and H-Bonded Base Pairs, *J. Phys. Chem.* **100**, 5590 (1996)
5. *A Primer in Density Functional Theory*, Lecture Notes in Physics **620**, ed. by C. Fiolhais, F. Nogueira, and M. Marques (Springer, Berlin Heidelberg New York 2003).
6. W. Kohn: Nobel Lecture: Electronic structure of matterwave functions and density functionals, *Rev. Mod. Phys.* **71**, 1253 (1999).
7. W. Kohn: In *Theory of the Inhomogeneous Electron Gas*, ed. by S. Lundqvist and N.H. March (Plenum Press, New York 1983)
8. R.M. Dreizler and E.K.U. Gross: *Density Functional Theory, an Approach to the Quantum Many Body Problem*, (Springer, Berlin Heidelberg New York 1990)
9. W. Koch and M.C. Holthausen: *A chemist's guide to density functional theory* (Wiley-VCH, Weinheim 2000)
10. P. Hohenberg and W. Kohn: Inhomogeneous Electron Gas, *Phys. Rev.* **136**, B864 (1964)
11. W. Kohn and L.J. Sham: Self-Consistent Equations Including Exchange and Correlation Effects, *Phys. Rev.* **140**, A1133 (1965)
12. R.A. Friesner and B.D. Dunietz: Large-Scale ab Initio Quantum Chemical Calculations on Biological Systems, *Acc. Chem. Res.* **34**, 351 (2001)
13. J. Park, A.N. Pasupathy, J.I. Goldsmith, C. Chang, Y. Yaish, J.R. Petta, M. Rinkoski, J.P. Sethna, H.D. Abrunña, P.L. McEuen, and D.C. Ralph: Coulomb blockade and the Kondo effect in single-atom transistors, *Nature* **417**, 722 (2002)
14. W. Liang, M.P. Shores, M. Bockrath, J.R. Long, and H. Park: Kondo resonance in a single-molecule transistor, *Nature* **417**, 725 (2002)

15. P. Jarillo-Herrero, S. Sapmaz, C. Dekker, L.P. Kouwenhoven, H.S.J. van der Zant: Electron-hole symmetry in a semiconducting carbon nanotube quantum dot, *Nature* **429**, 389 (2002)
16. S. Oberholzer, E.V. Sukhorukov, and C. Schönenberger: Crossover between classical and quantum shot noise in chaotic cavities, *Nature* **415**, 765 (2002)
17. E. Di Mauro and C.P. Hollenberg: DNA technology in chip construction, *Adv. Mater.* **5**, 384 (1993)
18. Y. Xia, J.A. Rogers, K.E. Paul, and G.M. Whitesides: Unconventional Methods for Fabricating and Patterning Nanostructures, *Chem. Rev.* **99**, 1823 (1999)
19. J.M. Lehn: Perspectives in supramolecular chemistry. From molecular recognition towards molecular information processing and self-organization, *Angew. Chem. Int. Ed.* **29**, 1304 (1990)
20. G.M. Whitesides and M. Boncheva: Supramolecular Chemistry And Self-assembly Special Feature: Beyond molecules: Self-assembly of mesoscopic and macroscopic components, *Proc. Natl. Acad. Sci. USA* **99**, 4769 (2002)
21. J.A. Pople, M. Head-Gordon, D.J. Fox, K. Raghavachari, and L.A. Curtiss: Gaussian-1 theory: A general procedure for prediction of molecular energies, *J. Chem. Phys.* **90**, 5622 (1989); <http://www.gaussian.com/>
22. J.M. Soler, E. Artacho, J.D. Gale, A. García, J. Junquera, P. Ordejón and D. Sánchez-Portal: The Siesta method for ab initio order-N materials simulation, *J. Phys.: Condens. Matter* **14**, 2745 (2002); <http://www.uam.es/departamentos/ciencias/fismateriac/siesta/>
23. S. Baroni, S. de Gironcoli, A. Dal Corso, and P. Giannozzi: Plane-Wave Self-Consistent Field, <http://www.pwscf.org>
24. M. Bockstedte, A. Kley, J. Neugebauer, and M. Scheffler: Density-functional theory calculations for poly-atomic systems: electronic structure, static and elastic properties and ab initio molecular dynamics, *Comput. Phys. Commun.* **107**, 187 (1997); <http://www.fhi-berlin.mpg.de/th/fhi98md/>
25. S. Ismail-Beigi and T.A. Arias: New algebraic formulation of density functional calculation, *Comput. Phys. Commun.* **128**, 1 (2000); <http://dft.physics.cornell.edu/>
26. CPMD consortium: Car Parrinello Molecular Dynamics, <http://www.cpmd.org>
27. S. Iijima: Helical microtubules of graphitic carbon, *Nature* **354**, 56 (1991)
28. R. Saito, G. Dresselhaus, and M. S. Dresselhaus: *Physical Properties of Carbon Nanotubes* (Imperial College Press, London 1998)
29. A. Rubio, J.L. Corkill, and M.L. Cohen: Theory of graphitic boron nitride nanotubes, *Phys. Rev. B* **49**, 5081 (1994)
30. X. Blase, A. Rubio, S.G. Louie, and M.L. Cohen: Stability and Band Gap Constancy of Boron-Nitride Nanotubes, *Europhys. Lett.* **28**, 335 (1994); Quasiparticle band structure of bulk hexagonal boron nitride and related systems, *Phys. Rev. B* **51**, 6868 (1995)
31. R.H. Baughman, A.A. Zakhidov, W.A. de Heer: Carbon Nanotubes—the Route Toward Applications, *Science* **297**, 787 (2002), and references therein
32. E. Thune and C. Strunk: *Quantum transport in carbon nanotubes*, in Lecture Notes in Physics **vvv**, ppp (yyyy)
33. S. Heinze, J. Tersoff, and P. Avouris: *Carbon nanotube electronics and optoelectronics*, in Lecture Notes in Physics **vvv**, ppp (yyyy)

34. J. Tersoff and D.R. Hamann: Theory and Application for the Scanning Tunneling Microscope, *Phys. Rev. Lett.* **50**, 1998 (1983)
35. A. Rubio, D. Sanchez-Portal, E. Artacho, P. Ordejón, and J.M. Soler: Electronic States in a Finite Carbon Nanotube: A One-Dimensional Quantum Box, *Phys. Rev. Lett.* **82**, 3520 (1999)
36. P. Delaney, H.J. Choi, J. Ihm, S.G. Louie, and M.L. Cohen: Broken symmetry and pseudogaps in ropes of carbon nanotubes, *Nature* **391**, 466 (1998)
37. M. Ouyang, J.L. Huang, C.L. Cheung, and C.M. Lieber: Energy Gaps in "Metallic" Single-Walled Carbon Nanotubes, *Science* **292**, 702 (2001)
38. A. Rubio: Spectroscopic Properties and STM Images of Carbon Nanotubes, *Appl. Phys. A* **68**, 275 (1999)
39. Y. Miyamoto, A. Rubio, S. Berber, M. Yoon, and D. Tománek: Spectroscopic characterization of Stone-Wales defects in nanotubes, *Phys. Rev. B* **69**, R121413 (2004)
40. Ph. Lambin, V. Meunier, and A. Rubio. In *Science and Applications of Carbon Nanotubes*, ed by D. Tománek, R.J. Enbody (Kluwer Academic, New York 2000), p. 17
41. D. Orlikowski, M. Buongiorno Nardelli, J. Bernholc, and C. Roland: Theoretical STM signatures and transport properties of native defects in carbon nanotubes, *Phys. Rev. B* **61**, 14194 (2000)
42. *Long-Range Charge Transfer in DNA*, vol. I and II, ed. by G. Schuster (Topics in Current Chemistry **236** and **237**, Springer, Berlin Heidelberg New York 2004)
43. P.J. de Pablo, F. Moreno-Herrero, J. Colchero, J. Gómez-Herrero, P. Herrero, A.M. Baró, P. Ordejón, J.M. Soler, and E. Artacho: Absence of dc-Conductivity in λ -DNA, *Phys. Rev. Lett.* **85**, 4992 (2000)
44. F.L. Gervasio, P. Carloni, and M. Parrinello: Electronic Structure of Wet DNA, *Phys. Rev. Lett.* **89**, 108102 (2002)
45. R.N. Barnett, C.L. Cleveland, A. Joy, U. Landmann, and G.B. Schuster: Charge Migration in DNA: Ion-Gated Transport, *Science* **294**, 567 (2001)
46. A. Calzolari, R. Di Felice, E. Molinari, and A. Garbesi: Electron Channels in Biomolecular Nanowires, *J. Phys. Chem. B* **108**, 2509 (2004); Correction: *J. Phys. Chem. B* **108**, 13058 (2004)
47. C.J. Murphy, M.A. Arkin, Y. Jenkins, N.D. Ghatlia, S. Bossman, N.J. Turro, and J.K. Barton: Long Range Photoinduced Electron Transfer through a DNA Helix, *Science* **262**, 1026 (1993)
48. D.B. Hall, R.E. Holmlin, and J.K. Barton: Oxidative DNA damage through long-range electron transfer, *Nature* **382**, 731 (1996)
49. E. Meggers, M.E. Michel-Beyerle, and B. Giese: Sequence Dependent Long Range Hole Transport in DNA, *J. Am. Chem. Soc.* **120**, 12950 (1998)
50. B. Giese, J. Amaudrut, A.K. Köhler, M. Spormann, and S. Wessely: Direct observation of hole transfer through DNA by hopping between adenine bases and by tunnelling, *Nature* **412**, 318 (2001)
51. P.T. Henderson, D. Jones, G. Hampikian, Y. Kan, and G. Schuster: Long-distance charge transport in duplex DNA: The phonon-assisted polaron-like hopping mechanism, *Proc. Natl. Acad. Sci. USA* **96**, 8353 (1999)
52. H.W. Fink and C. Schönenberger: Electrical conduction through DNA molecules, *Nature* **398**, 407 (1999)
53. E. Braun, Y. Eichen, U. Sivan, and G. Ben-Yoseph: DNA-templated assembly and electrode attachment of a conducting silver wire, *Nature* **391**, 775 (1998)

54. D. Porath, A. Bezryadin, S. de Vries, and C. Dekker: Direct measurement of electrical transport through DNA molecules, *Nature* **403**, 635 (2000)
55. A.Y. Kasumov, M. Kociak, S. Guerón, B. Reulet, V.T. Volkov, D.V. Klinov, and H. Bouchiat: Proximity-Induced Superconductivity in DNA, *Science* **291**, 280 (2001)
56. D. Porath, N. Lapidot, and J. Gómez-Herrero: *DNA-based devices*, in Lecture Notes in Physics **vvv**, xxx (yyyy)
57. R.A. Marcus and N. Sutin: Electron transfers in chemistry and biology, *Biochim. Biophys. Acta* **811**, 265 (1985)
58. M. Bixon and J. Jortner: Electron Transfer. From Isolated Molecules to Biomolecules, *Adv. Chem. Phys.* **106**, 35 (1999)
59. A. Nitzan: Electron transmission through molecules and molecular interfaces, *Annu. Rev. Phys. Chem.* **52**, 681 (2001)
60. A. Nitzan: The relationship between electron transfer rate and molecular conduction. 2. The sequential hopping case, *Isr. J. Chem.* **42**, 163 (2002)
61. J. Jortner, A. Nitzan, and M. A. Ratner: *Foundations of molecular electronics – charge transport in molecular conduction junctions*, in Lecture Notes in Physics **xxx**, ppp (yyyy)
62. R. Di Felice, A. Calzolari, E. Molinari, and A. Garbesi: Ab initio study of model guanine assemblies: The role of $\pi - \pi$ coupling and band transport, *Phys. Rev. B* **65**, 045104 (2002)
63. M. Bixon and J. Jortner: Charge Transport in DNA Via Thermally Induced Hopping, *J. Am. Chem. Soc.* **123**, 12556 (2001)
64. J. Jortner, M. Bixon, A.A. Voityuk, and N. Rösch: Superexchange Mediated Charge Hopping in DNA, *J. Phys. Chem. A* **106**, 7599 (2002)
65. K. Phillips, Z. Dauter, A.I.H. Murchie, D.M.J. Lilley, and B. Luisi: The crystal structure of a parallel-stranded guanine tetraplex at 0.95 Åresolution, *J. Mol. Biol.* **273**, 171 (1997)
66. G. Gottarelli, G.P. Spada, and A. Garbesi: Self-assembled Columnar Mesophases Based on Guanine-related Molecules. In *Comprehensive Supramolecular Chemistry*, vol 9, ed by J.L. Atwood, J.E.D. Davies, D. Mac-Nicol, F. Vögtle (Pergamon, Oxford UK 1996)
67. S.S. Alexandre, E. Artacho, J.M. Soler, and H. Chacham: Small Polarons in Dry DNA, *Phys. Rev. Lett.* **91**, 108105 (2003)
68. J.T. Davis: G-Quartets 40 Years Later: From 5-GMP to Molecular Biology and Supramolecular Chemistry, *Angew. Chem. Int. Ed.* **43**, 668 (2004)
69. R.G. Endres, D.L. Cox, and R.R.P. Singh: *Colloquium*: The quest for high-conductance DNA, *Rev. Mod. Phys.* **76**, 195 (2004)
70. A. Calzolari, R. Di Felice, E. Molinari, and A. Garbesi: G-quartet biomolecular nanowires, *Appl. Phys. Lett.* **80**, 3331 (2002)
71. E.K.U. Gross, J. Dobson, and M. Petersilka: Density Functional Theory of Time Dependent Phenomena. In: *Density Functional Theory II*, ed. by R.F. Nalewajski (Topics in Current Chemistry **181**, Springer, Berlin Heidelberg New York 1996) pp 81–172.
72. M.A.L. Marques and E.K.U. Gross: Time Dependent Density Functional Theory. In: *A Primer in Density Functional Theory*, Lecture Notes in Physics **620**, ed. by C. Fiolhais, F. Nogueira, and M. Marques (Springer, Berlin Heidelberg New York 2003) pp 144–184.
73. R. van Leeuwen: Key concepts of time-dependent density-functional theory, *Int. J. Mod. Phys. B* **15**, 1969 (2001)

74. R. Car and M. Parrinello: Unified Approach for Molecular Dynamics and Density-Functional Theory, *Phys. Rev. Lett.* **55**, 2471 (1985)
75. J.P. Perdew, K. Burke, and M. Ernzerhof: Generalized Gradient Approximation Made Simple, *Phys. Rev. Lett.* **77**, 3865 (1999)
76. K. Burke, M. Petersilka, and E.K.U. Gross: A hybrid functional for the exchange-correlation kernel in time-dependent density functional theory. In: *Recent Advances in Density Functional Methods*, ed. by P. Fantucci and A. Bencini (World Scientific, Singapore 2002) pp 67–79
77. G. Onida, L. Reining, and A. Rubio: Electronic excitations: density-functional versus many-body Green's-function approaches, *Rev. Mod. Phys.* **74**, 601 (2002)
78. E. Runge and E.K.U. Gross: Density-Functional Theory for Time-Dependent Systems, *Phys. Rev. Lett.* **52**, 997 (1984)
79. N.T. Maitra, K. Burke, and C. Woodward: Memory in Time-Dependent Density Functional Theory, *Phys. Rev. Lett.* **89**, 023002 (2002)
80. R. van Leeuwen: Mapping from Densities to Potentials in Time-Dependent Density-Functional Theory, *Phys. Rev. Lett.* **82**, 3863 (1999)
81. R. van Leeuwen: Causality and Symmetry in Time-Dependent Density-Functional Theory, *Phys. Rev. Lett.* **80**, 1280 (1998)
82. M. Petersilka, U.J. Gossman, and E.K.U. Gross: Excitation Energies from Time-Dependent Density-Functional Theory, *Phys. Rev. Lett.* **76**, 1212 (1996)
83. M. Petersilka and E.K.U. Gross: Spin-multiplet energies from time-dependent density functional theory, *Int. J. Quantum Chem.* **60**, 1393 (1996)
84. M. Casida. In *Recent Developments and Applications in Density Functional Theory*, ed. by J. Seminario (Elsevier, Amsterdam 1996) p 391
85. I. Vasiliev, S. Öğut, and J.R. Chelikowsky: Ab Initio Excitation Spectra and Collective Electronic Response in Atoms and Clusters, *Phys. Rev. Lett.* **82**, 1919 (1999)
86. I. Vasiliev, S. Öğut, and J.R. Chelikowsky: First-principles density-functional calculations for optical spectra of clusters and nanocrystals, *Phys. Rev. B* **65**, 115416 (2002)
87. H. Flocard, S.E. Koonin, and M. S. Weiss: Three-dimensional time-dependent Hartree-Fock calculations: Application to $^{16}O + ^{16}O$ collisions, *Phys. Rev. C* **17**, 1682 (1978)
88. K. Yabana and G.F. Bertsch: Time-dependent local-density approximation in real time, *Phys. Rev. B* **54**, 4484 (1996); K. Yabana and G.F. Bertsch: Z. Phys. D **42**, 219 (1997); K. Yabana and G.F. Bertsch: Oscillator strengths with pseudopotentials, *Phys. Rev. A* **58**, 2604 (1999)
89. K. Yabana and G.F. Bertsch: Application of the time-dependent local density approximation to optical activity, *Phys. Rev. A* **60**, 1271 (1999)
90. M.A.L Marques, X. López, D. Varsano, A. Castro, and A. Rubio: Time-Independent Density-Functional Approach for Biological Chromophores: The Case of the Green Fluorescent Protein, *Phys. Rev. Lett.* **90**, 258101 (2003)
91. M. A. L. Marques, A. Castro, G. F. Bertsch, and A. Rubio: octopus: a first-principles tool for excited electronion dynamics, *Comput. Phys. Commun.* **151**, 60 (2003). The code OCTOPUS is available at <http://www.tddft.org/programs/octopus>
92. W.G. Schmidt, S. Glutsch, P.H. Hahn, and F. Bechstedt: Efficient $O(N^2)$ method to solve the Bethe-Salpeter equation, *Phys. Rev. B* **67**, 085307 (2003)

93. <http://www.abinit.org>
94. P. Blaha, K. Schwarz, G. Madsen, D. Kvasnicka, and J. Luitz: <http://www.wien2k.at>
95. M. Städle, J.A. Majewski, P. Vogl, and A. Görling: Exact Kohn-Sham Exchange Potential in Semiconductors, *Phys. Rev. Lett.* **79**, 2089 (1997)
96. C.A. Ullrich, U.J. Gossmann, and E. K. U. Gross: Time-Dependent Optimized Effective Potential, *Phys. Rev. Lett.* **74**, 872 (1995)
97. L. Reining, V. Olevano, A. Rubio, and G. Onida: Excitonic Effects in Solids Described by Time-Dependent Density-Functional Theory, *Phys. Rev. Lett.* **88**, 066404 (2002); F. Sottile, V. Olevano, and L. Reining: Parameter-Free Calculation of Response Functions in Time-Dependent Density-Functional Theory, *Phys. Rev. Lett.* **91**, 056402 (2003); R. Del Sole, G. Adragna, V. Olevano, and L. Reining: Long-range behavior and frequency dependence of exchange-correlation kernels in solids, *Phys. Rev. B* **67**, 045207 (2003)
98. A. Marini, R. Del Sole, and A. Rubio: Bound Excitons in Time-Dependent Density-Functional Theory: Optical and Energy-Loss Spectra, *Phys. Rev. Lett.* **91**, 256402 (2003)
99. S. Albrecht, L. Reining, R. Del Sole, and G. Onida: Ab Initio Calculation of Excitonic Effects in the Optical Spectra of Semiconductors, *Phys. Rev. Lett.* **80**, 4510 (1998); L.X. Benedict, E.L. Shirley, and R.B. Bohn: Optical Absorption of Insulators and the Electron-Hole Interaction: An Ab Initio Calculation, *Phys. Rev. Lett.* **80**, 4514 (1998); M. Röhlffing and S.G. Louie: Electron-Hole Excitations in Semiconductors and Insulators, *Phys. Rev. Lett.* **81**, 2312 (1998); M. Röhlffing and S.G. Louie: Electron-hole excitations and optical spectra from first principles, *Phys. Rev. B* **62**, 4927 (2000)
100. Y.H. Kim and A. Görling: Excitonic Optical Spectrum of Semiconductors Obtained by Time-Dependent Density-Functional Theory with the Exact-Exchange Kernel, *Phys. Rev. Lett.* **89**, 096402 (2002); Exact Kohn-Sham exchange kernel for insulators and its long-wavelength behavior, *Phys. Rev. B* **66**, 035114 (2002)
101. X. Gonze, Ph. Ghosez, and R.W. Godby: Density-Polarization Functional Theory of the Response of a Periodic Insulating Solid to an Electric Field, *Phys. Rev. Lett.* **74**, 4035 (1995); Density-Functional Theory of Polar Insulators, *Phys. Rev. Lett.* **78**, 294 (1997); Polarization Dependence of the Exchange Energy, *Phys. Rev. Lett.* **78**, 2029 (1997); Ph. Ghosez, X. Gonze, and R.W. Godby: Long-wavelength behavior of the exchange-correlation kernel in the Kohn-Sham theory of periodic systems, *Phys. Rev. B* **56**, 12811 (1997)
102. R. Resta: Macroscopic polarization in crystalline dielectrics: the geometric phase approach, *Rev. Mod. Phys.* **66**, 899 (1994)
103. G.F. Bertsch, J.-I. Iwata, A. Rubio, and K. Yabana: Real-space, real-time method for the dielectric function, *Phys. Rev. B* **62**, 7998 (2000)
104. P.L. de Boeij, F. Kootstra, J.A. Berger, R. van Leeuwen, and J.G. Snijders: Current density functional theory for optical spectra: A polarization functional, *J. Chem. Phys.* **115**, 1995 (2001); M. van Faassen, P.L. de Boeij, R. van Leeuwen, J.A. Berger and J.G. Snijders: Application of time-dependent current-density-functional theory to nonlocal exchange-correlation effects in polymers, *J. Chem. Phys.* **118**, 1044 (2003); G. Vignale and W. Kohn: Current-Dependent Exchange-Correlation Potential for Dynamical Linear Response Theory, *Phys. Rev. Lett.* **77**, 2037 (1996)

105. T. Kreibich and E.K.U. Gross: Multicomponent Density-Functional Theory for Electrons and Nuclei, *Phys. Rev. Lett.* **86**, 2984 (2001)
106. T. Kreibich: Multicomponent Density-Functional Theory for Molecules in Strong Laser Pulses, PhD Thesis University of Würzburg, Germany (2000)
107. E.E. Koch and A. Otto: Optical absorption of benzene vapour for photon energies from 6 eV to 35 eV, *Chem. Phys. Lett.* **12**, 476 (1972)
108. S. Grimme and M. Parac: *Chem. Phys. Chem.* **3**, 292 (2003)
109. T.M.H. Creemers, A.J. Lock, V. Subramaniam, T.M. Jovin, and S. Völker: Photophysics and optical switching in green fluorescent protein mutants, *Proc. Natl. Acad. Sci. U.S.A.* **97**, 2974 (2000); Three photoconvertible forms of green fluorescent protein identified by spectral hole-burning, *Nature Struct. Biol.* **6**, 557 (1999)
110. S.B. Nielsen, A. Lapierre, J.U. Andersen, U.V. Pedersen, S. Tomita, and L.H. Andersen: Absorption Spectrum of the Green Fluorescent Protein Chromophore Anion In Vacuo, *Phys. Rev. Lett.* **87**, 228102 (2001)
111. B.R. Brooks, R.E. Bruccoleri, B.D. Olafson, D.J. States, S. Swaminathan, and M. Karplus: CHARMM: A program for macromolecular energy, minimization, and dynamics calculations, *J. Comput. Chem.* **2**, 187 (1983)
112. M.J. Field, P.A. Bash, and M. Karplus: A combined quantum mechanical and molecular mechanical potential for molecular dynamics simulations, *J. Comput. Chem.* **11**, 700 (1990)
113. J. Gao: Methods and applications of combined quantum mechanical and molecular mechanics potentials. In *Reviews in Computational Chemistry*, vol 7, ed by K.B. Lipkowitz, D.B. Boyd (VCH, New York 1995), pp 119–185
114. M.J.S. Dewar, E. Zoebisch, E.F. Healy, and J.J.P. Stewart: Development and use of quantum mechanical molecular models. 76. AM1: a new general purpose quantum mechanical molecular model, *J. Am. Chem. Soc.* **107**, 3902 (1995)
115. D. Varsano, A. Castro, M.A.L. Marques, R. Di Felice, and A. Rubio: A TDDFT study of excited states of DNA bases and base assemblies, work in progress
116. C.A. Sprecher and W.C. Johnson: Circular dichroism of the nucleic acid monomers, *Biopolymers* **16**, 2243 (1977)
117. L.B. Clark, G.G. Peschel, and I. Tinoco Jr.: Vapor Spectra and Heats of Vaporization of Some Purine and Pyrimidine Bases, *J. Phys. Chem.* **69**, 3615 (1965)
118. B. Mennucci, A. Tonniolo, and J. Tomasi: Theoretical Study of the Photophysics of Adenine in Solution: Tautomerism, Deactivation Mechanisms, and Comparison with the 2-Aminopurine Fluorescent Isomer, *J. Phys. Chem. A* **105**, 4749 (2001)
119. A. Broo: A Theoretical Investigation of the Physical Reason for the Very Different Luminescence Properties of the Two Isomers Adenine and 2-Aminopurine, *J. Phys. Chem. A* **102**, 526 (1998)
120. A.D. Becke: A new mixing of Hartree Fock and local density-functional theories, *J. Chem. Phys.* **98**, 1372 (1993); A.D. Becke: Density-functional thermochemistry. III. The role of exact exchange, *J. Chem. Phys.* **98**, 5648 (1993)
121. C. Jamorski, M.E. Casida, and D.R. Salahub: Dynamic polarizabilities and excitation spectra from a molecular implementation of time-dependent density-functional response theory: N₂ as a case study, *J. Chem. Phys.* **104**, 5134 (1996)
122. C.E. Crespo-Hernandez, B. Cohen, P.M. Hare, and B. Kohler: Ultrafast Excited-State Dynamics in Nucleic Acids, *Chem. Rev.* **104**, 1977 (2004)

123. P.R. Callis: Electronic states and luminescence of nucleic acid systems, *Annu. Rev. Phys. Chem.* **34**, 329 (1983)
124. G.H. Wannier: The Structure of Electronic Excitation Levels in Insulating Crystals, *Phys. Rev.* **52**, 191 (1937)
125. A.H. Romero, P.L. Silvestrelli, and M. Parrinello: Compton Anisotropy from Wannier Functions in the Case of Ice I_h, *phys. stat. sol. (b)* **220**, 703 (2000)
126. S.F. Boys: Construction of Some Molecular Orbitals to Be Approximately Invariant for Changes from One Molecule to Another, *Rev. Mod. Phys.* **32**, 296 (1960)
127. R. King-Smith and D. Vanderbilt: Theory of polarization of crystalline solids, *Phys. Rev. B* **47**, 1651 (1993)
128. S. Goedecker: Linear scaling electronic structure methods, *Rev. Mod. Phys.* **71**, 1085 (1999)
129. A.J. Williamson, R.Q. Hood, and J.C. Grossman: Linear-Scaling Quantum Monte Carlo Calculations, *Phys. Rev. Lett.* **87**, 246406 (2001)
130. F. Gygi, J.-L. Fattebert, and E. Schwegler: Computation of Maximally Localized Wannier Functions using a simultaneous diagonalization algorithm, *Comput. Phys. Comm.* **155**, 1 (2003)
131. L. Bernasconi and P.A. Madden: Optimally localized Wannier functions within the Vanderbilt ultrasoft pseudo-potential formalism, *J. Mol. Struct. (THEOCHEM)* **544**, 49 (2001)
132. A. Calzolari, N. Marzari, I. Souza, and M. Buongiorno Nardelli: Ab initio transport properties of nanostructures from maximally localized Wannier functions, *Phys. Rev. B* **69**, 035108 (2004)
133. I. Schnell, G. Czycholl, and C. Albers: Hubbard-U calculations for Cu from first-principle Wannier functions, *Phys. Rev. B* **65**, 075103 (2002)
134. W. Ku, H. Rosner, W.E. Pickett, and R.T. Scalettar: Insulating Ferromagnetism in La₄Ba₂Cu₂O₁₀: An Ab Initio Wannier Function Analysis, *Phys. Rev. Lett.* **89**, 167204 (2002)
135. I. Paul and G. Kotliar: Thermal transport for many-body tight-binding models, *Phys. Rev. B* **67**, 115131 (2003)
136. P.L. Silvestrelli, N. Marzari, D. Vanderbilt, and M. Parrinello: Maximally-localized Wannier functions for disordered systems: Application to amorphous silicon, *Sol. St. Commun.* **107**, 7 (1998)
137. P. Fernández, A. Dal Corso, A. Baldereschi, and F. Mauri: First-principles Wannier functions of silicon and gallium arsenide, *Phys. Rev. B* **55**, R1909 (1997)
138. B. Sporkmann and H. Bross: Calculation of Wannier functions for zinc-blende-type semiconductors, *J. Phys. Cond. Mat.* **9**, 5593 (1997)
139. N. Marzari and D. Vanderbilt: in *First-principles calculations for ferroelectrics*, vol 436, ed by R.E. Cohen (AIP Conference Proceedings, Woodbury NY 1998) pp 146
140. B. Sporkmann and H. Bross: Calculation of Wannier functions for fcc transition metals by Fourier transformation of Bloch functions, *Phys. Rev. B* **49**, 10869 (1994)
141. I. Schnell, G. Czycholl, and C. Albers: Unscreened Hartree-Fock calculations for metallic Fe, Co, Ni, and Cu from ab initio Hamiltonians, *Phys. Rev. B* **68**, 245102 (2003)

142. G. Cangiani, A. Baldereschi, M. Posternak, and H. Kakauer: Born charge differences of TiO₂ polytypes: Multipole expansion of Wannier charge densities, Phys. Rev. B **69**, R121101 (2004)
143. M. Le Vassor D'yerville, D. Monge, D. Cassagne, and J.P. Albert: Tight-binding method modelling of photonic crystal waveguides, Opt. Quantum Electron. **34**, 445 (2002)
144. D.M. Whittaker and M.P. Croucher: Maximally localized Wannier functions for photonic lattices, Phys. Rev. B **67**, 085204 (2003)
145. A. García-Martin, D. Hermann, F. Hagmann, K. Busch, and P. Wölfle: Defect computations in photonic crystals: a solid state theoretical approach, Nanotechnology **14**, 177 (2003)
146. I. Souza, R.M. Martin, N. Marzari, X. Zhao, and D. Vanderbilt: Wannier-function description of the electronic polarization and infrared absorption of high-pressure hydrogen, Phys. Rev. B **62**, 15505 (2000)
147. P.L. Silvestrelli and M. Parrinello: Water Molecule Dipole in the Gas and in the Liquid Phase, Phys. Rev. Lett. **82**, 3308 (1999); Structural, electronic, and bonding properties of liquid water from first principles, J. Chem. Phys. **111**, 3572 (1999)
148. M. Boero, K. Terakura, T. Ikeshoji, C. C. Liew, and M. Parrinello: Hydrogen Bonding and Dipole Moment of Water at Supercritical Conditions: A First-Principles Molecular Dynamics Study, Phys. Rev. Lett. **85**, 3245 (2000)
149. S. Nakhmanson, A. Calzolari, V. Meunier, J. Bernholc, and M. Buongiorno Nardelli: Spontaneous polarization and piezoelectricity in boron nitride nanotubes, Phys. Rev. B **67**, 235406 (2003)
150. A. Calzolari, C. Cavazzoni, and M. Buongiorno Nardelli: Electronic and Transport Properties of Artificial Gold Chains, Phys. Rev. Lett. **93**, 096404 (2004)
151. N. Marzari and D. Vanderbilt: Maximally localized generalized Wannier functions for composite energy bands, Phys. Rev. B **56**, 12847 (1997)
152. I. Souza, N. Marzari, and D. Vanderbilt: Maximally localized Wannier functions for entangled energy bands, Phys. Rev. B **65**, 035109 (2001)
153. *WanT package* by A. Calzolari, C. Cavazzoni, N. Marzari, and M. Buongiorno Nardelli: an integral approach to ab initio electronic transport from maximally-localized Wannier functions, <http://www.wannier-transport.org>
154. O.R. Chalvet and S. Daudel: *Localization and Delocalization in Quantum Chemistry* vols. I-IV, (Kluwer Academic Publishers, 1975)
155. D. Vanderbilt: Berry-phase theory of proper piezoelectric response, J. Phys. Chem. Solids. **61**, 147 (2000)
156. S. Datta: *Electronic transport in mesoscopic systems* (Cambridge Univ. Press 1995)
157. K. Stokbro, J. Taylor, M. Brandbyge, and H. Guo: *Ab-initio based nonequilibrium Green's function formalism for calculating electron transport in molecular devices*, in Lecture Notes in Physics **vvv**, ppp (yyyy)
158. A. Di Carlo, A. Pecchia, L. Latessa, T. Frauenheim, and G. Seifert: *Tight-binding DFT for molecular electronics (gDFTB)*, in Lecture Notes in Physics **vvv**, ppp (yyyy)
159. N. Bushong and M. Di Ventra: *Current-induced effects in nanoscale conductors*, in Lecture Notes in Physics **vvv**, ppp (yyyy)
160. D.S. Fischer and P.A. Lee: Relation between conductivity and transmission matrix, Phys. Rev. B **23**, 6851 (1981)

161. M. Buongiorno Nardelli: Electronic transport in extended systems: Application to carbon nanotubes, Phys. Rev. B **60**, 7828 (1999)
162. D. Lee and J. Joannopoulos: Simple scheme for surface-band calculations. I, Phys. Rev. B **23**, 4988 (1981)
163. F. Garcia-Moliner and V.R. Velasco: *Theory of Single and Multiple Interfaces* (World Scientific, Singapore 1992)
164. M. Brandbyge, J.-L. Mozos, P. Ordejon, J. Taylor, and Kurt Stokbro: Density-functional method for nonequilibrium electron transport, Phys. Rev. B. **65**, 165401 (2002)
165. Y. Xue, S. Datta, and M.A. Ratner: Charge transfer and “band lineup” in molecular electronic devices: A chemical and numerical interpretation, J. Chem. Phys. **115**, 4292 (2001)
166. X. Blase, L.X. Benedict, E.L. Shirley, and S.G. Louie: Hybridization effects and metallicity in small radius carbon nanotubes, Phys. Rev. Lett. **72**, 1878 (1994)
167. L. Chico, L.X. Benedict, S.G. Louie, and M. Cohen: Quantum conductance of carbon nanotubes with defects, Phys. Rev. B **54**, 2600 (1996)
168. A. Ferretti, A. Calzolari, R. Di Felice, F. Manghi, M. J. Caldas, M. Buongiorno Nardelli, and E. Molinari: First-principle theory of correlated transport through nano-junctions, Phys. Rev. Lett. (2004), in press.

Ab-initio Non-Equilibrium Green's Function Formalism for Calculating Electron Transport in Molecular Devices

K. Stokbro¹, J. Taylor², M. Brandbyge³ and H. Guo⁴

¹ Nanoscience Center, Universitetsparken 5d, 2100 Copenhagen East, Denmark
`ks@nano.ku.dk`

² Atomistix Inc, Juliane Maries Vej 30, 2100 Copenhagen East, Denmark
`jt@atomistix.com`

³ Department of Micro and Nanotechnology (MIC), Technical University of Denmark, Building 345 East, 2800 Kongens Lyngby, Denmark
`mbr@mic.dtu.dk`

⁴ Department of Physics, McGill University, Montreal (Quebec), PQ H3A 2T8, Canada
`guo@phys.mcgill.ca`

Abstract. The purpose of this chapter is to give a general reader an introduction to the Non Equilibrium Greens Function (NEGF) method for first principles modeling of current-voltage characteristics of molecular electronics devices. The molecular device is modeled on the atomic level, and we will use Density Functional Theory (DFT) to describe the electronic structure of the system. We will give a detailed description of all the steps involved in order to calculate the electron current. The steps involved are dividing the system into electrode and scattering region, determining the one-electron DFT Hamiltonian, setting up the NEGF, determining the charge density, and calculating the effective potential. The procedure sets up a set of selfconsistent equations, which result in an effective one-electron Hamiltonian description of the electron motion. From the one-electron Hamiltonian we can determine the electron current using the Landauer-Büttiger approach.

We present results obtained with the method for calculating the conductance of molecular resistors, and we will show that there are excellent agreement with recent experimental results. The non-equilibrium current will induce an additional force on the atoms. We investigate the origin of this force and present a simple model which relates the force to the charge rearrangement around the atoms in the scattering region.

Key words: Molecular electronics, first principles simulations, density functional theory, electron transport

1 Introduction

From the first proposal of a molecular rectifier by Aviram and Ratner [1], theoretical modeling has played an important role in progressing the field of molecular electronics. In the early phase, theoretical modeling was the only

means of gaining insight. Since then the experimental study of molecular devices have progressed tremendously, and several groups have been able to measure the electrical characteristics of systems with single or very few molecules between metallic contacts. However, the experiments are very technical demanding and often hard to interpretate and theoretical modeling therefore still plays a key role in advancing the field. Currently theoretical modeling techniques are improving in a similar pace as the experimental techniques, and theoretical modeling will most likely continue to be an important tool for advancing the field of molecular electronics.

The idea in molecular electronics is to use the large variation in the chemistry of molecules as a play ground for making new types of nanoscale devices. Thus, successful modeling of the devices must include the quantum chemical details of the molecules. The first model by Aviram and Ratner was based on chemical intuition [1]. Later models used semi-empirical descriptions of the chemistry [2–13] and recently full *ab initio* approaches have been introduced [14–26].

In this paper we will focus on *ab initio* approaches based on the Non Equilibrium Greens Function(NEGF) technique [27, 28]. Sofar this approach have been used to describe the coherent transport through a molecular device [18–20, 25, 26], i.e the quantum mechanical phase coherent transfer of an electron from one electrode to the other electrode, through the molecular region. However, the NEGF technique is also a promising approach for including the effect of phonon scattering, decoherence and external parameters like magnetic field.

In the following we will describe the NEGF approach for modeling molecular electronics devices. Our aim will be to make the approach understandable to non experts in theoretical modeling and NEGF techniques. In Sect. 2 we introduce Density Functional Theory (DFT) for quantum mechanical modeling of the electronic structure [29–32], and in Sect. 3 we show how NEGF can be used to solve the DFT equations for a molecule coupled to external electrodes with an applied bias. In Sect. 4 we briefly describe some implementations of the approach that we have been involved in, and Sects. 5 and 6 describes some insight obtained from using the methods. Section 5 is devoted to modeling high resistance molecular devices and in Sect. 6 we describe the origin of non-equilibrium forces arising due to the applied bias on the molecular electronics device. In Sect. 7 we conclude.

2 Mean Field Electronic Structure Theory

The purpose of atomic-scale modeling is to calculate the properties of molecules and materials from a description of the individual atoms in the systems. An atom consists of an ion core with charge Z , and an equal number of electrons that compensate this charge. We will use \mathbf{R}_μ, Z_μ to label the position and charge of the ions, where $\mu = 1, \dots, N$ and N is the number of ions.

The positions of the electrons are labeled by \mathbf{r}_i , $i = 1, \dots, n$ where n is the number of electrons.

Usually it is a good approximation to treat the ions as classical particles. The potential energy of the ions, $V(\mathbf{R}_1, \dots, \mathbf{R}_N)$, depends on the energy of the electronic system, E_0 , through

$$V(\mathbf{R}_1, \dots, \mathbf{R}_N) = E_0 + \frac{1}{2} \sum_{\mu, \mu'=1}^N \frac{Z_\mu Z_{\mu'} e^2}{|\mathbf{R}_\mu - \mathbf{R}_{\mu'}|} .$$

The electrons must be described as quantum particles, and the calculation of the electron energy requires that we solve the many-body Schrödinger wave equation.

$$\begin{aligned} \hat{H} \Psi(\mathbf{r}_1, \dots, \mathbf{r}_n) &= E_0 \Psi(\mathbf{r}_1, \dots, \mathbf{r}_n) \\ \hat{H} = - \sum_{i=1}^n \frac{\hbar^2}{2m} \nabla_i^2 - \sum_{i=1}^n \sum_{\mu=1}^N \frac{Z_\mu e^2}{|\mathbf{r}_i - \mathbf{R}_\mu|} \cdot \frac{1}{2} \sum_{i,j=1}^n + \frac{e^2}{|\mathbf{r}_i - \mathbf{r}_j|} . \end{aligned} \quad (1)$$

The “hat” over H denotes that it is an operator. The first term in (1) is the kinetic energy of the electrons, the second term the electrostatic electron-ion attraction, while the last term is the electrostatic electron-electron repulsion.

The last term couples different electrons, and gives rise to a correlated motion between the electrons. Due to this complication an exact solution of the many-body Schrödinger equation is only possible for systems with a single electron. Thus, approximations are required that can reduce the many-body Schrödinger equation into a practical, solvable model.

Several methods have been developed which transforms the many-body Schrödinger equation into an effective one-electron equation. Density Functional Theory (DFT) and Hartree Fock (HF) theory are examples of such methods. In these methods the electrons are described as non-interacting particles moving in an effective potential set up by the other electrons. The effective potential depends on the average position of the other electrons, and needs to be determined self-consistently.

In DFT the self-consistent loop includes the following steps:

$$\hat{H}_{1el} = -\frac{\hbar}{2m} \nabla^2 + V^{\text{eff}}[n](\mathbf{r}) \quad (2)$$

$$\hat{H}_{1el} \psi_\alpha(\mathbf{r}) = \varepsilon_\alpha \psi_\alpha(\mathbf{r}) \quad (3)$$

$$n(\mathbf{r}) = \sum_{\varepsilon_\alpha < \mu} |\psi_\alpha(\mathbf{r})|^2 \quad (4)$$

Equation (2) defines the one-electron Hamiltonian, where $-\frac{\hbar}{2m} \nabla^2$ describes the kinetic energy and $V^{\text{eff}}[n](\mathbf{r})$ the effective potential energy of the electron. The effective potential depends on the electron density, n . From the one-electron Hamiltonian we can determine the one-electron eigenstates by

Flowchart
The self-consistent loop in DFT methods

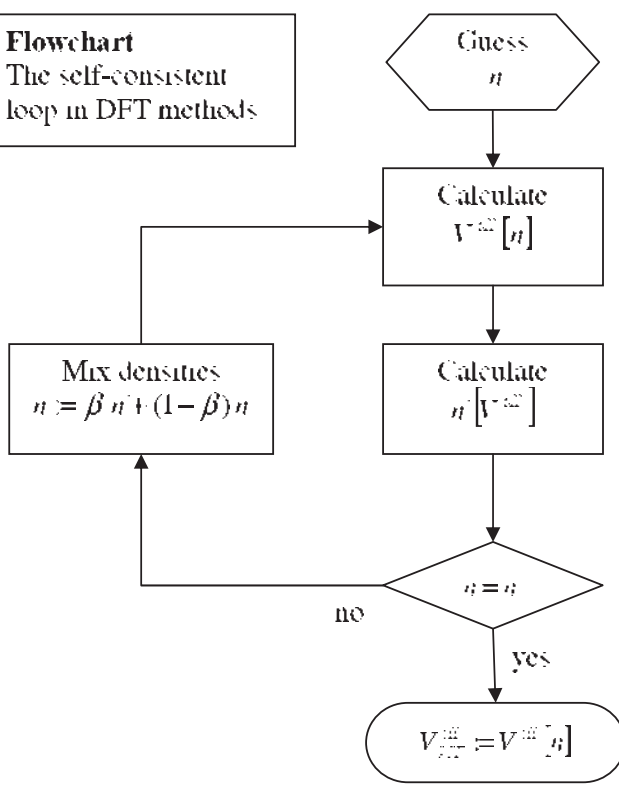


Fig. 1. Flowchart for DFT calculations, self-consistent loop

solving the one electron Schrödinger equation (3). The electron density is determined by summing all occupied one-electron eigenstates, i.e. one-electron states with an energy below the chemical potential of the system, μ . The flowchart in Fig. 1 illustrates the self-consistent loop required to solve the equations.

3 Application of DFT to Modeling Molecular Electronics Devices

Although the reduction of the many-body Schrödinger equation to an effective one-electron equation is a formidable simplification, the solution of the one-electron Schrödinger equation is not trivial. In the last 40 years an army of chemists and physicists have devoted their lives to tackling this problem, and their efforts have resulted in a number of successful methods to

accurately solve the one-electron Schrödinger equation. However, most of the methods require a simple geometry of the system, i.e. the system must be either isolated (a molecule) or periodic (a bulk crystal).

However, a molecular device is neither isolated nor periodic. It consists of two semi-infinite electrodes coupled with a molecular region. We call this an open system, because the molecule can exchange particles with the electrodes.

Figure 2 shows an example of a molecular device. We will divide the system into three regions, left electrode, right electrode and interaction region. In the electrode regions the potential is bulk like and the electron motion is governed by a bulk Hamiltonian. Usually the interaction region will consist of the molecule and a few layers of the electrode surfaces.

The left and right electrodes are electron reservoirs with chemical potentials, μ_L and μ_R . The two chemical potentials are different due to an applied voltage bias, V_b

$$\mu_L - \mu_R = eV_b a \quad (5)$$

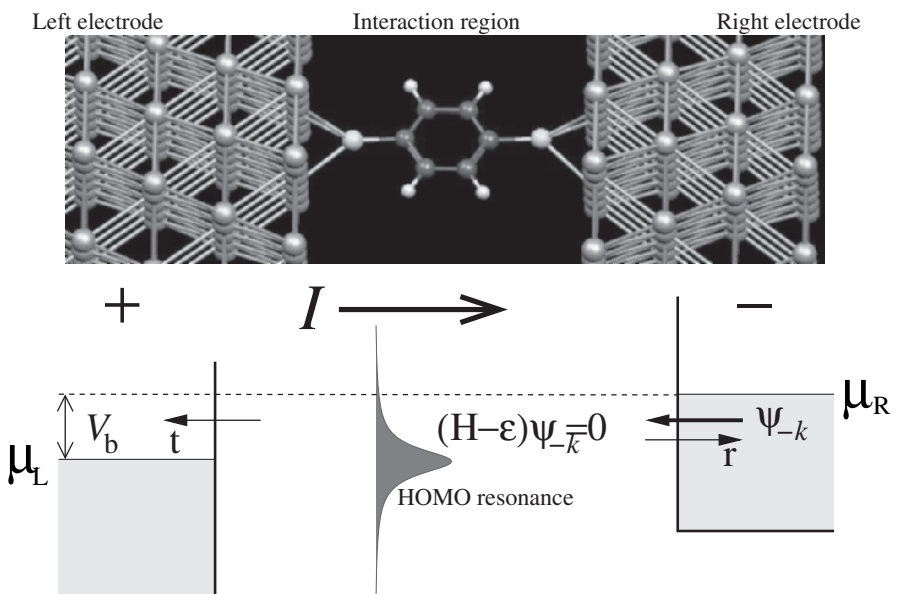


Fig. 2. A molecular coupled to metallic electrodes with applied bias V_b . The bias drives an electrical current from the left electrode to the right electrode. Due to the applied bias the electrodes have different electrochemical potentials, μ_L , μ_R . Electronic states on the molecule delocalize and molecular levels broaden into resonances. Electron scattering states are labeled by their momenta in the electrodes. The scattering states are determined by solving the Schrödinger equation in the interaction region using boundary conditions that match them with the momentum resolved bulk eigenstates

The difference in the electrochemical potentials sets up a steady state electron flow from the right to the left electrode. The system is in a non-equilibrium state and the electron distribution cannot be described by a single Fermi function. To determine the electron density we must calculate all the electronic eigenstates and assign each state to either the left or right reservoir in order to determine the occupation of the state. The division of the electronic eigenstates into left or right traveling waves, is obtained by for each energy, ε , calculating the solutions, $\psi_{kL}(\varepsilon), \psi_{kR}(\varepsilon)$, with a definite initial crystal momentum $\hbar kL$ in either the left (right) electrode. These are the so-called scattering states, referring to that an incoming Bloch wave is partly reflected and partly transmitted due to elastic scattering in the interaction region. The scattering states can be calculated in a similar way as used for calculating the transmission coefficient of a square potential barrier, a standard example used in most quantum mechanical text books (see for instance [33]). The procedure is to first calculate the Bloch waves for the left and the right electrode, and subsequently use these solutions as matching boundary conditions for the Schrödinger equation of the interaction region.

Once the scattering states are calculated the electron density can be determined using

$$n(\mathbf{r}) = \sum_{k_L, k_R} [| \psi_{kL} |^2 n_F(\varepsilon_{k_L} - \mu_L) + | \psi_{kR} |^2 n_F(\varepsilon_{k_R} - \mu_R)], \quad (6)$$

where n_F is the Fermi distribution function, k_L, ε_{k_L} label the crystal momentum and energy of scattering states from the left electrode, and k_R, ε_{k_R} label the corresponding quantities for the right electrode.

The calculation of the scattering states needs a different approach from the one used in traditional electronic structure calculations for isolated or periodic systems. However, efficient algorithms for calculating the scattering states have been developed [34, 35], and the main problem in determining the electron density from (6) is to make accurate evaluations of the sum over the crystal momentum. In the following subsections we will show how the non-equilibrium Green's function formalism in an efficient way solves this problem by calculating the electron density using complex contour integration.

3.1 The Screening Approximation

The standard procedure in electronic structure methods for isolated or periodic systems is to transform the one-electron Schrödinger equation into a matrix eigenvalue problem, which then can be solved with standard linear algebra packages. The transformation is obtained by writing the wavefunctions, ψ , as a linear combination of basis functions, $\psi(\mathbf{r}) = \sum_i a_i \phi_i(\mathbf{r})$. Many different choices exist for the basis functions, ϕ_i , some of the more popular are plane-waves or atom-based functions with shapes resembling the atomic wavefunctions. Using the basis functions the Schrödinger equation, (3) is transformed into

$$\sum_j H_{ij} a_j = \varepsilon \sum_j S_{ij} a_j ,$$

$$H_{ij} = \langle \phi_i | \hat{H}_{1el} | \phi_j \rangle ,$$

$$S_{ij} = \langle \phi_i | \phi_j \rangle$$

For a molecular system the Hamiltonian will be finite and the solution therefore trivial. For a periodic structure we only need to model a finite part of the system, which is then repeated to generate the entire solid. Thus, again the Hamiltonian will be finite and the solution trivial.

For the open system the reduction of the system size is less obvious. Here the trick is to separate the system into electrode and central regions, which can be solved separately.

Figure 3 shows a carbon nanotube coupled with a gold surface. The gold surface and the carbon nanotube are metallic. Because of the metallic nature of the semi-infinite electrodes, the perturbation due to the interaction region only propagates a few Å into the electrodes. We can therefore divide the

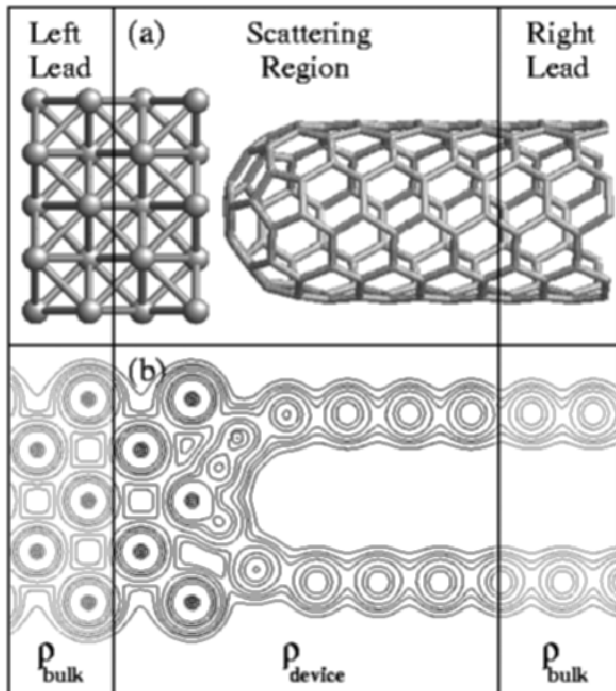


Fig. 3. (a) geometry of a carbon nanotube coupled with a gold surface. (b) The self-consistent charge density shown by contour lines in a cutplane. Outside the interaction region, the charge density is given by the bulk density of the electrodes

effective potential and the charge density into interaction region and electrode regions, where the values in the electrode regions are similar to the bulk values. This is called the screening approximation.

We will now expand the Hamiltonian operator in a basis set with finite range, and in this way separate the Hamiltonian Matrix into electrode and scattering region. There will be coupling elements between the different regions, but we will assume that the interaction range of the Hamiltonian is such, that there are no coupling between the left and right electrode. Thus the total Hamiltonian can be written as

$$H = \begin{pmatrix} \bar{H}_{LL} & \bar{H}_{LI} & 0 \\ \bar{H}_{IL} & \bar{H}_{II} & \bar{H}_{IR} \\ 0 & \bar{H}_{RI} & \bar{H}_{RR}, \end{pmatrix}$$

where \bar{H}_{LL} , \bar{H}_{II} , and \bar{H}_{RR} denote the Hamiltonian of the left electrode, interaction region, and right electrode, respectively, and \bar{H}_{LI} and \bar{H}_{IR} are the matrix elements involving the interaction region and the electrodes. With the bars above the letters, we indicate that the quantities are matrixes.

The eigenstates of this Hamiltonian are the scattering states, $\psi_{kL}(\varepsilon)$ and $\psi_{kR}(\varepsilon)$ described in the previous section, and the electron density is given by the sum of all the occupied eigenstates, see (4). In the next section we will show how the electron density can be calculated within a Green's function formalism, and in this way avoiding the calculation of the scattering states.

3.2 Calculating the Charge Density Using Green's Functions

We will now show how the charge density is obtained within the Green's function formalism. For this purpose we introduce the spectral-density operator, $\hat{\rho}(\varepsilon)$, and the electron density matrix \hat{D} . The electron density can be obtained from the density operator by taking the trace over a complete basis set.

$$n(\mathbf{r}) = \text{Tr} \hat{D} \quad (7)$$

The spectral density is the energy resolved electron density, and the total density is obtained by summing the spectral density over all occupied energies. Correspondingly, we have

$$\hat{\rho}(\varepsilon) = \delta(\varepsilon - \hat{H}), \quad (8)$$

$$\hat{D} = \int_{-\infty}^{\infty} \hat{\rho}(\varepsilon) n_F(\varepsilon - \mu) d\varepsilon,$$

where n_F is the Fermi function and μ the chemical potential of the system.

We will now calculate the electron density by taking the trace of the density matrix. For convenience we use the eigenstates, $\{\psi_\alpha\}$, as our complete basis set.

$$\begin{aligned}
n(\mathbf{r}) &= \sum_{\alpha} \psi_{\alpha}^*(\mathbf{r}) \hat{D} \psi_{\alpha}(\mathbf{r}) , \\
&= \sum_{\alpha} \int_{-\infty}^{\infty} \psi_{\alpha}^*(\mathbf{r}) \delta(\varepsilon - \hat{H}) \psi_{\alpha}(\mathbf{r}) n_F(\varepsilon - \mu) d\varepsilon , \\
&= \sum_{\alpha} \int_{-\infty}^{\infty} |\psi_{\alpha}(\mathbf{r})|^2 \delta(\varepsilon - \varepsilon_{\alpha}) n_F(\varepsilon - \mu) d\varepsilon , \\
&= \sum_{\alpha} |\psi_{\alpha}(\mathbf{r})|^2 n_F(\varepsilon_{\alpha} - \mu) .
\end{aligned}$$

Thus we see that from (7) we arrive at (4), and the two equations therefore identical.

The (retarded) Green's function is defined as

$$\hat{G}(\varepsilon) = \frac{1}{\varepsilon - \hat{H} + i \delta_+} , \quad (9)$$

where δ_+ is an infinitesimal positive number. We will use the Green's function formalism as a convenient way to obtain the spectral density and thereby the electron density of the system.

To relate the Greens function to the spectral density, we use the following relation from complex function theory

$$\text{Im} \frac{1}{x + i \delta_+} = \delta(x) . \quad (10)$$

Using this equation we combine (9) and (8) to obtain the relation

$$\hat{\rho}(\varepsilon) = \frac{1}{\pi} \text{Im} \hat{G}(\varepsilon) . \quad (11)$$

Expanding the operators in basis functions, we transform (8,9,11) into matrix equations,

$$\bar{G}(\varepsilon) = [\varepsilon + i \delta_+ \bar{S} - \bar{H}]^{-1} , \quad (12)$$

$$\bar{\rho}(\varepsilon) = \frac{1}{\pi} \text{Im} \bar{G}(\varepsilon) , \quad (13)$$

$$\bar{D} = \int_{-\infty}^{\infty} \bar{\rho}(\varepsilon) n_F(\varepsilon - \mu) d\varepsilon ,$$

$$n(\mathbf{r}) = \sum_{i,j} D_{ij} \phi_i^*(\mathbf{r}) \phi_j(\mathbf{r}) . \quad (14)$$

The problem of calculating the charge density is now reduced to the matrix inversion of (12). However, our system is open and the matrix to be inverted therefore infinite. Fortunately, the screening approximation means that we only need to calculate the charge density in the interaction region. From (14) we see that since our basis functions are localized, this means that we only need to calculate the Green's function matrix of the interaction region and a few layers of the electrodes.

3.3 Taking into Account the Electrode Region Through a Self Energy

In this section we will show how the Green's function matrix of the interaction region, G_{II} , can be calculated by inverting a matrix of similar size. For this purpose we will use perturbation theory in the coupling elements $\tilde{H}_{LI}(\varepsilon) = H_{LI} - \varepsilon S_{LI}$ and $\tilde{H}_{RI}(\varepsilon) = H_{RI} - \varepsilon S_{RI}$. The unperturbed Green's functions, G^0 , is calculated by setting $\tilde{H}_{LI} = \tilde{H}_{RI} = 0$, and using that in this case (12) is block diagonal

$$\bar{G}_{LL}^0(\varepsilon) = [(\varepsilon + i\delta_+) \bar{S}_{LL} - \bar{H}_{LL}]^{-1} .$$

$$\bar{G}_{II}^0(\varepsilon) = [(\varepsilon + i\delta_+) \bar{S}_{II} - \bar{H}_{II}]^{-1} .$$

$$\bar{G}_{RR}^0(\varepsilon) = [(\varepsilon + i\delta_+) \bar{S}_{RR} - \bar{H}_{RR}]^{-1} .$$

Now putting back the perturbation \tilde{H}_{LI} and \tilde{H}_{RI} we can obtain the perturbed Green's function from the Dyson's equation

$$\bar{G}_{II}(\varepsilon) = \bar{G}_{II}^0(\varepsilon) + \bar{G}_{II}^0(\varepsilon)[\bar{\Sigma}_{II}^L(\varepsilon) + \bar{\Sigma}_{II}^R(\varepsilon)]\bar{G}_{II}(\varepsilon) \quad (15)$$

$$\bar{\Sigma}_{II}^L(\varepsilon) = \tilde{H}_{IL}(\varepsilon)\bar{G}_{LL}^0(\varepsilon)\tilde{H}_{IL}(\varepsilon)^\dagger \quad (16)$$

$$\bar{\Sigma}_{II}^R(\varepsilon) = \tilde{H}_{IR}(\varepsilon)\bar{G}_{RR}^0(\varepsilon)\tilde{H}_{IR}(\varepsilon)^\dagger \quad (17)$$

Rearranging the terms in the Dyson's equation, we obtain

$$\bar{G}_{II}(\varepsilon) = [(\varepsilon + i\delta_+) \bar{S}_{II} - \bar{H}_{II} - \bar{\Sigma}_{II}^L(\varepsilon) - \bar{\Sigma}_{II}^R(\varepsilon)]^{-1} . \quad (18)$$

The terms $\bar{\Sigma}^L$ and $\bar{\Sigma}^R$ are called the self energies of the electrodes.

From (16,17) we see that the self energies is somehow a measure of the coupling strength between the interaction region and the electrodes. To understand the physics of the selfenergies, we divide it into a complex and a real part, $\Sigma^L = \sigma^L + i\Gamma^L$. To illustrate the significance of the real and the complex part we consider a system where H_{II} only have one orbital, i. e. $H_{II} = \alpha$ is a simple scalar and $S_{II} = 1$. We further assume that Σ^L , Σ^R are energy independent, the so-called wide-band limit. From (13,18) we obtain the spectral density matrix

$$\begin{aligned} \rho(\varepsilon) &= \frac{1}{\pi} \text{Im} \frac{1}{\varepsilon - \alpha - (\sigma^L + \sigma^R) - i(\Gamma^L + \Gamma^R)} \\ &= \frac{1}{\pi} \frac{(\Gamma^L + \Gamma^R)^2}{[\varepsilon - \alpha - (\sigma^L + \sigma^R)]^2 + (\Gamma^L + \Gamma^R)^2} \end{aligned} \quad (19)$$

Figure 2 illustrates the spectral density corresponding to the HOMO level for a DTB molecule coupled with a gold surface. From (19) we see that the real part of the self energy shifts the position of the resonance relative to the HOMO level, while the imaginary part broadens the HOMO level into a resonance.

The broadening of the molecular levels is a measure of the lifetime of the electronic states on the molecule. For an isolated molecule the molecular eigenstates are stationary states with almost infinite lifetime. When the molecule is coupled to metallic electrodes the electron can escape into the electrodes, and each electron will only spend a very short time on the molecule. The finite lifetime, τ , translates into an energy uncertainty, Γ , through Heisenberg's uncertainty relations

$$\Gamma\tau = \hbar. \quad (20)$$

Typical values are $\Gamma \sim 0.1\text{eV}$ for molecules covalently bound to metallic surfaces. Using (20) this translates into a lifetime of $\sim 10^{-14}\text{s}$.

3.4 Calculation of the Electrode Green's Function

In order to determine the self energies we need to calculate the unperturbed Green's function, \bar{G}_{LL}^0 , of the electrodes. Since, the Hamiltonian of the electrodes is semi-infinite, \bar{G}_{LL}^0 cannot be obtained by simple matrix inversion. However, in cases where the electrode Hamiltonian is periodic, there exists very efficient algorithms for obtaining \bar{G}_{LL}^0 . We will write the electrode Hamiltonian as periodic blocks, $\bar{H}_{L_1 L_1} = \bar{H}_{L_2 L_2} = \dots$ where the size of each block is such that only neighboring blocks interact,

$$\bar{H}_{LL} = \begin{pmatrix} \ddots & & & \\ & \bar{H}_{L_3 L_3} & \bar{H}_{L_3 L_2} & \\ & \bar{H}_{L_2 L_3} & \bar{H}_{L_2 L_2} & \bar{H}_{L_2 L_1} \\ & & \bar{H}_{L_1 L_2} & \bar{H}_{L_1 L_1} \end{pmatrix}$$

The Hamiltonian of each block, $\bar{H}_{L_1 L_1}$ and the coupling matrix, $\bar{H}_{L_1 L_2}$, can be obtained from a bulk calculation of the electrode system.

Using recursion, we can build up a series of approximations for the Green's function

$$\begin{aligned} \bar{G}_{L_1 L_1}^{0[0]} &= [(\varepsilon + i\delta_+) \bar{S}_{L_1 L_1} - \bar{H}_{L_1 L_1}]^{-1} \\ \bar{G}_{L_1 L_1}^{0[1]} &= [(\varepsilon + i\delta_+) \bar{S}_{L_1 L_1} - \bar{H}_{L_1 L_1} - \bar{H}_{L_1 L_2} \bar{G}_{L_2 L_2}^{0[0]} \bar{H}_{L_2 L_1}]^{-1} \\ \bar{G}_{L_1 L_1}^{0[2]} &= [(\varepsilon + i\delta_+) \bar{S}_{L_1 L_1} - \bar{H}_{L_1 L_1} - \bar{H}_{L_1 L_2} \bar{G}_{L_2 L_2}^{0[1]} \bar{H}_{L_2 L_1}]^{-1} \\ &\vdots \end{aligned}$$

Here the superscript $[n]$ refers to the order of the approximation. Usually it is necessary to go to order $n \approx 10000$ to obtain convergence, thus the algorithm can be quite time consuming. The poor convergence is because the error only gets reduced by $1/n$ as function of the number of steps n . Fortunately, there is a rescaled version of the algorithm where the error gets reduced by

$1/2^n$ [36]. Using this algorithm only a few steps are needed, $n \sim 20$, and the computational resources required to calculate the electrode Green's function is usually negligible compared to the resources required for the interaction part of the Green's function.

3.5 Integrating the Spectral Density with a Complex Contour

We now have all the ingredients required in (18) to obtain G_I and thereby the electron density, through

$$\begin{aligned} n(r) &= \sum_{ij} D_{ij} \phi_i(r) \phi_j(r) , \\ D_{ij} &= \int_{-\infty}^{\mu} \frac{1}{\pi} \text{Im}G_{ij}(\varepsilon) d\varepsilon . \end{aligned} \quad (21)$$

The problem with this equation is that the Green's function is a rapidly varying function along the real axis. See, for instance the simple spectral density of the DTB HOMO orbital shown in Fig. 2. Fortunately, it is possible to get around this problem using Complex Functions Theory. The Green's function is an analytical function, and can be extended into the complex plane. This means that the integral in (21) can be obtained by integrating along a contour in the complex plane. In the complex plane the Green's function is very smooth, as illustrated in Fig. 4. For realistic systems an accurate determination of the integral in (21) often requires more than 5000 energy points, while less than 50 points are required for an accurate determination of the integral along the complex contour. This factor 100 reduction in the computational complexity is crucial, and one of the most important virtues of the Green's function approach.

3.6 Non-Equilibrium Green's Functions for Finite Bias

In the above discussion we always assumed that the system has a single chemical potential, i.e. the system is in equilibrium. However, if we apply a potential bias, V_b , the two electrodes will have different chemical potential μ_L , μ_R that are linked through (5). Figure 2 illustrates the system setup, and as discussed in Sect. 2 the density must now be divided into partial contributions corresponding to their left ($\hat{\rho}^L$) or right ($\hat{\rho}^R$) origin

$$\hat{\rho}(\varepsilon) = \hat{\rho}^L(\varepsilon) + \hat{\rho}^R(\varepsilon) . \quad (22)$$

The density matrix for nonequilibrium is then found by filling the left and right originating states according to the respective chemical potentials [26,37],

$$\hat{D} = \int_{-\infty}^{\infty} d\varepsilon \hat{\rho}^L(\varepsilon) n_F(\varepsilon - \mu_L) + \hat{\rho}^R(\varepsilon) n_F(\varepsilon - \mu_R) . \quad (23)$$

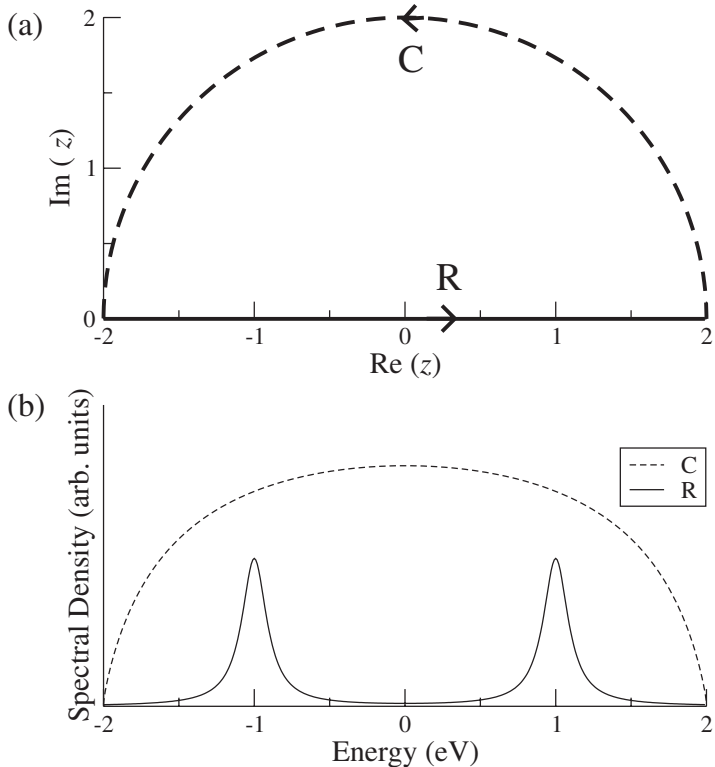


Fig. 4. (a) The integral of $G_I(z)$ is equivalent along the contour C and along the real axis R. (b) Variation of $\text{Im}G(z)$ along C (dashed) and along R (solid)

This division of the density can be accomplished using non-equilibrium Green's function theory, and we can write the partial spectral densities as

$$\hat{\rho}^L(\varepsilon) = -\hat{G}(\varepsilon) \text{Im}\hat{\Sigma}^L(\varepsilon) \hat{G}^\dagger(\varepsilon) , \quad (24)$$

$$\hat{\rho}^R(\varepsilon) = -\hat{G}(\varepsilon) \text{Im}\hat{\Sigma}^R(\varepsilon) \hat{G}^\dagger(\varepsilon) . \quad (25)$$

The foundation of these equations can be found in [26, 27], and here we will only show that (24, 25) indeed fulfills the sum rule (22). Using (18) in operator form we can write

$$\hat{G}^\dagger(\varepsilon) = \hat{G}(\varepsilon)[\varepsilon - \hat{H} - \hat{\Sigma}^L(\varepsilon) - \hat{\Sigma}^R(\varepsilon)]\hat{G}^\dagger(\varepsilon) \quad (26)$$

and we get

$$\rho(\varepsilon) = \frac{1}{\pi} \text{Im} \hat{G}, \quad (27)$$

$$= \frac{1}{2\pi} [\hat{G} + \hat{G}^\dagger], \quad (28)$$

$$= -\hat{G} \text{Im}[\hat{\Sigma}^L(\varepsilon) + \hat{\Sigma}^R(\varepsilon)] \hat{G}^\dagger. \quad (29)$$

which proves (22). This equation also proves (24,25) for cases where the interaction region only couples with one electrode. To see this note that if the interaction region only couples with the left electrode, then $\rho = \rho^L$ and $\hat{\Sigma}^R(\varepsilon) = 0$.

It is convenient to divide the energy axis into two regions, the energy range below both chemical potentials (the equilibrium region), and the energy range between the two chemical potentials (the non-equilibrium region or bias window). Similarly, we divide the density matrix into two parts,

$$\hat{D} = \hat{D}^{eq} + \hat{D}^{neq},$$

where \hat{D}^{eq} is the density matrix of the electrons with energies in the equilibrium region, and \hat{D}^{neq} the density matrix of the electrons with energies in the Non-equilibrium region. If $\mu_L < \mu_R$ we have, using (22, 23),

$$\hat{D}^{eq} = \int_{-\infty}^{\infty} \hat{\rho}(\varepsilon) n_F(\varepsilon - \mu_L) d\varepsilon, \quad (30)$$

$$\hat{D}^{neq} = \int_{-\infty}^{\infty} \hat{\rho}^R(\varepsilon) [n_F(\varepsilon - \mu_R) - n_F(\varepsilon - \mu_L)] d\varepsilon. \quad (31)$$

The calculation of the equilibrium part of the density matrix, \hat{D}^{eq} , is similar to the calculation of the density matrix for an equilibrium system and we can use the complex contour integration technique discussed in the previous section. To obtain the non-equilibrium part, \hat{D}^{neq} , we use (25, 31). However, $\hat{\rho}^R$ is not an analytical function, and it is therefore not possible to extend the integral in (31) into the complex plane, as used for the equilibrium part. Thus the integral in (31) must be performed along the real axis, and a dense set of integration points are needed to accurately evaluate the integral. For large biases the calculation of the non-equilibrium density is the most time consuming part of the calculation.

3.7 Calculating the Effective Potential from the Electron Density

The algorithms presented in the previous subsections allow us to calculate the density from the Hamiltonian. To complete the self-consistent cycle we also need to calculate the Hamiltonian from the density. From (2) we see that this means calculating the effective potential, $V^{\text{eff}}[n]$. In DFT the effective potential is given by

$$V^{\text{eff}}[n] = V^{\text{ion}}[n] + V^H[n] + V^{xc}[n], \quad (32)$$

where V^{ion} is the ion potential, $V^H[n]$ is the Hartree potential, and $V^{xc}[n]$ is the exchange correlation potential. The equations for the 3 potential terms are given by

$$\begin{aligned} V^{\text{ion}}(\mathbf{r}) &= \sum_{\mu=1}^N \frac{Z_{\mu}e^2}{|\mathbf{r} - \mathbf{R}_{\mu}|}, \\ \nabla^2 V^H[n](\mathbf{r}) &= -4\pi n(\mathbf{r}), \\ V^{xc}[n](\mathbf{r}) &= f(n(\mathbf{r}), \nabla n(\mathbf{r}), \nabla^2 n(\mathbf{r})). \end{aligned} \quad (33)$$

The ion potential is given by the electrostatic potential from the ion cores and does not depend on the density. For the exchange correlation potential we will use the Local Density Approximation [38] or Generalized Gradient Approximation [39], where V^{xc} is a local function of the density and possible gradients, and therefore easy to calculate.

The Hartree potential is defined as the electrostatic potential from the electron charge density and must be calculated from the Poisson's equation. Poisson's equation is a second-order differential equation and a boundary condition is required in order to fix the solution. Molecular systems have the boundary condition that the potential asymptotically goes to zero. In bulk systems the boundary condition is that the potential is periodic. Note, that the bulk boundary condition only determines the Hartree potential up to an additive constant, reflecting the physics that the bulk electrostatic potential does not have a fixed value relative to the vacuum level.

For the two-probe system we can calculate the Hartree potential in the electrodes using periodic boundary conditions. Since the electrodes are bulk systems the Hartree potentials are only determined up to additive constants, and the left and right Hartree potentials are floating relative to each other. However, the chemical potentials of the electrodes are calculated from their effective potentials, and we can therefore relate the Hartree potential to the chemical potential of the electrode. We may then use the relation in (5) between the chemical potentials to align the Hartree potential in the left electrode with that of the right electrode. The Hartree potentials in the electrodes now define boundary conditions for the Hartree potential in the central region. In the two directions perpendicular to the transport direction we will use periodic boundary conditions. Once we have sorted out the boundary conditions we can solve Poisson's equation of the central region using standard numerical differential equation solvers.

3.8 The Complete Self-Consistent Algorithm for the NEGF Calculation

Figure 5 shows all the steps required for the two-probe calculation. Initially we define the system geometry, and separate the system into interaction and

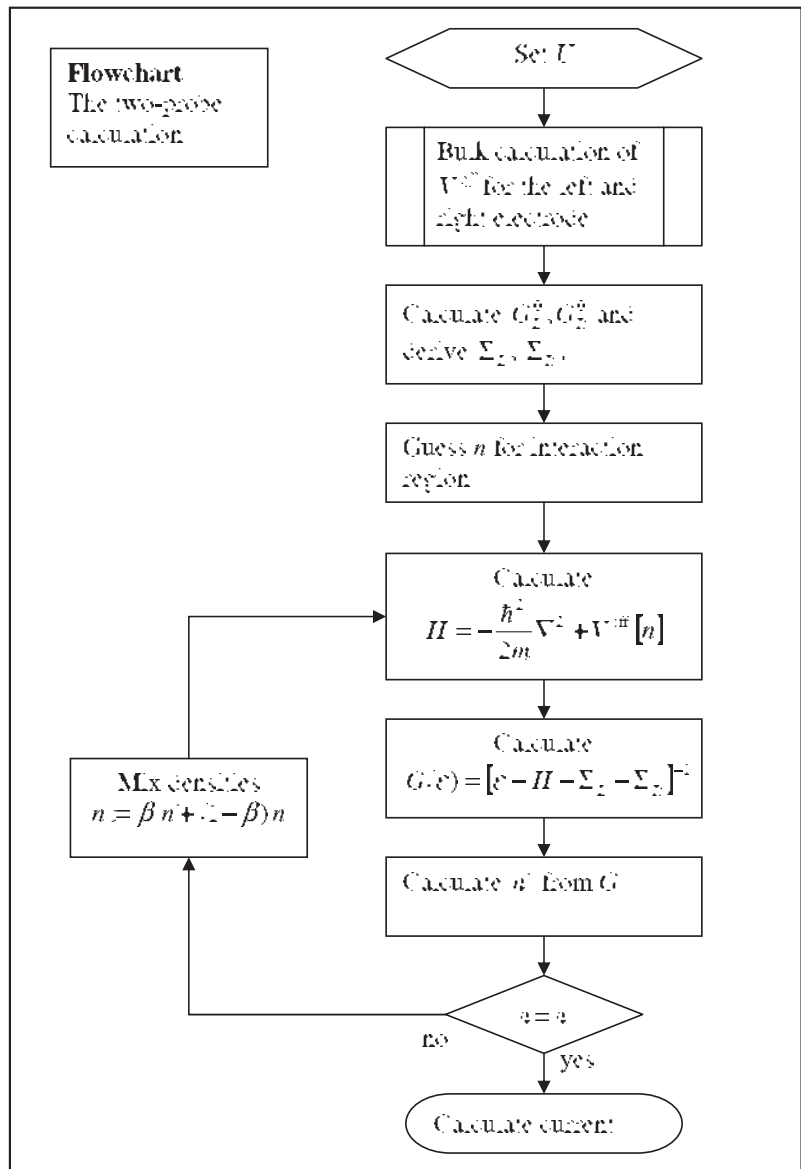


Fig. 5. The flowchart shows the steps required in order to perform a two-probe calculation

electrode regions. The first step is to perform independent self-consistent calculations for the electrodes. From these calculations we obtain the effective potential and density of the electrode regions, as illustrated in Fig. 3. From the self-consistent Hamiltonian of the electrodes, we also calculate the self energies, Σ_L , Σ_R using (16,17).

These initial calculations are now used as input to the two-probe calculation. Starting with an initial guess of the electron density, we construct the Hamiltonian of the interaction region from (2, 32). From the Hamiltonian and the electrode self energies we calculate the Green's function of the interaction region using (18). With the Green's function we can calculate the electron density using (21, 25, 30, 31) and thereby close the self-consistent cycle.

3.9 Electron Transport Coefficients and Currents Obtained from the Green's Function

With the self-consistent Hamiltonian we have a good description of the electronic structure of the molecular device. We will now use the self-consistent Hamiltonian to calculate the coherent electron transport through the device. The coherent transport is carried by the scattering states, which are eigenfunctions of the Hamiltonian with a definite crystal momentum k in the transport direction inside the electrodes. For each scattering state we define the transmission coefficient, T_k , as

$$T_k = \sum_{k'} t_{kk'}^\dagger t_{kk'} \quad (34)$$

where $t_{kk'}$ is the fraction of the wave which propagates through the device and into the outgoing channel with crystal momentum k' (see also Fig. 2).

In the Landauer-Büttiker formalism the current is given by summing the electron flow of all occupied waves. The current flow for each electron is given by $env_k T_k$, where $n = 1/V$ is the electron density (assuming the electrons are normalized in the volume V), $v_k = \frac{1}{\hbar} \frac{\partial \varepsilon_k}{\partial k}$ is the group velocity of the electrons, and the Transmission coefficient T_k gives the fraction of the electron wave which are transmitted. Let k denote crystal momentum of the scattering states going left to right and $-k'$ the crystal momentum of scattering states going right to left. The electron current is now given by

$$I = \frac{e}{V} \sum_k v_k T_k n_F(\varepsilon_k - \mu_L) + \frac{e}{L'} \sum_{-k'} v_{-k'} T_{-k'} n_F(\varepsilon_{-k'} - \mu_R) \quad (35)$$

where the Fermi functions, n_F , ensure that we only include the contributions from occupied electron states.

Transforming the sum into an integral (where the factor 2 account for spin)

$$\sum_k \rightarrow 2 \times \frac{V}{2\pi} \int dk \quad (36)$$

we obtain

$$I = \frac{2e}{h} \int_{-\infty}^{\infty} d\varepsilon [T_L(\varepsilon)n_F(\varepsilon - \mu_L) - T_R(\varepsilon)n_F(\varepsilon - \mu_R)] \quad (37)$$

where $T_L(\varepsilon) = \sum_k T_k \delta_{\varepsilon_k=\varepsilon}$ is the transmission coefficient of all electrons going left to right with energy ε . T_R is the corresponding quantity for electrons going right to left. In arriving at (37) we have used that left and right scattering states move in opposite direction, and therefore contribute with opposite sign. In fact, since the Hamiltonian has time reversal symmetry we must have $T_L = T_R = T(\varepsilon)$ (if $T_L \neq T_R$ we will have a different current when time is running backwards, thus breaking the time reversal symmetry). Using, this relation we arrive at

$$I = \frac{2e}{h} \int_{-\infty}^{\infty} d\varepsilon T(\varepsilon)[n_F(\varepsilon - \mu_L) - n_F(\varepsilon - \mu_R)] \quad (38)$$

From the Green's functions we can directly calculate the transmission coefficients, using the following results from NEGF theory

$$T(\varepsilon) = \text{Tr}[\text{Im}\hat{\Sigma}_L(\varepsilon)\hat{G}^\dagger(\varepsilon)\text{Im}\hat{\Sigma}_R(\varepsilon)\hat{G}(\varepsilon)] . \quad (39)$$

A derivation of this equation can be found in [27, 28]. Here we just note that the equation has some similarities with (24) and (25). Equations (24), (25) only involves one selfenergy term, reflecting that the interaction region can receive density by just coupling with one electrode. Equation (39) has two selfenergy terms, reflecting that in order to have transport through the interaction region the central region must couple with both electrodes.

4 Implementation: McDCAL, TranSIESTA, and Atomistix Virtual NanoLab

The NEGF approach described in the previous sections have now been implemented in several software packages for electron transport calculations. The authors have been involved in implementing the method in the McDCAL [25], TranSIESTA [26], and Atomistix Virtual NanoLab [40] software packages. Although the McDCAL, TranSIESTA, and Atomistix Virtual NanoLab packages are based on the same framework, there are small differences in the numerical implementations in the packages. Furthermore, the use of the NEGF framework leads to highly complex software and it is important to check the implementation for bugs that might lead to erroneous results.

In Figure 6 we show the transmission spectrum at bias voltages of 0 Volt (a) and 1 Volt (b) for a 7-atom carbon chain coupled to two Aluminium electrodes of finite cross section oriented along the (100) direction. A further description of this system can be found in [26]. Here we just note that there

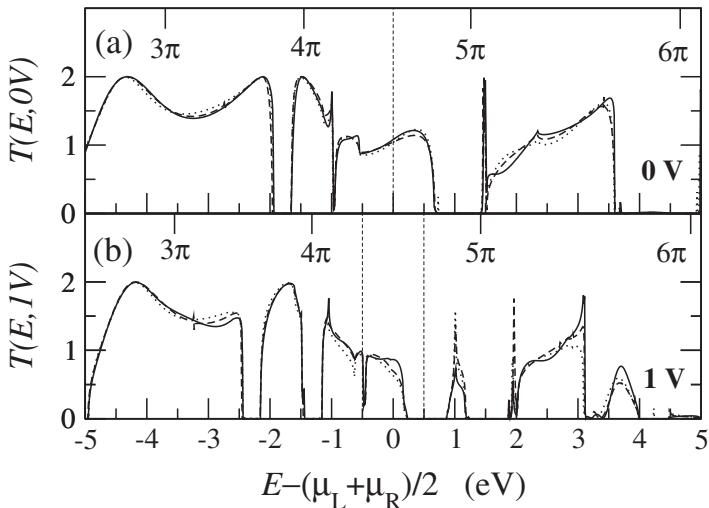


Fig. 6. (a) Zero bias transmission coefficient, $T(E, 0V)$, for a 7-atom carbon chain coupled to one dimensional Aluminium electrodes oriented in the (100) direction. (b) Transmission coefficient at 1 V, $T(E, 1V)$. *Solid lines* show results obtained with TranSIESTA, it *dotted lines* results obtained with McDCAL, and *dashed lines* are obtained with Atomistix Virtual NanoLab. The vertical *dashed lines* indicated the window between μ_L and μ_R . The position of the eigenstates of the carbon wire subsystem are also indicated at the top axis

is excellent agreement between the three different implementations of the NEGF methods. In the following sections we will describe some insight on the electron transport in nanoscale systems gained by using these software packages.

5 Resistance of Molecular Wires

A particular difficulty of understanding intrinsic properties of molecular conduction arises since charge transport properties of molecular devices are typically dominated by the properties of the molecule-electrode contacts rather than by the molecule itself [41, 42]. The contact geometry, quality, and chemistry therefore become very important. These details of contacts are often influenced by many uncontrollable experimental factors and stochastic events, hence producing data that cannot be easily reproduced. These problems also present difficulties to theoretical analyses which typically assume idealized contacts.

Recently, several experimental groups [43–49] have focused on studies of several molecular wires which have very large resistance, typically in the range of many $M\Omega$ at zero bias voltage. Such a large resistance dominates

transport features in two probe measurements of the metal-molecule-metal device configuration, thereby producing quantitatively consistent experimental data by different laboratories. These kinds of measurements are very important as they reveal the intrinsic properties of molecular scale conduction, rather than measuring details of particular metal-molecular contacts, for which good control has not yet been convincingly reported. In the following we present a calculation, using the NEGF-DFT technique discussed above, on the transport features of alkane-thiol, alkane-di-thiol, and oligophenylene molecular wires, and we make quantitative comparisons to measured data [43–49]. Very good agreement is obtained [50, 51].

We first consider transport properties of alkane-thiol molecular wires [50]. Alkane-thiol film formed on Au surfaces is a prototypical self-assembled monolayer (SAM) that has received considerable attention [52]. We focus on the following experimental findings of the metal-alkane-thiol-metal system collected by conducting atomic force microscope (AFM) measurements [42]: (i) for bias voltages between $\pm 0.3\text{V}$, the I-V curves are almost linear; (ii) the resistance of the alkane-thiol chains involving 4 to 8 carbons (C4–C8) is in the range of $0.2\text{ M}\Omega$ to $200\text{ M}\Omega$ at a load of 1nN in the conducting AFM study; (iii) the resistance roughly scales as $R = R_o \exp(\beta n)$, where $\beta \approx 1.0$ per carbon at low loads (less than 10nN) and n is the number of carbon atoms.

Since there has been no knowledge on contact geometry of the experimental devices [42], one assumes a plausible atomic configuration shown in Fig. 7 where an alkane-thiol chain [53] is contacted by two atomic scale metallic electrodes extending to reservoirs [54] at $z = \pm\infty$. The molecule-lead distance is fixed to be a constant for all the systems: the distance of the S-Au (from the sulfur atom to the surface of Au lead) and the H-Au is 4.0 a.u. Since the precise distance during charge transport is unknown, we choose these distances to be close to the equilibrium bond length suggested in literature [55].

Figure 8(a) plots the calculated I-V curves for the Au-alkane-thiol-Au wires [device in Fig. 7(a)]. They are almost linear over the range of the bias voltage applied. As the number of carbon atoms increases, the current decreases. The linear I-V curves give a resistance which is plotted in Fig. 8(b) in a semi-log form (resistances calculated at 0.1 V bias voltage), shown by the filled circles. The roughly linear increase of R in the semi-log plot suggests a rapid increase in R_n as the number of carbon atoms, n , increases. The data can indeed be fit to $R_n \approx R_o \exp(\beta n)$, where $R_o = 24\text{ k}\Omega$ and $\beta \approx 0.95$ per carbon. The corresponding experimental data was reported [42] to be $\beta \approx 1.0$ at low AFM loads ($< 10\text{nN}$). The theoretical β value is, therefore, in reasonable quantitative consistency with the experimental data. To check the stability of the calculated β against different contact distances, we calculated resistance by increasing/decreasing the contact distance by 0.5 a.u. Although the value of R_o can vary by as much as 17% , β is only varied by less than 1% .

This indicates that β is reasonably stable against such a change of contact structure.

The empty circles in Fig. 8(b) show the results for Al-alkane-thiol-Al junctions. One finds $\beta \approx 1.0$ and $R_o = 65 \text{ k}\Omega$. The Al junction has larger R_o than that of Au junction while the value of β is similar. This trend is consistent with experimental measurements [47] which show that a larger value of R_o is expected for leads with smaller work function. For an Al-alkane-thiol-Al device with a wider Al lead tempering into the molecule [see Fig. 7(b)], one finds $R_o \approx 105 \text{ k}\Omega$ and $\beta \approx 0.95$ per carbon, as shown by the empty triangles in Fig. 8(b). These results show that the coefficient R_o has a more sensitive dependence on device details, but the rate of resistance increase, β , is rather insensitive.

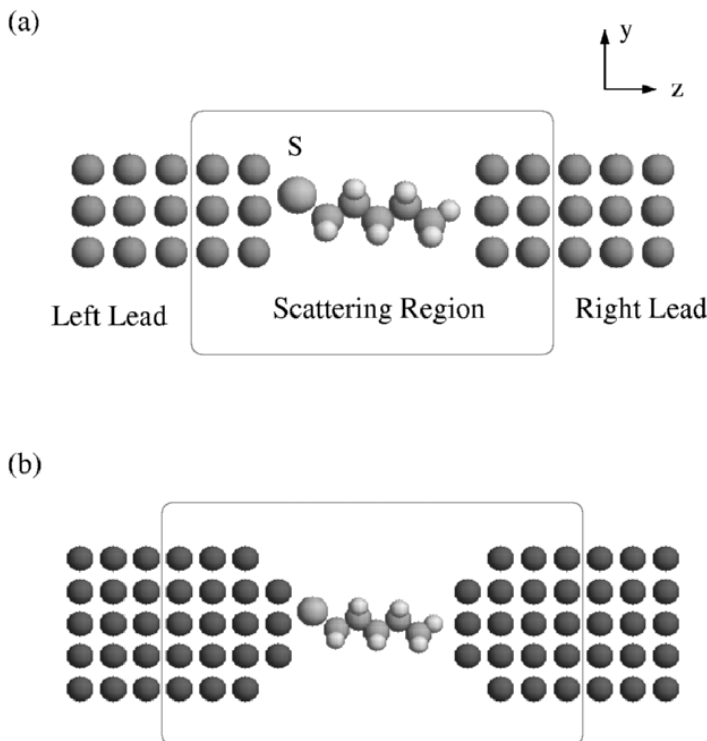


Fig. 7. (a) Schematic illustration of the Au-molecule-Au junction. The simulation box (device) is indicated by the scattering region, which includes a portion of the infinitely long electrodes and the alkane-thiol molecule. The distance of S-Au (surface) and H-Au is 4.0 a.u. Five alkane-thiol molecules are studied: $\text{CH}_3(\text{CH}_2)_{rmnS}$, $n = 3$ to 7. (b) Schematic illustration of an Al-alkanethiol-Al wire. The contact layer of Al atoms to the molecule is “tempered”

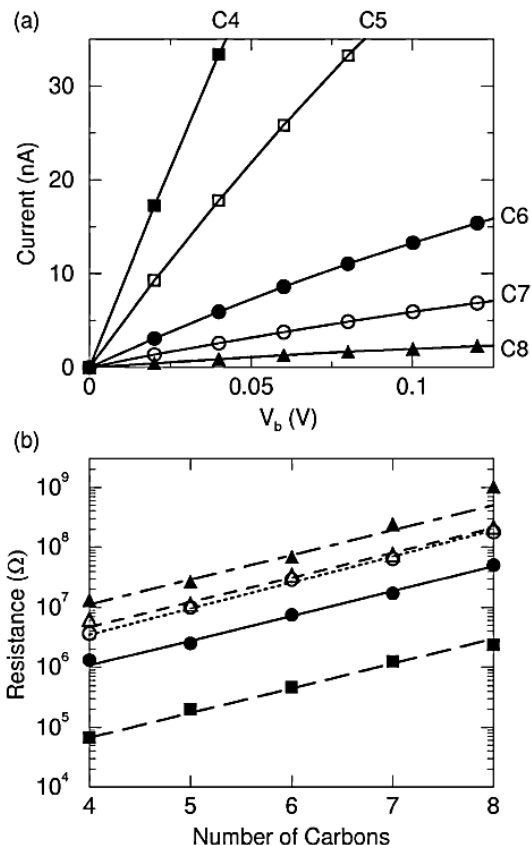


Fig. 8. (a) I-V characteristics of Au-alkanethiol-Au junctions as a function of the number of carbons in the alkane-thiol chains. (b) Semi-log plot of resistance versus number of carbon in the alkane chains. *Filled circles:* Au-alkanethiol-Au (fitted by solid line, $R_o = 24 \text{ k}\Omega$, $\beta = 0.95$); empty circles: for Al-alkanethiol-Al device where an Al unit cell has 18 Al atoms oriented in the (100) direction (dotted line, $R_o = 65 \text{ k}\Omega$, $\beta = 1.0$); empty triangles: still for Al-alkanethiol-Al device but with a larger lead tempered at the Al-molecule contact [see Fig. (1b)] (dashed line, $R_o = 105 \text{ k}\Omega$, $\beta = 0.95$); filled square: Au-alkanedithiol-Au (long dashed line, $R_o = 1.5 \text{ k}\Omega$, $\beta = 0.95$); filled triangles: Au-alkanethiol(CF_3)-Au (dot-dashed line, $R_o = 250 \text{ k}\Omega$, $\beta = 0.95$)

One can also investigate the effect of altering the contact group of the molecule to the leads. For an Au-alkanedithiol-Au device, both Au leads are contacted by an S atom, but one finds that the transport behavior is essentially the same as that of the alkane-thiol where only one Au surface is contacted by S. In particular, a linear I-V curve and an exponential length dependence of resistance are both found, and the values are $R_o \approx 1.5 \text{ k}\Omega$, $\beta \approx 0.95$, as shown in Fig. 8(b) as filled squares. The current through alka-

nedithiols is found to be larger than that of the alkane-thiol system, similar to that of experimental measurements [49, 56]. The smaller value of R_o for alkanedithiol wires indicates that the extra S atom provides a better coupling between the molecule to the lead. The value of $\beta \approx 0.95$ is near that of the recent experimental measurements [56, 160], which give $\beta \approx 1.1$, but is rather different from that reported in [57], which gave $\beta \approx 0.57$. The latter value of β is believed to be influenced by gold particle contact in the device setup in [57], which may behave as a quantum dot. Finally, a more drastic change of contact group can be achieved by replacing the end-group of alkane-thiols, CH_3 , with CF_3 -terminated [58]. Again, such a change does not alter the qualitative conduction behavior of the molecular wire, and one finds $R_o \approx 250 \text{ k}\Omega$ and $\beta \approx 0.95$, shown by the filled triangles in Fig. 8(b). The larger value of R_o for CF_3 -terminated molecule can be attributed to the longer contact distance between the F atom and the Au lead surface.

The quantitative consistency of the calculated and measured β values is encouraging; β is independent of the number of molecules in the contact region, and the single molecule model should indeed capture this quantity. On the other hand, it is interesting to observe that the calculated value of R_n is on the same order of magnitude as the experimental data. This is somewhat surprising, since R_n depends on the number of contacted molecules, which cannot be known exactly in an experimental setup. In [42], a contact area $\sim 15 \text{ nm}^2$ was estimated for an AFM tip of radius $\sim 50 \text{ nm}$ at an applied load of 1 nN, leading to an estimate of 75 molecules contacted at the junction. Similarly, 32 molecules have been estimated in [45], for a tip radius of 10 nm at a load of 4.5 nN (in liquid). Using these estimates, we would expect to see the experimental R_n to be tens of times smaller than the single molecule model predicted. Nevertheless, since R_n is a non-universal number, many factors may influence its value. The simplest possibility is that the number of conducting molecules in the AFM setup is actually fewer than estimated, i.e., not all molecules inside the AFM-substrate junction are contacted equally well. The same issues have also been raised in the recent work of Lee et al. [49] using the nanopore experimental setup. While the measured β and tunneling barrier are close to what we calculated [50], the estimate of the measured current density is smaller than the single molecule calculation. Again, the estimate of current density requires knowledge of how many molecules participate in conduction, which, at present, remains unknown.

Next, we consider [51] a different set of molecules, the oligophenylenes, which transport properties have also been studied experimentally in several laboratories [43, 44], and consistent results obtained. The oligophenylenes molecular wires we calculate are shown in Fig. 9, where a planar and a rotated ring structure are investigated. The molecule-electrode contact distance is fixed to be a constant for all three molecules (both conformations): the distance of the S-Au (from the sulfur atom to the surface of electrode) is 4.0 a.u. and H-Au is 2.2 a.u. [59].

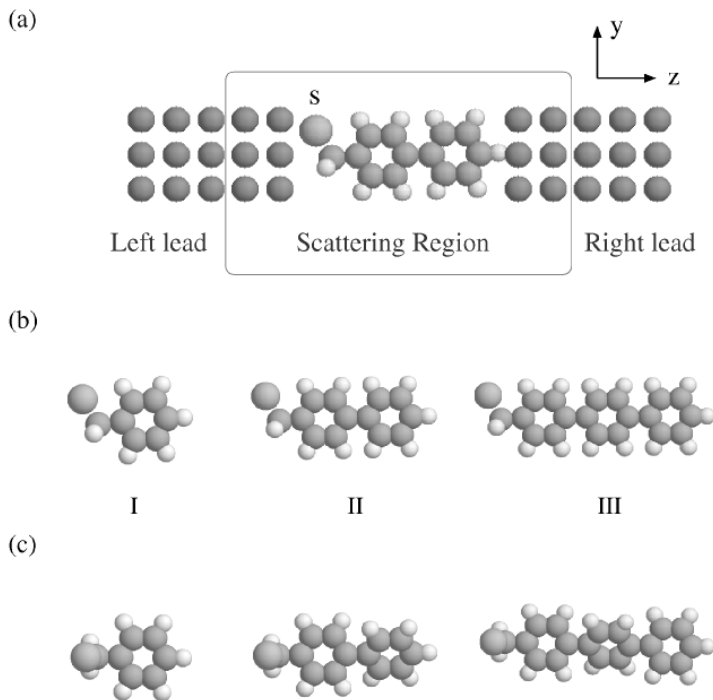


Fig. 9. (a) Schematic illustration of the oligophenylenes device. The simulation box (device) is indicated by the scattering region, which includes a portion of the infinitely long electrodes and the oligophenylenes thiolate molecule. The distance of S-Au (surface) is 4.0 a.u. and H-Au is 2.2 a.u. (b) Three molecules are studied: oligophenylenes derivatives I-III. Their molecular structures (planar) are shown. (c) Molecular structures in non-planar conformation. The SCH_2 -group is vertically (oriented by S-C bond) connected with a phenyl ring while the angle between two rings is 45 degrees

Figure 10(a) plots the calculated I-V curves for molecules I-III (planar structure, see Fig. 9). They are almost linear over the entire range of the bias voltage applied. The linear I-V curves give a voltage independent resistance which is plotted in Fig. 10(b) in a semi-log form (again, resistances are calculated at 0.1 V bias voltage). The data is, again, well fitted to $R_n \sim R_o \exp(\beta n)$ where n is the number of phenyl rings. We find the constants $R_o = 140 \text{ k}\Omega$ and $\beta \approx 1.76$, which translate to a length scale of 0.4 \AA . Figure 10(b) also shows resistances of non-planar molecules (filled triangle). For these non-planar molecular wires, we found $R_o = 30 \text{ k}\Omega$ and $\beta \approx 2.19$ which translates to a length scale of 0.51 \AA (the non-planar structures are slightly shorter than planar ones). Note that experimental data [43] were reported to be in the range $\beta \sim 0.35 \text{ \AA}$ to 0.5 \AA for three different AFM tips in the measurements. Our theoretical values are, therefore, quantitatively consistent with

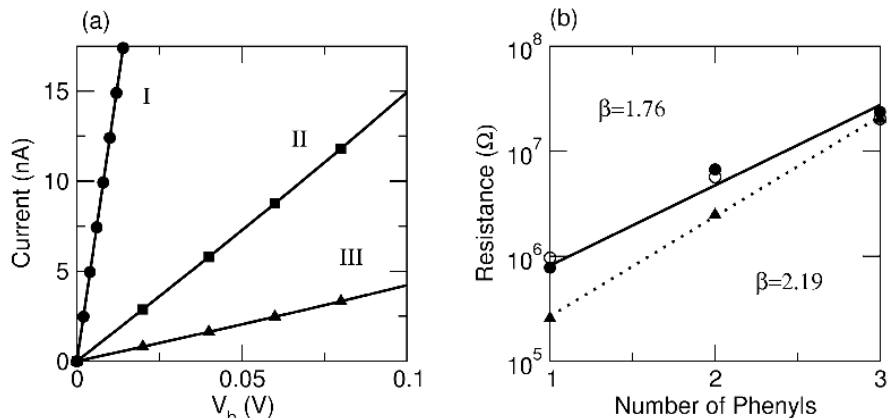


Fig. 10. (a) I-V characteristics for planar oligophenylene molecules of I-III of Fig. 9. (b) A semi-log plot of resistance versus number of phenyl groups in molecules of I-III. Filled circles: planar wires with Au electrodes; filled triangle: non-planar wires with Au electrodes; empty circles: planar wires with Al electrodes. The solid (dotted) line is a linear fit to the exponential equation where $R_o = 140 \text{ k } \Omega$ ($R_o = 30 \text{ k } \Omega$). Resistances (dI/dV) are calculated at bias of 0.1 V

them. Just as the data for alkane-thiol wires, the values of calculated R_o are within a factor of few to the experimental value. The difference is likely due to the fact that experimental devices involve more than one molecule. For planar molecules contacted by Al electrodes (empty circles in Fig. 10b), the value of β is slightly smaller and R_o is somewhat larger than those of the Au-oligophenylene-Au devices (for comparison, the Al-oligophenylene contact distance is fixed as that of the Au device).

The calculated results presented here [50, 51] for both Au-alkanethiol-Au and Au-oligophenylene-Au molecular wires are in good agreement with the experimental data, since the rate of resistance increase, β , is quantitatively comparable. For different contact structures, including different molecule end-groups, different leads, and different lead geometries, β does not change significantly. The resistance R_o , on the other hand, does change with these device details. The calculation allows us to conclude that transport in these molecular wires is largely determined by the molecule itself, and these systems therefore provide excellent testing grounds for ideas of molecular scale conduction, because they are less influenced by uncontrollable environmental factors.

6 Non-Equilibrium Forces

In the case of non-equilibrium the electronic density differ from the density found for thermal equilibrium, as discussed earlier. Thus the forces on the

atoms will change. For an relaxed atomic configuration initially in thermal equilibrium, the applied voltage bias and a resulting non-equilibrium steady-state situation will introduce “current-induced” forces on the atoms [37]. Understanding these effects from an atomistic view point is relevant in technological problems like the failure of interconnects in integrated circuits due to directionally biased diffusion of atoms caused by the presence of an electric current (electromigration) [60]. Traditionally the microscopic origin of the current induced force on an atom has been related to electrostatic forces and the momentum transfer by the electron flow, the so called electron wind force [60], but this division seems not to be necessary [37]. While there is a consensus on the definitions of these forces, the fundamental properties, such as the current-induced forces, are still under discussion [61].

In this section we discuss how the effect of current-induced bond weakening/strengthening can be understood in terms of the change in bond charge in the system using an atomic gold wire as an example [62]. The key to understanding the current-induced forces is the division of the bond charge into electrode-related left and right parts.

We consider a simple symmetric geometry consisting of three atoms connecting electrodes in both the (100) and (111) directions, see Fig. 11. The electrode-electrode distance is in both cases chosen to be 9.6 Å and the wire atoms are initially relaxed at zero bias. We choose this particular geometry since here the middle atom (2) can roughly be considered to have only two bonds namely to the left atom (1) and the right atom (3). When the voltage is applied we observe a substantial redistribution of the electronic charge. At 0 V the wires have a net negative charge of about 0.2 excess electrons. About half of this resides on atom 2. At 2V the excess electrons on atom 2 are almost halved. This charge redistribution results in an asymmetric voltage drop where the main drop is between the negative electrode and atom 2 (see Fig. 11).

In Fig. 12a we show the calculated bond forces for the (100)/(111) wires with atomic positions fixed at the relaxed values [63] obtained for zero bias. We find that the forces on the symmetric atoms 1 and 3 roughly follow each other, also beyond the linear bias regime [37]. We note that the order of magnitude and direction of the bond forces at 2 V are similar for (100)/(111) while the detailed behavior differs: the bond forces for the (100) wire stay linear up to 1 V and level off around 2 V while we observe an onset of the bond forces for (111) at 1 V.

Along with the bond force we also show the overlap population (OP) in Fig. 12a. The OP is a measure of the electronic charge residing in the bond. We note that except for the (111)-wire at low bias, the force and OP curves are almost mirrored. The result that an increase (decrease) in bond charge makes the bond force compressive (repulsive) is what we expect intuitively. In Fig. 12b we show the bond lengths after subsequent relaxation of the wire

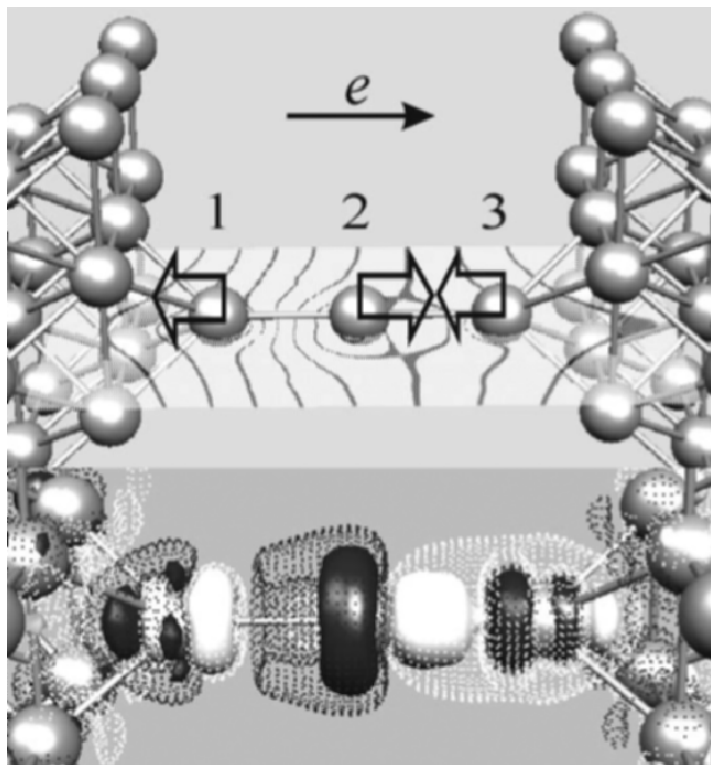


Fig. 11. (a) Direction of forces and voltage drop for the gold wire connecting (100) electrodes at 1 V bias. (b) Iso-density surfaces for the *change* in density from 0 V to 1 V. Dark is deficit and white is extra electron density. The *solid* (*dotted*) surface correspond to $\pm 5 \cdot 10^{-4} e/\text{\AA}^3$ ($\pm 2 \cdot 10^{-4} e/\text{\AA}^3$)

atoms for finite bias. The main relaxations take place in the wire bonds with smaller displacements in the wire-electrode bonds.

We aim at an qualitative picture of the current-induced forces. To this end we focus on the OP. We can express [64] the force acting on atom i due to the valence electrons using the force operator, \mathbf{F}_i , and the density matrix,

$$\mathbf{F}_i = \text{Tr}[\hat{\mathbf{F}}_i \hat{D}] \text{ where, } \hat{\mathbf{F}}_i = -\frac{\partial \hat{H}}{\partial \mathbf{R}_i}. \quad (40)$$

Consider the bonding between two atoms represented by orbitals $|\phi_1\rangle$ and $|\phi_2\rangle$ and separated by bond length b . From (40) we get the bond force,

$$F_{\text{bond}} = -2 \left(\frac{\langle \phi_2 | H' | \phi_1 \rangle}{\langle \phi_2 | \phi_1 \rangle} \right) O_{12}, \quad H' = \frac{\partial H}{\partial b}, \quad (41)$$

where we assume that only the hopping element, $\langle \phi_2 | H | \phi_1 \rangle$, changes with b . The bond force is proportional to the OP for the 12 bond,

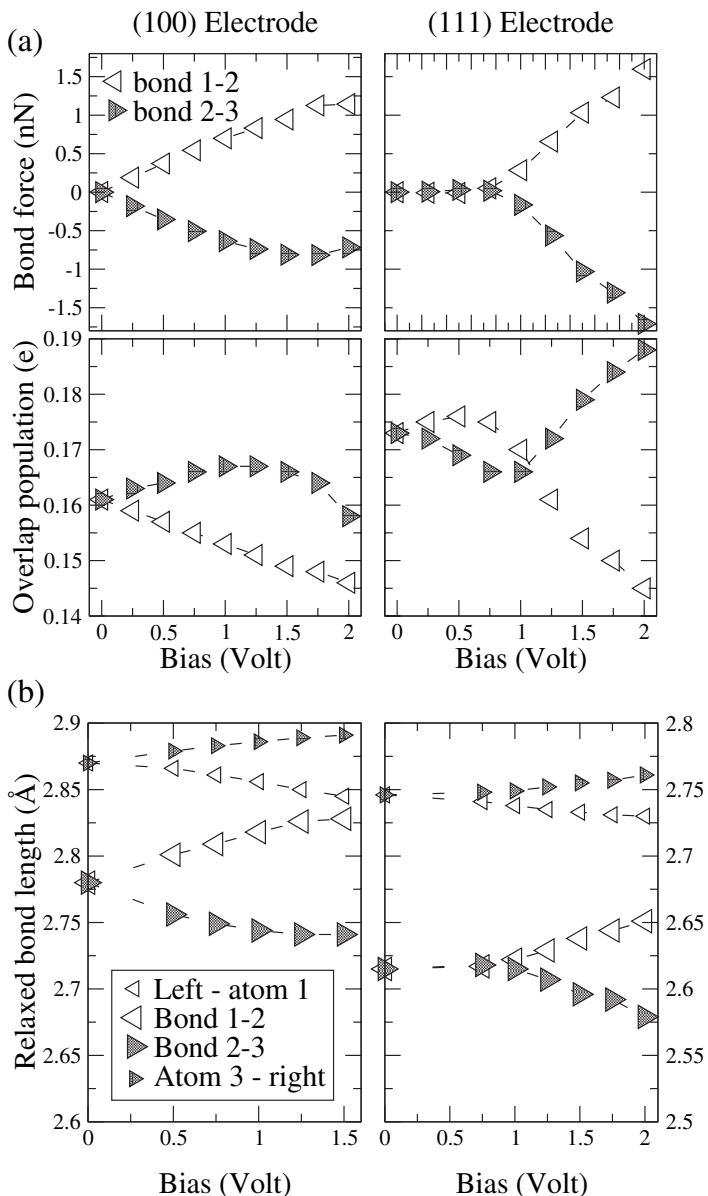


Fig. 12. (a) The bondforce and overlap (bond) population for the (100) and (111) connected wires. (b) The relaxed wire bondlengths for finite bias

$$O_{12} = 2 S_{12} D_{12} . \quad (42)$$

The OP is typically taken as a simple measure of the strength of a chemical bond as suggested by Mulliken for molecules [65]. In equilibrium we have,

$$O_{12} = 2 S_{12} \int_{-\infty}^{\infty} d\epsilon \rho_{12}(\epsilon) n_F(\epsilon - E_F) , \quad (43)$$

where n_F and E_F is the Fermi function and energy. The contribution from states at different energy(ϵ) in the extended system to the bonding between the two orbitals is described qualitatively by the OP weighted DOS (OPW-DOS) or COOP curve, $2S_{12} \rho_{12}(\epsilon)$, as discussed by Hoffmann [66].

Now we consider the nonequilibrium situation where an electrical current is running through a contact connecting two reservoirs, left and right (L, R), with different chemical potentials (μ_L, μ_R). The contact contains the 12 bond. In this case the bond force will change since the density and Hamiltonian matrices deviate from equilibrium values. The appropriate density matrix for the nonequilibrium situation is constructed from scattering states, and the total spectral density matrix (ρ) is split into partial contributions corresponding to their left ($\hat{\rho}^L$) or right ($\hat{\rho}^R$) origin as described in (22), and the density matrix for non-equilibrium is found by filling the left and right originating states according to the respective chemical potentials, see (23).

Similarly, we will split the overlap population (43), into its partial left and right components,

$$O_{12} = O_{12}^L + O_{12}^R , \quad (44)$$

where

$$O_{12}^L = 2 S_{12} \int_{-\infty}^{\infty} d\epsilon \rho_{12}^L(\epsilon) n_F(\epsilon - \mu_L) , \quad (45)$$

and likewise for R . When more orbitals are involved on atom 1 and 2 the overlap populations can be broken down in orbital components. In this case each orbital overlap will contribute with different weight to the bond force according to their different force matrix elements H' . This complication, together with the neglect of change in H' with applied voltage, makes the bond force and OP only roughly proportional, as we observe for the gold wires in Fig. 12. However, as a first approximation, we can explain the observed change in bond forces from the change in OP, which in turn means the change in left (ΔO^L) and right (ΔO^R) contributions.

In Fig. 13 we consider the change from 0 V to 1 V in left and right OP of the 12 and 23 bonds for the (100) case (we see a quite similar pattern for (111)). For both bonds ΔO^L is negative (decreasing bonding) while ΔO^R is positive (increasing bonding). We have resolved these further into the orbitals on atom 2 and display the main contributions in Fig. 13.

For the almost filled d_{yz}, d_{zx} states $\Delta O^R > 0$ while $\Delta O^L < 0$. The reason for this behavior is illustrated in Fig. 14. The increase in μ_L populate the d_{yz}, d_{zx} states which have *anti-bonding* around the Fermi level thus decreasing

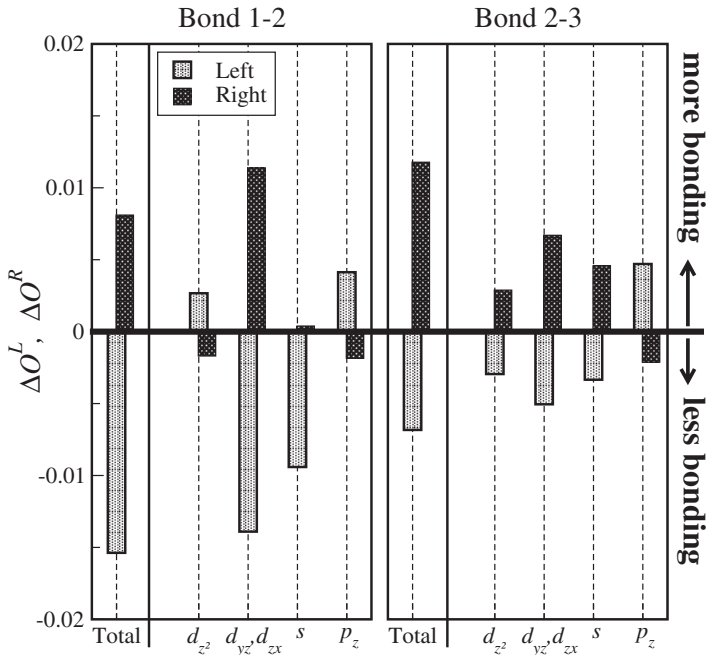


Fig. 13. The change in *left* and *right* partial OP, $\{O_{12}^L, O_{12}^R\}$ and $\{O_{23}^L, O_{23}^R\}$ for a change in bias from 0 V to 1 V for the (100) wire. These are broken into main orbital contributions with respect to the middle atom (2). We show the sum of the contributions for the degenerate d_{yz} and d_{zx}

the OP and therefore the bonding. On the other hand the decrease in μ_R has the opposite effect and increase the OP and the bonding. If we instead of almost filled states consider the almost empty p_z states we have *bonding* character around E_F and expect $\Delta O^L > 0$ while $\Delta O^R < 0$. This is exactly the behavior we observe in Fig. 13. Based on our simple picture in Fig. 14 we see that the almost completely filled states(d) and slightly more than half-filled states(s) together yield a *decrease* in O^L and *increase* in O^R . Since bond 12 couple more to the left electrode the total change in O^L will be bigger than the change in O^R . This explains the bond weakening of bond 12. The opposite is the case for bond 23. Also the voltage drop taking place in bond 12 will weaken this bond with respect to bond 23.

Thus in this simple example it seems clear that we can understand how the current-induced forces are due to a shift in the population of bonding and anti-bonding levels, and can be explained by examining the change in electrode decomposed bond charges(overlap population) with applied voltage. For systems with half-filled resonances dominating the bonding the situation may be less clear cut since both $O^L < 0$ and $O^R < 0$.

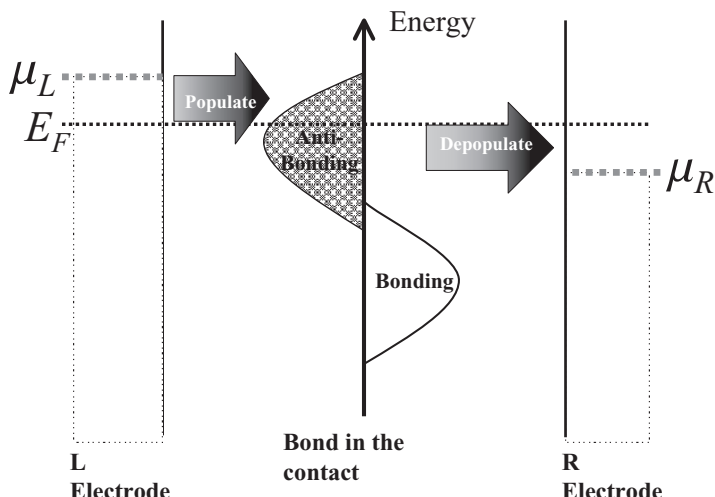


Fig. 14. Generic picture of the COOP (x-axis) curve for more than half-filling when the Fermi level is located in the anti-bonding region. The change in left and right bond populations is shown when the chemical potentials of the electrodes, μ_L, μ_R , deviate from the equilibrium, $\mu_L = \mu_R = E_F$

7 Conclusion

We have described the Non Equilibrium Green's Function (NEGF) formalism for modeling atomic-scale devices. With this technique it is possible to model the current-voltage characteristics of a molecular electronics device without any adjustable parameters, i.e. via *ab initio* techniques. We have used the method to calculate the resistance of molecules coupled with metallic electrodes, and obtained excellent agreement with experimental results.

We have discussed technical developments, such as complex contour integration, which greatly improves the computationally efficiency of the NEGF method. With these new improvements the computational efficiency of the NEGF method is approaching conventional quantum chemical methods, thus making virtual experiments on realistic molecular devices tenable.

Many new phenomena may be observed when a molecule is under non-equilibrium conditions. Of particular interest is the additional force on the atoms due to the electrical current through the structure. We have discussed the origin of these forces, and presented an intuitive chemical picture, which connects the non-equilibrium electron distribution with the atomic forces.

References

1. A. Aviram, M.A. Ratner: Molecular rectifiers, Chem. Phys. Lett. **29**, 277 (1974)

2. P. Pernas, A. Martin-Rodero, F. Flores: Electrochemical-potential variations across a constriction, *Phys. Rev. B* **41**, R8553 (1990)
3. W. Tian, S. Datta: Aharonov-bohm-type effect in graphene tubules: A landauer approach, *Phys. Rev. B* **49**, 5097 (1994)
4. L. Chico, M. Sancho, M. Munoz: Carbon-nanotube-based quantum dot, *Phys. Rev. Lett.* **81**, 1278 (1998)
5. A. de Parga, O.S. Hernan, R. Miranda, A.L. Yeyati, A. Martin-Rodero, F. Flores: Electron resonances in sharp tips and their role in tunneling spectroscopy, *Phys. Rev. Lett.* **80**, 357 (1998)
6. E.G. Emberley, G. Kirczenow: Electron standing-wave formation in atomic wires, *Phys. Rev. B* **60**, 6028 (1999)
7. M. Brandbyge, N. Kobayashi, M. Tsukada: Conduction channels at finite bias in single-atom gold contacts, *Phys. Rev. B* **60**, 17064 (1999)
8. H. Mehrez, J. Taylor, H. Guo, J. Wang, C. Roland: Carbon nanotube based magnetic tunnel junctions, *Phys. Rev. Lett.* **84**, 2682 (2000)
9. P. Sautet, C. Joachim: Interpretation of stm images: copper-phthalocyanine on copper, *Surf. Sci.* **271**, 387 (1992)
10. L.E. Hall, J.R. Reimers, N.S. Hush, K. Silverbrook: Formalism, analytical model, and a priori green's-function-based calculation of th current-voltage characteristics of molecular wires, *j. Chem. Phys.* **112**, 1510 (2000)
11. V. Mujica, A.E. Roitberg, M.A. Ratner: Molecular wire conductance: Electrostatic potential spatial profile, *J. Phys. Chem.* **112**, 6834 (2000)
12. F. Biscarini, C. Bustamante, V.M. Kenkre: Scanning tunneling microscopy. ii calculation of images of atomic and molecular adsorbates, *Phys. Rev. B* **51**, 11 089 (1995)
13. H. Ness, A. Fisher: Quantum inelastic conductance through molecular wires, *Phys. Rev. Lett.* **83**, 452 (1999)
14. N.D. Lang: Resistance of atomic wires, *Phys. Rev. B* **52**, 5335 (1995)
15. K. Hirose, M. Tsukada: First-principles calculation of the electronic structure for a bielectrode junction system under strong field and current, *Phys. Rev. B* **51**, 5278 (1995)
16. M.B. Nardelli: Electronic transport in extended systems: Application to carbon nanotubes, *Phys. Rev. B* **60**, 7828 (1999)
17. M.B. Nardelli, J. Bernholc: Mechanical deformations and coherent transport in carbon nanotubes, *Phys. Rev. B* **60**, R16 338 (1999)
18. S.N. Yaliraki, A.E. Roitberg, C. Gonzalez, V. Mujica, M.A. Ratner: The injecting energy at molecule/metal interfaces: Implications for conductance of molecular junctions from an ab initio molecular description, *J. Phys. Chem.* **111**, 6997 (1999)
19. P.A. Derosa, J.M. Seminario: Electron transport through single molecules: Scattering treatment using density functional and green function theories, *J. Phys. Chem. B* **105**, 471 (2001)
20. J. Palacios, A.J. Perez-Jimenez, E. Louis, J.A. Verges: Fullerene-based molecular nanobridges: A first principles study, *Phys. Rev. B* **64**, 115 411 (2001)
21. C.C. Wan, J.L. Mozos, G. Taraschi, J. Wang, H. Guo: *Appl. Phys. Lett.* **71**, 419 (1997)
22. H.J. Choi, J. Ihm: Ab initio pseudopotential method for the calculation of conductance in quantum wires, *Phys. Rev. B* **59**, 2267 (1999)
23. S. Corbel, J. Cerdà, P. Sautet: Ab initio calculations of scanning tunneling microscopy images within a scattering formalism, *Phys. Rev. B* **60**, 1989 (1999)

24. P.S. Damle, A.W. Ghosh, S. Datta: Unified description of molecular conduction: From molecules to metallic wires, Phys. Rev. B **64**, 201403 (2001)
25. J. Taylor, H. Guo, J. Wang: Ab initio modeling of open systems: Charge transfer, electron conduction, and molecular switching of a c-60 device, Phys. Rev. B **63**, 121104R (2001)
26. M. Brandbyge, J.L. Mozos, P. Ordejon, J. Taylor, K. Stokbro: Density functional method for nonequilibrium electron transport, Phys. Rev. B **65**, 165401 (2002)
27. H. Haug, A.P. Jauho: *Quantum kinetics in transport and optics of semiconductors* (Springer-Verlag, Berlin, Heidelberg, 1996)
28. S. Datta: *Electronic Transport in Mesoscopic Systems* (Cambridge Univ. Press., New York, 1996)
29. P. Hohenberg, W. Kohn: Inhomogeneous electron gas, Phys. Rev. **136**, B864 (1964)
30. W. Kohn, L.J. Sham: Self-consistent equations including exchange and correlation effects, Phys. Rev. **140**, A1133 (1965)
31. W. Kohn, A.D. Becke, R.G. Parr: Density functional theory of electronic structure, J. Phys. Chem. **100**, 12974 (1996)
32. R.G. Parr, W. Yang: *Density-Functional Theory of Atoms and Molecules* (Oxford University Press, New York, 1989, 1989)
33. L.I. Schiff: *Quantum Mechanics* (McGraw-Hill, Singapore, 1968)
34. E.G. Emberly, G. Kirczenow: Theoretical study of electrical conduction through a molecule connected to metallic nanocontacts, Phys. Rev. B **58**, 10911 (1998)
35. J. Taylor: (2000), Ph.D. thesis, McGill University
36. M. Lopez-Sancho, J. Lopez-Sancho, J. Rubio: Quick iterative scheme for the calculation of transfer matrices: application to mo (100), J. Phys. F **14**, 1205 (1984)
37. T.N. Todorov, J. Hoekstra, A.P. Sutton: Current-induced forces in atomic-scale conductors, Philos. Mag. B **80**, 421 (2000)
38. J.P. Perdew, A. Zunger: Self-interaction correction to density-functional approximations for many-electron systems, Phys. Rev. B **23**, 5048 (1981)
39. J.P. Perdew, K. Burke, M. Ernzerhof: Generalized gradient approximation made simple, Phys. Rev. Lett. **77**, 3865 (1996)
40. The atomistix virtual nanolab is an independent commercial software package that combines the technical achievements in McDCAL and TranSIESTA. For further information see www.atomistix.com.
41. D. Wold, C. Frisbie: Formation of metal-molecule-metal tunnel junctions: Microcontacts to alkanethiol monolayers with a conducting afm tip, J. Am. Chem. Soc. **122**, 2970 (2000)
42. D. Wold, C. Frisbie: Fabrication and characterization of metal-molecule-metal junctions by conducting probe atomic force microscopy, J. Am. Chem. Soc. **123**, 5549 (2001)
43. D. Wold, R. Haag, M. Rampi, C. Frisbie: Distance dependence of electron tunneling through self-assembled monolayers measured by conducting probe atomic force microscopy: Unsaturated versus saturated molecular junctions, J. Phys. Chem. B **106**, 2813 (2002)
44. T. Ishida, W. Mizutani, Y. Aya, H. Ogiso, S. Sasaki, H. Tokumoto: Electrical conduction of conjugated molecular sams studied by conductive atomic force microscopy, J. Phys. Chem. B **106**, 5886 (2002)

45. X. Cui, X. Zarate, J. Tomfohr, O. Sankey, A. Primak, A. Moore, T. Moore, D. Gust, G. Harris, S. Lindsay: Making electrical contacts to molecular monolayers, *Nanotechnology* **13**, 5 (2002)
46. J. Zhao, K. Uosaki: Formation of nanopatterns of a self-assembled monolayer (sam) within a sam of different molecules using a current sensing atomic force microscope, *Nano Lett.* **2**, 137 (2002)
47. J. Beebe, V. Engelkes, L. Miller, C. Frisbie: Contact resistance in metal-molecule-metal junctions based on aliphatic sams: Effects of surface linker and metal work function, *J. Am. Chem. Soc.* **124**, 11 268 (2002)
48. W. Wang, T. Lee, M. Reed: Mechanism of electron conduction in self-assembled alkanethiol monolayer devices, *Phys. Rev. B* **68**, 35 416 (2003)
49. T. Lee, V. Wang, J.F. Klemic, J.J. Zhan, J. Su, M.A. Reed: Comparison of electronic transport characterization methods for alkanethiol self-assembled monolayers, *J. Phys. Chem. B* **108**, 8742 (2004)
50. C. Kaun, H. Guo: Resistance of alkanethiol molecular wires, *Nano Lett.* **3**, 1521 (2003)
51. C. Kaun, B. Larade, H. Guo: Electrical transport through oligophenylene molecules: A first-principles study of the length dependence, *Phys. Rev. B* **67**, 121 411 (2003)
52. A. Ulman: *An Introduction to Ultrathin Organic Films from Langmuir-Blodgett to Self-Assembly* (Academic Press, Boston, 1991)
53. Gaussian 98, Revision A.7, M.J. Frisch, G.W. Trucks, H.B. Schlegel, G.E. Scusearia, M.A. Robb, J.R. Cheeseman, V.G. Zakrzewski, J.A. Montgomery, Jr., R.E. Stratmann, J.C. Burant, S. Dapprich, J.M. Millam, A.D. Daniels, K.N. Kudin, M.C. Strain, O. Farkas, J. Tomasi, V. Barone, M. Cossi, R. Cammi, B. Men-nucci, C. Pomelli, C. Adamo, S. Clifford, J. Ochterski, G.A. Petersson, P.Y. Ayala, Q. Cui, K. Morokuma, D.K. Malick, A.D. Rabuck, K. Raghavachari, J.B. Foresman, J. Cioslowski, J.V. Ortiz, A.G. Baboul, B.B. Stefanov, G. Liu, A. Liashenko, P. Piskorz, I. Komaromi, R. Gomperts, R.L. Martin, D.J. Fox, T. Keith, M.A. Al-Laham, C.Y. Peng, A. Nanayakkara, C. Gonzalez, M. Chal-lacombe, P.M.W. Gill, B. Johnson, W. Chen, M.W. Wong, J. L. Andres, C. Gonzalez, M. Head-Gordon, E.S. Replogle, and J.A. Pople, Gaussian, Inc., Pittsburgh PA, 1998.
54. In the calculations, a gold lead is composed of unit cells with 9 Au atoms oriented in the (100) direction repeated to $\pm\infty$, see Fig. 7a. For Al, two leads were used: the first has the same cross-section as the Au lead; the second is larger where each unit cell has 50 Al atoms repeated to $\pm\infty$ and the end surface of the lead is tempered as shown in Fig. 7b.
55. The junction distance in the experimental device is unknown. Wold et al. [43] suggested a value of 2.3 Å for Au-S bond and 2.0 Å for H-Au. Sellers et al. (H. Sellers, A. Ulman, Y. Shnidman, and J.E. Eilers, *J. Am. Chem. Soc.* **115**, 9389 (1993)) suggested that Au(100)-S distance at hollow site is 2.011 Å. We fixed the distances at 2.1 Å for Au-S and H-Au, close to these suggested equilibrium values. Furthermore, one knows that a pressure under 10 nN only has a tiny effect to conductance and the experimental data we compare were collected at around 1 nN, hence our choice of these junction distances should be reasonable.
56. V.B. Engelkes, private communication.
57. X. Cui, A. Primak, X. Zarate, J. Tomfohr, O. Sankey, A. Moore, T. Moore, D. Gust, L. Nagahara, S. Lindsay: Changes in the electronic properties of a molecule when it is wired into a circuit, *J. Phys. Chem. B* **106**, 8609 (2002)

58. The F-Au distance is fixed to be 2.6 Å, close to the suggested value of 2.7 Å.
See, J. Pflaum, G. Bracco, F. Schreiber, R. Colorado Jr., O.E. Shmakova, T.R. Lee, G. Scoles, and A. Kahn, *Surf. Sci.* **498**, 89 (2002).
59. These were the junction distances suggested in [43].
60. R.S. Sorbello: *Solid State Physics* **51**, 163 (1998)
61. M.D. Ventra, Y.C. Chen, T.N. Todorov: Are current-induced forces conservative?, *Phys. Rev. Lett.* **92**, 176 803 (2004)
62. M. Brandbyge, K. Stokbro, J. Taylor, J.L. Mozos, P. Ordejon: First principles calculation of current induced forces in an atomic gold wire, *Phys. Rev. B* **67**, 193 104 (2003)
63. The force is less than 0.02 nN on all wire atoms.
64. Terms which take into account incompleteness and non-orthogonality are included in pracsis, see P. Ordejon, E. Artacho, and J.M. Soler, *Phys. Rev. B*, **53**, R10441 (1996).
65. R.S. Mulliken: *J. Chem. Phys.* **23**, 1833 and 2343 (1955)
66. R. Hoffmann: A chemical and theoretical way to look at bonding on surfaces, *Rev. Mod. Phys.* **60**, 1988 (1988)

Tight-Binding DFT for Molecular Electronics (gDFTB)

A. Di Carlo¹, A. Pecchia¹, L. Latessa¹, Th. Frauenheim² and G. Seifert³

¹ Dept. Elect. Eng., University of Rome “Tor Vergata”, Via del Politecnico 1, 00133 Roma, Italy

dicarlo@ing.uniroma2.it

² Dept. of Theoretical Physics, University of Paderborn, 33098 Paderborn, Germany

³ Institut f. Physikalische Chemie, Technische Universität Dresden, 01062 Dresden, Germany

Abstract. We present a detailed description of the implementation of the non-equilibrium Green’s function technique on the density-functional-based tight-binding simulation tool (gDFTB). This approach can be used to compute electronic transport in organic and inorganic molecular-scale devices. The tight-binding formulation gives an efficient computational tool able to handle a large number of atoms. The non-equilibrium Green’s functions are used to compute the electronic density self-consistently with the open-boundary conditions naturally encountered in transport problems and the boundary conditions imposed by the potentials at the contacts. The Hartree potential of the density-functional Hamiltonian is obtained by solving the three-dimensional Poisson’s equation involving the non-equilibrium charge density. This method can treat, within a unified framework, coherent and incoherent transport mechanisms.

1 Introduction

Technological advances in fabrication, characterization and control at the nanoscale level have enabled the manufacturing of a variety of new organic and organic-inorganic structures with a good degree of reproducibility. This has allowed a level of miniaturization to the extreme scale where the active component of the electronic device can involve just a single molecule. This new field of research, which appropriately deserves the name of *molecular electronics*, is attracting more and more the attention of theoreticians and computational physicists both for its potential applications and for the interesting fundamental physics involved. Electronic conduction through a variety of different molecules has been studied experimentally by many research groups [1–5] and the recent breakthroughs [6] have given a demonstration of the potentialities of nonoscale electronics.

However, the exact nature of the transport mechanisms in many such systems remains still open to scientific debate [7]. The role of phonon scattering, coherent tunneling versus multiple incoherent hopping transport and redox-like processes are issues for investigation [8]. Certainly molecular devices

require new simulation approaches, since the inherent quantum-mechanical physics involved must be treated properly [9].

We have developed a new approach (*gDFTB*) for transport computations based on the well known density functional tight-binding (DFTB) method [10]. This approach has been extended to the non-equilibrium Green's function approach (NEGF) [11,12] for the computation of the charge density and electronic transport.

The gDFTB method allows a nearly first-principle treatment of systems comprising a large number of atoms. The Green's function technique enables the computation of the tunneling current flowing between two contacts in a manner consistent with the open boundary conditions that naturally arise in transport problems. On the other hand, the NEGF formalism allows to compute the charge density consistently with the non-equilibrium conditions in which a molecular device is driven when biased by an external field.

The key ingredient of the self-consistent loop is the solution of the Hartree potential needed in the density functional Hamiltonian. The Hartree potential is calculated by solving the three-dimensional Poisson's equation (with appropriate boundary conditions), for the corresponding non-equilibrium charge density computed via the NEGF formalism.

We give a full description of our methodology and show applications to molecular *devices* with fully self-consistent computation of the non-equilibrium wind-forces acting on the atoms, which enable us to explore the potentiality of molecular systems as electronic switches and bistable rectifiers. Our methodology also enables time-resolved current calculations along the steps of classical Molecular Dynamics simulations. The gDFTB tool can be accessed via the ICODE interface at the link: <http://icode.eln.uniroma2.it>.

The present paper has been structured as follows. Sections 2 and 3 are devoted to the introduction on DFTB method and to the transport problem we intend to tackle. In Sect. 4 we show how it is possible to map, within the standard Green's function formalism, the infinite contact-leads into complex self-energy terms, hence reducing the problem of open boundary conditions to the manipulation of finite matrices. The Green's functions formalism is used to compute the density matrix in non-equilibrium condition, starting from the scattering states of the system. Section 5 illustrates the equivalence between the results of Sect. 4 and the non-equilibrium Green's function formalism. Section 6 is dedicated to the computation of the terminal currents. One of the great advantages of the Green's function technique is that it can treat, within a unified mathematical framework, coherent and incoherent scattering. We give a general description of the correct current computation under non-equilibrium conditions in the cases of coherent and incoherent transport. We show that in absence of incoherent events the usual Landauer formula can be recovered. Section 7 summarizes the fundamental steps for the self-consistent charge computation in non-equilibrium systems. In Sect. 8 we give details on how to compute the non-equilibrium density matrix by an

appropriate contour integration, while the implementation of the Poisson's solver is reported in Sect. 9. Section 10 illustrates the computation of the atomic forces which are computed from the non-equilibrium density matrix. Application examples of the gDFTB code are given in Sect. 11. Section 12 illustrates how the Keldysh formalism can be extended to include incoherent electron-phonon scattering in molecular junctions. We conclude in the last section with a discussion on the applicability of DFT approaches to the transport problem.

2 The Self-Consistent Density-Functional Tight-Binding

Density-functional based methods permit an accurate and theoretically well founded description of the ground state properties for a large variety of materials.

The standard density-functional based tight-binding formalism has been explained in detail elsewhere, for a review see e.g. [10]. The particular choice in traditional DFTB is to use a minimal basis set of atomic orbitals in order to reduce the matrix dimensions for diagonalization speed-up. Furthermore, the integrals entering the matrices are calculated within the two-center approximation [13–15]. Therefore, the non-self-consistent part of the pair integrals is calculated at a step previous to the actual simulation and tabulated as a function of the inter atomic distance for each different pair of atomic species. This approach has proved to give transferable and accurate interaction potentials and the numerical efficiency of the method allows molecular dynamic simulations of large super-cells, containing several hundreds of atoms. The method has been extended to a self-consistent charge (SCC) DFTB method [16]. This methodology is particularly suitable to study the electronic properties and dynamics of large mesoscopic systems, particularly organic molecules such as CNTs, DNA strands or adsorbates on surfaces, semiconducting heterostructure etc. see [10, 17].

We briefly describe here the self-consistent DFTB method. The method is a development of the idea firstly introduced by Foulkes [18], where the electronic density is expanded as a sum of a reference density, $n^0(r)$, (that can be chosen as the superposition of neutral atomic densities) and a deviation, $\delta n(r)$, such that $n(r) = n^0(r) + \delta n(r)$. The total energy of the system can be described, up to second order in the local density fluctuations, as:

$$E_{tot}[n] = \sum_k n_k \langle \Psi_k | H^0 | \Psi_k \rangle + E_{rep}[n^0] + E^{(2)}[\delta n], \quad (1)$$

The first term in (1) can be written in terms of the TB Hamiltonian, which is given by

$$H_{\mu\nu}^0 = \begin{cases} \epsilon_{\mu}^{free-atom}, & \mu = \nu \\ \langle \phi_{\mu} | T + v_{eff}[n_i^0 + n_j^0] | \phi_{\nu} \rangle, & \mu \in i, \nu \in j \end{cases} \quad (2)$$

where ϕ_μ and ϕ_ν are the atomic orbitals localized around the atomic centers i and j ; T is the kinetic energy operator, and v_{eff} is the effective one-particle potential, which depends on the density of the two atomic centers i and j .

The term $E_{rep}[n^0]$ in (1) is the repulsive energy between the ions, screened by the electronic distribution and the exchange energy. This term is short-ranged because of the neutrality of the density $n^0(r)$ and can be expressed as a summation over atomic pair contributions as follows: [14]

$$E_{rep}[n^0] = \frac{1}{2} \sum_{\alpha\beta} U_{\alpha\beta}(n_\alpha^0, n_\beta^0). \quad (3)$$

The third term in (1) is the second order correction. This can be written as a sum of the second order correction to the Hartree potential and the exchange-correlation potential:

$$E^2[\delta n] = \frac{1}{2} \int \int \left[\frac{1}{|r - r'|} + \frac{\delta^2 E_{xc}}{\delta n(r)\delta n(r')} \right] \delta n(r)\delta n(r') dr dr' \quad (4)$$

This quantity is greatly simplified by retaining only the monopole term in the radial expansion of the atom-centered density fluctuations, which is written as [14].

$$\delta n_i(r) \approx \Delta q_i \frac{F_{00}^i(|r - R_i|)}{4\pi}. \quad (5)$$

The normalized spherical charge density at each atomic center is assumed to have a simple exponential decay, of the form

$$n_i(r) = \frac{\tau_i^3}{8\pi} \exp(-\tau_i |r - R_i|). \quad (6)$$

It follows that the second order correction can be written as

$$E^2 = \frac{1}{2} \sum_{i,j} \Delta q_i \Delta q_j \gamma_{ij}, \quad (7)$$

where

$$\gamma_{ij} = \int \int \Gamma[r, r', n^0] n_i(r') n_j(r) dr' dr \quad (8)$$

is introduced as a shorthand and Δq_i are the atomic charges.

Within the LDA approximation the exchange contribution vanishes for large atomic distances, hence in (8) the second order correction to E_{xc} can be neglected with respect to the Coulomb interaction. The term $\Gamma[r, r', n^0]$ becomes the usual Green's function of the Coulomb potential, $\frac{1}{|r - r'|}$, with vanishing boundary conditions at infinity. The on-site terms γ_{ii} can be related to the Hubbard parameter $U_i \equiv \gamma_{ii} = I_i - A_i$, where I_i and A_i are the atomic ionization potential and the electron affinity, respectively. Therefore, the expression for γ_{ij} only depends on the distance between the atoms i and

j and on the parameters U_i and U_j . The onsite Hubbard parameters can be calculated for any atom type within LDA-DFT as the second derivative of the total energy of the atom with respect to the occupation number of the highest occupied atomic orbital. These values are therefore neither adjustable nor empirical parameter [16].

The atomic charges can be easily calculated, using the Mulliken charge analysis. This consists on a simple projection of the eigenstates over the local orbitals,

$$\Delta q_i = \sum_k n_k \sum_{\mu \in i} \sum_{\nu} [c_{k\mu}^* c_{k\nu} S_{\mu\nu}] - q_i^0 . \quad (9)$$

Applying the variational principle to the energy functional of (1) together with (7) and using (9), it is possible to obtain a modified Hamiltonian for the Kohn-Sham equations:

$$H_{\mu\nu} = H_{\mu\nu}^0 + \frac{1}{2} S_{\mu\nu} \sum_k (\gamma_{ik} + \gamma_{jk}) \Delta q_k , \quad \forall \mu \in i, \nu \in j . \quad (10)$$

Since the atomic charges depend on the one-particle wave functions Ψ_k , a self-consistent procedure is required. The improvement of the self-consistent over the non self-consistent procedure is considerable in determining structural and energetic properties of molecular systems [16].

3 Setup of the Transport Problem

The type of systems under study can be represented as in the graph of Fig. 1. The system is subdivided into three parts: two contacts, C_1 and C_2 , and a device region, D . The contacts are semi-infinite leads and it is assumed that their properties coincide with those of bulk systems. The device is a conductor linking the two contacts, comprising the molecular *bridge*, M , and a portion of the surfaces of the conducting leads, S_1 and S_2 . This inclusion is necessary in order to ensure that the regions C_1 and C_2 can really be considered bulk-like. This assumption can be directly verified by checking that the charge density smoothly joins at the boundaries C_1/S_1 and C_2/S_2 . The number of contacting leads can be greater than two, but, for illustrative purposes, we will refer to two contacts only.

The two contacts are kept at different electrochemical potential, and a current is driven across the molecular *bridge*. The system can include external modulating fields, provided by gate plates. The problem of interest is to compute the current which flows in the *device*.

In solving for the transport problem it is not possible to make the assumption of local thermodynamical equilibrium, i.e., a global Fermi energy is not defined. The only assumption that can be made is that the connecting leads are kept at different potentials, and are considered large reservoirs where the electrons are effectively in equilibrium. In order to be consistent with this

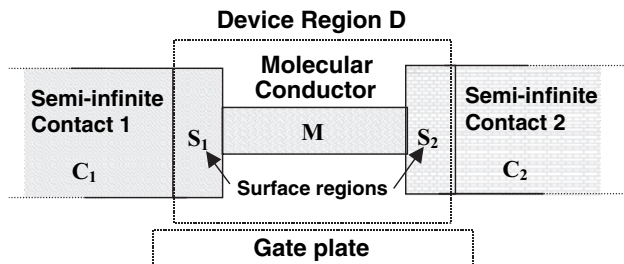


Fig. 1. Diagram showing the system comprising the contact regions, C₁ and C₂, the molecular region M, and the surface regions S₁ and S₂ included in the *device* region, A

scenario, the conducting bridge must offer the largest source of resistance to the flowing current. Only under this condition is it consistent to assume that the potential drops essentially across the device region, whilst the contacting leads are in equilibrium at two different constant potentials, as shown in Fig. 2. In this respect, the mesoscopic system plays the role of a large resistance in analogy to conventional electronics. However, it is useful to stress that there are fundamental differences between standard electronic devices and mesoscopic conductors. In macroscopic devices it is often possible, for example, to describe the electron dynamics as an equilibration process with a thermalised bath via inelastic scattering events, typically with phonons. Energy relaxations allow the system to reach equilibrium and to define, at the end, properties such as intrinsic mobility and conductivity which characterize a macroscopic material. For mesoscopic devices, the conduction is quantized and depends on the number of conducting channels. It is not possible to define an intrinsic conductivity of a molecule or any nanoscale system. Most of the properties of the device depend on the characteristics of the contact. When tunneling is coherent, the current depends critically on the coupling

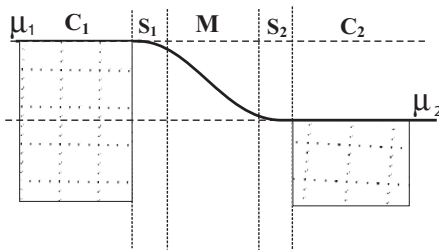


Fig. 2. Diagram showing the non equilibrium condition. The thick line is a representation of the average potential which is constant inside the contacts and drops in the molecular region. The potential smoothly joins to the bulk values in the surface regions, S₁ and S₂

between contact and molecule and on the position of the energy levels of the molecule relative to the Fermi level of the contacts.

Even when inelastic scattering occurs, these events are too few to allow perfect equilibration, and most of the energy relaxation occurs at the final contact. The device region is therefore out of equilibrium and a proper treatment must be employed. This is provided by the NEGF method firstly introduced by Keldysh [11] and later adapted to quantum transport problems by several authors [12, 19, 20].

4 The Green's Function Technique

In order to compute the current, open boundary conditions for the Kohn-Sham equations must be employed. Open boundary conditions are necessary in order to allow the eigenstates can carry a current. This can be described in the context of scattering theory. Following for instance the derivation given in [21] and in Chap. 4, it is possible to construct the scattering states by making use of the Lippmann-Schwinger equation

$$|\psi_1\rangle = |\phi_1\rangle + G^r V |\phi_1\rangle, \quad (11)$$

where G^r is the retarded Green's function of the system which links the exact scattering states $|\psi_1\rangle$ to the unperturbed states $|\phi_1\rangle$. The states $|\psi_1\rangle$ are states originating deep in lead 1 and propagating from lead 1 lead 2. Similarly it is possible to define a state propagating from lead 2 to lead 1. The potential V is the Hamiltonian coupling the Device region to the contacts, which can be treated as a perturbation.

The Green's function of the system is constructed exploiting the Dyson's equation and by constructing appropriate contact self-energies [12]. The self-energy can be calculated easily by exploiting the fact that the Hamiltonian describing the interaction between the *device* region and the contacts involves a finite number of atoms close to the junctions. Therefore, the required contact Green's function can be solved just for the matrix block corresponding to atoms close to the *device* region. This so-called surface Green's function can be calculated using, for example, the Decimation technique [?], which is a powerful recursive algorithm suitable to TB matrix representations.

The total density of states out of equilibrium can be expressed in terms of partial density of states propagating from lead 1 to 2 and vice versa. The key assumption is that the states $|\psi_1\rangle$ originate deep in contact 1 where there is an equilibrium condition with chemical potential μ_1 . Similarly the states $|\psi_2\rangle$ originate deep in contact 2 where there is an equilibrium condition with chemical potential μ_2 . Hence, the total density of these propagating states is [23]

$$\rho = \int_{-\infty}^{+\infty} dE [d_1(E)f(E - \mu_1) + d_2(E)f(E - \mu_2)] . \quad (12)$$

This expression for the density matrix, analogous to (20) of Chap. 4, can be used to calculate the electronic density needed for the density-functional Hamiltonian. It is important to note that this density matrix does not account for states localized within the molecular region because these states cannot be reached starting from scattering states originating in the leads. We will return to this crucial point in Sect. 8, when discussing the actual computation method of expression (12).

5 The Relationship with the Keldysh Green's Functions

The expression (12) for the density matrix, derived from the scattering states, is equivalent to a direct derivation from the NEGF formalism. The link with the Keldysh Green's function can be obtained combining (11) with (12) and finding an expression for d_1 and d_2 in terms of the retarded and the advanced Green's functions and the contact self-energies [21]. These expressions are

$$d_\alpha = \frac{1}{2\pi} G^r \Gamma_\alpha G^a , \quad (13)$$

where Γ_α is defined as:

$$\Gamma_\alpha = i [\Sigma_\alpha^r - \Sigma_\alpha^a] . \quad (14)$$

The Keldysh Green's functions, $G^<(E)$ and $G^>(E)$, are defined in terms of the retarded, the advanced Green's functions and the non-equilibrium self energies $\Sigma^<$ and $\Sigma^>$,

$$G^{<,>} = G^r \Sigma^{<,>} G^a , \quad (15)$$

In the general case, the self-energies $\Sigma^<$ and $\Sigma^>$ also include, beside the contact self-energy, terms corresponding to scattering sources. These can be provided by electron-phonon, electron-electron or electron-defect potentials interactions.

The total self-energies is a summation of the self-energies due to the leads and that due to the phase-breaking interactions [24]:

$$\Sigma^{<,>} = \Sigma_\phi^{<,>} + \sum_\alpha \Sigma_\alpha^{<,>} , \quad (16)$$

The contact self energy terms can be easily identified from (12), (14) and (15) with (Note the identity $f(-E) = 1 - f(E)$)

$$\Sigma_\alpha^{<,>} (E) = f(+, -(E - \mu_\alpha)) \Gamma_\alpha . \quad (17)$$

The self-energy due to the interactions can be expressed, in many-body perturbation theory, in terms of the Green's function itself, via the Dyson's [25]. This self-energy contains an imaginary part which plays the role of reshuffling electrons between different energy channels. The interactions can be

viewed as an exchange of particle with a virtual contact which absorbs electrons at a given energy (negative $I_\phi(E)$) and emits them at another energy (positive $I_\phi(E)$). The net virtual current should be zero, for current conservation. Combining (12) and (17), it is possible to find the general expression for the density matrix in terms of the NEGF:

$$\rho = \frac{1}{2\pi i} \int_{-\infty}^{+\infty} dE G^<(E). \quad (18)$$

The NEGF formalism is quite elegant and general and can treat, within a unified formalism, the complexity of non-equilibrium quantum processes and many-body theory. For example, it has been demonstrated that from NEGF it is possible to derive different limiting transport regimes in superlattices, [26] from miniband conduction to Wannier-Stark hopping and sequential tunneling. In practical computations, it is convenient to rewrite (12) as

$$\begin{aligned} \rho = & \int_{-\infty}^{+\infty} dE [d_1(E) + d_2(E)] f(E - \mu_1) + \\ & \int_{-\infty}^{+\infty} dE d_2(E) [f(E - \mu_2) - f(E - \mu_1)]. \end{aligned} \quad (19)$$

Using the definitions given in (13), and invoking time-reversal symmetry ($G^a = G^{r*}$), this expression can be written as:

$$\rho = -\frac{1}{\pi} \text{Im} \left[\int_{-\infty}^{+\infty} dE G^r(E) f(E - \mu_1) \right] + \Delta_2. \quad (20)$$

where Δ_2 is a shorthand defining the second integration in (19). Written in this form, it is easy to see that under equilibrium conditions ($\mu_1 = \mu_2$) the density matrix reduces to the well-known result of (27) of Chap. 4. It is worth noting that (20) accounts correctly for the states localized within the molecular region (at least up to the energy μ_1), whilst equation (19) does not. In fact, unless a relaxation mechanism is present, it is not possible to reach a localized state in the molecular region from a scattering state originating in the leads. For a state which does not couple to the leads $\Gamma_1 = \Gamma_2 = 0$ and there is no contribution to the density of states. This apparent contradiction is due to the fact that in going from (19) to (20) we have neglected the small imaginary part in the Green's function. The equality is actually not exact when $\Gamma_1 = \Gamma_2 = 0$. The use of (20) is correct and prevents underestimation of the electronic density because of contributions from localized states, which will be certainly populated because of energy relaxations always present in real devices.

The poles of G^r are slightly displaced below the real axis. The function is analytic on the upper half complex plane. The integration in (20) can be conveniently done by deforming the integration from the real axis into the

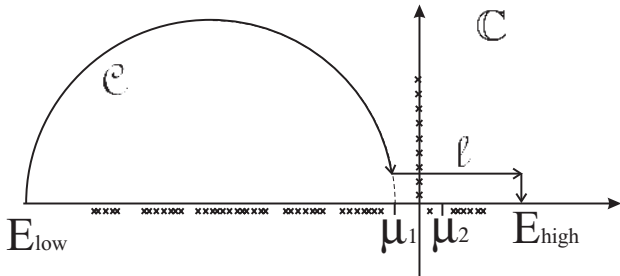


Fig. 3. Diagram showing the integration path in the complex plane needed to evaluate the non-equilibrium Green's function. The crosses below the real axis represent the poles of $G^r(z)$, and those on the imaginary axis the poles of the Fermi function

path $C + \ell$ shown in Fig. 3. The deformation is possible according to the residue theorem,

$$\oint dz G^r(z) f(z - \mu) = -2\pi i k T \sum_{\nu} G(z_{\nu}), \quad (21)$$

where $z_{\nu} = \mu + i\pi k T(2\nu + 1)$ are the poles of the Fermi function and the summation in (21) includes the poles enclosed within the contour. or $T > 0$ the integration path stays away from the real axis where $G^r(z)$ behaves regularly, with the exception of the points E_{low} and E_{high} , shown in Fig. 3. It is enough to choose the position of E_{low} far below the lowest energy of the electronic spectrum and E_{high} sufficiently greater than μ_1 , such that the Fermi function vanishes.

The integration involved in Δ_2 must be done on the real axis, since the function d_2 is analytic on the real axis only (it depends on G^r and G^a). This integration may be delicate and requires a fine mesh.

It is important to observe that this integration involves $d_2(E)$, and therefore, as discussed above, does not account for localized states not coupled to the leads. For any localized state lying within the energy range (μ_1, μ_2) it is necessary to manually provide the occupancy. Even though in practical computations this situation will seldom happen, the localized states can be counted if we express (19) in the alternative form:

$$\begin{aligned} \rho = & -\frac{1}{\pi} \operatorname{Im} \left[\int_{-\infty}^{+\infty} dE G^r(E) f(E - \mu_2) \right] \\ & - \int_{-\infty}^{+\infty} dE d_1(E) [f(E - \mu_2) - f(E - \mu_1)] . \end{aligned} \quad (22)$$

The first integration in (22) will now account for the localized states up to the energy μ_2 and will occupy them with one electron (actually two, if we account for the spin degeneracy). In some implementations [27] the

two alternative expressions (19) and (22) are compared to obtain a better accuracy for the density matrix. However we have seen that we can rely just on the first of the two computations, saving the high computational cost of the Green's functions.

6 The Terminal Currents

The current flowing in the system can be computed by defining an appropriate current operator [12, 28, 29]

$$I_{op}(r, r') = \frac{e}{\hbar} [G^<(r, r')H_D(r) - H_D(r)G^<(r, r')] , \quad (23)$$

whose diagonal elements give the divergence of the total current. An alternative derivation for deriving TB currents involves the definition of a bond-current operator [21] which is very useful for the calculation of local current fluxes [30]. The trace of the current operator gives the net outflow of current per unit energy across an imaginary surface enclosing the molecular region,

$$Tr[I_{op}] = \int \nabla \cdot J(r, E) dr . \quad (24)$$

Therefore, using (11), (14) and (15), the total outflow of current at any specific energy can be written as

$$Tr[I_{op}] = -\frac{e}{\hbar} Tr [\Sigma^<(E)G^>(E) - \Sigma^>(E)G^<(E)] , \quad (25)$$

which is obtained using the relationships $G^r - G^a = G^> - G^<$ and $\Sigma^r - \Sigma^a = \Sigma^> - \Sigma^<$. Inserting in (25) the expression for the total self-energy (16), it is possible to identify the terminal current contributions to the total current:

$$i_\alpha(E) = \frac{e}{\hbar} Tr [\Sigma_\alpha^<(E)G^>(E) - \Sigma_\alpha^>(E)G^<(E)] . \quad (26)$$

and the current contribution at the virtual contact:

$$i_\phi(E) = \frac{e}{\hbar} Tr [\Sigma_\phi^<(E)G^>(E) - \Sigma_\phi^>(E)G^<(E)] . \quad (27)$$

Expression (26) represents the net inflow of current from the α contact into the molecular region. The expression (27), instead, represents the inflow of current from the virtual contact. As observed above, current conservation must ensure that the net current exchange with the virtual contact is zero, or

$$\int i_\phi(E) dE = 0 . \quad (28)$$

Combining (15), (26) and (27) it is possible to separate the coherent and the incoherent contributions from the total current:

$$i_\alpha(E)_{coh} = \frac{e}{h} \sum_\beta Tr \left[\Sigma_\alpha^< G^r \Gamma_\beta G^a - \Gamma_\alpha G^r \Sigma_\beta^< G^a \right], \quad (29)$$

$$i_\alpha(E)_{incoh} = \frac{e}{h} \sum_\beta Tr \left[\Sigma_\alpha^< G^r \Gamma_\phi G^a - \Gamma_\alpha G^r \Sigma_\phi^< G^a \right]. \quad (30)$$

The incoherent part involves scattering contributions which give a non-vanishing $\Sigma_\phi^<$ and $\Sigma_\phi^>$.

In the case of two terminals and in the absence of incoherent scattering, the final expression for the current flowing from contact 1 to contact 2 can be written, using explicitly the relation (17), as:

$$i_{coh} = \frac{e}{h} \int_{-\infty}^{+\infty} Tr [T_2 G^r T_1 G^a] [f_2(E) - f_1(E)] dE \quad (31)$$

In this limit the usual expression of the Landauer theory is recovered. An additional factor of 2 usually must be added because of spin degeneracy.

7 The Poisson Equation

As anticipated in Sect. 7, the Hartree potential needed for the SCC iteration of the Kohn-Sham equations is computed by solving the Poisson's equation with the appropriate boundary conditions imposed by the contacts.

The Poisson's equation for the mean field electrostatic potential should be written as:

$$\begin{cases} \nabla^2 [V_{el} + V_{ions}] = -4\pi \sum_i [n_i^0(r) + \delta n_i(r) + \Delta q_i \delta(r - R_i)] \\ + \text{boundary conditions} \end{cases} \quad (32)$$

where $V_{el} + V_{ions}$ are respectively the contribution from the electrons (treated in mean field approximation) and the ions to the total electrostatic potentials, and Δq_i are the ionic charges.

The usual boundary condition assumed is that the potential vanishes at infinity. This gives the familiar solution for the electrostatic potential of a point charge, $e\Delta q$, as $e\Delta q / |r - r'|$, and the usual form for the Hartree energy.

In the DFTB implementation the only potential that can be modified self-consistently is the effective potential for the charge density, as written in (4). The effective potential for the reference density n^0 is included in H^0 and $E^{rep}[n^0]$ of (1) and cannot be directly accessed.

Therefore, by linearity, we split the Poisson's equation (32) into two equations:

$$\nabla^2 \left[V_{el}^{(0)} + V_{ions} \right] = -4\pi \sum_i [n_i^0(r) + \Delta q_i \delta(r - R_i)] \quad (33)$$

$$\nabla^2 V_{el}^{(2)} = -4\pi \sum_i \delta n_i(r) \quad (34)$$

Equation (33) gives the electrostatic field included in the zeroth-order terms of DFTB, if solved with the usual boundary conditions. If solved with the same boundary conditions, (34) will give back (4). This equation is solved, instead, with the boundary conditions imposed by the device. These conditions arise from the natural requirement that deep inside the contacts the effective potential for the Kohn-Sham equations must correspond to the bulk potentials. Therefore, at the boundaries between the *device* region and the contacts, the potential must match the intrinsic effective bulk potential (which originates from any equilibrium charge density) shifted by the applied bias. At the device-contacts interfaces, C_α/S_α , the potential must satisfy

$$V_{S_\alpha}^{(2)}(r)|_{C_\alpha/S_\alpha} = V_{C_\alpha, \text{bulk}}^{(2)}(r)|_{C_\alpha/S_\alpha} + \Delta V_\alpha , \quad (35)$$

where ΔV_α is the applied external potential to the α -contact.

For example, consider the case of GaAs contacts. The charge transfer between Ga and As, which occurs in equilibrium conditions, generates a non-uniform effective potential. The total potential inside the contacts can be obtained by adding the applied bias to this intrinsic potential and $V_{el}^{(2)}(r)$ of (34) should be matched at the boundaries between contacts and *device* regions to this total potential.

The decoupling of (33) and (34), which at first may seem arbitrary, is actually a good approximation since the zeroth-order densities are screened by the ionic charges, and therefore the pair potentials are not affected by the boundary conditions. On the contrary, the excess density produces a long-range Coulomb field that should respect the boundary conditions imposed by the device. For example, the charge which accumulates on the plates of a plane capacitor must be consistent with the applied bias.

In a planar capacitor geometry the potential could be solved by an infinite series of image charges [31]. Applying periodic boundary conditions it would be possible to solve the potential using FFT techniques [27]. We prefer to solve the Poisson's equation with a multi-grid technique, by expressing the charge density over a discrete mesh. Once the computation of $V_{el}^{(2)}(r)$ is done, the orbital energy terms, V_i , are computed by projection on the atomic centered densities (6). This technique allows an easier generalization to more complex device geometries, for example, a realistic FET configuration. The mesh is usually chosen as a trade-off between accuracy and computational speed. However the ansatz (6) for the atomic charge density is a quite smooth function and usually convergent results are obtained with a mesh spacing of 0.5 atomic units.

8 Atomic Forces

The atomic forces can be obtained using the Ehrenfest's theorem [32] or from a Lagrangian formulation of the equation of motion for the coupled electron-ion systems [33, 34] (See also Chap. 6). From both formulations it is found

that for a non complete (variational) basis set, the atomic forces also depend on the atomic velocities [34]. The adiabatic limit can be obtained under the assumption that the atomic velocities are sufficiently small and that the electron subsystem remains in a particular stationary state at any instantaneous ionic configuration. In this limit the atomic forces can be approximated by [14, 23, 35]

$$F_i = - \sum_k \sum_{\mu\nu} n_k c_{k\mu}^* c_{k\nu} \left[\frac{\partial H_{\mu\nu}^0}{\partial R_i} - \left(\varepsilon_k + \frac{V_\mu + V_\nu}{2} \right) \frac{\partial S_{\mu\nu}}{\partial R_i} \right] \quad (36)$$

$$- \sum_j \frac{\partial \gamma_{ij}}{\partial R_i} \Delta q_i \Delta q_j - \frac{\partial E^{rep}}{\partial R_i} \quad (37)$$

where V_μ is the energy shift of the atoms around which the orbital $|\phi_\mu\rangle$ is localized. Equation (37) can be also obtained by considering the gradient of the total energy of the system, expressed by the functional (1). Such total energy is a well defined quantity for closed and periodic systems. The generalization to contact leads connected to reservoirs can be formally by maximizing an appropriate entropy functional [23]. The complete expression becomes

$$F_i = - \sum_{\mu\nu} \left[\rho_{\mu\nu} \left(\frac{\partial H_{\mu\nu}^0}{\partial R_i} - \frac{V_\mu + V_\nu}{2} \frac{\partial S_{\mu\nu}}{\partial R_i} \right) + \varepsilon_{\mu\nu} \frac{\partial S_{\mu\nu}}{\partial R_i} \right] - V'_i \Delta q_i - \frac{\partial E^{rep}}{\partial R_i}, \quad (38)$$

where $\rho_{\mu\nu}$ is the non-equilibrium density matrix and $\varepsilon_{\mu\nu}$ is the energy-energy-weighted density matrix, defined by

$$\varepsilon_{\mu\nu} = \frac{1}{2\pi i} \int_{-\infty}^{+\infty} dE EG_{\mu\nu}^<(E). \quad (39)$$

The terms V'_i are derivatives of the potential given as

$$V'_i = \int V^{(2)}(r) \frac{\partial n_i(r)}{\partial R_i} dr, \quad (40)$$

which are computed numerically on the same grid where the Poisson equation is solved, using an analytic form for the gradient of $n_i(r)$ obtained from (6). Starting from (38) it is possible to derive an expression for the so-called current-induced forces for a system out of equilibrium. These extra forces arise from variations of the density matrix due to application of the bias and can be calculated using the non-equilibrium $\rho_{\mu\nu}$ and $\varepsilon_{\mu\nu}$. The sum of the extra forces over all the atoms add up to zero, a useful sumrule in numerical calculations. It is worth to mention that recently the conservative nature of current-induced forces has been questioned [36] showing a lively debate on the subject.

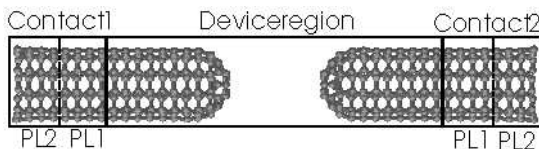


Fig. 4. Two tips of CNT (5,5) used in the simulation. The diagram shows the device region and the contact regions. The Principal Layers of the contacts are also indicated

9 gDFTB Example Applications

In this section we show results of self-consistent computations of the charge density and the potential under non-equilibrium conditions.

The first system comprises two CNT (5,5) capped by half- C_{70} molecules displaced tip-to-tip at close distance. The system is shown in Fig. 4, which also represents a practical example of the subdivision into device region and contacts. The two Principal Layers constituting the contacts are also indicated.

Figure 5a shows the charge distribution on the CNT tips, computed in equilibrium condition (no bias applied) and the charge density distributions at the tips when the CNTs are biased (Fig. 5b). The equilibrium charge density has deviations from the atomic neutrality of the order of $10^{-4}e$ which originates from the loss of symmetry in the CNT structures due to the capping. The charge redistribution occurs mainly at the junctions between the nanotubes and the caps. On the contrary, the bulk regions of the contacts are practically neutral.

The net charge accumulated under bias conditions, shown in Fig. 5c, demonstrates that opposite charges accumulates at the tips, as expected. The accumulated charge density is consistent with the applied potential; in fact the potential profile smoothly joins at the boundary between the device and the contacts. Both charge density and potential join smoothly at the contacts, confirming that the calculation is consistent with the assumption that the potential drops essentially within the device region.

In these computations we have not been interested in the tunneling current, but rather to verify the correct functioning of all the basic ingredients of the self-consistent iteration. The interplay between the computation of the charge density via the non-equilibrium Green's function formalism and the solution of the Poisson's equation for the self-consistent computation of the effective potential have been tested successfully.

In order to calculate the current flowing between the two nanotubes we will show some calculations related to a molecular system comprising of the two CNT tips bridged by a Tour wire (2'-amino-4-ethynylphenyl-4'-ethynylphenyl-5'-nitro-1-benzene), as shown in Fig. 6. Such kind of molecular wire were shown to posses two bistable states [37] of low and high conduc-

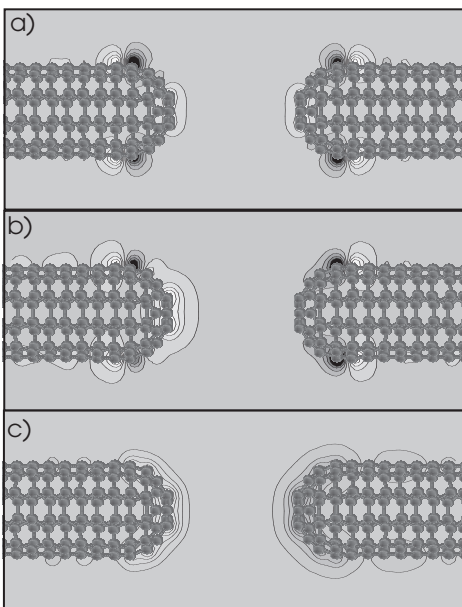


Fig. 5. Middle section of the charge density profile for two tips of CNT (5,5). *Dark areas* represent negative charge accumulation and *white areas* represent positive charge. (a) Charge density in equilibrium. (b) Charge density when 1 V bias is applied. (c) Net charge accumulated on the tips

tance that can be set on (off) by the application of a high forward (reverse) bias (>3 Volt). It is therefore relevant to investigate on the nature of such mechanisms. Previous analysis [38,39] have attributed the switching behavior to substantial electronic changes in the molecular orbitals which occurs upon molecular charging. Although these works certainly shed some light on the basic mechanisms involved in the switching, they have not been derived fully self-consistently with the flowing current and, furthermore, it is not obvious why the molecule should remain in the charged state (and therefore preserve the on-state) for the long times observed (400 s) when the bias is swept back to low values.

Figure 6 shows the self-consistent excess charge accumulated on the system when this is subject to a bias of 1.0 V. The figure is obtained by subtracting the self-consistent charge density of the biased system from the unbiased density. Black corresponds to accumulation of a negative charge and white corresponds to positive charge. It is possible to see the charges accumulated at the CNT tips which are consistent with the assumption that the potential drops essentially across the molecule. The same figure (Fig. 6b) shows the corresponding equipotential lines. Also in this case the relative difference between the potential of the biased system and potential obtained in equilibrium is shown.

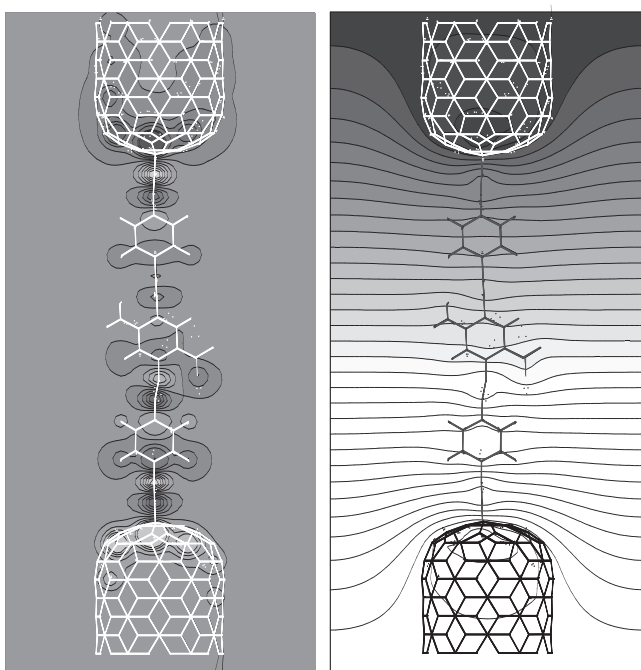


Fig. 6. Self-consistent charge (*Left*) and potential (*Right*) for a CNT-wire-CNT system at 1.0 V of bias

An increase of charge density on the molecular atoms is observed increasing the applied bias.

Figure 7 shows the self-consistent forces acting on the atoms at 0.5 V (Fig. 7a) and 1.0 V (Fig. 7b) for the structure relaxed under zero bias condition. The evident increase in all the atomic forces might be the signature of a conformational change related to the switching mechanism. Further investigations are necessary in this direction.

Figure 8 shows the I-V characteristics of the same system. The current sharply increases above 1.0 V of applied bias, indicating a resonant behavior. This can be expected as the Fermi energy of the CNT is at -4.56 eV, while the molecular orbitals HOMO and LUMO of the wire are at -5.85 eV and -3.0 eV respectively.

10 Incoherent Electron-Phonon Scattering

Temperature dependent transport and power dissipation in molecular devices is necessarily a problem that device design will need to face in the future. Only few works have dealt with this issue in recent years (see chapters by Nitzan and Di Ventra).

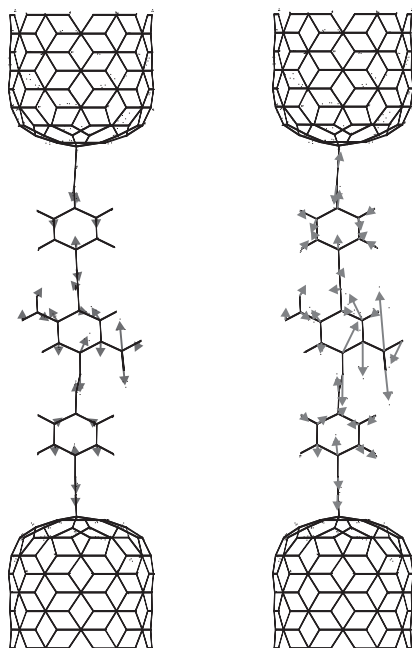


Fig. 7. Self-consistent forces acting on the atoms of the system at the biases of 0.5 V (Left) and 1.0 V (Right)

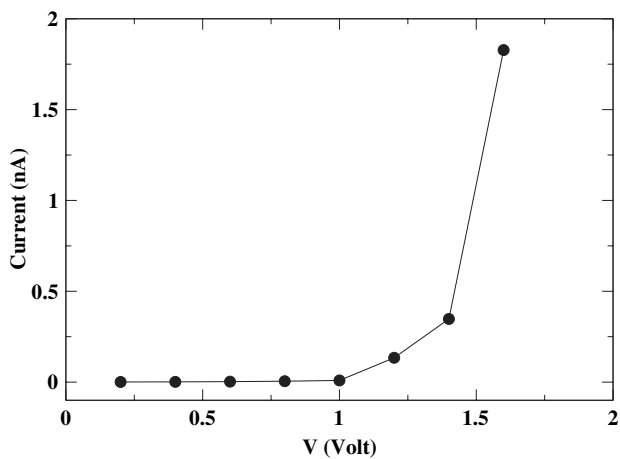


Fig. 8. Current-Voltage characteristics of the system in Fig. 6

Electron-phonon inelastic scattering is the main responsible for thermal relaxations in molecular junctions and their understanding is important for controlling molecular stability. Furthermore, electron-phonon scattering may provide paths for molecular isomerization, useful for switching mechanisms.

As explained in previous sections, the interatomic forces are obtained within the DFTB approach. This method has proven to be successful when applied to organic molecules, giving vibrational frequencies close to experimental results and similar in quality to sophisticated and time-consuming full ab-initio calculations [14, 15].

Inelastic electron-phonon scattering in molecular wires has been so far analyzed using model Hamiltonians [40–44]. Using the gDFTB method it is possible to simulate the electron-phonon coupling in a realistic molecular system by explicitly taking into account the molecular degrees of freedom, and analyzing in detail the contributions of the vibrational modes.

The usual procedure to treat molecular vibrations is to expand the effective nuclear potential up to the harmonic term, and to decouple the Hamiltonian as a superposition of independent one-dimensional oscillators, corresponding to the normal modes of vibration. Each vibrational mode will be labeled by q .

The quantization of the vibrational modes is obtained in the standard way and the ionic vibrations of a molecular wire can be described as a class of boson particles, here referred as *phonons*. This term may be slightly inappropriate, since phonons are usually regarded as lattice waves with a given momentum. In the present context, instead, one should refer more properly to *vibrons*, i.e., quantized molecular vibrations confined within one molecule. However, the term phonon is used to refer in a simple and direct way to the well-developed many-body formalism which has been borrowed from standard electron-phonon treatment in solids and adapted to the present context.

The electronic deformation potential is obtained by expanding the Hamiltonian to first order in the atomic displacements. Subsequently, the atomic coordinates are expressed as a superposition of creation-annihilation operators, a_q^+ and a_q , of phonon quanta in each vibrational mode q . The result is a term in the Hamiltonian describing the electron-phonon coupling,

$$H_{el-ph} = \sum_{q,\mu,\nu} \gamma_{\mu\nu}^q c_\mu^+ c_\nu [a_q^+ + a_q] , \quad (41)$$

where c_μ^+ and c_ν are, respectively, the creation and annihilation operators of one electron in the local basis and

$$\gamma_{\mu\nu}^\alpha = \sqrt{\frac{\hbar}{2\omega_q M_q}} \sum_\alpha \left[\frac{\partial H_{\mu\nu}}{\partial R_\alpha} - \sum_{\sigma,\lambda} \frac{\partial S_{\mu\sigma}}{\partial R_\alpha} S_{\sigma\lambda}^{-1} H_{\lambda\nu} + H_{\mu\lambda} S_{\lambda\sigma}^{-1} \frac{\partial S_{\sigma\nu}}{\partial R_\alpha} \right] \mathbf{e}_\alpha^q \quad (42)$$

are the electron-phonon coupling matrices. M_q are the atomic masses, ω_q the mode frequencies and \mathbf{e}_α^q are the normalized atomic displacements for each

mode. The non-orthogonality of the basis set is reflected by the presence of the overlap matrix, $S_{\mu\nu}$, and its derivative with respect to the ionic positions, R_α .

While crossing the system, the electrons interact with the molecular ionic vibrations from which they can be inelastically scattered. In the present context we assume that the metal ions do not move, henceforth the electron-phonon scattering within the leads is neglected. This is a good approximation given the very large difference in atomic masses between the *Au* atoms and the organic elements. Furthermore, we are specifically interested on the energy dissipated within the molecular degrees of freedom, since the inelastic electron-phonon scattering in the metallic leads is known to be small and not important for power dissipation issues. The present method neglects the coupling between contact and molecular modes. Indeed a degree of mixing between the acoustic modes of the metal and the low energy molecular modes can be expected. In principles such coupling can be included in the formalism. The relevant self-energy due to electron-phonon scattering is evaluated within the Born approximation (BA), graphically represented in Fig. 9.

Diagram I gives only a real contribution to the self-energy and is neglected (see below). Diagram II is translated into an analytic form by using the standard rules of Feynman's diagrams and the Langreth theorem for the analytic continuation rules of the Keldysh Green's functions [25]:

$$\Sigma_{ph}^{<(>)}(\omega) = i \sum_q \gamma_q^2 \int_{-\infty}^{+\infty} \frac{d\omega'}{2\pi} G^{<(>) }(\omega - \omega') D_q^{<(>)}(\omega') , \quad (43)$$

where $D_q^{<(>)}$ are the correlation functions related to the vibrational modes. In the actual calculations the zero-th order phonon propagator is used. In principle the exchange of energy between molecular phonon and thermal bath could be included explicitly by solving an additional kinetic equation. Such an approach is relevant in studying heat dissipations into the contacts.

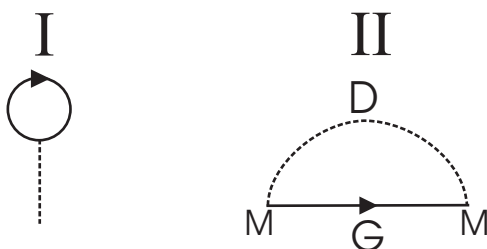


Fig. 9. First order Feynman diagrams of the electron-phonon interaction

Equation (43) is usually solved just to first-order, using the unperturbed $G_0^{<(>)}$ functions, obtained from (15) by setting $\Sigma_{ph}^{<(>)} = 0$. This is commonly called first order BA. However (43) and (15) can be solved in a self-consistent manner (SCBA) [45]. This corresponds to a partial summation of diagrams that goes beyond the simpler first order approximation. A self-consistent solution is computationally far more demanding, but leads to a result which is more satisfactory from a theoretical point of view. Only the self-consistent solution, in fact, preserves the contact current in (28), which is generally violated when using the simpler first order BA.

In self-consistent calculations the retarded (advanced) $G^{r(a)}(\omega)$ Green's functions which appear in (15) are, in principle, the exact GF of the electron-phonon coupled system, and should be renormalized with a corresponding electron-phonon self-energy. In general the electronic self-energy can be calculated from explicit applications of the Langreth evaluation rules of the non-equilibrium Feynman diagrams. Explicit expressions can be found, for instance, in [9]. Since we are mainly interested on incoherent phonon emission, we approximate the phonon self-energy to be purely imaginary, neglecting the shift of the van-Hoove singularities (i.e., essentially neglecting energy shifts due to polaron-like states). This assumption is valid since the molecular levels are far from the relevant range of injection energies and therefore the small shift will not modify appreciably the tunneling current. Within this assumption the imaginary part of the phonon self-energy can be obtained directly from the known relationship $\Sigma^r - \Sigma^a = \Sigma^> - \Sigma^<$. In any case the SCBA is valid in the small electron-phonon interaction limit and far from resonant situations where polaron effects should be taken into account.

10.1 Application to Alkane-Thiols

The mathematical machinery developed in the previous section is here applied to the tunneling of current through an alkanethiolate molecule, **Au-S(CH₂)₈S-Au**.

Alkanethiols are the archetypal of molecular electronic devices. Such type of molecules align on *Au* surfaces via covalent *S-Au* bonds to form regular and stable self-assembled monolayers (SAMs). They are characterized by a large optical bandgap (>5 eV), making them very stable to photo-degradation. The same large gap is responsible for a very low conduction via tunneling in Au/thiols/Au structures, giving good electrical stability. Although a simple and clear understanding of transport mechanisms has not been reached yet for most of the molecular compounds, transport in alkenethiols is essentially at a mature stage of experimental development.

The Au atoms, composing the two contacts are kept at fixed positions, corresponding to an ideal fcc crystal with Au-Au separations of 2.884 Å. First we relaxed the octanethiol saturated with a hydrogen termination, on top of one Au surface comprising six atomic layers. After this first step we removed

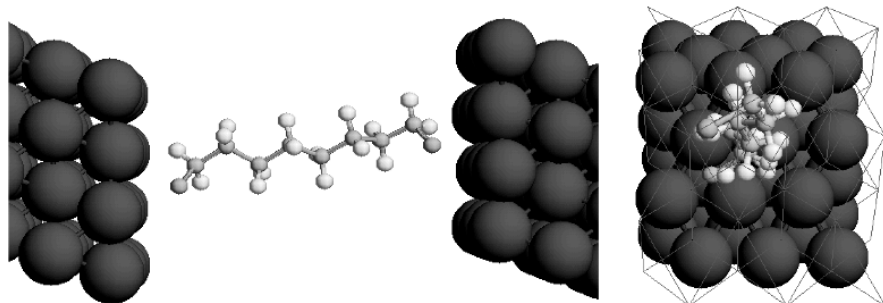


Fig. 10. Diagram representing the relaxed atomic coordinates of the octanedithiol between Au contacts

the hydrogen and put the second Au surface, taking care that the Au-S distance obtained at the first interface was reproduced at the second interface. Then we let this system to relax again. Periodic boundary conditions are used in all these calculations. The final relaxed structure is shown in Fig. 10. Although we found that the global minima of the isolated octanedithiol is the highest symmetry configuration, the relaxed structure of the molecule attached to Au electrodes does not show any particular symmetry. The vibrational frequencies are slightly affected by this, since many degeneracies are broken. However the differences in the whole spectrum are within 20%, which can be considered small and not relevant for the present analysis. The S atom is found to form a bond with an energy minimum at the hollow site of the Au(111) crystal. Actually, the exact minimal configuration is found with the sulfur atom slightly shifted from the hollow position, as reported in other ab-initio DFT calculations [46, 47]. The S atom is found at 2.76 Å from the Au plane. In Fig. 12 the computed conductance and the I-V characteristics of such system are reported. The theoretical curve is also compared to recent experimental results [48], obtained by measuring the current through a SAM assembled within a nanopore. Assuming that the SAM assemble in a lattice $R\sqrt{3} \times R\sqrt{3}$, from the measured nanopore diameter of 45 nm, we can estimate that approximately 10,000 molecules are sampled in parallel. Accordingly the experimental measurements are scaled by a factor 10^{-4} in order to compare with our calculations. The order of magnitude of the tunneling current is predicted well. This is important, particularly in relations to the absolute magnitude of the power dissipated in such system, as discussed later.

For each of the 78 modes we have computed the contribution to the inelastic current at $T = 0$ K and for an applied bias of 2 V. At $T = 0$, the incoherent part of the tunneling current (30) is related to the net phonon emission rate by $\tau^{-1} = I_{incoh}/e$. This quantity is used as a measure of the electron-phonon strength and is used to compare the different modes. A summary of such computations is reported in Table 1 and in Fig. 11a).

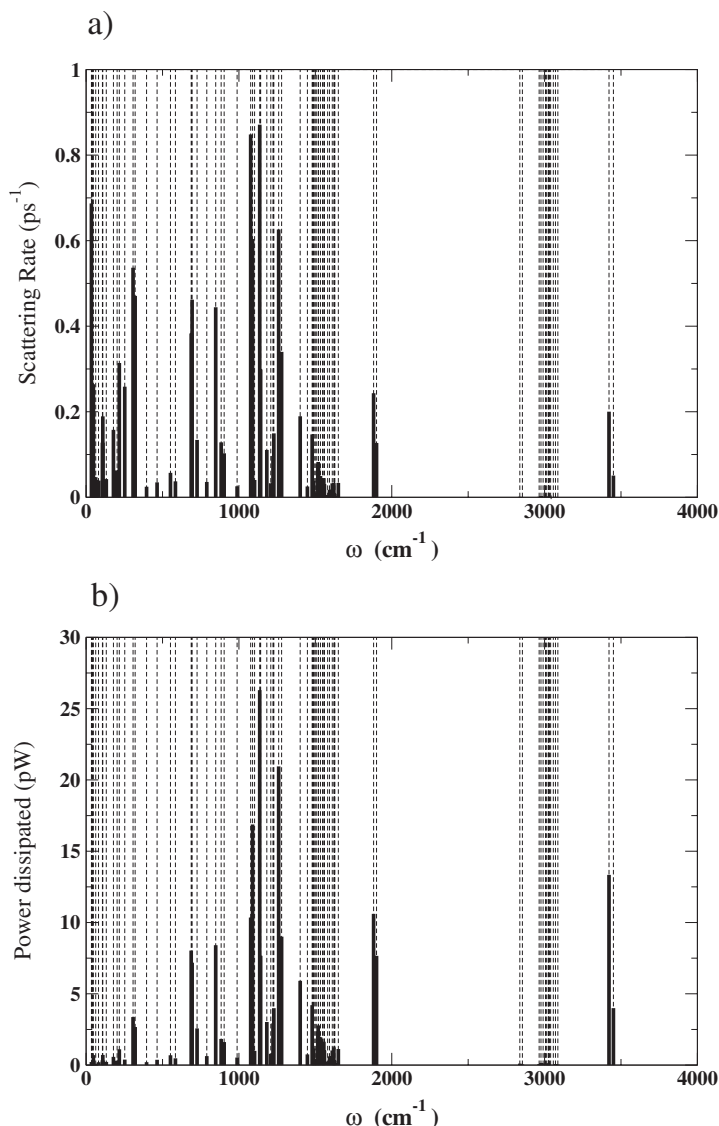


Fig. 11. (a) scattering rate and (b) power dissipated for each vibrational mode

The lowest vibrational modes correspond to oscillations of the carbon atoms in the back-bone plane, resembling the first harmonics of a string, and rigid twist around the C-C bonds of large subunits involving two or more CH_2 groups. The two sulfur atoms remain practically fixed or slide slightly over the Au surface. The frequencies of such modes are affected by large relative errors because they are sensitive to small differences in the atomic pair

Table 1. Summary of the most important frequencies (cm^{-1}) of the octanethiol, phonon emission rate (ps^{-1}), followed by a brief description of the mode and the typical experimental value, obtained by HREELS, Raman or IR [48]

ω	τ^{-1}	Description	ω exp.
34.8	0.687	(CH ₂) ₂ twist	–
106.9	0.127	“	–
109.3	0.189	“	–
178.8	0.157	“	–
217.0	0.314	Au-S stretch	225-
320.6	0.470	”	-255
687.5	0.383	S-C stretch	650-706
693.6	0.462	”	
848.1	0.444	CH ₂ rock	715-925
1076.8	0.848	C-C stretch	1050
1136.2	0.871	C-C stretch	1120
1222.8	0.097	CH ₂ wag	1300
1259.9	0.626	CH ₂ twist	1250
1479.2	0.147	“	
1518.2	0.082	CH ₂ scissor	1455
1881.0	0.243	CC+H swing	-
2976.5	0.0024	C-H stretch.	2860
3421.4	0.200	H-Au stretch	-

potentials and to the relaxed geometry. Furthermore, these modes are not easily accessible experimentally. We find that modes associated to internal twist of the C-C backbone involving the motion of (CH₂)₂ subunits are more effective in scattering electrons. As expected, the Au-S stretching modes, which is found in the range between 250 cm⁻¹ to 320 cm⁻¹, in agreement with experiments [48], is giving a large contribution to the electron-phonon scattering. Similarly, a large contribution is given by the C-S stretch modes, found around 690 cm⁻¹ [48]. The band of modes found between 1000 and 1100 cm⁻¹ corresponds to C-C stretch modes. These give the largest contribution to the incoherent current. A large contribution comes also from the modes related to motions of the CH₂ modes, particularly rocking and twisting. Wagging and scissoring modes, instead, give a smaller contribution.

In our analysis we also found non negligible signal from some modes which have not been discussed in experimental papers, since they are special to the Au/octanethiol/Au system and are not seen in isolated molecules. In particular two modes around 1900 cm⁻¹ (0.23 eV) which are associated to a slight rotation of the C-S bond, a stretch of the C-C bonds involving the motion of the C at position 2 and a pronounced swing of the H atom closest to the Au surface. Another mode affecting the inelastic current are related to the oscillation of the hydrogens closest to the Au surfaces. Such modes

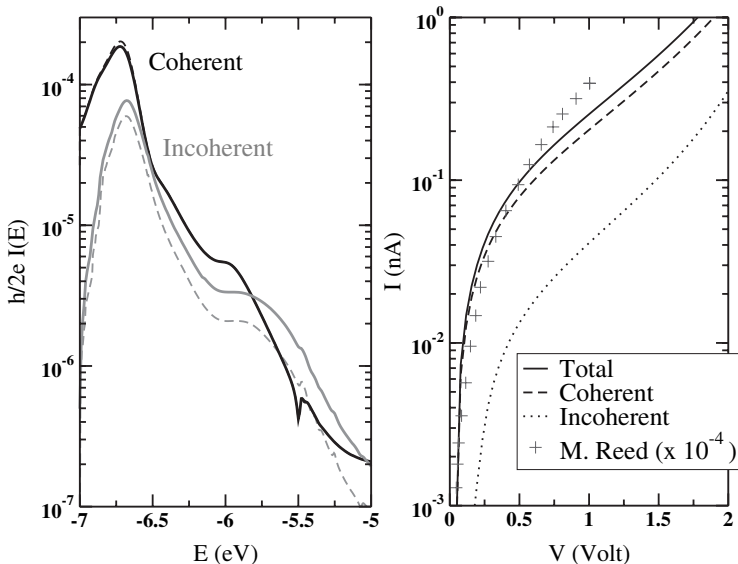


Fig. 12. *Left.* Tunneling probability as a function of injection energy across a molecule of octanethiol. The contribution of the incoherent (grey) and coherent (back) tunneling current are shown. the dashed curves are the first order BA, the solid ones are the SCBA. *Right.* the SCBA I-V characteristics of the system compared to recent experimental results (see text)

could be seen as a Au-H stretch and are found at a frequency of $\approx 3400 \text{ cm}^{-1}$ (0.42 eV).

The 34 modes giving an inelastic rate greater than 10^8 ps^{-1} have been included for the calculation of the incoherent current. Figure 12 shows the coherent and incoherent contributions to the total tunneling current resolved in energy for the bias of 2.0 V and the calculated I-V characteristics of the system.

The peaks in the transmission function correspond to features of the surface density of states of Au. In Fig. 12 we have compared the first order BA with the SCBA. It is important to remark that for this system the first order Born approximation gives already an acceptable result and the SC loop does not introduce substantial changes in the transmission probability in the relevant energy range. Differences are appreciable deep in the energy gap, where the transmission probability is already small and the total contribution to the current is negligible. A relevant quantity is the amount of power dissipated in the molecule due to inelastic phonon emission. This calculation can be obtained by considering the virtual contact current, as discussed for instance in [12].

The power dissipated is given by the net rate of energy transferred to the molecule and can be easily calculated as

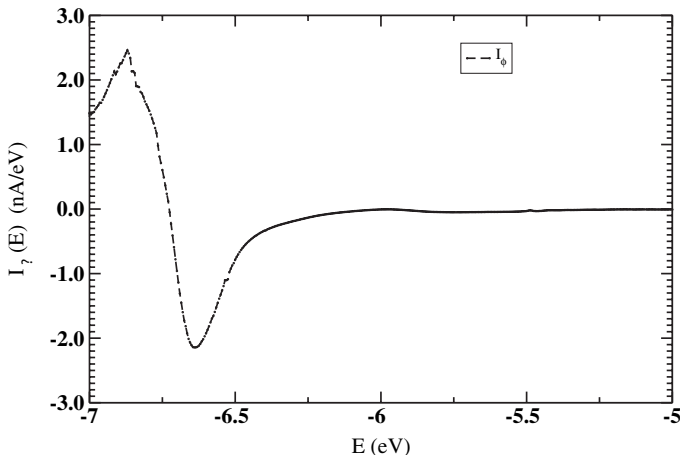


Fig. 13. Virtual contact current. Negative contribution corresponds to in-current and positive to out-current. The figure evidences a net transfer of electron energy

$$W = \frac{2}{h} \int_{-\infty}^{+\infty} \omega I_\phi(\omega) d\omega , \quad (44)$$

where $I_\phi(\omega)$ is the virtual contact current of (27). Figure 13 represents the virtual contact current for this system. The energy interval with a negative current corresponds to electrons incoming into the virtual contact, where positive current corresponds to electrons outgoing from the virtual contact. A net electron flux from higher to lower energies is evident from Fig. 13. Therefore, the NEGF can be used to compute energy relaxations in molecular systems. From (44) we calculate that the power dissipated in the octanethiol is $W = 0.16 \text{ nWatt}$ (1 eV/ps) at 2 V of applied bias.

It is interesting, however, to analyze the power dissipated in each vibrational mode, as shown in Fig. 11b). This is not directly proportional to the emission rate, since the power dissipated depends on the phonon energy as well. As expected, the low frequency modes contribute little to the dissipation, despite the relatively large scattering rates. The modes giving the largest contributing are found in the band of C-C stretch modes, the C-S stretch and the CH_2 rocking modes. Considerable power is also absorbed by the modes at 1900 and 3400 cm^{-1} , involving essentially movements of the hydrogens close to the Au surfaces.

The problem which needs to be addressed next is related to the dissipation of the absorbed heat, by coupling the vibrational modes to the environment. Computations of this kind, applied systematically to molecular bridges, allow the evaluation of molecular stability, assess the feasibility and help the engineering of future molecular electronic devices.

11 Comments on DFT Applied to Transport

The problem posed by a microscopic simulation of a quantum-mechanical system is genuinely a fantastic many-body problem. It should be clear that DFT theories (as well as Hartree-Fock theories) represent only a simple mean-field approximation to the exact solution [49, 50]. Fortunately, these approximations can give already accurate results in predicting the energy of crystals, surfaces, structural properties of clusters and can be used for the calculation of effective masses or other band-related properties. The main problems encountered both with HF and DFT are related to the computation of optical excitation energies, ionization potentials or electronic affinities, e.g., all those properties not strictly related to a N -electrons ground-state calculation. The Koopman's theorem states that the HF eigenvalues represent the energy required for the removal and addition of particles, but neglects relaxation and correlation energies. Indeed, ionization and affinity potentials are related to $N - 1$ and $N + 1$ particle states, respectively, and a N -particle calculation does not provide information about the relaxation of the electron-ion system due to the addition or removal of one electron. There is no equivalent of the Koopman's theorem for the Kohn-Sham eigenvalues [51] and there are no theoretical foundations that the eigenvalues of the Kohn-Sham equation are representative in any way of particle energies, with the exception of the highest occupied level, which in exact DFT corresponds to the ionization potential [52]. Unfortunately, the use of approximated functionals severely affects the result.

It is often said that HF does not account for correlation energies, although it accounts exactly for exchange effects, at least for the occupied states. On the other hand, DFT partially corrects for correlations, but does not include exactly the non-local exchange energy, which is treated within the local density or density gradient (GGA) approximations. For these reasons a N -particles HF calculation tends to overestimate the ionization and to underestimate the energy gained by the addition of an extra electron to the system (i.e., underestimates the electronic affinity). At the same time HF overestimates considerably the excitation gap energy (The energy required to take an electron from the ground state and bring it to the first excited state), since among the others the electron-hole interaction is neglected. DFT behaves exactly in the opposite way. For these reasons, some hybrid methods which mix with suitable balance various XC functionals [53–55] give, in general, good results for the energy gap of many materials and molecules.

This is clearly an issue in the calculation of coherent transport properties of materials, where the electronic gap is used to define a crucial quantity such as the tunneling barrier. Whether the barrier is provided by a semiconducting heterojunction, by an insulating oxide or by an organic molecule, the electronic band-gap enters critically into the calculation, affecting band alignment, charge transfer and ultimately the tunneling current (affected exponentially by the barrier height). For these reasons, empirical TB frequently

achieves a much better quantitative agreement with experimental currents. For these reasons transport calculations based on DFT (or HF) calculations should be taken with care. Indeed theory and experiment sometimes depart on the value of the absolute current by a factor of 100.

There are several ways in which the “gap problem” can be addressed [51]. Traditional chemistry methods, such as configuration interaction (CI) [50], scale very badly with system size (exponentially). The CI method has been recently applied to transport in open systems [56] showing that many-body corrections can give substantial quantitative improvements. A better scaling is possible with many-body perturbation theory, based on Green’s function methods. The DFT (or HF) calculations can be looked as the starting point for higher order corrections. Very successful has proven to be the *GW* approximation [57], which includes the description of the screened Coulomb and exchange interactions. The Many-body GF formalism implicitly takes into account for the addition of an extra particle in the system. We should also point out that the *GW* correction can be directly included in the NEGF formalism by proper definition of the self-energies. An extension of the gDFTB code to account for *GW* correction is under development [58].

The time-dependent DFT theory (See also Chap. 3) is an alternative method which contains information about exact optical excitation and encounters increasing success due to its relative simplicity. Adaptations of the TD-DFT to transport may provide important step forwards [59]. However, in many molecular structures the optical gap is quite different from the transport gap (TD-DFT describe the excitation of a system of constant N electrons), thus a direct application of TD-DFT to transport problems may still have some limits.

12 Conclusions

Nanometer scale devices require new simulation tools which treats properly the quantum-mechanical aspects of the electronic and transport properties. Density functional methods have become the standard for solid-state computations. We have implemented the non-equilibrium Green’s function technique for transport computations into the density-functional based code DFTB. Such a method has been modified in order to be completely consistent with the open boundary conditions needed for transport computations. Our methodology bridges the gap between completely empirical Tight-Binding and ab-initio methods. To obtain this, we use the non-equilibrium Green’s function formalism for the computation of the density matrix. The electronic density determines the Hartree potential of the density-functional Hamiltonian. We show how to compute the Hartree potential by solving the Poisson’s equation for the density fluctuations.

The multi-grid Poisson solver can easily handle boundary conditions that can satisfy realistic contacts, three terminal devices and novel architectures with complex gate geometries.

The new code can compute coherent and incoherent tunneling current flowing in a molecular device self-consistently with the boundary conditions imposed on the Hamiltonian of the system. Atomic forces can be also computed at the same time. The code enables molecular dynamics simulations that can be coupled to real-time current computations [60].

The self-consistent code was employed to study the electronic properties of two carbon nanotubes tips in equilibrium and under a 1 V bias difference. The computation of the displaced charge density via the non-equilibrium Green's function is fully consistent with the applied bias.

References

1. C. Joachim, J.K. Gimzewski, R.R. Schittler, C. Chavy: Electronic transparency of a single C_{60} molecule, *Phys. Rev. Lett.* **74**, 2102 (1995)
2. R.M. Metzger, B. Chen, U. Hopfner, M.V. Lakshminantham, D. Vuillaume, T. Kawai, X.L. Wu, H. Tachibana, T.V. Hughes, H. Sakurai, J.W. Baldwin, C. Hosch, M.P. Cava, L. Brehmer, C.J. Ashwell: Unimolecular electrical rectification in hexadecylquinolinium tricyanoquinodimethanide, *J. Am. Chem. Soc.* **119**, 10 455 (1997)
3. C. Zhou, M.R. Deshpande, M.A. Reed, L. Jones, J.M. Tour: Conductance of a molecular junction, *Appl. Phys. Lett.* **71**, 611 (1997)
4. W. Tian, S. Datta, S. Hong, R. Reifenberger, J.I. Henderson, C.P. Kubiak: Conductance spectra of molecular wires, *J. Chem. Phys.* **109**, 2874 (1998)
5. C.P. Collier, E.W. Wong, M. Belohradský, F.M. Raymo, J.F. Stoddart, P.J. Kuekes, R.S. Williams, J.R. Heath: Electronically configurable molecular-based logic gates, *Science* **285**, 391 (1999)
6. B. Xu, N.J. Tao: Measurement of single-molecule resistance by repeated formation of molecular junctions, *Science* **301**, 1221 (2003)
7. J.F. Stoddart, J.R. Heath, R.S. Williams: More on molecular electronics, *Science* **303**, 1136 (2004)
8. A. Nitzan, M.A. Ratner: Electron transport in molecular wire junctions, *Science* **300**, 1384 (2003)
9. A. Pecchia, A. Di Carlo: Atomistic theory of transport in organic and inorganic nanostructures, *Rep. Prog. Phys.* **67**, 1497 (2004)
10. T. Frauenheim, G. Seifert, M. Elstner, T. Niehaus, C. Kohler, M. Amkreutz, M. Sternberg, Z. Hajnal, A. Di Carlo, S. Suhai: Atomistic simulations of complex materials: ground-state and excited-state properties, *J. Phys.: Condensed Matter* **14**, 3015 (2002)
11. L.V. Keldysh: Diagram Technique for Nonequilibrium Processes, *Sov. Phys. JEPT* **20**, 1018 (1965)
12. S. Datta: *Electronic Transport in Mesoscopic System* (Cambridge University Press, -, 1995)
13. G. Seifert, H. Eshrig: LCAO-X alpha calculations of transition metal clusters, *Phys. Stat. Sol.(b)* **127**, 573 (1985)

14. D. Porezag, M.R. Pederson, T. Frauenheim, T. Köhler: Structure, stability and vibrational properties of polymerized C_{60} , Phys. Rev. B **52**, 14 963 (1995)
15. G. Seifert, D. Porezag, T. Frauenheim: Calculations of molecules clusters and solids with a simplified LCAO-LDA scheme quantum chemistry, Int. J.Q. Chem. **98**, 185 (1996)
16. M. Elstner, D. Prezag, G. Jugnickel, J. Elsner, M. Haugk, T. Frauenheim, S. Suhai, G. Seifer: Self-consistent charge density tight-binding method for simulation of complex materials properties, Phys. Rev. B **58**, 7260 (1998)
17. P. Maragakis, R.L. Barnett, E. Kaxiras, M. Elstner, T. Frauenheim: Electronic structure of overstretched dna, Phys. Rev. B **66**, 241 104 (2002)
18. W. Foulkes, R. Haydock: Tight-binding models and density-functional theory, Phys. Rev. B **39**, 12 520 (1989)
19. A. Svizhenko, M.P. Anantram, T.R. Govindan, B. Biegel, R. Venugopal: Two-dimensional quantum mechanical modeling of nanotransistors, J. Appl. Phys. **91**, 2343 (2002)
20. R.C. Bowen, G. Klimeck, R.K. Lake, W.R. Frenzley, T. Moise: Quantitative resonant tunneling diode simulation, J. Appl. Phys. **81**, 3207 (1997)
21. T.N. Todorov: Tight-binding simulation of current-carrying nanostructures, J. Physics: Condens. Matter **14**, 3049 (2002)
22. F. Guinea, C. Tejedor, F. Flores, E. Louis: Effective two dimensional hamiltonian at surfaces, Phys. Rev. B **28**, 4397 (1983)
23. T.N. Todorov, J. Hoekstra, A.P. Sutton: Current-induced forces in atomic scale conductors, Phil. Mag. B **80**, 421 (2000)
24. S. Datta: Nanoscale device simulation: The green's function formalism, Superlattices and Microstructures **28**, 253 (2000)
25. H. Haung, A.P. Jauho: *Quantum Kinetics in Transport and Optics of Semiconductors*, Vol. 123 (Springer Series in Sol. State Sci., -, 1993)
26. A. Wacker, A.P. Jauho: Quantum transport: the link between standard approaches in superlattices, Phys. Rev. Lett. **80**, 369 (1998)
27. M. Brandbyge, J.L. Mozos, P. Ordejon, J. Taylor, K. Stokbro: Density functional method for nonequilibrium electron transport, Phys. Rev. B **65**, 165 401 (2002)
28. C. Caroli, R. Combescot, P. Nozieres, D. Saint-James: Direct calculation of the tunneling current, J. Phys. C: Solid State Phys. **4**, 916 (1971)
29. Y. Xue, S. Datta, M.A. Ratner: First-principles based matrix green's function approach to molecular electronic devices: general formalism, Chem. Phys. **281**, 151 (2002)
30. A. Pecchia, M. Gheorghe, A. Di Carlo, P. Lugli: Modulation of the electronic transport properties of carbon nanotubes with adsorbed molecules, Synt. Met. **138**, 89 (2002)
31. J. Taylor, H. Guo, J. Wang: Ab initio modelling of quantum transport properties of molecular electronic devices, Phys. Rev. B **63**, 245 407 (2001)
32. M. Di Ventra, S.T. Pantelides, N.D. Lang: Current-induced forces in molecular wires, Phys. Rev. Lett. **88**, 046 801 (2002)
33. K.J. Schafer, J.D. Garcia, N.H. Kwong: Self-consistent trajectories for surface scattering via classical-quantal coupling, Phys. Rev. B **36**, 1872 (1987)
34. T.N. Todorov: Time-dependent tight binding, J. Physics: Condens. Matter **13**, 10 125 (2001)
35. A.P. Sutton, M.W. Finniss, D.G. Pettifor, Y. Ohta: The tight-binding bond model, J. Phys. C: Solid State Phys. **21**, 35 (1988)

36. M. Di Ventra, Y.C. Chen, T.N. Todorov: Are current-induced forces conservative?, Phys. Rev. Lett. **92**, 176803 (2004)
37. M.A. Reed, J. Chen, A.M. Rawlett, D.W. Price, J.M. Tour: Molecular random access memory cell, Appl. Phys. Lett. **78**, 3735 (2001)
38. J.M. Seminario, A.G. Zacarias, J.M. Tour: Theoretical study of a molecular resonant tunneling diode, J. Am. Chem. Soc. **122**, 3015 (2000)
39. J.M. Seminario, A.G. Zacarias, P.A. Derosa: Analysis of a dinitro based molecular device, J. Chem. Phys. **116**, 1671 (2002)
40. N. Mingo, K. Makoshi: Calculation of the inelastic scanning tunneling image of acetylene on Cu(100), Phys. Rev. Lett. **84**, 3694 (2000)
41. K. Stokbro, B.Y.K. Hu, C. Thirstrup, X.C. Xie: First-principles theory of inelastic currents in a scanning tunneling microscope, Phys. Rev. B **58**, 8038 (1998)
42. E.G. Emberly, G. Kirczenow: Landauer theory, inelastic scattering, and electron transport in molecular wires, Phys. Rev. B **61**, 5740 (2000)
43. H. Ness, A.J. Fisher: Coherent electron injection and transport in molecular wires: inelastic tunneling and electron-phonon interactions, Chem. Phys. **281**, 279 (2002)
44. B. Dong, H.L. Cui, X.L. Lei: Photon-phonon-assisted tunneling through a single molecule quantum dot, Phys. Rev. B **68**, 205315 (2004)
45. M. Galperin, M. Ratner, A. Nitzan: On the line widths of vibrational features in inelastic electron tunneling spectroscopy, Nano Lett. **4**, 1605 (2004)
46. Y. Yourdshahyan, H.K. Zhang, A.M. Rappe: n-alkyl thiol head-group interactions with the au(111) surface, Phys. Rev. B **63**, 081405R (2001)
47. J. Gottschlk, B. Hammer: A density functional theory study of the adsorption of sulfur, marcapto, and methylthiolate on Au(111), J. Chem. Phys. **116**, 784 (2002)
48. W. Wang, T. Lee, I. Kretzschmar, M. Reed: Inelastic electron tunneling spectroscopy of an alkanedithiol self-assembled monolayer, Nano Lett. **4**, 643 (2004)
49. R.O. Jones, O. Gunnarsson: The density functional formalism, its applications and prospects, Rev. Mod. Phys. **61**, 689 (1989)
50. A. Szabo, N.S. Ostlund: *Modern Quantum Chemistry* (Dover, 1996)
51. G. Onida, L. Reining, A. Rubio: Electronic excitations: density-functional versus many-body green's function approaches, Rev. Mod. Phys. **74**, 601 (2002)
52. C.O. Almbladh, U. von Barth: Exact results for the charge and spin densities, exchange-correlation potentials, and density-functional eigenvalues, Phys. Rev. B **31**, 3231 (1985)
53. J.P. Perdew: Density-functional approximation for the correlation energy of the inhomogeneous electron gas, Phys. Rev. B **33**, 8822 (1986)
54. C. Lee, W. Yang, R.G. Parr: Development of the colle-salvetti correlation energy formula into a functional of the electron density, Phys. Rev. B **37**, 785 (1987)
55. A.D. Becke: Density-functional thermochemistry. the role of exact exchange, J. Chem. Phys. **98**, 5648 (1993)
56. P. Delaney, J.C. Greer: Correlated electron transport in molecular electronics, Phys. Rev. Lett. **93**, 036805 (2004)
57. L. Hedin: New Method for Calculating the One-Particle Green's Function with Application to the Electron-Gas Problem, Phys. Rev. **139**, A796 (1965)

58. T.A. Niehaus, M. Rohlffing, F. Della Sala, A. Di Carlo, T. Frauenheim: Quasiparticle energies for large molecules: a tight-binding gw approach, To appear on Phys. Rev. B pp. cond-mat/0411024 (2004)
59. N.T. Maitra, I. Souza, K. Burke: Current-density functional theory of the response of solids, Phys. Rev. B **68**, 045109 (2003)
60. A. Pecchia, M. Gheorghe, A. Di Carlo, P. Lugli, T. Niehaus, R. Sholz: Role of thermal vibrations in molecular wire conduction, Phys. Rev. B **68**, 235321 (2003)

Current-Induced Effects in Nanoscale Conductors

Neil Bushong¹ and Massimiliano Di Ventra²

¹ Department of Physics, University of California, San Diego, La Jolla, CA 92093-0319, USA

bushong@physics.ucsd.edu

² Department of Physics, University of California, San Diego, La Jolla, CA 92093-0319, USA

diventra@physics.ucsd.edu

Abstract. We present an overview of current-induced effects in nanoscale conductors with emphasis on their description at the atomic level. In particular, we discuss steady-state current fluctuations, current-induced forces, inelastic scattering and local heating. All of these properties are calculated in terms of single-particle wavefunctions computed using a scattering approach within the static density-functional theory of many-electron systems. Examples of current-induced effects in atomic and molecular wires will be given and comparison with experimental results will be provided when available.

1 Current Through a Nanoscale Junction

Transport of electrical charge across a nanoscale junction is accompanied by many effects, such as fluctuations of the average current; transfer of energy between electrons and ions and consequent heating of the junction; and forces on ions due to current-induced variations of the electronic distribution [1]. In this chapter we will discuss these effects separately, and we will focus on their description at the atomic level. It is, however, important to realize that there has to be a (yet unknown) relation between these different properties. Such relation would constitute an important contribution to our understanding of transport in nanoscale systems.

The static scattering approach to electrical conduction will be the underlying theme of this review. However, we point out that novel time-dependent formulations of the transport problem may lead us to a better understanding of these effects [2, 3]. In what follows we picture a nanoscale junction as formed by two semi-infinite electrodes held a fixed distance apart, with a nanoscale object bridging the gap between them. The nanoscale object could be a single atom, a chain of atoms, a molecule, or any system with nanoscale dimensions [4–16]. We then consider the problem of DC current flow from one electrode to the other as the result of an applied bias V_B . If we take the left electrode to be positively biased, electrons will flow from the right electrode to the left one. A buildup of negative charge will be present on the surface of the right electrode within a screening length of the electrode

surface. Similarly, a buildup of positive charge will exist on the surface of the left electrode due to a corresponding depletion of electrons [14, 15]. We will assume that, far away from the junction, the electrons in each electrode are in local thermal equilibrium and their statistics are described by the Fermi-Dirac distribution, so that $V_B = E_{FR} - E_{FL}$, where $E_{FL(R)}$ is the chemical potential deep in the left (right) electrode. (Here, as in the rest of the chapter, we use atomic units.)

We calculate the transport properties of this system by expanding the stationary states of the Hamiltonian into a set of left- and right-moving waves. We then sum each left- and right-moving state, weighting them with a Fermi function according to their energy. The stationary scattering states of the bare electrodes have the form

$$\Psi_{E\mathbf{K}_{\parallel}}^0(\mathbf{r}) = e^{i\mathbf{K}_{\parallel}\cdot\mathbf{Y}} u_{E\mathbf{K}_{\parallel}}(z), \quad (1)$$

with the following boundary conditions [17]:

$$u_{E\mathbf{K}_{\parallel}}(z) = (2\pi)^{3/2} k_R^{-1/2} \times \begin{cases} e^{-ik_R z} + R e^{ik_R z}, & z \rightarrow \infty \\ T e^{-ik_L z}, & z \rightarrow -\infty. \end{cases} \quad (2)$$

\mathbf{K}_{\parallel} is the electron momentum in the plane parallel to the electrode surfaces. We have defined $\frac{1}{2}k_R^2 = E - \frac{1}{2}|\mathbf{K}_{\parallel}|^2 - v_{eff}(\infty)$, and $\frac{1}{2}k_L^2 = E - \frac{1}{2}|\mathbf{K}_{\parallel}|^2 - v_{eff}(-\infty)$. \mathbf{Y} is the component of the position vector in a plane parallel to the electrode surfaces, and z is the coordinate perpendicular to them. $v_{eff}(\pm\infty)$ is the bottom of the electronic energy band deep within the right/left electrode. The wavefunctions Ψ^0 satisfy the continuum normalization condition

$$\int d^3\mathbf{r} [\Psi_{E'\mathbf{K}'_{\parallel}}^0(\mathbf{r})]^* \Psi_{E\mathbf{K}_{\parallel}}^0(\mathbf{r}) = \delta(E' - E) \delta(\mathbf{K}'_{\parallel} - \mathbf{K}_{\parallel}). \quad (3)$$

Since the details of the electrodes are not important up to the interface with the sample, we represent them using a uniform-background (jellium) model [14, 15]. The potential V the electrons experience when they scatter through the nanojunction is³

$$V(\mathbf{r}, \mathbf{r}') = v_{ps}(\mathbf{r}, \mathbf{r}') + \left[v_{xc}[n(\mathbf{r})] - v_{xc}[n^0(\mathbf{r})] + \int d^3\mathbf{r}'' \frac{\delta n(\mathbf{r}'')}{|\mathbf{r} - \mathbf{r}''|} \right] \delta(\mathbf{r} - \mathbf{r}'). \quad (4)$$

The term v_{ps} is the electron-ion interaction potential that we represent with (nonlocal) pseudopotentials; v_{xc} is the exchange-correlation potential computed using the local-density approximation to density functional theory (DFT).⁴; $n^0(\mathbf{r})$ is the electronic density for the pair of biased bare electrodes;

³For the detailed implementation of the approach outlined in this chapter see the original papers [14, 15].

⁴One possible choice of exchange-correlation functional is the one given in [18], as parametrized in [19]. For an extended discussion of the local density approximation, see Chap. 5 of this collection [20].

$n(\mathbf{r})$ is the electronic density for the total system, and $\delta n(\mathbf{r})$ is their difference. We are implicitly assuming that static DFT gives a reasonable account of the scattering properties of a nanoscale system, at least in linear response. While this may be true for metallic junctions it is not obvious for molecular junctions [21]. However, in linear response and far from the resonant regime, we expect basic physical trends for these systems to be reproduced well by static DFT [21].

The full Hamiltonian of the system is $H = H_0 + V$, where H_0 is the Hamiltonian due to the bare biased electrodes, and V is the scattering potential. Our next task is to find the self-consistent solutions to the equation $H\Psi_E = E\Psi_E$, which we can put into the Lippmann-Schwinger form:

$$\Psi_{E\mathbf{K}_{\parallel}}(\mathbf{r}) = \Psi_{E\mathbf{K}_{\parallel}}^0(\mathbf{r}) + \int d^3\mathbf{r}' d^3\mathbf{r}'' G_E^0(\mathbf{r}, \mathbf{r}') V(\mathbf{r}', \mathbf{r}'') \Psi_{E\mathbf{K}_{\parallel}}(\mathbf{r}''). \quad (5)$$

The quantity G_E^0 is the Green's function for the bare electrodes, and needs to be calculated for each energy E .

Lastly, the total density of the system is

$$n(\mathbf{r}) = 2 \sum_i |\Psi_i(\mathbf{r})|^2 + 2 \int dE \int d^2\mathbf{K}_{\parallel} |\Psi_{E\mathbf{K}_{\parallel}}(\mathbf{r})|^2, \quad (6)$$

where we have included a factor of 2 due to spin degeneracy. The Ψ_i 's are the bound states of H , if any exist. They can be calculated by direct diagonalization of the full Hamiltonian H . In order to find a self-consistent solution for the density, (4), (5) and (6) are solved iteratively.

One has the freedom to choose a basis set to represent the wave functions. Due to the non-variational nature of the electrical current, the issue of which basis set to use in a given calculation is far from trivial [22]. In the examples that follow, plane waves have been used as basis set⁵, which allows easy testing of the convergence of the results [22].

Once the wavefunctions have been calculated self-consistently, the total electric current density (at zero temperature) is given by

$$\mathbf{j}(\mathbf{r}) = -2 \int_{E_{\text{FL}}}^{E_{\text{FR}}} dE \int d^2\mathbf{K}_{\parallel} \text{Im}\{[\Psi_{E\mathbf{K}_{\parallel}}(\mathbf{r})]^* \nabla \Psi_{E\mathbf{K}_{\parallel}}(\mathbf{r})\}. \quad (7)$$

The quantity we are interested in is the extra current δJ due to presence of the nanojunction [24–27] (two semi-infinite contacts have infinite surface area, and thus pass infinite current)

$$\delta J = \int d^2\mathbf{Y} \hat{\mathbf{z}} \cdot [\mathbf{j}(\mathbf{r}) - \mathbf{j}^0(\mathbf{r})], \quad (8)$$

⁵For other examples of calculations using different basis sets, see Sect. 2.2 of Chap. 4 of this collection, and the references therein [23].

where \mathbf{j} is the electric current density, and we have defined \mathbf{j}^0 to be the current density in the absence of the nanojunction. The current defined in (8) is the average current that flows across the nanojunction. Fluctuations with respect to that average are expected and will be described in Sect. 3.

It is worth noting that, in contrast to Chaps. 1, 2, 4 and 5 of this collection [20, 23, 28, 29], we do not calculate the electrical current using any of the Landauer formulas [30, 31]; rather, the current is calculated as the expectation value of the current operator over single-particle states. Clearly, it can be proven that when the transmission probabilities are extracted from the single-particle scattering wavefunctions, we recover from (8) the conventional two-probe Landauer formula [32].

2 Current-Induced Forces

Now that we have computed the stationary scattering states and corresponding current we can look at one of the effects induced by electron flow. We first focus on current-induced forces, i.e. the phenomenon by which atoms in a current-carrying wire are subject to forces due to the local change in self-consistent electronic distribution [33, 34]. There are several open questions related to current-induced forces, the most notable of which is their conservative nature [35]. Here we will focus on their dependence on some microscopic properties. We will show that these forces are a non-linear function of the junction properties, such as its current density, charge density and length.

Let us first define forces in a current-carrying wire. We first note that in this non-equilibrium problem the usual Hellman-Feynman theorem is not valid [33, 35]. A meaningful definition of force on ions can then be obtained by either the classical limit of Ehrenfest's theorem applied to the rate of change of ionic momentum [33] or from the Euler-Lagrange equation of motion for the classical ions [37]. Both approaches yield the same expression for the force on an ion, with position \mathbf{R} , due to the self-consistent electronic density $\rho(\mathbf{r})$ under current flow [37],

$$\mathbf{F} = - \int d\mathbf{r} \frac{\partial v_{ps}}{\partial \mathbf{R}} \rho(\mathbf{r}), \quad (9)$$

which can be equivalently written as [33]

$$\mathbf{F} = - \sum_i \left\langle \psi_i \left| \frac{\partial v_{ps}}{\partial \mathbf{R}} \right| \psi_i \right\rangle - \lim_{\Delta \rightarrow 0} \int_{\sigma} dE \left\langle \psi_{\Delta} \left| \frac{\partial v_{ps}}{\partial \mathbf{R}} \right| \psi_{\Delta} \right\rangle. \quad (10)$$

The first term on the RHS of (10) is similar to the usual Hellmann-Feynman contribution to the force due to localized electronic states $|\psi_i\rangle$. The second term is the contribution due to continuum states [33]. The wavefunctions

$|\psi_\Delta\rangle$ are eigendifferentials for each energy interval Δ in the continuum σ [33]. Finally, an additional contribution from ion-ion interactions needs to be taken into account.

For convenience we can separate the total force into two contributions. We define “direct force” to be the portion of the total force due to the charge distribution of the biased bare electrodes. We then call the remaining term the “electron wind force”⁶. There exists an inelastic portion of the electron wind force due to energy transfer from electrons to ions, in the form of phonon excitations; however, this contribution is generally negligible compared to the elastic one and will be neglected here [36].

We note that atomic relaxations induced by current flow do not have a large effect on the absolute value of the current that passes through the junction, even in the limit of high voltages and current densities [33,36,39,40]. While this result says nothing about the mechanical stability of current-carrying wires under bias, it allows us to study several transport properties assuming atomic positions fixed at their zero bias value.

Let us now look at the dependence of these forces on microscopic details. As an example, in Fig. 1 we consider a nanoscopic wire composed of three silicon atoms between two bulk electrodes. We keep atomic positions fixed at their zero bias values. For each atom in the junction, we plot the direct force, the electron wind force due to the continuum states, and the electron wind force due to the discrete part of the spectrum.

The direct force is almost linear with applied bias, with the force on the central atom being the largest. Closer to the electrode surfaces, the electrostatic potential ceases to be a linear function of position, causing the force on the other two atoms to be slightly smaller. Note that the force on the central atom due to states in the continuum is positive (i.e. pushes the atom to the left, in the same direction as the electron flow). However, the force on the central atom due to states in the discrete spectrum is almost zero, even at larger biases. The reason for this behavior is that the amount of charge localized around the central atom is almost constant in the applied bias, and so the corresponding force is also constant [36].

Figure 2(a) through (c) shows the force on specific atoms in silicon wires composed of varying numbers of atoms, while Fig. 2(d) shows the average force on the total wires. It is difficult to extract overall trends from Figs. 2(a) through (c), although it is interesting to note that the second atom from the left (labeled Si₂) is consistently the atom that experiences the greatest force. Figure 2(d), however, follows an obvious trend: the average force saturates with increasing number of atoms. This comes from the fact that, as the length of the wire increases, the boundary effects due to the electrodes become less important. This result suggests that longer wires are more difficult to break under current flow, an important factor to consider in nanoscale devices.

⁶Note that this definition of “direct force”, and corresponding “wind force”, is not universal in literature. For a discussion of the various definitions, see [38].

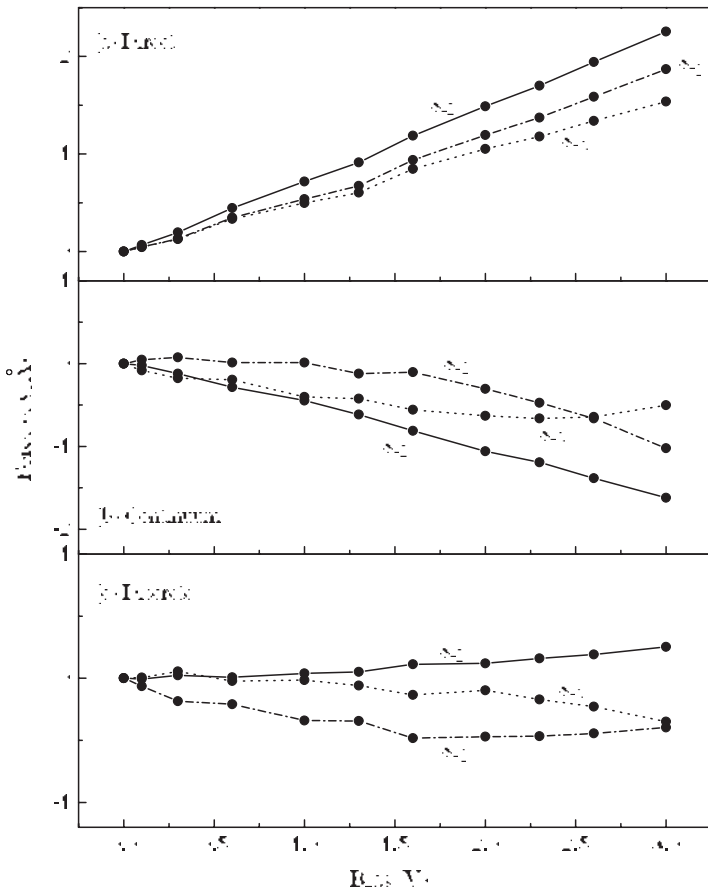


Fig. 1. Different contributions to the total force for each of the three atoms composing a silicon wire, as a function of bias. See text for details. Reprinted figure with permission from [36]. Copyright 2003 by the American Physical Society

3 Shot Noise

In this section we will discuss steady-state current fluctuations that occur due to the quantization of charge. Shot noise is quite distinct from (equilibrium) thermal noise and is generally unavoidable, even at zero temperature [41].

We will first derive an expression of shot noise in terms of single-particle wavefunctions. In order to do so, let us write the field operator for electrons $\hat{\Psi}$ as combination of a field operator due to electrons incident from the left, and one due to electrons incident from the right [32, 42]

$$\hat{\Psi} = \hat{\Psi}^L + \hat{\Psi}^R . \quad (11)$$

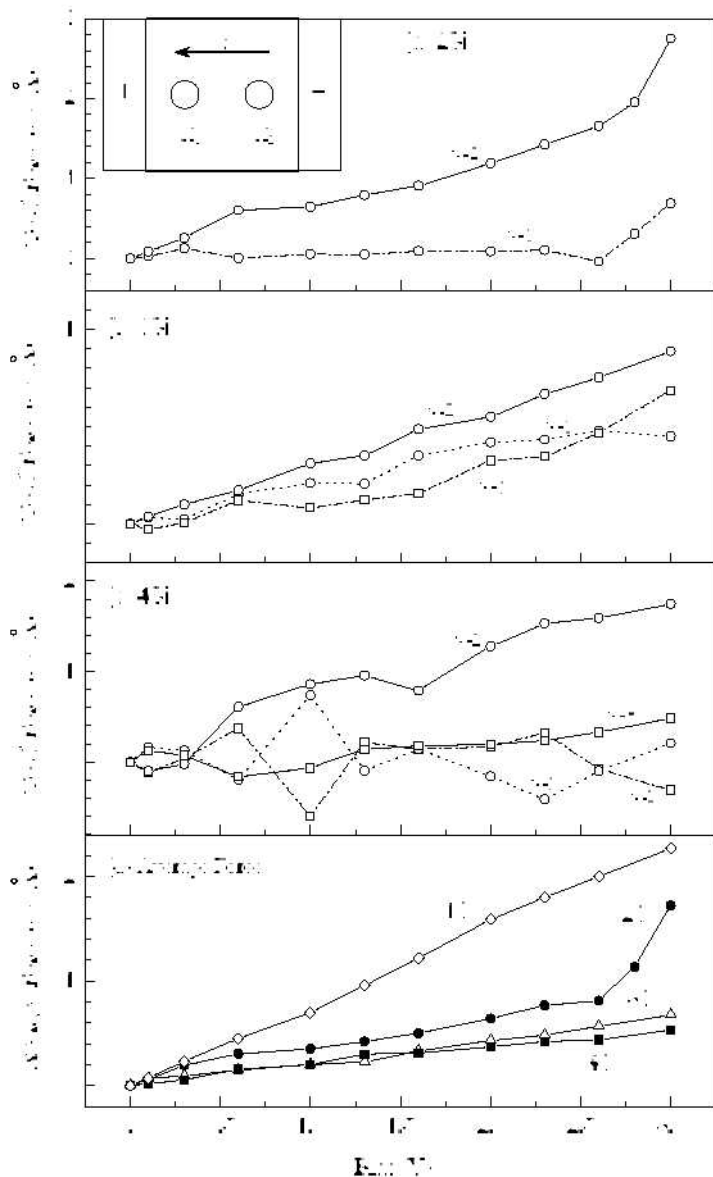


Fig. 2. Total force on each atom in atomic wires consisting of (a) two, (b) three, and (c) four silicon atoms. The inset shows a schematic of the wire that is composed of two silicon atoms. (d) The average force on each wire. Reprinted figure with permission from [36]. Copyright 2003 by the American Physical Society

We can further expand each of these field operators into the single particle wave functions (5):

$$\hat{\Psi}^{L(R)} = \sum_E e^{-i\omega t} a_E^{L(R)} \Psi_E^{L(R)}(\mathbf{r}, \mathbf{K}_\parallel). \quad (12)$$

Again, we have used \mathbf{K}_\parallel to denote the component of the electron's incident momentum that is parallel to the surfaces of the electrodes.⁷

The coefficients $a_E^{L(R)}$ are the annihilation operators for electrons incident from the left (right) reservoir. These operators satisfy the usual anticommutation relation $\{a_E^\phi, a_{E'}^{\chi\dagger}\} = \delta_{\phi\chi}\delta(E - E')$, where $\phi, \chi = R, L$. We will again assume that the electrons coming from the left (right) reservoir are in local thermal equilibrium at a temperature T_e far away from the junction, so that their statistics are given by the Fermi-Dirac distribution function $f_E^{L(R)}$, i.e.

$$\langle a_E^{\phi\dagger} a_{E'}^\chi \rangle = \delta_{\phi\chi} \delta(E - E') f_E^\phi \quad (13)$$

$$= \frac{\delta_{\phi\chi} \delta(E - E')}{e^{[E - E_F\phi]/k_B T_e} + 1}. \quad (14)$$

Using the field operator (11), we can define the current operator

$$\hat{I}(z, t) = -i \int d\mathbf{Y} \int d\mathbf{K}_\parallel (\hat{\Psi}^\dagger \partial_z \hat{\Psi} - \partial_z \hat{\Psi}^\dagger \hat{\Psi}). \quad (15)$$

In the limit of zero temperature, the Fermi distribution reduces to a step function; if we again assume the chemical potential in the right reservoir E_{FR} is higher than the chemical potential in the left reservoir E_{FL} , then at zero temperature the average value of the current is just

$$\langle \hat{I} \rangle = -i \int_{E_{FL}}^{E_{FR}} dE \int d\mathbf{Y} \int d\mathbf{K}_\parallel \tilde{I}_{E,E}^{R,R}, \quad (16)$$

where

$$\tilde{I}_{E,E'}^{\phi,\chi} = (\Psi_E^\phi)^* \nabla \Psi_{E'}^\chi - \nabla (\Psi_E^\phi)^* \Psi_{E'}^\chi, \quad (17)$$

and * denotes complex conjugation.

We define shot noise as the Fourier transform of the electric current autocorrelation function in the limit of zero frequency and zero temperature [41, 43]:

$$2\pi S(\omega) = \int dt e^{i\omega t} \langle \Delta \hat{I}(t) \Delta \hat{I}(0) \rangle, \quad (18)$$

where the excess current operator $\Delta \hat{I}(t)$ is equal to $\hat{I}(t) - \langle \hat{I} \rangle$. The evaluation of this expression is quite cumbersome and therefore we do not include it here.

⁷The presence of the nanojunction causes \mathbf{K}_\parallel to cease to be a good quantum number; we still use it here as a “label” to enumerate scattering states.

We only mention that we need to evaluate terms of the form $\langle \hat{A}_4 \hat{A}_3 \hat{A}_2 \hat{A}_1 \rangle$, where the \hat{A}_i 's are raising and lowering operators. We can evaluate these terms with the Bloch-De Dominicis theorem [44]:

$$\langle \hat{A}_4 \hat{A}_3 \hat{A}_2 \hat{A}_1 \rangle = \langle \hat{A}_4 \hat{A}_3 \rangle \langle \hat{A}_2 \hat{A}_1 \rangle + \eta \langle \hat{A}_4 \hat{A}_2 \rangle \langle \hat{A}_3 \hat{A}_1 \rangle + \eta^2 \langle \hat{A}_4 \hat{A}_1 \rangle \langle \hat{A}_3 \hat{A}_2 \rangle , \quad (19)$$

where $\eta = -1$ for fermions, and $+1$ for bosons. The end result is

$$S(\omega) = \sum_{\phi, \chi=L,R} \int dE f_{E+\omega}^\phi (1 - f_E^\chi) \int d\mathbf{Y}_1 \int d\mathbf{K}_1 \tilde{I}_{E+\omega, E}^{\phi\chi} \int d\mathbf{Y}_2 \int d\mathbf{K}_2 \tilde{I}_{E, E+\omega}^{\chi\phi} . \quad (20)$$

In the limit of zero frequency and zero temperature, (20) reduces to [32, 42]

$$S = \int_{E_{\text{FL}}}^{E_{\text{FR}}} dE \left| \int d\mathbf{R} \int d\mathbf{K} \tilde{I}_{E, E}^{\text{LR}} \right|^2 . \quad (21)$$

This is the desired expression relating shot noise to single-particle wavefunctions⁸.

In the case of uncorrelated electrons, the magnitude of the shot noise becomes $S_P = 2eI$, where e is the electron charge, and I is the dc current. This corresponds to the noise of a series of incident particles, the time between the arrivals of which follows a Poissonian distribution function. For this reason, S_P is sometimes called the Poisson value for the shot noise [41, 46]. In general, however, the magnitude of the shot noise will be less than the Poisson value. A relative measure of noise is therefore the Fano factor F , defined as the ratio between shot noise S and the Poisson limit S_P .

We are now ready to discuss an example of noise properties of a nanoscale junction. We again look at the properties of a junction formed by a short wire of silicon atoms between two bulk electrodes. Other examples of noise in atomic-scale systems can be found in [42] and [32].

Figure 3 shows the results of conductance and Fano factor for such a system for a bias of 0.01 V. We first notice that the Fano factor is strongly nonlinear as a function of bias. It is also considerably enhanced for very short wires due to the large contribution from the metal electrodes. In addition, the Fano factor oscillates as a function of number of silicon atoms. The conductance shows a similar but opposite oscillatory trend. Both the noise and conductance oscillations are due to the fact that a Si wire made up of an even number of atoms has fully-occupied π orbitals, while a wire made up of an odd number of atoms has a half-filled π state at the Fermi level [47].

Other interesting properties of shot noise in nanoscale systems include its dependence on contact geometry and interwire interactions [32]. We refer the reader to the original papers for a discussion of these effects.

⁸As for the current, this expression can be reduced to the well-known result $S = \frac{V_B}{\pi} \sum_n T_n (1 - T_n)$ [45] if the transmission probabilities T_n of each mode are extracted from the scattering wavefunctions; see [32].

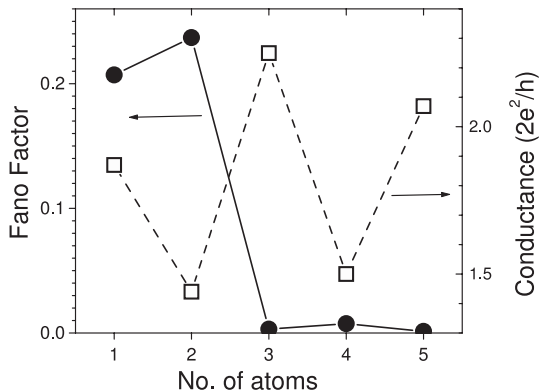


Fig. 3. Fano factor and conductance for a nanojunction composed of different numbers of silicon atoms. Reprinted figure with permission from [42]. Copyright 2003 by the American Physical Society

4 Local Heating

Local heating occurs when electrons in a current-carrying wire exchange energy with phonons [48–52]. Accordingly, there are four main processes that contribute to local heating in the junction:

1. Cooling processes in which an electron incident from the left absorbs a phonon, which we will denote by the superscript L, 1;
2. Heating processes in which an electron incident from the left emits a phonon, denoted by the superscript L, 2;
3. Cooling processes in which an electron incident from the right absorbs a phonon, denoted by the superscript R, 1; and
4. Heating processes in which an electron incident from the right emits a phonon, denoted by the superscript R, 2.

The power generated in a nanoscale junction is given by the sum of the average power generated by those four processes, summed over all possible vibrational modes:

$$W_{\text{tot}}^{\text{avg.}} = \sum_{\text{vib. modes}} (\langle W^{R,2} \rangle + \langle W^{L,2} \rangle - \langle W^{R,1} \rangle - \langle W^{L,1} \rangle) \quad (22)$$

In addition to the above processes, cooling occurs due to dissipation of energy in the bulk electrodes.⁹ In order to evaluate the power generated by each of those processes, we first need to consider the full many-body Hamiltonian of the system:

⁹We assume here that at those biases when current-induced forces are large heating is small. This is generally true if dissipation into the bulk electrodes is efficient [53].

$$H = H_{\text{el}} + H_{\text{ion}} + H_{\text{el-ion}} \quad (23)$$

Here, H_{el} is the electronic Hamiltonian (including electron-electron effects), H_{ion} is the ionic Hamiltonian, given by

$$H_{\text{ion}} = \sum_{i=1}^N \frac{\mathbf{P}_i^2}{2M_i} + \sum_{i,j} V_{\text{ion}}(\mathbf{R}_i - \mathbf{R}_j), \quad (24)$$

and $H_{\text{el-ion}}$ is the electron-ion interaction,

$$H_{\text{el-ion}} = \sum_{i,j} V_{\text{el-ion}}(\mathbf{r}_i - \mathbf{R}_j). \quad (25)$$

\mathbf{P}_i , M_i and \mathbf{R}_i denote the momentum, mass and position of the i th ion (out of a total of N ions), while \mathbf{r}_i denotes the position of the i th electron.

We assume that each ion executes a small vibration about its equilibrium position \mathbf{R}_j^0 so that its displacement is given by $\mathbf{Q}_j = \mathbf{R}_j - \mathbf{R}_j^0$. We can decouple these ionic vibrations by introducing normal coordinates $\{q_{j\beta}\}$ so that the α^{th} component ($\alpha = x, y, z$) of \mathbf{Q}_i is given by

$$(\mathbf{Q}_i)_\alpha = \sum_{j=1}^N \sum_{\beta=1}^3 A_{i\alpha,j\beta} q_{j\beta}. \quad (26)$$

The coefficients $A_{i\alpha,j\beta}$ obey the orthonormality relations $\sum_{i,\alpha} M_i A_{i\alpha,j\beta} \times A_{i\alpha,j'\beta'} = \delta_{j\beta,j'\beta'}$. We now can solve this problem in the usual way by introducing boson creation and annihilation operators $b_{j\beta}^\dagger$ and $b_{j\beta}$ for the $(j\beta)$ th mode; the creation and annihilation operators obey the commutation relation $[b_{j\beta}, b_{j'\beta'}^\dagger] = \delta_{j\beta,j'\beta'}$. With this transformation, the total ionic Hamiltonian is just the sum of the Hamiltonians for each normal mode:

$$H_{\text{ion}} = \sum_{j,\beta} \left(b_{j\beta}^\dagger b_{j\beta} + \frac{1}{2} \right) \omega_{j\beta} \quad (27)$$

Next, much like in Sect. 3, we expand the field operator for the electrons into a part that describes electrons incident from the left, and a part that describes electrons incident from the right: $\hat{\Psi} = \hat{\Psi}^L + \hat{\Psi}^R$.

We now express $H_{\text{el-ion}}$ in terms of the fermionic and bosonic creation and annihilation operators [48]:

$$H_{\text{el-ion}} = \int d\mathbf{r} \sum_i V_{\text{el-ion}}(\mathbf{r} - \mathbf{R}_i) \quad (28)$$

$$= \int d\mathbf{r} \sum_i \mathbf{Q}_i \cdot \nabla_{\mathbf{R}} V_{\text{el-ion}}(\mathbf{r} - \mathbf{R}_i^0) + O(Q^2) \quad (29)$$

$$= \sum_{\varphi,\chi} \sum_{E_1,E_2} \sum_{i\alpha,j\beta \in \text{vib.}} \sqrt{\frac{1}{2\omega_{j\beta}}} A_{i\alpha,j\beta} J_{E_1,E_2}^{i\alpha,\varphi\chi} a_{E_1}^{\varphi\dagger} a_{E_2}^{\chi} (b_{j\beta} + b_{j\beta}^\dagger), \quad (30)$$

since we have $(\mathbf{Q}_i)_\alpha = \sum_{j\beta \in \text{vib.}} A_{i\alpha,j\beta} \sqrt{\frac{1}{2\omega_{j\beta}}} (b_{j\beta} + b_{j\beta}^\dagger)$. The electron-phonon coupling constant is given by

$$J_{E_1, E_2}^{i\alpha, \varphi\chi} = \int d\mathbf{r} \int d\mathbf{K}_\parallel \Psi_{E_1}^{\phi*}(\mathbf{r}, \mathbf{K}_\parallel) \frac{\partial}{\partial R_\alpha} V^{\text{ps}}(\mathbf{r}, \mathbf{R}_i^0) \Psi_{E_2}^\chi(\mathbf{r}, \mathbf{K}_\parallel), \quad (31)$$

where $V^{\text{ps}}(\mathbf{r}, \mathbf{R}_i^0)$ denotes the pseudopotential due to the i^{th} atomic core. It is interesting to note that, unlike the equilibrium case, in a current-carrying wire the electron-phonon coupling constant depends on two types of stationary states: left- and right-moving states.

We now assume that after continuous exchange of energy, both the electronic and phonon subsystems have reached a steady-state temperature and therefore assign a temperature T_e to the electron gas, and a temperature T_ω to the phonons (see schematic in Fig. 4), so that the statistics of the phonons in the junction can be described by the Bose-Einstein distribution:

$$g_{j\beta} = \frac{1}{e^{[n_{j\beta} + \frac{1}{2}]\omega_{j\beta}/k_B T_\omega} - 1}, \quad (32)$$

where T_ω is the local temperature of the junction, and $n_{j\beta}$ is the occupation number of the $(j\beta)^{\text{th}}$ mode.

We can now use the Fermi's Golden Rule to infer rates of phonon emission and absorption, and thus explicitly evaluate (22) [48–50]. Accordingly, the

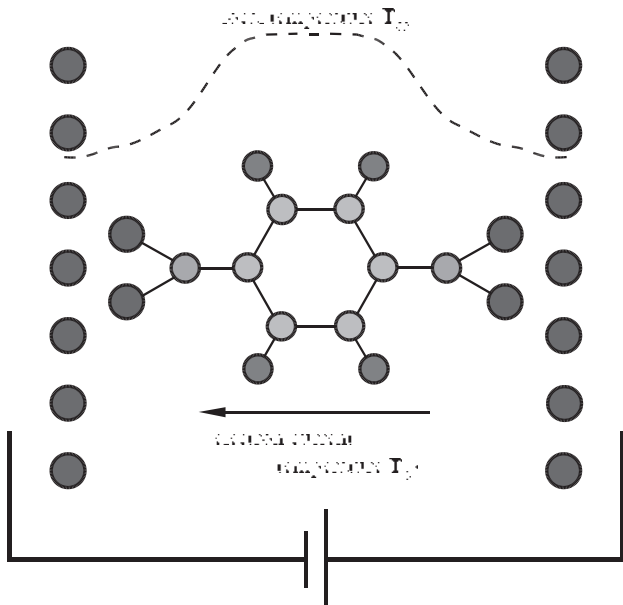


Fig. 4. Molecular junction undergoing local heating as a result of transport. The electron gas has a temperature T_e , and the phonons a temperature T_ω

transition rate from an initial state $|i\rangle$ to a final state $|f\rangle$ is

$$R_{j\beta} = 2\pi|\langle i|H_{\text{el-ion}}^{j\beta}|f\rangle|^2\delta(E_f - E_i - \omega_{j\beta}) . \quad (33)$$

Here, we are only considering the transition rate for an electron interacting with the $(j\beta)$ th mode, and so we have defined $H_{\text{el-ion}}^{j\beta}$ to be the $(j\beta)$ th term in the $H_{\text{el-ion}}$ Hamiltonian (see (30)).

Let us consider the case where an electron incident from the right emits a phonon. In this context, $|i\rangle$ denotes the $(j\beta)$ th mode in its original state, and $|f\rangle$ denotes the same mode after excitation to a higher occupation number. We can therefore evaluate the statistical average of the square of the matrix element of the Hamiltonian in (33) to obtain

$$\begin{aligned} & \langle |\langle i|H_{\text{el-ion}}^{j\beta,\text{R},2}|f\rangle|^2 \rangle \\ &= \left| \sum_{i\alpha} \sqrt{\frac{1}{2\omega_{j\beta}}} A_{i\alpha,j\beta} J_{E-\omega_{j\beta},E}^{i\alpha,\text{LR}} \sqrt{(1 + \langle g_{j\beta} \rangle)} f_E^{\text{R}} (1 - f_{E-\omega_{j\beta}}^{\text{L}}) \right|^2 . \end{aligned} \quad (34)$$

Note that the 1 that is added to $g_{j\beta}$ corresponds to spontaneous emission.

The power emitted by right-incident electrons into vibrational modes that undergo transitions from a state with energy E_i to a state with energy E_f is simply

$$w_{j\beta}^{\text{R},2}(E_i, E_f) = (E_f - E_i) R_{j\beta} \quad (35)$$

$$= 2\pi|\langle i|H_{\text{el-ion}}^{j\beta}|f\rangle|^2(E_f - E_i)\delta(E_f - E_i - \omega_{j\beta}) . \quad (36)$$

The total power emitted by right-incident electrons to the $(j\beta)$ th mode is the sum over all initial and final states:

$$W_{j\beta}^{\text{R},2} = 2 \sum_{E_i} \sum_{E_f} w_{j\beta}^{\text{R},2}(E_i, E_f) \quad (37)$$

$$= 2 \sum_{E_i} \sum_{E_f} 2\pi|\langle i|H_{\text{el-ion}}^{j\beta}|f\rangle|^2(E_f - E_i)\delta(E_f - E_i - \omega_{j\beta}) \quad (38)$$

$$\begin{aligned} &= 2 \int dE_i D_{E_i}^{\text{R}} \int dE_f D_{E_f}^{\text{L}} 2\pi|\langle i|H_{\text{el-ion}}|f\rangle|^2 \\ &\quad \times (E_f - E_i)\delta(E_f - E_i - \omega_{j\beta}) \end{aligned} \quad (39)$$

$$= 4\pi \int dE_i D_{E_i}^{\text{R}} D_{E_i - \omega_{j\beta}}^{\text{L}} |\langle i|H_{\text{el-ion}}|f\rangle|^2 \omega_{j\beta} , \quad (40)$$

where we have multiplied by a factor of 2 due to spin degeneracy. In taking the continuum limit, we have introduced $D_E^{\text{R(L)}}$, which is the partial density of states of electrons moving to the right (left) with energy E .

Finally, the total power emitted by right-incident electrons to the $(j\beta)$ th mode is therefore

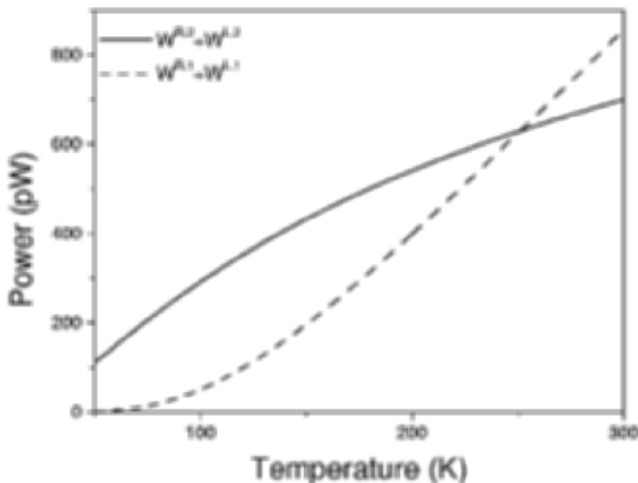


Fig. 5. Absolute magnitude of the power due to electron-phonon interactions as a function of T_ω . The intersection of the two curves gives the steady-state temperature of the junction

$$\langle W_{j\beta}^{R,2} \rangle = 2\pi[1 + \langle g_{j\beta}(n_{j\beta}) \rangle] \int dE \left| \sum_{i\alpha} A_{i\alpha,j\beta} J_{E-\omega_{j\beta}}^{i\alpha,LR} \right|^2 \times f_E^R (1 - f_{E-\omega_{j\beta}}) D_E^R D_{E-\omega_{j\beta}}^L. \quad (41)$$

Similar considerations apply to all other processes that contribute to (22).

The local temperature of the junction T_ω is evaluated (at a fixed electronic temperature T_e) when the total power (22) is zero. This is illustrated in Fig. 5 where the magnitude of the sum of the heating processes is plotted on the same graph as the magnitude of the sum of the cooling processes as a function of T_ω . The point where the two curves intersect is the steady-state temperature of the nanojunction.

Let us now discuss two examples. We first neglect cooling due to dissipation into the electrodes. Figure 6 shows the steady-state temperature as a function of applied bias for two different nanojunctions, a gold point contact and a molecular junction. We note that local heating occurs when a certain threshold bias is reached. This is because a given vibrational mode cannot be excited unless the incident electron is energetic enough to supply the requisite amount of energy; that is, $V_{\text{Bias}}^{(\text{crit.})} = \min\{\omega_{i\alpha}\}$. The onset bias for heating is in good agreement with experimental observations in the gold point-contact case [54]. Once the threshold bias is reached, however, the local temperature of the junction rises quickly, since cooling processes cannot effectively compensate for heating processes. Note that, in this case, very large temperatures can be reached at very small biases.

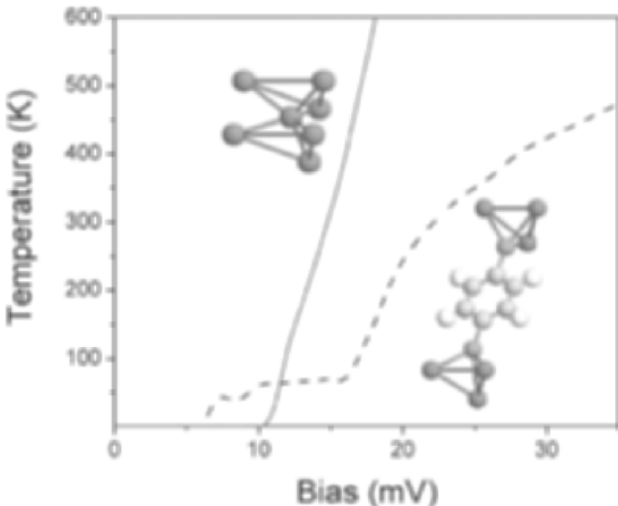


Fig. 6. Steady-state temperature as a function of applied bias for two different contact geometries: a molecular junction, and a single gold atom contact. A schematic of the contact geometry is shown as an inset for each case. For both contact geometries, the nanojunction is not in thermal contact with the bulk electrodes. Reprinted with permission from [48]

This is in contrast to Fig. 7, which depicts the same process, but with an important difference: the nanojunction and contacts are now assumed to be thermally coupled with each other, i.e. energy can be dissipated into the bulk electrodes. In order to estimate this energy transfer we use the following expression for elastic phonon scattering between a bulk material A in contact with another bulk material B via a weak mechanical link (the nanojunction) [55]:

$$I_{\text{th}} = 4\pi K^2 \int d\varepsilon \varepsilon N_A(\varepsilon) N_B(\varepsilon) [g(T_A, \varepsilon) - g(T_B, \varepsilon)], \quad (42)$$

where $g(T_{A(B)}, \varepsilon)$ is the Bose-Einstein distribution at a temperature $T_{A(B)}$ and energy ε and $N_{A(B)}$ is the phonon spectral density of states of surface A(B) [55]. The weak mechanical link is modeled via a harmonic oscillator with stiffness K .

Applying (42) to our case we obtain the results of Fig. 7 [48]. Notice that the bias scale in Fig. 7 is much different than the one in Fig. 6, i.e. the majority of heat generated in the junction is dissipated into the bulk electrodes. However, in real devices poor thermal contact between the junction and the electrodes can actually occur, as can localized phonon modes within the junction which have low coupling with the continuum of modes of the bulk electrodes [50]. Such instances can lead to very large local temperatures in the junction with consequent structural instabilities [48, 50, 53]. Such insta-

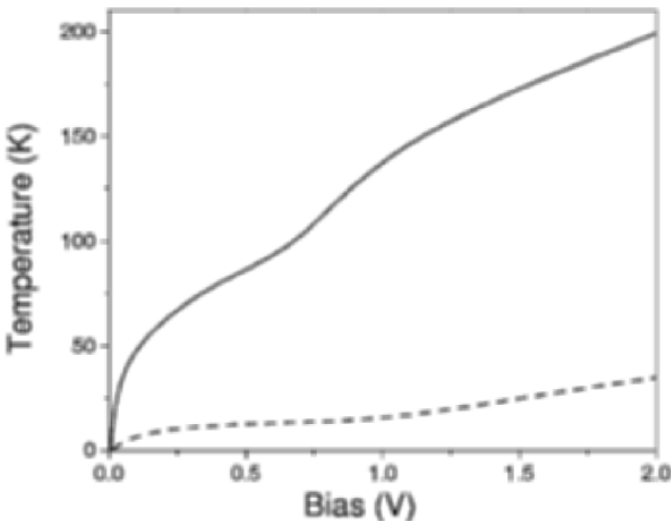


Fig. 7. Steady-state temperature as a function of applied bias for the same geometries as in Fig. 6, where the *dashed line* corresponds to the molecular junction, and the solid line corresponds to the gold point contact. Dissipation into the bulk electrodes is taken into account. Reprinted with permission from [48]

bilities have been actually observed in metallic point contacts [56] and may be responsible for the low yield in fabricating molecular junctions [57].

5 Inelastic Conductance

In addition to local heating, electron-phonon coupling can yield a lot of information on the internal structure of nanoscale junctions: discontinuities in the conductance can occur when the energy of incident electrons becomes large enough to excite different vibrational modes of the junction.

In order to calculate the inelastic current, let us consider the case of an electron incident from the right. By treating the electron-phonon interaction as a perturbation, the total wavefunctions of the (electron plus phonon) system can be written in terms of the states $|\Psi_E^R; n_{i\alpha}\rangle = |\Psi_E^R\rangle \otimes |n_{i\alpha}\rangle$. The wavefunction of the system, including electron-phonon interactions is therefore (to first order): $|\Phi_E^R; n_{i\alpha}\rangle = |\Psi_E^R; n_{i\alpha}\rangle + |\delta\Psi_E^R; n_{i\alpha}\rangle$, where $|\delta\Psi_E^R; n_{i\alpha}\rangle$ is the leading-order change in the wavefunction due to electron-phonon interaction. We can then calculate the leading correction to the total wavefunction:

$$|\delta\Psi_E^R; n_{j\beta}\rangle = \lim_{\varepsilon \rightarrow 0^+} \sum_{\phi'=\text{L,R}} \sum_{j',\beta'} \int dE' D_{E'}^{\phi'} \times \frac{\langle \Psi_{E'}^{\phi'}; n_{j'\beta'} | H_{\text{el-ion}} | \Psi_E^R; n_{j\beta} \rangle \langle \Psi_{E'}^{\phi'}; n_{j'\beta'} \rangle}{\varepsilon(E, n_{j\beta}) - \varepsilon(E', n_{j'\beta'}) - i\varepsilon}. \quad (43)$$

Once again, $D_E^{\text{L(R)}}$ is the partial density of states for electrons incident from the left (right). $\varepsilon(E, n_{j\beta}) = E + (n_{j\beta} + \frac{1}{2})\omega_{j\beta}$ is the energy of state $|\Psi_E^\phi; n_{j\beta}\rangle$.¹⁰

Using the identity $\lim_{\varepsilon \rightarrow 0} \frac{1}{z - i\varepsilon} = P(\frac{1}{z}) + i\pi\delta(z)$, where $P(x)$ denotes the principle value of x , together with the matrix element that leads to (34), we obtain

$$\begin{aligned} |\delta\Psi_E^{\text{R}}; n_{j\beta}\rangle &= i\pi \sum_{i\alpha} \sqrt{\frac{1}{2\omega_{j\beta}}} A_{i\alpha, j\beta} \left[D_{E+\omega_{j\beta}}^{\text{L}} \sqrt{\langle g(n_{j\beta}) \rangle f_E^{\text{R}} (1 - f_{E+\omega_{j\beta}}^{\text{L}})} \right. \\ &\quad \times J_{E+\omega_{j\beta}}^{i\alpha, \text{LR}} |\Psi_{E+\omega_{j\beta}, E}^{\text{L}}; n_{j\beta} - 1\rangle \\ &\quad + D_{E-\omega_{j\beta}}^{\text{L}} \sqrt{(1 + \langle g(n_{j\beta}) \rangle) f_E^{\text{R}} (1 - f_{E-\omega_{j\beta}}^{\text{L}})} \\ &\quad \left. \times J_{E-\omega_{j\beta}}^{i\alpha, \text{LR}} |\Psi_{E-\omega_{j\beta}, E}^{\text{L}}; n_{j\beta} + 1\rangle \right] \end{aligned} \quad (44)$$

The brackets $\langle \quad \rangle$ denote a statistical average. The analagous expression for $|\delta\Psi_E^{\text{L}}; n_{j\beta}\rangle$ is obtained by simply interchanging all R's with L's.

As an axample let us assume that the electronic temperature T_e is equal to zero. In that case, for an external bias $V = E_{\text{FL}} - E_{\text{FR}}$, only normal modes with energies $\omega_{j\beta} < V$ can be excited. (Again, we are assuming the left electrode is positively biased.) Furthermore, if we assume negligible local heating, and that the few excited phonons decay on a short time scale, then we have $\langle g(n_{j\beta}) \rangle = 0$. In this case, the inelastic contribution to the current is:

$$\delta I = -i \int_{E_{\text{FL}}}^{E_{\text{FR}}} dE \int d\mathbf{R} \int d\mathbf{K}_{\parallel} [(\delta\Psi_E^{\text{R}})^* \partial_z \delta\Psi_E^{\text{R}} - \partial_z (\delta\Psi_E^{\text{R}})^* \delta\Psi_E^{\text{R}}]. \quad (45)$$

In Fig. 8 we plot the inelastic conductance of a molecular junction. It is evident that only specific modes with large longitudinal component (with respect to the direction of current flow) dominate the inelastic conductance, while modes with large transverse component contribute negligibly. In addition, it is shown in [58] that inelastic current-voltage characteristics are quite sensitive to the structure of the contact between the molecule and the electrodes thus providing a powerful tool to extract the bonding geometry in molecular wires.

¹⁰Since the electron-phonon coupling is small for the systems considered here, we assume the energy E is the unperturbed electronic energy, i.e. the elastic correction to the electronic energy is negligible.

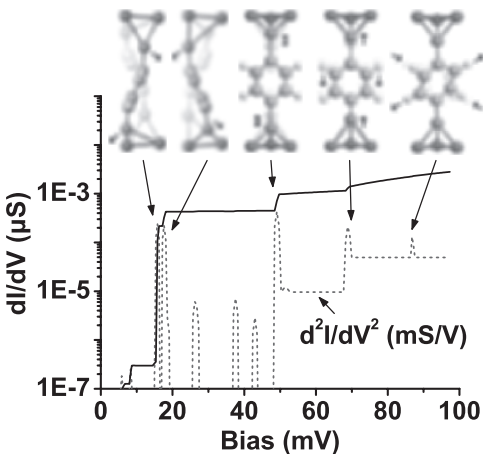


Fig. 8. Magnitude of the differential conductance through a molecular junction made of a benzene-dithiolate molecule. The *dashed line* gives the derivative of the differential conductance, while the insets illustrate the major longitudinal phonon modes Reprinted with permission from [58]. Copyright 2004 American Chemical Society

6 Conclusions

We have presented a review of several current-induced effects in nanoscale conductors and their description at the atomic level. These effects provide a wealth of information on the transport properties of atomic and molecular junctions beyond the value of the average current. In addition, their understanding is paramount to the possible application of nanoscale systems in electronics.

Acknowledgements

One of us (MD) is indebted to the students and research associates who have worked with him over the past years on the issues described in this review: M. Zwolak, J. Lagerqvist, Y.-C. Chen, M. Chshiev and Z. Yang. We are also thankful for illuminating discussions with N.D. Lang and T.N. Todorov. We acknowledge support from the NSF Grant No. DMR-01-33075.

References

1. M. Di Ventra, S. Evoy, J.R. Hefflin: *Introduction to Nanoscale Science and Technology* (Kluwer Academic Publishers, Boston, 2004)

2. M. Di Ventra, T.N. Todorov: Transport in nanoscale systems: the microcanonical versus grand-canonical picture, *J. Phys.-Condens. Matter* **16**, 8025–8034 (2004)
3. A.P. Horsfield, D.R. Bowler, A.J. Fisher, T.N. Todorov, M.J. Montgomery: Power dissipation in nanoscale conductors: classical, semi-classical and quantum dynamics, *J. Phys.-Condens. Matter* **16**, 3609–3622 (2004)
4. H. Ohnishi, Y. Kondo, K. Takayanagi: Quantized conductance through individual rows of suspended gold atoms, *Nature* **395**, 780 (1998)
5. A. Yazdani, D.M. Eigler, N.D. Lang: Off-resonance conduction through atomic wires, *Science* **272**, 1921 (1996)
6. V. Rodrigues, D. Ugarte: Real-time imaging of atomistic process in one-atom-thick metal junctions, *Phys. Rev. B* **63**, 073405 (2001)
7. R.M. Metzger, B. Chen, U. Höpfner, M.V. Lakshminantham, D. Vuillaume, T. Kawai, X. Wu, H. Tachibana, T.V. Hughes, H. Sakurai, J.W. Baldwin, C. Hosch, M.P. Cava, L. Brehmer, G.J. Ashwell: Unimolecular electrical rectification in hexadecylquinolinium tricyanoquinodimethane, *J. Am. Chem. Soc.* **119**, 10455–10466 (1997)
8. C. Zhou, M.R. Deshpande, M.A. Reed, L.J. II, J.M. Tour: Nanoscale metal/self-assembled monolayer/metal heterostructures, *Appl. Phys. Lett.* **71**, 611–613 (1997)
9. M.A. Reed, C. Zhou, C.J. Muller, T.P. Burgin, J.M. Tour: Conductance of a molecular junction, *Science* **278**, 252–254 (1997)
10. S. Datta, W. Tian, S. Hong, R. Reifenberger, J. Henderson, C.P. Kubiak: Current-voltage characteristics of self-assembled monolayers by scanning tunneling microscopy, *Phys. Rev. Lett.* **79**, 2530–2533 (1997)
11. J. Gimzewski, C. Joachim: Nanoscale science of single molecules using local probes, *Science* **283**, 1683–1688 (1999)
12. J. Chen, M.A. Reed, A.M. Rawlett, J.M. Tour: Large on-off ratios and negative differential resistance in a molecular electronic device, *Science* **286**, 1550–1552 (1999)
13. M.A. Reed, J. Chen, A.M. Rawlett, D.W. Price, J.M. Tour: Molecular random access memory cell, *Appl. Phys. Lett.* **78**, 3735–3737 (2001)
14. N.D. Lang, P. Avouris: Carbon-atom wires: Charge-transfer doping, voltage drop, and the effect of distortions, *Phys. Rev. Lett.* **84**, 358–361 (2000)
15. M. Di Ventra, N.D. Lang: Transport in nanoscale conductors from first principles, *Phys. Rev. B* **65**, 045402 (2002)
16. J. Tomfohr, G. Ramachandran, O.F. Sankey, S.M. Lindsay: in *Introducing Molecular Electronics*, ed. by G. Cuniberti, G. Fagas, K. Richter (Springer, New York, 2005), Vol. vvv of Lecture Notes in Physics, p. xxx; Chap. 11 of this collection
17. A. Messiah: *Quantum Mechanics* (Dover Publications, Inc., New York, 1999)
18. D.M. Ceperley, B. Alder: Ground state of the electron gas by a stochastic method, *Phys. Rev. Lett.* **45**, 566 (1980)
19. J.P. Perdew, A. Zunger: Self-interaction correction to density-functional approximations for many-electron systems, *Phys. Rev. B* **23**, 5048 (1981)
20. A. Di Carlo, A. Pecchia, L. Latessa, T. Frauenheim, G. Seifert: in *Introducing Molecular Electronics*, ed. by G. Cuniberti, G. Fagas, K. Richter (Springer, New York, 2005), Vol. vvv of Lecture Notes in Physics, p. xxx; Chap. 5 of this collection

21. N. Sai, M. Zwolak, G. Vignale, M. Di Ventra: Non-local corrections to the DFT-LDA electron conductance in nanoscale systems, cond-mat/0411098 (2004)
22. Z. Yang, A. Tackett, M. Di Ventra: Variational and nonvariational principles in quantum transport calculations, Phys. Rev. B **66**, 041405(R) (2002)
23. K. Stokbro, J. Taylor, M. Brandbyge, H. Guo: in *Introducing Molecular Electronics*, ed. by G. Cuniberti, G. Fagas, K. Richter (Springer, New York, 2005), Vol. vvv of Lecture Notes in Physics, p. xxx; Chap. 4 of this collection
24. N.D. Lang: Field-induced transfer of an atom between two closely spaced electrodes, Phys. Rev. B **45**, 13599–13606 (1992)
25. N.D. Lang: Erratum: Field-induced transfer of an atom between two closely spaced electrodes, Phys. Rev. B **51**, 2029(E) (1995)
26. N.D. Lang: Bias-induced transfer of an aluminum atom in the scanning tunneling microscope, Phys. Rev. B **49**, 2067–2071 (1994)
27. N.D. Lang: Resistance of atomic wires, Phys. Rev. B **52**, 5335–5342 (1995)
28. J. Jortner, A. Nitzan, M.A. Ratner: in *Introducing Molecular Electronics*, ed. by G. Cuniberti, G. Fagas, K. Richter (Springer, New York, 2005), Vol. vvv of Lecture Notes in Physics, p. xxx; Chap. 1 of this collection
29. P. Hänggi, S. Kohler, J. Lehmann, M. Strass: in *Introducing Molecular Electronics*, ed. by G. Cuniberti, G. Fagas, K. Richter (Springer, New York, 2005), Vol. vvv of Lecture Notes in Physics, p. xxx; Chap. 2 of this collection
30. R. Landauer: Conductance from transmission: Common sense points, Physica Scripta **T42**, 110–114 (1992)
31. R. Landauer: Electrical transport in open and closed systems, Zeitschrift fur Physik B– Condensed Matter **68**, 217–228 (1987)
32. J. Lagerqvist, Y.C. Chen, M. Di Ventra: Shot noise in parallel wires, Nanotechnology **15**, S459–S464(1) (2004)
33. M. Di Ventra, S. Pantelides: Hellmann-Feynman theorem and the definition of forces in quantum time-dependent and transport problems, Phys. Rev. B **61**, 16207 (2000)
34. T. Seideman: Current-driven dynamics in molecular-scale devices, J. Phys.-Condens. Matter **15**, R521–R549 (2003)
35. M. Di Ventra, Y.C. Chen, T.N. Todorov: Are current-induced forces conservative?, Phys. Rev. Lett. **92**, 176803 (2004)
36. Z. Yang, M. Di Ventra: Nonlinear current-induced forces in Si atomic wires, Phys. Rev. B **67**, 161311(R) (2003)
37. T.N. Todorov: Time-dependent tight binding, J. Phys.-Condens. Matter **13**, 10125–10148 (2001)
38. S.S. Sorbello: *Solid State Physics*, Vol. 51 (Academic Press, Inc., New York, 1998)
39. M. Di Ventra, S. Pantelides, N. Lang: Current-induced forces in molecular wires, Phys. Rev. Lett. **88**, 046801 (2002)
40. M. Di Ventra, N.D. Lang, S. Pantelides: Electronic transport in single molecules, Chem. Phys. **281**, 189 (2002)
41. Y.M. Blanter, M. Büttiker: Shot noise in mesoscopic conductors, Physics Reports **336**, 1–166 (2000)
42. Y.C. Chen, M. Di Ventra: Shot noise in nanoscale conductors from first principles, Phys. Rev. B **67**, 1553304 (2003)
43. S. Camalet, J. Lehmann, S. Kohler, P. Hänggi: Current noise in ac-driven nanoscale conductors, Phys. Rev. Lett. **90**, 210602 (2003)

44. R. Kubo, M. Toda, N. Hashitsume: *Statistical Physics II: Nonequilibrium Statistical Mechanics* (Springer, New York, 1992)
45. M. Büttiker: Scattering theory of thermal and excess noise in open conductors, Phys. Rev. Lett. **65**, 2901–2904 (1990)
46. W. Schottky: Über spontane stromschwankungen in verschiedenen elektrizitätsleitern, Annals of Physics **57**, 541 (1918)
47. N.D. Lang: Anomalous dependence of resistance on length in atomic wires, Phys. Rev. Lett. **79**, 1357–1360 (1997)
48. Y.C. Chen, M. Zwolak, M. Di Ventra: Local heating in nanoscale conductors, Nano Lett. **3**, 1691 (2003)
49. M.J. Montgomery, T.N. Todorov, A.P. Sutton: Power dissipation in nanoscale conductors, J. Phys.-Condens. Matter **14**, 5377–5389 (2002)
50. M.J. Montgomery, T.N. Todorov: Electron-phonon interaction in atomic-scale conductors: Einstein oscillators versus full phonon modes, J. Phys.-Condens. Matter **15**, 8781–8795 (2003)
51. D. Segal, A. Nitzan, W.B. Davis, M.R. Wasielewski, M.A. Ratner: Electron transfer rates in bridged molecular systems 2: A steady-state analysis of coherent tunneling and thermal transitions, J. Phys. Chem. B **104**, 3817–3829 (2000)
52. A. Troisi, M.A. Ratner, A. Nitzan: Vibronic effects in off-resonant molecular wire conduction, J. Chem. Phys. **118**, 6072–6082 (2003)
53. Z. Yang, M. Chshiev, M. Zwolak, Y. Chen, M. Di Ventra: Role of heating and current-induced forces in the stability of atomic wires, Phys. Rev. B **71**, 041402(R) (2005)
54. N. Agrait, C. Untiedt, G. Rubio-Bollinger, S. Vieira: Onset of energy dissipation in ballistic atomic wires, Phys. Rev. Lett. **88**, 216803 (2002)
55. K.R. Patton, M.R. Geller: Thermal transport through a mesoscopic weak link, Phys. Rev. B **64**, 155320 (2001)
56. R.H.M. Smit, C. Untiedt, J.M. van Ruitenbeek: The high-bias stability of monatomic chains, Nanotechnology **15**, S472–S478 (2004)
57. N.B. Zhitenev, A. Erbe, Z. Bao: Single- and multigrain nanojunctions with a self-assembled monolayer of conjugated molecules, Phys. Rev. Lett. **92**, 186805 (2004)
58. Y. Chen, M. Zwolak, M. Di Ventra: Inelastic current-voltage characteristics of atomic and molecular junctions, Nano Letters **4**, 1709–1712 (2004)

Single Electron Tunneling in Small Molecules

Maarten R. Wegewijs¹, Matthias H. Hettler², Christian Romeike¹, Axel Thielmann², Katja Nowack¹, and Jürgen König³

¹ Institut für Theoretische Physik A, RWTH Aachen, 52056 Aachen, Germany

² Forschungszentrum Karlsruhe, Institut für Nanotechnologie, 76021 Karlsruhe, Germany

³ Institut für Theoretische Physik III, Ruhr-Universität Bochum, 44780 Bochum, Germany

Abstract. We discuss current- and noise-spectroscopy of small molecules weakly coupled to electrodes using master equations. The Coulomb interaction and size quantization effect on the molecule restrict the transport to the tunneling of single electrons. We consider situations where orbital-, spin- or vibrational excitations localized on the molecule play a role or even dominate the transport. For each case, we analyze mechanisms which lead to negative differential conductance (NDC) and even total suppression of the current. The shot noise is shown to provide additional information due to its sensitivity to asymmetries in state- and electrode- specific tunnel couplings. Combined current-noise spectroscopy could be very useful for characterization of experiments.

1 Introduction

Non-linear electron transport through small molecules *weakly* coupled to electrodes and with coupling to a gate electrode has been realized in many recent experiments [1–5]. The control of transport via the gate voltage is an advantage of the electromigration technique [6] over other measurement setups. It is an essential tool for identifying the nature of non-linear conductance resonances [7]. Since excitations of different charge states shift differently with the gate voltage detailed information about the molecular states involved and coupling to the electrodes can be extracted. One of the main challenges in this field is the study of the many types of excitations localized on the molecule (electronic/orbital, spin, vibrational) under strongly non-equilibrium transport conditions due to the applied bias voltage. Low voltage phenomena such as Kondo-tunneling related to spin- and/or orbital degeneracy are also of interest but will not be considered here. In all these situations Coulomb interactions provide a large, important energy scale. We consider here molecules with size up to a few nanometers, which are considered as a “zero-dimensional” object, i.e. all quantum mechanical states are localized on the small object. As it is the quantitative nature of these molecular states that determines the electronic transport we require an exact description within the effective model chosen. This effective model must incorporate the degrees of freedom deemed relevant for a particular transport situation and molecule. In longer,

quasi one-dimensional molecules such as carbon nanotubes Coulomb interactions give rise to interesting effects discussed in Chaps. 9 and 14 of this book. We focus here on the situation where the molecule is weakly coupled to the external controlled reservoirs (electrodes and light-sources [8]) and external dissipative environments (mechanical or electromagnetic). Strong coupling phenomena such as Kondo-tunneling are discussed in [9, 10] and the references therein. We consider here only stationary non-equilibrium states resulting from time-independent external signals. Effects that appear in driven systems are discussed in Chap. 3. Neglecting Coulomb interactions one expects the tunneling current to increase with bias voltage since current contributions from the independent “transport channels” can simply be added. Coulomb interactions can prevent the simultaneous occupation of states on a molecule, thereby correlating the spin- and/or orbital “channels” and making states *compete* in the transport. Together with the Pauli principle they introduce magnetic interactions between electrons within the molecule, thereby effecting the transport through the total molecular spin. This can lead to two possible surprises: the current does not change *where* one would naively expect it to change (Coulomb blockade, spin blockade, phonon blockade, Kondo effect) or, the current changes *where* it is expected but in an *opposite* way (i.e. negative differential conductance (NDC) or current peaks). In the latter case, mechanisms which can only become effective at some finite voltage “trap” the molecule in a state from which it cannot easily escape. Such situations are the topic of this chapter. We first introduce the central ideas of current and noise spectroscopy and its description using master equations in Sect. 2. We then demonstrate how different types of excitations localized on a molecule may strongly influence the transport. These can be orbital excitations (Sect. 3), spin excitations (Sect. 4), or vibrational excitations (Sect. 5). In Sect. 6 we demonstrate that by combining the current- and shot noise-spectroscopy new insight can be gained in the transport effects discussed in Sects. 3–5.

2 Tunneling Transport

2.1 Current and Shot-Noise Spectroscopy

In Fig. 1a we depict the basic setup and the main effects which we consider. A small molecule is coupled by tunnel junctions to electrodes L , R and capacitively coupled to a gate electrode at potential V_g . The bias voltage is applied symmetrically, $\mu_L = \mu + V/2$, $\mu_R = \mu - V/2$.

The quantities of interest are the stationary current I and the shot noise S in dependence on applied voltages. Let E_N denote the ground-state energies for successive charge states of the molecule. At zero applied voltages and low temperature T the number of electrons on the molecule is determined by the maximal N for which $E_N - E_{N-1} < \mu$. For a given sample and

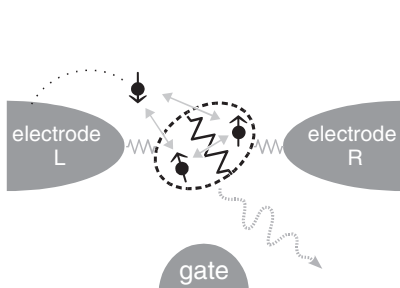


Fig. 1a. Molecular device: The extra electron strongly interacts with the electrons which are present, and must change the molecular spin precisely by $\Delta S = 1/2$. The molecule may exchange quantized vibrational energy with the electron (springs) or dissipate energy into the external environment

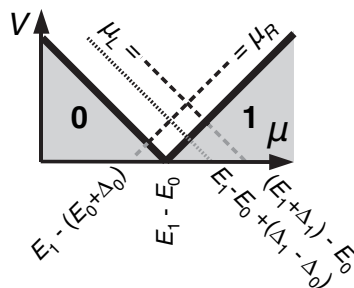


Fig. 1b. Stability diagram for $V > 0$: lines indicate the resonance condition for a transition between two ground (full) or excited states (dotted) and between one ground- and one excited state (dashed) In the gray areas the $N = 0$ or 1 ground state is stable and the excited states play no role

molecule this value is usually unknown since it depends on many uncontrollable details of the junction. By varying the gate voltage one uniformly shifts $E_N - E_{N-1} \propto V_g$ independent of N . One can simply search for the nearest charge-degeneracy point $E_{N+1} - E_N = \mu$ where an extra electron can enter and leave the molecule without energy cost. Here a current can flow at low bias. At low temperature the finite separation between subsequent degeneracy points causes linear transport to be suppressed except for discrete values of the gate voltage. The energy gaps are roughly determined by two major energy scales related to the molecule. First, the electrostatic interaction among electrons on the molecule gives a contribution $\propto N^2$ to E_N . The corresponding extra energy required for electron addition is $e^2/(2C)$, where C is the “capacitance” of the molecule (Coulomb blockade effect). Secondly, if the extra electron will occupy an unoccupied orbital, the orbital energy difference presents an additional energy barrier (size-quantization effect). Typical values of the addition energy gaps in experiments are 100 meV or larger. Recent experiments [5] indicate that for molecules other contributions to the addition energies show significant non-linear gate voltage dependence (in contrast to quantum-dot “artificial atoms”). This provides additional detailed information but in a first approximation can be neglected. At sufficiently high bias voltage excited states start to contribute to the transport. Whereas ground-state energies depend on robust features, excitations probe more detailed and sensitive properties of the molecule. In Sects. 3–6 we will present examples where such excitations dominate the transport completely. Here we show how they appear in current spectroscopy. An intensity plot of the nonlinear conductance dI/dV as a function of gate voltage V_g (or equivalently μ) and bias voltage V provides a concise map of the energetic conditions for a change in

the current (“stability diagram”). For symmetric junction capacitances the energies of the molecular states are independent of the symmetrically applied bias voltage and $E_{N+1} - E_N \propto V_g$. The current can change when an additional transition becomes allowed whereby an electron can enter the molecule from the left electrode or exit the molecule to the right electrode. This occurs whenever the bias voltage crosses a line in the (μ, V) diagram with negative or positive slope respectively. This situation is depicted in Fig. 1b near a single charge-degeneracy point $N = 0, 1$ where the lowest excited states lie at energies $E_N + \Delta_N$ and $\Delta_1 > \Delta_0$. The excitation lines only appear in the region where the ground-state transitions are already allowed, $\mu_L > E_1 - E_0$ and $E_1 - E_0 < \mu_R$.

The current-noise in dependence of V and V_g is of interest also. In contrast to the mean value of the measured current, the time-dependent fluctuations about this value can have various origins [11]. For experiments on nanostructured devices like molecules, the most dominant contribution to the current noise is $1/f$ -noise associated with fluctuations of the applied bias voltage, for example, induced by site fluctuations of atoms in the electrodes. The power spectrum of this noise contribution decays typically as a power law with the frequency f of the fluctuations. In addition to $1/f$ -noise, there is *shot noise* that is due to the fact that the electronic charge is quantized in units of $-e$. The shot noise is independent of the frequency to first order in f and is strongly dependent on the details of the electronic transport through the molecule [12]. It will therefore also change at the resonance lines Fig. 1b. For simple systems, the shot noise S is proportional to the average current $S \propto I$. Therefore, one often presents the so-called Fano factor $F = S/2eI$. The “poissonian value” of the shot noise $F = 1$ is reached, if the electrons that make up the current are uncorrelated. “Sub-poissonian noise”, $F < 1$, is generally expected for electrons due to Pauli exclusion principle [11]. E.g. for transport through two symmetric potential barriers without electron-electron interaction, one obtains $F = 1/2$. For transport through resonant tunneling diodes, one can observe “super-poissonian noise”, $F > 1$, above a bias threshold where negative differential conductance (NDC) is observed. In such situations, the electron transport is therefore noisy above the level one would expect from uncorrelated electrons. The Fano-factor in dependence of the voltages V and V_g thus is an important spectroscopic tool which contains extra information about correlations of the tunneling electrons.

2.2 Master Equations Current and Shot-Noise

We consider the minimal transport model $H = H_M + \sum_r H_r + H_T$ incorporating the molecule (M), reservoirs $r = L, R$ and the tunneling (T):

$$H_r = \sum_{k\sigma} \epsilon_{kr} a_{k\sigma r}^\dagger a_{k\sigma r} \quad (1)$$

$$H_T = \sum_{ki\sigma r} t_i^r a_{k\sigma r}^\dagger c_{i\sigma} + h.c. \quad (2)$$

We employ units $\hbar = k_B = 1$ and $-e$ is the electron charge. The molecular part H_M is chosen to contain the various strong interactions on the molecule which require an exact treatment. It will be discussed in detail in each section below. Generally, it is expressed in a basis of single-electron operators $c_{i\sigma}$ for orbitals on the molecule labeled by i and spin projection σ and operators relating to relevant internal vibrational coordinates. After diagonalization we can write $H_M = \sum_s E_s |s\rangle\langle s|$, where the discrete *molecular* many-body states have a summary label s which includes the total charge N , spin S , and other possible quantum numbers. Equation (1) models the electrodes $r = L, R$ as non-interacting quasi-particle reservoirs which are fixed at electro-chemical potential $\mu_r = \mu \pm V/2$ and temperature T . Here $a_{k\sigma r}$ are electron operators of electrode r labeled by k and spin σ . The density of states in the electrodes ρ_e is assumed to be flat around the Fermi-energy in order to focus on effects of the molecular part. This assumption may be too stringent for the energy scales of typical molecular systems but we want to suppress effects coming exclusively from the electronic structure of the electrodes. The tunneling term (2) describes charge transfer between electrode and molecule on a very small time scale. The level dependent coupling strength is characterized by the intrinsic line width $\Gamma_i^r = 2\pi|t_i^r|^2 \rho_e$. $\Gamma = \max \Gamma_i^r$ denotes the overall coupling strength (in units of energy) between electrodes and the molecule and serves to define the current scale. The molecular states may additionally be coupled to the electromagnetic field (photons) and/or a mechanical environment which dissipate the energy accumulated on the molecule due to the tunneling. Whereas this does not change the charge of the molecule, it does have an effect on the non-equilibrium distribution of the molecular states and may thereby strongly influence the current as we demonstrate in Sect. 3. We do not explicitly discuss here the coupling to such bosonic reservoirs since they are readily incorporated.

For the transport properties it is crucial to treat the strong Coulomb (and possibly other) interactions on the small molecule exactly. We therefore treat the tunneling to the reservoirs in a systematic perturbation theory in the electrode-molecule tunneling (2). The small parameter is Γ/T , a ratio of two time scales. $1/\Gamma$ is the typical time between two tunneling events and $1/T$ is the time scale on which the excitations created in the reservoirs by each of these tunneling events are thermalized. For $\Gamma \ll T$ we have *single-electron tunneling*: quantum-correlations between subsequent tunneling events [13] are not important here. The corresponding lowest order perturbation theory in Γ and couplings to dissipative environments leads to the master equations for the occupation probabilities p_s of molecular many-body states s . Obviously, this approach is limited by the necessity to have sufficiently weak

electrode-molecule coupling and/or high temperature. However, the important non-equilibrium effects involving the strong molecular interactions are captured correctly. Also, the results can be improved systematically by going to higher orders in Γ . Finally, in interpreting many experiments the lowest order result is at least the most useful starting point. Below we only summarize the equations necessary to compute the current and shot noise in lowest order perturbation theory in the coupling strengths Γ . Their systematic derivation using a diagrammatic technique has been discussed for the current in [14, 15] and extended for the noise in [12], see also Chap. 3. As the applied bias is static, the time derivative of the probabilities p_s vanishes in the stationary state. The stationary non-equilibrium probabilities p_s^{st} are uniquely determined by the transition rates $W_{ss'}$ from state s' to s (forming a matrix \mathbf{W}) through the stationary master equation $\mathbf{W}\mathbf{p}^{\text{st}} = \mathbf{0}$ together with the normalization $\sum_s p_s = 1$. The property $\sum_s W_{ss'} = 0$ guarantees the normalization of the distribution p_s for arbitrary times and the existence of a stationary state. We can then write

$$\mathbf{p}^{\text{st}} = (\tilde{\mathbf{W}})^{-1} \mathbf{v}, \quad (3)$$

where matrix $\tilde{\mathbf{W}}$ is identical to \mathbf{W} but with one (arbitrarily chosen) row s_0 replaced with (Γ, \dots, Γ) and \mathbf{v} is a vector, $v_s = \Gamma \delta_{ss_0}$. The transition rates $W_{ss'}, s \neq s'$ (in the absence of bosonic coupling) are the sum $W_{ss'} = \sum_r W_{ss'}^r$ of the Golden rule rates for the tunneling of an electron to/from electrode $r = L, R$:

$$W_{ss'}^r = 2\pi\rho_e \sum_\sigma \begin{cases} f_r^+(E_s - E_{s'}) \left| \sum_i t_i^r \langle s | c_{i\sigma}^\dagger | s' \rangle \right|^2 & N_{s'} < N_s \\ f_r^-(E_{s'} - E_s) \left| \sum_l t_l^r \langle s | c_{l\sigma} | s' \rangle \right|^2 & N_{s'} > N_s \end{cases} \quad (4)$$

were $f(x) = 1/(\exp(x/T) + 1)$ is the Fermi function, $f_r^+(x) = f(x - \mu_r)$ and $f_r^-(x) = 1 - f(x - \mu_r)$. The decay rates are $W_{ss} = -\sum_{s' \neq s} W_{ss'}$. The stationary current $I = \langle \hat{I} \rangle$ and the (zero-frequency) current-noise

$$S = \int_{-\infty}^{\infty} dt \langle \delta \hat{I}(t) \delta \hat{I}(0) + \delta \hat{I}(0) \delta \hat{I}(t) \rangle \quad (5)$$

are related to the current operator $\hat{I} = (\hat{I}_R - \hat{I}_L)/2$ and its fluctuation $\delta \hat{I}(t) = \hat{I}(t) - \langle \hat{I} \rangle$. We can use the symmetrized combination of currents $\hat{I}_r = -ie \sum_{ik\sigma} (t_i^r a_{k\sigma r}^\dagger c_{i\sigma} - h.c.)$ into electrode $r = L, R$ since in the stationary limit $\langle \hat{I}_R \rangle = -\langle \hat{I}_L \rangle$. The current and the noise can be explicitly calculated from the expressions

$$I = \frac{e}{2} \mathbf{e}^T \mathbf{W}^I \mathbf{p}^{\text{st}} \quad (6)$$

$$S = e^2 \mathbf{e}^T (\mathbf{W}^{II} \mathbf{p}^{\text{st}} + \mathbf{W}^I \mathbf{P} \mathbf{W}^I \mathbf{p}^{\text{st}}). \quad (7)$$

The vector \mathbf{e} is given by $e_s = 1$ for all s . The rates entering the current and noise expressions are

$$W_{ss'}^I = \pm(W_{ss'}^R - W_{ss'}^L), N_s \leq N_{s'} \quad (8)$$

$$W_{ss'}^{II} = \frac{1}{4}(W_{ss'}^R + W_{ss'}^L)(1 - 2\delta_{ss'}) \quad (9)$$

The matrix \mathbf{P} is a “normalized propagator” [12] which to lowest order in Γ can be expressed similar to (3)

$$\mathbf{P} = (\tilde{\mathbf{W}})^{-1}\mathbf{Q} \quad (10)$$

with $Q_{ss'} = (p_s^{\text{st}} - \delta_{ss'})(1 - \delta_{ss_0})$. It is of order Γ^{-1} , thus leading to a non-vanishing contribution of the second part in (7) even in lowest (first) order. The inclusion of dissipative environments (photons, phonons) will only modify the rates \mathbf{W} and thereby \mathbf{p}^{st} and \mathbf{P} (cf. (3), (10)), the rates \mathbf{W}^I and \mathbf{W}^{II} are not affected. Similar expressions for the calculation of current and noise were derived by other means by Hershfield et al. in [16] and Korotkov in [17].

3 Electronic Excitations of a Benzene Ring

To calculate the tunneling current through a benzene ring, we extract an effective model from electronic structure calculations. For benzene, transport is assumed to be dominated by the π -electron system, but generalizations are straightforward. We first perform Hartree-Fock calculations in a suitable basis and then transform the Hamiltonian to the molecular orbital basis. We then integrate out the σ electrons arriving at an effective *interacting* model Hamiltonian for the π electrons in the presence of the atomic cores and the “frozen” density of the σ electrons:

$$H_M = \sum_{ij\sigma} \epsilon_{ij} c_{\sigma i}^\dagger c_{\sigma j} + \sum_{ijkl\sigma\sigma'} U_{ijkl} c_{\sigma i}^\dagger c_{\sigma' j}^\dagger c_{\sigma' k} c_{\sigma l} \quad (11)$$

Operators $c_{\sigma i}^\dagger, c_{\sigma i}$ create/destroy electrons of spin σ in orthogonalized Wannier-like orbitals $\Phi_i, i = 1, \dots, 6$ centered at the carbon atoms. While this model neglects σ - π mixing for certain excited states of the molecule [18, 19], its parameters account for the detailed electronic structure of the molecule. We compute the model parameters only once. This neglects the higher order effect of electric field screening by σ electrons and its impact on the π electrons, however, we fully include screening by the π electrons (see below). We find that the low-energy spectrum of benzene obtained from the diagonalization of the effective Hamilton operator (11) compares favorably with the spectrum directly obtained from accurate multi-reference configuration interaction calculations [19, 20]. To account for the effect of an external potential drop along the transport (x -)direction on the electrons we include an external potential in the Hamiltonian:

$$H_{bias} = e \sum_{ij\sigma} V_{ij}^{\text{ext}} c_{\sigma i}^\dagger c_{\sigma j} \quad (12)$$

with $V_{ij}^{ext} = \int d\mathbf{r}\Phi_i(\mathbf{r})V^{ext}(\hat{\mathbf{r}})\Phi_j(\mathbf{r})$ and $V^{ext}(\hat{\mathbf{r}}) = [(\mu_L + \mu_R)/2e - (\mu_L - \mu_R)/e]\hat{\mathbf{r}}_x/L$ where $\mathbf{r} = 0$ is the center of the molecule. The length over which the external bias falls off is chosen $L = 0.4$ nm. The matrix elements V_{ij}^{ext} result from the same electronic structure calculation described above. We exactly diagonalize the many-electron Hamiltonian (11) in the finite basis (Wannier orbital per carbon site) to obtain the many-body eigenstates $|s\rangle$ with the corresponding energies E_s .

Tunneling contact and relaxation. For simplicity, we assume that tunneling is only possible through two “contact” carbon atoms which we choose to be at either the 1- and 4-(*para*-) positions or 1- and 3-(*meta*). When including relaxation by radiative transitions, we use the dipole approximation with dipole transition moments $\mathbf{d}_{i,j} = \int d\mathbf{r}\Phi_i(\mathbf{r})\hat{\mathbf{r}}\Phi_j(\mathbf{r})$ obtained from the electronic structure calculations. The corresponding transition rates are

$$W_{ss'}^d = \frac{4e^2}{3c^3}(E_s - E_{s'})^3 n(E_s - E_{s'}) |<s|\mathbf{d}|s'>|^2 \quad (13)$$

where $n(E) = 1/(e^{E/T} - 1)$ denotes the equilibrium Bose function [N.B. for emission $E_s - E_{s'} < 0$ and $n(-|E|) = -(1 + n(|E|))$]. We have chosen Γ such that $\Gamma \ll T \approx 25$ meV (room temperature) and that the maximum tunneling rate $W_{ss'}$ is about 0.15 meV (corresponding to 6 nA current). This is still about a factor of 5 larger than the maximum of the relaxation rates $W_{s,s'}^d$. However, the effect shown below does not depend on the ratio of rates within reasonable ranges.

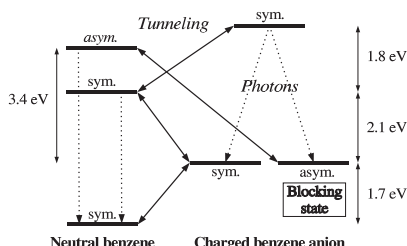


Fig. 2a. Relevant neutral and anion states: tunneling transitions and photon emission

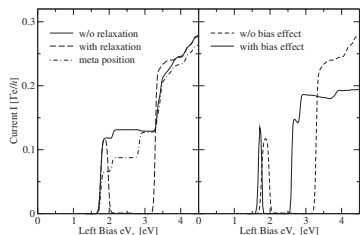


Fig. 2b. $I - V$ characteristics with (right) and without inclusion of bias effect (left)

Transport: NDC and blocking state. Without the effect of the applied field and radiative relaxation (solid line in left panel of Fig. 2b) the $I - V$ curve consists of a series of steps of which only a few are well resolved on this scale. The first step is associated with the population of the first π^* orbital of molecule (molecular charge = $-e$), see Fig. 2a. An electron hops onto the lowest available level and then hops off again. At slightly larger bias, a transition of the anion to the first excited state of the neutral molecule becomes

possible, resulting in a slight increase of the current. If the bias is sufficiently large this excited state may now accept another electron to populate higher excited states of the anion or low-lying states of the di-anion, resulting in a rapidly growing cascade of transitions between hundreds of states of the system. In the model considered here the growth of this cascade leads to quasi-ohmic behavior above 3.6 eV. In our calculation the first states of the di-anion become occupied at about 4.5 eV. The inclusion of radiative transitions has a dramatic effect on the $I - V$ curve (dashed line in left panel Fig. 2b). We observe a collapse of the current over a substantial range of the applied bias (2.1–3.4 eV). The reason for this collapse is the population of a “blocking” state in the cascade of transitions that becomes possible when excited states of the neutral molecule and anion become accessible. Above approximately 2.1 eV bias an excited state of the anion at about 5.6 eV (see Fig. 2a), becomes partially populated in the transport cascade. This state can decay by photon emission to either a symmetric or an antisymmetric many body state (with respect to the plane through the transport axis and perpendicular to the molecular plane) of the anion. In the bias range of the current collapse this state cannot decay by coupling to the leads, because the lowest neutral states are symmetric and the tunneling preserves the symmetry. Since there are no further radiative transitions possible on the molecule in the stationary state, the probability of occupying the “blocking” state is unity and the current ceases to flow. At a larger bias (3.4 eV) the system can decay to the first antisymmetric excited state of the neutral molecule, which can then decay further by photon emission. The solid line in the right panel of Fig. 2b shows the $I - V$ curve of the benzene with radiative relaxation and with the effect of the external potential applied parallel to the transport axis. The differential screening effects on all of the states in the cascade result in a significant renormalization of the $I - V$ curve since the various states couple differently to the applied field. However, the current collapse still occurs, although the voltage window is reduced. If we couple the right electrode at the *meta*-position of benzene we find no current collapse with/without relaxation or bias effect, see Fig. 2b, left panel, dash-dotted line. This can be readily understood by the fact that at the *meta*-position the wave function of the formerly blocking state is non-vanishing and electrons can tunnel out to the right electrode. Consequently, we observe a series of current steps similar (but not identical) to the case of coupling at the *para*-position without relaxation.

4 Spin Excitations of a [2 × 2] Grid Molecule

Single-molecular grid complexes [21] consist of rationally designed ligands and metal-ions which arrange by self-assembly. Each metal-ion is located at the contact point between two ligands, which provide a highly symmetric ligand cage. Low-temperature intramolecular metal-ion spin coupling [22, 23] as well as the electrochemical properties where the charge was reversibly

modulated [24] were successfully explained by considering the metal-ions and ligands as weakly coupled components. It is known [25] that the ligands as well as metal-ions can accept extra electrons, depending on synthetically controlled chemical details. We analyze a phenomenological model for such type of grid molecule consisting of four ions on a $[2 \times 2]$ grid connected by four bridging ligands as depicted in Fig. 3. For simplicity, we assume the metal-ion to exhibit a strong ligand field which splits the atomic d -shells into two subshells, of which the lower one is filled and the upper one is empty. For both ligands and metal-ions we retain one orbital per site but we account for their different nature. The Hamiltonian $H_M = H_t + H_l + H_m$ captures these features:

$$H_t = \sum_{\langle ij \rangle} \sum_{\sigma} t C_{i\sigma}^{\dagger} c_{j\sigma} + \text{h.c.} \quad (14)$$

$$H_l = \sum_j (\epsilon n_j + u n_{j\uparrow} n_{j\downarrow} + v n_j n_{j+1}) + w \sum_{j=1,2} n_j n_{j+2} \quad (15)$$

$$H_m = \sum_i (E N_i + U N_{i\uparrow} N_{i\downarrow}) \quad (16)$$

Here $c_{j\sigma}, n_{j\sigma} = c_{j\sigma}^{\dagger} c_{j\sigma}, n_j = \sum_{\sigma} n_{j\sigma}$ and $C_{i\sigma}, N_{i\sigma} = C_{i\sigma}^{\dagger} C_{i\sigma}, N_i = \sum_{\sigma} N_{i\sigma}$ refer to orbitals on the ligands and metal-ions respectively which are numbered cyclically by $j, i = 1, 2, 3, 4$. The ligand-part of the Hamiltonian (15) consists of an orbital energy ϵ , the short-range Coulomb repulsion terms on the ligand (u) and between adjacent (v) and the opposite ligands (w). Due to decreasing overlap with distance we have $u > v > w$, as is found in experiments [24]. Hamiltonian (16) describes the metal-ion orbitals with energy E and short-range interaction U on a single ion [d orbital overlap between neighboring ions can be typically neglected]. Figure 3 indicates the interactions schematically. The tunneling term (14) describes electron hopping within the molecule between nearest neighbor ($\langle ij \rangle$) ligand- and metal-ion redox centers. We consider the case $\epsilon < \epsilon + u < E < E + U$ where

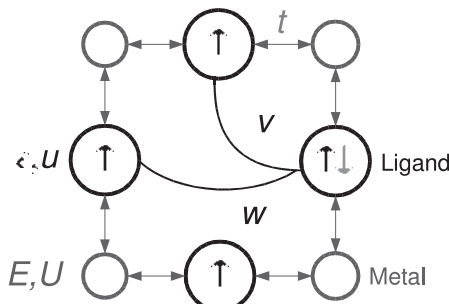


Fig. 3. Grid molecule: small and large circles represent metal-ion and ligand orbitals, respectively

the first eight extra electrons will occupy four equivalent ligand centered orbitals. Such a situation has been well-documented for a number of grid-molecules [24]. The metal ligand charge-transfer (MLCT) barrier is assumed to suppress the direct hopping of extra electrons on the ligands to unoccupied metal-ions: $\Delta = E - \epsilon \gg |t|$. However, fluctuations of the metal-orbital occupations allow these extra electrons to hop *between ligands* via intermediate metal-ion orbitals with an effective matrix element $t' = t^2/\Delta$. We can eliminate the charge degrees of freedom on the metal-ion sites by a Schrieffer-Wolff transformation [26] and obtain an effective 4-site model $H_{\text{Meff}} = -\sum_{\langle jk \rangle} \sum_{\sigma} t'/2 c_{j\sigma}^\dagger c_{k\sigma} + H_l$. Similar “ionic” or “double-shell” models have been studied in other contexts [10, 27–29]. When neglecting the hopping t' , the charging energies $u > v > w$ dictate that the first electron reduces one of the four ligands, say $j = 1$. The next one goes onto the opposite ligand 3 in order to minimize the Coulomb interaction. The next electrons reduce the adjacent ligands 2 and 4. For the next four electrons, ligand orbitals are doubly occupied in the same sequence. The gaps in the addition spectrum $w, 2v-w, w, u, w, 2v-w, w$ (*extra* energy required for the next electron) thus directly relate to the geometrical features of the grid [24]. We have calculated the exact eigenstates of the effective model for charges $N = 0 - 8$. The tunneling current was calculated assuming that electrons enter the molecule through two “contact” ligands, $j = 1, 3$. The variation of the ground-state spin as successive electrons are added to the ligands depends on the ratio of the short-range interaction strength and the hopping, u/t' , compared to a threshold value $r = r(v, w)$. The latter depends on the longer-ranged interactions only. We now discuss the two possible situations which can occur.

Maximal-spin ground state. For two special charge numbers of the molecule, $N = 3, 5$ the strong short-range Coulomb interaction u gives rise to the well-known Nagaoka effect [30]. Due to the suppression of double occupied ligand orbitals the set of lowest energy states must all have a single hole/electron relative to the half-filled state $N = 4$. It can only maximally gain kinetic energy when the background of the other electrons is fully spin polarized due to the Pauli principle. This highly charge sensitive ferromagnetic tendency competes with the antiferromagnetic spin coupling due to superexchange processes between neighboring ligand orbitals via metal-ions. For sufficiently large u and small t' such that $u/t' \geq r(v, w)$ the ground state spin for $N = 3, 5$ has the maximal value $S = 3/2$ supported by the extra electrons on the ligands. For even N the spin is $S = 0$ and for $N = 1, 7$ $S = 1/2$. The gap ΔE_{Nag} between the Nagaoka state and lowest excited state is of kinetic origin: it saturates for large u to a value proportional to t' . The hopping t' thus has to remain moderate in order to have an observable effect. Taking typical estimates for parameters [24], $u \approx 0.1\text{eV} = 4|t|$, $\Delta \approx 1\text{eV}$, hence $\Delta E_{\text{Nag}} \approx t' = t^2/\Delta \approx 0.1\text{meV} \approx 1\text{K}$. In Fig. 4aa the differential conductance exhibits *spin-blockade of tunneling* [31] due to the presence of a maximal-spin ground-state at selected charge numbers. Transport involving

groundstates with charge $N = 2 - 6$ is completely blocked for small bias and low temperature, $T, V < \Delta E_{\text{Nag}}$ and the Coulomb diamonds for $N = 2 - 6$ do not close. Even though the ground state transitions are energetically allowed, the rates are zero due the spin selection rule $\Delta S = 1/2$.

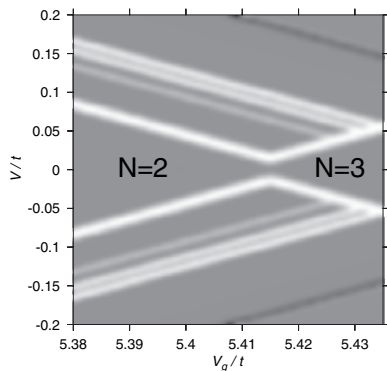


Fig. 4a. $dI/dV(V_g, V)$ grayscale plot (gray = 0, white/black $\gtrless 0$) for $u = 5t, v = 2.25t, w = t, \Delta = 20t, T = 2 \cdot 10^{-4}t$

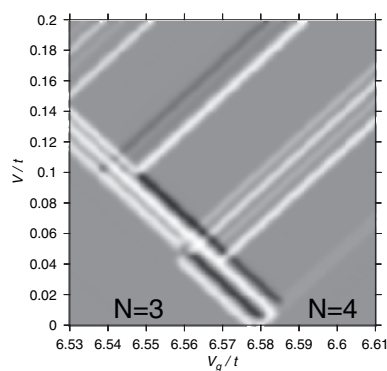


Fig. 4b. Same parameters as Fig. 4a except $u = 4.05t$ and around a different charge degeneracy point

Maximal-spin excited state. If the Coulomb interaction u is too small for fixed t' to stabilize a maximal spin ground state, the total spin alternates between $S = 0$ and $S = 1/2$ for even/odd number of electrons N . No spin blockade occurs. However, depending on the gate voltage, NDC and even complete current blocking can occur at finite bias voltage [31] when the Nagaoka state is the lowest spin-excitation at the special charge states $N = 3, 5$ (i.e. $u/t' \lesssim r(v, w)$). The typical result is depicted in Fig. 4b. Near the charge-degeneracy point two NDC lines (black) with negative slope appear which are due to the low lying $S = 3/2$ Nagaoka state. At the lower NDC line the Nagaoka excitation starts to populate the $N = 4, S = 1$ excited state thereby reducing the current. The Nagaoka state itself can only be populated via thermally activated tunneling. This indeed occurs already at low voltages due to a spin-related asymmetry in the transition rates: the Nagaoka state cannot decay to the $N = 4, S = 0$ ground state. Further away from the degeneracy point ($V_g/t \lesssim 6.56$ in Fig. 4b), the lower NDC line turns into a conductance peak. Simultaneously, the ground-state transition line below it disappears. This is related to a complete population inversion among the $N = 3$ molecular states: the Nagaoka excited state becomes *fully* occupied at the expense of the $S = 1/2$ ground state. This already occurs at low voltage in Coulomb blockade regime. The upper NDC line is caused by the occupation of the high lying maximal-spin state $N = 4, S = 2$ since it cannot decay to states with one electron less and higher spin [31]. Only due the presence

of the low-lying Nagaoka state $S = 3/2$ at $N = 3$ this state can be reached already at low voltages.

5 Vibrational Excitations and Multiple Orbitals

We now consider a molecule with two electron-accepting orbitals $i = 1, 2$ with energies ϵ_i ($n_{i\sigma} = c_{i\sigma}^\dagger c_{i\sigma}$, $n_i = \sum_\sigma n_{i\sigma}$):

$$H_M = \sum_{i=1,2} \epsilon_i n_i + \omega(b^\dagger b + 1/2) + \omega \sum_{i=1,2} \lambda_i n_i (b^\dagger + b) \quad (17)$$

We have not written in (17) terms corresponding to the largest energy scale in the problem, the short-range Coulomb interactions on and between the orbitals (see Sect. 6). Here they can be taken into account correctly by excluding doubly occupied states (di-anion) from the many-electron basis states, $\sum_i n_i \leq 1$, and accounting for spin degeneracy. We can then simply discuss two charged electronic states, labeled by the occupied orbital $i = 1, 2$, with excitation energy $\Delta = \epsilon_2 - \epsilon_1$ and a neutral state labeled $i = 0$. We consider the situation where both charged states of the molecule couple to a single internal vibrational mode with frequency ω and coordinate $Q = (b + b^\dagger)/\sqrt{2}$ normalized to the nuclear zero-point motion by $(M\omega)^{-1/2}$ (M = nuclear mass involved). Here b^\dagger excites the vibrational mode by one quantum ω . When the molecule is charged by occupying orbital $i = 1, 2$ the harmonic adiabatic potential for the nuclear motion shifts relative to the neutral state by $\delta Q = \sqrt{2}\lambda_i$. The dimensionless Huang-Rhys factors [32] λ_i measure whether the distortion of the nuclear equilibrium geometry is small ($\lambda_i < 1$) or large ($\lambda_i > 1$) relative to the quantum fluctuations of the positions of the nuclei. The related energy scale is the increase in the elastic energy $\omega\lambda_i^2$ if one would keep the nuclear geometry fixed when adding an electron to orbital i . We diagonalize the molecular Hamiltonian (17) by the standard Lang-Firsov [33] unitary transformation $U = \prod_{i=1,2} (X_i)^{n_i}$, $X_i = e^{-\lambda_i(b^\dagger - b)}$ and obtain $H'_M = \sum_i \epsilon'_i n_i + \omega(b^\dagger b + \frac{1}{2})$. We will label the lowest of the renormalized energies, $\epsilon'_i = \epsilon_i - \omega\lambda_i^2$, by $i = 1$ and the excited state by $i = 2$ i.e. by definition $\Delta' = \epsilon'_2 - \epsilon'_1 = \Delta + \omega(\lambda_1^2 - \lambda_2^2) > 0$. Here we demonstrate the most salient features which appear when the couplings are asymmetric, $\lambda_1 \gg 1 \gg \lambda_2$, and the renormalized excitation energy is small, $\Delta' \lesssim \omega$. In this limit the “bare” electronic excitation energy Δ is comparable in magnitude with the elastic energy change of the strongly coupled state 1, but opposite in sign: $\Delta \sim -\omega\lambda_1^2 < 0$. The electrode-molecule tunneling (2) now reads: $H_T = \sum_{kior} t_i^r X_i a_{k\sigma r}^\dagger \bar{c}_{i\sigma} + h.c.$ Here $\bar{c}_{i\sigma}^\dagger$ creates a polaron state i_0 with vibrational excitations i_q , $q = 1, 2, \dots$. We assume tunneling rates independent of orbital and electrode: $\Gamma_i^r = 2\pi|t_i^r|^2 \rho_e = \Gamma$. An electron entering the molecule will induce all possible transitions $0_q \rightarrow i_q$ due to the nuclear translation operators X_i . The occupation probabilities p_q^i , $i = 0, 1, 2$ ($\sum_q \sum_{i=0,1,2} p_q^i = 1$)

are calculated from the master (3) with transition rates

$$W_{iq \leftarrow 0q'}^r = \Gamma_{qq'}^i f_r^+(\mu_{q-q'}^i), W_{0q \leftarrow iq'}^r = \Gamma_{qq'}^i f_r^-(\mu_{q'-q}^i) \quad (18)$$

Energy conservation for the transition $i_{q'} \leftarrow 0_q$ is incorporated through the addition energies $\mu_{q'-q}^i = \epsilon'_i + (q' - q)\omega$, which only depend on the *change* in vibration number $q' - q$. The linear shift of the levels ϵ'_i with gate voltage is accounted for by varying μ relative to μ_0^1 . The tunneling rates $\Gamma_{qq'}^i$ depend on both q and q' individually through the Franck-Condon reduction factors [34]: $\Gamma_{qq'}^i / \Gamma = \Gamma_{q'q}^i / \Gamma = |\langle q | X_i | q' \rangle|^2$ which are only appreciable for $q, q' \sim \lambda_1^2$. Since $\lambda_2^2 \ll 1$, all transitions to state 2 which do not conserve the vibrational number are exponentially suppressed with $|q' - q|$. The remaining transitions with $q = q'$ all become allowed at the same energy. Since $\lambda_1^2 \gg 1$, transitions which change the vibrational number by as much as $\sim \lambda_1^2$ are possible. The envelope of the rapid variations of the rates with q, q' varies on the scale λ_1^2 set by the elastic energy. Importantly, this envelope initially *increases exponentially* for $q, q' \ll \lambda_1^2$. The resulting $dI/dV(\mu, V)$ map Fig. 5a and $I-V$ curves Figs. 5c, 5d exhibit a rich structure due to the vibrational excitations. For comparison we plot in Figs. 5c, 5d the analytic result we obtained in the limit of complete relaxation of the vibrational distribution before each tunneling event (due to some dissipative environment). The current shows a finite gap $\geq \Delta'$ at any gate voltage, which signals the large change of the ground state nuclear geometry upon charging the molecule. In the region where the excited state 2 is not yet accessible, $\mu_0^2 > \mu_L > \mu_0^1$ and $\mu_0^1 > \mu_R$ in Fig. 5b, the only allowed transitions $1_0 \leftrightarrow 0_0$ have exponentially small Franck-Condon factors, $\Gamma_{00}^1 \ll \Gamma$, leading to the current gap. At finite voltages above the gap, $V > \Delta'$, the order in which transitions become allowed depends on the gate voltage and gives rise to basically three different situations labeled I-III in Fig. 5b.

Ground state trapping (I). In the “fuzzy” region on the right in Fig. 5a, $\mu_L > \mu_0^2$ and $\mu > \mu_0^2$, a current could be expected to flow since $2_{q'} \leftrightarrow 0_q$ and $1_{q'} \leftrightarrow 0_q$ are energetically allowed for several q, q' . Instead the current is strongly suppressed. Due to the more positive gate voltage state 1_0 has more transitions which populate it than those which “drain” it. One always returns to the state 1_0 via a cascade of transitions such as $1_0 \leftrightarrow 0_0 \leftrightarrow 1_1 \leftrightarrow 0_1 \leftrightarrow \dots \leftrightarrow 1_{q-1} \leftrightarrow 0_{q-1} \leftrightarrow 1_q \leftrightarrow 0_q \rightarrow 1_0$ where the inverse of the last transition, $0_q \leftarrow 1_0$, is not allowed for sufficiently large q , see Fig. 5a. The rates of these few extra transitions populating the state are *exponentially larger* than all escape rates due to the Franck-Condon factors. This “feedback” loop of transitions keeps state 1_0 fully occupied with increasing bias. This is the basic mechanism whereby vibrational excitations dominate the transport.

Isolated region (II). The small diamond-shaped region in Fig. 5a isolated at finite voltages $\Delta' < V < 2\omega$ is remarkable. Inside it the current is non-zero and along its four defining boundaries the current is completely suppressed. This region can be understood by considering the truncated set of states

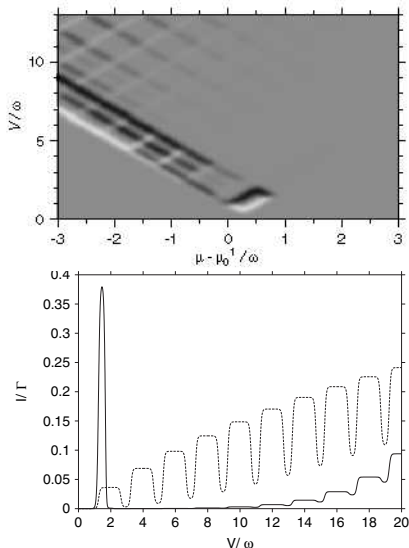


Fig. 5a. $dI/dV(\mu, V)$ in grayscale (gray = 0, white/black ≥ 0) for $\lambda_1 = 5, \lambda_2 = 0.1, \Delta'/\omega = 0.5, T/\omega = 0.025$

Fig. 5c. $I(V)$ for $\mu - \mu_0^1 = 0.625\omega$ in Fig. 5a, for non-equilibrium (full) and equilibrium vibrations (dashed)

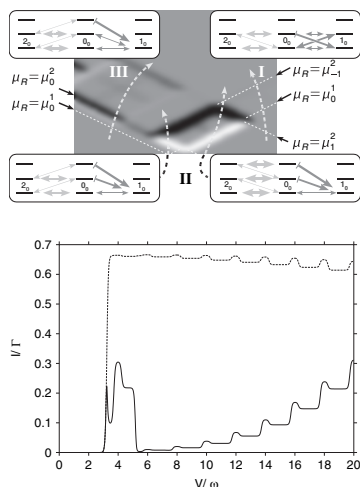


Fig. 5b. Low bias region of Fig. 5a and “feedback” cascades of vibration-assisted transitions

Fig. 5d. Same as Fig. 5c but for $\mu - \mu^1 = -1.125\omega$. Notice the initial sharp current peak

$0_0, 0_1, 2_0, 2_1$ and 1_0 , see Fig. 5b. The current suppression at the low bias side is due to Coulomb blockade and the Franck-Condon suppression factors discussed above. Inside the region only the transitions $2_0 \leftrightarrow 0_0 \leftrightarrow 1_0$ are allowed and we find: $p_0^0 \approx 1/5, p_0^1 \approx p_0^2 \approx 2/5$. The transitions to and from the charged state 2_0 are solely responsible for the current: $I \approx \Gamma_{00}^2 p_0^2 \approx 2/5\Gamma$. The strong current suppression defining the region at higher voltage occurs when either $2_0 \rightarrow 0_1$ (NDC line with positive slope) or $0_0 \rightarrow 2_1 \rightarrow 0_1$ (NDC line with negative slope) becomes allowed. A second transition $0_1 \rightarrow 1_0$ can then rapidly populate the state 1_0 . The reverse transition $0_1 \leftarrow 1_0$ is not allowed at low temperature $T \ll \Delta' - \omega$. This brings us back to the low-current “fuzzy region” discussed above.

Current peak (III). Another remarkable feature is the current *peak* along the resonance line $\mu_L = \mu_0^2$ (white/black double line on the left in Fig. 5a). Here state 2_0 becomes accessible and strongly competes with state 1_0 in a small energy window. The current first rises as expected in Fig. 5d when approaching from $\mu_L - \mu_0^2 \sim -T$ since the small transition rate $W_{20 \leftarrow 00}^L$ has already increased sufficiently to enhance the current over the low value $\sim \Gamma_{00}^1$ supported by the transitions $1_0 \leftrightarrow 0_0$ alone. However, this transition rate has not reached its maximum value $\Gamma_{00}^2 \gg \Gamma_{00}^1$. The “feedback” loops such as $0_0 \leftrightarrow 2_0 \leftrightarrow 0_1 \rightarrow 1_0$ are not thus not relevant yet, since the vibrationally

excited states are barely occupied. This is no longer the case at the falling side of the peak, $\mu_L - \mu_0^2 \sim T$, where the vibrational distributions p_q^2, p_q^0 are sufficiently driven out of equilibrium. The “feedback” starts to trap the molecule in the strongly coupled state 1_0 and reduces the current again, producing a sharp peak in Fig. 5d. The current is completely suppressed once the transition $0_0 \rightarrow 2_1$ also becomes allowed. All above strong NDC effects are not possible in a single-orbital model [35] and its generalization to degenerate orbitals [36] as long as the coupling to the vibration is voltage-independent (compare [37]).

6 Current Noise (Shot Noise)

We discuss current and shot noise for the transport model (1) and (2), taking a molecular Hamiltonian with two non-degenerate orbitals with excitation energy $\Delta = \epsilon_2 - \epsilon_1$ (compare (15), (17)):

$$H_M = \sum_{i\sigma} \epsilon_i n_{i\sigma} + \sum_i u n_{i\uparrow} n_{i\downarrow} + v n_1 n_2 , \quad (19)$$

We consider electronic energy scales where the molecule can acquire 16 possible states: each orbital can be either unoccupied, occupied with spin \uparrow or \downarrow , or doubly occupied. We thus have to write explicitly the “on-site” Coulomb interaction u and inter-orbital Coulomb repulsion v (implicitly included in Sect. 5). The largest tunnel coupling $\Gamma = \max \Gamma_i^r$ sets the current scale and we consider the weak coupling regime with temperature $T = 10\Gamma$. The Fano factor or noise-to-current-ratio $F = S/2eI$, provides additional information about transport properties, not contained in the $I - V$ characteristics alone. Therefore, we are interested in studying its dependence on the various couplings to the electrodes in order to draw conclusions about the size of these parameters for a given experiment. For a single orbital model with interaction u (i.e only $i = 1$ term in (19)) a comprehensive study of the shot noise and the Fano factor is given in [12]. Here, we consider a situation where the competition of transport through the two molecular orbitals gives rise to NDC and its connection to super-poissonian noise. We choose the energy parameters of the molecule Hamiltonian as $\epsilon_1 = 0.5\text{eV}$, $\epsilon_2 = 1.5\text{eV}$, $u = 3.5\text{eV}$, $v = 2\text{eV}$. Here ϵ_i is defined relative to μ for symmetric bias $\mu_r = \mu \pm V/2$, $r = L, R$. The molecule is uncharged at zero bias, since the addition energy to occupy the first molecular orbital is $\epsilon_1 = 0.5\text{ eV}$ (doublet D_1). In contrast to the single orbital system discussed in [12] we find an NDC regime, see Fig. 6a, in dependence on the different coupling strengths between the molecular orbitals and the reservoirs, as was previously discussed in [38, 39]. The shot noise behaves qualitatively similar to the current, the important quantitative details are discussed in the following.

Current and NDC. If we choose equal tunnel couplings, $\Gamma_i^r = \Gamma$ (solid line in Fig. 6a, with $\Gamma = 2.5\text{ meV}$), we find that current and shot noise S

increase, each time, as a new transport “channel” (controlled by the excitation energies) opens. This leads to plateaus, separated by thermally broadened steps. The first four plateaus are shown and discussed in the following. At a bias voltage of 1 V, sequential transport through the doublet D_1 with one electron on the lower lying orbital becomes possible. At 3 V, additionally transport through the doublet D_2 opens up, with the upper orbital being occupied with one electron. For a bias voltage above 5 V, transport channels with two or more electrons on the molecule open up. The different regions of interest are labeled by I_i, S_i with $i = 0, 1, 2$. All results in Figs. 6a, 6b are normalized to the values $I_{\max} = e2\Gamma$ and $S_{\max} = e^22\Gamma$ reached in the large-bias regime (not indicated in the plots) for symmetric coupling.

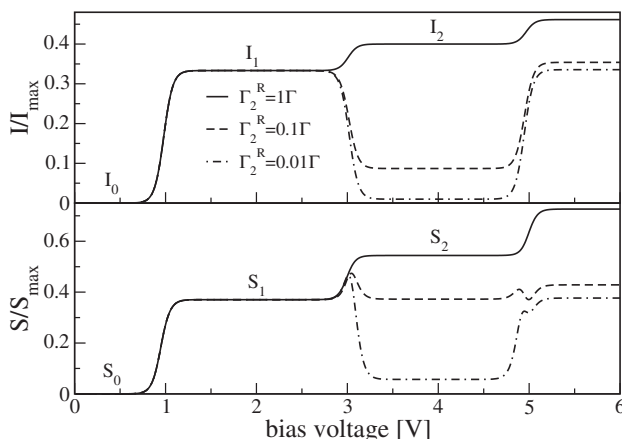


Fig. 6a. Current I and shot noise S vs. bias voltage

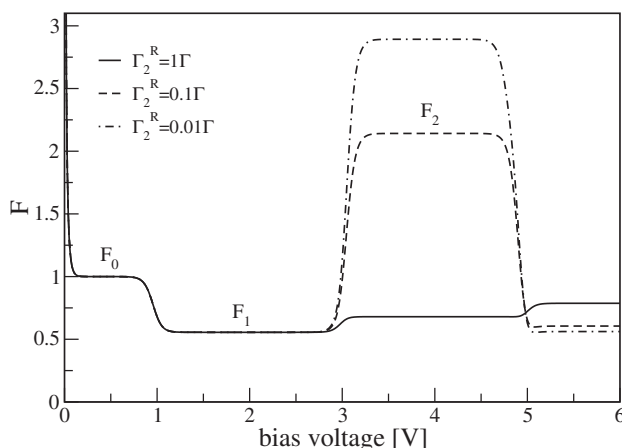


Fig. 6b. Fano factor F vs. bias voltage for the same parameters as in Fig. 6a

If now the coupling parameter Γ_2^R is reduced with respect to the other couplings, the current and shot noise are suppressed in region 2. This results in NDC at the threshold of 3V where the doublet D_2 becomes relevant, see Fig. 6a for $\Gamma_2^R = 0.1\Gamma$ and 0.01Γ . The reason for the NDC is a combination of the Pauli principle, Coulomb blockade and suppressed coupling, as discussed in Sect. 3 and [38, 40]. In our case, an electron, entering the upper molecular orbital from the left electrode, cannot leave the molecule, if the coupling of this orbital to the right electrode is entirely suppressed. Transport through the lower molecular orbital is also not possible, since the simultaneous occupation of both orbitals is energetically forbidden in the considered bias regime. The electron gets stuck in the upper molecular orbital blocking other electrons from tunneling through the molecule. Consequently, the current collapses. Since in lowest-order perturbation theory in Γ the plateau *heights* are given by the coupling parameters only, we find, that for $\Gamma_2^R < 2/3\Gamma$ NDC can be observed, whereas the shot noise is suppressed below its lower bias plateau only, if $\Gamma_2^R < 0.1\Gamma$. This difference can already give a rough idea about the coupling strength Γ_2^R for a given set of current and noise measurements. If the shot noise is sufficiently suppressed in the NDC region, a *peak* in the shot noise appears around the resonance energy of the second orbital. This peak is due to temperature induced fluctuations that in certain situations enhance the shot noise over the surrounding plateau values (where temperature fluctuations are exponentially suppressed). As the resonance is approached from lower bias, within the range of temperature broadening the noise “detects” the opening of the second transport channel and increases. If the bias is beyond the resonance, the redistribution of occupation has taken place and the noise is algebraically suppressed. The result is the observed peak with a width that scales with temperature. However, the peak height is only determined by the coupling parameters and is independent of the temperature. For the considered model the current does not show such a peak, as it usually decreases proportional due to the loss of occupation of the first orbital, the transport channel with “good” coupling. However, see Sect. 5 for situations where also peaks in the current can appear.

Fano factor, super-poissonian noise. The effect of NDC on the Fano factor, which is given by $F = S/2eI$, is shown in Fig. 6b. At small bias, $eV \ll T$, the noise is dominated by thermal noise, described by the well known hyperbolic cotangent behavior which leads to a divergence of the Fano factor [11, 41]. The plateau for bias voltages below 1V (region 0) corresponds to the Coulomb blockade regime, where transport is exponentially suppressed. In the regions 1 (2) transport through the state D_1 (D_2) is possible. The suppressed coupling strength Γ_2^R does not affect the plateau height F_1 , whereas F_2 reaches values larger than 1, and up to 3 [39]. This “super-poissonian” noise ($F > 1$) is predicted for $\Gamma_2^R < 0.44\Gamma$. If the bias is larger than 5V tunneling through states is allowed where both orbitals are occupied simultaneously, i.e. the molecule can be doubly occupied. The Fano factor is sub-poissonian again ($F < 1$)

in this regime. Comparing the Figs. 6a and 6b graphically allows one to determine roughly the strength of the suppression of Γ_2^R . In general, however, depending on the underlying energy parameters (giving the ordering of a sequence of plateaus) and the coupling parameters (giving their height) other values for the Fano factor are possible. In the Coulomb blockade regime (region 0), for example, there can also be super-poissonian noise, if both orbital energies lie below the equilibrium Fermi energy. Super-poissonian noise is also possible for a single orbital, if the spin degeneracy is lifted by a magnetic field (in the Coulomb blockade regime) or by ferromagnetic leads, see [42–45]. The energy and coupling parameters can be fully determined only by considering several transport regimes, e.g. by application of a gate voltage.

7 Conclusions

We have presented several examples of current suppression effects ultimately related to Coulomb interactions on small molecules. We found that the decay of electronic excitations on a conjugated molecular ring via *spontaneous emission* can result in strong NDC and current collapse over a significant voltage window. The emitted photon changes the symmetry of the electronic state of the charged molecule and thereby switches off the current. The true many-particle features and symmetry properties of the π electron-states of the molecule were shown to be of central importance. For a grid type molecule we have shown that interaction effects can lead to a charge-switchable large molecular spin due to the *Nagaoka mechanism*. Such a maximal spin state as ground-state (or low-lying excitation) shows up in spin-blockade of the tunneling current (or NDC). The relevance of the Nagaoka mechanism in the context of band-magnetism is limited by this extreme charge sensitivity. In single molecule devices, one can modulate the total charge with single-electron precision by a gate voltage [1, 2] due to the Coulomb blockade effect. Even more pervasive NDC effects were found for a molecule with two competing non-degenerate orbitals coupled to the same vibrational mode of a molecule. The accumulation of vibrational energy eventually traps the molecule in the state most strongly coupled to the vibration, reducing or even totally suppressing the current. Interestingly, this vibration related NDC does not require electrode- or electronic-state- specific asymmetries in the tunneling rates nor complex many-particle spin-effects. It is due to the *intramolecular* electron-vibration coupling and may therefore be more amendable to “molecular engineering”. Finally, the analysis of the shot noise of the electronic current revealed that it gives information about the various tunneling parameters that are difficult to control in experiments and hard (if at all) to determine from the current alone. *Current-noise* spectroscopy can allow the determination of a complete set of parameters for a given effective model. This would lead to a much better characterization of experiments, and in

turn make possible meaningful comparisons of experiments with the same molecule but widely differing measurement setups.

Acknowledgments

We acknowledge stimulating collaborations and discussions with Wolfgang Wenzel, Herbert Schoeller, Philipp Stampfuß, Jens Kortus, Mario Ruben and Karsten Flensberg.

References

1. H. Park, J. Park, A.K.L. Lim, E.H. Anderson, A.P. Alivisatos, P.L. McEuen: Nanomechanical oscillations in a single- C_{60} transistor, *Nature* **407**, 57 (2000)
2. J. Park, A.N. Pasupathy, J.I. Goldsmith, C. Chang, Y. Yaish, J.R. Petta, M. Rinkoski, J.P. Sethna, H.D. Abruna, P.L. McEuen, D.C. Ralph: Coulomb blockade and the Kondo effect in single-atom transistors, *Nature* **417**, 722 (2002)
3. A.N. Pasupathy, J. Park, C. Chang, A.V. Soldatov, S. Lebedkin, R.C. Bialczak, J.E. Grose, L.A.K. Donev, J.P. Sethna, D.C. Ralph, P.L. McEuen: Vibration-assisted electron tunneling in C140 single-molecule transistors, *Nano Lett.* **5**, 203 (2005)
4. W. Liang, M.P. Shores, M. Bockrath, J.R. Long, H. Park: Kondo resonance in a single-molecule transistor, *Nature* **417**, 725 (2002)
5. G. Lientschnig: Simulating Hybrid Circuits of Single-Electron Transistors and Field-Effect Transistors, Ph.D. thesis, TU Delft (2003)
6. H. Park, A.K.L. Lim, A.P. Alivisatos, J. Park, P.L. McEuen: Fabrication of metallic electrodes with nanometer separation by electromigration, *Appl. Phys. Lett.* **75**, 301 (1999)
7. L. Kouwenhoven, C. Marcus, P. McEuen, S. Tarucha, R. Westervelt, N. Wingreen: Electron transport in quantum dots, *Mesoscopic Electron Transport* (Kluwer, 1997), p. 105
8. D. Dulic, S.J. van der Molen, T. Kudernac, H.T. Jonkman, J.J.D. de Jong, T.N. Bowden, J. van Esch, B.L. Feringa, B.J. van Wees: One-Way Optoelectronic Switching of Photochromic Molecules on Gold, *Phys. Rev. Lett.* **91**, 207402 (2003)
9. M. Pustilnik, L. Glazman: Kondo effect in quantum dots, *J. Phys. Condens. Matter* (2004)
10. T. Kuzmenko, K. Kikoin, Y. Avishai: Kondo effect in systems with dynamical symmetries, *Phys. Rev. B* **69**, 195109 (2004)
11. Y.M. Blanter, M. Büttiker: Shot Noise in Mesoscopic Conductors, *Phys. Rep.* **336**, 1 (2000)
12. A. Thielmann, M.H. Hettler, J. König, G. Schön: Shot noise in tunneling transport through molecules and quantum dots, *Phys. Rev. B* **68**, 115105 (2003)
13. G. Ingold, Y.V. Nazarov: Charge Tunneling Rates in Ultrasmall Junctions, *Single Charge Tunneling* (Plenum Press, New York, 1992)

14. J. König, H. Schoeller, G. Schön: Zero-bias anomalies and boson-assisted tunneling through quantum dots, *Phys. Rev. Lett.* **76**, 1715 (1996)
15. J. König, J. Schmid, H. Schoeller, G. Schön: Resonant tunneling through ultrasmall quantum dots: Zero-bias anomalies, magnetic-field dependence, and boson-assisted transport, *Phys. Rev. B* **54**, 16820 (1996)
16. S. Hershfield, J.H. Davies, P. Hyldgaard, C.J. Stanton, J.W. Wilkins: Zero-frequency current noise for the double-tunnel-junction Coulomb blockade, *Phys. Rev. B* **47**, 1967 (1993)
17. A.N. Korotkov: Intrinsic noise of the single-electron transistor, *Phys. Rev. B* **49**, 10381 (1994)
18. B.O. Roos, K. Andersson, M.P. Fülscher: Towards an accurate molecular orbital theory for excited states: the benzene molecule, *Chem. Phys. Lett.* **192**, 5 (1992)
19. T. Hashimoto, H. Nakano, K. Hirao: Theoretical study of valence and Rydberg excited states of benzene revisited, *J. Mol. Struct.* **451**, 25 (1998)
20. P. Stampfuß, W. Wenzel: The parallel implementation of configuration-selecting multireference configuration interaction method, *J. Comput. Chem.* **20**, 1559 (1999)
21. M. Ruben, J. Rojo, F. Romero-Salguero, L. Uppadine, J.M. Lehn: Grid-type metal ion architectures: Functional metallosupramolecular arrays, *Angew. Chem. Int. Ed.* (2004)
22. O. Waldmann, J. Hassmann, P. Müller, G.S. Hanan, D. Volkmer, U.S. Schubert, J.M. Lehn: Intramolecular Antiferromagnetic Coupling in Supramolecular Grid Structures with Co^{2+} Metal Centers, *Phys. Rev. Lett.* **78**, 3390 (1997)
23. O. Waldmann, M. Ruben, U. Ziener, J.M. Lehn: *Europhys. Lett.* preprint
24. M. Ruben, E. Breuning, M. Barbouï, J.M. Gisselbrecht, J.M. Lehn: *Chem. Eur. J.* **9**, 291 (2003)
25. A.A. Vlček: *Coord. Chem. Rev.* p. 39 (1982)
26. J.R. Schrieffer, P.A. Wolff: Relation between the Anderson and Kondo Hamiltonians, *Phys. Rev.* **149**, 491 (1966)
27. J. Torrence, J. Vazques, J. Mayerle, V. Lee: Discovery of a Neutral-to-Ionic Phase Transition in Organic Materials, *Phys. Rev. Lett.* **46**, 253 (1981)
28. S. Ishihara, T. Egami, M. Tachiki: Enhancement of the electron-lattice interaction due to strong electron correlation, *Phys. Rev. B* **49**, 8944 (1994)
29. K. Kikoin, Y. Avishai: Double quantum dot as a spin rotator, *Phys. Rev. B* **65**, 115329 (2002)
30. Y. Nagaoka: Ferromagnetism in a Narrow, Almost Half-Filled s Band, *Phys. Rev.* **147**, 392 (1966)
31. D. Weinmann, W. Häusler, B. Kramer: Spin Blockades in Linear and Nonlinear Transport through Quantum Dots, *Phys. Rev. Lett.* **74**, 984 (1995)
32. K. Huang, A. Rhys: *Proc. Roy. Soc. London Ser. A* **204**, 406 (1950)
33. I.G. Lang, Y.A. Firsov: *Sov. Phys. JETP* **16**, 1301 (1963)
34. G. Mahan: *Many-Particle Physics* (Plenum, 1990)
35. D. Boese, H. Schoeller: Influence of nanomechanical properties on single-electron tunneling: A vibrating single-electron transistor, *Eur. Phys. Lett.* **54**, 668 (2001)
36. A. Mitra, I. Aleiner, A.J. Millis: Phonon effects in molecular transistors: Quantal and classical treatment, *Phys. Rev. B* **69**, 245302 (2004)
37. K.D. McCarthy, N. Prokoféev, M.T. Tuominen: Incoherent dynamics of vibrating single-molecule transistors, *Phys. Rev. B* **67**, 245415 (2003)

38. M. Hettler, H. Schoeller, W. Wenzel: *Nano-Physics and Bio-Electronics: A New Odyssey* (Elsevier, Amsterdam, 2002), pp. 303–322
39. G. Michalek, B.R. Bulka: Current and shot noise in two capacitively coupled single electron transistors with an atomic sized spacer, *Eur. Phys. J. B* **121**, 28 (2002)
40. M.H. Hettler, W. Wenzel, M.R. Wegewijs, H. Schoeller: Current Collapse in Tunneling Transport through Benzene, *Phys. Rev. Lett.* **90**, 076805 (2003)
41. E.V. Sukhorukov, G. Burkard, D. Loss: Noise of a quantum dot system in the cotunneling regime, *Phys. Rev. B* **63**, 125315 (2001)
42. A. Cottet, W. Belzig: Dynamical spin-blockade in a quantum dot with paramagnetic leads, *Eur. Phys. Lett.* **66**, 405 (2004)
43. B.R. Bulka: Current and power spectrum in a magnetic tunnel device with an atomic-size spacer, *Phys. Rev. B* **62**, 1186 (2000)
44. A. Cottet, W. Belzig, C. Bruder: Positive Cross Correlations in a Three-Terminal Quantum Dot with Ferromagnetic Contacts, *Phys. Rev. Lett.* **92**, 206801 (2004)
45. A. Cottet, W. Belzig, C. Bruder: Positive cross-correlations due to dynamical channel blockade in a three-terminal quantum dot, *Phys. Rev. B* **70**, 115315 (2004)

Transport through Intrinsic Quantum Dots in Interacting Carbon Nanotubes

M. Thorwart¹, R. Egger¹, and M. Grifoni²

¹ Institut für Theoretische Physik, Heinrich-Heine-Universität, Universitätsstr. 1, 40225 Düsseldorf, Germany

² Institut für Theoretische Physik, Universität Regensburg, Universitätsstr. 31, 93035 Regensburg, Germany

Abstract. Single-wall carbon nanotubes (SWNTs) constitute molecular wires with remarkable electronic properties. Due to the special nature of their electronic bands, SWNTs have been predicted to exhibit Tomonaga-Luttinger liquid (TLL) rather than Fermi liquid behavior at low energy scales. We focus on the effects of electronic correlations, treated within a TLL model, in a SWNT containing two impurities defining a small island for electrons (i.e., a quantum dot). We present analytical and numerical results for the linear conductance, obtained from a master equation approach and dynamical quantum Monte Carlo simulations, respectively. The one-dimensional character of transport is reflected in unconventional Coulomb blockade features for temperatures smaller than the level spacing in the dot. In this regime, TLL correlations among tunneling events require a generalization of the standard uncorrelated sequential tunneling picture for intermediate barrier transmission and strong interactions. In that case, correlated sequential tunneling processes can dominate, which lead to a different temperature dependence of the peak conductance. For sufficiently low temperatures, the simulations reveal a universal coherent resonant tunneling regime for arbitrary barrier transmission.

1 Introduction

The startling properties of one-dimensional (1D) interacting electrons, first pointed out by Tomonaga [1] and Luttinger [2], are generally referred to as (non-chiral) Tomonaga-Luttinger liquid (TLL) behavior [3–5]. TLL physics has moved into the center of attention in the mesoscopic physics community after the successful demonstration of electrical transport experiments for a variety of 1D materials, such as semiconductor quantum wires [6,7], fractional quantum Hall edge states [8], and single-wall carbon nanotubes (SWNTs) [9]. An more general introduction into the structure of SWNTs is given in Chap. 13 of this book, including their synthesis and various tranport properties. Beyond the study of fundamental physical aspects like many-body correlation effects, etc., SWNTs also have promising applications in molecular electronics and optoelectronics, see Chap. 14 in this book.

In this Chapter, we focus on electrical transport in SWNTs, which constitute an important realization of molecular wires. Shortly after the theoretical proposal of TLL behavior in nanotubes [10–13], which is briefly reviewed in

Sect. 2 below, first experimental evidence for this peculiar many-body state has been reported [14, 15]. Those researchers found the expected TLL power-law scaling of the tunneling density of states in SWNTs [12, 16]. In later experiments [17, 18], transport through an intrinsic quantum dot formed by a double barrier within the SWNT has been probed. Such a setup allows to study the typical resonant or sequential tunneling effects for the case of leads consisting of correlated electrons. A power-law scaling of the linear conductance maximum with temperature, i.e., $G_{\max} \sim T^\alpha$ was found. However, the observed exponent did not agree with the expected value $\alpha_{\text{UST}} = 1/g - 2$, where the Luttinger parameter $g < 1$ describes the effects of electron-electron interactions, see below. As it will be discussed below, the experimentally observed exponent can be explained theoretically in terms of what has been denoted as correlated sequential tunneling (CST) [17, 18]. This extends the previously known uncorrelated sequential tunneling (UST) picture [16, 19, 20] by systematically including higher-order correlated tunneling processes yielding CST. The latter have been neglected in the previous UST treatment.

We also mention related experiments on SWNTs, where Fabry-Perot type oscillations in the conductance of a nearly transparent double barrier were observed [21–24]. Remarkably, it is possible to tune the barrier strength via additional gates, and a crossover from Fabry-Perot behavior to sequential tunneling (Coulomb blockade) peaks has been observed [24]. Throughout this Chapter, we shall restrict ourselves to the most interesting case of a symmetric double barrier, and we put $\hbar = k_B = 1$.

2 Electrical Transport in Individual SWNTs

In order to keep this Chapter self-contained, we first briefly outline why a SWNT can be modeled by TLL theory, following [12]. In the second part of this section, we then describe the double-barrier problem and comment on its current theoretical understanding.

2.1 Field Theory of a Clean SWNT

The electronic properties of SWNTs essentially follow from the band structure of π electrons in a 2D graphene sheet. For graphene, one finds precisely two independent Fermi points $\alpha\mathbf{K}$ with $\alpha = \pm$ instead of a continuous Fermi surface [9]. Up to energy scales $E < D$, with bandwidth $D \approx 0.5$ to 1 eV, the dispersion relation around the Fermi points is highly linear and forms a ‘Dirac cone’. Since the basis of the honeycomb lattice contains two atoms, one has two sublattices $p = \pm$, and hence two degenerate Bloch states. In order to describe nanotubes, one then wraps the graphene sheet onto a cylinder. This is an accurate procedure for not too thin SWNTs with radius $R \gtrsim 5$ Å, which are the object of our study. The Bloch states are then given by $\varphi_{p\alpha}(\mathbf{r}) = (2\pi R)^{-1/2} \exp(-i\alpha\mathbf{K}\mathbf{r})$ for Fermi point $\alpha = \pm$. Here, $\mathbf{r} = (x, y)$

is defined on the respective sublattice p , and the Bloch functions live separately on each sublattice. Imposing periodic boundary conditions around the circumference of the SWNT, the Dirac cone dispersion relation implies a linear 1D dispersion relation for metallic SWNTs. Taking the x -axis along the tube direction and $0 < y < 2\pi R$ around the circumference, transverse quantization implies a factor $\exp(imy/R)$ (with integer angular momentum m) in the wavefunction. The population of states other than $m = 0$ involves a huge energy cost of the order $v_F/R \approx D$, where v_F denotes the Fermi velocity. Assuming that the SWNT is not excessively doped, one can thus discard all transport bands except $m = 0$ in a low-energy description. Then the nanotube forms a 1D quantum wire with only two spin-degenerate transport bands intersecting the Fermi energy E_F . The electron operator for spin $\sigma = \pm$ is thus written as

$$\Psi_\sigma(x, y) = \sum_{p\alpha} \varphi_{p\alpha}(x, y) \psi_{p\alpha\sigma}(x), \quad (1)$$

which introduces slowly varying 1D fermion operators $\psi_{p\alpha\sigma}(x)$ that depend only on the x coordinate. Neglecting Coulomb interactions for the moment, we obtain two copies of a massless 1D Dirac Hamiltonian for each spin direction,

$$H_0 = -v_F \sum_{p\alpha\sigma} p \int dx \psi_{p\alpha\sigma}^\dagger \partial_x \psi_{-p\alpha\sigma}. \quad (2)$$

Therefore a perfectly contacted clean SWNT has quantized conductance $4e^2/h$.

Next we examine Coulomb interactions characterized by the potential $U(\mathbf{r} - \mathbf{r}')$, whose detailed form depends on properties of the substrate, nearby metallic gates, and the geometry of the setup. In the simplest case, bound electrons and the effects of an insulating substrate are described by a dielectric constant κ , and in the absence of external screening, we get

$$U(\mathbf{r} - \mathbf{r}') = \frac{e^2/\kappa}{\sqrt{(x - x')^2 + 4R^2 \sin^2[(y - y')/2R] + a_z^2}}, \quad (3)$$

where a_z is the average distance between a $2p_z$ electron and the nucleus. Neglecting relativistic effects, electron-electron interactions are described by

$$H_I = \frac{1}{2} \sum_{\sigma\sigma'} \int d\mathbf{r} \int d\mathbf{r}' \Psi_\sigma^\dagger(\mathbf{r}) \Psi_{\sigma'}^\dagger(\mathbf{r}') U(\mathbf{r} - \mathbf{r}') \Psi_{\sigma'}(\mathbf{r}') \Psi_\sigma(\mathbf{r}), \quad (4)$$

which can be reduced to a 1D form by inserting the expansion (1). We can then exploit the large arsenal of theoretical methods readily available for 1D models [4]. The result looks complicated, but can be simplified considerably by exploiting momentum conservation. Usually SWNTs are intrinsically doped, such that Umklapp processes can be ignored. Then only forward and

backward scattering processes are allowed. In passing, we note that the role of umklapp scattering in a TLL in presence of a periodic potential has been studied in [25]. Using a 1D potential

$$V_0(x - x') = \int_0^{2\pi R} \frac{dy}{2\pi R} \int_0^{2\pi R} \frac{dy'}{2\pi R} U(\mathbf{r} - \mathbf{r}') , \quad (5)$$

which can be explicitly evaluated for the interaction (3) [12], the forward scattering interaction potential reads $V_0(x) + \delta_{p,-p'}\delta V_p(x)$. The term

$$\delta V_p(x) = \int_0^{2\pi R} \frac{dy dy'}{(2\pi R)^2} [U(x + pd_x, y - y' + pd_y) - U(x, y - y')] \quad (6)$$

is only present if \mathbf{r} and \mathbf{r}' are located on different sublattices. Here \mathbf{d} is the shift vector between sublattices. Thereby important information about the graphene lattice structure is kept even within the low-energy continuum approximation. Since $V_0(x)$ treats both sublattices on equal footing, the resulting part of the forward scattering interactions couples only the total 1D electron densities,

$$H_I^{(0)} = \frac{1}{2} \int dx dx' \rho(x) V_0(x - x') \rho(x') , \quad (7)$$

where the 1D density is $\rho = \sum_{p\alpha\sigma} \psi_{p\alpha\sigma}^\dagger \psi_{p\alpha\sigma}$. This part of the interaction dominates in practice and implies TLL behavior. Notice that it is connected to the *long-ranged* tail of the Coulomb interaction. All the remaining interactions are linked to short-ranged processes, which in turn are averaged over the circumference of the tube. Hence their amplitude is proportional to $1/R$, and is below argued to cause at worst exponentially small gaps. For $|x| \gg a$, where $a = 0.246$ nm is the graphene lattice spacing, one sees easily that $\delta V_p(x)$ is negligible. However, for $|x| \leq a$, an additional term beyond (7) arises. At those length scales, the difference between inter- and intra-sublattice interactions could matter. A microscopic consideration then finds the additional forward scattering term [12]

$$H_I^{(1)} = -f \int dx \sum_{p\alpha\alpha'\sigma\sigma'} \psi_{p\alpha\sigma}^\dagger \psi_{-p\alpha'\sigma'}^\dagger \psi_{-p\alpha'\sigma'} \psi_{p\alpha\sigma} , \quad (8)$$

where $f/a = \gamma_f e^2/R$. An estimate for armchair SWNTs yields $\gamma_f \approx 0.05$ [12]. A similar reasoning applies to backscattering, where the presence of an oscillating phase factor implies an effectively local interaction again,

$$H_I^{(2)} = b \int dx \sum_{pp'\alpha\sigma\sigma'} \psi_{p\alpha\sigma}^\dagger \psi_{p'-\alpha\sigma'}^\dagger \psi_{p'\alpha\sigma'} \psi_{p-\alpha\sigma} . \quad (9)$$

Taking the interaction (3), $b/a = \gamma_b e^2/R$ with $\gamma_b \approx \gamma_f$.

Further progress is possible using the bosonization approach [4]. For that purpose, we perform a unitary transformation of the non-interacting Hamiltonian (2) into the form of the 1D Dirac model by switching from sublattice states ($p = \pm$) to right- and left-movers ($r = \pm$). Then a bosonization formula [4, 10–12] applies, with four bosonic phase fields $\theta_a(x)$ and their canonical momenta $\Pi_a(x)$. These four channels follow from combining charge and spin degrees of freedom as well as symmetric and antisymmetric combinations of the two Fermi points, $a = c+, c-, s+, s-$. The bosonized form of H_0 and $H_I^{(0)}$ is

$$H_0 = \sum_a \frac{v_F}{2} \int dx [\Pi_a^2 + g_a^{-2}(\partial_x \theta_a)^2], \quad (10)$$

$$H_I^{(0)} = \frac{2}{\pi} \int dx dx' \partial_x \theta_{c+}(x) V_0(x - x') \partial_{x'} \theta_{c+}(x'). \quad (11)$$

The bosonized form of $H_I^{(1,2)}$ [10] gives nonlinear contributions in the θ_a fields for $a \neq c+$. Although bosonization of (2) gives $g_a = 1$ in (10), interactions change these parameters. In particular, for long wavelengths, $H_I^{(0)}$ is incorporated into H_0 by putting $g_{c+} = [1 + 4\tilde{V}_0(k \approx 0)/\pi v_F]^{-1/2}$, with $\tilde{V}_0(k)$ being the Fourier transform of $V_0(x)$. For all other channels, there is only a negligible renormalization $g_{a \neq c+} = 1 + f/\pi v_F \approx 1$. The velocities of the four modes are $v_a = v_F/g_a$. The charged mode propagates therefore with higher velocity than the three neutral modes. For the long-ranged interaction (3), there is a logarithmic singularity in $\tilde{V}_0(k)$. Due to the finite SWNT length L , this divergence is cut off by $k = 2\pi/L$ in practice, giving the dimensionless TLL parameter

$$g_{c+} = \left\{ 1 + \frac{8e^2}{\pi \kappa v_F} \ln(L/2\pi R) \right\}^{-1/2} \approx 0.2 \dots 0.3 \quad (12)$$

for typical $L/R \approx 10^3$. The fact that $g_{c+} \ll 1$ implies that an individual metallic SWNT on an insulating substrate is a strongly correlated system with pronounced non-Fermi liquid effects. For $f = b = 0$, a SWNT then constitutes a realization of the TLL. Let us then briefly address the role of the nonlinearities associated with the coupling constants f and b . Formally, this can be studied via the renormalization group and a Majorana refermionization approach [12], allowing for the essentially complete characterization of the non-Fermi-liquid ground state of a clean SWNT. It turns out that for temperatures above $T_b = D \exp[-\pi v_F / \sqrt{2}b] \approx 0.1$ mK, a SWNT is a TLL, and $H_I^{(1,2)}$ can be neglected [12]. In the remainder, we focus on temperatures well above T_b .

2.2 Double Barrier Problem in a TLL

For the investigation of the linear conductance through a double barrier in a SWNT at resonance, it turns out that neither spin nor the K point degeneracy

introduce qualitatively new features [26, 27]. We therefore focus on the spinless case in what follows, where the appropriate g follows from $g^{-1} = (3 + g_{c+}^{-1})/4$ [12]. For example, taking $g_{c+} = 0.3$ would give $g = 0.63$. The TLL is then characterized by the single field $\theta(x)$ (corresponding to the $c+$ mode) with conjugate momentum $\Pi(x)$. When the double barrier is included, the Hamiltonian reads

$$H = \frac{v_F}{2} \int dx \left\{ \Pi^2 + \frac{1}{g^2} (\partial_x \theta)^2 \right\} + U_{\text{imp}} \sum_{p=\pm} \cos[\sqrt{4\pi} \theta(px_0/2) + eVt + p\pi N_0] . \quad (13)$$

Here, V is the applied bias voltage, and U_{imp} denotes the strength of the symmetric double barrier located at $x = \pm x_0/2$. We then have an intrinsic quantum dot with a plasmon level spacing $\varepsilon = E_s/g$, where $E_s = \pi v_F/x_0$ is the single-particle level spacing, and charging energy $E_c = E_s/g^2$, containing the average number N_0 of electrons determined by external gate voltages. The plasmon level spacing ε directly reflects the spatial quantization of the TLL modes in the quantum dot. The charging energy E_c well-known for systems with Coulomb blockade describes the energy necessary to add an electron on the dot. Note that the two leads are modeled here as effectively semi-infinite TLLs. Their correlated lead electrons are finally responsible for the occurrence of power laws, e.g., for the linear conductance $G = dI/dV(V \rightarrow 0)$, on which we focus. It can be computed from the relation

$$I = G_0 V + \frac{e}{\sqrt{\pi}} \langle \partial_t \theta(x, t) \rangle , \quad (14)$$

where $G_0 = e^2/h$ is the conductance quantum, and the quantum average is evaluated in the stationary long-time limit. The conductance is periodic in N_0 , and we restrict ourselves to one period, $0 \leq N_0 \leq 1$, where G has a resonance peak at $N_0 = 1/2$. One can compute G analytically for the Fermi-liquid limit, $g = 1$, by refermionizing this model [27],

$$\frac{G_{g=1}(N_0, T)}{G_0} = \int_{-\infty}^{\infty} dE \frac{1}{4T \cosh^2(E/2T)} \frac{w^2}{\cos^2(\pi[N_0 + E/E_s]) + w^2} , \quad (15)$$

with the dimensionless parameter $w = (4 - \lambda^2)^2/[8\lambda(4 + \lambda^2)]$, where $\lambda = \pi U_{\text{imp}}/D$. For strong barriers, (15) leads to a lineshape of Breit-Wigner form with linewidth $\Gamma_0 = wE_s/\pi$. For $g = 1$, the infinite-barrier limit is reached already for $\lambda = 2$, where the associated phase shift is $\pi/2$.

As the model is not integrable for $g < 1$, exact solutions are out of reach. Analytical progress then generally has to rely on approximations. Initial work [16, 19, 28] pursued perturbative approaches, using the renormalization group, instanton methods or cumulant expansions, both for strong and weak barriers. Furusaki [20] has presented a detailed study of the *incoherent sequential tunneling* regime, including also cotunneling contributions important away from the resonance peak. The regime of incoherent sequential tunneling

is characterized by rare independent tunneling processes from the leads onto and off the dot. In other words, the decay width Γ of the dot states is much smaller than temperature. Due to the clear separation of time-scales, the incoherent regime allows for a *Markovian master equation approach*, whose validity requires that the peak conductance satisfies $G_{\max} \ll G_0$. Keeping only rates to lowest order in Γ_0 from the TLL ‘leads’ onto the island (dot), the standard uncorrelated sequential tunneling (UST) mechanism follows, with [20]

$$\frac{G_{\text{UST}}(N_0, T)}{G_0} = \frac{\Gamma_0(\pi T/D)^{-1+1/g}}{4\Gamma(1/g)T \cosh(\delta/2T)} \left| \Gamma \left(\frac{1}{2g} + i \frac{\delta}{2\pi T} \right) \right|^2, \quad (16)$$

where $\Gamma(x)$ denotes the Gamma function, and $\delta = E_c|N_0 - 1/2|$. The line-shape (16) is rather close to the Fermi-liquid form (15) for large barrier heights, and characterized by a linear T dependence of the linewidth. In the tails of a peak, the conductance (16) vanishes exponentially, but then also (elastic) cotunneling has to be included [19, 20, 28]. As cotunneling is a process of second-order in the Γ_0 which involves only a *virtual* population of the dot, it can dominate away from resonance. Note that the UST peak conductance in (16) scales as $G_{\max} \propto T^{1/g-2}$. Finally, at low temperatures, instead of sequential tunneling, *coherent resonant tunneling* is possible. Then, the electrons tunnel through the two barriers in a coherent way, i.e., keeping all the correlations which are suppressed in the incoherent regime. An analysis using a Markovian master equation breaks down and the regime is then characterized by non-Lorentzian universal lineshapes [16],

$$\frac{G_{\text{res}}(N_0, T)}{G_0} = f_g(X), \quad X = d_g|N_0 - 1/2|/T^{1-g}, \quad (17)$$

with a dimensionful constant d_g , such that detailed parameters show up only via the quantity X . The linewidth then scales as T^{1-g} . The universal scaling function has the limiting behaviors $1 - f_g(X) \propto X^2$ for $X \ll 1$, and $f_g(X) \propto X^{-2/g}$ for $X \gg 1$. While for strong barriers, $T = 0$ resonant tunneling requires $g > 1/2$, in the weak-barrier limit, it should survive for $g > 1/4$ [16]. Note that now $G_{\max} = G_0$.

Remarkably, the experimental data of [17, 18] are incompatible with this picture, since the observed temperature dependence of the conductance peak does not follow the $T^{1/g-2}$ UST scaling. In analogy to the bridged electron transfer theory of Hu and Mukamel [29], the master equation approach of [20] has recently been generalized to include higher-order processes [30], see Sect. 3. There is an additional conduction channel in the sequential regime, which has been dubbed “correlated sequential tunneling” (CST) [18] and can lead to the $G_{\max} \propto T^{2/g-3}$ scaling found experimentally [17, 18] in certain parameter regions identified below. Interestingly enough, also the QMC results in Sect. 4 show the CST scaling law in the appropriate regime.

Another line of work [31, 32] approaches the double-barrier problem by considering weak interactions, g close to 1. Within the range of applicability, [31, 32] confirmed the picture of [16, 19, 20] for infinite level spacing, showing no sign of CST behaviors. However, as CST theory shows that finite E_s is necessary for the mechanism, this result is hardly surprising. We note that [32] predicted that for weak barriers, a sharp Lorentzian resonance peak is possible whose linewidth vanishes as a power law at low temperatures. This finding is confirmed from our simulations in Sect. 4. Furthermore, Komnik and Gogolin presented an exact solution of a related model at the point $g = 1/2$ [33]. In their model, however, there is no sequential tunneling regime at all, and therefore we believe that it represents a non-generic situation. A functional renormalization group approach has been applied to this problem by Meden et al. [34]. Within the parameter regime studied mainly numerically, no signature of CST has been found. However, their scheme is perturbative in the electron interaction and involves approximations on the evaluation of the self-energy whose validity is hard to assess. Moreover, the correct parameter regime for CST may simply have been missed. Finally, we note that we are dealing with zero-range electronic interaction throughout this work, in contrast to [18], where a finite interaction range has been used to find a quantitative description of the experimental data. The zero-range interaction is the proper low-energy limit of a finite-range model illustrating that finite-range effects are only relevant at higher energies. Since we are interested here in the principal transport mechanisms at low energies, we directly start from the case of zero-range interaction.

3 Markovian Master Equation Approach

3.1 Rate Equations

For large tunnel barriers, it is useful to switch to a dual version of the Hamiltonian (13), where the dynamics is described by hopping events connecting minima of the periodic double-barrier potential

$$H_{\text{imp}} = 2U_{\text{imp}} \cos(\pi N) \cos(\pi n) \quad (18)$$

in the (N, n) -plane [16], where

$$-eN = -e\pi^{-1/2}[\theta(x_0/2) + \theta(-x_0/2)]$$

gives the charge difference between the left and right leads, and

$$-en = -e\pi^{-1/2}[\theta(x_0/2) - \theta(-x_0/2)]$$

is the charge occupying the dot. Note that the Hamiltonian (18) is particularly convenient for describing strong barriers within a perturbative treatment of

the tunneling process through the barriers (see below). On the other hand, the Hamiltonian (13) is appropriate when one starts with weak barriers. Nevertheless, both Hamiltonians are equivalent. The effective tunneling amplitude connecting neighboring minima of the potential (18) can be estimated using instanton techniques, and is given by [28]

$$\Delta = \pi^{-1} \Gamma(1 + 1/g) \Gamma^{1/g}(1 + g) (\pi U_{\text{imp}}/D)^{-1/g} D . \quad (19)$$

Tunneling events induce a change $n \rightarrow n \pm 1$ for tunneling onto/out of the dot, and $N \rightarrow N \mp 1$ for tunneling towards the right/left. Hence transfer of one unit of charge across the complete double barrier structure requires $N \rightarrow N \pm 2$. The current (14) through the double barrier is then given by $I = e\langle \dot{N} \rangle / 2$, evaluated in the stationary (i.e., long-time) limit.

This discrete hopping dynamics can be described by a Markovian master (rate) equation for the probability $P_N(n, t)$ of being in state (N, n) at time t . The rates can be extracted as irreducible diagrams for the self-energy [28], which to lowest order are Golden Rule rates [20]. Alternatively, the rates can be derived using the projection operator formalism [29]. The first-order UST contributions to the transition rates imply $N \rightarrow N \pm 1$ jumps. Taking into account transition rates to second order in the hybridization $\Gamma_0 = 2\pi\rho_0\Delta^2$, where $\rho_0 = 1/\pi v_F$ denotes the bare 1D density of states in the leads, one encounters nontrivial divergences. The origin of the divergences is that formally, the width of the intermediate diagonal states, being states of the quantum dot with a real *physical* population of electrons, is zero for each diagram at a fixed order. This unphysical feature can be cured on the formal level by a resummation of higher-order diagrams yielding a finite linewidth of the dot states. This is achieved in [30] by an effective procedure which involves the well-known Weisskopf-Wigner approximation. On the one hand, this procedure yields direct CST processes, $N \rightarrow N \pm 2$. On the other hand, additional contributions to the transition rates for $N \rightarrow N \pm 1$ arise. The master equation for $P_N(n, t)$ then reads

$$\begin{aligned} \dot{P}_N(n) = & -\gamma(n)P_N(n) + \Gamma_R^f(n+1)P_{N+1}(n+1) \\ & + \Gamma_L^b(n+1)P_{N-1}(n+1) + \Gamma_L^f(n-1)P_{N+1}(n-1) \\ & + \Gamma_R^b(n-1)P_{N-1}(n-1) + \Gamma_{CST}^f(n)P_{N+2}(n) \\ & + \Gamma_{CST}^b(n)P_{N-2}(n) - \Gamma_{CST}^f(n)P_N(n) - \Gamma_{CST}^b(n)P_N(n) , \end{aligned} \quad (20)$$

where $\Gamma_{L/R}^{f/b}(n)$ denotes the forward/backward rate for a transition over the left/right barrier, having started with n electrons on the dot. In addition, $\Gamma_{CST}^{f/b}(n)$ denotes the forward/backward rate for a direct CST transition $N \rightarrow N \pm 2$. Moreover,

$$\gamma(n) = \Gamma_R^f(n) + \Gamma_L^f(n) + \Gamma_R^b(n) + \Gamma_L^b(n) \quad (21)$$

is related to the linewidth. Below we are interested in the peak conductance only, where cotunneling processes are always subleading [20]. For that reason,

cotunneling rates are not included in the master equation (20). This is of course not a fundamental restriction, but simplifies matters somewhat.

In the stationary long-time limit, the probability

$$p(n) = \sum_{N=-\infty}^{+\infty} P_N(n, t \rightarrow \infty)$$

for the dot being occupied with n electrons follows from (20) after some algebra in the form of a detailed balance relation,

$$\frac{p(n)}{p(n+1)} = \frac{\Gamma_L^b(n+1) + \Gamma_R^f(n+1)}{\Gamma_L^f(n) + \Gamma_R^b(n)}, \quad (22)$$

which in turn determines the current I according to

$$I = -\frac{e}{2} \sum_n \left(\Gamma_R^f(n) + \Gamma_L^f(n) - \Gamma_R^b(n) - \Gamma_L^b(n) + 2\Gamma_{CST}^f(n) - 2\Gamma_{CST}^b(n) \right) p(n). \quad (23)$$

In the low-temperature linear transport regime, $eV, T \ll E_c$, at most two charge states, say $n = 0$ and $n = -1$, can contribute, and the rates $\Gamma_L^f(0)$, $\Gamma_R^f(-1)$, $\Gamma_R^b(0)$, and $\Gamma_L^b(-1)$ are effectively zero, since they involve excluded states $n = +1$ or $n = -2$.

3.2 Conductance Peak Height

Focusing on the linear conductance at the maximum of the peak ($N_0 = 1/2$), the above relations give two contributions, $G_{\max}(T) = G_{\max,A} + G_{\max,B}$, where

$$G_{\max,A} = \frac{e^2}{T\gamma} \left(\Gamma^{(1)} \right)^2 \quad (24)$$

and

$$G_{\max,B} = -e\Gamma^{(2)\prime} - 2e\Gamma'_{CST} + \frac{e^2}{T\gamma} \Gamma^{(1)} \Gamma^{(2)}. \quad (25)$$

Here we have decomposed the rates $\Gamma_{L/R}^{f/b}$ into first-order and second-order contributions (the latter must be kept for consistency when one includes CST rates), and used that these rates all coincide at resonance. Moreover, on resonance we also have $\gamma(0) = \gamma(-1) = \gamma$. The prime in (25) denotes the derivative d/dV at $V = 0$. Next, the rates for the model (13) have to be computed which has been done in [30], where the evaluation of the triple time-integral representations for the various irreducible rate contributions is described in detail.

Remarkably, in the time integration τ_2 corresponding to the intermediate (diagonal) state, one encounters a nontrivial divergence. Physically, this

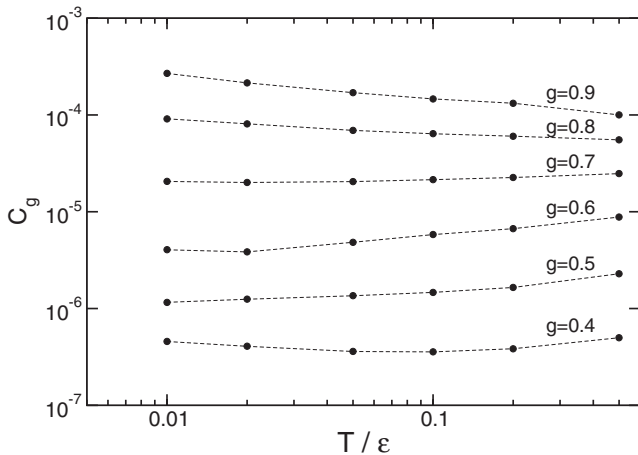


Fig. 1. Temperature dependence of C_g for various g . The energy unit is $\epsilon = E_s/g$, and we take $D = 10\epsilon$

divergence is cured by including higher-order contributions to the rates, causing a finite lifetime of the intermediate state. This lifetime is linked to the linewidth γ , and within the Weisskopf-Wigner approach, γ should then be self-consistently fixed by acting as cutoff to the τ_2 integration and at the same time following from (21). On resonance, this procedure can be carried out analytically, and the self-consistently determined linewidth γ follows in the form [30]

$$\gamma \simeq 4(\Gamma^{(1)} + \Delta^4 C_g), \quad (26)$$

where $\Gamma^{(1)}$ is the UST rate given by Furusaki [20], scaling as $\Gamma^{(1)} \propto T^{1/g-1}$. The Weisskopf-Wigner approximation breaks down if $\xi > 1$, where we use

$$\xi = \frac{\Delta^4 A_g}{(\Gamma^{(1)} + \Delta^4 C_g)^2}. \quad (27)$$

The Δ -independent quantities A_g and C_g encapsulate the second-order contributions $\Gamma^{(2)}$ on resonance. The expressions which have to be evaluated in order to obtain A_g and C_g are rather involved and are given explicitly in Sect. III of [30]. Here, we show the results for C_g from a numerical evaluation of these expressions for various TLL parameters in Fig. 1. We find that C_g is basically temperature independent, and therefore a crossover occurs from $\gamma \propto T^{1/g-1}$ at high temperatures ($T > T_c$) to a constant γ at low temperatures, $T < T_c$, see Fig. 2. However, A_g generally is temperature-dependent [30] and therefore the criterion $\xi < 1$ is violated below some temperature T_l where $\xi(T_l) = 1$, see (27). The crossover scale T_c is shown in Fig. 3. We shall see that this crossover generates a transition from the UST to the CST regime. We note that in addition to $\xi < 1$, the validity of the Markovian master equation always requires $G_{\max} \ll G_0$ [20].

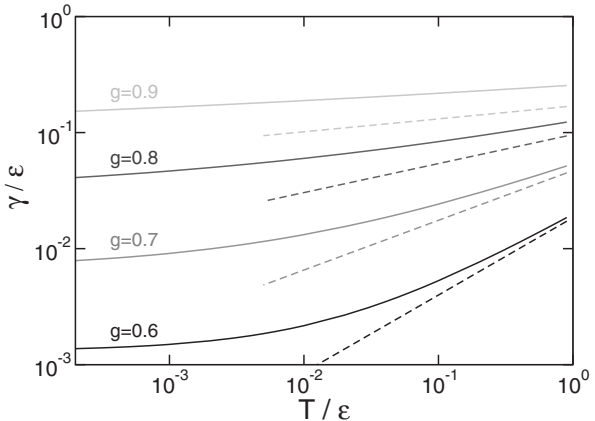


Fig. 2. Temperature dependence of the linewidth γ (solid lines) for $\Delta = 3\varepsilon$ and $g = 0.6$ (bottom) to $g = 0.9$ (top). Dashed lines show $T^{1/g-1}$

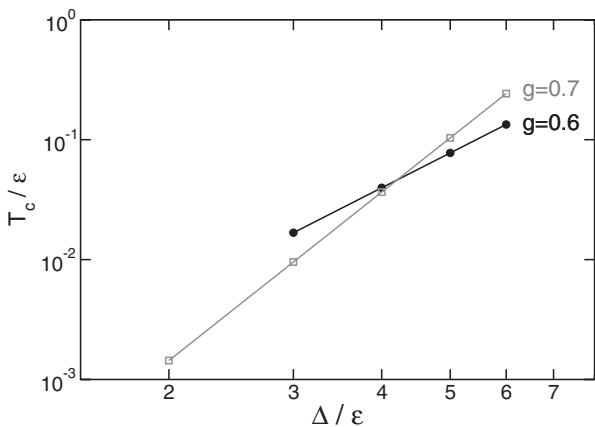


Fig. 3. Crossover temperature T_c separating UST and CST behavior for $D = 10\varepsilon$

When analyzing the conductance (25), it turns out that $G_{\max,B}$ vanishes. This is the result of a remarkable cancellation of the CST rates Γ_{CST} with higher-order contributions $\Gamma^{(2)}$ to nearest-neighbor rates. We do not have an analytical proof for the cancellation, but numerically it appears to be a perfect one [30]. The peak conductance is then simply given by (24), and from (26) the crossover temperature T_c follows,

$$T_c = \left(\frac{\Delta^2 C_g}{\eta_g} \right)^{g/(1-g)}, \quad (28)$$

where we use the abbreviation

$$\eta_g = \frac{(1 - e^{-\varepsilon/D})^{1/g} \Gamma^2(1/2g)}{4D\Gamma(1/g)} (2\pi/D)^{1/g-1}.$$

Below T_c , CST effects will then dominate. In that regime, γ is essentially constant with temperature, and hence one finds the approximate CST power law

$$G_{\max} \propto T^{2/g-3}, \quad (29)$$

implying the CST exponent $\alpha_{\text{CST}} = -3 + 2/g$. Above T_c , however, the usual UST picture is recovered. In Fig. 3, results for T_c are shown as a function of Δ for two TLL parameters g , always respecting the conditions $\xi(T_c) < 1$ and $G_{\max}(T_c) \ll G_0$. Generally, T_c increases with increasing Δ and with decreasing g , i.e., for more transparent barriers and/or strong interactions. For $g \simeq 1$, the CST regime is restricted to very low T and large Δ , making it unlikely to be observable. For strong interactions, however, CST effects can be pronounced even for moderately transparent barriers at low temperatures.

We show results for $G_{\max}(T)$ for $\Delta = 3\varepsilon$ in Fig. 4. At low temperatures, $G_{\max}(T)$ follows the approximate CST power law (29) given by the dotted curves. Note that for these cases, our approach is self-consistently valid, since $\xi < 1$ and $G_{\max} \ll G_0$. At high temperatures, the cross-over to the regime of uncorrelated sequential tunneling occurs, with the UST power law $G_{\max}(T) \propto \alpha_{\text{UST}}$, see dashed lines. For larger values of $g \gtrsim$, we find $G_{\max} > G_0$, such that our approach breaks down in this parameter regime.

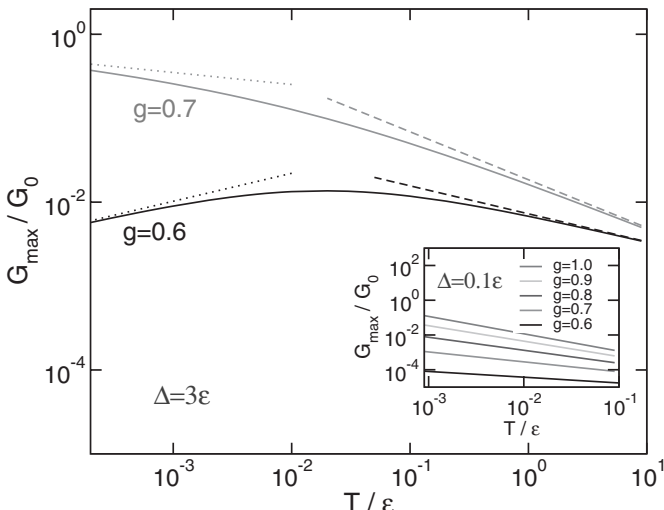


Fig. 4. Temperature dependence of the conductance maximum G_{\max} (solid lines) for $\Delta = 3\varepsilon$ and $g = 0.6$ (bottom) and $g = 0.7$ (top). The dotted lines mark the CST power law, while the dashed lines indicate UST scaling behavior. Inset: G_{\max} for $\Delta = 0.1\varepsilon$ and $g = 0.6$ (bottom) to $g = 1$ (top). The slopes now coincide with the UST prediction α_{UST}

On the other hand, for $g < 0.6$, we find $\xi > 1$, which then again invalidates our treatment. Nevertheless, there is a well-defined region of applicability, where the approximate CST scaling is predicted. Finally, for $\Delta = 0.1\varepsilon$, the UST scaling is recovered, see inset of Fig. 4 and the master equation approach breaks down before the CST effects dominate when temperature is lowered.

To summarize, the exponent α_{CST} emerges due to a modification of the linewidth γ by higher-order processes and reflects the physics of this correlated transport mechanism. For $T < \varepsilon$, plasmon modes excited on the dot lead to a correlation among electrons in different leads, such that the sequential tunneling process cannot be separated into two distinguishable steps as under the UST mechanism. Therefore the end-tunneling density of states, $\rho(E) \propto E^{1/g-1}$ [16] appears twice, and one arrives — apart from the usual $1/T$ factor — at a doubled exponent compared to the UST value.

4 Quantum Monte Carlo Simulations

4.1 Dynamical Simulations

In this section, we study the model (13) by numerically exact quantum Monte Carlo (QMC) methods. Since we are interested in the conductance G , we have to employ a real-time (Keldysh) functional integral approach. An alternative would be to use standard Euclidean-time QMC simulations, and then use analytic continuation techniques to extract the conductance. In [35], the latter approach was chosen for the single-barrier problem, where the analytic continuation was performed using Padé approximants. We have also tried this for the double-barrier problem, but found it to be completely uncontrolled and unreliable. This is not too surprising as the analytic continuation of numerical data is mathematically ill-defined and known to work only in fortunate cases. In contrast, the Keldysh-QMC simulation suffers from the well-known sign problem due to quantum interference of different real-time paths. This poses a problem to simulations at very low temperatures, but nevertheless allows us to study a wide parameter regime of interest in a controlled way. The single-barrier problem was studied successfully by this technique before [36, 37], and the generalization of the method to the double-barrier case has been described in [27], see also [26] for details. For lack of space, we here only discuss results of these simulations. The correctness of the QMC scheme has been checked in detail against the exact solution (15) for $g = 1$.

4.2 Strong Barrier Transmission

Let us then start with the case of strong transmission, taking $U_{\text{imp}}/D = 0.05$ and $E_s/D = \pi/2$. Remarkably, for $T/D > 0.01$, Path Integral Monte Carlo data are quantitatively described by the Fermi liquid lineshape (15) provided $w = w_g(T)$ is treated as a fit parameter. This allows for the interpretation

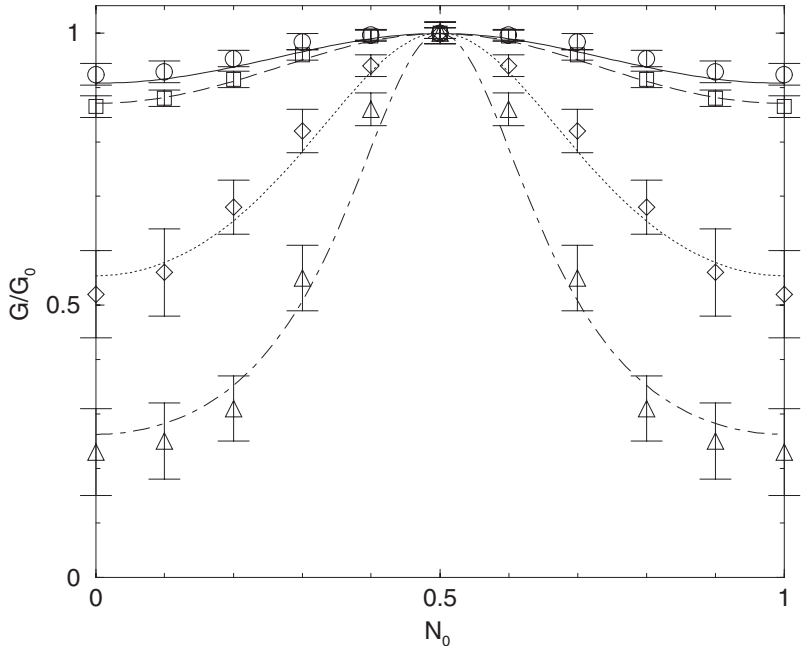


Fig. 5. Conductance lineshape $G(N_0)$ for various g in the strong transmission limit, $U_{\text{imp}}/D = 0.05$, with $E_s/D = \pi/2$ and $T/D = 0.025$. QMC data are shown as circles ($g = 1$), squares ($g = 0.9$), diamonds ($g = 0.6$), and triangles ($g = 0.3$), respectively. Vertical bars indicate MC error estimates (one standard variance). The solid curve is the exact result (15) for $g = 1$. The other curves represent best fits to (15) with w as fit parameter

that the dimensionality does not qualitatively affect the lineshape but enters only via the peak height and the linewidth. This is shown for $T/D = 0.025$ in Fig. 5, which also shows the comparison of our QMC data to (15) at $g = 1$. (The comparison for other U_{imp} is given in [27].) The results of extensive QMC simulations then allow to extract $w_g(T)$, see Fig. 6 for $g = 0.3$ and $g = 0.6$, where each data point was obtained from QMC data for the full conductance lineshape. Most interestingly, the linewidth parameter $w_g(T)$ is found to exhibit power-law behavior, $w_g(T) \propto T^{\alpha_g}$, with a g -dependent exponent α_g . In particular, we find the numerical values $\alpha_{0.3} \approx 0.84$ and $\alpha_{0.6} \approx 0.72$. No analytical theory for these values at such strong interactions is known at present. Apparently, the strong-transmission peaks become narrower and narrower as T is lowered, see also [32]. The lineshape (15) resembles experimental results for strong-transmission (Fabry-Perot) oscillations in nanotubes [21–24]. We then identify this regime of weak barriers and not too low temperature as the *Fabry-Perot regime*. For $g < 1$, these Fabry-Perot oscillations include remnants of Coulomb blockade effects, which are partly washed out due to

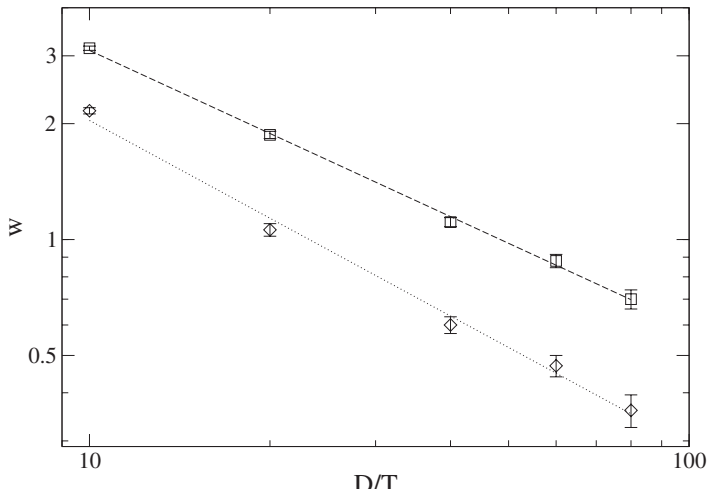


Fig. 6. Fit parameter $w_g(T)$ for conductance lineshape (15) as obtained from QMC data at $g = 0.3$ (diamonds) and $g = 0.6$ (squares), for $E_s/D = \pi/2$ and $U_{\text{imp}}/D = 0.05$. Dotted and dashed lines are guides to the eye only

quantum fluctuations, but still are effective in narrowing the resonance peak when lowering T . No sharp conductance dips were observed in our simulations, in contrast to experimental findings [21]. Such dips are probably related to special barrier scattering processes not contained in our model (13).

At lower T , deviations from the Fermi-liquid lineshape (15) become apparent. However, in that case it is possible to collapse data for different parameters (but for fixed value of g) onto a universal scaling curve $f_g(X)$, see Fig. 7 for $g = 0.3$. Very similar results were found for $g = 0.6$ as well. For small $X = c|N_0 - 1/2|/T^{1-g}$, the scaling function indeed obeys $1 - f_g(X) \propto X^2$, and is also consistent with $f_g(X) \propto X^{-2/g}$ for $X \gg 1$. Therefore these universal lineshapes can be identified as *coherent resonant tunneling peaks* [16]. Although for strong barriers, resonant tunneling exists only for $g > 1/2$, we observe a perfect resonance peak at $g = 0.3$. This agrees with the weak-barrier arguments of [16], suggesting resonant tunneling to survive in that limit for $g > 1/4$. Noteworthy, we emphasize that despite the presence of the sign problem it is here possible to enter the asymptotic low-energy regime of coherent resonant tunneling with a Keldysh-Monte-Carlo simulation.

4.3 Weak Barrier Transmission

Finally, we turn to a stronger barrier, $U_{\text{imp}}/D = 0.2$, where one expects sequential tunneling at not too low temperatures. In Fig. 8, numerical results for the conductance peak height are shown for $g = 0.6$. This value of g is relevant to SWNT experiments [17, 18, 30]. At low temperatures,

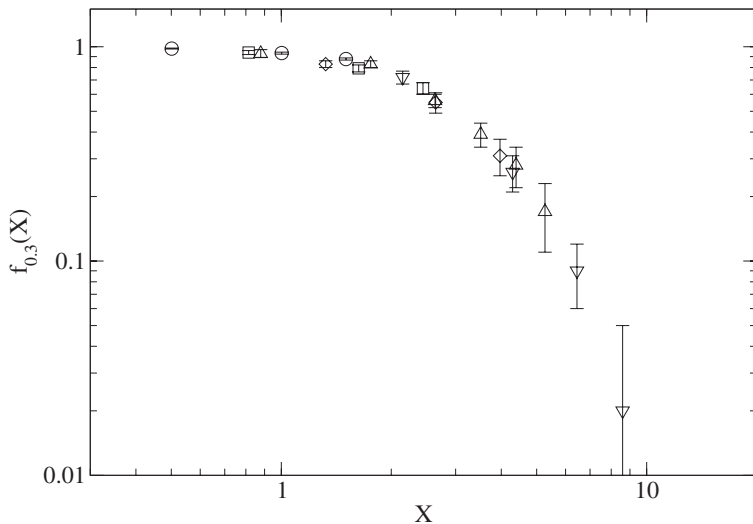


Fig. 7. Low-temperature QMC data for various N_0, T at $E_s/D = \pi/2, U_{\text{imp}}/D = 0.05$, plotted according to (17) for $g = 0.3$. Different symbols refer to different temperatures

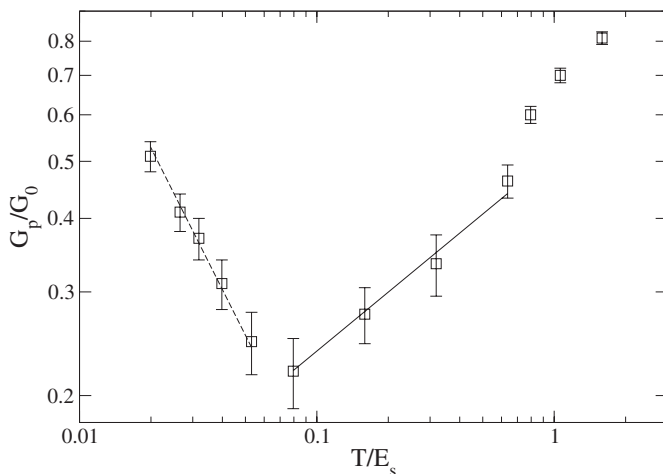


Fig. 8. Temperature dependence of the peak conductance $G_p \equiv G_{\max}$ for $g = 0.6, U_{\text{imp}}/D = 0.2$, and $E_s/D = \pi/20$. The dashed line reflects a $T^{-0.8}$ power law, the solid line a $T^{1/3}$ law

G_{\max} approaches the quantum conductance G_0 expected in the resonant tunneling regime. For intermediate temperatures, $G_{\max}(T)$ goes through a minimum, and then sequential processes start to dominate. Still well below E_s , we observe a a power-law increase of the conductance peak height, $G_{\max}(T) \propto T^\alpha$. Interestingly enough, our data are consistent with the CST scaling, $\alpha = \alpha_{\text{CST}} = -3 + 2/g = 1/3$, but not with the corresponding UST prediction, $\alpha_{\text{UST}} = -2 + 1/g = -1/3$, which would even have a different sign. We stress that other exponents, e.g., $\alpha_1 = 2/g - 2 = 4/3$, as expected for the effective single-impurity problem arising at $T \gg E_s$ [20] can safely be ruled out. Therefore our simulations confirm that the CST mechanism can indeed be crucial and even exceed the UST contribution. For the parameters in Fig. 8, we find $\Delta \approx 3.3\varepsilon$ from (19), consistent with the expectation that CST effects require rather transparent barriers, $\Delta > \varepsilon$, and strong interactions, see Sect. 3. As a side remark, we mention that Fig. 8 shows similar $T \approx E_s$ features as the experimental data of [17]. However, the upturn towards the resonant tunneling regime in $G_{\max}(T)$ seen in Fig. 8 for $T/E_s < 0.1$ has not yet been observed experimentally [17].

5 Conclusions

By using a master equation approach and real-time QMC simulations, linear transport in a Tomonaga-Luttinger liquid (TLL) with two tunneling barriers forming a quantum dot has been studied. This is a situation that can be studied experimentally in single-wall nanotubes [17, 21].

From the rate equation approach, we find a characteristic power-law temperature dependence of the peak height of the linear conductance in the sequential tunneling regime. By including second-order contributions to the tunneling rates in combination with a self-consistent Weisskopf-Wigner regularization, a comprehensive picture has been obtained in Sect. 3. For temperatures below the level spacing determined by the energy scale $\varepsilon = \pi v_F/gx_0$, for dot size x_0 and TLL parameter g , the power-law exponent of the peak conductance depends on the transparency Δ of the tunneling barriers. For sufficiently transparent barriers, $\Delta > \varepsilon$, not too low temperatures (within a window $T_l < T < T_c$), and strong interactions, we find that correlated sequential tunneling (CST) is possible, with the CST exponent $\alpha_{\text{CST}} = -3 + 2/g$. For very high barriers ($\Delta \rightarrow 0$), however, the uncorrelated sequential tunneling (UST) exponent $\alpha_{\text{UST}} = -2 + 1/g$ is always recovered. Note that despite the large Δ reported here for the CST regime, the Markovian master equation is still applicable, as the peak conductance remains small throughout the temperature regime of interest. We have determined the crossover temperature T_c separating both regimes, see (28) and Fig. 3. For $T < T_c$, the CST mechanism is effective, while for $T > T_c$, the UST picture is recovered.

CST scaling is also observed in the numerically exact simulations described in Sect. 4 using the real-time Quantum Monte Carlo method.

Furthermore, regarding the SWNT experiments of [17], where the CST power law has been reported, one can check that it is likely that also rather transparent barriers have been present. Concrete estimates give $\Delta \approx 1.2\varepsilon$ [30], consistent with the statements in Sect. 3. For CST to be operative, one needs finite level spacing, low (but not too low) temperatures, relatively strong interactions, and not too high barriers. The regime where one can expect to find CST effects is therefore rather narrow, but has clearly been shown to exist.

Using dynamical quantum Monte Carlo simulations, it is in fact possible to avoid any approximation and study the conductance in a numerically exact fashion. Despite the well-known sign problem, it is possible to use this method even in the low-temperature coherent resonant tunneling regime, where we have found the predicted universal lineshapes of the linear conductance. Moreover, for weak barrier transmission, we have shown that there is a Fabry-Perot regime, where the linewidth at not too low temperatures follows the noninteracting lineshape, but with a temperature dependent linewidth scaling in a g -dependent power-law form. In particular, as T decreases, the peak becomes sharper and sharper, and finally one enters the coherent resonant tunneling regime.

Finally, we note that the CST scaling law (29) has been obtained in [18] starting from finite-range interactions among the electrons. The divergence has been regularized by summing up a selection of higher-order terms. However, this selection was too strict [30], leading to the incorrect conclusion that finite-range interactions would be a prerequisite for CST to occur. As shown in this work, also zero-range interactions suffice, as long as the tunneling barriers are not too high.

Acknowledgments

We acknowledge support by the DFG under the Gerhard-Hess program, the SFB Transregio 12, and the EU network DIENOW. This reported work is based on collaborations with G. Cuniberti, C. Dekker, S. Hügle, and H. Postma. We thank A.O. Gogolin, A. Komnik, V. Meden, Yu. Nazarov, K. Schönhammer, J. Stockburger, and U. Weiss for useful discussions.

References

1. S. Tomonaga: Remarks on Bloch's method of sound waves applied to many-fermion problems, *Prog. Theor. Phys.* **5**, 544 (1950)
2. J.M. Luttinger: An exactly soluble model of a many-fermion system, *J. Math. Phys. (N.Y.)* **4**, 1154 (1963)
3. F.D.M. Haldane: Luttinger liquid theory of one-dimensional quantum fluids.
1. Properties of the Luttinger model and their extension to the general 1D interacting spinless Fermi gas, *J. Phys. C* **14**, 2585 (1981)

4. A.O. Gogolin, A.A. Nersesyan, A.M. Tsvelik: *Bosonization and Strongly Correlated Systems* (Cambridge University Press, 1998)
5. K. Schönhammer: The Luttinger liquid concept for interacting electrons in one dimension, *J. Phys.: Cond. Matt.* **14**, 12783 (2002).
6. O.M. Auslaender, A. Yacoby, R. de Picciotto, K.W. Baldwin, L.N. Pfeiffer, and K.W. West: Experimental Evidence for Resonant Tunneling in a Luttinger Liquid, *Phys. Rev. Lett.* **84**, 1764 (2000).
7. M. Rother, W. Wegscheider, R.A. Deutschmann, M. Bichler, G. Abstreiter: Evidence of Luttinger liquid behavior in GaAs/AlGaAs quantum wires, *Physica E* **6**, 551 (2000).
8. A.M. Chang: Chiral Luttinger liquids at the fractional quantum Hall edge, *Rev. Mod. Phys.* **75**, 1449 (2003)
9. C. Dekker: Carbon nanotubes as molecular quantum wires, *Phys. Today* **52**(5), 22 (1999)
10. R. Egger, A.O. Gogolin: Effective Low-Energy Theory for Correlated Carbon Nanotubes, *Phys. Rev. Lett.* **79**, 5082 (1997)
11. C.L. Kane, L. Balents, M.P.A. Fisher: Coulomb Interactions and Mesoscopic Effects in Carbon Nanotubes, *Phys. Rev. Lett.* **79**, 5086 (1997)
12. R. Egger, A.O. Gogolin: Correlated transport and non-Fermi-liquid behavior in single-wall carbon nanotubes, *Eur. Phys. J B* **3**, 281 (1998)
13. R. Egger, A. Bachtold, M.S. Fuhrer, M. Bockrath, D. Cobden, and P. McEuen: Luttinger liquid behavior in metallic carbon nanotubes, In *Interacting Electrons in Nanostructures*, ed. by R. Haug, H. Schoeller (Springer Lecture Notes in Physics, 2001)
14. M. Bockrath, D.H. Cobden, J. Lu, A.G. Rinzler, R.E. Smalley, L. Balents, and P.L. McEuen: Luttinger-liquid behaviour in carbon nanotubes, *Nature* **397**, 598 (1999)
15. Z. Yao, H.W.J. Postma, L. Balents, C. Dekker: Carbon nanotube intramolecular junctions, *Nature* **402**, 273 (1999)
16. C.L. Kane, M.P.A. Fisher: Transmission through barriers and resonant tunneling in an interacting one-dimensional electron gas, *Phys. Rev. B* **46**, 15233 (1992)
17. H.W.Ch. Postma, T. Teepen, Z. Yao, M. Grifoni, and C. Dekker: Carbon Nanotube Single-Electron Transistors at Room Temperature, *Science* **76**, 293 (2001)
18. M. Thorwart, M. Grifoni, G. Cuniberti, H. Postma, and C. Dekker: Correlated tunneling in intramolecular carbon nanotube quantum dots, *Phys. Rev. Lett.* **89**, 196402 (2002)
19. A. Furusaki, N. Nagaosa: Resonant Tunneling in a Luttinger liquid, *Phys. Rev. B* **47**, 3827 (1993)
20. A. Furusaki: Resonant tunneling through a quantum dot weakly coupled to quantum wires or quantum Hall edge states, *Phys. Rev. B* **57**, 7141 (1998)
21. W. Liang, M. Bockrath, D. Bozovic et al: *Nature* **411**, 665 (2001)
22. J. Kong, E. Yenilmez, T. Tombler et al: *Phys. Rev. Lett.* **87**, 106801 (2001)
23. M. Bockrath, W. Liang, D. Bozovic, J.H. Hafner, C.M. Lieber, M. Tinkham M, and H.K. Park, Resonant electron scattering by defects in single-wall carbon nanotubes, *Science* **291**, 283 (2001)
24. J.W. Park, J.B. Choi, K.H. Yoo: Formation of a quantum dot in a single-wall carbon nanotube using the Al top-gates, *Appl. Phys. Lett.* **81**, 2644 (2002)

25. A. Rosch and N. Andrei: Conductivity of a Clean One-Dimensional Wire, Phys. Rev. Lett. **85**, 1092 (2000)
26. S. Hügle, PhD Thesis, University of Düsseldorf (2003)
27. S. Hügle, R. Egger: Resonant tunneling in a Luttinger liquid for arbitrary barrier transmission, Europhys. Lett. **66**, 565 (2004)
28. M. Sassetti, F. Napoli, U. Weiss: Coherent transport of charge through a double-barrier in a Luttinger liquid, Phys. Rev. B **52**, 11213 (1995)
29. Y. Hu, S. Mukamel: Tunneling versus sequential long-range electron-transfer - Analogy with pump probe spectroscopy, J. Chem. Phys. **91**, 6973 (1989)
30. M. Thorwart, R. Egger, M. Grifoni: Correlated sequential tunneling through a double barrier for interacting one-dimensional electrons, preprint cond-mat/0407751
31. Yu. Nazarov, L.I. Glazman: Resonant Tunneling of Interacting Electrons in a One-Dimensional Wire, Phys. Rev. Lett. **91**, 126804 (2003)
32. D.G. Polyakov, I.V. Gornyi: Transport of interacting electrons through a double barrier in quantum wires, Phys. Rev. B **68**, 035421 (2003)
33. A. Komnik, A.O. Gogolin: Resonant Tunneling between Luttinger Liquids: A Solvable Case, Phys. Rev. Lett. **90**, 246403 (2003)
34. V. Meden, T. Enss, S. Andergassen, W. Metzner, and K. Schönhammer, Correlation effects on resonant tunneling in one-dimensional quantum wires, Phys. Rev. B **71**, 041302 (2005)
35. K. Moon, H. Yi, C. L. Kane, S. M. Girvin, and M. P. A. Fisher: Resonant tunneling between quantum Hall edge states, Phys. Rev. Lett. **71**, 4381 (1993)
36. K. Leung, R. Egger, C.H. Mak: Dynamical Simulation of Transport in One-Dimensional Quantum Wires, Phys. Rev. Lett. **75**, 3344 (1995)
37. C.H. Mak, R. Egger: Quantum Monte Carlo study of tunneling diffusion in a dissipative multistate system, Phys. Rev. E **49**, 1997 (1994)

Contacting Individual Molecules Using Mechanically Controllable Break Junctions

Jan van Ruitenbeek¹, Elke Scheer² and Heiko B. Weber^{3,4}

¹ Kamerlingh Onnes Laboratorium, Universiteit Leiden, Postbus 9504, 2300 RA Leiden, The Netherlands

Ruitenbeek@physics.leidenuniv.nl

² Universität Konstanz, Fachbereich Physik, Universitätsstr. 10, 78464 Konstanz, Germany

Elke.Scheer@uni-konstanz.de

³ Institut für Angewandte Physik, Universität Erlangen-Nürnberg, 91058 Erlangen, Germany

Heiko.Weber@physik.uni-erlangen.de

⁴ Forschungszentrum Karlsruhe, Institut für Nanotechnologie, 76021 Karlsruhe, Germany

Abstract. Among the experimental techniques employed in contacting individual molecules Mechanically Controllable Break Junctions are being frequently used. Some of the advantages are (1) straight-forward preparation of clean surfaces for anchoring the molecule; (2) the possibility to produce many different single-molecule junctions in one experiment, allowing obtaining statistical averages; (3) adapting the electrode gap to the molecules' length; (4) control over the mechanical stress of the molecule. We briefly review results obtained on organic molecules anchored to gold electrodes by thiol groups, both at room temperature and at cryogenic temperatures, and experiments on simple molecules chemisorbed to platinum electrodes.

1 Introduction

For studying the electronic transport through individual molecules , several experimental techniques, including scanning tunnelling microscopy (STM) [1], conducting atomic force microscopy (CAFM) [2] or microfabricated electrodes provided by different schemes have been considered [3–5]. Here we will focus on experiments employing Mechanically Controllable Break Junctions (MCBJ), which have a number of attractive features compared to the other methods used.

In STM and CAFM a certain quantity of the molecular compound under investigation is deposited onto a conducting surface. By varying the substrate material the interaction strength between the molecule and the surface can be tailored, which has been shown to be crucial for the interpretation of the electronic properties of the system [6, 7]. However, for a given substrate, the configuration of the molecule cannot be altered in a controlled manner. Since in those measurements the scanning probe is usually kept at a distance to the molecules, no chemical bond is formed between the molecule and the

tip, giving rise to a strongly asymmetric configuration of the electrochemical potentials of the system. When the amount of the deposited molecule is varied, interaction and self organization effects between the molecules can be studied [8, 9]. With high-speed STM the diffusion of molecules on surfaces was investigated even in real time [9, 10]. However, these methods usually require intensive cleaning procedures and ultrahigh vacuum techniques (UHV) in order to obtain reproducible conditions. Furthermore, scanning tunnelling spectroscopy at room temperature has a limited energy resolution in the range of 100 mV and changing external parameters as e.g. temperature or magnetic field give rise to position drifts that hamper the systematic study of an individual molecule. One of the main advantages of it is the fact that the actual configuration can be manipulated atom by atom or molecule by molecule [11] and monitored with atomic or even subatomic resolution [12]. Recently, a STM arranged logical device, consisting of about 300 CO molecules on a copper surface has been demonstrated [13]. The relatively complicated and expensive setup can be regarded, however, as a crucial drawback of STM and CAFM. Therefore, for defining devices for a possible use in nanoelectronics, direct and scalable electrodes that are separated by the typical size of the object under study are desirable.

With standard electron-beam lithography, electrode pairs with spacings below approximately 20 nm are difficult to define reproducibly. Therefore, several alternative methods, including electromigration methods [3] or electro-deposition [14], have been proposed and used successfully for special applications. For the study of the electronic properties of small ensembles of molecules, different techniques using self assembled monolayers and shadow evaporated, electron-beam defined electrodes have been used [15]. However, the success rate for these methods is usually rather low and the deposition of metal on top of a layer of molecules risks inducing uncontrolled chemical modifications. Another drawback of using electrodes that are fixed on a substrate is the lack of flexibility, concerning the contact configuration once the molecule or molecules of interest have been contacted.

A gap-width of the order of nanometers between two metal electrodes is easily adjusted mechanically by exploiting the MCBJ technique, which will be discussed in more detail below. It relies on mechanically breaking a metal wire, thus exposing clean fracture surfaces. This circumvents the problem of UHV surface preparation necessary in STM-type of experiments. The two wire ends are mounted on a bendable substrate at close proximity, so that the distance can be repeatedly adjusted by mechanically controlling the bending of the substrate and the junction is rather insensitive to the influence of external vibrations since both wire ends are fixed to the same substrate. The fresh fracture surfaces can then be exposed to the molecules of interest and the junction can be repeatedly opened and closed to search for characteristic conductance levels associated with a molecular bridge.

Once a molecular junction has been established, this junction may be stressed or deformed mechanically, resulting in different configurations and thus different electronic properties. Due to the small dimensions of the experimental device, the stability of the molecular junction is sufficient to allow investigating the same junction on a time scale that permits the systematic variation of control parameters such as temperature or magnetic field. Contacts can be opened and closed to large contacts repeatedly in the presence of the molecules of interest, thus allowing to gather statistical information on a certain molecular species. When necessary, by applying high voltage pulses to the electrodes they can even be cleaned and can be re-used for the same study without replacing the device. On the other hand, obvious drawbacks of the existing techniques are the lack of information of the atomic scale configuration of the junction and the fact that both electrodes are necessarily made of the same metal. Although in principle lithographically fabricated MCBJ devices can be incorporated into more complex electronic circuits, the mechanical control setup is rather large and does not easily allow the independent control of more than one junction. Thus, the MCBJ technique, although very useful for investigating fundamental properties of the electronic transport on the molecular scale, might be less appropriate for the fabrication of highly integrated molecular electronics devices. For the realization of molecular field effect transistors a third electrode controlling the electrostatic potential of the molecule is required, and has recently been achieved with MCBJ in combination with breaking by electromigration [16].

2 Experimental Techniques

2.1 Fabrication of the Electrodes

In a seminal experiment by Reed et al. [17], it has been demonstrated that molecules can be contacted by MCBJ [18–20]. Since then, different variations of MCBJ have been developed and used for this purpose [21–25]. The MCBJ technique was first proposed by Moreland and Ekin [18] for the fabrication of tunable tunnel junctions. Later the method has been refined and used for the investigation of stable single-atom contacts [19]. The principle of a MCBJ is shown in Fig. 1a. It consists of a wire with a manually fabricated constriction having a cross section of the order a few tens of micrometers. The wire is glued on both sides of the constriction to a flexible substrate, which is mounted on a three-point bending mechanism consisting of a pushing rod and two counter supports. By bending of the substrate with the help of a piezo drive, the wire is elongated such that the mechanical stress is concentrated in the constriction area. In the last stages of the elongation the lateral size of the constriction is gradually reduced to the size of a few atoms until it eventually breaks forming two separated electrodes. By controllably relaxing the bending of the substrate, the contact between them can be re-established. As a result

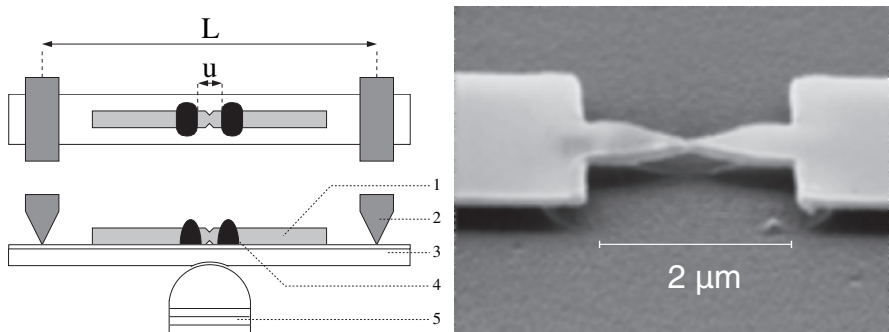


Fig. 1. (a) Schematic top and side view of the mounting of a MCBJ , having a notched wire (1), two fixed counter supports (2), a bending beam (3), two drops of epoxy adhesive (4), and a pushing rod consisting of stacked piezo element (5). (b) Electron micrograph of a lithographically fabricated MCBJ made of Co with a metal thickness of 150 nm

of the chosen geometry the setup itself acts as a reduction gear for the motion of the pushing rod with respect to the resulting relative displacement of the two electrodes. The reduction ratio is given by

$$r = \frac{\delta u}{\delta x} = \frac{6tu}{l^2} \quad (1)$$

where δu denotes the change of the electrode separation u when moving the pushing rod by δx (vertically in Fig. 1a). Since the substrate thickness t and the distance L of the counter supports cannot be easily varied over a wide range, the separation u between the anchor points of the bridge arms (i.e. the distance of the glue drops) controls the reduction ratio r . As this distance has a lower bound of a few tens of micrometers with the technique just described, a microfabricated version of the MCBJ technique has been put forward [20, 26]. An electron micrograph of such a lithographic MCBJ is given in Fig. 1b. By electron beam lithography a metallic nanowire is patterned, having a width of about 100 nm and a similar thickness, onto a flexible metallic substrate covered with an insulating sacrificial layer. The sacrificial layer is then partially removed by dry etching in order to suspend the nanobridge over a length of approximately 2 μ m. By virtue of the small length of the bridge the displacement ratio is of order 10^{-4} . In general, the displacement of the pushing rod that can be achieved with a piezo element corresponds to an electrode gap variation of ≈ 0.1 nm, in particular in low-temperature applications. The adjustment of the contact is therefore achieved by a purely mechanical drive. The stability of the atomic-sized contacts or molecular junctions formed with these devices has a higher stability than with the conventional MCBJ because external mechanical perturbations are reduced by the same displacement ratio. The main drawbacks of the use of a mechanical drive lie in the fact that mechanical systems have a larger backlash

(hysteresis), are slower, and their motion may lead to some heat generation. Furthermore, a mechanical drive rod needs to be installed that may give rise to additional heat load on low-temperature measurements. Nevertheless, the lithographic MCBJs have shown to be very useful for the formation and investigation of molecular junctions since they allow to fabricate particularly stable electrodes. The long-time stability can be estimated by recording the resistance of a clean metallic bridge when it is broken to form a tunnel junction. Taking the bulk value for the work function Φ of the metal and using the relation

$$R_T \propto \exp \left[\frac{2}{\hbar} \sqrt{2m^* \Phi} \cdot d \right] \quad (2)$$

for the tunnelling resistance R_T , where m^* is the electron effective mass, a value for the increment in the distance d between the electrodes can be obtained from a measurement of the change in resistance. We find that the stability at ambient conditions has a typical value of 250 pm (standard deviation averaged over 24 h) and achieves values of less than 1 pm at low temperature.

Thus, the MCBJ technique provides a simple method to prepare atomically spaced, clean and tunable pairs of electrodes. By controlling the distance of the electrodes they can be adapted to different sizes of molecules. Since both electrodes are of the same material and dimensions, symmetric contacting of the molecule is possible. By suitable choice of the electrode material and molecule, strong chemical bonds without extrinsic tunnel barriers are obtained. Depending on the nature of the molecule of interest, different techniques are used to deposit the molecules and to establish the contact between the electrodes and the molecules.

2.2 Deposition of Molecules

For the investigation of the transport through small molecules such as hydrogen, acetylene, carbon monoxide, or others presented in Sect. 3, a standard “notched-wire” MCBJ is broken at low temperature, i.e. under cryogenic UHV conditions. Platinum is chosen as electrode material for several reasons. First, it strongly chemisorbs some interesting small molecules. Secondly, due to its electronic properties, it is possible to detect unambiguously the presence of the molecules (see below). A small amount of the gaseous molecules, which is controlled by controlling the pressure in a small reservoir, is then inserted into the vacuum of the sample space. Only hydrogen has a finite vapor pressure at the desired measuring temperature that, for reasons of stability, spectroscopic resolution, and vacuum conditions, is kept at 4.2 K. For other substances the gasses were admitted through a capillary that can be temporarily heated by a resistive wire running all the way down its interior. Because of the large temperature gradient between the gas inlet at room temperature and the electrodes at low temperature, the amount of deposited gas molecules arriving on the electrodes is difficult to quantify. However, an

amount of $\approx 5 \mu$ mole has been shown to be suitable for the experiments described below. After the addition of the molecules the system is allowed to equilibrate for about one hour before the electronic measurements are started.

For the investigation of larger conjugated molecules, usually gold electrodes are employed because the molecules can be terminated by thiol groups that allow to establish a strong chemical bond to gold. This requires some wet chemistry at room temperatures. The first series of experiments were limited to room temperature [17, 21, 22], but procedures for low-temperature experiments have recently been established [27]. Once the MCBJ has been mounted onto the mechanical bending gear and measuring leads have been attached to the two ends of the junction, the electrodes are broken under ambient conditions to a distance of about 5 nm. A droplet of a solution containing a distinct concentration of the molecules is deposited onto an opened lithographic MCBJ. After a certain reaction time the molecules that did not establish a chemical bond are washed away by the addition of the pure solvent and a subsequent cleaning and drying procedure. After these steps the device is brought into high vacuum and room-temperature measurements can be performed immediately. For low-temperature measurements, particular care has to be taken to avoid insulating barriers e.g. due to ice formation. Furthermore, a single-molecule junction adjusted at room temperature cannot be held fixed during the cool-down procedure due to the difference in thermal contraction of the various construction materials used in the setup. In order to prevent the molecular bridge from contaminating, the MCBJ junction is closed thoroughly and opened again repeatedly before cool-down. Since the chemical bond between the thiol endgroups and the gold atoms of the electrodes is stronger than the gold-gold bonds within the outermost planes of the electrodes, the junction is expected to break within the electrodes themselves upon elongation. The result is that the molecules are attached with one thiol end to one of the electrodes, while the other thiol end is capped by a small gold cluster. After these preparations, the setup is cooled down to the desired measuring temperature that is usually about 30 K, or below. The gold electrodes and clusters are expected to remain fairly clean and a cold weld of the cluster cap to the other electrode can be made by bringing the electrodes closer together.

It is also possible to deposit molecules by thermal evaporation, as was recently done for fullerene molecules (C_{60}) [24]. A lithographic gold break junction (electrically connected to the measuring circuit) is broken at room temperature under high vacuum conditions $p \simeq 10^{-8}$ mbar to a distance of approximately 2–3 nm. The fullerenes are evaporated from a tungsten boat and the deposition is controlled by a quartz crystal. When half a monolayer is deposited, the evaporation is stopped and the bridge is closed. The fullerene molecules, which presumably land on the surface, are attracted into the gap both by diffusion and by dielectrophoresis, when a voltage is applied to the electrodes.

2.3 Measurement Techniques

One of the main advantages of the MCBJ technique is the possibility to manipulate the molecular junctions and to modify the measuring configuration. Depending on the system under study, different characterization procedures for the electrodes and for the junctions are performed that are described in Sects. 3 and 4, respectively. Here, we mention briefly the electronics for the setups.

The typical resistances of molecular junctions range from a few $k\Omega$ up to several $G\Omega$. Since most organic molecules present a large gap between filled and empty molecular orbitals, the current-voltage characteristics (IV) are often nonlinear, with differential resistances up to $T\Omega$ at low bias. In this resistance range it is advantageous to source a voltage and to measure the resulting current. This is either performed by a commercial automatic source-measure unit that allows to apply bias voltages from a few μV up to 10 V and to record currents from a few fA up to mA. The differential conductance can then be calculated numerically from the IV. However, for detecting small variations of the differential conductance as described in Sect. 3 it is advantageous to measure directly the differential conductance dI/dV by a lock-in technique. The absolute accuracy of the determination of the linear resistance is of the order of 1%, while relative changes down to 10^{-5} can be detected. However, two problems should be mentioned: First, usually this precision is not achieved at room temperature due to fluctuations of the junctions. Second, such measurements are slow compared to the relatively fast IV recording and may exceed the lifetime of the junction. In particular at high bias voltage ($V \sim 1V$) and at room temperature, the junction may be altered during the measurement.

When measurements of the conductance as a function of the inter-electrode distance are performed, e.g. for the recording of conductance histograms or the study of individual so-called opening or closing curves, a constant dc-bias voltage is applied, the current is recorded and the position of the electrodes is controlled by ramping the piezo voltage or running the motor linearly with a certain turning speed.

3 Simple Molecules

The early experiments aimed at probing the electronic transport properties of individual organic molecules have shown that it is difficult to identify the number of molecules actually contacted and that the characteristics observed vary widely between experiments. Under such conditions it is not surprising that there is also very little agreement with calculations. This situation forms a strong motivation to study simple systems that by themselves will not be useful as molecular devices, but that may provide a more viable test system to identify the problems in experiment and theory. The simplest molecule

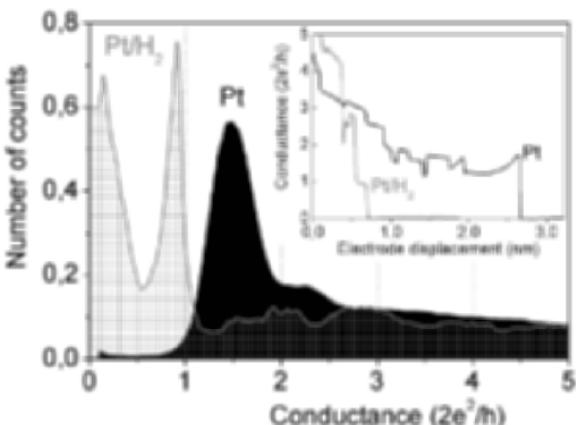


Fig. 2. Conductance curves and histograms for clean Pt, and Pt in a H₂ atmosphere. The curves for Pt in the inset and the histogram in the main panel were measured at a bias of 10 mV. The curve for Pt with H₂ in the inset was measured at 100 mV, and the histogram was obtained at 140 mV. All data were taken at 4.2 K under cryogenic vacuum. From [23]

is dihydrogen, which, as has been shown, can be contacted between platinum electrodes [23]. The discussion of the hydrogen experiments will occupy most of this section. Towards the end, experiments on slightly more complex molecules will be presented briefly.

Smit et al. [23] obtained molecular junctions of a hydrogen molecule between platinum leads by the method outlined in the previous section. The inset to Fig. 2 shows a conductance curve for clean Pt (black) at 4.2 K, before admitting H₂ gas into the system. About 10,000 similar curves were used to build the conductance histogram shown in the main panel (black, normalized by the area). After introducing hydrogen gas the conductance curves were observed to change qualitatively as illustrated by the gray curve in the inset. The dramatic change is most clearly brought out by the conductance histogram (gray, hatched).

Clean Pt contacts show a typical conductance of $1.5 \pm 0.2 G_0$ for a single-atom contact [†], as can be inferred from the position and width of the first peak in the Pt conductance histogram. Below $1 G_0$ very few data points are recorded, since Pt contacts tend to show an abrupt jump from the one-atom contact value into the tunnelling regime towards tunnel conductance values well below $0.1 G_0$. In contrast, after admitting hydrogen gas a lot of structure is found in the entire range below $1.5 G_0$, including a pronounced peak in the histogram near $1 G_0$. The research to date on this system has been focused on the molecular arrangement responsible for this sharp peak. Clearly, many

[†] $G_0 = 2e^2/h$ is the quantum unit of conductance

other junction configurations can be at the origin of the large density of data points a lower conductance, but they have not yet been studied in detail.

The interpretation of the peak at $1 G_0$ was obtained from combination of measurements, including vibrational spectroscopy and the analysis of conductance fluctuations, and Density Functional Theory (DFT) calculations. Experimentally, the vibration modes of the molecular structure were investigated by exploiting the principle of point contact spectroscopy for contacts adjusted to sit on a plateau in the conductance near $1 G_0$. The principle of point contact spectroscopy is similar to inelastic tunnelling spectroscopy (IETS, cf. Chap. 10), but differs somewhat in a few important details. As for IETS, the differential conductance is measured using a small modulation superimposed on a dc bias that is slowly swept over a wide voltage range. When the bias increases from 0 and crosses a voltage corresponding to the energy of a vibration mode in the contact, $eV = \hbar\omega$, a new channel for electron scattering opens. For an ideal one-channel contact the only option is backscattering since all forward propagating states are occupied. Thus, in contrast to IETS, to first approximation scattering by vibration modes leads to a drop in the conductance.

Figure 3 shows examples for Pt-H₂ and Pt-D₂ junctions at a plateau near $1 G_0$. The conductance is seen to drop by about 1 or 2%, symmetrically at positive and negative bias, as expected for electron-phonon scattering. The energies are in the range 50–60 meV, well above the Debye energy of ~20 meV for Pt metal. A high energy for a vibration mode implies that a light element

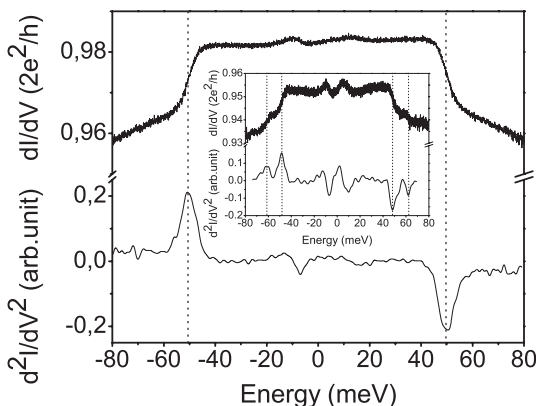


Fig. 3. Differential conductance curve for a molecule of D₂ contacted by Pt leads. The dI/dV curve (*top*) was recorded over 1 minute, using a standard lock-in technique with a voltage bias modulation of 1 meV at a frequency of 700 Hz. The lower curve shows the numerically obtained derivative. The spectrum for H₂ in the inset shows two phonon energies, at 48 and 62 meV. All spectra show some, usually weak, anomalies near zero bias that can be partly due to excitation of modes in the Pt leads, partly due to two-level systems near the contact. From [28]

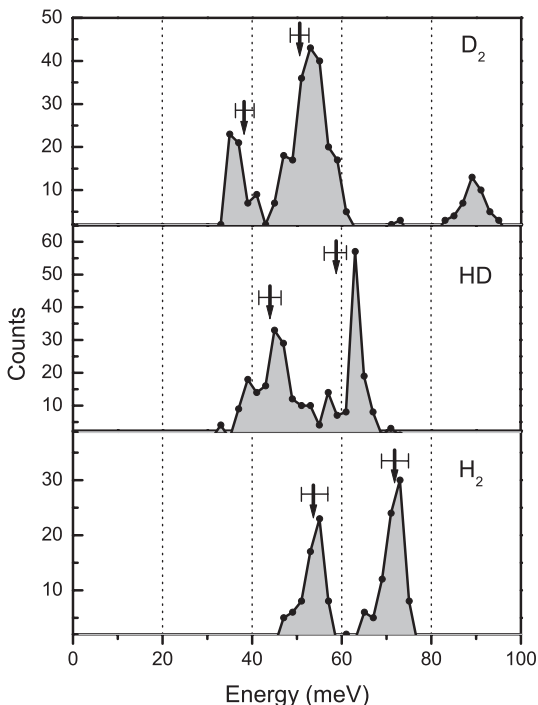


Fig. 4. Distribution of vibration mode energies observed for H₂, HD, and D₂ between Pt electrodes, with a bin size of 2 meV. The peaks in the distribution for H₂ are marked by arrows and their widths by error margins. These positions and widths were scaled by the expected isotope shifts, $\sqrt{2/3}$ for HD and $\sqrt{1/2}$ for D₂, from which the arrows and margins in the upper two panels have been obtained. From [28]

is involved, since the frequency is given by $\omega = \sqrt{\kappa/M}$ with κ an effective spring constant and M the mass of the vibrating object. The proof that the spectral features are indeed associated with hydrogen vibration modes comes from further experiments where H₂ was substituted by the heavier isotopes D₂ and HD. The positions of the peaks in the spectra of d^2I/dV^2 vary within some range between measurements on different junctions, which can be attributed to variations in the atomic geometry of the leads to which the molecules bind. Figure 4 shows histograms for the vibration modes observed in a large number of spectra for each of the three isotopes.

Two pronounced peaks are observed in each of the distributions, that scale approximately as the square root of the mass of the molecules, as expected. The two modes can often be observed together, as in the inset to Fig. 3. For D₂ an additional mode appears near 90 meV. This mode cannot easily be observed for the other two isotopes, since the lighter HD and H₂ mass shifts the mode above 100 meV where the junctions become very unstable. For a given

junction with spectra as in Fig. 3 it is often possible to stretch the contact and follow the evolution of the vibration modes. The frequencies for the two lower modes were seen to increase with stretching, while the high mode for D₂ is seen to shift downward. This unambiguously identifies the lower two modes as transverse modes and the higher one as a longitudinal mode for the molecule. This interpretation agrees nearly quantitatively with DFT calculations for a configuration of a Pt-H-H-Pt bridge in between Pt pyramidal shaped leads [28, 29]. The conductance obtained in the DFT calculations [23, 28, 29] also reproduces the value of nearly 1 G₀ for this configuration. The number of conduction channels found in the calculations is one, which agrees with the analysis of conductance fluctuations in the experiment of [23, 30]. The fact that the conductance is carried by a single channel demonstrates that there is indeed just a single molecule involved.

Several other DFT calculations have been performed, see e.g. [31, 32], where the agreement is only partial. Although Cuevas et al. [32] find a similar high value for the conductance, the molecular orbitals responsible for the transport are the bonding orbitals, while [23, 28, 29] attribute the transport almost entirely to the antibonding orbitals. This difference implies that the sign of the charge transfer between the molecule and the metal leads differs between the two types of calculations. Using a slightly different approach Garcia et al. [31] agree with Cuevas et al. on the bonding orbitals as the transport channel, but they obtain a conductance well below 1 G₀. They propose an alternative atomic arrangement to explain the high conductance for the Pt-H bridge, consisting of a Pt-Pt-bridge with two H atoms bonded to the sides. However, this configuration gives rise to three conductance channels, which is excluded based on the analysis of the conductance fluctuations as discussed above. The rather strong disagreement between various approaches in DFT calculations for this simple molecule show that there is a need for a reliable set of experimental data against which the various methods can be tested. The hydrogen metal-molecule-metal bridge may provide a good starting point since it is the simplest and it can be compared in detail by virtue of the many parameters that have been obtained experimentally.

Conductance histograms recorded using Fe, Co or Ni electrodes in the presence of hydrogen also show a pronounced peak near 1 G₀ [33], indicating that many transition metals may form similar single-molecule junctions. Also Pd seemed a good candidate, but Csonka et al. [30] did not observe the same suppression of conductance fluctuations as for Pt. There is an additional peak at 0.5 G₀ in the conductance histogram, and it was argued that hydrogen is incorporated into the bulk of the Pd metal electrodes.

Going beyond the simplest molecule using similar techniques much work is still in progress. Preliminary results have been obtained for CO and for C₂H₂ between Pt electrodes [33, 34]. By its high symmetry buckminster fullerene, C₆₀, also forms an excellent system to start with, and we will end this section by briefly reviewing the recent results.

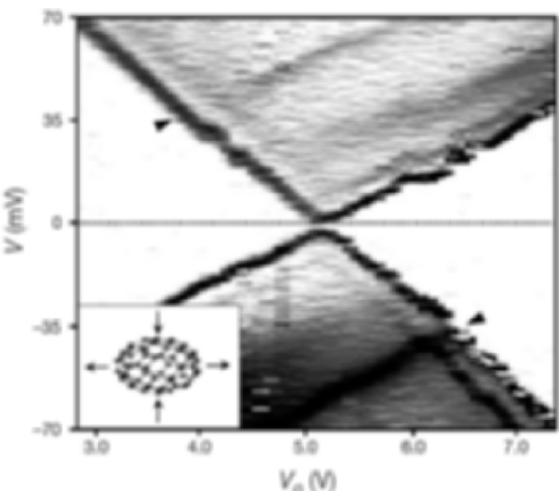


Fig. 5. Differential conductance gray-scale plot for a C_{60} molecule in a gold junction, obtained by electromigration breaking. High levels of dI/dV are shown in black and low levels white and these are plotted as a function of the gate voltage (ordinate) and the source-drain voltage (abscissa). Arrows mark the energy levels with an energy of 35 meV that are attributed to the excitation of the internal vibration mode illustrated in the inset. From [35]

Single-molecule junctions for C_{60} were first obtained by Park et al. [35], using pairs of gold electrodes broken by electromigration. The molecule in this case is weakly coupled to the electrodes, presumably by van der Waals forces and the low-bias conductance is extremely low (below 1 nS). However, the molecular levels can be shifted into resonance with the Fermi levels of the electrodes, either by increasing the source-drain bias voltage, or by use of a gate voltage, see Fig. 5. The gold electrodes for this device have been fabricated onto SiO_2 layer on top of a doped silicon wafer, that was employed as a back-gate. The molecular levels were observed to behave just as expected for the levels in a weakly coupled quantum dot. However, new features appeared as weak additional current jumps with energies of about 5 meV and 35 meV above threshold. They fit very well to the energies expected for a center-of-mass bouncing mode of the molecule as a whole, and an internal mode (Fig. 5, inset), respectively.

More recently Champagne et al. [16] combined the electromigration break technique and back gate with a mechanical adjustment of the junction by bending of the substrate, as mentioned above. Although they did not resolve the vibration modes they could manipulate the position of the energy levels for a C_{60} molecule and the strength of the coupling to the electrodes by controlling the gate voltage and the mechanical bending of the substrate, respectively. This will be an important tool for further investigations of

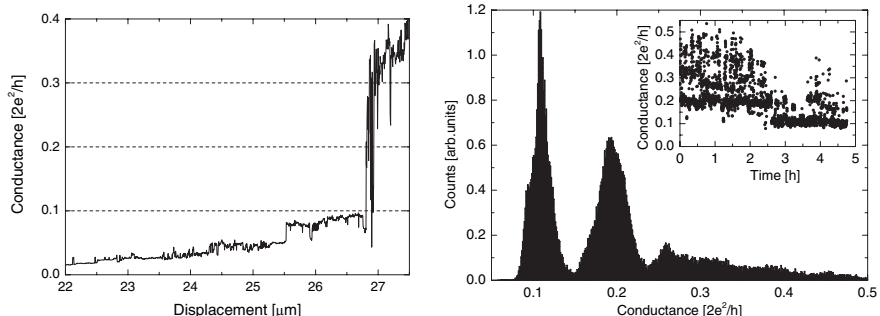


Fig. 6. Room temperature experiments on contacting C_{60} molecules in a lithographically fabricated MCBJ device. The left panel shows a typical trace of conductance vs. distance of the pushing rod while closing the contact after evaporation of the fullerene molecules. One often observes a plateau near $0.1 G_0$. For some contacts a spontaneous fluctuation is observed (right panel, inset) that is dominantly between two conductance levels of about 0.1 and $0.2 G_0$ as shown by the histogram. From [36]

single-molecule junctions. Again, the low-bias conductance in these experiments is very low which leads to sharply defined molecular levels.

Room temperature measurements [24,36] on the system C_{60} between gold electrodes reveal the possibility to establish low-resistance contacts between the metal and the molecules. Using a lithographically fabricated MCBJ device and evaporation of the molecules as described in Sect. 2.2, the bridge was opened slowly and the conductance was monitored. A typical trace is shown in Fig. 6 (left). In contrast to the measurements on the pure gold electrodes before deposition of the molecules, one often observes a conductance plateau close to $0.1 G_0$. When further closing the contact and then stopping the motion of the pushing rod, fluctuations as a function of time between two or three preferred conductance values may occur. An example is given in Fig. 6 (right), showing a histogram of such two-level fluctuations in the main panel and the corresponding conductance trace in the inset. The conductance fluctuates between $0.1 G_0$ and $0.2 G_0$, suggesting that a molecular junction is established by one fullerene molecule or two, respectively. The conductance plateau at $0.1 G_0$ is also regularly observed when opening the bridge. It is therefore interpreted as the preferred conductance of a single C_{60} molecule between metallically clean gold electrodes. This value is one to two orders of magnitude larger than that reported when contacting the molecules by other techniques [16, 35] which usually require the exposure of the electrodes to ambient conditions. and more experiments at low temperatures are needed to investigate this further.

4 Molecules Bonded by Thiol Groups to Gold

For conductance measurements on single, or few, organic molecules under controlled local environment, MCB's, but also an electrochemical STM can be used [37]. The STM of the Tao group was equipped with a gold covered tip and was repeatedly brought in contact with a gold surface such that gold filaments were formed and then retracted. These measurements were performed at room temperature in an ultrapure electrolyte. The phenomena observed are rather similar to the MCBJ experiments in the previous section: conductance plateaus at multiples of $G_0 = 2e^2/h$ occurred immediately before the disruption, which was analyzed by histogram techniques very similar to Fig. 2. Then an organic molecule was added to the electrolyte, for example a 4,4'-bipyridine which forms relatively stable bonds between the nitrogen atoms at both ends of the molecule and the Au surfaces. It turns out that the conductance plateaus close to $1G_0$ were more or less unaffected by the presence of the molecules, but in the histograms an additional peak at $\approx 0.01G_0$ and integer multiples thereof appeared. This was attributed to a single-molecule junction which temporarily was formed when the tip distance was such that a molecule fitted between the STM tip and the surface. In principle, the electrochemical setup is advantageous because it allows for an additional tuning parameter: the electrical potential within the electrolyte. For larger objects, this may be regarded as a gate electrode [38]. Here, the consequences of the reference voltage is mainly to stabilize or destabilize the nitrogen-gold bond. Experiments similar to those performed in Tao's group with STM in a wet cell, can also be done with a MCBJ approach, as demonstrated in [39].

The small molecules mentioned in Sect. 3 above are investigated at low temperatures and under clean conditions. There is an advantage in studying organic molecules which are designed to form stable covalent bonds to both electrodes. When the combination thiol endgroup (of the molecule) and gold electrode is chosen, the bonds are strong enough to form metal-molecule-metal contacts, which are stable even when one slightly pulls the electrodes apart. For example it has been measured with AFM techniques that the disruption force of thiol-ended molecules on gold is in the nano-Newton regime [40], and it has been calculated that when one pulls slightly at the molecules, a small atomically sharp tip forms, and finally (if one pulls further) some gold is pulled off the surface [41]. This has two consequences: First, these properties are favorable when *single*-molecule junctions are desired, because a broader contact will be reduced in diameter during pulling at the contact. Second, the strong thiol-gold bonds turn out to be strong enough to withstand relatively high currents and voltages even at room temperature. This is, of course, important for nanoelectronic applications.

As mentioned before, the first measurements have been performed by Reed and coworkers, who used the MCBJ technique to investigate 1,4-benzenedithiol [17]. The molecules were self assembled on the gold surface from solution and then the bridge was broken. Stable junctions were formed

and stable, reproducible IVs were recorded, which were clearly nonlinear. One of the final conclusions was “*The reproducibility of the minimum conductance at a consistent value implies that the number of active molecules could be as few as one*” [17]. This work stimulated a large number of theoretical calculations of the charge transport, the majority of which, however, overestimated the conductance by orders of magnitude compared to the experimental results.

Two years later, Kergueris *et al* published results from a similar experiment with a different molecule, based on thiophene units in the molecular backbone [21]. One important finding was that two stable configurations were observed, namely a symmetric one, but also one which was asymmetric in shape, a fact that could only be explained by an asymmetric geometrical realization of the metal-molecule-metal junction.

At this stage, many open question arose. Whereas the results obtained with molecules were clearly differing from blind experiments without molecules, no clear information was available on the number of molecules or how the molecules were arranged in the junction. Neither the experiment nor the theory were able to clarify the geometry.

Further insight was obtained from comparative studies with different molecules. As an example, Reichert *et al.* used an MCBJ device with molecules that were specially designed for this purpose [22,27]. In a first step, two molecular ‘rods’ were synthesized of comparable length with a conjugated inner part. The main difference is their symmetry, see Fig. 7: Molecule **1** has a mirror symmetry with the mirror plane between the electrodes and therefore both current directions are equivalent. This symmetry is absent in Molecule **2** due to two different side groups in the central unit. Consequently one could expect a different behavior for the two possible current directions and, consequently, an asymmetric IV.

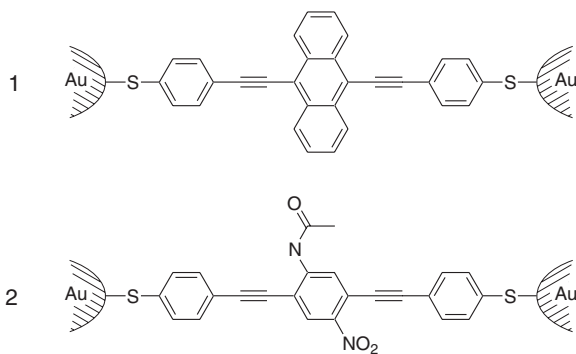


Fig. 7. Thiol-ended molecules **1** and **2**: a spatially symmetric (9,10-Bis((2'-para-mercaptophenyl)-ethinyl)-anthracene) and an asymmetric molecule (1,4-Bis((2'-para-mercaptophenyl)ethinyl)-2-acetyl-amino-5-nitro-benzene) in between two gold electrodes

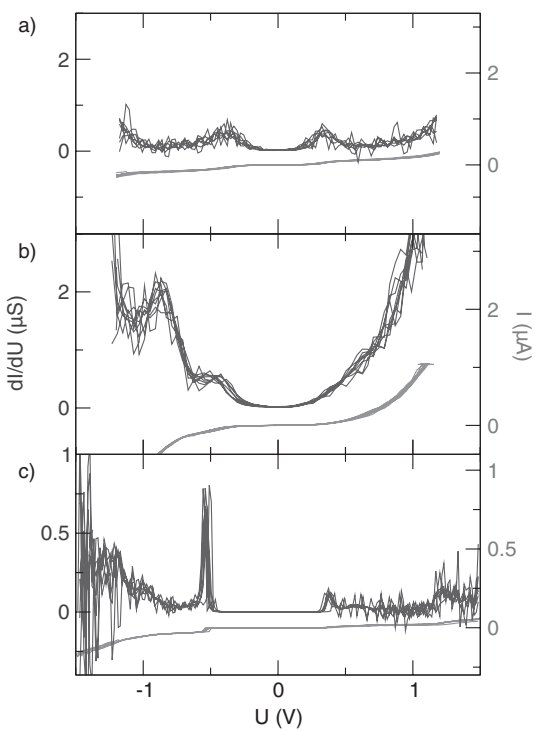


Fig. 8. Current voltage characteristics, reproducibly recorded for a stable junction in a MCBJ (red) and their numerical derivative dI/dU (blue). (a) with molecule **1** at room temperature, (b) with molecule **2** at room temperature, (c) with molecule **2** at $T = 30.6\text{K}$

The junctions were formed by a continuous opening and closing procedure, which results frequently in stable junctions before the contact disrupts (observed as a sudden decrease of the current), where nearly identical IVs could be detected subsequently several times. Figure 8 displays data thus obtained, both the IVs as well as its numerical derivative (blue). The junction is stable up to $V \approx 1.1$ V, allowing to trace the same IV several times. The current level ranges up to $1\mu\text{A}$. The IV curve is clearly nonlinear, having a broad step-like feature at $V = \pm 0.35$ V, which presumably corresponds to the onset of conductance when the first molecular orbital comes in resonance with the electrochemical potential of the electrodes. The blue curve is the differential conductance dI/dV , obtained by numerical differentiation of $I(V)$. It displays two peaks and the overall structure is to a good approximation symmetric. The corresponding curve for the asymmetric molecules is shown in Fig. 8b, it is clearly asymmetric. There are two important conclusions that can be drawn from this comparison: (i) the fact that the symmetric molecule gives symmetric IVs and the asymmetric molecule gives asymmetric IVs

proves that indeed the molecule is forming the contact (and not water or dust or anything else). (ii) the number of molecules is very small, perhaps even a single one: a large ensemble of molecules, being randomly oriented during the deposition on both electrodes, would result in a symmetric IV. These findings, together with additional observations described in [22] do not unambiguously prove, but indicate strongly that indeed a single molecule or at most a few molecules form the junction.

The data shown in Figs. 8a and 8b are typical examples of IV curves. When the measurement is repeated, the shapes of the IVs change: The peak position may shift up and down by 100 mV or it may appear at the opposite voltage sign, the overall conductance may vary within a factor of 10 as well as the peak height and peak width vary within a certain range. For the symmetric molecule **1**, sometimes also asymmetric IVs occur, which can be attributed to strongly asymmetric contacts, whereas for **2** the asymmetry is always observed. These sample to sample fluctuations are an intrinsic feature of *single* molecule junctions: The wave function of the molecule is sensitive to the molecule's local environment, which differs from junction to junction. This effect, which is the origin also for sample-to-sample fluctuations in optical experiments [42] will also affect the electronic transport properties. For single-molecule contacts, an additional effect comes into play: the sulphur can bond to different sites of the gold electrode tip because they are not well-defined on the atomic scale. Upon contact, however, this bond has become one part of the molecules' wave function. It has been shown theoretically that different atomic geometries in the contacts lead to a different charging of the molecules and in the peak shifts, similar to the phenomena observed in the experiment [43, 44].

One important finding is that the conductance of this type of molecule is significantly lower than for the short molecules discussed in Sect. 3. There are several factors that may play a role in explaining the difference. For a high transmission probability of the electrons, and therefore a high conductance, there should be at least one electronic orbital on the molecule that extends all the way across to the two ends. In addition, this orbital needs to hybridize strongly with the metallic states near the Fermi level in the leads. The sulphur atom, which accumulates some charge upon contact with the electrodes due to its high electronegativity forms an effective tunnel barrier, which reduces the transparency of the junction. The important role of the details of the molecular structure and, in particular, the role of the sulphur atom on the conductance properties has been demonstrated in [45, 46]. It is noteworthy that the spatial structure of a molecular junction is inhomogeneous, which plays an important role for the transport process. In particular for thiol-ended conjugated molecules, the conjugated part can be considered as an island, which is electronically decoupled from the electrodes by the sulphur atoms.

4.1 Low Temperatures

There are important advantages in taking the experiment to lower temperatures. Electronic excitations and in particular vibrational degrees of freedom are expected to be frozen out, giving rise to much sharper spectroscopic features. For the formation of the molecule-electrode bond, on the other hand, room-temperature conditions are required to enable the diffusion of the reaction products and to provide sufficient activation energy (other combinations than acetyl-protected thiol vs. gold might be suitable under different conditions, but have not yet been tested). The two requirements can be met by using the following procedure: Once a molecular junction is established at room temperature, it is reopened because it is difficult to control the electrode distance during the cool-down process. After cooling down to cryogenic temperatures the junction is closed again until stable IVs are observed. A detailed description of the experimental protocol can be found in [27]. The data thus obtained with molecules **2** are displayed in Fig. 8c). By comparing with Fig. 8b) one notes, as an example, that the broad minimum observed at room temperature develops at low temperature towards a blockade of the current around zero bias. Looking at the shoulder-like structure around -0.5 V in Fig. 8b), the features have a peak width of several hundred millivolts. In contrast, the peaks are much better resolved at low temperature. The molecule is indeed oscillating very fast at room temperature and the measurement thus averages over many configurations. The increase in stability can also be inferred from the larger accessible stable bias window, which spans from -1.5 V to 1.5 V at low temperature. In addition, the noise, which is intrinsic to the nanocontact and not due to experimental limitations, is substantially reduced.

Hence, molecules are soft objects and at finite temperature and at finite current they may tremble! This is clearly a qualitative difference to purely electronic phenomena in semiconductor quantum dots and may also be of certain interest for applications: mechanical degrees of freedom may be exploited as resistance switches and the oscillations observed with molecule **2** can be regarded as a precursor to such a switching event.

A chemically defined switching of the conductance between high and low states may be controlled by light, as demonstrated by Dulić et al. [47]. They used a photochromic molecule that can be switched from a high-conductance state to a low-conductance state under the influence of visible light and back under near UV irradiation. The two states had been investigated before in detail in solution. Dulić et al. used a lithographically fabricated MCBJ device to contact individual molecules of this kind, modified to have thiol-anchoring groups. They observed switching of the conductance of a molecule from the high-conductance state to the low-conductance state, but the reverse step was not obtained. They present evidence that the reverse step is suppressed as a result of the interaction of the UV light with surface plasmons in the gold electrodes.

5 Conclusions and Prospects

Although the field of molecular electronics has seen several false starts, we are now seeing some experiments that may provide a reliable basis for further development. The mechanically controllable break junction technique is likely to play an important role in these developments. However, in all cases the information obtained in the experiments is limited to whatever can be learned through current and voltage measurement and control. Imaging is still not possible, and the interpretation of the data is seldomly straightforward or unique. It is important to maintain a critical attitude towards the data and the interpretations, but there is good reason for optimism. It will be important to extend the collection of available experimental tools, e.g. by combining gate electrodes and force sensors, and by measuring shot noise, conductance fluctuations, interaction with light, and more. There is a lot that remains to be done, but we have a start.

Acknowledgements

We thank our coworkers T. Böhler, D. Djukic, J. Grebing, M. Di Leo, H. v. Löhneysen, Y. Noat, R. Ochs, J. Reichert, D. Secker, R.H.M. Smit, C. Untiedt, and J. Würfel, for their contributions to this work. Special thanks to M. Mayor for the intense collaboration and the synthesis of molecule **1** and **2**. Financial support by the Deutsche Forschungsgemeinschaft, Stichting FOM, the Alfried Krupp von Bohlen und Halbach-Stiftung, the Helmholtz association and the Volkswagen Foundation, is gratefully acknowledged.

References

1. C. Joachim, J.K. Gimzewski, R.R. Schlitter, C. Chavy: Electronic transparency of a single C₆₀ molecule, *Phys. Rev. Lett.* **74**, 2102–2105 (1995)
2. X.D. Cui, A. Primak, X. Zarate, J. Tomfohr, O.F. Sankey, A.L. Moore, T.A. Moore, D. Gust, G. Harris, S.M. Lindsay: Reproducible measurement of single-molecule conductivity, *Science* **294**, 571–574 (2001)
3. H. Park, A.K.L. Lim, A.P. Alivisatos, J. Park, P.L.M. Euen: Fabrication of metallic electrodes with nanometer separation by electromigration, *Appl. Phys. Lett.* **75**, 301–303 (1999)
4. S. Kubatkin, A. Danilov, M. Hjort, J. Cornil, J.L. Brédas, N. Stuhr-Hansen, P. Hedegård, T. Bjørnholm: Single-electron transistor of a single organic molecule with access to several redox states, *Nature (London)* **425**, 698–701 (2003)
5. Y.V. Kervennic, J.M. Thijssen, D. Vanmaekelbergh, R. Dabirian, C.A. van Walree, L.W. Jenneskens, H.S.J. van der Zant: “Orbital transport in a molecular transistor”, unpublished
6. A.Y. Kasumov, D. Klinov, P.E. Roche, S. Gueron, H. Bouchiat: Thickness and low-temperature conductivity of DNA molecules, *Appl. Phys. Lett.* **84**, 1007–1009 (2004)

7. T. Heim, D. Deresmes, D. Vuillaume: Conductivity of DNA probed by conducting-atomic force microscopy: effects of contact electrode, DNA structure, and surface interactions., *J. Appl. Phys.* **96**, 2927–2936 (2004)
8. M. Morgenstern, J. Kljn, C. Meyer, D. Haude, R. Wiesendanger: Visualizing the influence of interactions on the nanoscale: simple electron systems, American Institute of Physics Conference Proceedings pp. 11–19 (2003)
9. R. Schaub, E. Wahlstrom, A. Ronnau, E. Laegsgaard, I. Stensgaard, F. Besenbacher: Oxygen-mediated diffusion of oxygen vacancies on the TiO₂/(110) surface, *Science* **299**, 377–379 (2003)
10. L. Kuipers, M. Hoogeman, J. Frenken, H. van Beijeren: Step and kink dynamics on Au (110) and Pb (111) studied with a high-speed stm., *Phys. Rev. B* **52**, 11 387–11 397 (1995)
11. D.M. Eigler, E.K. Schweizer: Positioning single atoms with a scanning tunnelling microscope., *Nature* **344**, 524–526 (1990)
12. M. Herz, F.J. Giessibl, J. Mannhart: Probing the shape of atoms in real space, *Phys. Rev. B* **68**, 045 301 (2003)
13. A.J. Heinrich, C.P. Lutz, J.A. Gupta, D.M. Eigler: Molecule cascades, *Science* **298**, 1381–1387 (2002)
14. A.F. Morpurgo, C.M. Marcus, D.B. Robinson: Controlled fabrication of metallic electrodes with atomic separation, *Phys. Rev. Lett.* **74**, 2084–2086 (1999)
15. N.B. Zhitenev, A. Erbe, Z. Bao: Single- and multigrain nanojunctions with a self-assembled monolayer of conjugated molecules, *Phys. Rev. Lett.* **92**, 186 805/1–4 (2004)
16. A.R. Champagne, A.N. Pasupathy, D.C. Ralph: “Mechanically-adjustable and electrically-gated single-molecule transistors”, preprint, cond-mat/0409134
17. M.A. Reed, C. Zhou, C.J. Muller, T.P. Burgin, J. M.Tour: Conductance of a molecular junction, *Science* **278**, 252–254 (1997)
18. J. Moreland, J.W. Ekin: Electron tunneling experiments using Nb-Sn ‘break’ junctions, *J. Appl. Phys.* **58**, 3888–3895 (1985)
19. C.J. Muller, J.M. van Ruitenbeek, L.J. de Jongh: Experimental observation of the transition from weak link to tunnel junction, *Physica C* **191**, 485–492 (1992)
20. J.M. van Ruitenbeek, A. Alvarez, I. Pineyro, C. Grahmann, P. Joyez, M.H. Devoret, D. Esteve, C. Urbina: Adjustable nanofabricated atomic size contacts, *Rev. Sci. Instrum.* **67**, 108–111 (1996)
21. C. Kergueris, J.P. Bourgoin, S. Palacin, D. Esteve, U. Urbina, M. Magoga, C. Joachim: Electron transport through a metal-molecule-metal junction, *Phys. Rev. B* **59**, 12 505–12 513 (1999)
22. J. Reichert, R. Ochs, D. Beckmann, H. Weber, M. Mayor, H. v. Löhneysen: Driving current through single organic molecules, *Phys. Rev. Lett.* **88**, 176 804/1–4 (2002)
23. R.H.M. Smit, Y. Noat, C. Untiedt, N.D. Lang, M.C. van Hemert, J.M. van Ruitenbeek: Measurement of a conductance of a hydrogen molecule, *Nature* **419**, 906–908 (2002)
24. T. Böhler, J. Grebing, A. Mayer-Gindner, H. v. Löhneysen, E. Scheer: Mechanically controllable breakjunctions for use as electrodes for molecular electronics, *Nanotechnology* **15**, 465–471 (2004)
25. N. Agraït, A.L. Yeyati, J.M. van Ruitenbeek: Quantum properties of atomic-sized conductors, *Phys. Rep.* **377**, 81–279 (2003)

26. C. Zhou, C.J. Muller, M.R. Deshpande, J.W. Sleigh, M.A. Reed: Microfabrication of a mechanically controllable break junction in silicon, *Appl. Phys. Lett.* **67**, 1160–1162 (1995)
27. J. Reichert, H.B. Weber, M. Mayor, H. von Löhneysen: Low-temperature conductance measurements on single molecules, *Appl. Phys. Lett.* **82**, 4137–4139 (2003)
28. D. Djukic, K.S. Thygesen, C. Untiedt, R.H.M. Smit, K.W. Jacobsen, J. van Ruitenbeek: “Stretching dependence of the vibration modes of a single-molecule Pt-H₂-Pt bridge”, preprint, cond-mat/0409640
29. K.S. Thygesen, K.W. Jacobsen: Conduction mechanism in a molecular hydrogen contact, *Phys. Rev. Lett.* **94**, 036 807/1–4 (2005)
30. S. Csonka, A. Halbritter, G. Mihály, O.I. Shklyarevskii, S. Speller, H. van Kempen: Conductance of Pd-H nanojunctions, *Phys. Rev. Lett.* **93**, 016 802/1–4 (2004)
31. Y. García, J.J. Palacios, E. SanFabián, J.A. Vergés, A.J. Pérez-Jiménez, E. Louis: Electronic transport and vibrational modes in a small molecular bridge: H₂ in Pt nanocontacts, *Phys. Rev. B* **69**, 041 402/1–4 (2004)
32. J.C. Cuevas, J. Heurich, F. Pauly, W. Wenzel, G. Schön: Theoretical description of a electrical conduction in atomic and molecular junctions, *Nanotechnology* **14**, R29–R38 (2003)
33. C. Untiedt, D.M.T. Dekker, D. Djukic, J.M. van Ruitenbeek: *Phys. Rev. B* **69**, 081 401(R)/1–4
34. D. Djukic, J.M. van Ruitenbeek: Unpublished
35. H. Park, J. Park, A.K.L. Kim, P.L.M.E. E. H. Anderson A. P. Alivisatos: Nanomechanical oscillations in a single C₆₀ transistor, *Nature* **407**, 57–59 (2000)
36. T. Böhler, J. Grebing, E. Scheer: “Electronic transport through individual fullerene molecules”, unpublished
37. B. Xu, N.J. Tao: Measurement of single-molecule resistance by repeated formation of molecular junctions, *Science* **302**, 1221–1223 (2003)
38. M. Krueger, M. Buitelaar, T. Nussbaumer, L. Forro, C. Schönenberger: Electrochemical carbon nanotube field-effect transistor, *Appl. Phys. Lett.* **78**, 1291–1293 (2001)
39. L. Grüter, M.T. González, R. Huber, M. Calame, C. Schönenberger: “Conductance of atomic contacts in liquid environment”, preprint, cond-mat/0401666
40. M. Grandbois, M. Beyer, M. Rief, H. Clausen-Schaumann, H.E. Gaub: How strong is a covalent bond?, *Science* **283**, 1727–1729 (1999)
41. D. Krüger, H. Fuchs, R. Rousseau, D. Marx, M. Parrinello: Pulling monatomic gold wires with single molecules: An ab initio simulation, *Phys. Rev. Lett.* **89**, 186 402/1–4 (2002)
42. P. Tamarat, A. Maali, B. Lounis, M. Orrit: Ten years of single-molecule spectroscopy, *J. Phys. Chem. A* **104**, 1 (2000)
43. H.B. Weber, J. Reichert, F. Weigend, R. Ochs, D. Beckmann, M. Mayor, R. Ahlrichs, H. v. Löhneysen: Electronic transport through single conjugated molecules, *Chem. Phys.* **281**, 113 (2002)
44. F. Evers, F. Weigend, M. Köntopp: Conductance of molecular wires and transport calculations based on density-functional theory, *Phys. Rev. B* **69**, 235 411 (2004)

45. M. Mayor, H.B. Weber, J. Reichert, M. Elbing, C. v. Hänisch, D. Beckmann, M. Fischer: Electric current through a molecular rod – relevance of the anchor group position, *Angewandte Chemie Int. Ed.* **42**, 5834 (2003)
46. M. Mayor, C. v. Hänisch, H.B. Weber, J. Reichert, D. Beckmann, M. Fischer: A *trans*-Pt(ii) als single-molecule insulator, *Angewandte Chemie Int. Ed.* **41**, 1183 (2002)
47. D. Dulić, S.J. van der Molen, T. Kudernac, H.T. Jonkman, J.J.D. de Jong, T.N. Bowden, J. van Esch, B.L. Feringa, B.J. van Wees: One-way optoelectronic switching of photochromic molecules on gold, *Phys. Rev. Lett.* **91**, 207402/1–4 (2003)

Intrinsic Electronic Conduction Mechanisms in Self-Assembled Monolayers

Wenyong Wang¹, Takhee Lee², and Mark A. Reed³

¹ Semiconductor Electronics Division, National Institute of Standards and Technology, M.S. 8120, Gaithersburg, MD 20899-8120, USA

² Department of Materials Science and Engineering, Gwangju Institute of Science and Technology, Gwangju 500-712, Korea

³ Departments of Electrical Engineering and Applied Physics, Yale University, P.O. Box 208284, New Haven, CT 06520, USA
mark.reed@yale.edu

Abstract. A review on the mechanisms and characterization methods of molecular electronic transport is presented. Using self-assembled monolayers (SAMs) of alkanethiols in a nanometer scale device structure, tunneling is unambiguously demonstrated as the main conduction mechanism for large bandgap SAMs, exhibiting well-known temperature and length dependencies. Inelastic electron tunneling spectroscopy exhibits clear vibrational modes of the molecules in the device, presenting the first direct evidence of the presence of molecules in a molecular device.

1 Introduction

The suggestion [1] and demonstration [2] of utilizing molecules as the active region of electronic devices has recently generated considerable interest in both the basic transport physics and potential technological applications of “molecular electronics” [3, 4]. However some reports of molecular mechanisms in electronic devices [5, 6] have been shown to be premature and due to filamentary conduction [7], highlighting the fabrication sensitivity of molecular structures and the need to institute reliable controls and methods to validate true molecular transport [8]. A related problem is the characterization of molecules in the active device structure, including their configuration, bonding, and indeed even their very presence. Here we present results on well-understood molecular assemblies, which exhibit an understood classical transport behavior, and which can be used as a control for eliminating (or understanding) fabrication variables. Utilizing tunneling spectroscopic methods, we present the first unambiguous evidence of the presence of molecules in the junction.

A molecular system whose structure and configuration are sufficiently well-characterized such that it can serve as a standard is the extensively studied alkanethiol ($\text{CH}_3(\text{CH})_{n-1}\text{SH}$) self-assembled monolayer (SAM) [9]. This system is useful as a control since properly prepared SAMs form single van der Waals crystals [9, 10], and presents a simple classical metal-insulator-metal (M-I-M) tunnel junction when fabricated between metallic contacts due

to the large HOMO-LUMO gap (HOMO: highest occupied molecular orbital, LUMO: lowest unoccupied molecular orbital) of approximately 8 eV [11, 12].

Various surface analytical tools have been utilized to investigate the surface and bulk properties of the alkanethiol SAMs, such as X-ray photoelectron spectroscopy [13], Fourier transform infrared spectroscopy (FTIR) [14], Raman spectroscopy [15], scanning tunneling microscopy (STM) [10], etc. Studies have shown that the bonding of the thiolate group to the gold surface is strong with a bonding energy of ~ 1.7 eV [9]. STM topography examinations revealed that alkanethiols adopt the commensurate crystalline lattice characterized by a $c(4 \times 2)$ superlattice of a $(\sqrt{3} \times \sqrt{3})R30^\circ$ [10, 16]. FTIR investigation showed that the orientation of the alkanethiol SAMs on Au(111) surfaces are tilted $\sim 30^\circ$ from the surface normal [17].

Electronic transport through alkanethiol SAMs have also been characterized by STM [18, 19], conducting atomic force microscopy [20–23], mercury-drop junctions [24–27], cross-wire junctions [28], and electrochemical methods [29–31]. These investigations are exclusively at ambient temperature – clearly useful – but insufficient for an unambiguous claim that the transport mechanism is tunneling (of course expected, assuming that the Fermi levels of the contacts lie within the large HOMO-LUMO gap). However in the absence of temperature-dependent current-voltage ($I(V,T)$) characteristics, other conduction mechanisms (such as thermionic, hopping, or filamentary conduction) can contribute and complicate the analysis, and thus such a claim is premature.

Utilizing a nanometer scale device structure that incorporates alkanethiol SAMs, we demonstrate devices that allow $I(V,T)$ and structure-dependent measurements [32, 33] with results that can be compared with accepted theoretical models of M-I-M tunneling. The use of this fabrication approach is not special in any way (other than that we have so far found it to be successful) – indeed we stress that any successful device fabrication method should yield the results described below if one is characterizing the intrinsic molecular transport properties.

The electronic transport is further investigated with the technique of inelastic electron tunneling spectroscopy (IETS) [33]. IETS was developed in the 1960's as a powerful spectroscopic tool to study the vibrational spectrum of organic molecules confined inside metal-oxide-metal junctions [34–38]. In our study IETS is utilized for the purpose of molecule identification, chemical bonding, and conduction mechanism investigation of the “control” SAMs. The exclusive presence of well-known vibrational modes of the alkanes used are direct evidence of the molecules in the device structure, something that has to date only been inferred (with good reason, but nonetheless not unambiguously). The vibrational modes, exclusively identified as alkanes (as well as contact modes) are difficult to interpret in any other way other than as components in the active region of the device. The specific spectral lines also yield intrinsic linewidths that may give insight into molecular conformation,

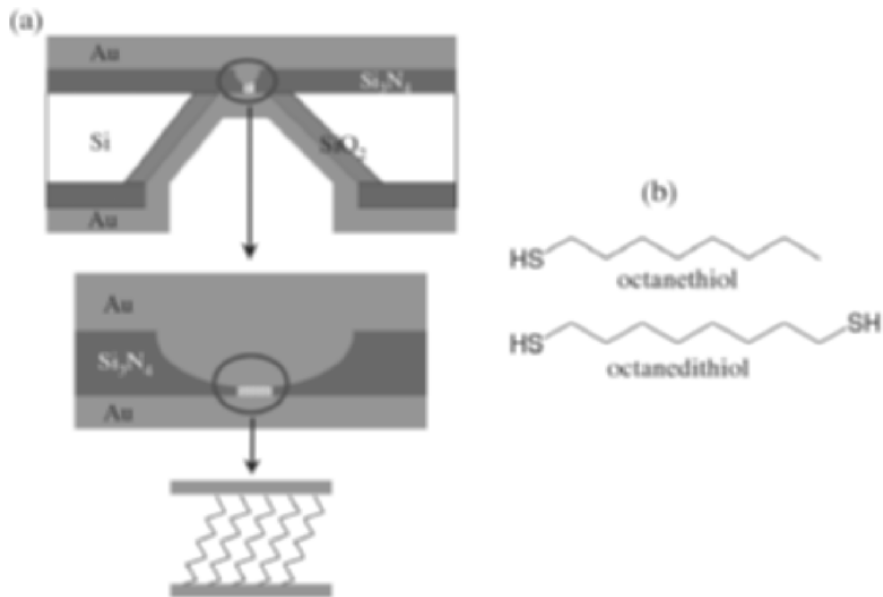


Fig. 1. Schematics of a nanometer scale device used in this study. (a) Top schematic is the cross section of a silicon wafer with a nanometer scale pore etched through a suspended silicon nitride membrane. Middle and bottom schematics show a Au/SAM/Au junction formed in the pore area. (b) The structures of octanethiol and octanedithiol are shown as examples

and may prove to be a powerful tool in future molecular device characterization.

2 Experiment

Electronic transport measurements on alkanethiol SAMs were performed using a device structure similar to one reported previously [32, 33, 39–41]. In this device, as illustrated in Fig. 1(a), a number of molecules (~several thousands) are sandwiched between two metallic contacts. This technique provides a stable device structure and makes cryogenic measurements possible. The device fabrication starts with a high resistivity silicon wafer with low stress Si₃N₄ film deposited on both sides by low pressure chemical vapor deposition (LPCVD). By standard photolithography processing, a suspended Si₃N₄ membrane (size of 40 μm × 40 μm and thickness of ~70 nm) is fabricated on the topside of the wafer. Subsequent e-beam lithography and reactive ion etching creates a single pore with a diameter of tens of nanometers through the membrane. As the next step, 150 nm gold is thermally evaporated onto the topside of the wafer to fill the pore and form one of the metallic contacts.

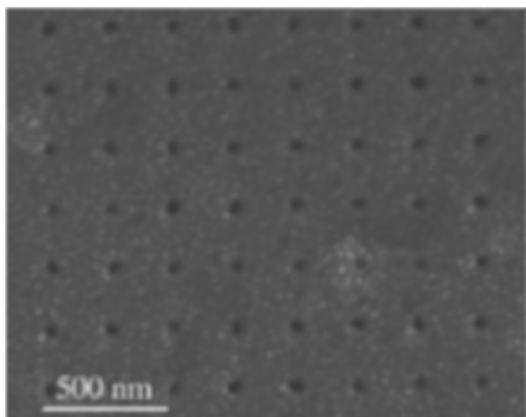


Fig. 2. A scanning electron microscope image of a representative array of pores used to calibrate device size. The scale bar is 500 nm

The device is then transferred into a molecular solution to deposit the SAM layer. For our experiments, a ~5 mM alkanethiol solution is prepared by adding ~10 μ L alkanethiols into 10 mL ethanol. The deposition is done in solution for 24 hours inside a nitrogen filled glove box with an oxygen level of less than 100 ppm. Three alkanemonothiol molecules of different molecular lengths-octanethiol [$\text{CH}_3(\text{CH}_2)_7\text{SH}$; denoted as C8, for the number of alkyl units], dodecanethiol [$\text{CH}_3(\text{CH}_2)_{11}\text{SH}$, denoted as C12], and hexadecanethiol [$\text{CH}_3(\text{CH}_2)_{15}\text{SH}$, denoted as C16] and one alkanedithiol molecule-octanedithiol [$\text{HS}(\text{CH}_2)_8\text{SH}$, denoted as C8-dithiol] were used to form the active molecular components. As representative examples, the chemical structures of octanethiol and octanedithiol are shown in Fig. 1(b).

In order to statistically determine the pore size, test patterns (arrays of pores) were created under similar fabrication conditions. Figure 2 shows a scanning electron microscope (SEM) image of such test pattern arrays. This indirect measurement of device size is done since SEM examination of the actual device can cause hydrocarbon contamination of the device and subsequent contamination of the monolayer. From regression analysis of 298 pores, the device sizes of the C8, C12, C16, and C8-dithiol samples are 50 ± 8 , 45 ± 2 , 45 ± 2 , and 51 ± 5 nm in diameters, respectively. A more ideal (less parasitics) C8 sample supersedes that of previous reports [32], and derived parameters from the two data sets agree to within a standard error. We will use these device areas as the effective contact areas. Although one could postulate that the actual area of metal that contacts the molecules may be different, there is little reason to propose it would be different as a function of length over the range of alkanethiols used, and at most would be a constant systematic error. Further on we will show that the results from the current density agree with the results from length dependence, giving an independent check that the effective area is in fact the actual area.

The sample is then transferred in ambient conditions to an evaporator that has a cooling stage to deposit the opposing Au contact. During the thermal evaporation (under the pressure of $\sim 10^{-8}$ Torr), liquid nitrogen is kept flowing through the cooling stage in order to avoid thermal damage to the molecular layer [32, 42]. This technique reduces the kinetic energy of evaporated Au atoms at the surface of the monolayer, thus preventing Au atoms from punching through the monolayer. For the same reason the evaporation rate is kept very low. For the first 10 nm gold evaporated, the rate is less than 0.1 Å/s. Then the rate is increased slowly to 0.5 Å/s for the rest of the evaporation and a total of 200 nm gold is deposited to form the contact.

The device is subsequently packaged and loaded into a low temperature cryostat. The sample temperature is varied from 300 to 4.2 K by flowing cryogen vapor onto the sample (and thermometer) using a closed loop temperature controller. Two-terminal dc I(V) measurements are performed using a semiconductor parameter analyzer. Inelastic electron tunneling spectra are obtained via a standard lock-in second harmonic measurement technique [34, 35]. A synthesized function generator is used to provide both the modulation and the lock-in reference signal. The second harmonic signal (proportional to d^2I/dV^2) is directly measured using a lock-in amplifier, which is checked to be consistent with a numerical derivative of the first harmonic signal (proportional to dI/dV). Various modulation amplitudes and frequencies are utilized to obtain the spectra. The ac modulation is added to a dc bias using operational amplifier-based custom circuitry [43].

3 Theoretical Basis

3.1 Possible Conduction Mechanisms

In Table 1, possible conduction mechanisms are listed with their characteristic current, temperature- and voltage-dependencies [44] (We do not discuss filamentary tunneling mechanisms, which are easier to categorize [45]. Based on whether thermal activation is involved, the conduction mechanisms fall into two distinct categories: (i) thermionic or hopping conduction which has temperature-dependent I(V) behavior and (ii) direct tunneling or Fowler-Nordheim tunneling which does not have temperature-dependent I(V) behavior. For example, thermionic and hopping conductances have been observed for 4-thioacetyl biphenyl SAMs [39] and 1,4-phenylene diisocyanide SAMs [40]. On the other hand, the conduction mechanism is expected to be tunneling when the Fermi levels of contacts lie within the large HOMO-LOMO gap for short length molecule, as for the case of alkanethiol molecular system [11, 12]. Previous work on Langmuir-Blodgett alkane monolayers [46] exhibited a significant impurity-dominated transport component, complicating the analysis. I(V) measurements on self-assembled alkanethiol monolayers have also been

Table 1. Possible conduction mechanisms. Adapted from [44]

Conduction Mechanism	Characteristic Behavior	Temperature Dependence	Voltage Dependence
Direct tunneling*	$J \propto V \exp\left(-\frac{2d}{\hbar}\sqrt{2m\Phi}\right)$	none	$J \propto V$
Fowler-Lordheim tunneling	$J \propto V^2 \exp\left(-\frac{4d\sqrt{2m}\Phi^{3/2}}{3q\hbar V}\right)$	none	$\ln(J/V^2) \propto 1/V$
Thermionic emission	$J \propto T^2 \exp\left(-\frac{\Phi-q\sqrt{qV/4\pi e d}}{kT}\right)$	$\ln(J/T^2) \propto 1/T$	$\ln(J) \propto V^{1/2}$
Hopping conduction	$J \propto V \exp\left(-\frac{\Phi}{kT}\right)$	$\ln(J/V) \propto 1/T$	$J \propto V$

* This characteristic of direct tunneling is valid for the low bias regime [see (3)].

reported [18, 28, 47]; however all of these measurements were performed at fixed temperature (300 K) which is insufficient to prove tunneling as the dominant mechanism.

3.2 Tunneling Models

To describe the transport through a molecular system having HOMO and LUMO energy levels, one of the applicable models is the Franz two-band model [48, 51]. This model provides a non-parabolic energy-momentum $E(k)$ dispersion relationship by considering the contributions of both the HOMO and LUMO energy levels [48]:

$$k^2 = \frac{2m^*}{\hbar^2} E \left(1 + \frac{E}{E_g} \right) \quad (1)$$

where k is the imaginary part of wave vector of electrons, m^* is the electron effective mass, $\hbar (= 2\pi\hbar)$ is Planck's constant, E is the electron energy, and E_g is the HOMO-LUMO energy gap. From this non-parabolic $E(k)$ relationship, the effective mass of the electron tunneling through the SAM can be deduced by knowing the barrier height of the metal-SAM-metal junction.

When the Fermi level of the metal is aligned close enough to one energy level (either HOMO or LUMO), the effect of the other distant energy level on the tunneling transport is negligible, and the widely used Simmons model [52] is an excellent approximation [53]. Simmons model expressed the tunneling current density through a barrier in the tunneling regime of $V < \Phi_B/e$ as [24, 52]

$$J = \frac{e}{4\pi^2\hbar d^2} \left\{ \left(\Phi_B - \frac{eV}{2} \right) \times \exp \left[-\frac{2(2m)^{1/2}}{\hbar} \alpha \left(\Phi_B - \frac{eV}{2} \right) d \right] \right. \\ \left. - \left(\Phi_B + \frac{eV}{2} \right) \times \exp \left[-\frac{2(2m)^{1/2}}{\hbar} \alpha \left(\Phi_B + \frac{eV}{2} \right) d \right] \right\} \quad (2)$$

where m is the electron mass, d is the barrier width, Φ_B is the barrier height, and V is the applied bias. For molecular systems, the Simmons model has been modified with a parameter α [24,32]. α is a unitless adjustable parameter that is introduced to provide either a way of applying the tunneling model of a rectangular barrier to tunneling through a nonrectangular barrier [24], or an adjustment to account for the effective mass (m^*) of the tunneling electrons through a rectangular barrier [24,32,51,54], or both. $\alpha = 1$ corresponds to the case for a rectangular barrier and bare electron mass. By fitting individual I(V) data using (2), Φ_B and α values can be obtained.

Equation (1) can be approximated in two limits: low bias and high bias as compared with the barrier height Φ_B . For the low bias range, (2) can be approximated as [52]

$$J \approx \left(\frac{(2m\Phi_B)^{1/2} e^2 \alpha}{\hbar^2 d} \right) V \exp \left[-\frac{2(2m)^{1/2}}{\hbar} \alpha (\Phi_B)^{1/2} d \right] \quad (3)$$

To determine the high bias limit, we compare the relative magnitudes of the first and second exponential terms in (2). At high bias, the first term is dominant and thus the current density can be approximated as

$$J \approx \left(\frac{e}{4\pi^2\hbar d^2} \right) \left\{ \left(\Phi_B - \frac{eV}{2} \right) \times \exp \left[-\frac{2(2m)^{1/2}}{\hbar} \alpha \left(\Phi_B - \frac{eV}{2} \right) d \right] \right\} \quad (4)$$

The tunneling currents in both bias regimes are exponentially dependent on the barrier width d. In the low bias regime the tunneling current density is $J \propto \frac{1}{d} \exp(-\beta_0 d)$, where β_0 is bias-independent decay coefficient:

$$\beta_0 = \frac{2(2m)^{1/2}}{\hbar} \alpha (\Phi_B)^{1/2} \quad (5)$$

while in the high bias regime, $J \propto \frac{1}{d^2} \exp(-\beta_V d)$, where β_V is bias-dependent decay coefficient:

$$\beta_V = \frac{2(2m)^{1/2}}{\hbar} \alpha \left(\Phi_B - \frac{eV}{2} \right)^{1/2} = \beta_0 \left(1 - \frac{eV}{2\Phi_B} \right)^{1/2} \quad (6)$$

At high bias β_V decreases as bias increases, which results from barrier lowering effect due to the applied bias.

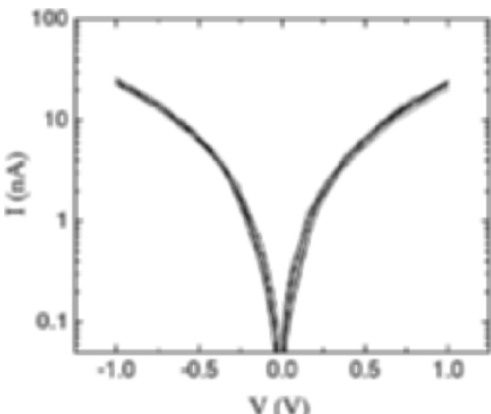


Fig. 3. Temperature-dependent $I(V)$ characteristics of dodecanethiol (C12). $I(V)$ data at temperatures from 300 to 80 K with 20 K steps are plotted on a log scale

4 Results

4.1 Current-Voltage Characteristics

Temperature-Variable Current-Voltage ($I(V,T)$) Measurement

In order to determine the conduction mechanism of self-assembled alkanethiol molecular systems $I(V)$ measurements in a sufficiently wide temperature range (300 to 80 K) and resolution (10 K) were performed. Figure 3 shows a representative $I(V,T)$ characteristic of dodecanethiol (C12) measured with the device structure as shown in Fig. 1(a). Positive bias corresponds to electrons injected from the physisorbed Au contact [bottom contact in Fig. 1(a)] into the molecules. By using the contact area of 45 ± 2 nm in diameter determined from SEM study, a current density of $1,500 \pm 200$ A/cm² at 1.0 Volt is determined. No significant temperature dependence of the characteristics (from $V = 0$ to 1.0 Volt) is observed over the range from 300 to 80 K. An Arrhenius plot ($\ln(I)$ versus $1/T$) of this is shown in Fig. 4(a), exhibiting little temperature dependence in the slopes of $\ln(I)$ versus $1/T$ at different bias and thus indicating the absence of thermal activation. Therefore, we conclude that the conduction mechanism through alkanethiol is tunneling contingent on demonstrating a correct molecular length dependence. The tunneling through alkanethiol SAMs has been assumed as “through-bond” tunneling, i.e., along the tilted molecular chains between the metal contacts [21, 22, 31, 55]. Based on the applied bias as compared with the barrier height (Φ_B), the tunneling through a SAM layer can be categorized into either direct ($V < \Phi_B/e$) or Fowler-Nordheim ($V > \Phi_B/e$) tunneling. These two tunneling mechanisms can be distinguished due to their distinct voltage dependencies (see Table 1). Analysis of $\ln(I^2/V)$ versus $1/V$ [in Fig. 4(b)] shows no significant voltage

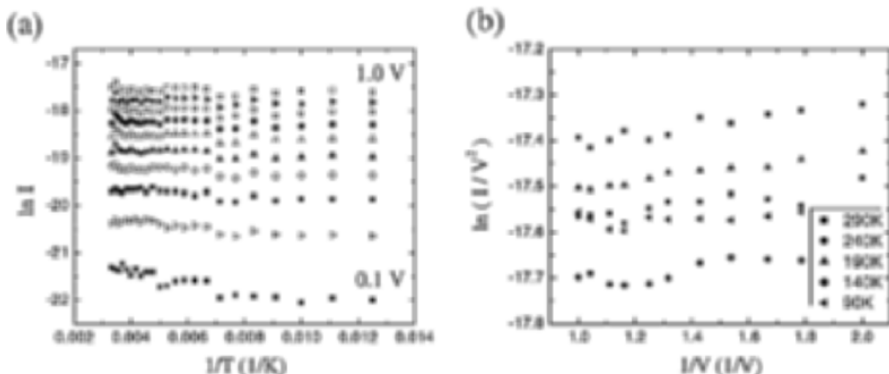


Fig. 4. (a) Arrhenius plot generated from the I(V) data in Fig. 3, at voltages from 0.1 to 1.0 Volt with 0.1 Volt steps. (b) Plot of $\ln(I^2/V)$ versus $1/V$ at selected temperatures

dependence, indicating no obvious Fowler-Nordheim transport behavior in this bias range (0 to 1.0 Volt) and thus determining that the barrier height is larger than the applied bias, i.e., $\Phi_B > 1.0$ eV. This study is restricted to applied biases ≤ 1.0 Volt and the transition from direct to Fowler-Nordheim tunneling requires higher bias. Having established tunneling as the conduction mechanism, we can now obtain the barrier height by comparing our experimental I(V) data with theoretical calculations from the aforementioned tunneling models.

Tunneling Characteristics through Alkanethiols

From the modified Simmons model [see (2)] by adjusting two parameters Φ_B and α , a nonlinear least squares fitting can be performed to fit the measured C12 I(V) data (calculation assuming $\alpha = 1$ has been previously shown not to fit I(V) data well for some alkanethiol measurements at fixed temperature (300 K)) [24]. By using a device size of 45 nm in diameter, the best fitting parameters (minimizing χ^2) for the room temperature C12 I(V) data were found to be $\Phi_B = 1.42 \pm 0.04$ eV and $\alpha = 0.65 \pm 0.01$, where the error ranges of Φ_B and α are dominated by potential device size fluctuations of 2 nm. Likewise, data sets were obtained and fittings were done for octanethiol (C8) and hexadecanethiol (C16), which yielded values $\{\Phi_B = 1.83 \pm 0.10$ eV and $\alpha = 0.61 \pm 0.01\}$ and $\{\Phi_B = 1.40 \pm 0.03$ eV, $\alpha = 0.68 \pm 0.01\}$, respectively.

Using $\Phi_B = 1.42$ eV and $\alpha = 0.65$, a calculated I(V) for C12 is plotted as a solid curve on a linear scale [Fig. 5(a)] and a semi-log scale [Fig. 5(b)]. A calculated I(V) for $\alpha = 1$ and $\Phi_B = 0.65$ eV (which gives the best fit at low bias range) is shown as the dashed curve in the same figure, illustrating that with $\alpha = 1$ only limited regions of the I(V) can be fit (specifically here, for V

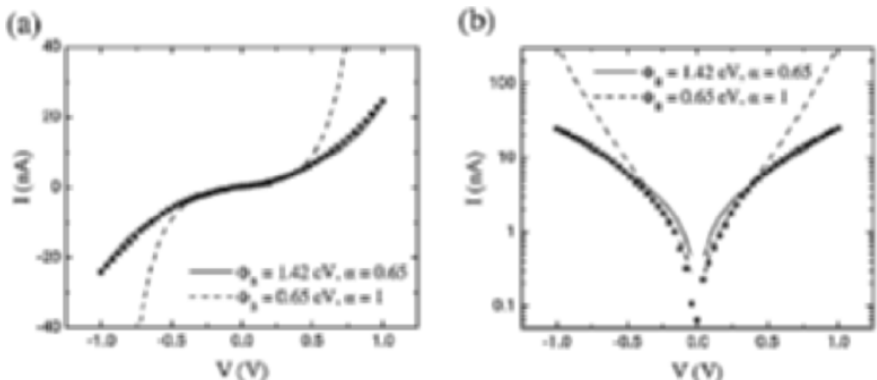


Fig. 5. Measured C12 I(V) data (*circular symbols*) is compared with calculation (*solid curve*) using the optimum fitting parameters of $\Phi_B = 1.42$ eV and $\alpha = 0.65$. The calculated I(V) from a simple rectangular model ($\alpha = 1$) with $\Phi_B = 0.65$ eV is also shown as the dashed curve. Current is plotted (a) on linear scale and (b) on log scale

< 0.3 Volt). For the case of a rectangular barrier, the parameter fit presented above corresponds to an effective mass m^* ($= \alpha^2 m$) of 0.42 m. In order to investigate the dependency of the Simmons model fitting on Φ_B and α , a fitting minimization analysis was undertaken on the individual Φ_B and α values as well as their product form of $\alpha\Phi_B^{1/2}$ in (5). $\Delta(\Phi_B, \alpha) = (\sum |I_{\text{exp},V} - I_{\text{cal},V}|^2)^{1/2}$ was calculated and plotted where $I_{\text{exp},V}$ is the experimental current-voltage values and $I_{\text{cal},V}$ is calculated using (2). 7,500 different $\{\Phi_B, \alpha\}$ pairs were used in the fittings with Φ_B ranging from 1.0 to 2.5 eV (0.01 eV increment) and α from 0.5 to 1.0 (0.01 increment). Figure 6(a) is a representative contour plot of $\Delta(\Phi_B, \alpha)$ versus Φ_B and α values generated for the C12 I(V) data where darker regions correspond to smaller $\Delta(\Phi_B, \alpha)$ and various shades represent half order of magnitude $\Delta(\Phi_B, \alpha)$ steps. The darker regions represent better fits of (1) to the measured I(V) data. In the inset in Fig. 6(a) one can see there is a range of possible Φ_B and α values yielding minimum fitting parameters. Although the tunneling parameters determined from the previous Simmons tunneling fitting $\{\Phi_B = 1.42$ eV and $\alpha = 0.65\}$ lie within this minimum region in this figure, there is a distribution of other possible values.

A plot of $\Delta(\Phi_B, \alpha)$ versus $\alpha\Phi_B^{1/2}$ for the same device reveals a more pronounced dependence, and is shown in Fig. 6(b). This plot indicates the fitting to the Simmons model sharply depends on the product of $\alpha\Phi_B^{1/2}$. For this plot the $\Delta(\Phi_B, \alpha)$ is minimized at $\alpha\Phi_B^{1/2}$ of 0.77 (eV) $^{1/2}$ corresponding to a β_0 value of 0.79 Å $^{-1}$ from (5). The C8 and C16 devices showed similar results, indicating the Simmons tunneling model has a strong $\alpha\Phi_B^{1/2}$ dependence.

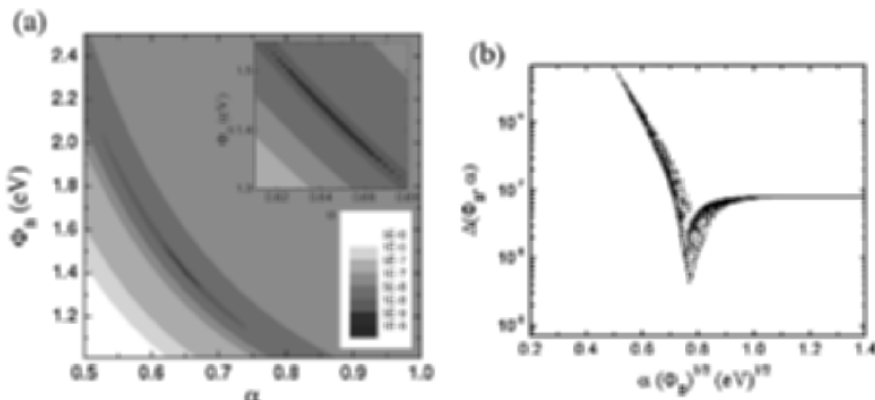


Fig. 6. (a) Contour plot of $\Delta(\Phi_B, \alpha)$ values for C12 nanopore device as a function of Φ_B and α , where the darker region corresponds to a better fitting. Inset shows detail minimization fitting regions. (b) A plot of $\Delta(\Phi_B, \alpha)$ as a function of a $\alpha\Phi_B^{1/2}$

Length-Dependent Tunneling through Alkanethiols

Three alkanethiols of different molecular length, C8, C12, and C16 were investigated to study length-dependent tunneling behavior. Figure 7 is a semi-log plot of tunneling current densities multiplied by molecular length (J_d at low bias and J_d^2 at high bias) as a function of the molecular length for these alkanethiols. The molecular lengths used in this plot are 13.3, 18.2, and 23.2 Å for C8, C12, and C16, respectively (each molecular length was determined by adding an Au-thiol bonding length to the length of molecule [21]). Note that these lengths assume through-bond tunneling [21, 22, 31, 55]. The high and low bias regimes are defined somewhat arbitrarily by comparing the relative magnitudes of the first and second exponential terms in (2). Using $\Phi_B = 1.42$ eV and $\alpha = 0.65$ obtained from nonlinear least squares fitting of the C12 I(V) data, the second term becomes less than $\sim 10\%$ of the first term at ~ 0.5 Volt that is chosen as the boundary of low and high bias ranges.

As seen in Fig. 7, the tunneling current shows exponential dependence on molecular length, which is consistent with the Simmons tunneling model [see (3) and (4)]. The β values can be determined from the slope at each bias and are plotted in Fig. 8. The error bar of an individual β value in this plot was obtained by considering both the device size uncertainties and the linear fitting errors.

The determined β values are almost independent of bias in the low bias range ($V < \sim 0.5$ V), and an average β of 0.77 ± 0.06 Å⁻¹ in this region (from 0 to 0.5 V) can be calculated from Fig. 8. The β value (0.77 ± 0.06 Å⁻¹ ≈ 0.96 ± 0.08 per methylene) for alkanethiols reported here is comparable to previously reported values as summarized in Table 2. This β value agrees with the value of 0.79 Å⁻¹(β_0) calculated via (5) from fitting individual I(V)

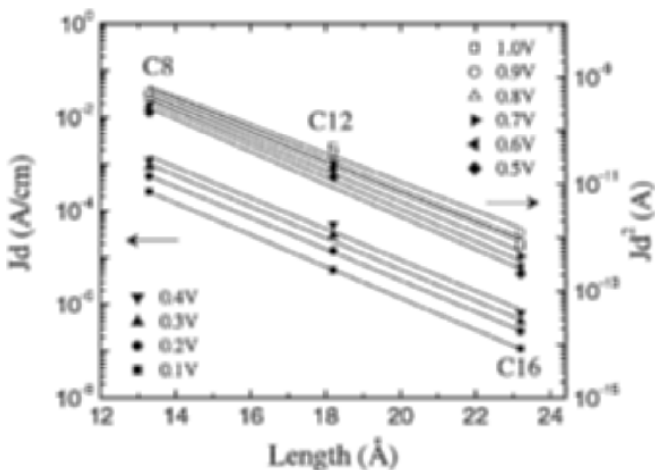


Fig. 7. Log plot of tunneling current densities multiplied by molecular length d at low bias and by d^2 at high bias (symbols) versus molecular lengths. The lines through the data points are linear fittings

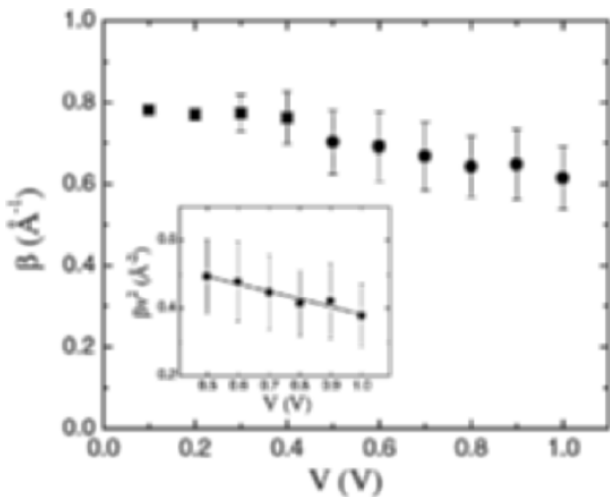


Fig. 8. Plot of β versus bias in the low bias range (square symbols) and high bias ranges (circular symbols). The inset shows a plot of β_V^2 versus bias with a linear fitting

characteristic of the C12 device. The calculated β_0 of C8 and C16 devices also have similar values, as summarized in Table 3.

According to (6), β_V^2 depends on bias V linearly in the high bias range. The inset in Fig. 8 is a plot of β_V^2 versus V in this range (0.5 to 1.0 Volt) along with linear fitting of the data. From this fitting, $\Phi_B = 1.35 \pm 0.20$ eV and

Table 2. Summary of alkanethiol tunneling characteristic parameters

Junction	β (\AA^{-1})	J (A/cm^2) at 1 V	Φ_B (eV)	Technique	
(bilayer) monothiol	0.87 ± 0.1	25–200 ^{a)}	2.1 ^{e)}	Hg-junction	[24]
(bilayer) monothiol	0.71 ± 0.08	0.7–3.5 ^{a)}		Hg-junction	[26]
monothiol	0.79 ± 0.01	$1500 \pm 200^b)$	1.4 ^{e)}	Solid M-I-M	[32]
monothiol	1.2			STM	[18]
dithiol	0.8 ± 0.08	$3.7\text{--}5 \times 10^5^c)$	$5 \pm 2^f)$	STM	[19]
monothiol	0.73–0.95	1100–1900 ^{d)}	2.2 ^{e)}	CAFM	[20]
monothiol	0.64–0.8	10–50 ^{d)}	2.3 ^{e)}	CAFM	[22]
dithiol	0.46 ± 0.02	$3\text{--}6 \times 10^5^c)$	1.3–1.5 ^{e)}	CAFM	[23]
monothiol	1.37 ± 0.03		1.8 ^{f)}	Tuning fork AFM	[47]
monothiol	0.97 ± 0.04			Electrochemical	[29]
monothiol	0.85			Electrochemical	[30]
monothiol	0.91 ± 0.08			Electrochemical	[31]
monothiol	0.76	2×10^4 (at 0.1 V)	1.3–3.4 ^{g)}	Theory	[56]
monothiol	0.76			Theory	[57]
monothiol	0.79			Theory	[54]

Note:

Some decay coefficients b were converted into the unit of \AA^{-1} from the unit of per methylene.

The junction areas were estimated by optical microscope^{a)}, SEM^{b)}, assuming single molecule^{c)}, and Hertzian contact theory^{d)}.

Current densities (J) for C12 monothiol or dithiol at 1 V are extrapolated from published results for other length molecules by using conductance $\propto \exp(-\beta d)$ relationship.

Barrier height Φ_B values were obtained from Simmons equation^{e)}, bias-dependence of $\beta^f)$, and a theoretical calculation^{g)}.

$\alpha = 0.66 \pm 0.04$ were obtained from the intercept and the slope, respectively, consistent with the values $\{\Phi_B = 1.42$ eV and $\alpha = 0.65\}$ obtained from the nonlinear least squares fitting in the previous section.

β values for alkanethiols obtained by various experimental techniques have previously been reported and are summarized in Table 2 [18–32, 47]. In order to compare with these reported β values, we also performed length-dependent analysis on our experimental data according to the generally used equation [19–27, 32]:

$$G = G_0 \exp(-\beta d). \quad (7)$$

This gives a β value from 0.84 to 0.73 \AA^{-1} in the bias range from 0.1 to 1.0 volt, which is comparable to results reported previously. For example, Holmlin, et al, reported a β value of 0.87\AA^{-1} by mercury drop experiments [24], and Wold, et al, have reported β of 0.94\AA^{-1} and Cui, et al, reported β of 0.64\AA^{-1} for various alkanethiols by using a conducting atomic force microscope technique [20, 22]. These reported β were treated as bias-independent

Table 3. Summary of alkanethiol tunneling parameters in this study

Molecules	J (A/cm ²) at 1 V	Φ_B (eV)	α	m^* (m)	β_0 (Å ⁻¹) [*]
C8	31,000 ± 10,000	1.83 ± 0.10	0.61 ± 0.01	0.37	0.85 ± 0.04
C12	1,500 ± 200	1.42 ± 0.04	0.65 ± 0.01	0.42	0.79 ± 0.02
C16	23 ± 2	1.40 ± 0.03	0.68 ± 0.01	0.46	0.82 ± 0.02
C8-dithiol	93,000 ± 18,000	1.20 ± 0.03	0.59 ± 0.01	0.35	0.66 ± 0.02

* β_0 values were calculated from (5) using Φ_B and α .

quantities, contrary to the results reported here and that observed in a slightly different alkane system (ligand-encapsulated nanoparticle/alkane-dithiol molecules) [23]. We also caution again the use of parameters that have not been checked against a temperature-dependent analysis, since small non-tunneling components can dramatically affect derived values of β .

Franz Model

We have analyzed our experimental data using a Franz two-band model [48–51]. Since there is no reliable experimental data on the Fermi level alignment in these metal-SAM-metal systems, Φ_B and m^* are treated as adjustable parameters. We performed a least squares fit on our data with the Franz non-parabolic E(k) relationship [see (1)] using an alkanethiol HOMO-LUMO gap of 8 eV.¹ Figure 9 shows the resultant E(k) relationship and the corresponding energy band diagrams. The zero of energy in this plot was chosen as the LUMO energy. The best fitting parameters obtained by minimizing χ^2 were $\Phi_B = 1.49 \pm 0.51$ eV and $m^* = 0.43 \pm 0.15$ m, where the error ranges of Φ_B and m^* are dominated by the error fluctuations of β [$-k^2 = (\beta/2)^2$]. Both electron tunneling near the LUMO and hole tunneling near the HOMO can be described by these parameters. $\Phi_B = 1.49$ eV indicates that the Fermi level is aligned close to one energy level in either case, therefore the Simmons model is a valid approximation. The Φ_B and m^* values obtained here are in reasonable agreement with the previous results obtained from the Simmons model.

4.2 Inelastic Tunneling

Inelastic Electron Tunneling Spectroscopy

Electronic transport through alkanethiol SAMs is further investigated with the technique of inelastic electron tunneling spectroscopy [33], such as the

¹ Although the HOMO-LUMO gap of alkyl chain type molecules has been reported (see [12]), there is no experimental data on the HOMO-LUMO gap for Au/alkanethiol SAM/Au system. 8 eV is commonly used as HOMO-LUMO gap of alkanethiol

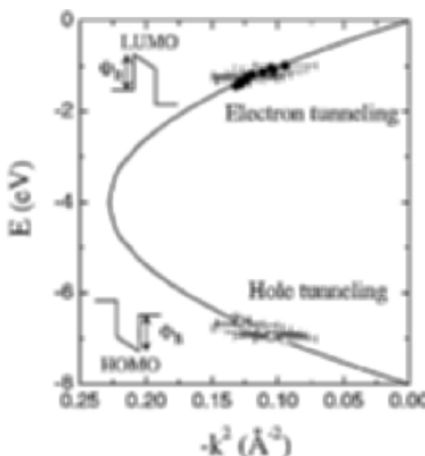


Fig. 9. $E(k)$ relationship (symbols) generated from the length-dependent measurement data for alkanethiols. Solid and open symbols correspond to electron and hole, respectively. The insets show the corresponding energy band diagrams. The solid curve is the Franz two-band expression for $m^* = 0.43 \text{ m}$

works of 1966 by Jaklevic and Lambe who studied the conductance of a tunnel junctions with encased organic molecules [34]. Since then it has become a powerful spectroscopic tool for chemical identification, chemical bonding investigation, and surface chemistry and physics studies [37]. In an inelastic tunneling process the electron loses energy to a localized vibrational mode with a frequency when the applied bias satisfies the condition of $eV = h\nu$. As a result, an additional tunneling channel is opened for the electron, resulting in an increase in the total current at the applied bias corresponding to the vibrational mode energy [36]. Typically only a small fraction of tunneling electrons are involved in the inelastic tunneling process (determined by the electron – vibronic mode coupling coefficient), resulting in a small conductance change, which is commonly measured in the second harmonics of a phase-sensitive detector that yields the characteristic frequencies of the corresponding vibrational modes as well as other information [35–37].

$I(V,T)$ measurements and additional IETS studies have been performed on an octanedithiol (C8-dithiol) SAM using the aforementioned device structure shown in Fig. 1(a) [33]. Figure 10(a) is the $I(V,T)$ data for this device obtained from 300 to 4.2 K. An Arrhenius plot shown in Fig. 10(b) exhibits little temperature dependence, verifying that tunneling is the main transport mechanism for C8-dithiol SAM. This result is in good agreement with the tunneling transport characteristics observed previously. Figure 11 shows the room temperature $I(V)$ measurement result. Using a junction area of $51 \pm 5 \text{ nm}$ in diameter (obtained from statistical studies of the nanopore size with SEM), a current density of $(9.3 \pm 1.8) \times 10^4 \text{ A/cm}^2$ at 1.0 Volt is calculated.

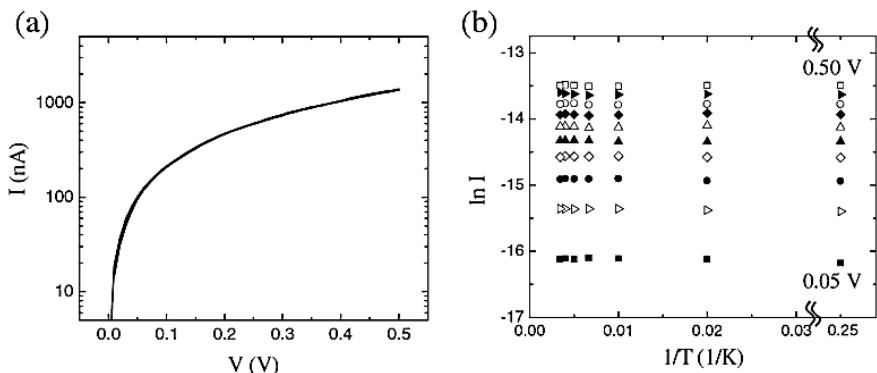


Fig. 10. (a) $I(V,T)$ characteristics of C8-dithiol SAM at selected temperatures (4.2, 50, 100, 150, 200, 250, and 290 K). (b) Arrhenius plot generated from the data in (a), at voltages from 0.1 to 0.5 Volt with 0.05 Volt steps

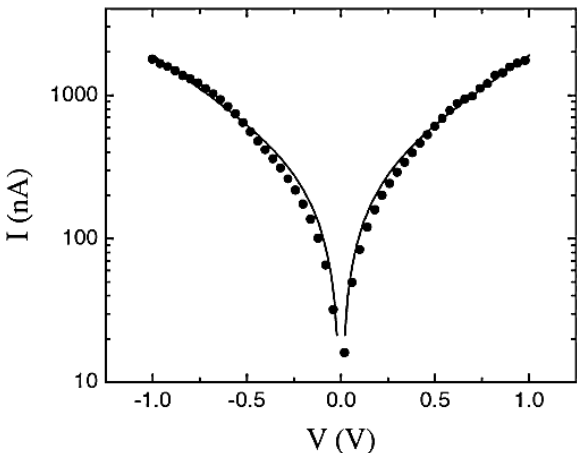


Fig. 11. Measured C8-dithiol $I(V)$ data (*circular symbols*) is compared with calculation (*solid curve*) using the optimum fitting parameters of $\Phi_B = 1.20$ eV and $\alpha = 0.59$

As a comparison, the current density of $(3.1 \pm 1.0) \times 10^4$ A/cm² at 1.0 Volt was observed for C8 monothiol SAM. Using the modified Simmons model [see (2)], the transport parameters of $\Phi_B = 1.20 \pm 0.03$ eV and $\alpha = 0.59 \pm 0.01$ ($m^* = 0.34$ m) were obtained for this C8-dithiol SAM.

Figure 12 shows the IETS spectrum of the same C8-dithiol SAM device obtained at $T = 4.2$ K. An ac modulation of 8.70 mV (rms value) at a frequency of 503 Hz was applied to the sample to acquire the second harmonic signals. The spectra are stable and repeatable upon successive bias sweeps. The spectrum at 4.2 K is characterized by three pronounced peaks in the

0 to 200 mV region at 33, 133, and 158 mV. From comparison with previously reported infrared (IR), Raman, and high resolution electron energy loss (HREEL) spectra of SAM covered gold surfaces (Table 4), these three peaks are assigned to $\nu(\text{Au-S})$, $\nu(\text{C-C})$, and $\gamma_w(\text{CH}_2)$ modes of a surface bound alkanethiolate² [58–60]. The absence of a strong $\nu(\text{S-H})$ signal at ~ 329 mV suggests that most of the thiol groups have reacted with the gold bottom and top contacts. Peaks are also reproducibly observed at 80, 107, and 186 mV. They correspond to $\nu(\text{C-S})$, $\delta_r(\text{CH}_2)$, and $\delta_s(\text{CH}_2)$ modes. The stretching mode of the CH_2 groups, $\nu(\text{CH}_2)$, appears as a shoulder at 357 meV. The peak at 15 mV is due to vibrations from either Si, Au, or $\delta(\text{C-C-C})$ [61]. We note that all alkanethiolate peaks without exception or omission occur in the spectra. Peaks at 58, 257, 277, and 302, as well as above 375 mV are likely to originate from Si-H and N-H vibrations related to the silicon nitride membrane [61, 62], which forms the SAM encasement. Measurement of the background spectrum of an “empty” nanopore device with only gold contacts to obtain background contributions from Si_3N_4 is hampered by either too low (open circuit) or too high (short circuit) currents in such a device. However, to the best of our knowledge alkanethiols have no vibrational signatures in these regions. Similar IETS result has also been obtained using a different test structure recently [63].

Although there are no selection rules in IETS as there are in IR and Raman spectroscopy, certain selection preferences have been established. According to the IETS theory [64], molecular vibrations with net dipole moments perpendicular to the interface of the tunneling junction have larger peak intensities than vibrations with net dipole moments parallel to the interface (for dipoles close to the electrodes). Thus vibrations perpendicular to the electrode interface, i.e., $\nu(\text{Au-S})$, $\nu(\text{C-S})$, $\nu(\text{C-C})$, and $\gamma_w(\text{CH}_2)$ dominate the IETS spectrum while modes parallel to the interface, i.e., $\delta_{r,s}(\text{CH}_2)$ and $\nu(\text{CH}_2)$, are weak, as clearly shown in Fig. 12.

Linewidth Study

In order to verify that the observed spectra are indeed valid IETS data, the peak width broadening was examined as a function of temperature and modulation voltage. IETS was performed with different ac modulations at a fixed temperature, and at different temperatures with a fixed ac modulation. Figure 13(a) shows the modulation dependence of the IETS spectra obtained at 4.2 K, and Fig. 13(b) shows the modulation broadening of the C-C stretching mode at 133 meV. The circular symbols are the full widths at half maximum (FWHMs) of the experimental peak at $T = 4.2$ K with various modulation voltages. A Gaussian distribution function was utilized to obtain a FWHM and the error range [65]. The square symbols are calculated

²The symbols δ , γ , and ν denote in-plane rocking (r) and scissoring (s), out-of-plane wagging (w) and twisting (t), and stretching modes, respectively

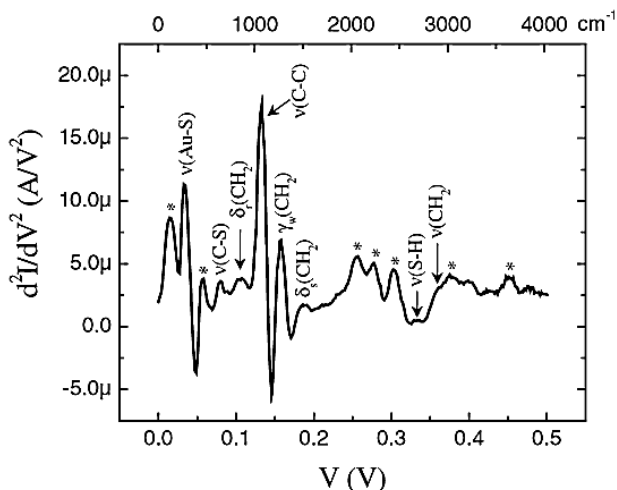


Fig. 12. Inelastic electron tunneling spectra of C8-dithiol SAM obtained from lock-in second harmonic measurements with an ac modulation of 8.70 mV (rms value) at a frequency of 503 Hz ($T = 4.2\text{ K}$). Peaks labeled * are most probably background due to the encasing Si_3N_4

FWHM values ($W_{\text{theoretical}}$) taking into account both a finite temperature effect ($W_{\text{thermal}} \sim 5.4\text{ k}_B\text{T}$) and a finite voltage modulation effect ($W_{\text{modulation}} \sim 1.7\text{ Vac}_{\text{rms}}$) [66]. These two broadening contributions add as the squares: $W_{\text{theoretical}}^2 = W_{\text{thermal}}^2 + W_{\text{modulation}}^2$. The agreement is excellent over most of the modulation range, but we note a saturation of the linewidth at low modulation bias indicating the influence of a non-negligible intrinsic linewidth. Taking into account the known thermal and modulation broadenings, and including the intrinsic linewidth (W_I) [67] broadening as a fitting parameter, the measured peak width (W_{exp}) is given by

$$W_{\text{exp}} = \sqrt{W_I^2 + W_{\text{thermal}}^2 + W_{\text{modulation}}^2} \quad (8)$$

W_I can be determined by using a nonlinear least squares fit to the ac modulation data (Fig. 13) with (8), giving an intrinsic linewidth of $3.73 \pm 0.98\text{ meV}$ for this line. This is shown (with the error range) in Fig. 13(b) as a shaded bar, including the thermal contribution.

We can independently check the thermal broadening of the line at fixed modulation width. Figure 14 shows the temperature dependence of the IETS spectra obtained with an ac modulation of 8.70 mV (rms value). In Fig. 14(b) the circular symbols (and corresponding error bars) are experimental FWHM values of the C-C stretching mode from Fig. 14(a), determined by a Gaussian fit (and error of the fit) to the experimental lineshape. For simplicity we have only considered Gaussian lineshapes [65] resulting in increased error bars for the lower temperature range due to an asymmetric lineshape. The

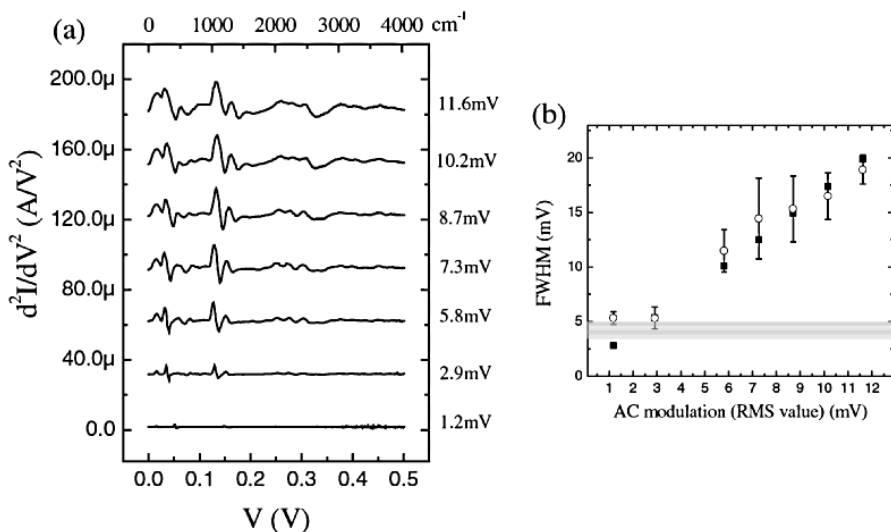


Fig. 13. (a) Modulation dependence of IETS spectra obtained at 4.2 K. (b) Line (C-C stretching mode) broadening as a function of ac modulation. The circular symbols are experimental FWHMs and the square symbols are theoretical calculations considering both modulation and thermal contributions. The shaded bar denotes the expected saturation due to the derived intrinsic linewidth (including a $5.4 k_B T$ thermal contribution) of 3.73 ± 0.98 meV

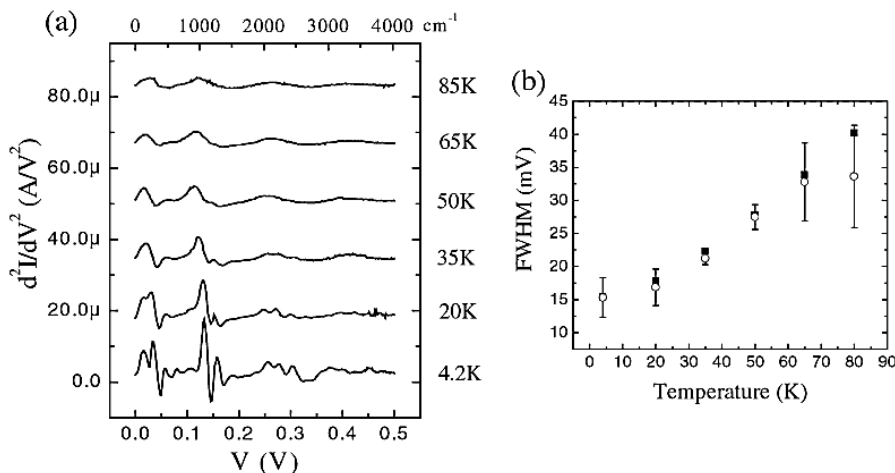


Fig. 14. (a) Temperature dependence of IETS spectra obtained at a fixed ac modulation of 8.70 mV (rms value). (b) Line (C-C stretching mode) broadening as a function of temperature. The circular symbols are experimental FWHMs and the square symbols are theoretical calculations considering thermal broadening, modulation broadening, and the intrinsic linewidth

Table 4. Summary* of the major vibrational modes of alkanethiolates. Taken from [58–60]

Modes	Methods	Wavenumber (cm^{-1})	(meV)
$\nu(\text{Au-S})$	HREELS	225	28
$\nu(\text{Au-S})$	Raman	641	79
	Raman	706	88
	HREELS	715	89
$\delta_r(\text{CH}_2)$	IR	720	89
	IR	766	95
	IR	925	115
	HREELS	1050	130
$\nu(\text{C-C})$	Raman	1064	132
	Raman	1120	139
	IR	1230	152
$\gamma_{w,t}(\text{CH}_2)$	HREELS	1265	157
	IR	1283	159
	IR	1330	165
$\delta_s(\text{CH}_2)$	HREELS	1455	180
$\nu(\text{S-H})$	Raman	2575	319
$\nu_s(\text{CH}_2)$	Raman	2854	354
	HREELS	2860	355
	Raman	2880	357
$\nu_{as}(\text{CH}_2)$	Raman	2907	360
	HREELS	2925	363

* There is a vast amount of literature with spectroscopic assignments for alkanethiols. The references given are representative for IR [60], Raman [58], and HREELS [59] assignments.

square symbols are theoretical calculations considering thermal broadening, modulation broadening, and the intrinsic linewidth determined above. The error ranges of the calculation (due to the intrinsic linewidth error) are approximately the size of the data points. The agreement between theory and experiment is very good, spanning a temperature range from below ($\times 0.5$) to above ($\times 10$) the thermally broadened intrinsic linewidth. This linewidth should be a sensitive test to compare to theoretical models of transmission probabilities [68].

Similar intrinsic linewidths have been determined for the Au-S stretching mode (33 meV) and CH_2 wagging mode (158 meV), and the results are shown in Fig. 15. For the Au-S stretching mode, the deviation of experimental data from calculated values is little, indicating that its intrinsic linewidth is small. A linewidth upper limit of 1.69 meV is determined for this vibrational mode. For the CH_2 wagging mode, nonlinear least squares fit to (8)

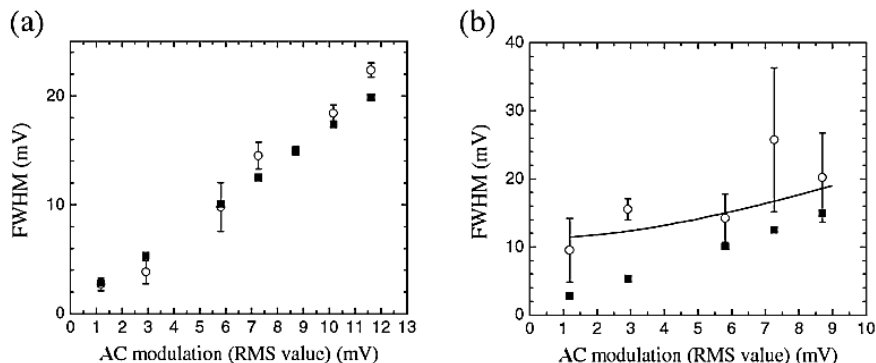


Fig. 15. Line broadenings as function of ac modulation for IETS spectra obtained at 4.2 K for (a) the Au-S stretching mode and (b) the CH₂ wagging mode. The circular symbols are experimental FWHMs and the square symbols are theoretical calculations considering both modulation and thermal contributions (but not intrinsic linewidth). Nonlinear least squares fitting to (8) to determine intrinsic linewidth is shown as the solid curve in (b)

[the solid curve in Fig. 15(b)] gave intrinsic linewidth of 13.5 ± 2.4 meV. The linewidths and their variation throughout the molecule are potentially due to inhomogeneous line broadening, and a more detailed understanding may give detailed structural information of these device structures.

5 Conclusions

We present here a study of electron tunneling through alkanethiol SAMs, with the intent that this system can serve as a simple control for the development of well-characterized molecular junctions. The characteristics are consistent with accepted models of M-I-M tunneling junctions, as well as presenting a system on which tunneling spectroscopy can be performed.

The field of “molecular electronics” is rich in the proposal and promise of numerous device concepts [69, 70] but unfortunately has an absence of reliable data and characterization techniques upon which to test these ideas. It is incumbent upon the experimentalist to carefully institute controls to carefully validate claims of intrinsic molecular behavior. Systematic controls, such as the model system presented here, should assist in guiding further work toward a rational development of the fascinating device structures and systems that the field promises.

Acknowledgements

The authors would like to thank J. F. Klemic, X. Li, and R. Munden for helpful discussions and assistance. We especially thank I. Kretzschmar for assistance in identification of the IETS spectra. This work was supported by DARPA/ONR (N00014-01-1-0657), ARO (DAAD19-01-1-0592), AFOSR (F49620-01-1-0358), NSF (DMR-0095215), and NASA (NCC 2-1363). The fabrication was performed in part at the Cornell Nano-Scale Science & Technology Facility.

References

1. M.A. Reed, J.M. Tour: Computing with molecules, *Scientific American* 2000, June 86–93
2. M.A. Reed, C. Zhou, C.J. Muller et al: Conductance of a molecular junction, *Science* **278**, 252–254 (1997)
3. M.A. Reed, T. Lee, eds. *Molecular Nanoelectronics* (American Scientific Publishers, Stevenson Ranch, 2003)
4. J.R. Heath, M.A. Ratner: Molecular electronics, *Physics Today* 2003, May 43–49; A. Nitzan, M.A. Ratner: Electron transport in molecular wire junctions, *Science* **300**, 1384–1389 (2003)
5. Y. Chen, G.-Y. Jung, D.A. Ohlberg et al: Nanoscale molecular-switch crossbar circuits, *Nanotechnology* **14**, 462–468 (2003); Beyond Silicon: Breakthroughs in Molecular Electronics, <http://www.hpl.hp.com/research/qsr/> (Hewlett-Packard Quantum Science Research)
6. Y. Luo, C.P. Collier, J.O. Jeppesen et al: Two-dimensional molecular electronics circuits, *Chem. Phys. Chem.* **3**, 519–525 (2002); C.P. Collier, G. Mattersteig, E.W. Wong et al: A [2]catenane-based solid state electronically reconfigurable switch, *Science* **289**, 1172–1175 (2000)
7. D.R. Stewart, D.A.A. Ohlberg, P.A. Beck et al: Molecule-independent electrical switching in Pt/organic monolayer/Ti devices, *Nano Lett.* **4**, 133–136 (2004); C.N. Lau, D.R. Stewart, R.S. Williams et al: Direct observation of nanoscale switching centers in metal/molecule/metal structures, *Nano Lett.* **4**, 569–572 (2004)
8. T. Lee, W. Wang, J.F. Klemic et al: Comparison of electronic transport characterization methods for alkanethiol self-assembled monolayers, *J. Phys. Chem. B* **108**, 8742–8750 (2004)
9. A. Ulman: *An Introduction to Ultrathin Organic Films from Langmuir-Blodgett to Self-Assembly* (Academic Press, Boston, 1991)
10. G.E. Poirier: Characterization of organosulfur molecular monolayers on Au(111) using scanning tunneling microscopy, *Chem. Rev.* **97**, 1117–1127 (1997)
11. M.A. Ratner, B. Davis, M. Kemp et al: in *Molecular Electronics: Science and Technology*, The Annals of the New York Academy of Sciences, vol 852, ed by A. Aviram, M.A. Ratner (The New York Academy of Sciences, New York 1998)

12. C. Boulas, J.V. Davidovits, F. Rondelez et al: Suppression of charge carrier tunneling through organic self-assembled monolayers, *Phys. Rev. Lett.* **76**, 4797–4800 (1996); M. Fujihira, H. Inokuchi: Photoemission from polyethylene, *Chem. Phys. Lett.* **17**, 554–556 (1972); S.G. Lias, J.E. Bartmess, J.F. Liebman et al: *Gas-Phase Ion and Neutral Thermochemistry*, *J. Phys. Chem. Ref. Data*, **17**(1), 24 (1998)
13. M.W. Walczak, C. Chung, S.M. Stole et al: Structure and interfacial properties of spontaneously adsorbed n-alkanethiolate monolayers on evaporated silver surfaces, *J. Am. Chem. Soc.* **113**, 2370–2378 (1991)
14. R.G. Nuzzo, B.R. Zegarski, L.H. Dubois: Fundamental studies of the chemisorption of organosulfur compounds on gold(111). Implications for molecular self-assembly on gold surfaces, *J. Am. Chem. Soc.* **109**, 733–740 (1987)
15. C.A. Widrig, C. Chung, M.D. Porter: The electrochemical desorption of n-alkanethiol monolayers from polycrystalline Au and Ag electrodes, *J. Electroanal. Chem.* **310**, 335–359 (1991)
16. G.E. Poirier, M.J. Tarlov: The c(4×2) superlattice of n-alkanethiol monolayers self-assembled on Au(111), *Langmuir* **10**, 2853–2856 (1994)
17. M.D. Porter, T.B. Bright, D.L. Allara et al: Spontaneously organized molecular assemblies. 4. Structural characterization of n-alkyl thiol monolayers on gold by optical ellipsometry, infrared spectroscopy, and electrochemistry, *J. Am. Chem. Soc.* **109**, 3559–3568 (1987)
18. L.A. Bumm, J.J. Arnold, T.D. Dunbar et al: Electron transfer through organic molecules, *J. Phys. Chem. B* **103**, 8122–8127 (1999)
19. B. Xu, N.J. Tao: Measurement of single-molecule resistance by repeated formation of molecular junctions, *Science* **301**, 1221–1223 (2003)
20. D.J. Wold, C.D. Frisbie: Fabrication and characterization of metal-molecule-metal junctions by conducting probe atomic force microscopy, *J. Am. Chem. Soc.* **123**, 5549–5556 (2001)
21. D.J. Wold, R. Haag, M.A. Rampi et al: Distance dependence of electron tunneling through self-assembled monolayers measured by conducting probe atomic force microscopy: unsaturated versus saturated molecular junction, *J. Phys. Chem. B* **106**, 2813–2816 (2002)
22. X.D. Cui, X. Zarate, J. Tomfohr et al: Making electrical contacts to molecular monolayers, *Nanotechnology* **13**, 5–14 (2002)
23. X.D. Cui, A. Primak, X. Zarate et al: Changes in the electronic properties of a molecule when it is wired into a circuit, *J. Phys. Chem. B* **106**, 8609–8614 (2002)
24. R. Holmlin, R. Haag, M.L. Chabinyc et al: Electron transport through thin organic films in metal-insulator-metal junctions based on self-assembled monolayers, *J. Am. Chem. Soc.* **123**, 5075–5085 (2001)
25. M.A. Rampi, G.M. Whitesides: A versatile experimental approach for understanding electron transport through organic materials, *Chem. Phys.* **281**, 373–391 (2002)
26. K. Slowinski, H.K.Y. Fong, M. Majda: Mercury-mercury tunneling junctions. 1. Electron tunneling across symmetric and asymmetric alkanethiolate bilayers, *J. Am. Chem. Soc.* **121**, 7257–7621 (1999)
27. R.L. York, P.T. Nguyen, K. Slowinski: Long-range electron transfer through monolayers and bilayers of alkanethiols in electrochemically controlled Hg-Hg tunneling junctions, *J. Am. Chem. Soc.* **125**, 5948–5953 (2003)

28. J.G. Kushmerick, D.B. Holt, S.K. Pollack et al: Effect of bond-length alternation in molecular wires, *J. Am. Chem. Soc.* **124**, 10654–10655 (2002)
29. J.F. Smalley, S.W. Feldberg, C.E.D. Chidsey et al: The kinetics of electron transfer through ferrocene-terminated alkanethiol monolayers on gold, *J. Phys. Chem.* **99**, 13141–13149 (1995)
30. K. Weber, L. Hockett, S. Creager: Long-range electronic coupling between ferrocene and gold in alkanethiolate-based monolayers on electrodes, *J. Phys. Chem. B* **101**, 8286–8291 (1997)
31. K. Slowinski, R.V. Chamberlain, C.J. Miller et al: Through-bond and chain-to-chain coupling. Two pathways in electron tunneling through liquid alkanethiol monolayers on mercury electrodes, *J. Am. Chem. Soc.* **119**, 11910–11919 (1997)
32. W. Wang, T. Lee, M.A. Reed: Mechanism of electron conduction in self-assembled alkanethiol monolayer devices, *Phys. Rev. B* **68**, 035416 (2003)
33. W. Wang, T. Lee, I. Kretzschmar et al: Inelastic electron tunneling spectroscopy of an alkanedithiol self-assembled monolayer, *Nano Lett.* **4**, 643–646 (2004)
34. R.C. Jaklevic, J. Lambe: Molecular vibration spectra by electron tunneling, *Phys. Rev. Lett.* **17**, 1139–1140 (1966)
35. J. Lambe, R.C. Jaklevic: Molecular vibration spectra by inelastic electron tunneling, *Phys. Rev.* **165**, 821–832 (1968)
36. C.J. Adkins, W.A. Phillips: Inelastic electron tunnelling spectroscopy, *J. Phys. C: Solid State Phys.* **18**, 1313–1346 (1985)
37. P.K. Hansma, Ed. *Tunneling Spectroscopy: Capabilities, Applications, and New Techniques* (Plenum, New York, 1982)
38. B.C. Stipe, M.A. Rezaei, W. Ho: Single-molecule vibrational spectroscopy and microscopy, *Science* **280**, 1732–1735 (1998)
39. C. Zhou, M.R. Deshpande, M.A. Reed et al: Nanoscale metal/self-assembled monolayer/metal heterostructures, *Appl. Phys. Lett.* **71**, 611–613 (1997)
40. J. Chen, M.A. Reed, A.M. Rawlett et al: Large on-off ratios and negative differential resistance in a molecular electronic device, *Science* **286**, 1550–1552 (1999); J. Chen, L.C. Calvet, M.A. Reed et al: Electronic transport through metal-1,4-phenylene diisocyanide-metal junctions, *Chem. Phys. Lett.* **313**, 741–748 (1999)
41. K.S. Ralls, R.A. Buhrman, R.C. Tiberio: Fabrication of thin-film metal nanobridges, *Appl. Phys. Lett.* **55**, 2459–2461 (1989)
42. R.M. Metzger, B. Chen, U. Holpfner et al: Unimolecular electrical rectification in hexadecylquinolinium tricyanoquinodimethanide, *J. Am. Chem. Soc.* **119**, 10455–10466 (1997)
43. P. Horowitz, W. Hill: *The Art of Electronics*, (Cambridge University Press, New York, 1989)
44. S.M. Sze: *Physics of Semiconductor Devices* (Wiley, New York, 1981)
45. R.E. Thurstans, D.P. Oxley: The electroformed metal-insulator-metal structure: a comprehensive model, *J. Phys. D: Appl. Phys.* **35**, 802–809 (2002); J.C. Simmons, R.R. Verderber: New conduction of reversible memory phenomena in thin insulating films, *Prof. Roy. Soc. A.* **301**, 77–102 (1967); G. Dearnaley, A.M. Stoneham, D.V. Morgan: Electrical phenomena in amorphous oxide films, *Rep. Prog. Phys.* **33**, 1129–1191 (1970)
46. B. Mann, H.J. Kuhn: Tunneling through fatty acid salt monolayers, *J. Appl. Phys.* **42**, 4398–4405 (1971); E.E. Polymeropoulos, J. Sagiv: Electrical conduction through adsorbed monolayers, *J. Chem. Phys.* **69**, 1836–1847 (1978)

47. F.F. Fan, J. Yang, L. Cai et al: Charge transport through self-assembled monolayers of compounds of interest in molecular electronics, *J. Am. Chem. Soc.* **124**, 5550–5560 (2002)
48. W. Franz: In *Handbuch der Physik*, vol 17, ed by S. Flugge (Springer-Verlag, Berlin, 1956)
49. G. Lewicki, C.A. Mead: Experimental determination of E-k relationship in electron tunneling, *Phys. Rev. Lett.* **16**, 939–941 (1966); R. Stratton, G. Lewicki, C.A. Mead: The effect of nonparabolic energy bands on tunneling through thin insulating films, *J. Phys. Chem. Solids.* **27**, 1599–1604 (1966); G.H. Parker, C.A. Mead: Electron-momentum relationship in InAs, *Phys. Rev. Lett.* **21**, 605–607 (1968)
50. B. Brar, G.D. Wilk, A.C. Seabaugh: Direct extraction of the electron tunneling effective mass in ultrathin SiO₂, *Appl. Phys. Lett.* **69**, 2728–2370 (1996)
51. C. Joachim, M. Magoga: The effective mass of an electron when tunneling through a molecular wire, *Chem. Phys.* **281**, 347–352 (2002)
52. J.G. Simmons: Generalized formula for the electric tunnel effect between similar electrodes separated by a thin insulating film, *J. Appl. Phys.* **34**, 1793–1803 (1963)
53. J.G. Simmons: Conduction in thin dielectric films, *J. Phys. D* **4**, 613–657 (1971); J. Maserjian, G.P. Petersson: Tunneling through thin MOS structures: Dependence on energy (E-k), *Appl. Phys. Lett.* **25**, 50–52 (1974)
54. J.K. Tomfohr, O.F. Sankey: Complex band structure, decay lengths, and Fermi level alignment in simple molecular electronic systems, *Phys. Rev. B* **65**, 245105 (2002)
55. H. Yamamoto, D.H. Waldeck: Effect of tilt-angle on electron tunneling through organic monolayer films, *J. Phys. Chem. B* **106**, 7469–7473 (2002); A.M. Napper, H. Liu, D.H. Waldeck: The nature of electronic coupling between ferrocene and gold through alkanethiolate monolayers on electrodes: The importance of chain composition, interchain coupling, and quantum interference, *J. Phys. Chem. B* **105**, 7699–7707 (2001)
56. C.-C. Kaun, H. Guo: Resistance of alkanethiol molecular wires, *Nano Lett.* **3**, 1521–1525 (2003)
57. S. Piccinin, A. Selloni, S. Scandolo et al: Electronic properties of metal-molecule-metal systems at zero bias: A periodic density functional study, *J. Chem. Phys.* **119**, 6729–6735 (2003)
58. M.A. Bryant, J.E. Pemberton: Surface Raman scattering of self-assembled monolayers formed from 1-alkanethiols: Behavior of films at Au and comparison to films at Ag, *J. Am. Chem. Soc.* **113**, 8284–8293 (1991)
59. H.S. Kato, J. Noh, M. Hara et al: An HREELS study of alkanethiol self-assembled monolayers on Au(111), *J. Phys. Chem. B* **106**, 9655–9658 (2002)
60. C. Castiglioni, M. Gussoni, G. Zerbi: Charge mobility in a-bonded molecules: The infrared spectrum of polymethylene chains in the solid and liquid phases, *J. Chem. Phys.* **95**, 7144–7149 (1991)
61. M. Molinary, H. Rinnert, M. Vergnat et al: Evolution with annealing treatments of the size of silicon nanocrystallites embedded in a SiN_x matrix and correlation with optical properties, *Mat. Sci. Eng. B* **101**, 186–189 (2003); P.D. Bogdanoff, B. Fultz, S. Rosenkranz: Vibrational entropy of L1₂Cu₃Au measured by inelastic neutron scattering, *Phys. Rev. B* **60**, 3976–3981 (1999); U. Mazur, K.W. Hipps: Spectroscopic characterization of tricyanovinyl alcoholate

- and pentacyanopropenide salts in solid, solution, and adsorbed phases: nuclear magnetic resonance, infrared, Raman, and tunneling spectra, *J. Phys. Chem.* **86**, 2854–2860 (1982)
- 62. U. Mazur, K.W. Hipp: Characterization of alumina-supported OySiH by inelastic electron tunneling spectroscopy, *J. Phys. Chem.* **85**, 2244–2249 (1981); H. Kurata, M. Hirose, Y. Osaka: Wide optical-gap, photoconductive a-Si_xN_{1-x}:H, *Jap. J. Appl. Phys.* **20**, L811-L813 (1981)
 - 63. J.G. Kushmerick, J. Lazarcik, C.H. Patterson et al: Vibronic contributions to charge transport across molecular junctions, *Nano Lett.* **4**, 639–642 (2004)
 - 64. J. Kirtley, J.T. Hall: Theory of intensities in inelastic-electron tunneling spectroscopy orientation of adsorbed molecules, *Phys. Rev. B* **22**, 848–856 (1980)
 - 65. I.J. Lauhon, W. Ho: Single-molecule vibrational spectroscopy and microscopy: CO on Cu(001) and Cu(110), *Phys. Rev. B* **60**, R8525–R8528 (1999)
 - 66. J. Klein, A. Leger, M. Belin et al: Inelastic-electron-tunneling-spectroscopy of metal-insulator-metal junctions, *Phys. Rev. B* **7**, 2336–2348 (1973)
 - 67. L.J. Lauhon, W. Ho: Effects of temperature and other experimental variables on single molecule vibrational spectroscopy with the scanning tunneling microscope, *Rev. Sci. Instrum.* **72**, 216–223 (2001)
 - 68. M.A. Kastner: Physics Today 1993, January 24–31
 - 69. A. Aviram, M. Ratner, eds. *Molecular Electronics: Science and Technology*, The Annals of the New York Academy of Sciences, vol. 852 (The New York Academy of Sciences, New York, 1998)
 - 70. J. Reimers, C. Picconatto, J. Ellenbogen et al: *Molecular Electronics III*, The Annals of the New York Academy of Sciences, vol. 1006 (The New York Academy of Sciences, New York, 2003)

Making Contacts to Single Molecules: Are We There Yet?

J. Tomfohr¹, G.K. Ramachandran¹, O.F. Sankey¹ and S.M. Lindsay^{1,2}

¹ Department of Physics and Astronomy

² The Biodesign Institute Arizona State University, Tempe, AZ 85287, USA

Abstract. The problem of connecting two wires to a single molecule has several practical solutions, varying from break junctions, to gaps formed by controlled evaporation and self-assembled structures. Here, we focus on gold nanoparticle self-assembled junctions, and break junctions, two techniques that allow the number of molecules in the gap to be determined. We show that the nanoparticle junctions are affected by the electronic properties of the nanoparticles, and that corrections for these effects tend to bring the data into closer agreement with both break-junction measurements and *ab initio* calculations.

1 Introduction

How well do we understand charge transport through a molecule connected at each end to conducting electrodes? Modern computational techniques make quantitative predictions about molecular conduction, yet, to take one controversial example, experiments show DNA to be an insulator [1], semiconductor [2], conductor [3] and even superconductor [4] (though the issue is now probably resolved [5]).

A reliable method for contacting molecules is needed, and, if quantitative comparison with theory is the goal, then the number of molecules that are contacted should be countable. Methods for contacting molecules include scanning tunneling microscopy (STM) [6–8] conducting atomic force microscopy (AFM) [9, 10], break junctions [11–13] (and see the discussion by Wang, lee and Reed in [38]), fixed-gap nanojunctions [14, 15], nanopores [16, 38], mercury drop contacts [17] and crosswire assmeblies [18]. Each method has some particular advantage [16] but the difficulty of counting the number of contacted molecules, and the characterization of their bonding, remain difficult problems. These problems probably underlie the wide range of data reported for similar molecules [19], though a tour-de-force assembly mechanism for placing molecules into nanojunctions has produced some striking results [20, 21].

We chose to study simple (and already much studied) molecules, the alkane dithiols [10, 22], using a self-assembled system in which a well defined number of molecules are connected, by covalent bonds, to metal electrodes. A self-assembled monolayer of (in this case) octanethiol is placed in contact

with a solvent so that some molecules leave (taking a gold atom with them, such is the lability of the gold surface covered with thiols [23]). Thus, such a surface, when placed in a solution of dithiolated molecules, will open up spaces for the dithiolated molecules to enter the monolayer [24]. The result is dithiolated molecules inserted into a monolayer of monothiols in a well-defined orientation, and bonded at their lower end to the gold substrate. It is still not easy to make an electrical contact to the inserted molecules, because the atoms of a top contact must line up correctly with the (now fixed) upper thiol, so that a chemical bond can form. To solve this problem, the monolayer is next incubated with a suspension of gold nanoparticles (NPs). We used 1.5 nm diameter gold stabilized with triphenylphosphine [25] as this ligand is readily displaced by the more reactive thiol. The NPs find the protruding thiols and attach to them. The attached NPs then make excellent “large” targets for a conducting atomic force microscope probe. A gold-coated probe is pushed into the NP to complete a circuit. The result is highly reproducible data showing a quantized series of current-voltage curves that are multiples of the current-voltage curve for a single molecule [22]. Importantly, the single molecule data are quite close to the results of first-principles calculations [22]. This rosy picture is clouded by further studies of transport as a function of alkane chain length [26] which yield a value for the inverse electronic decay length, β , that are too small and too voltage-dependent.

Xu and Tao [27] have recently introduced an elegant extension of the break-junction method. They operate an STM as an automated break junction, pushing a gold tip (under computer control) into a gold substrate immersed in a solution of dithiolated molecules. The bias between tip and substrate is fixed and the current recorded as the tip is pulled away from the surface. The current plotted vs. distance shows discrete plateaus (regions of constant current over a significant distance of the pull). When these values of current plateau are histogrammed, distinct peaks are seen in the conductance, probably corresponding to 1, 2, 3 etc. molecules bridging the gap [27]. The plateaus in the current vs. distance plots form because gold filaments are very ductile, so a single molecule dominates the gap resistance as the gold to which it is attached is drawn out from the tip and substrate [28]. This method is simple to carry out and gives reproducible data, though complete current-voltage curves must be obtained through repeated experiments at different biases. These measurements are made in solution and we expect that the environment matters considerably for redox active molecules, but we doubt that this is critical for simple tunnel transport.

Do these plateau regions really correspond to integer numbers of molecules in well-defined geometries? Values of conductance measured in this way [27] are close to, but systematically higher than, those measured by the method of self-assembled junctions [22, 26]. Importantly, the Xu-Tao method yields much more realistic values for β [27]. It is the aim of this paper to show that electronic effects of the nanoparticle contact account, at least qualitatively,

for differences between the two techniques (which are relatively small in any case). This lends credence to the interpretation of the current-plateaus as corresponding to integer numbers of molecules in the gap. Thus the method of Xu and Tao [27] represents a significant improvement over our self-assembly based method [22], yielding data that is quite close to the results of first-principles simulation and resolving the issue of anomalous values for the electronic decay constant [26]. Some issues remain to be resolved, but these are minor relative to the scale of recent progress.

2 Contact Resistance in NP Contact Experiments

Our original, probably naive, interpretation of our experimental data assumed that the contact between the gold-coated AFM probe and the NP was good (i.e., the system acts like a bulk metal). Yet this is surely not true. The particle probably remains coated with triphenylphosphine (as evidenced by a low measured adhesion force between the AFM probe and the NP). Any significant resistance (i.e., greater than the resistance quantum, $h/2e^2 \approx 12.6 \text{ k}\Omega$) would lead to independent charging of the NP, with consequent Coulomb blockading [29]. The matter is complicated further by the possibility that very small (< 5 nm diameter) gold NPs may suffer from an intrinsic gap as a consequence of quantum size effects [30].

The current-voltage curves taken via a gold NP show clear evidence of a zero-bias gap (Fig. 1). This shows the mean, and standard deviation (as vertical bars) for current data points for about 1000 measurements of octanedithiol molecules between a gold NP ($d = 1.5 \text{ nm}$) and a gold (111) surface. The derivative, dI/dV , is shown on the same plot, illustrating a zero bias gap on the order of 0.5 V. It is tempting, and probably partially correct, to attribute this gap to a Coulomb blockade caused by charging of the gold NP. Interpretation is, however, complicated by the fact that gold NPs of this size show evidence of electronic structure with level spacings on the order of 100 meV [30]. Unfortunately, this problem is difficult to circumvent, as the NP technique relies on the use of (easily-displaced) triphenylphosphine ligand, limiting the particle size to 1.5 nm [25] (or smaller, see below). Note that this ligand is probably not important from a strictly electronic viewpoint as it is not easily reduced or oxidized.

The problem is not easily dealt with from a theoretical viewpoint either. This is because it requires a detailed electronic structure calculation for the NP with explicit inclusion of electron-electron interactions in order to deal with the Coulomb charging problem. Simple estimates, based on “particle in a box” pictures do not give a good account of the details of the observed structure [30]. We therefore proceed to treat the Coulomb blockade aspect the simplest way we can, using the results of the fits to assess the degree to which this approach is flawed in practice.

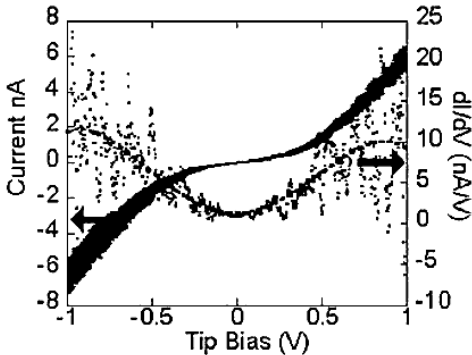


Fig. 1. Current vs. bias ($T = 300\text{K}$) for octanedithiol in a gold-molecule-gold junction (*left axis*) with the corresponding derivative (*right axis*). Data are averages for 1000 molecules with the standard deviation on each current shown by a vertical bar (giving the curve its width). Despite the averaging process, noise dominated the numerical derivative, so a 4th order polynomial fit is shown as the *dashed line*

At its simplest, this problem can be treated by considering the junction as a resistance (proportional to inverse tunneling rate) in parallel with a capacitor to represent the AFM to gold particle contact and a second parallel resistor-capacitor combination in series with the first to represent the gold particle to gold substrate contact (illustrated in the inset in Fig. 2a). Such an arrangement has been treated in detail by Hanna and Tinkham [31] and the current-voltage characteristic is calculated as follows:

With R_1 corresponding to the probe-to-particle tunnel junction resistance, C_1 to its capacitance, R_2 corresponding to the particle-to-substrate tunnel junction resistance and C_2 its capacitance, and allowing for a charge accumulation Q_0 on the nanoparticle, the current is obtained from

$$I(V) = e \sum_{n=-\infty}^{\infty} \sigma(n) [\Gamma_2^+(n) - \Gamma_2^-(n)] = e \sum_{n=-\infty}^{\infty} \sigma(n) [\Gamma_1^-(n) - \Gamma_1^+(n)] . \quad (1)$$

Here,

$$\Gamma_j^{\pm}(n) = \frac{1}{R_j e^2} \left(\frac{-\Delta E_j^{\pm}}{1 - \exp(\Delta E_j^{\pm}/k_B T)} \right), \quad j = 1, 2 \quad (2)$$

and

$$\Delta E_1^{\pm} = \frac{e}{C_1 + C_2} \left(\frac{e}{2} \pm (ne + Q_0) \pm C_2 V \right) \quad (3)$$

$$\Delta E_2^{\pm} = \frac{e}{C_1 + C_2} \left(\frac{e}{2} \pm (ne + Q_0) \pm C_1 V \right) . \quad (4)$$

The residual charge on the nanoparticle, Q_0 , was set to zero in the fits that follow as non-zero values give asymmetric I-V curves, contrary to experiment. In (2), the electron distribution abides by the following ratios and equations:

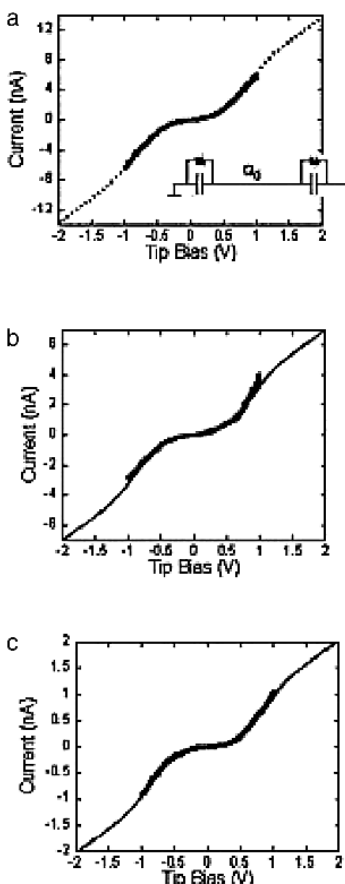


Fig. 2. Experimental single molecule current-voltage data (averages for many molecules) are shown as the *thick lines* superimposed on the theoretical Coulomb-blockade fits (*thin lines*) for (a) octanedithiol, (b) decanedithiol and (c) dodecanedithiol. Fitting parameters are listed in Table 1

$$\frac{\sigma(n)}{\sigma(n+1)} = \frac{\Gamma_1^-(n+1) + \Gamma_2^-(n+1)}{\Gamma_1^-(n) + \Gamma_2^+(n)} \quad (5)$$

and

$$\sum_{n=-\infty}^{\infty} \sigma(n) = 1 . \quad (6)$$

C_2 should be at least equal to the free space capacitance of the sphere, $4\pi\epsilon_0 R$ where $R \approx 1.5$ nm, giving $0.08aF$ ($1aF = 10^{-18}F$). Fits to averaged data for octane, decane and dodecanedithiol are shown in Fig. 2 (for details of the statistical distribution of this data see [26]). The fits are good, but we

Table 1. Fitting parameters for the Coulomb blockade model for the various n-alkanes with 1.5 nm Au contacts (C_8 = octanedithiol, C_{10} = decanedithiol, C_{12} = dodecanedithiol)

Sample	C_1 (aF)	C_2 (aF)	R_1 (MΩ)	R_2 (MΩ)
C_8	0.318 ± 0.02	0.085 ± 0.02	<1	128 ± 5
C_{10}	0.318 ± 0.02	0.085 ± 0.02	<1	252 ± 10
C_{12}	0.318 ± 0.02	0.085 ± 0.02	<1	875 ± 40

show the modeled curves over a higher bias range than the experimental data to emphasize the fact that structure in the curves lies beyond the range of experimental observation (set by sample stability). The parameters for these fits are listed in Table 1. Once the octanedithiol data were fitted, the remaining data could be fitted with the same values for the tip-NP capacitance, C_1 , and NP-surface capacitance C_2 , to yield values for the molecular resistance, R_2 . The tip-to-NP resistance was too low to be determined accurately by the fits. The values of R_2 are closer to those that have been calculated [22,32–35] and the value of C_2 is of the right order, but too low, given that the appropriate relative dielectric constant must be > 1 . The essentially constant value for C_2 is reasonable, given the small changes in the relatively large NP-surface distance. Of more concern is the failure of the corrected data to produce a reasonable value for β . A plot of the values of R_2 vs. chain length (in units of methylene groups) is shown in Fig. 3. The best exponential fit is shown by the dashed line. The fit is clearly quite poor, and the corresponding value of $\beta(0.48)$ anomalously low [26]. How might the intrinsic electronic properties of the sphere interfere with an otherwise exponential decay? A simple, if utterly classical, representation would be to introduce a “contact resistance”.

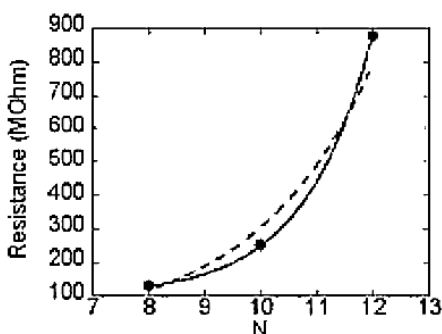


Fig. 3. Resistance vs. chain length (N = number of methylene groups) shown as the black dots. Best-fit exponential ($b = 0.48$) is shown by the dashed line. The modified decay (exponential plus constant) is shown by the solid line

This concept has no validity in a quantum system, but might be valid if the tunneling steps (tip to NP, NP to surface) were incoherent, perhaps as a consequence of thermal vibrations. Fitting to $R_0 + R_1 \exp(\beta N)$ produces a much better fit and improved value for β of 0.83 (solid line in Fig. 3.) with $R_0 = 98\text{ M}\Omega$. We point this out to raise the possibility that a resolution of the remaining inconsistencies lies with the electronic properties of the NP. A definitive answer awaits development of an electronic structure calculation incorporating electron interactions properly.

3 Changing the NP Size

Given the need for triphenylphosphine stabilization, the only experimentally accessible procedure is to go down in size, and we used the method of Woerhle et al. [36] to synthesize NPs of nominal diameter 0.7 nm. HRTEM showed that the resulting particles were smaller than the 1.5 nm NPs originally used, but resolution and contrast were too poor for a quantitative size distribution to be determined. Nonetheless, it proved possible to attach these particles to octanethiol monolayers containing inserted octanedithiols. STM images of a monolayer with attached NPs and a control sample (no inserted dithiols and hence no attached NPs) are shown in Fig. 4 (experimental procedures were

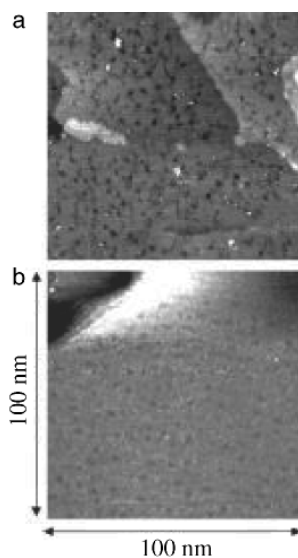


Fig. 4. STM image of (a) octanethiol monolayer with inserted octanedithiol molecules after incubation with 0.7 nm gold particles followed by rinsing. Similar treatment of an octanethiol monolayer (no inserted octanedithiol) results in a clean surface with no gold clusters adhering (b)

Table 2. Apparent heights and widths of the bare thiols and the two gold NPs in STM images

Sample	Height (nm)	Width (nm)
Protruding thiol	0.69 ± 0.08	2.4 ± 0.4
0.7 nm particle attached	2.4 ± 0.4	5.0 ± 1
1.5 nm particle attached	2.8 ± 0.4	6.1 ± 1.5

as described in [22]). The measured dimensions of the small NPs differ from those measured for the 1.5 nm NPs and the bare thiols (Table 2). These data were obtained from STM images and important role of electronic structure in the contrast is evident: The changes in dimensions trend in the right direction, but the absolute numbers do not correspond to physical size differences.

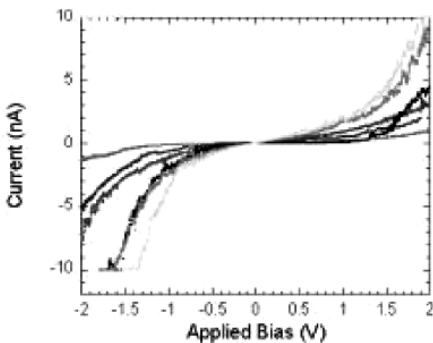


Fig. 5. A representative sample of the range of current-voltage curves obtained using the 0.7 nm gold spheres as contacts. Though the data are spread considerably, the zero-bias gap is consistently larger than that obtained with a 1.5 nm diameter contact

Current-voltage data obtained with these NPs were quite variable, and we were unable to construct meaningful distributions corresponding to multiples of a fundamental curve (as was done for the larger NP [22]). However, the curves were broadly similar, as shown by the representative sample in Fig. 5. Comparison with Figs. 1 and 2 shows quite clearly that the low bias region of suppressed (or partially suppressed) current is roughly doubled (± 1 V cf. ± 0.5 V) as the particle size is halved. Wang et al. [30] did not explore the effect of particle size in the region (> 5 nm) where the electronic structure of the NP becomes important, so this observation of a Coulomb-blockade-like behavior (blockade scaling with $1/\text{radius}$) is novel, and suggests that elements of the Coulomb blockade model apply in this small size regime also.

4 Status of Single Molecule Measurements

The results and analysis presented above suggest that (a) measurements on NP-contacted junctions are distorted by the electronic properties of the NP, (b) the distortions are partially explained with classical Coulomb blockade theory, though substantial deviations indicate the importance of the intrinsic electronic structure of the NP and (c) the consequence is a reduction of measured current in the low bias region corresponding to the Coulomb blockade and/or low bias gap of the NP states. While not fully quantitative, these factors could explain the discrepancies between the data obtained with NP contacts [22, 26] and those obtained with break junctions [27]. Values of the low-bias resistance for octanedithiol connected between gold contacts are summarized in Table 3. The theoretical values come from initial DFT simulations [22], refined calculations that dealt with the interfacial dipole self-consistently [32, 35] and simple estimates based on the known value of β [32, 34]. These simple estimates might be expected to work quite well for the wide HOMO-LUMO gap of the alkane, so it appears that the break junction data and the latter two theoretical values are in reasonable agreement. The NP raw data disagree with these data by a factor of nearly 20, improved to about a factor 2 with the Coulomb blockade correction.

Table 3. Measured (top three entries) and calculated (lower three entries) resistances at low bias for octanedithiol connected to gold electrodes

Method (Reference)	Resistance ($M\Omega$)
Self-assembled junction [22]	900 ± 50
Coulomb-blockade-corrected, this work.	128 ± 5
Break junction [27]	51 ± 5
DFT [22]	150
DFT [32,33]	40
Simple estimate [32,33]	38.5

Thus, we conclude that rather good single molecule data are available from the method of Xu and Tao [27]. The molecule is under some strain in these junctions, though electromechanical measurements indicate that these effects do not dominate the data for a number of molecules [28]. In addition to being easier to interpret, the new approach is experimentally quite simple and flexible. For example, the use of partially-insulated STM probes [37] permits measurement in aqueous electrolytes, a feature exploited in the measurement of the electronic properties of DNA molecules in their native state [5].

Thus, in answer to the question posed in our title, reliable single molecule measurements of conductance are at hand. The measurement of temperature

dependence [16] for a well-defined single molecule junction remains as an important experimental challenge.

Acknowledgements

This work was funded by a NIRT grant of the National Science Foundation (ECS 01101175). NPs were synthesized by Franklin Milton and HRTEM was carried out by Peter Crozier. We thank Devens Gust, Tom and Ana Moore, Larry Nagahara and Nongjian Tao for useful discussions.

References

1. D.D. Dunlap, R. Garcia, E. Schabtach, and C. Bustamante: Masking generates contiguous segments of metal coated and bare DNA for STM imaging. *Proc. Natl. Acad. Sci. (USA)* **90**, 7652 (1993).
2. D. Porath, A. Bezryadin, S. de Vries, and C. Dekkar: Direct measurement of electrical transport through DNA molecules, *Nature* **403**, 635 (2000).
3. H.-W. Fink and C. Schoenberger: Electrical conduction through DNA molecules, *Nature* **398**, 407 (1999).
4. A.Y. Kasumov, M. Kociak, S. Guéron, B. Reulet, V.T. Volkov, D.V. Klinov, and H. Bouchiat: Proximity-Induced Superconductivity in DNA, *Science* **291**, 280 (2001).
5. B. Xu, P.M. Zhang, X.L. Li, and N.J. Tao: Direct Conductance Measurement of Single DNA Molecules in Aqueous Solution, *Nanolett.* **4**, 1105 (2004).
6. L.A. Bumm, J.J. Arnold, M.T. Cygan, T.D. Dunbar, T.P. Burgin, L. Jones, D.L. Allara, J.M. Tour, and P.S. Weiss: Are single molecular wires conducting? *Science* **271**, 1705 (1996).
7. N. Tao: Probing potential-tuned resonant tunneling through redox molecules with scanning tunneling microscopy. *Phys. Rev. Letts.* **76**, 4066 (1996).
8. W. Han, E.N. Duranitini, T.A. Moore, A.L. Moore, D. Gust, P. Rez, G. Leatherman, G.R. Seely, N. Tao, and S.M. Lindsay: STM contrast, electron-transfer chemistry and conduction in molecules, *J. Phys. Chem.* **101**, 10719 (1997).
9. D.J. Wold and C.D. Frisbie: Formation of metal-molecule-metal tunnel junctions: Microcontacts to alkanethiol monolayers with a conducting AFM tip, *J. Am. Chem. Soc.* **122**, 2970 (2000).
10. X.D. Cui, X. Zarate, J. Tomfohr, A. Primak, A.L. Moore, T.A. Moore, D. Gust, G. Harris, O.F. Sankey, and S.M. Lindsay: Making electrical contacts to molecular monolayers, *Nanotechnology* **13**, 5 (2002).
11. M.A. Reed, C. Zhou, C.J. Muller, T.P. Burgin, and J.M. Tour: Conductance of a molecular junction, *Science* **278**, 252 (1997).
12. J. Reichert, R. Ochs, D. Beckmann, H.B. Weber, M. Mayor, and H. von Lohneysen: Driving current through single organic molecules, *Phys Rev. Lett.* **88**, 176804 (2002).
13. J. Reichert, H.B. Weber, M. Mayor, and H. von Lohneysen: Low-temperature conductance measurements on single molecules, *Applied Physics Letters* **82**, 4137 (2003).

14. H. Park, A.K.L. Lim, Alivisatos, A.P., J. Park, and P.L. McEuen: Fabrication of metallic electrodes with nanometer separation by electromigration, *Applied Physics Letters* **74**, 301 (1999).
15. J. Park, A.N. Pasupathy, J.I. Goldsmith, C. Chang, Y. Yaish, J.R. Petta, M. Rinkoski, J.P. Sethna, H.D. Abruna, P.L. McEuen, and D.C. Ralph: Coulomb Blockade and the Kondo Effect in single atom transistors, *Nature* **417**, 722 (2002).
16. T. Lee, W. Wang, J.F. Klemic, J.J. Zhang, J. Su, and M.A. Reed: Comparison of electronic transport characterization methods for alkanethiol self-assembled monolayers, *J. Phys. Chem.* B published on web May 2004 (2004).
17. E. Holmlin, R. Haag, M.L. Chabinyc, R.F. Ismagilov, A.E. Cohen, A. Terfort, M.A. Rampi, and G.M. Whitesides: Electron transport through thin organic films in metal-insulator-metal junctions based on self-assembled monolayers, *J. Am. Chem. Soc.* **123**, 5075 (2001).
18. J.G. Kushmerick, D.B. Holt, J.C. Yang, J. Naciri, M.H. Moore, and R. Shashidhar: Metal-Molecule Contacts and Charge Transport across Monomolecular Layers: Measurement and Theory. *Phys Rev. Lett.* **89**, 086802/1 (2002).
19. A. Salomon, D. Cahen, S. Lindsay, J. Tomfohr, V.B. Engelkes, and C.D. Frisbie: Comparison of electronic transport measurements on organic molecules, *Advanced Materials* **15**, 1881 (2003).
20. S. Kubatkin, A. Danilov, M. Hjort, J. Cornil, J.-L. Bredas, N. Stuhr-Hansen, P. Hedegard, and T. Bjornholm: Single electron transistor of a single organic molecule with access to several redox states, *Nature* **425**, 698 (2003).
21. S. Kubatkin, A. Danilov, H. Olin, and T. Claeson: Tunneling through a single quench-condensed cluster, *J. Low Temp. Phys.* **118**, 307 (2000).
22. X.D. Cui, A. Primak, X. Zarate, J. Tomfohr, O.F. Sankey, A.L. Moore, T.A. Moore, D. Gust, H. G., and S.M. Lindsay: Reproducible measurement of single-molecule conductivity, *Science* **294**, 571 (2001).
23. J.A.M. Sondag-Huethorst, C. Schonenberger, and L.G.J. Fokkink: Formation of Holes in Alkanethiol Monolayers on Gold, *J. Phys. Chem.* **98**, 6826 (1994).
24. M.T. Cygan, T.D. Dunbar, J.J. Arnold, L.A. Bumm, N.F. Shedlock, T.P. Burgin, L. Jones, D.L. Allara, J.M. Tour, and P.S. Weiss: Insertion, conductivity and structure of conjugated organic oligomers in self-assembled alkanethiol monolayers on Au(111), *J. Am. Chem. Soc.* **120**, 2721 (1998).
25. W.W. Weare, S.M. Reed, M.G. Warner, and J.E. Huchison: Improved synthesis of small (d-core=1.5nm) phosphine-stabilized gold nanoparticles, *J. Am. Chem. Soc.* **122**, 12890 (2000).
26. X.D. Cui, A. Primak, X. Zarate, J. Tomfohr, O.F. Sankey, A.L. Moore, T.A. Moore, D. Gust, L.A. Nagahara, and S.M. Lindsay: Changes in the electronic properties of a molecule when it is wired into a circuit, *J. Phys. Chem. B* **106**, 8609 (2002).
27. B. Xu and N.J. Tao: Measurement of Single-Molecule Resistance by Repeated Formation of Molecular Junctions, *Science* **301**, 1221 (2003).
28. B. Xu, X. Xiao, and N.J. Tao: Measurements of Single-Molecule Electromechanical Properties, *J. Am. Chem. Soc.* **125**, 16164 (2003).
29. S. Datta, W. Tian, S. Hong, R. Reifenberger, J.I. Henderson, and C.P. Kuobiak: Current-voltage characteristics of self-assembled monolayers by scanning tunneling microscopy, *Phys. Rev. Lett.* **79**, 2530 (1997).

30. B. Wang, H. Wang, H. Li, C. Zeng, and J.G. Hou: Tunable single-electron tunneling behavior of ligand-stabilized gold particles on self-assembled monolayers, *Phys. Rev. B* **63**, 035403 (2000).
31. A.E. Hanna and M. Tinkham: Variation of the Coulomb staircase in a two-junction system by fractional electron charge, *Physical Review B* **44**, 5919 (1991).
32. J. Tomfohr, *Electron tunneling transport theory for molecules*, in *Physics*. 2002, Arizona State University: Tempe.
33. J.K. Tomfohr and O.F. Sankey: Theoretical analysis of electron transport through organic molecules, *J. Chem. Phys.* **120**, 1542 (2004).
34. J. Tomfohr and O.F. Sankey: Simple estimates of the electron transport properties of molecules, *Phys. Stat. Sol. B – Basic Research* **233**, 59 (2002).
35. J. Tomfohr and O.F. Sankey: Complex bandstructure, decay lengths and Fermi level alignment in simple molecular electronic systems, *Phys. Rev. B* **65**, 245105 (2002).
36. G.H. Woerhle, M.G. Warner, and J.E. Huchison: Ligand exchange reactions yield sub-nanometer, thiol-stabilzed gold particles with defined optical transisitons, *J. Chem. Phys. B* **106**, (2002).
37. L.A. Nagahara, T. Thundat, and S.M. Lindsay: Preparation and Characterization of STM Tips for Electrochemical Studies, *Rev. Sci. Instrum.* **60**, 3128 (1989).
38. W. Wang, T. Lee, M. Reed: Intrinsic electronic conduction mechanisms in self-assembled monolayers , *Lecture Notes in Physics* vvv, xxx (2005); Chap. 10 of this collection.

Six Unimolecular Rectifiers and What Lies Ahead

Robert M. Metzger

Department of Chemistry, Box 870336, University of Alabama, Tuscaloosa,
AL 35487-0336, USA

Abstract. Six unimolecular rectifiers are discussed: γ -hexadecylquinolinium tricyanoquinodimethanide, **1**, and two thioacetyl derivatives of **1**, namely (Z)- α -cyano- β -[N-tetradecylthioacetylquinolin-4-ylum)-4-styryl-dicyanomethanide, **2**, and (Z)- α -cyano- β -[N-hexadecylthioacetylquinolin-4-ylum)-4-styryl-dicyanomethanide, **3**, and three other rectifiers of very different structure: 2,6-di[butyylaminophenylvinyl]-1-butylpyridinium iodide, **4**, dimethylanilino-aza[C₆₀]-fullerene, **5**, and fullerene-bis-[4-diphenylamino-4"--(N-ethyl-N-2"-ethyl)amino-1,4-diphenyl-1,3-butadiene] malonate, **6**. Monolayers of these molecules exhibit asymmetric electrical conductivity between Au or Al electrodes. We also suggest approaches towards one-molecule electronic devices, useful for the ultimate reduction in circuit sizes.

Key words: “A” rectifiers; asymmetric intramolecular electron conduction; Aviram-Ratner model; break-junction; carbon nanotubes; catenanes; combining SAMs and LB techniques; cold gold; Coulomb blockade; cryocooling sample; electromigration of Au; gold-monolayer-gold sandwich hexadecylquinolinium tricyanoquinodimethanide; Inelastic Electron Tunneling Spectroscopy; Landauer quantum of conductance; Langmuir-Blodgett monolayer; Langmuir-Schaefer monolayer; LB films; “molecule-independent” switching; Scanning Tunneling Spectroscopy; single-electron transistor; “S” rectifiers; stalactites and stalagmites of Au; through-bond tunneling; through-space tunneling; “U” rectifiers; unimolecular amplifier; unimolecular rectification.

1 Introduction

“Molecular electronics”, or “molecular-scale” electronics, defined narrowly, is the study of electrical and electronic processes measured or controlled on the scale of a single molecule or cluster [1]. In contrast, molecular electronics, defined broadly, is the “molecule-based” study of bulk electronic properties of crystals or polymer aggregates [1]. We focus here on the former, narrower definition; i.e. on conduction processes that involve one molecule, or very few molecules: we baptize this area “unimolecular electronics” (UE). This implies “reaching out and touching” individual molecules with electrodes, without damaging them, and exploiting their chemical structure to control the flow of electrical signals. Given the size of molecules (about 0.5 to 3 nm), UE may be thought as the *reductio ad absurdum* of standard highly integrated

electronics. The electronic properties of single molecules have been studied by spectroscopy for almost a century, since photons can blithely interrogate molecules in the gas phase, solid-state, or in solution, without knowing exactly where the molecules are, and without electrical leads. In contrast, electrical circuits using photons as control elements cannot easily be reduced to nm dimensions! Touching single molecules electrically and without damage is somewhat more problematical.

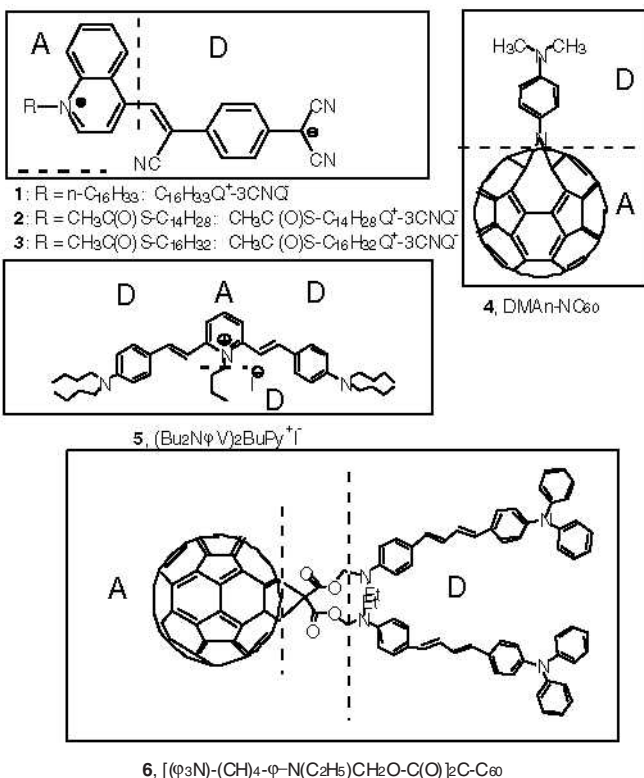


Fig. 1. Six Rectifiers. The electron donor (acceptor) regions are shown as "D" (as "A")

UE may have been implied or considered by Richard Phillips Feynman ("there is plenty of room at the bottom") [2], but he explicitly mentioned assemblies of atoms, and not molecules. UE was also considered in an early U.S. Department of Defense initiative. UE saw its first serious paper when Aviram and Ratner proposed in 1974 electrical rectification, or diode behavior, by a single molecule with suitable electronic asymmetry [3]. In the early 1980's, three topical conferences organized by the late Forrest L. Carter galvanized some interest, and, alas, some vacuous press-agentry. In the late 1990's, the

United States Defense Advanced Projects Agency sponsored serious attempts towards molecular integrated circuits and UE, but this also generated some grandiloquent publicity. Since 2000, the world-wide interest in nanotechnology has encouraged new and serious efforts in UE. Nobody doubts that molecules may function as electronic components (as one-electron donors or acceptors), but a huge technical challenge is how to address them electrically. The electrical conductivity has been measured for individual molecules by scanning tunneling microscopy (STM), for monolayers of molecules assembled by the Langmuir-Blodgett (LB) method, by the Langmuir-Shaefer (LS) method, or for “self-assembled monolayers” (SAMs) covalently bonded to an inorganic bulk substrate (e.g. organothiols on gold). We have finally “touched” molecules. A single molecule can be touched on a bulk electrically conducting surface, by an STM tip, by a conducting-tip atomic force microscopy (AFM) tip, or between two Au “break junction” tips, or by making electrical contacts to sandwiches of organic monolayers placed between super-thin inorganic metal pads (with areas from $1\text{ }\mu\text{m}^2$ to 1 cm^2). The current vs. voltage (IV) characteristics can be measured either for a single molecule, or, in parallel, for a monolayer of molecules, or many layers, either locally, by scanning tunneling spectroscopy (STS) or, as a macroscopic average, over a pad. The challenge is to fabricate the “metal | organic | metal” sandwiches or cells, while not over-heating or damaging the organic layer, or avoiding the penetration of metal filaments into the organic layer.

UE is receiving great recent attention, in part, because of the public-relations discovery of “nanoscale science”, but in greater part, because there is a hope that molecules could become technologically useful active electronic devices. There are concerns about how small silicon-based integrated circuits can be shrunk, to make components closer, and the speed of computing faster. Since the mid 1960’s the computing power has doubled, at first every two years and, presently, every 18 months or so (Moore’s “law”) [4]. This occurs, as the “design rules” for integrated circuits (i.e. the smallest distance between adjacent components) get smaller and smaller [5]. By now, design rules below 100 nm are common in commerce, and will approach 50 nm in research; however, this shrinkage cannot go on forever. There is a widely held opinion that, below design rules of perhaps 20 nm, huge technical hurdles may face silicon-based electronics, while molecules, with sizes 0.5 to 3 nm, can presumably do similar tasks with great facility. The market-driven diligence and inventiveness of scientists and engineers advancing silicon-based electronics may provide unexpected technical break-throughs: they may be a “moving target” for UE. But it is fun to try to be both successful in the *reductio ad absurdum* and useful to industry and commerce.

Other articles in this volume deal with the conductivity in self-assembled monolayers of relatively symmetrical thiols and bithiols [6–9].

Here is a brief and subjective list of recent advances in UE:

- (1) STS showed that the currents across alkanethiols and aromatic thiols bonded to Au are larger when the molecules have aromatic, rather than aliphatic, moieties [10]. This result confirms what Henry Taube and co-workers had established by kinetics experiments [11].
- (2) By a “break junction” technique, a thin Au film, deposited above a thinned-out Si wafer, was broken reproducibly, by restraining the Si wafer between two static wedges, and moving a piston by a piezoelectric scanner towards a thinned-out central area of the wafer. When the Si cracked, so did the Au, and a very narrow gap between the Au shards could be controlled by the scanner to $\pm 1 \text{ \AA}$. When a benzene solution of 1,4-benzenethiol was poured on this break junction, some bithiols bonded to one shard, and some to both shards; the latter provided a one-molecule conductive path, with a measured resistance of several $M\Omega$ [12], much larger than Landauer’s quantum of resistance $(h/2 e^2)/N = 12.91/N \text{ k}\Omega$ [15], where N is the spin degeneracy ($N = 1$ or 2). This technique has been implemented elsewhere [13, 14], and is discussed in this volume [9].
- (3) Using a “nanopore” technique, molecules of 2'-amino-4-ethynylphenyl-4'-ethynylphenyl-5'-nitro-benzene-1-thiolate, attached to Au on one side and topped by a Ti electrode on the other, exhibit negative differential resistance (NDR) [16]; this molecule, when studied by STM, shows time-dependent oscillations in conductance, presumably due to a change in tilt angle of the organothiolate with respect to the Au substrate [17]. If the second “top” metal is deposited at room temperature in either high vacuum (10^{-6} Torr) or ultra-high vacuum (10^{-8} Torr), then evidence of chemical reactions at the open surface of alkoxyorganothiolates (Al, Cu, Ag, and especially the very reactive Ti) or of interpenetration to the bottom of the SAM, close to the Au-S interface (Au), has been presented [18, 19]. The conductivity of alkanethiolates as a function of temperature was studied [20], and recently inelastic electron tunneling spectroscopy was used to prove that the current has traversed the molecules inelastically, exciting intramolecular vibrations and also vibrations of the bonds to the Au surface [21]. This is reviewed in this volume [8].
- (4) The Landauer quantum of resistance, $12.9 \text{ k}\Omega$ [15] was measured at room temperature between a multi-walled carbon nanotube, glued to a conducting atomic force microscope (AFM) tip, and a pool of liquid Hg [22]. Alas, this experiment does not seem to have been duplicated elsewhere.
- (5) FET behavior was observed by STM for a single-walled carbon nanotube curled over parallel Au lines, with the STM acting as a gate electrode [23]. This experiment has been implemented and extended elsewhere [24].
- (6) An LB monolayer of a bistable [3] catenane closed-loop molecule, with a naphthalene group as one “station”, and tetrathiafulvalene as the second “station”, and a tetracationic catenane hexafluorophosphate salt traveling on the catenane, like a “train” on a closed track, was deposited on poly-Si as one electrode, and topped by a 5 nm Ti layer and a 100 nm Al elec-

trode. The current-voltage plot is asymmetric as a function of bias (which may move the train on the track), and a succession of read-write cycles shows that the resistance changes stepwise, as the train(s) move from the lower-conductivity station(s) to the higher-conductivity station(s) [25]. However, a recent admission that LB monolayers of alkanes and rotaxanes show “molecule-independent switching” [26] (evidenced by an ohmic “return” current which can be attributed to either stalactites or stalagmites of Au or to some chemical reaction of the monolayer with Ti [18]) may cast some doubt on the catenane result.

- (7) The organometallic equivalent of a single-electron transistor (SET) was realized at 0.1 K with an organometallic Co(II) complex, using two electromigrated Au electrodes covalently bonded to the molecule, and a Si gate electrode at 30 nm from the molecule [27]. A new SET (again, no gain) has been reported [28]: these devices can exhibit no power gain: it is a well-controlled Coulomb blockade device with an elegant name to describe the role of the gate electrode in controlling the oxidation level. Other variants of this experiment have been reported [29, 30].
- (8) Unimolecular rectification across an LB monolayer of hexadecylquolinium tricyanoquinodimethanide, **1**, (Fig. 1) was first detected between Mg and Pt electrodes [31, 32], and later thoroughly confirmed between Al electrodes [33, 34] and, most recently, even between oxide-free Au electrodes [35, 36], to be a variant of the Aviram-Ratner (AR) [3] mechanism.

We focus here on unimolecular rectification, and update several recent reviews [37–39].

As explained below, the AR proposal [3] suggested a D- σ -A molecule connecting an electron donor moiety (D) to an electron acceptor moiety (A) through an insulating saturated “sigma” bridge σ ; the mechanism of action involves inelastic tunneling through the molecule from its first electronic excited state $D^+ - \sigma - A^-$ to the less polar ground state $D^0 - \sigma - A^0$ [3]. The first confirmed rectifier [31–36] was, instead, by happenstance, a ground-state zwitterion $D^+ - \pi - A^-$, connected by a twisted pi bridge, rather than a sigma bridge, and used inelastic tunneling from the lower-polarity excited state $D^0 - \pi - A^0$ to the higher-polarity ground state [40]. Gradual changes in the electrical conductivity of an LB monolayer of **1** upon repeated measurement led to combining the LB and SAM techniques and measuring two thioacetyl variants **2** and **3**, which could bind strongly to Au electrodes [41]. Two other LB monolayer rectifiers have been found, when sandwiched between Au electrodes: a pyridinium salt **4**, in which the rectification seems to be due to back-charge transfer from the anion to the pyridinium ion [42], and dimethylaminophenylazafullerene **5**, which is a moderate rectifier but can also exhibit a tremendous apparent rectification ratio (as high as 20,000) [43] due to a partial penetration of stalagmites of gold, which behave ohmically [43]. Finally, very sturdy rectification was seen in a Langmuir-Shaefer (LS) monolayer of fullerene-bis-(4-diphenylamino-4”-(N-ethyl-N-2”)-

hydroxyethylamino-1,4-diphenyl-1,3-butadiene malo-nate **6** between Au electrodes [44].

This review will first discuss metallic contacts. Next, it re-explains the AR proposal, and presents the assembly techniques needed to study the molecules of interest. Then it discusses three mechanisms that can cause rectification, and what is known about electron transport through organic films. The attention then shifts to the main experimental results of asymmetric current-voltage plots for the confirmed unimolecular rectifiers. Finally, it makes some guesses for future progress.

2 Metal Contacts

All-organic computers have been conceived, but at present the synthetic complexity of such a venture (making organic electronic components and also making organic or polymeric interconnects) may deter even the most optimistic visionaries. At the present time, only two-terminal devices, such as resistors, insulators, or rectifiers have been studied: all these are interrogated by inorganic metal contacts (Au, Ti, Al, Mg, graphite, etc.).

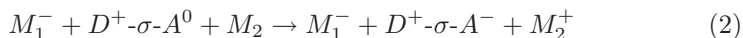
A technology of fabricating three metal electrodes, which can be brought into simultaneous covalent contact with a single molecular device, does not yet exist. At present, one can do binary logic with two-terminal diodes, or with negative differential resistance devices, or by three-terminal FET logic, which is in widespread industrial use. It would be very useful to bring three-terminal metal filaments within 1 nm of each other, without short circuits, then synthesize molecules with three terminations, to bridge and connect across these narrow gaps. The goal of bringing such electrodes together has interested several laboratories [27, 45]. When that goal is reached, and power gain is demonstrated through such three-terminal molecules, then all the necessary molecular electronic devices needed for unimolecular electronic circuits are present, and one can construct an all-organic computer, by jettisoning the metal contacts and synthesizing all-organic backbones (using, for instance, conducting oligomers and polymers or single-walled carbon nanotubes: another non-trivial goal!). It seems premature to worry about the organic backbones, when the zoo of available molecular devices does not yet include molecules with gain.

Another design criterion is that one must do with molecules what cannot easily be done with inorganic compounds. Otherwise, a me-too competition with proven commercial devices will always favor the existing technology.

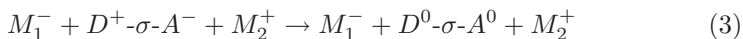
3 The Aviram-Ratner Ansatz

The first concrete suggestion for UE was the 1974 AR proposal [3] that a one-molecule rectifier could be achieved with a D- σ -A molecule, where D is a good

one-electron donor with relatively first low ionization potential I_D , where σ is some saturated covalent “sigma” bridge, and where A is a good one-electron acceptor with relatively high electron affinity E_A , when this molecule is placed between two appropriate metal contacts M_1 and M_2 . The purpose of σ is to decouple the molecular orbitals of the donor moiety D from the molecular orbitals of the acceptor moiety A. Of course, this language is approximate: the molecular orbitals belong to the whole molecule, but they often are more localized on one moiety than the other [3]. If the decoupling between D and A is complete, then intramolecular electron transfer becomes impossible. The molecular ground state of $D-\sigma-A$ has a lower dipole moment, and can be written as $D^0-\sigma-A^0$, while the first excited state is much more polar, has a higher dipole moment, and can be written as the zwitterionic or betaine state $D^+-\sigma-A^-$ [3]. Given what is known about organic molecules, it is likely that resonant transfer would be possible (Figs. 2 and 3) when the Fermi energy E_F of M_2 is resonant with the lowest unoccupied molecular orbital (LUMO) of the A moiety or part (which is close to the negative of the electron affinity A_A of the A moiety), and the highest occupied molecular orbital (HOMO) of the D moiety (which is close to the negative of the ionization potential I_D of the D moiety), is on resonance with E_F of the metal M_1 (upon the application of a positive bias V onto M_1). The intramolecular electron transfer would be an inelastic tunneling from the excited electronic state $D^+-\sigma-A^-$ to the ground electronic state $D^0-\sigma-A^0$. The mechanism would consist of two resonant electron transfers across metal-organic interfaces:

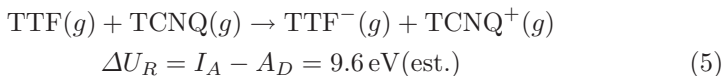
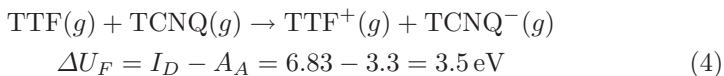


followed by (or simultaneous with) an inelastic down-hill intramolecular electron transfer:



which achieves, overall, the migration of one electron from M_2 to M_1 [3].

AR suggested, for the $D-\sigma-A$ molecule **7**, D = tetrathiafulvalene (TTF, **9**), A = tetracyanoquinodimethan (TCNQ, **13**), because these were, respectively, a good organic donor D , and one of the best organic acceptors A , as evidenced by the following data (for ions at infinite separation):



The AR proposal involves an electronic transition, which should be fast (ps to ns), compared with translations [25], conformational transitions, or molecular rearrangements (s to μ s).

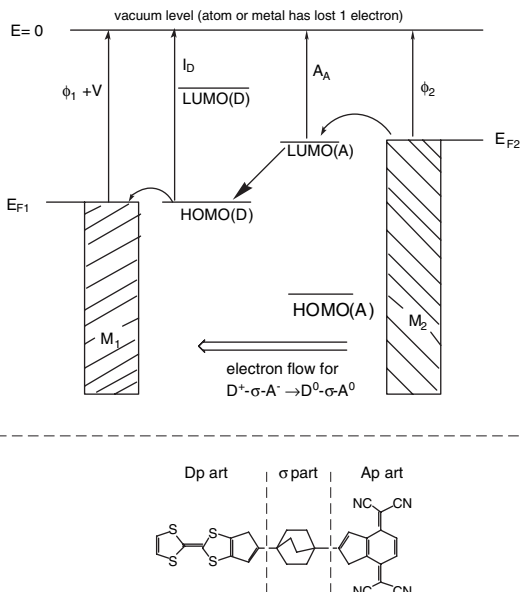


Fig. 2. The AR Ansatz [3], showing a proposed $D\text{-}\sigma\text{-}A$ -molecule (or “Gedankenmolekül”) 7 (which was never synthesized) and the through-molecule electron flow from the excited zwitterion state $D^+\text{-}\sigma\text{-}A^-$ to the undissociated ground state $D^0\text{-}\sigma\text{-}A^0$ when the molecule is placed between two metal electrodes M_1 and M_2 . Here $E = 0$ is the vacuum level, ϕ is the work function of the metal electrodes, V is the potential applied on the left electrode (the right electrode is grounded), I_D is the ionization potential of the donor moiety D , A_A is the electron affinity of the acceptor moiety A , and E_{F1} and E_{F2} are the Fermi levels of the metal electrodes, and the HOMO and LUMO levels are the highest occupied molecular orbitals or lowest unoccupied molecular orbitals of the D and A moieties

4 Three Processes for Rectification by Organic Monolayers

There are three distinct processes for asymmetrical conduction, i.e. rectification, in “metal | organic | metal” assemblies. The first process is due to Schottky barriers [46] at the “metal | organic” interfaces: a surface dipole will be formed at one or both interfaces, and, if these dipoles are different in size, then the currents at positive bias will be different than those at negative bias [46]. We shall call molecules that rectify by this process “S” (for Schottky) rectifiers [47, 48].

The second process arises, if the “chromophore” (i.e. the part of the molecule whose molecular orbital must be accessed during conduction) is placed asymmetrically within a “metal | molecule | metal” sandwich, e.g. because of the presence of a long alkyl “tail” [49, 50]. We shall call molecules that rectify by this process “A” (for “asymmetric”) rectifiers [51, 52].

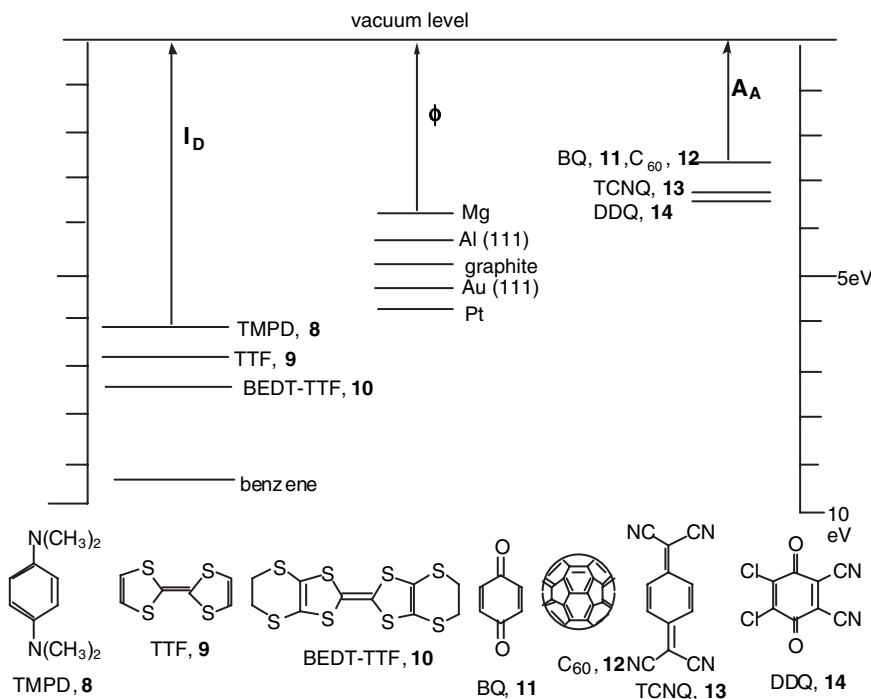


Fig. 3. Energy levels: HOMOs of some donors (8-10; left), work functions ϕ of some metals (middle), LUMOs of some acceptors (11-14, right)

The third process occurs when the current passing through a molecule, or monolayer of molecules, involves electron transfers between molecular orbitals, whose significant probability amplitudes are asymmetrically placed within the chromophore: this third process we think of as true “unimolecular rectification”, and we shall call this process “U” (for unimolecular) rectification [49]; these “U” rectifiers are what we endeavour to achieve.

The practical requirements for assembling organic molecules between two inorganic metal electrodes may mean that the monolayer may behave simultaneously as an “A”, or “S”, or “U” rectifier: thus, pure “U” rectifiers are rare [50].

5 Current and Resistance Across a Metal-Molecule-Metal System

The electron transport from metal to organic material to metal has received theoretical attention [49,53]. First, asymmetries in current-voltage plots (often ascribed to rectification) also occur if a chromophore is placed asymmetrically within the electrode gap [49] (“A” rectifiers). This has been seen in

early STM experiments [54]. Second, elastic electron transfer between a metal and a single molecular orbital of a molecule can be expressed by [36, 53, 55]:

$$I = I_0 \{ \tan^{-1}[\theta(E_0 + peV)] - \tan^{-1}[\theta(E_0 - (1-p)eV)] \} \quad (6)$$

where E_0 is the molecular orbital energy, V is the applied potential, and p is the fractional distance of the molecule from, say, the left electrode. If the molecule is centered in the gap, then $p = 1/2$. To obtain the efficiency of the current, the prefactor I_0 can be compared to $Q N_S$, where Q is the quantum of conductance (7.75×10^{-5} Siemens), and N_S is the number of molecules sampled simultaneously in parallel. Tunneling across molecules is expected to be approximately exponential to some power of the potential, so a sigmoidal curve is usually seen, symmetrical about $I = 0$ and $V = 0$. The various models have been discussed [36]. When the connection to the metal electrodes is macroscopic, i.e. involves a very large number of channels ($N \rightarrow \infty$), or if scattering occurs during the electron transport [56], then Ohm's law holds:

$$V = IR \quad (7)$$

In assessing rectification, one measures the rectification ratio (RR), defined as the current at a positive bias V divided by the absolute value of the current at the corresponding negative bias $-V$:

$$\text{RR}(V) = |I(V)|/|I(-V)| \quad (8)$$

There is also an interesting quantum limit: if an electron is confined to a small quantum dot (a two-dimensional confined region, of capacitance C), when the ratio $e^2/2C < kT$ (where k is Boltzmann's constant, and T is the absolute temperature), then a Coulomb blockade occurs: no more charges can be added, for a threshold voltage $V < (kT/e)$. The "single-electron transistor" (SET) [27] uses this Coulomb blockade.

6 Assembly Techniques: Physisorption Versus Chemisorption

In designing molecules for unimolecular rectifiers or, in the future, for unimolecular amplifiers, one must also decide how the molecules will be assembled and measured. For putting a molecule on a metal electrode, two techniques are available, physisorption and chemisorption.

Physisorption includes the random deposition from a vapor onto a solid substrate, or the organized transfer of an ordered monolayer (Langmuir or Pockels-Langmuir (PL) film) from the air-water interface onto a solid substrate. If this substrate is pushed vertically into the water and out of it, then an LB monolayer or, if the transfer is repeated, an LB multilayer is formed.

If the PL monolayer does not adhere well to a vertically inserted substrate, it may, instead, adhere well when the substrate is lowered horizontally atop the PL film, resulting in a Langmuir-Schaefer (LS) monolayer on the substrate. LB or LS physisorption has 2 advantages: (1) the percent coverage of the surface at the moment of transfer can be measured directly as the film transfer ratio; (2) is that Schottky barriers due to surface dipoles, formed during chemisorption, are avoided. Physisorption has 2 limitations: (1) after transfer, the structure of the vapor-deposited film, or of the LB monolayer or multilayers, may change over time, as the film tends towards a thermodynamic steady state; (2) any other adsorbates already present on the metal electrode are not displaced, but covered by the LB or LS layer(s).

Chemisorption includes the formation of a covalent bond of thiols and similar compounds to gold and similar metals, or of chlorosilanes to hydroxyl-covered silicon surfaces: these have been labeled as “self-assembled monolayers” (SAMs). Chemisorption involves large heats of bond formation, and has 2 advantages: (1) the chemical reaction displaces from the surface any previously physisorbed adsorbates; (2) the adsorbed species, once bonded, are difficult to remove. Chemisorption has 3 disadvantages: (1) the uncertain degree of coverage, (2) the possibility of further chemical reactions, and (3) the formation of surface dipoles. One can hope that by exposing a surface long enough (e.g. a few days) to the adsorbate, the heat of reaction will help drive the reaction to produce “full coverage” of a Langmuir, or monolayer, on the solid surface. There are spectroscopic techniques to monitor this deposition, but they are accurate to only maybe ± 0.1 Langmuir. For thiolates, the bonding to Au is partially ionic, so one creates a surface dipole (1 or 2 Debyes): i.e. an “S” rectifier. The polarity of silane links on Si is lower, but there is also less known about ordering the silanes on Si.

7 The “Organic Rectifier Project”

As mentioned above, the AR “Ansatz” requires that one couple a strong donor, or reducing agent D with a strong acceptor, or oxidizing agent A in the same molecule by some covalent bridge, preferably saturated (Figs. 2 and 3): this is a difficult synthetic challenge, also encountered in artificial photosynthetic systems. In addition, the rectifier must include appropriate terminations for the molecule, to allow its assembly between metal electrodes.

The “Organic Rectifier Project” at the University of Mississippi (1982–1991) was committed to the LB method. Many molecules were made which did indeed form LB films (structures **15–23** in Fig. 4). They were all obtained by using the carbamate coupling reaction as the last synthetic step (it was not possible to convert a weak acceptor into a strong acceptor in the presence of a strong donor after the covalent bridge is already built; rather, the coupling reaction must strongly favor the bridge building over the competing formation of an ionic charge-transfer salt). An ester coupling was also successful [57,58].

The various D- σ -A molecules that form LB films were the carbamates **15–23** mentioned above. Of these, **20–23** were “trial molecules” with the weak ethoxynitrophenyl (ENP) acceptor group.

Alas, rectification experiments failed, because of primitive techniques [57, 58].

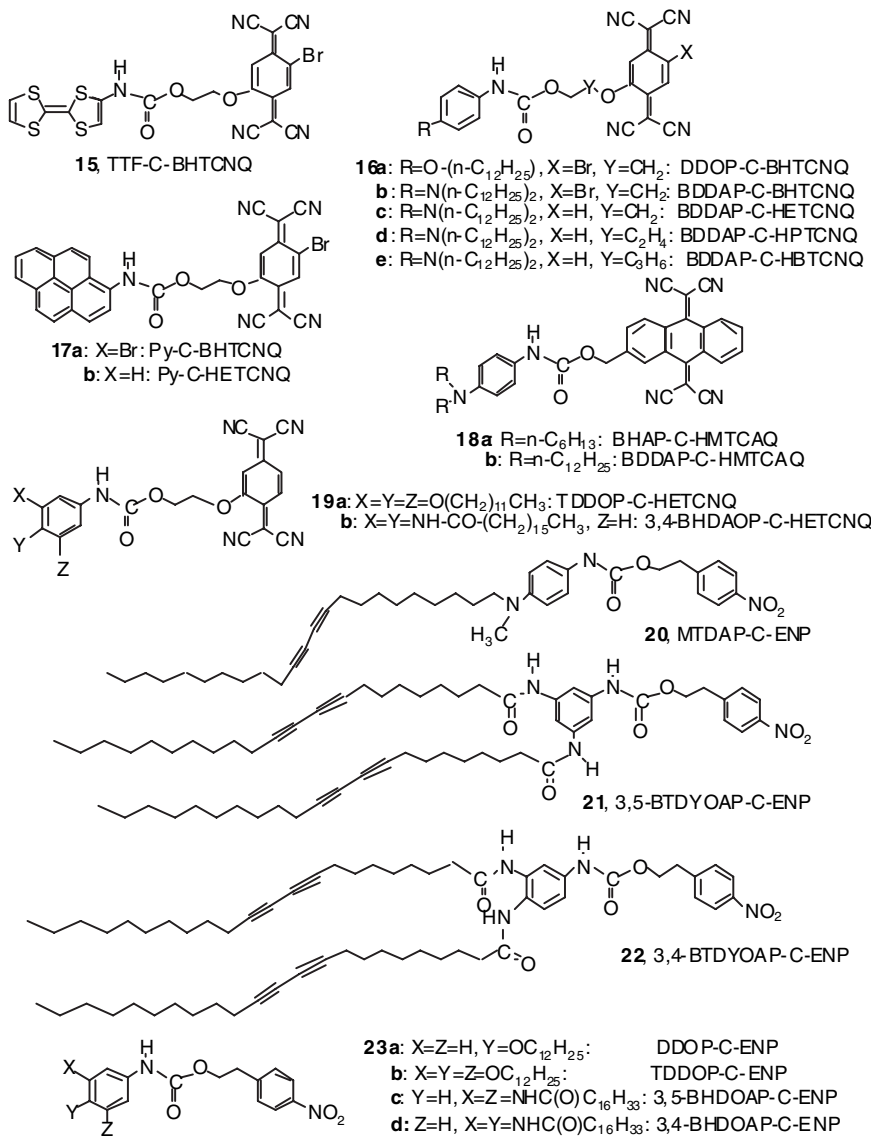


Fig. 4. D- σ -A molecules **15–23** synthesized at the University of Mississippi (1982–1991)

8 Electrical Properties of Monolayers and Multilayers

It is easy enough to transfer an organic monolayer or multilayer atop a sufficiently flat metal layer by the LB method [59, 60], or by chemisorption [61]. It is much more difficult to then deposit a second metal electrode atop the organic layer, without damaging the organic layer. The electrical properties of LB multilayers had been studied for decades [62], [63–65]. A dramatic improvement in the method of making “metal-LB layers | metal” sandwiches was accomplished by J. Roy Sambles and co-workers at Exeter University, who found that Mg vapor and thin Mg films would damage the LB films least; they thus studied molecular rectification [31, 66]. The first molecule studied was DDOP-C-BHTCNQ, **16a** [67], which had an asymmetric current-voltage curve [66]. However, later work [68] showed that a Schottky barrier between Mg and the BHTCNQ termination of **16a** (i.e. an interfacial Mg^{++} TCNQ⁻⁻ or Mg^{++} (TCNQ⁻)₂salt) was probably responsible for the rectification, rather than asymmetric conduction through the molecule, as in the AR [3] proposal: the LB multilayer of **16a** yielded an “S” rectifier [68].

The second molecule studied by Sambles was γ -hexadecylquinolinium tricyanoquinodimethanide, $C_{16}H_{33}Q\text{-}3\text{CNQ}$, **1**, (Fig. 1) [31]. Molecule **1** is one of a series of zwitterionic molecules synthesized by the group of Goeffrey J. Ashwell at Cranfield University for their nonlinear optical properties [70]. The rectification measured for LB monolayers and multilayers of **1**, when sandwiched between a Pt electrode on one side and a Mg electrode on the other (with an overcoat of Ag) [31] was at first put into some doubt [58, 71, 72]; but it was confirmed, when insulating LB layers of tricosenoic acid were added between the electroactive layers of **1** and the electrodes [32], and yet the rectification persisted [32].

9 Rectification of $C_{16}H_{33}Q\text{-}3\text{CNQ}$

The work at the University of Alabama by Cava, Metzger, and co-workers has aimed, since 1996, at confirming unimolecular rectification by eliminating asymmetries in the current-voltage plots due to electrodes of dissimilar metals, and at seeking the mechanism for the observed asymmetries. For instance, molecule **1** was studied by using the same metallic electrode on both sides on an LB monolayer or multilayer (at first Al [33, 34], and more recently Au [35, 43]), by concentrating on “metal | LB monolayer | metal” sandwiches, rather than “metal | LB multilayer | metal” sandwiches, and by resorting to a thorough chemical and spectroscopic characterization of the molecular species responsible for rectification [40, 42].

10 Molecular Properties of C₁₆H₃₃Q-3CNQ

The synthesis was improved: a 2-fold molar excess of the reagent LiTCNQ yielded C₁₆H₃₃Q-3CNQ, **1** in good yield [33]. Molecule **1** is slightly soluble in polar solvents and insoluble in non-polar solvents. It does crystallize, but afforded crystal habits that were so intertwined that a unit cell could not be indexed [33]. The cyclic voltammogram of **1** showed a reversible reduction at $E_{1/2} = -0.54$ vs SCE (this potential resembles that of p-benzoquinone, **11**); **1** has a second irreversible reduction, and a single irreversible oxidation [33]. The molecular ground-state static electric dipole moment of **1** is $\mu_{GS} = 43 \pm 8$ Debyes at infinite dilution in CH₂Cl₂ [33]. The absorption spectrum in solution shows a relatively narrow and hypsochromic band, peaked between 600 and 900 nm; this band is an intervalence transfer (IVT) or internal charge-transfer band [33, 40]. This band fluoresces in the near IR region [40]. From the Stokes shift, the experimental value of μ_{GS} , and also from a theoretical treatment of the solvation of ellipsoidal molecules in polar solvents, the excited-state dipole moment was estimated as $\mu_{ES} = 3$ to 9 Debyes [40]. Molecule **1** does not form large enough single crystals for a structure determination, despite many efforts [33]; spectroscopic evidence shows that **1** is clearly zwitterionic in the ground state (D⁺-A⁻), and less dissociated (D⁰-A⁰) in the first excited state. In the crystal structure of the closely related picolyl tricyanoquinodimethan (or picolinium tricyanoquinodimethanide) [69], the twist angle is 30.13° between the picolinium ring and the benzene ring of the tricyanoquinodimethane moiety [69]; there should be a similar twist angle between the benzene and the quinolinium rings in structure **1**; these angles are non-zero for steric reasons, and prevent the ultra-short pi-electron bridge in structure **1** from allowing complete mixing of the quinolinium or pyridinium electrons with the electrons on the 3CNQ part. Since the molecule is hypsochromic, the ground state must be D⁺-A⁻, and the first electronically excited state must be D⁰-A⁰. Despite the twist, the short bridge in **1** allows for an intense IVT band between the D and A ends of the molecule.

The VUV spectrum of LB multilayers of **1** on quartz, exhibits a strong peak at 570 nm [33]; this peak was measured at 565 ± 5 nm for a monolayer at the air-water interface; [73], but there is a long absorbance tail that extends into the IR [33, 73]. A second peak can appear at the air-water interface, at 670 nm, which fades with time [73]. For **1** dissolved in low-polarity solvents, there are two peaks, which were interpreted as vibronic sub-bands [40], and which shift with solvent dielectric constant [40], but shift less, when plotted against Reichardt's normalized solvent polarity parameter [73, 74]. In solvents of greater polarity, **1** exhibits only one peak, whose hypsochromic shift is pronounced [40, 73]. The earlier assignment was that two vibronic sub-bands are resolved in the lower-polarity solvents, but not in the higher-polarity solvents [40]; the more recent assignment attributes the higher-energy sub-band in low-polarity solvents to the formation of centrosymmetric solvated

association dimers [73], which can survive, for some time, even in a monolayer of **1** assembled at the air-water interface [73].

The HOMO of **1** shows a delocalized charge density, spread on both the D⁺ part and the 3CNQ⁻ part, while the LUMO is localized on the A⁻ part, as confirmed by EPR spectroscopy [40].

11 Film Properties of C₁₆H₃₃Q-3CNQ

Molecule **1** forms good amphiphilic Pockels-Langmuir monolayers at the air-water interface, with a collapse pressure of 34 mN m⁻¹ and collapse areas of 50 Å² at 20°C [33]. It transfers well on the upstroke, with transfer ratios around 100% onto hydrophilic glass, quartz, or aluminum [33, 75] or fresh hydrophilic Au [35, 36]. It transfers poorly on the downstroke onto graphite, with a transfer ratio of about 50% [75]. Thereafter, the monolayers transfer only on the upstroke, with 100% transfer ratios, onto all surfaces, forming Z-type LB multilayers [33, 70, 75] (except for that first poorly transferred layer on HOPG [75]). Some promise was shown by a derivative of **1** with R = alkylthioacetyl [76].

The LB monolayer thickness of **1** was determined by X-ray diffraction (23 Å [33] and 29 Å [36]), spectroscopic ellipsometry (23 Å) [36], surface plasmon resonance (22 Å) [33, 77], and by X-ray photoelectron spectrometry (XPS) (25 Å) [77]. Assuming an average monolayer thickness of 23 Å and a calculated molecular length of 33 Å (with an all-trans geometry for the C₁₆H₃₃ “tail”), one gets a tilt angle of 46° from the surface normal [33]. The XPS spectrum of one monolayer of **1** on Au shows two N(1s) peaks [77]. An angle-resolved XPS spectrum shows that the cyano nitrogens lie closer to the Au substrate, than does the quinolinium N atom [77]. The valence-band portion of the XPS spectrum agrees roughly with the density of molecular energy states [40]. The contact angle of a drop of water on “hydrophilic Au” is measured to be 40° (it should be zero if the gold were perfectly free of hydrophobic adsorbates); this angle increases to 92° if a monolayer of **1** is transferred atop fresh hydrophobic Au [77].

What evolves is a picture of molecules of **1** that adhere somewhat by the two terminal CN groups onto a hydrophilic substrate, are tilted maybe 45° from the surface normal, and present alkyl chains to the air. This is confirmed by a grazing-angle FTIR study of **1** on Al [33] or on Au [77]. Since a monolayer survives in the ultra-high vacuum of an XPS instrument, it must adhere rather well to it, i.e. it does not desorb very rapidly. The absorption spectrum of an 11-layer LB film shows an intense IVT band at 570 nm or 2.17 eV [33]. LB multilayers of **1** have a strong second harmonic signal $\chi_{zzz}^{(2)} = 180 \text{ pm V}^{-l}$, whose strength is partly due to resonance enhancement at 532 nm from the tail of the absorption band [78]. The STM image of **1** on HOPG has been measured (Fig. 5) [33]: since **1** adheres (poorly) with the alkyl chains closest to the graphite, one sees an unresolved image of the molecule seen

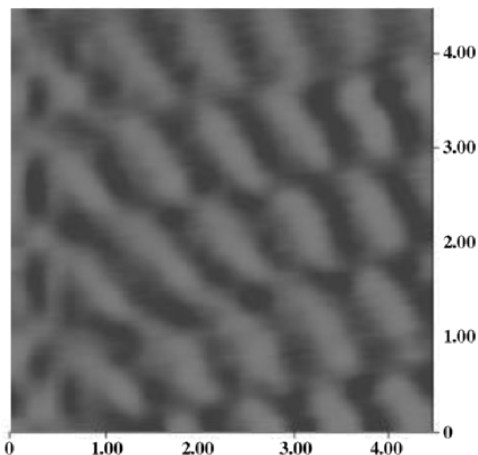


Fig. 5. STM image of a LB monolayer of $C_{16}H_{33}Q\text{-}3CNQ$, **1** on HOPG, with Pt/Ir tip (Nanoscope III). Scan size = 4.5 nm × 4.5 nm, Z-range = 2.3 pA, bias = -316 mV; setpoint current = 3.2 pA [33]

from the dicyanomethylene end, with a repeat distance of $6 \text{ \AA} \times 12 \text{ \AA}$ [33], somewhat larger than the collapse area per molecule of 50 \AA^2 . The poor adhesion to graphite, and the low coverage explain why the image in Fig. 5 slowly migrates across the surface [33].

12 Metal – LB Film – Metal Sandwiches of $C_{16}H_{33}Q\text{-}3CNQ$

To perform rectification measurements, LB monolayers and multilayers of $C_{16}H_{33}Q\text{-}3CNQ$, **1** were sandwiched between macroscopic Al electrodes [33], and most recently using the “cold gold” technique (Fig. 6), between Au electrodes [35,36]. First, the bottom electrode (either Al [33], or an adhesion layer of Cr followed by Au [36]) is evaporated onto a glass or quartz or Si substrate; second, the LB monolayer or multilayer of **1** is transferred above it; third, the structure is dried for 2 days to remove any adventitious water; fourth, the second electrode is deposited through a shadow mask [33] or a contact mask [35,36], to make 30 to 48 pads per substrate (most recently of area of 0.283 mm^2 each [36]); fifth, a droplet of either Ag paste or Ga/In eutectic is put above the bottom electrode and (very gently) sequentially on one of the pads of the top electrode, and electrical measurements are made. During the evaporation of the top electrode, a copper plate holding the sample is cooled by a liquid nitrogen bath; this suffices for an Al deposition [33] but not for an Au deposition. For Au deposition (Fig. 6), two additional precautions are taken, one, to add 10^{-3} torr of Ar gas to the evaporation chamber [79], the

other, to protect the substrate from direct thermal radiance from the heated Au source by hiding the sample on the opposite side of the copper plate (always cooled to liquid nitrogen temperatures). This “cold gold” deposition [79] forces the Au atoms to undergo multiple scattering by Ar atoms before they reach the substrate [35,36]. The final metal-LB film-metal geometry is shown in Fig. 7 for Au electrodes [35,36] (the geometry is similar for Al electrodes).

The Al layers are covered by its oxide, as is the Ga/In eutectic drop, while the Au electrodes have no oxide covering.

13 Unimolecular Rectification by C₁₆H₃₃Q-3CNQ

A monolayer or multilayer of arachidic acid, C₁₉H₃₉COOH, sandwiched between Al electrodes as in Fig. 14, has a sigmoidal and almost symmetrical curve under both positive bias and negative bias (as expected) [33]; the same results are seen when Au electrodes are used [36]. When a monolayer of C₁₆H₃₃Q-3CNQ, **1** is placed between Al electrodes (with their inevitable patchy and defect-ridden covering of oxide), then a dramatically asymmetric current is seen (Fig. 8). For **1**, the rectification ratio (8) is RR = 26 at 1.5 Volts [33]. Assuming a molecular area of 50 Å², the total current at 1.5 Volts corresponds to 0.33 electrons molecule⁻¹ s⁻¹ [33]. The rectification ratios vary somewhat from pad to pad, as does the total current, because these are all two-probe measurements, with all electrical resistances (Al, Ga/In or Ag paste, wires, etc.) in series. As high potentials are scanned repeatedly, the IV curves show progressively less asymmetry; the rectification ratios decrease gradually with measurement, i.e. with repeated cycling of the bias across the monolayer. One should remember that putting 1.5 Volts across a monolayer of thickness 2.3 nm creates an electrical field of 0.65 GV m⁻¹, which is very large; under such fields, many zwitterionic molecules in the monolayer may turn around, end over end, to minimize the total energy. The more “liquid”-like the monolayer, the easier this process would be. Measurements of the temperature dependence of rectification of **1** between Al electrodes, in the range 105 K < T < 390 K, established that the asymmetry is not temperature-dependent [34], but that the currents increase with temperature; this may be due to temperature effects across the several metal-oxide-metal junctions [34].

Although the experiments with Al electrodes measured the rectification of several molecules in parallel, or unimolecular rectification, this conclusion rested on the assumption that the oxide covering of the Al electrodes was sufficiently defective to allow “ohmic” contact with the molecules, in other words, that no substantial electrical contact was made wherever the oxide coverage was thick, and that the current measured flowed mostly through those sites, where the oxide coating was very thin or non-existent. This conclusion may not have been completely convincing to all readers. With Au electrodes the current through the pads increased dramatically, as expected,

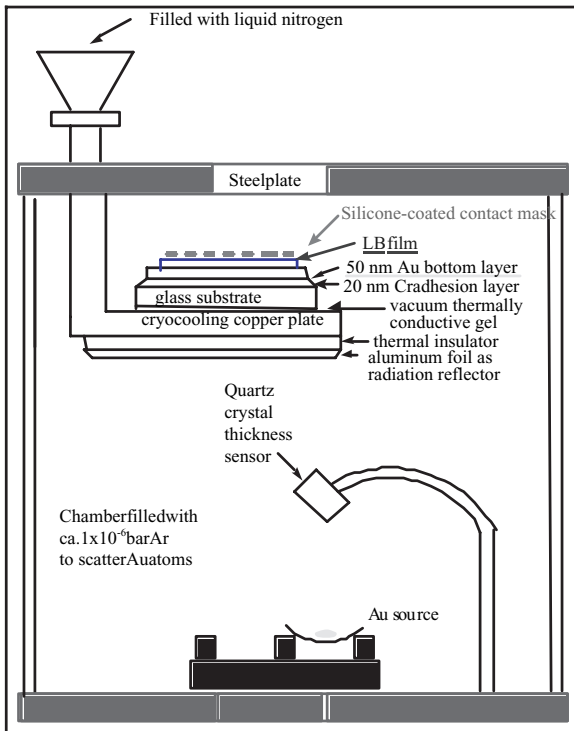
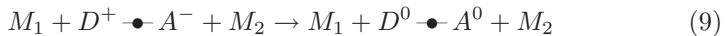


Fig. 6. Geometry of “cold gold” evaporation [36]

but the asymmetry persisted: this confirmed that the same asymmetric conduction through the molecules could be measured using either Au or Al electrodes [35, 36].

Figures 9 to 12 give details the results with Au electrodes. Figure 9 shows the best rectification ratio at 2.2 Volts ($RR = 27.53$). Figure 10 shows how the rectification ratio decreases from cycles 1 to 6. Figure 11 shows the highest current (90,400 electrons per molecule per second). Some cells exhibit, as in Fig. 12, a saturation in the forward current. For some other cells (not shown), the current increases until breakdown occurs; in some cells this happens at 5.0 Volts, i.e. the cells suffer dielectric breakdown only at a field close to 2 GV m^{-1} [36]. It is quite clear that rectification by a one-molecule thick layer of $\text{C}_{16}\text{H}_{33}\text{Q-3CNQ}$, **1** is an established fact.

One plausible mechanism for rectification by $\text{C}_{16}\text{H}_{33}\text{Q-3CNQ}$, **1** is a minor change in the AR proposal, so that (2), (2), and (3) are replaced by:



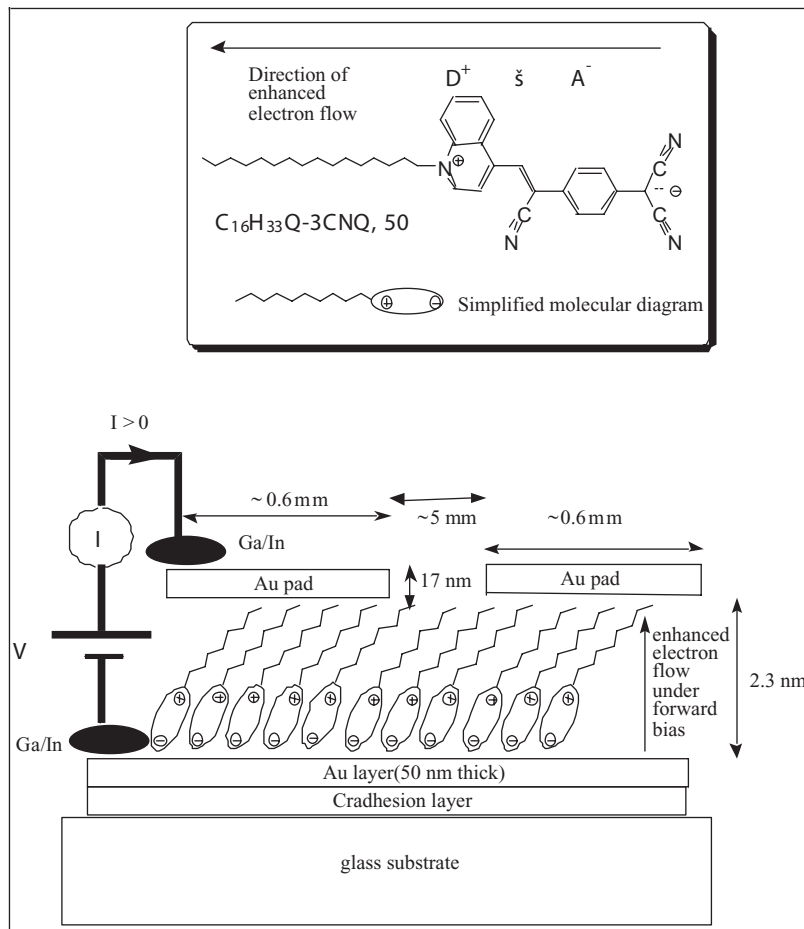


Fig. 7. Molecular structure and geometry of LB monolayer of $C_{16}H_{33}Q\text{-}3\text{CNQ}$, **1** sandwiched between Au electrodes, with an arrow showing the direction of enhanced electron flow under positive, or forward bias. The glass substrate, 50 mm × 50 mm × 0.4 mm, covered either by a Cr adhesion layer, or by a hydrophobic xylene covering, followed by an evaporated Au film 50 mm × 50 mm × 50 nm, then the LB monolayer or multilayer, then by 48 cylindrical Au pads, 17 nm thick and with an area of 0.283 mm² each [36]

where the first step is the electric field-driven excitation from ground to excited state, followed by electron transfers across the two “molecule | metal” interfaces [33].

Independently, it was confirmed that Z-type 30-layer films of **1** rectify between Au electrodes [73]. The currents for the multilayer [73] were three orders of magnitude smaller than those reported for the monolayer [36], either

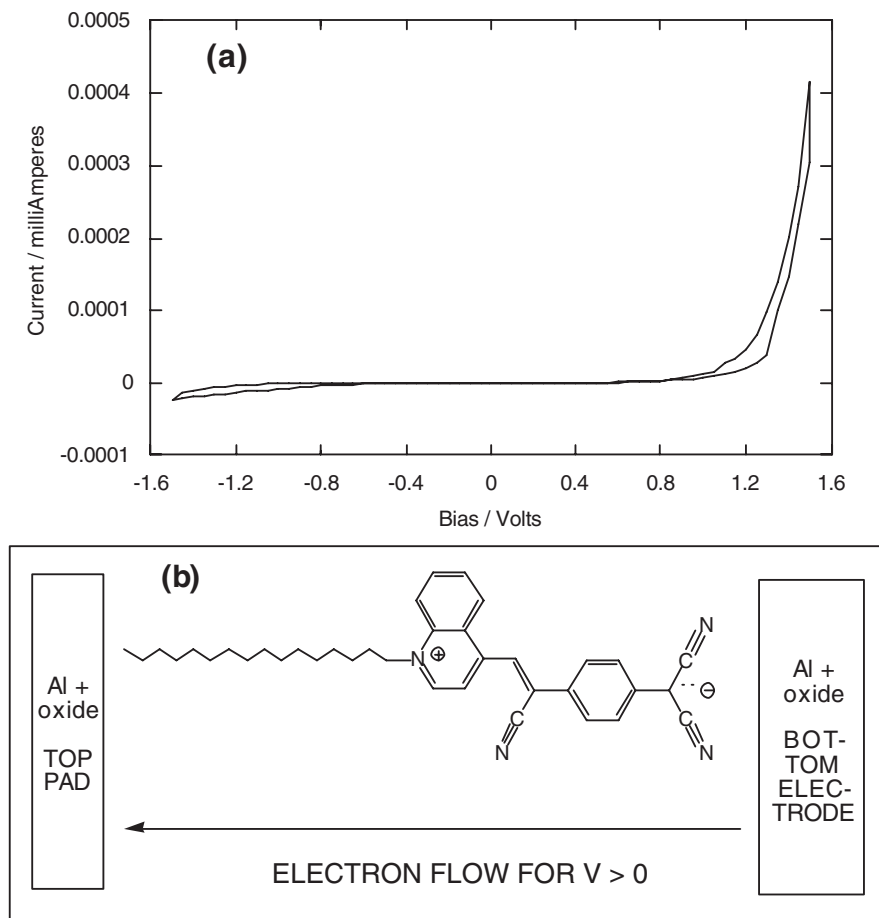


Fig. 8. (a) DC current I versus the DC applied voltage V (I - V plot) through a single monolayer of $\text{C}_{16}\text{H}_{33}\text{Q}-3\text{CNQ}$, **1** sandwiched between Al electrodes (top Al pad area 4.5 mm^2 , thickness 100 nm), using Ga/In eutectic and Au wires. Voltage sweep rate = 10 mV s^{-1} . RR = 26 at 1.5 Volts. (b) Direction of electron flow at $V > 0$ [33]

because of inefficient electron transport between adjacent layers, or because of current contributions from Au filaments within the LB monolayer [73].

14 Chemisorbed Monolayer Rectifiers

Thioacetyl variations of **1** have been synthesized [41, 76], with the aim of preparing molecules that can form Langmuir (or Pockels-Langmuir) monolayers at the air-water interface, and then bind covalently to an Au substrate after

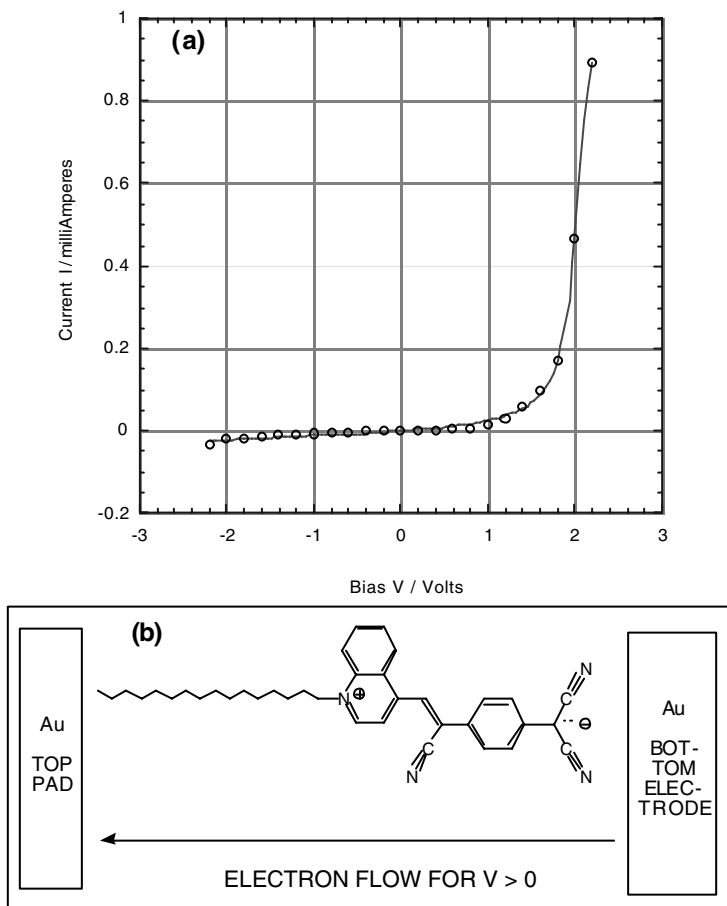


Fig. 9. (a) Current-voltage (I-V) plot for a cell “Au | monolayer of C₁₆H₃₃Q-3CNQ, 1 | Au”. The resistance at 2.2 Volts is $R = 2.47 \text{ k}\Omega$; the current at 2.2 Volts is $I = 9.83 \times 10^3 \text{ electrons molecule}^{-1} \text{ s}^{-1}$. The rectification ratio at 2.2 V is $RR = 27.53$ in the first cycle (shown), but decreases to 10.1, 4.76, 2.44, and 1.86 in cycles 2, 3, 4, and 5, respectively (not shown). (b) Direction of electron flow for $V > 0$ [36]

either LB or LS transfer: the idea was to combine the good ordering possible at the air-water interface, a good transfer to a substrate, and a very sturdy chemical bond to the substrate after transfer. The first molecule [76] with an undecyl “tail” followed by a thioacetyl termination (“C11 thioacetyl”) gave disappointing results: the pressure-area isotherm that the Pockels-Langmuir film collapsed at relatively low surface pressures, compared to 1, and yielded disordered LB monolayers, with competition between strong physisorption by the dicyanomethide end of the molecule and Au-to-thiolate chemisorption. The monolayer rectified in either direction, depending on where in the LB

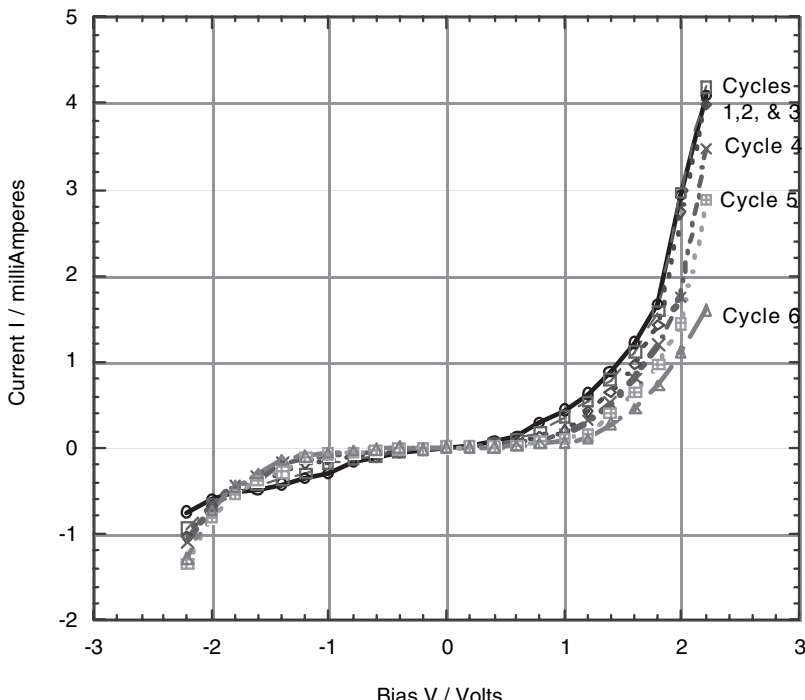


Fig. 10. I-V plot for a cell “Au | monolayer of $C_{16}H_{33}Q\text{-}3CNQ$, **1** | Au”, showing the decrease in rectification ratio. At 2.2 V in the first cycle, $R = 538 \Omega$, $I = 4.09 \text{ mA} = 4.5 \times 10^4 \text{ electrons molecule}^{-1} \text{ s}^{-1}$, and $RR = 5.39$. Cycle 1: circles \circ ; cycle 2: squares \square ; cycle 3: diamonds \diamond ; cycle 4: x's \times ; cycle 5: squares with crosses \oplus ; cycle 6: triangles \triangle . The direction of electron flow for $V > 0$ is the same as shown in Fig. 9 [36]

monolayer, i.e. on which molecule (“right side up” or “upside down”) the STM tip was probing [76]. Better results were seen with thioacetyl variants **2** (“C14 thioacetyl”) and **3** (“C16 thoacetyl”) [41]. The pressure-area isotherm indicated much sturdier films, which transferred well to solid substrates by either LB or LS transfer [76]. The intensity of the IVT band in monolayers and multilayers on quartz (but not in solution) was lower for **2** and **3** than for **1**, probably because the twist angle is unexpectedly greater in **1** than in **2** or **3** [41]. The rectification is best for LS films: Fig. 13 shows the IV plot for an LS monolayer of **2** on Au, while Fig. 14 shows the same result for **3** [41]. The enhanced current occurs at $V < 0$, because LS monolayers of **2** and **3** have the molecular chromophores oriented in the direction opposite to their orientation for **1** in Figs. 8–12 [41]. The rectification for **3** and **4** persists, and does not disappear with cycling [41].

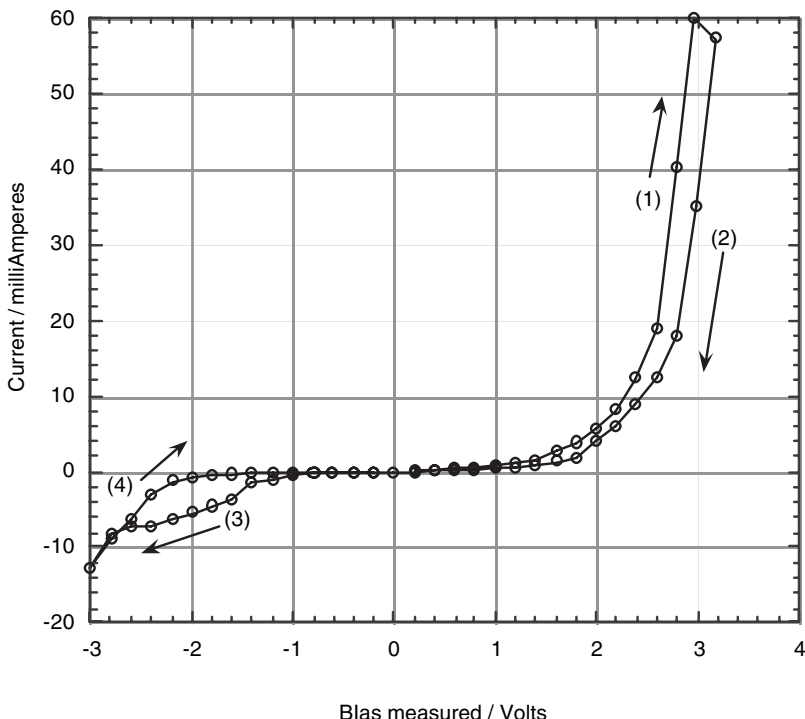


Fig. 11. I-V plot for a cell “Au | monolayer of $C_{16}H_{33}Q\text{-}3CNQ$, **1** | Au”, showing hysteresis At 2.2 V in the first cycle, $R = 268 \Omega$, $I = 8.20 \text{ mA} = 9.04 \times 10^4$ electrons molecule $^{-1}$ s $^{-1}$, and RR = 6.62. The direction of electron flow for $V > 0$ is the same as shown in Fig. 9 [36]

15 Three More Rectifiers

Recently three more molecules were studied at the University of Alabama: 2,6-di[dibutylamino-phenylvinyl]-1-butylpyridinium iodide, $(Bu_2N\varphi V)_2 Bu Py^+I^-$, **4** [42] dimethylanilino-aza[C_{60}]fullerene, DMAAn- NC_{60} , **5** [43], and the fullerene derivative **6** (Fig. 1): all three are unimolecular rectifiers.

$(Bu_2N\varphi V)_2 Bu Py^+I^-$, **4** forms a Pockels-Langmuir film at the air-water interface, and transfers to hydrophilic substrates as a Z-type multilayer. The monolayer thickness was estimated as 0.7 nm by spectroscopic ellipsometry, and 1.15 nm by surface plasmon resonance (at $\lambda = 532$ nm) or 1.18 nm (at $\lambda = 632.8$ nm); X-ray diffraction suggests a layer thickness of 1.3 nm [42]. The films exhibit an absorption maximum at 490 nm (which is slightly hypsochromic in solution), attributable to iodide-to-pyridinium back-charge-transfer, and a second harmonic signal $\chi^{(2)} = 50 \text{ pm V}^{-1}$ at normal incidence ($\lambda = 1064 \text{ nm}$) and 150 pm V^{-1} at 45° [42]. X-ray photoelectron spectroscopy of a multilayer of **4** on a gold substrate finds only 30% of the

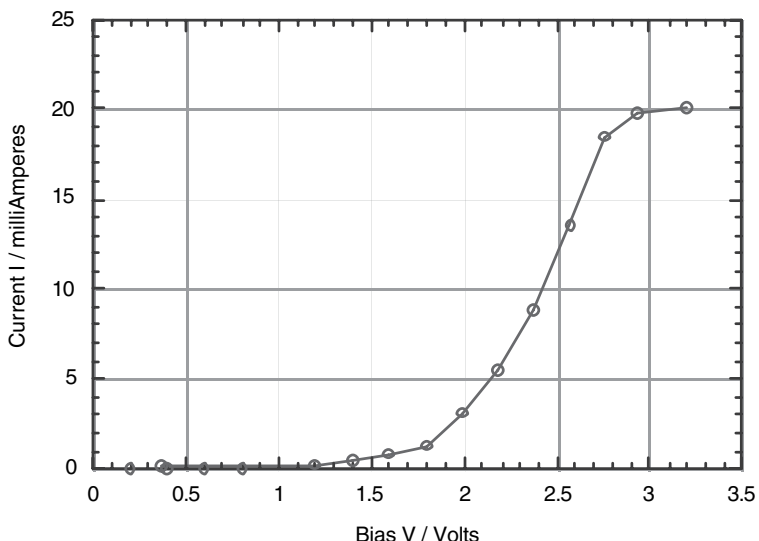


Fig. 12. I-V plot for a cell “Au | monolayer of $C_{16}H_{33}Q\text{-}3CNQ$, **1** | Au”, that shows saturation in the forward current $I = 20$ mA at 3.2 Volts (this cell broke down at 3.4 Volts) The direction of electron flow for $V > 0$ is the same as shown in Fig. 9 [36]

expected signal from the iodide; it is likely that the iodide anion is partially replaced by a more abundant hydroxide anion during LB transfer [42]. The rectification is shown in Fig. 15: once again, there is a decrease of rectification upon successive cycles. Some cells have initial rectification ratios as high as 60. The favored direction of electron flow is from the gegenion to the pyridinium ion, i.e. in the direction of “back chargetransfer”, and the rectification in $(Bu_2N\varphi V)_2BuPy^+\text{I}^-$, **4** can be attributed to an interionic electron transfer, rather than to an intramolecular electron transfer [43].

The azafullerene DMA_n-NC₆₀, **5** consists of a weak electron donor (dimethylaniline) bonded to a moderate electron acceptor (N-capped C₆₀). It is a blue compound, with a significant IVT peak at 720 nm [43]. The pressure-area isotherm [43] is shown in Fig. 16. The Langmuir film is very rigid, i.e. the slope of the isotherm is relatively large. However, the molecular areas are 70 Å² at extrapolated zero pressure, and 50 Å² at the chosen LB film transfer pressure of 22 mN m⁻¹ [43], whereas the true molecular area of C₆₀ is close to 100 Å². Therefore it is thought that the molecules **5**, transferred onto Au on the upstroke, are somewhat staggered, as is shown in the inserts of Figs. 17 and 18, with the more hydrophilic dimethylamino group closer to the bottom Au electrode. The film thickness is estimated as 2.2 nm (XPS) [43]. The monolayer is covered, as previously [35, 36, 42], with 17 nm-thick Au pads deposited by the “cold gold” technique. The dimethylamino groups in the LB film are probably not as close-packed as the azafullerenes. Angle-resolved

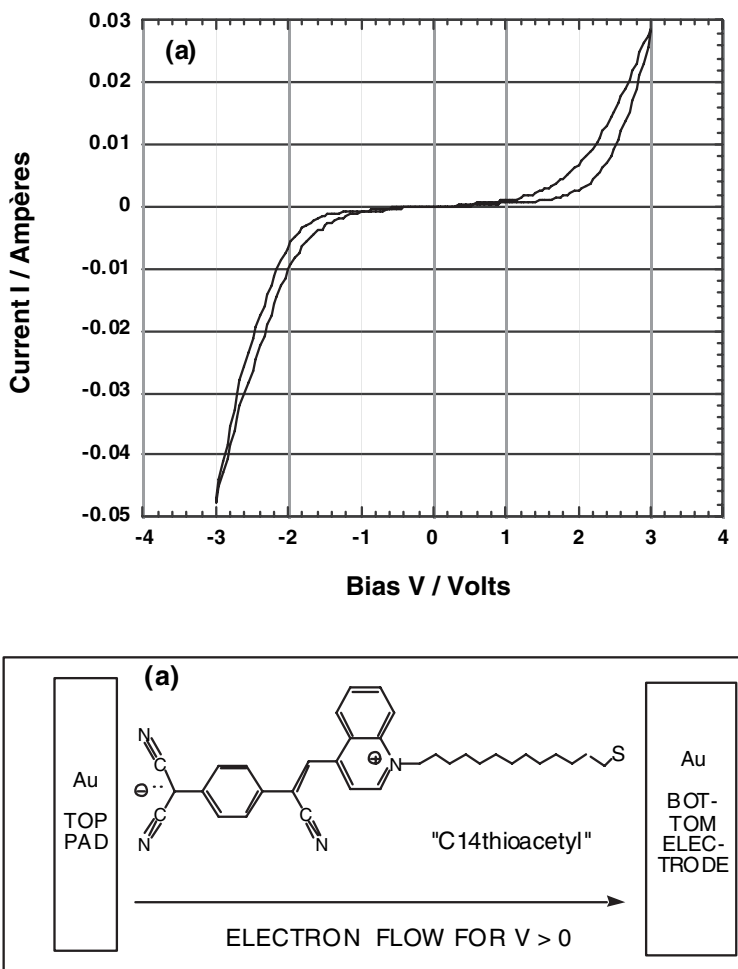


Fig. 13. (a) I-V plot for a cell “Au | LS monolayer of S-C₁₄H₂₈Q-3CNQ, **2** | Au”. (b) Direction of electron flow for $V > 0$ [41]

N(1s) XPS spectra confirm that the two N atoms are closer to the bottom Au electrode than is the C₆₀ cage [43]. The current-voltage plot shown in Fig. 17 is a dramatic but unwelcome surprise [43]. The top pads have an area of 0.283 mm², as before [36, 40], and the cell now supports 1 Ampere of current across it! (per molecule, that would be an absurdly large number such as 5×10^{11} electrons molecule⁻¹ s⁻¹). Moreover, the high current between 1.5 Volts and -0.5 Volts in the “return” path (3 and 4 in Fig. 17) is ohmic. The asymmetry decreases upon cycling (not shown here) [43]. Probably, metallic Au filaments have formed within the monolayer, which do not pierce the fullerene ends of the monolayer, and are progressively destroyed

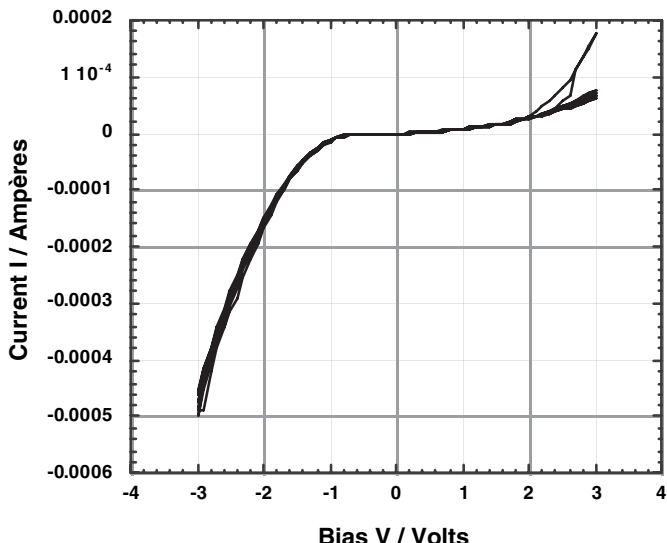


Fig. 14. I-V plot for a cell “Au | LS monolayer of S-C₁₆H₃₂Q-3CNQ, **3** | Au”. The direction of electron flow for $V > 0$ the same as for Fig. 13 [41]

by cycling the voltage: these Au stalagmites are shown in Fig. 16 as jagged arrows or thunderbolts. In contrast, some cells show no such large current, but a much smaller current, which is “marginally” rectifying in the forward direction, with a rectification ratio RR of about 2 (Fig. 18) [43].

Molecule **6** is a new rectifier, based on triphenylamines (one-electron donors) and fullerene (weak one-electron acceptor), which has a very novel property: under conditions similar to those used for **1**, **4** and **5**, a Langmuir-Schaefer monolayer of **6** rectifies (Fig. 19), but the rectification ratio does not decrease at all upon successive cycling. The monolayer is probably very dense and stiff, so stiff, in fact, that it cannot be transferred onto an Au substrate by the usual vertical LB process, but adheres to Au if it is transferred by the horizontal, or Langmuir-Schaefer process [44].

16 Direction of “Forward Current” in Rectifiers

Now a few words of interpretation. The direction of electron flow for $V > 0$, shown in the insets to Figs. 8–15, 18 and 19, can be compared to the “D” and “A” regions shown for molecules **1–6** in Fig. 1. Clearly, the “rectification signal”, or enhanced electron flow, or “forward current” corresponds, in all six cases, to electron flow from the electron-rich donor region D to the electron-poor acceptor region A. That is a nice and reassuring confirmation of the ideas proposed by Aviram and Ratner in 1974 [3]. Much work must still be

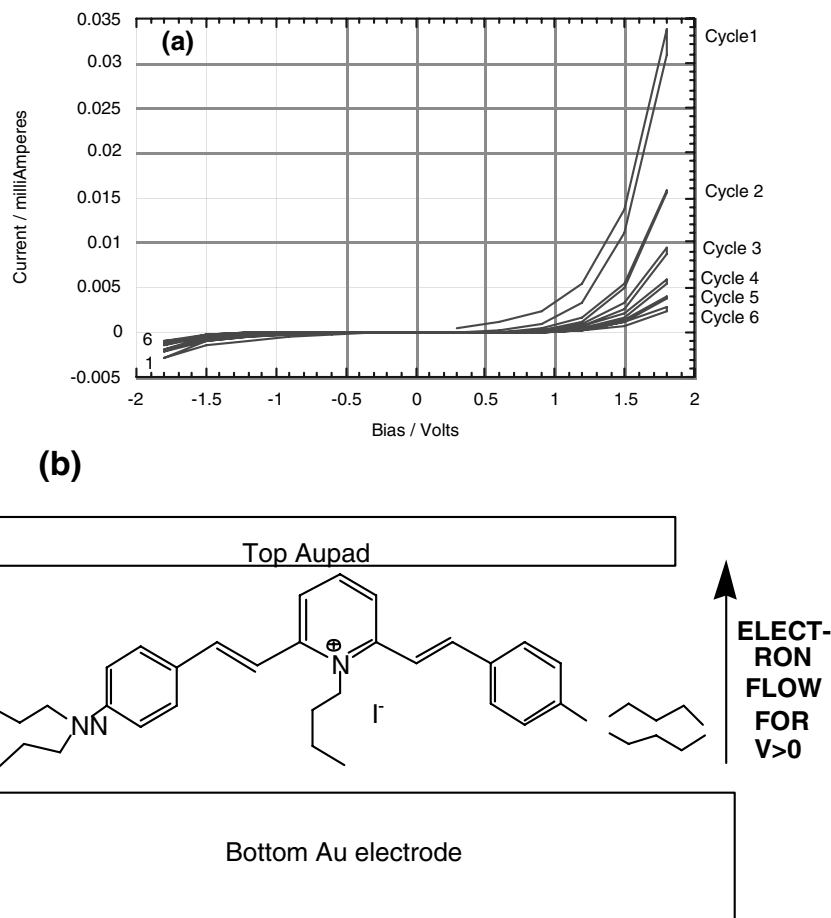


Fig. 15. (a) I-V plots for $(\text{Bu}_2\text{N}\varphi\text{V})_2\text{BuPy}^+\text{I}^-$, **4**, measured in a “Au | LB monolayer of **4** | Au“ cell, for six successive cycles of measurement. The rectification ratios are $\text{RR} = 12, 7, 5, 4, 3, 3$, for cycles 1 through 6, respectively. (b) The direction of electron flow for $V > 0$ [42]

done, to confirm the details of how, and how fast, these electrons flow through the monolayers.

17 Challenges for the Near Future

Although unimolecular rectification has been fully confirmed, there are still open questions for the near term:

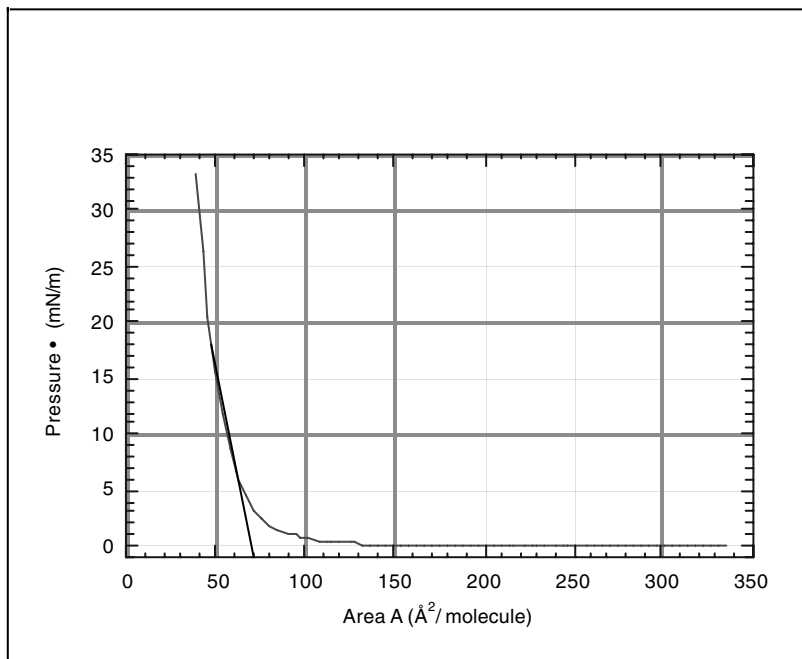


Fig. 16. Pressure-area isotherm for DMAAn-NC₆₀, **5** [43]

1. Can inelastic electron tunneling spectroscopy confirm that the electron really does go through the molecule (instead of tunneling through space)? The answer is yes [21].
2. How fast is the rectification process?
3. What is the role of the metal electrodes during a room-temperature metal vapor deposition process [18, 19], or during the measuring process? Can they form stalagmites and stalactites within the monolayer [43]? Can this process be controlled? A recent admission by the Hewlett-Packard group that their previously well-advertised work on self-assembled monolayers is plagued by metal filaments [26] (similar to what we reported earlier [43] and showed above in Fig. 17) has helped to clarify what is intrinsic conduction through molecules and what is artifact.
4. Do we know whether the currents measured scale with the area of the electrodes used? This has been difficult to determine, when the measurements may have been limited by varying resistances at the oxide-bearing Ga/In eutectic drop – to – gold interfaces.
5. Can one investigate optically what occurs during the electrical measurements? Can we “peek” under the monolayer?
6. What is the role of image dipoles induced in the metal electrodes by the molecular dipole moments in either the ground state or the excited state?

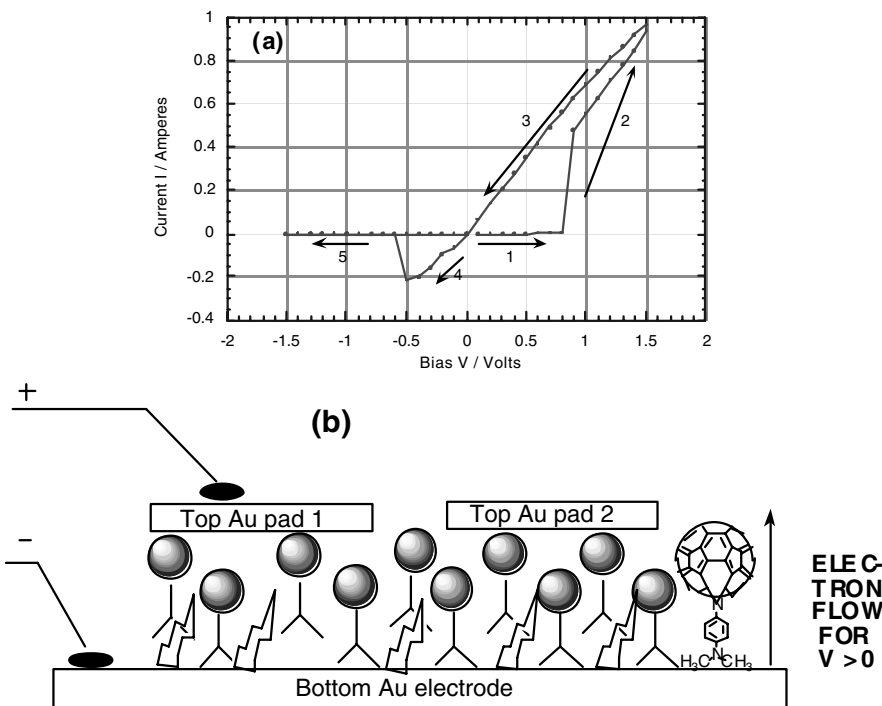


Fig. 17. (a) I-V plots for DMAAn-NC₆₀, **5**, measured in a “Au | LB monolayer of **5** | Au” cell, with numbers indicating the measuring sequence. This is filamentary conduction through Au stalagmites and **5**. (b) Direction of electron flow for $V > 0$ [43]

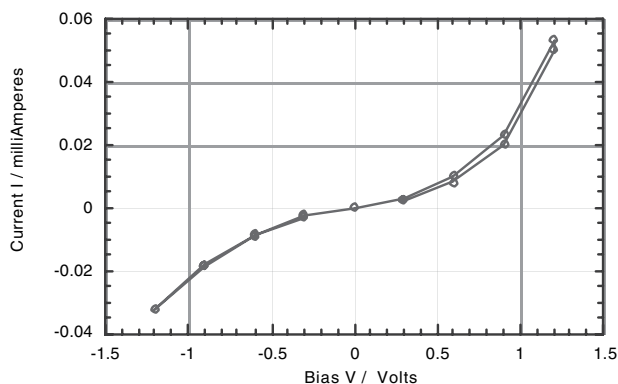


Fig. 18. Current-voltage plots for DMAAn-NC₆₀, **5**, measured in a “Au | LB monolayer of **5** | Au” cell, in which the current stays small: this should be the current due to the molecules **5** and not to the Au filaments. The direction of electron flow for $V > 0$ the same as for Fig. 17 [43]

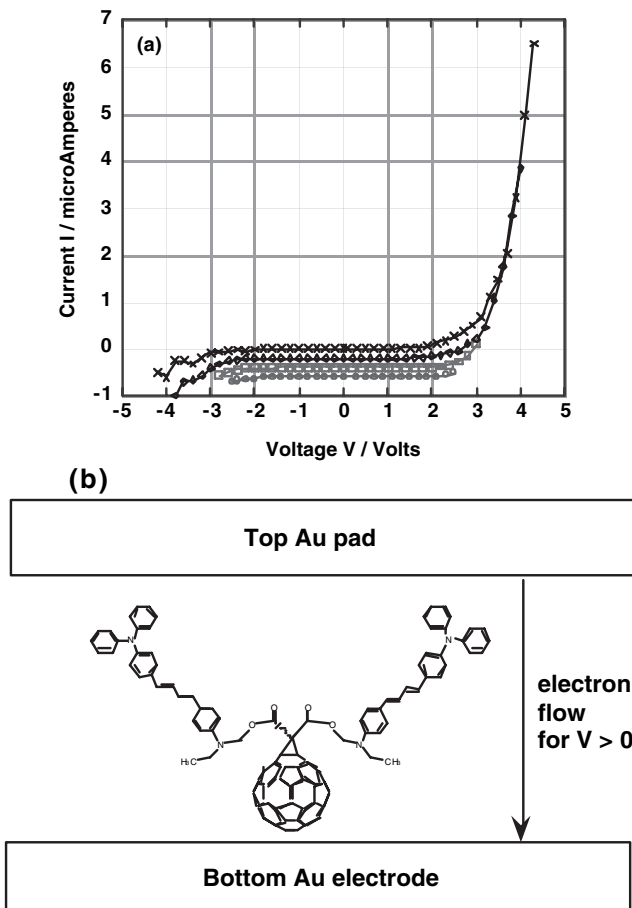


Fig. 19. (a) Multiple I-V scans for a LS monolayer of **6**. Inset shows the upper and lower limit voltage for the scans with the indicated marker. For clarity, each curve is moved along the y-axis by multiples of $2 \times 10^{-7} \text{ A}$. (b) Direction of electron flow for $V > 0$ [44]

7. Can rectifiers and bridges and strands of conducting polymers be grafted together to form a molecular amplifier, or transistor, with power gain [80–82]? We show in Fig. 20 one such idea [82]: if a molecule with three moieties A, B, and C covalently bonded together is such that either the electron mobility from A to B is large that the mobility from C to B, then the molecule may function as amolecular amplifier, as ana analog of an npn' bip;olar junction transistor. Alternately, if this mechanism does not work, perhaps a field effect would function between moieties C and B, thus narrowing the channel or conductivity of the main current from A to B. However, it is very hard to prepare three electrodes, say two of

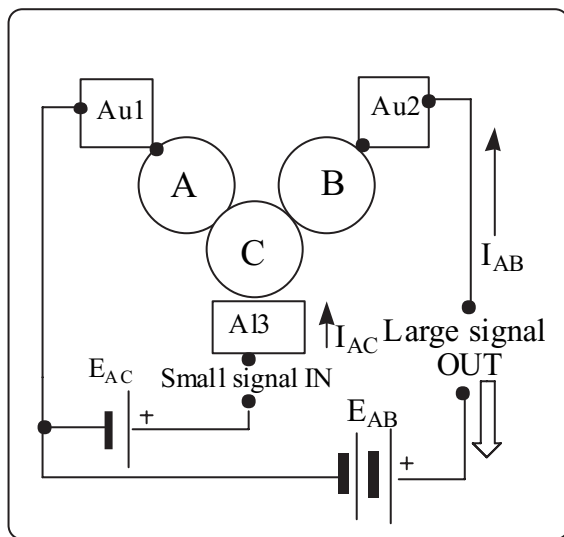


Fig. 20. Proposed unimolecular amplifier, shown very schematically as molecule ABC, contacted by two Au electrodes (Au1 and Au2) and a third, different, electrode (Al3) [82]

Au (Au 1 and Au2, to bond thiol terminations of a molecule) and one different one of Al (to bond a carboxylic acid termination) such that the gap between all of the electrodes is molecule-sized, i.e. 1 to 2 nm. This goal is an ongoing effort in many laboratories.

18 Conclusion

We have presented here a review of unimolecular rectification, which, thirty years after it was first proposed, has become an established reality. May this progress produce many new ideas for molecular devices to power the ultimate computers of the future.

19 End-Notes

The technique of cryocooling the substrate during Al or Au vapor deposition [33, 36], which may retard a chemical attack of the LB monolayer, is acknowledged in [8]. The “U” rectifier results for **6** were explained by proposing that the Fermi level does not move linearly with distance within a molecule [44]: it is reassuring to see [6] that a Poisson-Schrödinger calculation also predicted a non-linear variation of the Fermi level or the chemical

potential across a molecule [83]: see Fig. 12 of [6]. The Inelastic Electron Tunneling Spectroscopy technique [8, 21] is being implemented in our laboratory: we hope to show soon that the through-molecule current due to "U" rectification also excites intramolecular vibrations.

Acknowledgments

This work was generously supported by the United States National Science Foundation (grants NSF-DMR-FRG-00-95215, DMR-00-99674, and DMR-01-20967), and was made possible by the diligence and insight of many colleagues, students, and post-doctoral fellows.

References

1. R. M. Metzger, Prospects for Truly Unimolecular Devices. *NATO ASI Series B* **248**, 659–666 (1991).
2. R. P. Feynman, There is Plenty of Room at the Bottom. In *Miniatrization*, Gilbert, H. D., Ed. (Reinhold, New York, 1961) p. 282.
3. A. Aviram and M. A. Ratner, Molecular Rectifiers. *Chem. Phys. Lett.* **29**, 277–283 (1974).
4. G. E. Moore, Cramming More Components onto Integrated Circuits. *Electronics* **38**(8), 114–117 (10 April 1965).
5. International Technology Roadmap for Semiconductors, 2001: <http://public.itrs.net/Files/2001ITRS/Home.htm>
6. J. Jortner, A. Nitzan, and M. A. Ratner, Foundations of Molecular Electronics – Charge Transport in Molecular Conduction Junctions. *This Volume*, Chap. 1.
7. M. R. Wegewijs, M. H. Hettler, J. König, A. Thielmann, C. Romeike, and K. Nowack, Single-Electron Tunneling in Small Molecules. *This Volume*, Chap. 7.
8. W. Wang, T. Lee, and M. A. Reed, Intrinsic Electronic Conduction Mechanisms in Self-Assembled Monolayers. *This Volume*, Chap. 10.
9. J. Tomfohr, G. Ramachandran, O. F. Sankey, and S. M. Lindsay, Making Contacts in Single Molecules: Are We There Yet? *This Volume*, Chap. 11.
10. L. A. Bumm, J. J. Arnold, M. T. Cygan, T. D. Dunbar, T. P. Burgin, L. Jones II, D. L. Allara, J. M. Tour, and P. S. Weiss, Are Single Molecular Wires Conducting? *Science* **271**, 1705–1707 (1996).
11. H. Taube, Electron Transfer between Metal Complexes – A Retrospective View (Nobel Lecture). *Angew. Chem. Intl. Ed. Engl.* **23**, 329–339 (1984).
12. M. A. Reed, C. Zhou, C. J. Muller, T. P. Burgin, and J. M. Tour, Conductance of a Molecular Junction. *Science* **278**, 252–253 (1997).
13. J. Reichert, R. Ochs, D. Beckmann, H. B. Weber, M. Mayor, and H. von Löhneysen, Driving Current through Single Organic Molecules. *Phys Rev. Lett.* **88**, 176804 (2002).
14. J. Reichert, H. B. Weber, M. Mayor and H. von Löhneysen, Low-Temperature Conductance Measurements on Single Molecules. *Appl. Phys. Lett.* **82**, 4137–4139 (2003).

15. R. Landauer, Spatial Variation of Currents and Fields Due to Localized Scatterers in Metallic Conduction. *IBM J. Res. Dev.* **1**, 223–231 (1957).
16. J. Chen, M. A. Reed, A. M. Rawlett, and J. M. Tour, Large On-Off Ratios and Negative Differential Resistance in a Molecular Electronic Device. *Science* **286**, 1550–1552 (1999).
17. Z. J. Donhauser, B. A. Mantooth, K. F. Kelly, L. A. Bumm, J. D. Monnell, J. J. Stapleton, D. W. Price, Jr., A. M. Rawlett, D. L. Allara, J. M. Tour, and P. S. Weiss, Conductance Switching in Single Molecules Through Conformational Changes. *Science* **292**, 2303–2307 (2001).
18. B. C. Haynie, A. V. Walker, T. B. Tighe, D. L. Allara, and N. Winograd, Adventures in Molecular Electronics: How to Attach Wires to Molecules. *Appl. Surf. Sci.* **203–204**, 433–436 (2003).
19. A. V. Walker, T. B. Tighe, O. M. Cabarcos, M. D. Reinard, B. C. Haynie, S. Uppili, N. Winograd, and D. L. Allara, The Dynamics of Noble Metal Atom Penetration through Methoxy-Terminated Alkanethiolate Monolayers. *J. Am. Chem. Soc.* **126**, 3954–3963 (2004).
20. W. Wang, T. Lee, and M. A. Reed, Mechanism of Electron Conduction in Self-Assembled Alkanethiol Monolayer Devices. *Phys. Rev.* **B68**, #035416 (2003).
21. W. Wang, T. Lee, I. Kretschmar, and M. A. Reed, Inelastic Electron Tunneling Spectroscopy of an Alkanedithiol Self-Assembled Monolayer. *Nano Lett.* **4**, 643–646 (2004).
22. S. Frank, P. Poncharal, Z. L. Wang, and W. A. de Heer, Carbon Nanotube Quantum Resistors. *Science* **280**, 1744–1746 (1999).
23. S. J. Tans, M. H. Devoret, H. Dai, A. Thess, R. E. Smalley, L. J. Geerligs, and C. Dekker, Individual Single-Wall Carbon Nanotubes as Quantum Wires. *Nature* **386**, 474–477 (1997).
24. V. Derycke, R. Martel, J. Appenzeller, and Ph. Avouris, Carbon Nanotube Inter- and Intramolecular Logic Gates. *Nano Lett.* **1**, 453–456 (2001).
25. C. P. Collier, G. Mattersteig, E. W. Wong, K. Beverly, J. Sampaio, F. M. Raymo, J. F. Stoddart, and J. R. Heath, A [2] Catenane Based Solid-State Electronically Reconfigurable Switch. *Science* **289**, 1172–1175 (2000).
26. D. R. Stewart, D. A. A. Ohlberg, P. A. Beck, Y. Chen, R. S. Williams, J. O. Jeppesen, K. A. Nielsen, and J. F. Stoddart, Molecule-Independent Electrical Switching in Pt/Organic Monolayer/Ti devices. *Nano Lett.* **4**, 133–136 (2004).
27. J. Park, A. N. Pasupathy, J. I. Goldsmith, C. Chang, Y. Yaish, J. R. Petta, M. Rinkoski, J. P. Sethna, H. D. Abruña, P. L. McEuen, and D. C. Ralph, Coulomb Blockade and the Kondo Effect in Single-Atom Transistors. *Nature* **417**, 722–725 (2002).
28. S. Kubatkin, A. Danilov, M. Hjort, J. Cornil, J.-L. Brédas, N. Stuhr-Hansen, P. Hedegård, and T. Bjørnholm, Single-Electron Transistor of a Single Organic Molecule with Access to Several Redox States. *Nature* **425**, 698–701 (2003).
29. Y. Selzer, M. A. Cabassi, T. S. Mayer, D. L. Allara, Thermally Activated Conduction in Molecular Junctions. *J. Am. Chem. Soc.* **126**, 4052–4053 (2004).
30. Y. Selzer, L. Cai, M. A. Cabassi, Y. Yao, J. M. Tour, T. S. Mayer, and D. L. Allara, Effect of Local Environment on Molecular Conduction: Isolated Molecule versus Self-Assembled Monolayer. *Nano Lett.* **5**: 61–65 (2005).
31. G. J. Ashwell, J. R. Sambles, A. S. Martin, W. G. Parker, and M. Szablewski, Rectifying Characteristics of Mg | (C₁₆H₃₃-Q3CNQ LB Film) | Pt Structures. *J. Chem. Soc. Chem. Commun.* 1374–1376 (1990).

32. A. S. Martin, J. R. Sambles, and G. J. Ashwell, Molecular Rectifier. *Phys. Rev. Lett.* **70**, 218–221 (1993).
33. R. M. Metzger, B. Chen, U. Höpfner, M. V. Lakshmikantham, D. Vuillaume, T. Kawai, X. Wu, H. Tachibana, T. V. Hughes, H. Sakurai, J. W. Baldwin, C. Hosch, M. P. Cava, L. Brehmer, and G. J. Ashwell, Unimolecular Electrical Rectification in Hexadecylquinolinium Tricyanoquinodimethanide. *J. Am. Chem. Soc.* **119**, 10455–10466 (1997).
34. B. Chen and R. M. Metzger, Rectification between 370 K and 105 K in Hexadecylquinolinium Tricyanoquinodimethanide. *J. Phys. Chem.* **B103**, 4447–4451 (1999).
35. T. Xu, I. R. Peterson, M. V. Lakshmikantham, and R. M. Metzger, Rectification by a Monolayer of Hexadecylquinolinium Tricyanoquinodimethanide between Gold Electrodes. *Angew. Chem. Int'l. Ed.* **40**, 1749–1752 (2001).
36. R. M. Metzger, T. Xu, and I. R. Peterson, Electrical Rectification by a Monolayer of Hexadecylquinolinium Tricyano-quinodimethanide Measured between Macroscopic Gold Electrodes. *J. Phys. Chem.* **B105**, 7280–7290 (2001).
37. R. M. Metzger, Electrical Rectification by a Molecule: The Advent of Unimolecular Electronic Devices. *Acc. Chem. Res.* **32**, 950–957 (1999).
38. R. M. Metzger, Unimolecular Electrical Rectifiers. *Chem. Reviews* **103**, 3803–3834 (2003).
39. R. M. Metzger, Unimolecular Rectifiers and Prospects for Other Unimolecular Electronic Devices. *Chem. Record* **4**, 291–304 (2004).
40. J. W. Baldwin, B. Chen, S. C. Street, V. V. Konovalov, H. Sakurai, T. V. Hughes, C. S. Simpson, M. V. Lakshmikantham, M. P. Cava, L. D. Kispert, and R. M. Metzger, Spectroscopic Studies of Hexadecylquinolinium Tricyanoquinodimethanide. *J. Phys. Chem.* **B103**, 4269–4277 (1999).
41. A. Jaiswal, D. Rajagopal, M. V. Lakshmikantham, M. P. Cava, and R. M. Metzger, unpublished.
42. J. W. Baldwin, R. R. Amaresh, I. R. Peterson, W. J. Shumate, M. P. Cava, M. A. Amiri, R. Hamilton, G. J. Ashwell, and R. M. Metzger, Rectification and Nonlinear Optical Properties of a Langmuir-Blodgett Monolayer of a Pyridinium Dye. *J. Phys. Chem.* **B106**, 12158–12164 (2002).
43. R. M. Metzger, J. W. Baldwin, W. J. Shumate, I. R. Peterson, P. Mani, G. J. Mankey, T. Morris, G. Szulczewski, S. Bosi, M. Prato, A. Comito, and Y. Rubin, Large Current Asymmetries and Potential Device Properties of a Langmuir-Blodgett Monolayer of Dimethylanilinoazafullerene Sandwiched between Gold Electrodes. *J. Phys. Chem.* **B107**, 1021–1027 (2003).
44. A. Honciuc, A. Jaiswal, A. Gong, K. Ashworth, C. W. Spangler, I. R. Peterson, L. R. Dalton, and R. M. Metzger, Current Rectification in a Langmuir-Schaefer Monolayer of Fullerene-bis-[4-diphenylamino-4”-(N-ethyl-N-2”-ethyl)amino-1,4-diphenyl-1,3-butadiene] Malonate between Au Electrodes. *J. Phys. Chem.* **B109**, 857–871 (2005).
45. J. M. Tour, A. M. Rawlett, M. Kozaki, Y. Yao, R. C. Jagessar, S. M. Dirk, D. W. Price, M. A. Reed, C.-W. Zhou, J. Chen, W. Wang, and I. Campbell, Synthesis and Preliminary Testing of Molecular Wires and Devices. *Chem. Eur. J.* **7**, 5118–5134 (2001).
46. W. Schottky, Simplified and Extended Theory of Barrier-Layer Rectifiers. *Z. Phys.* **118**, 539–592 (1942).

47. Y. Liu, Y. Xu, J. Wu, and D. Zhu, Preparation of LB Films of C₆₀-doped poly(3-alkylthiophene)s and Electronic Properties of their Schottky Diodes. *Solid St. Commun.* **95**, 695–704 (1995).
48. Y. Liu, Y. Xu, and D. Zhu, Schottky Diodes Fabricated with Langmuir-Blodgett Films of C₆₀-doped Poly(3-alkylthiophene)s. *Synth. Metals* **90**, 143–146 (1997).
49. C. Krzeminski, C. Delerue, G. Allan, D. Vuillaume, and R. M. Metzger, Theory of Rectification in a Molecular Monolayer. *Phys. Rev.* **B64**, #085405 (2001).
50. V. Mujica, M. A. Ratner, and A. Nitzan, Molecular Rectification: Why Is It So Rare? *Chem. Phys.* **281**, 147–150 (2002).
51. M. L. Chabinyc, X. Chen, R. E. Holmlin, H. Jacobs, H. Skulason, C. D. Frisbie, V. Mujica, M. A. Ratner, M. A. Rampi, and G. M. Whitesides, Molecular Rectification in a Metal-Insulator-Metal Junction Based on Self-Assembled Monolayers. *J. Am. Chem. Soc.* **124**, 11730–11736 (2002).
52. S. Roth, S. Blumentritt, M. Burghard, C. M. Fischer, G. Philipp, and C. Müller-Schwannecke, Charge Transport in LB Microsandwiches. *Synth. Metals* **86**, 2415–2418 (1997).
53. I. R. Peterson, D. Vuillaume, and R. M. Metzger, Analytical Model for Molecular-Scale Charge Transport. *J. Phys. Chem.* **A105**, 4702–4707 (2001).
54. A. Stabel, P. Herwig, K. Müllen, and J. P. Rabe, Diodelike Current-Voltage Curves for a Single Molecule-Tunneling Spectroscopy with Submolecular Resolution of an Alkylated, *peri*-Condensed Hexabenzocoronene. *Angew. Chem. Int. Ed.* **34**, 1609–1611 (1995).
55. L. E. Hall, J. R. Reimers, N. S. Hush, and K. Silverbrook, Formalism, Analytical Model, and A-priori Green's Function-Based Calculations on the Current-Voltage Characteristics of Molecular Wires. *J. Chem. Phys.* **112**, 1510–1521 (2000).
56. W. B. Davis, M. R. Wasiliewski, M. A. Ratner, V. Mujica, and A. Nitzan, Electron Transfer Rates in Bridged Molecular Systems: A Phenomenological Approach to Relaxation. *J. Phys. Chem.* **A101**, 6158–6164 (1997).
57. R. M. Metzger and C. A. Panetta, The Quest for Unimolecular Rectifiers. *New J. Chem.* **15**, 209–221 (1991).
58. R. M. Metzger, D- σ -A Unimolecular Rectifiers. *Matrls. Sci. Engrg.* **C3**, 277–285 (1995).
59. K. B. Blodgett, Films Built by Depositing Successive Monomolecular Layers on a Solid Surface. *J. Am. Chem. Soc.* **57**, 1007–1022 (1935).
60. K. B. Blodgett and I. Langmuir, Built-Up Films of Barium Stearate and Their Optical Properties. *Phys. Rev.* **51**, 964–982 (1937).
61. W. C. Bigelow, D. L. Pickett, and W. A. Zisman, Oleophobic Monolayers. I. Films Adsorbed from Solution in Nonpolar Liquids. *J. Colloid Sci.* **1**, 513–538 (1946).
62. B. Mann and H. Kuhn, Tunneling through Fatty Acid Salt Monolayers. *J. Appl. Phys.* **42**, 4398–4405 (1971).
63. R. M. Handy and L. C. Scala, Electrical and Structural Properties of Langmuir Films. *J. Electrochem. Soc.* **113**, 109–116 (1966).
64. R. H. Tredgold, A. J. Vickers, and R. A. Allen, Structural Effects on the Electrical Conductivity of Langmuir-Blodgett Multilayers of Cadmium Stearate. *J. Phys.* **D17**, L5–L8 (1984).
65. G. G. Roberts, P. S. Vincett, and W. A. Barlow, AC and DC Conduction in Fatty Acid Langmuir Films. *J. Phys.* **C11**, 2077–2085 (1978).

66. N. J. Geddes, J. R. Sambles, D. J. Jarvis, W. G. Parker, and D. J. Sandman, Fabrication and Investigation of Asymmetric Current-Voltage Characteristics of a Metal/Langmuir-Blodgett Monolayer/Metal Structure. *Appl. Phys. Lett.* **56**, 1916–1918 (1990).
67. R. M. Metzger, C. A. Panetta, N. E. Heimer, A. M. Bhatti, E. Torres, G. F. Blackburn, S. K. Tripathy, and L. A. Samuelson, Toward Organic Rectifiers: Langmuir-Blodgett Films and Redox Properties of the N-4-n-Dodecyloxyphenyl and N-1-Pyrenyl Carbamates of 2-Bromo,5-(2'-hydroxyethoxy)TCNQ. *J. Mol. Electronics* **2**, 119–124 (1986).
68. N. J. Geddes, J. R. Sambles, D. J. Jarvis, W. G. Parker, and D. J. Sandman, The Electrical Properties of Metal-Sandwiched Langmuir-Blodgett Multilayers and Monolayers of a Redox-Active Organic Molecular Compound. *J. Appl. Phys.* **71**, 756–768 (1992).
69. R. M. Metzger, N. E. Heimer, and G. J. Ashwell, Crystal and Molecular Structure and Properties of Picolytricyano-quinodimethan, the Zwitterionic Donor-Pi-Acceptor Adduct between Li^+TCNQ^- and 1,2-Dimethylpyrididium Iodide. *Mol. Cryst. Liq. Cryst.* **107**, 133–149 (1984).
70. N. A. Bell, R. A. Broughton, J. S. Brooks, T. A. Jones, S. C. Thorpe, and G. J. Ashwell, Synthesis and Langmuir-Blodgett Films of a Zwitterionic D-A Adduct of Tetracyanoquinodimethane (TCNQ). *J. Chem. Soc. Chem. Commun.* 325–326 (1990).
71. R. M. Metzger, The Search for Organic Unimolecular Rectifiers. *Am. Inst. Phys. Conf. Proc.* **262**, 85–92 (1992).
72. R. M. Metzger, The Quest for D- σ -A Unimolecular Rectifiers and Related Topics in Molecular Electronics. *Am. Chem. Soc. Adv. in Chem. Ser.* **240**, 81–129 (1994).
73. G. J. Ashwell and G. A. N. Paxton, Multifunctional Properties of Z- β -(N-Hexadecylquinolinium)- α -cyano-4-styryldicyano-methanide: a Molecular Rectifier, Optically Non-Linear Dye, and Ammonia Sensor. *Austr. J. Chem.* **55**, 199–204 (2002).
74. C. Reichardt, *Solvents and Solvent Effects in Organic Chemistry*, Second Edition (VCH, Weinheim, Germany 1990).
75. R. M. Metzger, H. Tachibana, X. Wu, U. Höpfner, B. Chen, M. V. Lakshminikantham, and M. P. Cava, Is Ashwell's Zwitterion a Molecular Diode? *Synth. Metals* **85**, 1359–1360 (1997).
76. A. Jaiswal, R. R. Amaresh, M. V. Lakshminikantham, A. Honciuc, M. P. Cava, and R. M. Metzger, Electrical Rectification in a Monolayer of Zwitterions Assembled by Either Physisorption or Chemisorption. *Langmuir* **19**, 9043–9050 (2003).
77. T. Xu, T. A. Morris, G. J. Szulczewski, R. R. Amaresh, Y. Gao, S. C. Street, L. D. Kispert, R. M. Metzger, and F. Terenziani, A Spectroscopic Study of Hexadecylquinolinium Tricyanoquinodimethanide as a Monolayer and in Bulk. *J. Phys. Chem.* **B106**, 10374–10381 (2002).
78. G. J. Ashwell, Improved Second Harmonic Generation from Monolayer and Multilayer Langmuir-Blodgett Film Structures. In *Organic Materials for Non-linear Optics III*, G. J. Ashwell and D. Bloor, Eds. (Royal Soc. of Chem., Cambridge, 1993), pp. 31–39.
79. N. Okazaki and J. R. Sambles, A New Fabrication Technique and Current-Voltage Properties of a Au/LB/Au Structure. In *Extended Abstracts of the International Symposium on Organic Molecular Electronics, Nagoya, Japan*, pp. 66–67 (2000).

80. M. A. Reed, Sub-Nanoscale Electronic Systems and Devices. *United States Patent* **5,475,341** (12 Dec. 1995).
81. J. C. Ellenbogen, Monomolecular Electronic Device Including a Molecular Diode Having at Least One Barrier Insulating Group. *United States Patent* **6,339,227** (15 Jan. 2002).
82. R. M. Metzger, unpublished.
83. V. Mujica, A. E. Roitberg, and M. Ratner, Molecular Wire Conductance: Electrostatic Potential Spatial Profile. *J. Chem Phys.* **112**, 6834–6839 (2000).

Quantum Transport in Carbon Nanotubes

Elsa Thune and Christoph Strunk

Institute of Experimental and Applied Physics, University of Regensburg,
Universitätsstr. 31, 93040 Regensburg, Germany
elsa.thune@physik.uni-regensburg.de
christoph.strunk@physik.uni-regensburg.de

We present a tutorial introduction into the structure and electronic properties of carbon nanotubes which may serve as an entry point into the literature on the field. Some of the original experiments in the field are selected to illustrate the richness of quantum transport in single-and multi-wall carbon nanotubes.

1 Introduction

Prior to the discovery of fullerenes, graphite and diamond were the only known crystalline forms of carbon. The sp^2 hybridization in graphite links carbon atoms in a two-dimensional (2d) honeycomb lattice (Fig. 1a). A single sheet of graphite is called graphene. The p_z orbitals, which are perpendicular to the plane of graphene, give rise to partially filled bands with the capability of electric conduction. Diamond is sp^3 -hybridized and forms a three-dimensional (3d) network of tetrahedral units (Fig. 1b). The structural differences between graphite and diamond cause profound differences in the electrical properties: graphite is a semimetal, while diamond is an insulator with a band gap of ~ 6 eV.

In 1985 a new form of carbon, the fullerenes, was discovered by Kroto et al. [1]. The best known of these molecules is Buckminster fullerene, C_{60} , which has sixty carbon atoms forming a truncated-icosahedral structure with twelve pentagonal rings as shown in Fig. 1c. These molecules have the structure of a soccer ball (the so-called “buckyballs”). When the fullerenes were discovered, it became evident that graphene layers exist not only as planar sheets but also as spherically curved and closed shells. This becomes possible by the integration of other polygons, e.g. pentagons, into the hexagonal lattice. In 1992, Ugarte discovered that under high electron irradiation of fullerene soot, nested giant fullerenes made of concentric spherical shells of graphite, forming onion-like structures (Fig. 1d) can be generated [2]. The discovery and subsequent synthesis of fullerenes in macroscopic quantities has initiated a new field in chemistry and physics of carbon. In 1991 Iijima discovered a cylindrical form of the “buckyball”, known as a carbon nanotube (CNT) [3] (Fig. 1e).

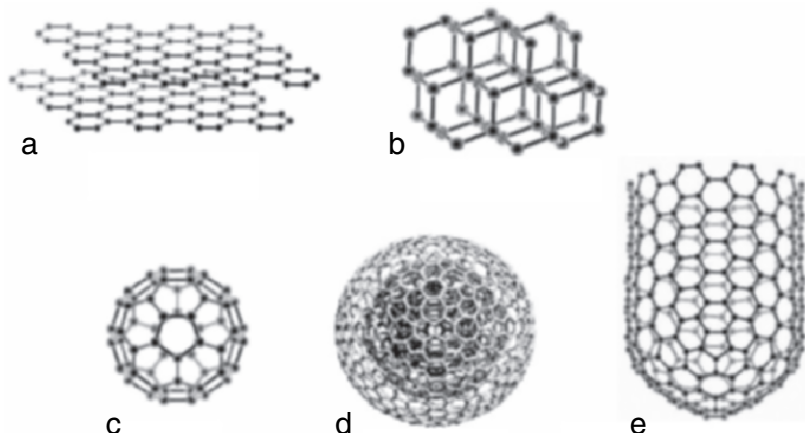


Fig. 1. Five different forms of carbon materials: (a) graphite structure of carbon; (b) diamond structure of carbon; (c) C₆₀ fullerene; (d) onion-like structure, from [4] reproduced by permission of the Royal Society of Chemistry; (e) tubular structure of carbon, which is regarded as an elongated fullerene

Nanotubes belong to the family of fullerenes and can be considered as elongated buckyballs. They fall into two broad classes: single-and multi-wall. An ideal single-wall carbon nanotube (SWNT) is a single graphene shell, that has been rolled up to form a seamless hollow cylinder (Fig. 2a and b), while a multi-wall carbon nanotube (MWNT) is a coaxial arrangement of numbers of SWNTs, i.e. several concentric graphene shells (Fig. 2c and d). Both kinds of tubes have sp²-hybridized structure, like graphite, and in the ideal case they are terminated at the ends by perfectly fitting fullerene caps.

2 Synthesis

Carbon nanotubes can be synthesized by various methods, including arc-discharge, laser ablation, chemical vapor deposition, and high pressure CO conversion [5]. In the arc-discharge method, carbon atoms are evaporated in a plasma of helium gas ignited by high currents passing through opposing carbon electrodes. The carbon atoms nucleate on a metal catalyst and grow up to several micrometers in length. A similar principle is adopted in the laser ablation method where intense laser pulses are used to ablate a carbon target containing a metal catalyst. During laser ablation, a flow of inert gas is passed through the growth chamber to carry the grown nanotube downstream to a cold collection finger. The produced SWNTs mostly bunch in the form of ropes with tens of individual nanotubes close-packed via Van der Waals interactions as shown in Fig. 2a and b. In chemical vapor deposition, a flowing hydrocarbon gas is decomposed by metal catalysts at a growth temperature

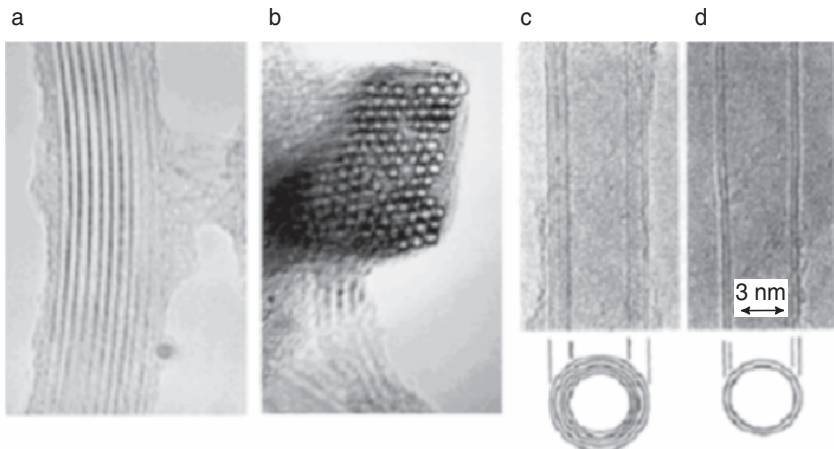


Fig. 2. High-resolution transmission electron microscope (HRTEM) micrographs of carbon nanotubes. (a) A thin bundle of single-wall carbon nanotubes. The parallel lines are the walls of individual tubes. The outermost boundary of the nanotube bundle is covered by amorphous carbon. (b) Cross sectional view of a nanotube bundle. (c) and (d) multi-wall nanotubes with five and two shells, respectively. Below the images the cross sectional structure of the two tubes is shown. From [3], by permission

between 500 and 1000 °C. The precipitation of carbon from the saturated phase in metal particles leads to the formation of a tubular carbon solid. The high pressure CO disproportionation process (HiPco) is a technique for catalytic production of SWNTs in a continuous-flow gas phase using CO as the carbon feedstock and Fe(CO)₅ as the iron-containing catalyst precursor. SWNTs are produced by flowing CO, mixed with a small amount of Fe(CO)₅ through a heated reactor. Size and diameter distribution of the nanotubes can be roughly selected by controlling the pressure of CO. This process is promising for bulk production of CNTs.

Since their discovery and high-yield synthesis, carbon nanotubes have attracted great interest among the research community due to their remarkable mechanical and electronic properties. This comes not only from the fact that CNTs have inherited some of the unique features of graphite, but also from their one-dimensional (1d) character. For instance, the Young's modulus in CNTs can be as high as ~1 TPa [6]. This makes the nanotube an excellent candidate for strengthening the matrix in composite materials. On the other hand, CNTs are examples of molecular wires which allow the study of electric transport through single molecules. They may become building blocks for nanoelectronic devices, and some day seriously compete with conventional silicon-based microelectronics [7] in some areas.

3 The Structure of Carbon Nanotubes

3.1 Lattice Structure

As described above, a carbon nanotube (CNT) can be considered as seamless cylinders made of a single graphene sheet. In general, an infinite number of nanotube geometries can exist. These differ not only in diameter, but also in the orientation of cylinder axis with respect to the underlying honeycomb lattice. Figure 3 is a schematic of a graphene sheet that can be cut along the dashed lines and rolled up along an arbitrary lattice vector \vec{C} to construct a tube. The vector \vec{C} is called the chiral vector and expressed as $n \vec{a}_1 + m \vec{a}_2$, where \vec{a}_1 and \vec{a}_2 are the basis vectors of the hexagonal lattice and n, m are integers. One specific tube is characterized by the diameter d , the chiral angle Θ between \vec{C} and \vec{a}_1 or, equivalently, by the chiral indices (n, m) which are related to d and Θ according to:

$$d = \frac{C}{\pi} = \frac{a}{\pi} (m^2 + mn + n^2)^{1/2} \quad (1)$$

$$\Theta = \arctan \left(\frac{\sqrt{3}m}{(m + 2n)} \right) \quad (2)$$

Here $a = \sqrt{3}a_{cc}$ is the lattice constant of graphene and a_{cc} the nearest neighbor carbon-carbon distance (0.142 nm in graphite). The shortest lattice vector \vec{T} , which is perpendicular to \vec{C} and parallel to the nanotube axis, defines the lattice translations along the tube axis. The lattice edges cut by the two sets of parallel dashed lines shown in Fig. 3 can be perfectly mapped onto each other when forming the tube. Arbitrary chiral angles Θ produce in general chiral tubes, which have axial chiral symmetry, as can be seen in the lowest panel in Fig. 4. There are two special chiral angles, i.e. $\Theta = 0^\circ$ and $\Theta = 30^\circ$ which correspond to highly symmetric non-chiral nanotubes. These are termed “zigzag” and “armchair”, having chiral indices $(n, 0)$ and (n, n) , respectively. The labels zigzag and armchair refer to the pattern of carbon bonds along the circumference, which are shown bold in Fig. 3.

3.2 Structural Investigations of Carbon Nanotubes

As grown, SWNTs usually have a dispersion of chirality and diameter [8, 9] because the nanotube structural energy is only weakly dependent on chirality [10]. Hence, a critical issue in CNT research and applications is the determination of the chiral indices of a given individual tube [11], which requires the measurement of both diameter and chiral angle. A complete determination of the structure with enough spatial resolution to identify an individual nanotube is in practice a difficult task. The measuring technique

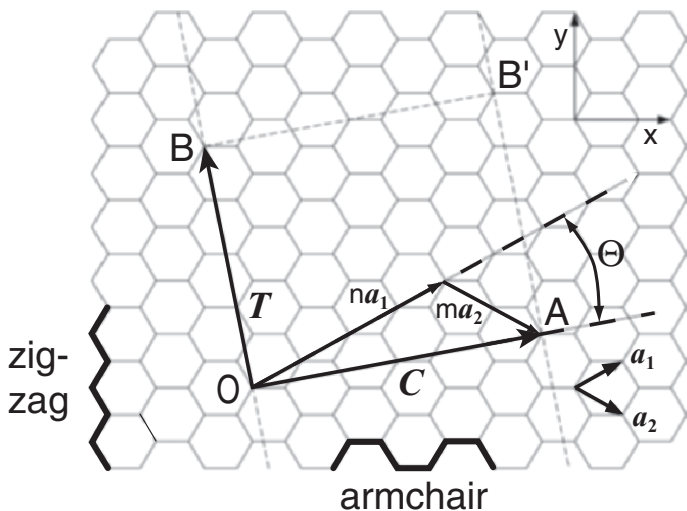


Fig. 3. Hexagonal network of a graphene sheet. The tube with index $(n, m) = (4, 2)$ is constructed when the dotted strip is rolled up in such a way that point O matches point A, and point B matches point B'. Θ denotes the chiral angle of a specific tube and varies between $0^\circ \leq \Theta \leq 30^\circ$. \vec{C} is the chiral vector and perpendicular to the translational vector \vec{T} which determines the length of the unit cell of the tube and the boundary of the first Brillouin zone: $-\pi/T \leq k \leq \pi/T$

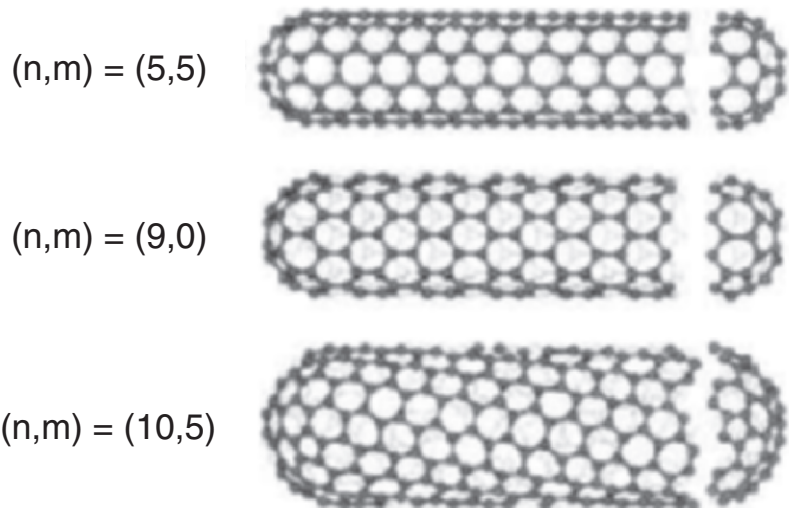


Fig. 4. Three examples of nanotubes. From top to bottom: armchair (5,5), zigzag (9,0) and chiral (10,5). From [12], by permission

has to provide a high enough signal to noise ratio to compare the experimental data with corresponding theoretical simulations. With this in mind, two types of techniques can be used. A first type of measurements relies on the direct determination of d and Θ either in real space by Scanning Tunneling Microscopy (STM) or in reciprocal space by Selected Area Electron Diffraction (SAED). A second type of methods exploits the physical properties connected to the structure and is based on spectroscopic measurements, either by Scanning Tunnelling Spectroscopy (STS) or by Raman spectroscopy. Since Iijima's initial study, many articles have been published on structural characterization using electron diffraction [3,13–18], STM [19,20] and Raman spectroscopy [11,21,22]. STM images the lattice structure of a part of the outer wall of carbon nanotube to measure the chiral angle. However, a unique identification of one specific tube using STM remains difficult. Electron diffraction in principle can determine more unambiguously both the chirality and diameter of tubes.

The chiral indices (n, m) of an individual nanotube can be identified using electron diffraction as follows: in the reciprocal space of the nanotubes [18,23,24] the intensity in a given diffraction direction is determined by the Bragg reflections of the cylindrical graphene sheet. The diffraction pattern depends on the chirality and the tilt angle of the tube with respect to the incident electron beam. The intensities are localized along horizontal lines perpendicular to the nanotube axis. Along each line, the intensity is modulated. The diffraction pattern has an underlying hexagonal symmetry coming from the graphene lattice. However, each reflection has several satellites along the horizontal lines. These are caused by the finite diameter of the nanotube, in close analogy with the Fraunhofer diffraction pattern of a single slit in wave optics. This can be seen in the computer-generated diffraction patterns of two non-chiral nanotubes shown in Fig. 5a and 5c. The inner diffraction spots are located at the corners of a hexagon and represent the first order graphite-like diffraction spots, e.g., $(10\bar{1}0)$. There is another larger hexagon, formed by the second order diffraction spots, e.g., $(11\bar{2}0)$. All reflections are elongated in the direction normal to the tube axis. This results from the continuous shortening of the apparent lattice parameter seen by the electrons in the direction normal to the axis when moving from the center to the edges of the tube. The spots are the intersections of the Ewald sphere with the rods that form the reciprocal lattice of the nanotube [23].

In chiral tubes a splitting of the diffraction reflections is observed (see Fig. 5b). The first order diffraction spots form now two hexagons, which are rotated against each other. This originates from the two halves of the nanotube located on both sides of the plane through the central axis of tube, which is perpendicular to the electron beam. The projections of the lattice structure of the two nanotube halves in this plane are rotated with respect to each other by twice the chiral angle. The resulting diffraction patterns are rotated by the same angle, allowing a direct determination of the chiral

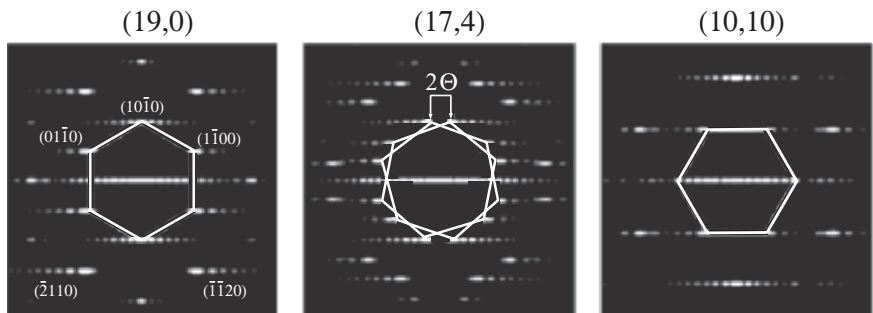


Fig. 5. Computer-generated electron diffraction patterns of three single-wall nanotubes, from left to right: (19,0), (17,4), and (10,10). Some of the spots in left panel are labelled. The chiral (17,4) tube shows a splitting of the diffraction spots, which allows the determination of the chiral angle. The chiral angles Θ are 0° , 10.3° , and 30° , respectively. In each case, the nanotube is oriented along the vertical direction, and the electron beam is normal to the tube axis, perpendicular to the plane of the graph. From [27], by permission

angle of the nanotube. The helicity of the lattice structure of a nanotube can therefore be directly extracted from the diffraction pattern [3, 18]. When the electron beam is not perpendicular to the tube axis, a correction must be applied to determine Θ from the observed angular splitting of the $(10\bar{1}0)$ reflections [25].

Most of the experimental studies of nanotubes by electron diffraction have been realized on multi-wall systems (MWNT and SWNT bundles). On rare occasions, individual SWNTs have been investigated by this technique [13, 26], since individual SWNTs produce very low intensities.

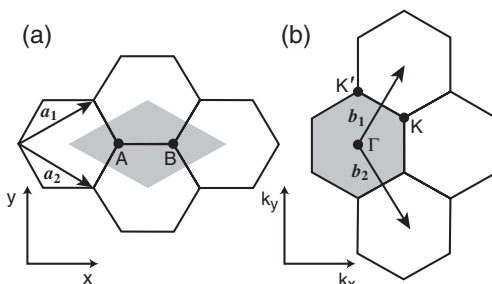


Fig. 6. (a) Fractions of the graphene lattice in real space and (b) the corresponding reciprocal lattice. A unit cell in the graphene lattice and the first Brillouin zone are indicated by the shaded rhombus and hexagon, respectively. a_i , and b_i , ($i = 1, 2$) are the basis vectors of the direct and the reciprocal lattice

4 Electronic Structure of Nanotubes

4.1 Energy Dispersion and Density of States of Graphene

To understand the electronic properties of nanotubes, we begin with the band structure of graphene, which underlies also the band structure of the nanotubes [28]. It is convenient to start by calculating the band structure of a graphite sheet within the tight-binding approximation [29, 30] and then to superimpose the periodic boundary conditions along the circumferential direction, which result from the cylindric character of the nanotubes. Figure 6a shows the hexagonal lattice of a graphene sheet in real space, with the basis vectors $\vec{a}_1 = (\sqrt{3}a/2, a/2)$ and $\vec{a}_2 = (\sqrt{3}a/2, -a/2)$ where $a = \sqrt{3}a_{cc}$ is the graphene lattice constant. Figure 6b shows the reciprocal lattice and its basis vectors $\vec{b}_1 = (2\pi/\sqrt{3}a, 2\pi/a)$ and $\vec{b}_2 = (2\pi/\sqrt{3}a, -2\pi/a)$. The first Brillouin zone is indicated by a grey hexagon. Carbon has four valence electrons per atom, three of which are used to form sp^2 bonds with neighboring atoms in σ orbitals. The corresponding energy bands lie far below the Fermi level and do not contribute to the electrical conduction. The transport properties are determined by the remaining π electrons, which occupy the bonding and antibonding band resulting from the superposition of the $2p_z$ orbitals. The resulting energy dispersion for the bands reads in a tight binding approximation [30]:

$$E(k_x, k_y) = \pm \gamma_0 \left[1 + 4 \cos\left(\frac{\sqrt{3}k_x a}{2}\right) \cos\left(\frac{k_y a}{2}\right) + 4 \cos^2\left(\frac{k_y a}{2}\right) \right]^{1/2} \quad (3)$$

where $\gamma_0 = 2.5$ eV is the overlap integral between nearest neighbors [10]. This equation describes the two bands resulting from bonding and antibonding states. Figure 7 shows a surface plot of the energy dispersion according to (3). The bonding and antibonding bands touch at six K points at the corners of the first Brillouin zone, as shown in Fig. 7. We note that there are two triplets of Fermi points, K and K' which are inequivalent under translations of the reciprocal lattice. On the other hand, the hexagonal lattice symmetry provides an equivalence under 60° -rotations. Because of this symmetry, the K and K' points are energetically degenerate and lead to the peculiar touching of the conduction and the valence band. At zero temperature, the bonding bands are completely filled and the antibonding bands are empty. Thus, undoped graphite may be classified as a zero-gap semiconductor. The undoped state, where the Fermi surface contains only the six K-points is called the charge neutrality point (CNP). In practice, there will always be a little doping, which slightly shifts the Fermi energy away from the CNP and leads to a small density of states $N(E_F)$, which is responsible for the relatively poor conductivity of graphite.

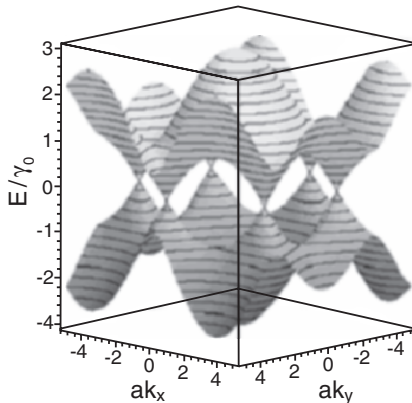


Fig. 7. Band structure of graphene. The bonding (π) and antibonding (π^*) bands touch at the K and K' points. Because there are two electrons in the unit cell, the π band is completely filled and the π^* band is empty

4.2 Band Structure and Density of States of Carbon Nanotubes

We can now obtain the band structure of nanotubes by imposing the periodic boundary condition along the circumferential direction defined by the chiral vector \vec{C} . The transversal component of the wave vector is thus quantized: $k_{\perp} = \vec{k} \cdot \vec{C} = 2\pi q$, ($q = 0, 1, 2 \dots 2n$). This gives rise to a discrete number of parallel equidistant lines, representing the allowed k_{\perp} modes in the reciprocal space of the graphene. Each line corresponds to a 1d subband for conduction along the nanotube. The distance between adjacent lines, $\Delta k = 2/d$, is inversely proportional to the nanotube diameter d , and the orientation of the lines with respect to the reciprocal lattice are given by the chiral angle Θ . The length of these lines is $2\pi/T$, as determined from the length T of the translation vector \vec{T} . For armchair tubes we have $T = a$, while for zigzag tubes holds $T = \sqrt{3}a$, where $a = \sqrt{3}a_{cc}$ is again the graphene lattice constant. Figure 8 shows a contour plot of the bonding band in the first Brillouin zone. The quantization condition for armchair nanotubes is $\sqrt{3}nak_x = 2\pi q$, whereas $nak_y = 2\pi q$ applies for zigzag nanotubes. In both cases q runs from 0 to $2n$. The parallel lines shown in Fig. 8 are examples of allowed k modes in armchair nanotubes. The $q = n$ modes in this case touch the K and K' points, implying that armchair tubes are always metallic. The dispersion relations for armchair and zigzag nanotubes can be obtained by inserting these quantization conditions into (3):

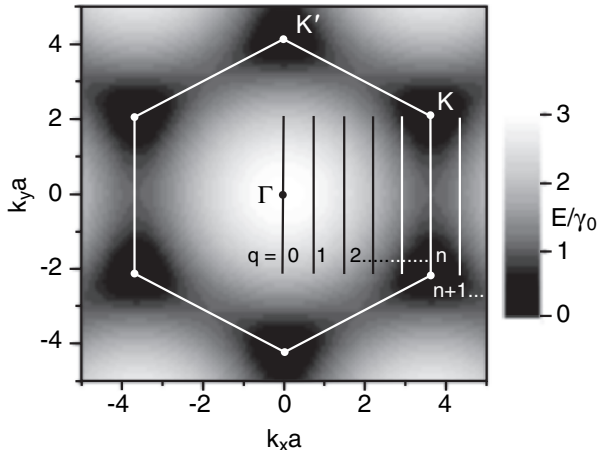


Fig. 8. Grey scale plot of the antibonding π^* band of graphene. The corners of the hexagonal Brillouin zone define the six K and K' points. In the absence of doping, the Fermi level is located at the corner points of the hexagonal Brillouin zone. The periodic boundary conditions along the circumference of the tube confine the allowed k values indicated to the parallel lines from $q = 0$ to $q = 2n$. The length of the lines is $2\pi/a$ (here we consider an armchair tube). In general, the chiral angle determines the orientation of the allowed k lines with respect to the reciprocal lattice

$$E_{\text{armchair}}(k_y) = \pm \gamma_0 \left[1 \pm 4 \cos\left(\frac{\pi q}{n}\right) \cos\left(\frac{k_y a}{2}\right) + 4 \cos^2\left(\frac{k_y a}{2}\right) \right]^{1/2} \quad (4)$$

$$E_{\text{zigzag}}(k_x) = \pm \gamma_0 \left[1 \pm 4 \cos\left(\frac{\sqrt{3} k_x a}{2}\right) \cos\left(\frac{\pi q}{n}\right) + 4 \cos^2\left(\frac{\pi q}{n}\right) \right]^{1/2} \quad (5)$$

Figure 9 shows two normalized band structures plotted as E/γ_0 vs. k and the density of states (DOS) corresponding to armchair and zigzag nanotubes, respectively. For undoped armchair nanotubes, there are two subbands which cross the Fermi energy at $E_F = 0$ since the 2d graphite energy bands cross at the K point of the 2d Brillouin zone. As a rule, those tubes are metallic, which satisfy the condition that $2n + m$ is a multiple of 3. As a result 1/3 of all possible structures correspond to metallic and 2/3 to semiconducting tubes. In very thin tubes, this rule can be violated because the curvature of the graphene layer can induce a small gap between valence and conduction band [31].

As opposed to graphene, where the six K -points have zero weight in the 2d Brillouin zone, there is a large 1d density of states at the K point in the armchair NTs. Away from the charge neutrality point (CNP), the onset of the next subbands leads to van Hove singularities (VHS) in the DOS. In one dimension the DOS diverges as $1/\sqrt{E}$. The van Hove singularities appear at

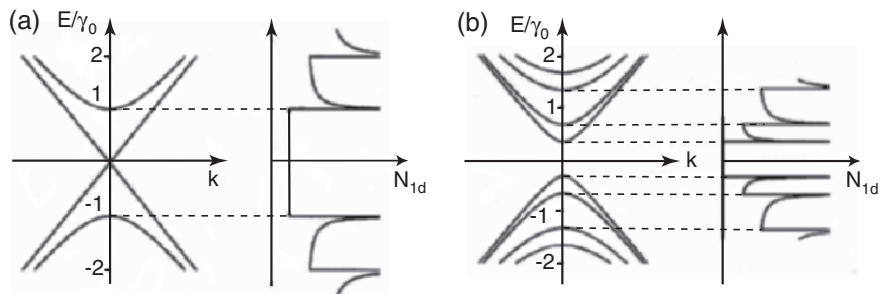


Fig. 9. Approximate one-dimensional energy dispersion relations and corresponding density of states for (a) metallic carbon nanotubes and (b) semiconducting carbon nanotubes. The number of 1d-subbands depends on the vector \vec{C} . The energy at the Fermi level is set to zero

points k_i in the 2d Brillouin zone where the allowed k lines are tangential to the contours of constant energy. In semiconducting nanotubes, there are no allowed k lines passing through the K or K' points. The allowed k lines closest to K contributes to the first band edge, which form again van Hove singularities in the density of states. In this case, there is an energy gap E_g which is inversely proportional to the nanotube diameter, i.e. $E_g = 2a_{cc}\gamma_0/d$. The right-hand panel in Fig. 9a and b shows the density of states derived from the corresponding band structure in the left panel. Both the spatial resolved atomic structure of carbon nanotubes and the corresponding electronic density of states have been demonstrated experimentally by investigations with a scanning tunneling microscope [19, 20, 32]. An example is shown in Fig. 10, where tunneling spectra of several SWNTs with diameters around 1 nm are displayed. The tubes with a small band gap around 0.6 eV are identified as semi-conducting, while the metallic tubes display a significantly larger spacing between the VHS around 2 eV. In the latter case, the DOS between the VHS is finite.

5 Electron Transport Experiments

By measurements of the electronic transport properties, many features of the electronic structure of the CNTs can be revealed. There are several classes of experiments that can be performed, which differ by the purity of the samples and the transparency of the interface between the tube and the metallic contact electrodes.

5.1 Electric Contacts

Individual carbon nanotubes can be contacted using nanostructured metal electrodes. The purified tube material is first brought into suspension and

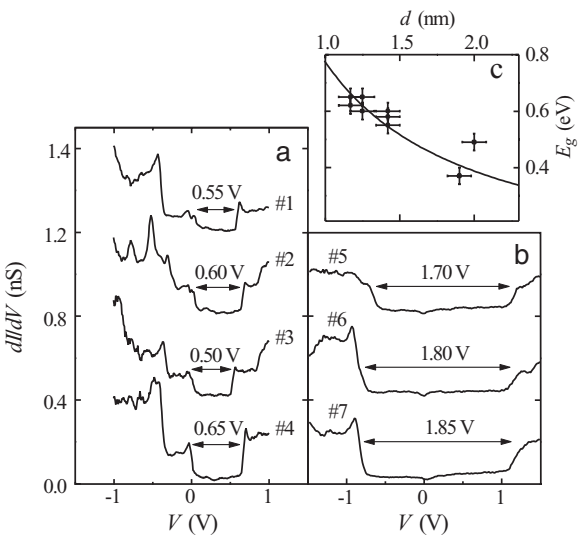


Fig. 10. Tunneling density of states of individual single-wall nanotubes on an Au surface measured by scanning tunneling spectroscopy (adapted from [20], by permission). A tunneling contact is formed between the STM-tip and the nanotube. The measured differential conductance dI/dV is proportional to the density of states. For clarity, curves are offset vertically by multiples of 0.4 nS. The gaps between the van Hove singularities corresponding to the onset of 1d-subbands are indicated by the arrows. (a) Semiconducting tubes with gap values around 0.6 eV. (b) Metallic tubes with gap values around 1.8 eV. (c) Variation of the measured energy gap of different tubes with diameter. The *solid line* is a fit according to $E_g = 2a_{cc}\gamma_0/d$ with $\gamma_0 = 2.7$ eV

then sprayed over a suitable substrate, e.g. oxidized silicon. If the silicon wafer is highly doped, it can serve as a backgate to tune the number of electrons on the tubes. Using alignment marks on the substrate, isolated nanotubes are identified and by electron beam lithography a resist mask with the contact pattern is written. After development of the resist, metallization and lift-off, the samples are ready for measurement. Deposition of the metal on top of the tubes usually results in a lower contact resistance and allows a higher yield than the reverse sequence. An example is shown in Fig. 11. Contact resistances down to $1\text{ k}\Omega$ have been realized in single- and multi-wall carbon nanotubes.

Alternatively, a scanning tunneling microscope or an atomic force microscope with metallized tip can be used to probe the electrochemical potential drop even as a function of position [33,34]. In the tunneling regime tunneling spectroscopy allows to measure also the local density of states [20,35,36].

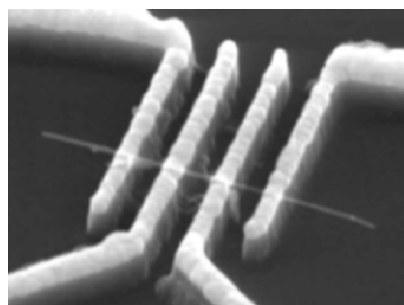


Fig. 11. Scanning electron micrograph of an individual multi-wall nanotube with four Au contacts. The contact separation is 300 nm. The SiO substrate has been etched away to create a freely suspended nanotube (Courtesy C. Schönenberger)

5.2 Ballistic Transport

Depending on the fabrication process, the structural quality of carbon nanotubes can be very high. Hence, they are promising candidates for ballistic one-dimensional conductors. For ideal, i.e., highly transparent contacts and perfect tubes, the one-dimensional subbands as described in Sect. 4.2 form one-dimensional conduction channels in the sense of the Landauer-Büttiker theory of quantum transport [37]. Each of these channels contributes $2e^2/h$ to the conductance, if the different spin orientations are degenerate. Because of the double degeneracy of the states at the corner points of the Brillouin zone, two spin degenerate channels contribute to the transport, resulting in a conductance of $G = 4e^2/h = (6.4k\Omega)^{-1}$. In practice, the non-ideal transparency of the contacts limits the conductance to about $G \approx 3e^2/h$.

The possibility of ballistic transport in metallic single-wall nanotubes has been beautifully demonstrated in an electron interference experiment by Liang et al. [38]. At the charge neutrality point (CNP), the electron states have the wave vector $k_0 = \pi/a$, where $a = 0.246$ nm is the graphene lattice constant. The Fermi wave length λ_F can be tuned with the gate voltage U_G applied between the Si substrate and the sample. In this way the Fermi level of the tube is shifted away from the charge neutrality point by ΔE_F ; resulting in a corresponding shift of the Fermi wave vector: $k_F = k_0 + \Delta E_F/\hbar v_F$. The injected electrons travel ballistically within the tube, but are reflected back and forth between the contacts. Depending on the ratio between Fermi wave length $\lambda_F = 2\pi/k_F(U_G)$ and the distance between the contacts, this is expected to lead to the formation of transmission resonances just as in an optical Fabry-Perot interferometer.

As a result of the alternation of constructive and destructive interference between directly transmitted and multiply reflected waves it is expected that the conductance as a function of gate voltage shows periodic oscillations with U_G . The measurement in Fig. 12 indeed shows such a periodic variation of

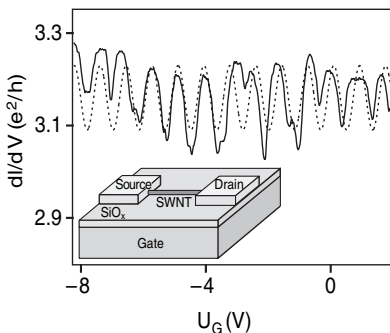


Fig. 12. Oscillatory zero-bias differential conductance (dI/dV) of a 200-nm long SWNT device plotted against gate voltage (U_G) (solid line). For comparison, a single sine function with the same periodicity is added (dashed line). From [38], by permission

the conductance as a function of gate voltage. Some smaller features are superimposed on the basic oscillation, which are most probably caused by some residual weak potential fluctuations along the tube.

A few experiments on multi-wall nanotubes succeeded in observing a conductance quantized in units of $2e^2/h$ [39, 40], similar to those of quantum point contacts in ballistic semiconductor heterostructures [41, 42]. The quantization is caused by the successive opening of one conductance channel after the other. In these measurements an STM tip is used to establish the electric contact at room temperature. At present it is not clear, why the transport in this configuration seems to be perfectly ballistic as opposed to experiments described in the next section in which the tubes are contacted by the lithographic methods.

5.3 Diffusive Transport

Besides the Fermi momentum $p_F = \hbar k_F$, the magnetic field offers another convenient possibility to control the phase of the electron wave function. The majority of experiments on carbon nanotubes uses lithographically prepared contacts in order to perform conductance measurements down to very low temperatures. If the average distance between two elastic scattering events l_{el} is significantly smaller than the distance between the contacts, the motion of electrons becomes diffusive and in the simplest description the conductivity of the sample is given by the Einstein relation $\sigma = e^2 D(T, B) N(E_F, B)$, where D is the diffusion constant and N the density of states. While the classical motion of the electrons results in a value $D = 1/2 v_F l_{el}$, it turns out, that there are important quantum corrections to this result, which depend on temperature and magnetic field [43]. In addition the density of states at the Fermi energy depends on magnetic field [44, 45]. Under these conditions

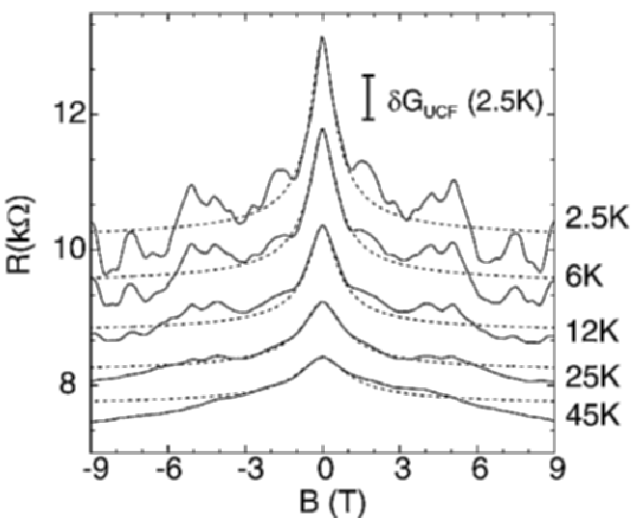


Fig. 13. Transversal magnetoresistance $R(B)$ of a multi-wall nanotube (*solid lines*) for several temperatures. The contact separation is $1.9 \mu\text{m}$. The central peak is well reproduced by the theory of weak localization (*dashed lines*). At low temperatures an aperiodic fluctuating background appears. The amplitude of these fluctuations agrees well with the expected magnitude of the universal conductance fluctuations (*vertical bar*) from [46], by permission

no quantized conductance is observed. The conductance gradually drops as the temperature is decreased. This drop in conductance or increase in resistance turns out to depend strongly on magnetic field. If the orientation of the magnetic field B is perpendicular to the tube, a single peak centered around $B = 0$ is observed, which becomes higher and sharper as the temperature is decreased. This is illustrated in Fig. 13, where $R(B)$ traces are plotted for several temperatures [46]. Besides the central peak, an aperiodic fluctuation pattern is seen. These fluctuations are reproducible as long as the sample is kept cold, but vary upon thermal cycling up to room temperature as well as from sample to sample. Both phenomena the central peak and the aperiodic background are closely related to the famous Aharonov-Bohm effect [43] and represent a hallmark of diffusive quantum transport [47–50]. Aharonov and Bohm predicted that the interference of an electron travelling on two different paths, which connect two points in space, leads to an oscillatory h/e -periodic dependence of the propagation probability on the magnetic flux enclosed by the two paths. In a diffusive medium, electrons transferred between two contact electrodes have a very large number of quasi-classical trajectories to choose. All of these interfere with different Aharonov-Bohm phases, leading to a superposition of many Aharonov-Bohm periods in the transmission probability and thus also in the magnetoresistance. There is

an upper limit for the length of interfering paths, which is determined by the phase coherence length $L_\varphi = \sqrt{D\tau_\varphi}$, where τ_φ denotes the average time between scattering events which randomize the phase of the electron wave function. A small value of L_φ suppresses the interference effects. Earlier experiments on thin disordered metal films have shown that several types of interference effects emerge from this superposition [43].

One of them is known as weak localization [51] and its signature is precisely the peak in $R(B)$ centered around $B = 0$, as it can be seen in Fig. 13. It is caused by an enhanced backscattering probability of pairs of time reversed diffusion paths. In absence of a magnetic field, the wave function of an electron travelling on a closed quasi-classical path experiences a certain phase shift depending on the Fermi wave vector, the path length and the elastic scattering events on the way. However, the time reversed state travelling in opposite direction along the same path exhibits precisely the same phase shift, provided that no interactions occur that break the time reversal symmetry. Thus, the two paths interfere always constructively, resulting in a quantum mechanical enhancement of the classical return probability by a factor of 2. This corresponds to an increase of the resistance. In a finite magnetic field the time reversal symmetry is broken and the Aharonov-Bohm oscillations of closed loops with different area A have different periodicity $2e/hA$ and average out above a certain magnetic field. The value of this field is determined by the condition $B \times A_{\max} \approx h/2e$, where A_{\max} is the area enclosed by the longest phase coherent diffusion path. The width of the weak localization peak is thus given by $2e/hL_\varphi^2$ in a two-dimensional sample of width $w \gg L_\varphi$ and $2e/hwL_\varphi$ in a quasi one-dimensional sample of width $w \ll L_\varphi$. Depending on temperature and the degree of disorder, carbon nanotubes can be in both limits. Using the established theory of weak localization [52], the values of L_φ can be extracted from fits to the magnetoresistance (dashed lines in Fig. 13).

The contribution of the coherent backscattering has an universal amplitude of $\Delta G = e^2/h$. In the classic experiments on disordered metal films and wires with a typical resistance of the order of a few 10Ω it used to be a rather small effect since $\Delta R/R = -\Delta G \cdot R \approx 10^{-4}$. In carbon nanotubes, however, the number of conduction channels is so small, that the quantum interference contribution to the conductance can be 20% or even larger.

The second feature seen in Fig. 13, i.e. the aperiodic fluctuations, is another quantum interference effect known as universal conductance fluctuations (UCF) [43]. These result from the superposition of all transmission channels through the sample. The random phases of the different diffusion paths lead to an interference contribution, which varies randomly as a function of magnetic field or Fermi wave vector. These random fluctuations do not average out to zero, but produce another universal contribution to the conductance of magnitude $\approx e^2/h$ to the conductance, provided that the phase coherence length exceeds the sample size. If L_φ is shorter than the sample

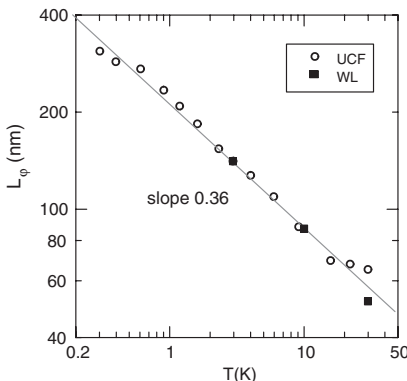


Fig. 14. Phase coherence lenght L_φ extracted from the weak localization fits (■) and the amplitude of the UCF (○). The solid line corresponds to a power law fit with an exponent of 0.36. From [53], by permission

length, the fluctuations in the different segments of length L_φ sum up independently and the relative amplitude $\delta G/G$ of the UCF is suppressed by stochastic ensemble averaging proportional to $(L_\varphi/L)^{1/2}$. Hence, L_φ can also be determined from the amplitude of the universal conductance fluctuations. The resulting temperature dependence of the phase coherence length is plotted in Fig. 14 [53]. The data extracted from the width of the weak localization peak and the amplitude of the conductance fluctuations agree well. At low bias voltage, the mean free path for electron-phonon scattering exceeds 1 μm even at room temperature [54]. Hence, the electron-phonon interaction is negligible in carbon nanotubes at low temperatures. The measurement indeed shows that L_φ increases proportional to $T^{-1/3}$ over the observed range of temperatures. This is in good agreement with the theoretical prediction by the theory of the disorder-enhanced electron-electron scattering [55].

The final proof that the scenario of diffusive quantum transport is correct is provided by measurements in a magnetic field parallel to the tube axis. As opposed to the case of transversal field, not a single peak, but a *periodic* variation in $R(B)$ is expected. The cross section πR^2 of the tube defines a well defined magnetic field period $\Delta B = h/2e\pi R^2$ for all diffusion path on the tube provided that the electric current is carried predominantly by the outermost conducting shells. The weak localization-like contribution from closed time-reversed paths has a fundamental period of $h/2e$, because the tube is encircled twice [56], i.e., once by the two time-reversed paths. If L_φ is long enough to allow the contribution of multiple turns around the tube, also higher harmonics occur and the peaks in $R(B)$ become sharper. This effect has been predicted by Altshuler, Aronov and Spivak (AAS) [56] and experimentally observed by Sharvin and Sharvin [57]. In principle also h/e -periodic contributions are expected. However, these rapidly vanish upon ensemble averaging.

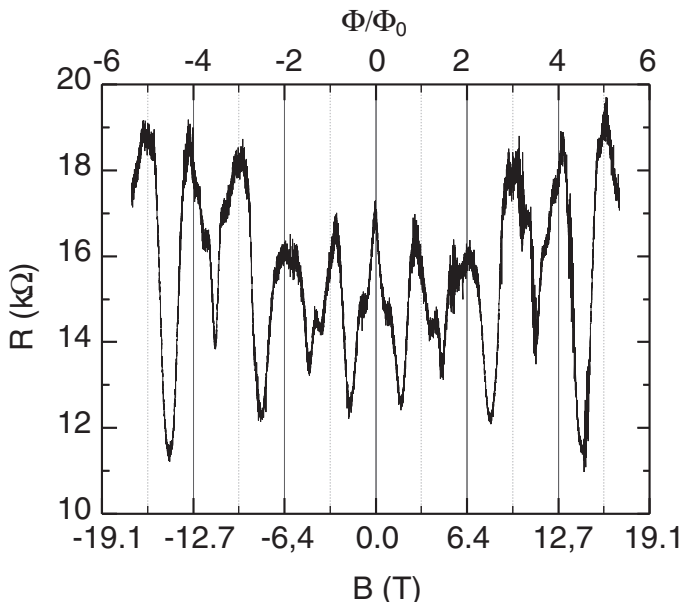


Fig. 15. Magnetoresistance of a 28 nm thick tube as a function of parallel magnetic field. The contact spacing was 350 nm. From [59], by permission

The magnetic fields corresponding to $h/2e$ depend strongly on the diameter of the tubes. For multi-wall tubes with an outer diameter of 16 nm a $h/2e$ period around 9 Tesla is expected. In single-wall tubes the required magnetic fields drastically exceed the laboratory scale. Because of these large field scales only 1 or 1.5 periods could be observed in the earlier experiments [46, 58]. Figure 15 shows a more recent measurement of the parallel magnetoresistance of multi-wall tube with an outer diameter around 28 nm [59]. Resistance oscillations with a period of 3.2 Tesla are observed. This agrees well with the expected $h/2e$ -period of 3.4 Tesla. The height of adjacent peaks alternates, which indicates the presence of a h/e component superimposed on top of the $h/2e$ -periodic AAS-like contribution. Again, an aperiodic background resulting from UCF is observed. Current experiments address the dependence of the Aharonov-Bohm phenomena on the position of the Fermi level [60].

5.4 Effects of the Electron-Electron Interaction

In macroscopic conductors the effects of the electron-electron interaction (EEI) are usually very weak, because the long range part of the Coulomb interaction is effectively suppressed and only an exponentially screened interaction potential remains. This allows a decomposition of the interacting electron system into weakly interacting fermionic quasi-particles. In one- and two-dimensional conductors, or in reduced dimensions, the screening is much

less effective, resulting in an anomaly in the density of the quasi-particle states near the Fermi energy, while the quasi-particles still form a Fermi liquid. In strictly one-dimensional ballistic systems such as the single-wall carbon nanotubes the Fermi liquid theory breaks down completely and the lowest energy excitations are plasma oscillations with a bosonic character. This is the famous Tomomaga-Luttinger liquid. In the case of weak coupling between the tube and fermionic contact electrodes the transport through the nanotubes is hindered by the Coulomb energy required to put an excess electron to the tube. In this regime, the nanotube can be considered as a one-dimensional quantum dot, assuming simple electron tunneling and a capacitive coupling to the leads. Below, we will briefly describe these regimes, while the interesting case of a quantum dot coupled to Luttinger liquid leads is considered in the article by Thorwart et al. in this volume [61].

Coulomb Blockade

Coulomb blockade [62] occurs, when a small metallic island is coupled to metallic leads via tunnel junctions (see the schematic in Fig. 16a). We know from electrostatics that a certain charging energy $E_C = e^2/2C$ has to be paid to increase the number of electrons on the island by one. Here, C is the sum of the contact and gate capacitances. For simplicity we assume that the tunneling resistance is much larger than h/e^2 and that E_C is independent of the occupation of the single particle states (Constant Interaction model). If the tunnel junctions are small enough, E_C exceeds the thermal energy $k_B T$ at sufficiently low temperatures and the charging energy has to be supplied by the external voltage sources, i.e. by the bias voltage V_{sd} or the gate potential U_G . At small V_{sd} the transport through the quantum dot is blocked, unless the gate potential is tuned to a value, where the N and $N + 1$ electron states are degenerate E_C (see Fig. 16b).

As drawn in Fig. 16c this leads to diamond-shaped regions in the U_G - V_{sd} -plane, in which the current is blocked. If the island is large, the distance between the transmission resonances on the U -axis is given by E_C alone (see Fig. 16). On the other hand, if the island is very small there is also a finite level spacing δE , which adds on top of E_C and is usually determined by the size of the island, i.e., the length of the nanotube. In this case the distance between the transmission resonances, the *addition energy* E_{add} required to add one electron to the dot is given by $E_{add} = E_C + \delta E$.

Because of the small diameter of the nanotubes, the capacitances are very small and the Coulomb blockade occurs below some 10 Kelvin for single-wall tubes [63, 64] and below 1 K for multi-wall tubes [65]. For illustration, we show in Fig. 17 a recent example of a semiconducting tube of very high purity [66]. The tube can be symmetrically charged with electrons and holes. The diamonds shrink with increasing number of charges, because the capacitance of the leads increases with the charge. This is specific for semiconducting tubes. These are coupled to the leads via Schottky barriers, whose width

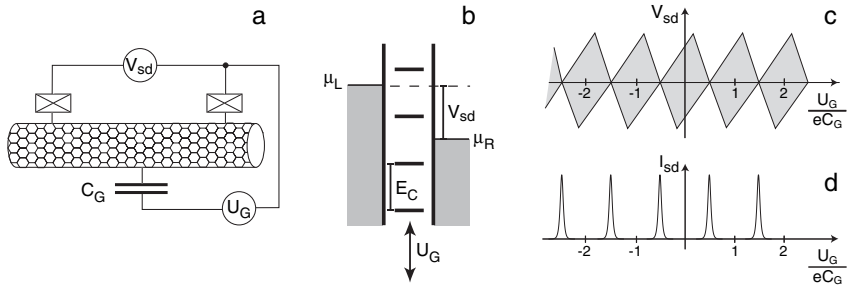


Fig. 16. (a) A nanotube connected to a voltage source via two tunnel junctions. The electric potential on the tube is controlled by the gate voltage U_G . (b) The difference in chemical potential between the two contact electrodes is tuned by the bias voltage V_{sd} . The energy level of electrons on the tube are equally spaced by the Coulomb energy E_C . Electric current can flow, only if one of the levels falls within the window V_{sd} between the electrochemical potentials μ_L and μ_R of the electrodes. (c) Typical diamond pattern of the Coulomb blockaded regions in the V_{sd} - U_G plane. The diamonds are asymmetric if the two junctions are not identical. (d) Coulomb resonances between the blockaded regions at $V_{sd} = 0$. The width of the peaks is proportional to T

depends on the gate potential [67]. The additional lines of high transmission above and below the Coulomb diamonds correspond to excited states of the electrons in the tube. The excitation spectrum is perfectly symmetric upon addition of electrons or holes. In many cases, residual disorder splits the nanotube in several quantum dots. This is reflected in irregularities in the Coulomb diamonds [68].

Similar experiment have been performed on multi-wall tubes. In [65] it has been shown that the addition energy has a four electron periodicity with three small steps of size E_C and one large step of $E_C + \delta E$. This is a direct

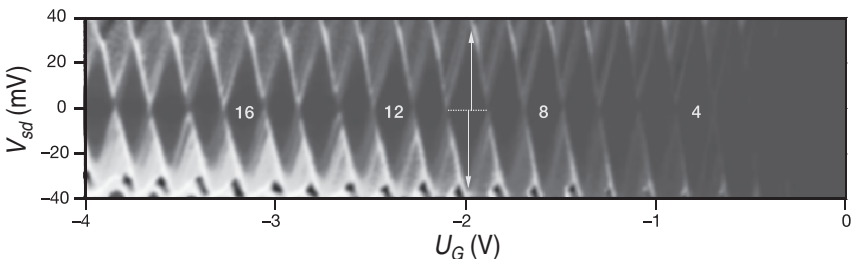


Fig. 17. Two dimensional plot of the differential conductance dI/dV_{sd} versus V_{sd} and U_G at $T = 4\text{ K}$ (black and white correspond to $G = 0$ and $G = 3\mu\text{S}$, respectively). In the black diamond-shaped regions, the current is blocked and the number of holes (indicated by the numbers) is fixed by Coulomb blockade. From [66], by permission

proof for the channel degeneracy at the charge neutrality point (also called K-K' degeneracy), which is linked to the hexagonal lattice symmetry (see Sect. 4.2).

Kondo Effect

With increasing transparency of the contacts the wave function of the electrons trapped by Coulomb blockade on the nanotubes extends into the leads. This leads to a very peculiar even-odd effect in the Coulomb oscillations [69]: the Coulomb valleys with an unpaired electron, i.e. an odd number of electrons, show an *increase* of the conductance with decreasing temperature as shown in Fig. 18a. This is opposite to the conventional Coulomb blockade found in the valleys with an even number of electrons, where the conductance is exponentially suppressed: $G \propto \exp(-E_C/k_B T)$. The conductance enhancement appears as a narrow horizontal ridge in the odd Coulomb diamonds as illustrated in Fig. 18b. The reason is the Kondo-effect, one of the fundamental many-body effects in solid state physics. It is well known from magnetic impurities in noble metals (e.g. Fe in Au) [70], or more recently, from open semiconductor quantum dots [71, 72]. If the transparency of the tunnel contacts is sufficiently large, the electron transport through the quantum dot is more and more dominated by second order processes, where the spin-up electron leaves the quantum dot, and is replaced by a spin-down electron (see Fig. 18d). This peculiar spin flip process is resonantly enhanced around a characteristic temperature [73, 74], the Kondo temperature T_K and leads to a typical logarithmic increase of the conductance at low temperatures as shown in Fig. 18c. The Kondo temperature sets the temperature, respectively the voltage scale above which the Kondo-resonance is suppressed, i.e. the width of the Kondo-ridges in the V_{sd} - U_G -diagram. This is illustrated for two Kondo-ridges (X,Y) in Fig. 18c.

At very low temperatures the spin-flip processes are suppressed again and the tunneling model breaks down, because scattering processes of any order contribute to the transport. The result is a very peculiar many-body state, which couples the left and right contact electrode with a very high transmission probability (i.e. much larger than the transmission probability of the single tunnel contacts) that approaches *one* in the unitary limit [75]. The many body state can be qualitatively visualized in the following way: in the even valleys the Pauli-principle induces a repulsion of the adjacent electrons in the leads, similar to the well known exchange hole around an electron in the homogeneous electron gas. In the odd valleys, where the nanotube is occupied, e.g. with a spin-up electron, the adjacent spin-down electrons in the leads do not suffer from the Pauli repulsion. This leads to an increase of the density of the spin down electrons close to the nanotube and thus a *screening* of the unpaired spin trapped on the nanotube. The antiparallel coupling between the localized spin on the nanotube and its delocalized neighbors on the leads can be viewed as an exchange interaction like in antiferromagnetism.

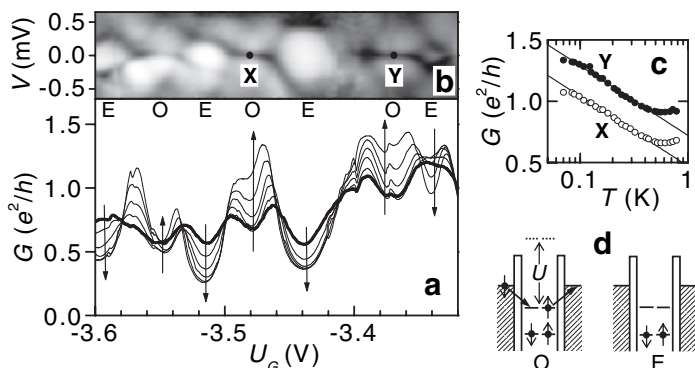


Fig. 18. Characteristics of a SWNT with contacts of intermediate transmission probabilities. (a) Zero bias conductance vs. gate voltage of a SWNT at $T = 75, 125, 180, 245, 320, 490, 560$ and (thicker line) 780 mK. With decreasing temperature the conductance drops in the even (**E**) valleys and increases in the odd (**O**) valleys. (b) Grey scale plot of the conductance in the V_{sd} - U_G -plane. Notice the pronounced Kondo ridges in valleys **X** and **Y**. (c) Temperature dependence of the conductance at points **X** and **Y**. (d) Schematic of the spin-flip process as described in the text. From [69], by permission

The strength of the exchange interaction is again determined by the Kondo temperature. An applied magnetic field suppresses the antiferromagnetic coupling and leads to a splitting of the Kondo resonance. Using carbon nanotube and C_60 quantum dots, it very recently became possible to study the competition between the Kondo effect and other electron-electron interaction effects like superconductivity [76, 77] or ferromagnetism [78].

Zero Bias Anomalies

At temperatures $k_B T \gtrsim E_C$ or tunneling conductances $G \gtrsim E_C$, the Coulomb blockade is suppressed. However, this suppression is far from being complete and can persist in weaker form up to much higher temperature or conductance. This manifests itself in so-called “zero bias anomalies”, i.e. an algebraic suppression of the tunneling conductance with $G \propto V_{sd}^\alpha$ and T^α , respectively. Typically, α ranges between 0.2 and 0.7. Again, we have to distinguish between single-wall nanotubes (two channels and ballistic) and multi-wall nanotubes (typically many channels and diffusive).

In single-wall tubes the motion of electrons is strictly one-dimensional and the electron-electron interaction is only very weakly screened. The screening usually suppresses the long range part of the Coulomb interaction and saves for most purposes the simple single-particle picture. Formally, this is described by the Fermi liquid theory, which is based on a one-to-one mapping of free electron states and fermionic quasiparticle states. The remaining screened

electron-electron interaction is short ranged and induces a slight change in the Fermi velocity and a finite life time of the single particle states. In strictly one-dimensional conductors the screening becomes so weak that the Fermi liquid theory becomes invalid and has to be replaced by the Tomonaga-Luttinger theory [79, 80]. Instead of electron-like fermionic quasi-particles, the lowest energy excitations of the system are bosonic plasmon like density oscillations without spin. In addition, there exist also spinwave-like excitations without charge and with a different velocity. This separation of charge and spin degrees of freedom is a unique signature of the Luttinger liquid. To our knowledge, experiments on carbon nanotubes detected up to now only the charge degrees of freedom.

One important consequence of the unscreened electron-electron interaction in Luttinger liquids is that there are no single particle states, in which an electron from a fermionic lead can tunnel. Instead, an electron state has to be built from many plasmons and spin waves. This requires extra energy, which can be provided only by the external voltage source driving the tunneling current. As opposed to the case of tunneling between Fermi liquids, the tunneling conductance between a Fermi liquid and a Luttinger liquid is not linear at small bias voltages, but vanishes as a power law $G \propto V^\alpha$. The power law exponent α is dependent on the strength of the electron-electron interaction and on the position of the tunneling contact on the tube: if it is at the end of the tube α is smaller than in the middle, because at the end a tunneling electron has to push away the electron in the tube in one direction, at the center it has to push away electrons in both directions.

The suppressed tunneling density of states has been detected in several experiments on individual SWNTs and SWNT-bundles [81, 82]. An example is shown in Fig. 19, where dI/dV_{sd} is plotted as a function of V_{sd} for end contacted (a) and bulk contacted (b) ropes. In the first case, the contacts are deposited on top of the tubes and are more invasive when compared to the latter, where tube has been put on top of the contacts. At voltages $V_{sd} < k_B T/e$ the curves saturate, because of thermal excitation of the tunneling electrons. An important prediction of the theory [83, 84] is an universal scaling of the differential conductance for different temperatures. As seen from the main panel in Fig. 19, the measurements at different temperatures indeed follow the predicted universal curve. In addition, the dependence of α on the location of the tunnel junction was correctly reproduced. Also the case of tunneling between two Luttinger liquids has been investigated [82] and resulted in reasonable agreement with the theoretical expectations.

On the other hand, similar experiments in multi-wall nanotubes have revealed power law behavior of the dI/dV_{sd} -curves as well [85–87] with very similar values of the exponent α . In [87] it has been shown that α even rapidly fluctuates as function of gate voltage. This can hardly be linked to Luttinger liquid behavior because the inner shells of the MWNTs effectively screen the electron-electron interaction [88]. An alternative explanation for the zero-bias

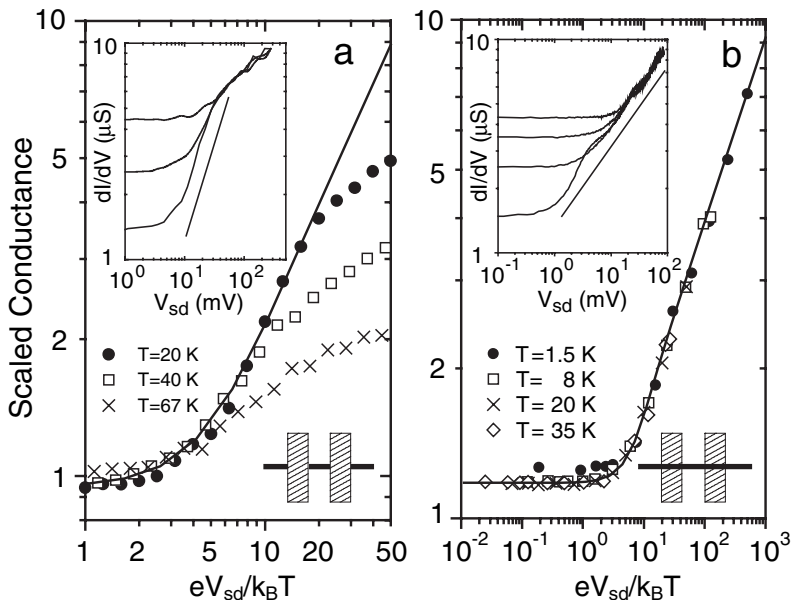


Fig. 19. The differential conductance dI/dV of SWNT-ropes measured at various temperatures. (a) inset: dI/dV traces taken on an end-contacted rope. (b) dI/dV traces taken on an bulk-contacted rope. In both insets, a straight line on the log-log plot is shown as a guide to the eye to indicate power-law behavior. The main panels show these measurements collapsed onto a universal scaling curve. The *solid line* is the theoretical result fit to the data using g as a fitting parameter. The values of g resulting in the best fit to the data are $g = 0.46$ in (a) and $g = 0.63$ in (b). After [81], by permission

anomalies observed in the tunneling conductance of MWNTs is based on a theory by Altshuler and Aronov [89], which predicted a two-particle interference mechanism resulting again in a power law ($\alpha = 0.5$ in two dimensions) suppression of the tunneling density of states located at the Fermi energy. This theory has been adapted for the different regimes and dimensionalities of MWNTs [90–92]. The resulting zero bias anomalies are difficult to distinguish from those predicted by the Luttinger liquid theory. As a consequence, the tunneling experiments alone cannot be taken as unambiguous evidence for the Luttinger liquid. Very recent measurements rely on Coulomb drag effects in order to provide more unique signatures of the Luttinger liquid state [93]. However, the “holy grail” of this field, i.e., the detection of the spin-charge separation still remains an experimental challenge.

6 Conclusions

The research on electron transport in carbon nanotubes continues to develop very rapidly. Recent experiments investigate the connection of electric and mechanical degrees of freedom in nano-electro-mechanical systems (NEMS) based on carbon nanotubes [94, 95] as well as spin-dependent transport [96, 97]. Other works try to functionalize carbon nanotubes using methods of biochemistry [98]. Transistor and optoelectronic applications of carbon nanotubes start to reach levels of performance that can be compared to those of silicon and GaAs-based semiconductor devices [67, 99, 100]. With these new directions nanotube research is expected to have large potential for both fundamental research and device applications.

Acknowledgements

We gratefully acknowledge financial support from the Deutsche Forschungsgemeinschaft (DFG) within the Graduiertenkolleg 638.

References

1. H. W. Kroto, J. R. Heath, S. C. O'Brien, R. F. Curl, and R. E. Smalley: C₆₀: Buckminsterfullerene, *Nature* **318**, 162 (1985).
2. D. Ugarte: Curling and closure of graphitic networks under electron-beam irradiation, *Nature* **359**, 707 (1992).
3. S. Iijima: Helical microtubules of graphitic carbon, *Nature* **354**, 56 (1991).
4. H. Terrones, M. Terrones: Beyond C₆₀: Graphite structures for the future, *Chem. Soc. Rev.* **24**, 341 (1995).
5. M. S. Dresselhaus, G. Dresselhaus, and Ph. Avouris: *Carbon nanotubes: Synthesis, Structure Properties and Applications* (Springer-Verlag, Berlin, 2001).
6. J.-P. Salvetat, G. A. D. Briggs, J.-M. Bonard, R. R. Bacsa, A. J. Kulik, T. Stöckli, N. A. Burnham, and L. Forró: Elastic and Shear Moduli of Single-Walled Carbon Nanotube Ropes, *Phys. Rev. Lett.* **82**, 944 (1999).
7. Ph. Avouris: Carbon nanotube electronics, *Chem. Phys.* **281**, 429 (2002).
8. R. Saito, G. Dresselhaus, and M. S. Dresselhaus: *Physical Properties of Carbon Nanotubes* (Imperial College Press, London, 1998).
9. R. H. Baughman, A. A. Zakhidov, and W. A. de Heer: Carbon Nanotubes—the Route Toward Applications, *Science* **297**, 787 (2002).
10. J. W. Mintmire and C. T. White: Electronic and structural properties of carbon nanotubes, *Carbon* **33**, 893 (1995).
11. A. Jorio, R. Saito, J. H. Hafner, C. M. Lieber, M. Hunter, T. McClure, G. Dresselhaus, and M. S. Dresselhaus: Structural (n, m) Determination of Isolated Single-Wall Carbon Nanotubes by Resonant Raman Scattering, *Phys. Rev. Lett.* **86**, 1118 (2001).
12. Image gallery of R. E. Smalley: <http://smalley.rice.edu/>.

13. S. Iijima and T. Ichihashi: Single-shell carbon nanotubes of 1-nm diameter, *Nature* **363**, 603 (1993).
14. L.-C. Qin, S. Iijima, H. Kataura, Y. Maniwa, S. Suzuki, and Y. Achiba: Helicity and packing of single-walled carbon nanotubes studied by electron nanodiffraction, *Chem. Phys. Lett.* **268**, 101 (1997).
15. J. M. Cowley, P. Nikolaev, A. Thess, and R. E. Smalley: Electron nanodiffraction study of carbon single-walled nanotube ropes, *Chem. Phys. Lett.* **265**, 379 (1997).
16. M. Kociak, K. Suenaga, K. Hirahara, Y. Saito, T. Nakahira, and S. Iijima: Linking Chiral Indices and Transport Properties of Double-Walled Carbon Nanotubes, *Phys. Rev. Lett.* **89**, 155501 (2002).
17. J.-F. Colomer, L. Henrard, Ph. Lambin, and G. Van Tendeloo: Electron diffraction study of small bundles of single-wall carbon nanotubes with unique helicity, *Phys. Rev. B* **64**, 125425 (2001).
18. S. Amelinckx, A. Lucas, and Ph. Lambin: Electron diffraction and microscopy of nanotubes, *Rep. Prog. Phys.* **62**, 1471 (1999).
19. T. W. Odom, J.-L. Huang, P. Kim, and C. M. Lieber: Atomic structure and electronic properties of single-walled carbon nanotubes, *Nature* **391**, 62 (1998).
20. J. W. G. Wildöer, L. C. Venema, A. G. Rinzler, R. E. Smalley, and C. Dekker: Electronic structure of atomically resolved carbon nanotubes, *Nature* **391**, 59 (1998).
21. Ch. Kramberger, R. Pfeiffer, H. Kuzmany, V. Zolyomi, and J. Kurti: Assignment of chiral vectors in carbon nanotubes, *Phys. Rev. B* **68**, 235404 (2003).
22. S. B. Cronin, R. Bamett, M. Tinkham, S. G. Chou, O. Rabin, M. S. Dresselhaus, A. K. Swan, M. S. Ünlü, and B. B. Goldberg: Electrochemical gating of individual single-wall carbon nanotubes observed by electron transport measurements and resonant Raman spectroscopy, *Appl. Phys. Lett.* **84**, 2052 (2004).
23. X. B. Zhang, X. F. Zhang, S. Amelinckx, G. Van Tendeloo, and J. Van Landuyt: The reciprocal space of carbon tubes: a detailed interpretation of the electron diffraction effects, *Ultramicroscopy* **54**, 237 (1994).
24. X. F. Zhang, X. B. Zhang, G. Van Tendeloo, S. Amelinckx, M. Op. de Beek, and J. Van Landuyt: Carbon nano-tubes; their formation process and observation by electron microscopy, *J. Cryst. Growth* **130**, 368 (1993).
25. X. B. Zhang and S. Amelinckx: On the measurements of the helix angles of carbon nanotubes, *Carbon* **32**, 1537 (1994).
26. M. Gao, M. Zuo, R. D. Tweten, I. Petrov, L. A. Nagahara, and R. Zhang: Structure determination of individual single-wall carbon nanotubes by nanoarea electron diffraction, *App. Phys. Lett.* **82**, 2703 (2003).
27. Ph. Lambin, A. Loiseau, C. Culot, and L. P. Biro: Structure of carbon nanotubes probed by local and global probes, *Carbon* **40**, 1635 (2002).
28. C. T. White, D. H. Robertson, and J. W. Mintmire: Helical and rotational symmetries of nanoscale graphitic tubules, *Phys. Rev. B* **47**, 5485 (1993).
29. T. W. Odom, J.-L. Huang, P. Kim, and C. M. Lieber: Structure and Electronic Properties of Carbon Nanotubes, *J. Phys. Chem. B* **104**, 2794 (2000).
30. R. Saito, M. Fujita, G. Dresselhaus, and M. S. Dresselhaus: Electronic structure of graphene tubules based on C_{60} , *Phys. Rev. B* **46**, 1804 (1992).

31. Ch. Zhou, J. Kong, and H. Dai: Intrinsic Electrical Properties of Individual Single-Walled Carbon Nanotubes with Small Band Gaps, *Phys. Rev. Lett.* **84**, 5604 (2000).
32. M. Ouyang, J.-L. Huang, C. L. Cheung, and C. M. Lieber: Energy Gaps in "Metallic" Single-Walled Carbon Nanotubes, *Science* **292**, 702 (2001).
33. A. Bachtold, M. S. Fuhrer, S. Plyasunov, M. Forero, E. H. Anderson, A. Zettl, and P. L. McEuen: Scanned Probe Microscopy of Electronic Transport in Carbon Nanotubes, *Phys. Rev. Lett.* **84**, 6082 (2000).
34. P. J. de Pablo, C. Gómez-Navarro, J. Colchero, P. A. Serena, J. Gómez-Herrero, and A. M. Baró: Nonlinear Resistance versus Length in Single-Walled Carbon Nanotubes, *Phys. Rev. Lett.* **88**, 036804 (2002).
35. P. Kim, T. W. Odom, J.-L. Huang, and C. M. Lieber: Electronic Density of States of Atomically Resolved Single-Walled Carbon Nanotubes: Van Hove Singularities and End States, *Phys. Rev. Lett.* **82**, 1225 (1999).
36. L. C. Venema, J. W. G. Wildöer, J. W. Janssen, S. J. Tans, H. L. J. Temminck Tuinstra, L. P. Kouwenhoven, and C. Dekker: Imaging Electron Wave Functions of Quantized Energy Levels in Carbon Nanotubes, *Science* **283**, 52 (1999).
37. S. Datta, *Electronic Transport in Mesoscopic Systems* (Cambridge University Press, Cambridge 1995).
38. W. Liang, M. Bockrath, D. Bozovic, J. H. Hafner, M. Tinkham, and H. Park: Fabry - Perot interference in a nanotube electron waveguide, *Nature* **411**, 665 (2001).
39. S. Frank, P. Poncharal, Z. L. Wang, and W. A. de Heer: Carbon Nanotube Quantum Resistors, *Science* **280**, 1744 (1998).
40. A. Urbina, I. Echeverria, A. Perez-Garrido, A. Dias-Sanchez, and J. Abellan: Quantum Conductance Steps in Solutions of Multiwalled Carbon Nanotubes, *Phys. Rev. Lett.* **90**, 106603 (2003).
41. B. J. van Wees, H. van Houten, C. W. J. Beenakker, J. G. Williamson, L. P. Kouwenhoven, D. van der Marel, and C. T. Foxon: Quantized conductance of point contacts in a two-dimensional electron gas, *Phys. Rev. Lett.* **60**, 848 (1988).
42. A. Wharam, T. J. Thornton, R. Newbury, M. Pepper, H. Ahmed, J. E. F. Frost, D. G. Hasko, D. C. Peacock, D. A. Ritchie, and G. A. C. Jones: One-dimensional transport and the quantisation of the ballistic resistance, *J. Phys. C* **21**, L 209 (1988).
43. For a review, see e.g.: S. Washburn and R. Webb: Quantum transport in small disordered samples from the diffusive to the ballistic regime, *Rep. Prog. Phys.* **55**, 1311 (1992).
44. H. Ajiki and T. Ando: Electronic States of Carbon Nanotubes, *Phys. Soc. of Jpn* **62**, 1255 (1993).
45. S. Roche and R. Saito: Magnetoresistance of Carbon Nanotubes: From Molecular to Mesoscopic Fingerprints, *Phys. Rev. Lett.* **87**, 246803 (2001).
46. C. Schönenberger, A. Bachtold, C. Strunk, J. P. Salvetat, L. Forró: Interference and Interaction in multi-wall carbon nanotubes, *App. Phys. A* **69**, 283 (1999).
47. L. Langer, V. Bayot, E. Grivei, J. P. Issi, J. P. Heremans, C. H. Olk, L. Stockman, C. Van Haesendonck, and Y. Bruynseraede: Quantum Transport in a Multiwalled Carbon Nanotube, *Phys. Rev. Lett.* **76**, 479 (1996).

48. K. Liu, S. Roth, G. S. Düsberg, G. T. Kim, D. Popa, K. Mkhopadhyay, R. Doome, and J. B. Nagy: Antilocalization in multiwalled carbon nanotubes, Phys. Rev. B **61**, 2375 (2000).
49. K. Liu, Ph. Avouris, R. Martel, and W. K. Hsu: Electrical transport in doped multiwalled carbon nanotubes, Phys. Rev. B **63**, 161404 (2001).
50. R. Tarkiainen, M. Ahlskog, J. Penttilä, L. Roschier, P. Hakonen, M. Paalanen, and E. Sonin: Multiwalled carbon nanotube: Luttinger versus Fermi liquid, Phys. Rev. B **64**, 195412 (2001).
51. P. A. Lee, T. V. Ramakrishnan: Disordered electronic systems, Rev. Mod. Phys **57**, 287 (1985).
52. B. L. Altshuler and A. G. Aronov: Magnetoresistance of thin films and of wires in a longitudinal magnetic field, JETP Lett. **33**, 499 (1981).
53. M. Buitelaar: Electron Transport in Multiwall Carbon Nanotubes, Dissertation, University of Basel (2002).
54. J.-Y Park, S. Rosenblatt, Y. Yaish, V. Sazonova, H. Üstünel, S. Braig, T. A. Arias, P. W. Brouwer, and P. L. McEuen: Electron-Phonon Scattering in Metallic Single-Walled Carbon Nanotubes, Nano Lett. **4**, 517 (2004).
55. B. L. Altshuler, A. G. Aronov, and D. E. Khmel'nitzkii: Suppression of localization effects by the high frequency field and the nyquist noise, Solid State Communications **39**, 619 (1981).
56. B. L. Altshuler, A. G. Aronov, and B. Z. Spivak: The Aharonov-Bohm effect in disordered conductors, Pis'ma Zh. Eksp. Teor. Fiz. **33**, 101 (1981), [JETP Lett. **33**, 94 (1981)].
57. Y. Sharvin and Y. V. Sharvin: Magnetic-flux quantization in a cylindrical film of a normal metal, Pis'ma Zh. Eksp. Teor. Fiz. **34**, 285 (1981), [JETP Lett. **34**, 272 (1981)].
58. A. Bachtold, C. Strunk, J. P. Salvetat, L. Forró, T. Nussbaumer, and C. Schönenberger: Aharonov-Bohm oscillations in carbon nanotubes, Nature **397**, 673 (1999).
59. B. Stojetz: Interplay of Bandstructure and Quantum Interference in Multi Wall Carbon Nanotubes, Dissertation, University of Regensburg (2004).
60. B. Stojetz, C. Miko, L. Forró, C. Strunk: Effect of Band Structure on Quantum Interference in Multiwall Carbon Nanotubes, to be published in Phys. Rev. Lett.
61. M. Thorwart, M. Grifoni, and R. Egger: Transport through intrinsic quantum dots in interacting carbon nanotubes, in this volume.
62. For a review see, e.g.: H. Grabert and M. H. Devoret (Edts.), *Single Charge tunneling*, NATO ASI Series B: **294** (Plenum Press, New York 1992).
63. S. J. Tans, A. R. M. Verschueren, and C. Dekker: Room-temperature transistor based on a single carbon nanotube, Nature **393**, 49 (1998).
64. S. J. Tans, M. H. Devoret, H. Dai, A. Thess, R. E. Smalley, L. J. Geerlings, and C. Dekker: Individual single-wall carbon nanotubes as quantum wires, Nature **386**, 474 (1997).
65. M. R. Buitelaar, A. Bachtold, T. Nussbaumer, M. Iqbal, and C. Schönenberger: Multiwall Carbon Nanotubes as Quantum Dots, Phys. Rev. Lett. **88**, 156801 (2002).
66. P. Jarillo-Herrero, S. Sapmaz, C. Dekker, L. P. Kouwenhoven, and H. S. J. van der Zant: Electron-hole symmetry in a semiconducting carbon nanotube quantum dot, Nature **429**, 389 (2004).

67. S. Heinze, J. Tersoff, and Ph. Avouris: Carbon nanotube electronics and optoelectronics, in this volume.
68. A. Bezryadin, A. R. M. Verschueren, S. J. Tans, and C. Dekker: Multiprobe Transport Experiments on Individual Single-Wall Carbon Nanotubes, *Phys. Rev. Lett.* **80**, 4036 (1998).
69. J. Nygard, D. H. Cobden, and P. E. Lindelof: Kondo physics in carbon nanotubes, *Nature* **408**, 342 (2000).
70. G. Grüner and A. Zawadowski: Magnetic impurities in non-magnetic metals, *Rep. Prog. Phys.* **37**, 1497 (1974).
71. D. Goldhaber-Gordon, H. Shtrikman, D. Mahalu, D. Abusch-Magder, U. Meirav, and M. A. Kastner: Kondo effect in a single-electron transistor, *Nature* **391**, 156 (1998).
72. S. M. Cronenwett, T. H. Oosterkamp, and L. P. Kouwenhoven: A Tunable Kondo Effect in Quantum Dots, *Science* **281**, 540 (1998).
73. C. V. Haesendonck, J. Vranken, and Y. Bruynseraeede: Resonant Kondo Scattering of Weakly Localized Electrons, *Phys. Rev. Lett.* **58**, 1968 (1987).
74. R. P. Peters, G. Bergmann, and R. M. Mueller: Kondo Maximum of Magnetic Scattering, *Phys. Rev. Lett.* **58**, 1964 (1987).
75. W. G. van der Wiel, S. de Franceschi, T. Fujisawa, J. M. Elzerman, S. Tarucha, and L. P. Kouwenhoven: The Kondo Effect in the Unitary Limit, *Science* **289**, 2105 (2000).
76. M. R. Buitelaar, T. Nussbaumer, and C. Schönenberger: Quantum Dot in the Kondo Regime Coupled to Superconductors, *Phys. Rev. Lett.* **89**, 256801 (2002).
77. M. R. Buitelaar, W. Belzig, T. Nussbaumer, B. Babic, C. Bruder, and C. Schönenberger: Multiple Andreev Reflections in a Carbon Nanotube Quantum Dot, *Phys. Rev. Lett.* **91**, 057005 (2003).
78. A. N. Pasupathy, R. C. Bialczak, J. Martinek, J. E. Grose, L. A. K. Donev, P. L. McEuen, and D. C. Ralph: The Kondo Effect in the Presence of Ferromagnetism, *Science* **306**, 86 (2004).
79. R. Egger and A. O. Gogolin: Effective Low-Energy Theory for Correlated Carbon Nanotubes, *Phys. Rev. Lett.* **79**, 5082 (1997).
80. C. Kane, L. Balents, and M. A. Fisher: Coulomb Interactions and Mesoscopic Effects in Carbon Nanotubes, *Phys. Rev. Lett.* **79**, 5086 (1997).
81. M. Bockrath, D. H. Cobden, A. G. Rinzler, R. E. Smalley, L. Balents, and Paul L. McEuen: Luttinger-liquid behaviour in carbon nanotubes, *Nature* **397**, 598 (1999).
82. Z. Yao, H.W.Ch. Postma, L. Balents, and C. Dekker: Carbon nanotube intramolecular junctions, *Nature* **402**, 273 (1999).
83. M. P. A. Fisher and A. Dorsey: Dissipative Quantum Tunneling in a Biased Double-Well System at Finite Temperatures, *Phys. Rev. Lett.* **54**, 1609 (1985).
84. H. Grabert and U. Weiss: Quantum Tunneling Rates for Asymmetric Double-Well Systems with Ohmic Dissipation, *Phys. Rev. Lett.* **54**, 1605 (1985).
85. A. Bachtold, M. de Jonge, K. Grove-Rasmussen, P. L. McEuen, M. Buitelaar, and C. Schönenberger: Suppression of Tunneling into Multiwall Carbon Nanotubes, *Phys. Rev. Lett.* **87**, 166801 (2001).
86. W. Yi, L. Lu, H. Hu, Z. W. Pan, and S. S. Xie: Tunneling into Multiwalled Carbon Nanotubes: Coulomb Blockade and the Fano Resonance, *Phys. Rev. Lett.* **91**, 076801 (2003).

87. A. Kanda, K. Tsukagoshi, Y. Aoyagi, and Y. Ootuka: Gate-Voltage Dependence of Zero-Bias Anomalies in Multiwall Carbon Nanotubes, *Phys. Rev. Lett.* **92**, 036801 (2004).
88. R. Egger: Luttinger Liquid Behavior in Multiwall Carbon Nanotubes, *Phys. Rev. Lett.* **83**, 5547 (1999).
89. B. L. Altshuler and A. G. Aronov, *Electron-electron Interactions in Disordered Systems*, edited by A. L. Efros and M. Pollak (Elsevier, Amsterdam, 1985).
90. R. Egger and A. O. Gogolin: Bulk and Boundary Zero-Bias Anomaly in Multiwall Carbon Nanotubes, *Phys. Rev. Lett.* **87**, 066401 (2001).
91. E. G. Mishchenko, A. V. Andreev, and L. I. Glazman: Zero-Bias Anomaly in Disordered Wires, *Phys. Rev. Lett.* **87**, 246801 (2001).
92. J. Rollbühler and H. Grabert: Coulomb Blockade of Tunneling between Disordered Conductors, *Phys. Rev. Lett.* **87**, 126804 (2001).
93. B. Gao, A. Komnik, R. Egger, D. C. Glattli, and A. Bachtold: Evidence for Luttinger-Liquid Behavior in Crossed Metallic Single-Wall Nanotubes, *Phys. Rev. Lett.* **92**, 216804 (2004).
94. B. Reulet, A. Yu. Kasumov, M. Kociak, R. Deblock, I. I. Khodos, Yu. B. Gorbatov, V. T. Volkov, C. Journet, and H. Bouchiat: Acoustoelectric Effects in Carbon Nanotubes, *Phys. Rev. Lett.* **85**, 2829 (2000).
95. V. Sazonova, Y. Yaish, H. Üstünel, D. Roundy, T. A. Arias, and P. L. McEuen: A tunable carbon nanotube electromechanical oscillator, *Nature* **431**, 284 (2004).
96. K. Tsukagoshi, B. W. Alphenaar, and H. Ago: Coherent transport of electron spin in a ferromagnetically contacted carbon nanotube, *Nature* **401**, 572 (1999).
97. B. Zhao, I. Mönch, H. Vinzelberg, T. Mühl, and C. M. Schneider: Spin-coherent transport in ferromagnetically contacted carbon nanotubes, *Appl. Phys. Lett.* **80**, 3144 (2002).
98. K. Keren, R. S. Berman, E. Buchstab, U. Sivan, and E. Braun: DNA-Templated Carbon Nanotube Field-Effect Transistor, *Science* **302**, 1380 (2003).
99. J. A. Misewich, R. Martel, Ph. Avouris, J. C. Tsang, S. Heinze, and J. Tersoff: Electrically Induced Optical Emission from a Carbon Nanotube FET, *Science* **300**, 783 (2003).
100. S. Li, Z. Yu, S.-F. Yen, W. C. Tang, P. J. Burke: Carbon Nanotube Transistor Operation at 2.6 GHz, *Nano Lett.* **4**, 753 (2004).

Carbon Nanotube Electronics and Optoelectronics

S. Heinze¹, J. Tersoff², and Ph. Avouris²

¹ Institute of Applied Physics, University of Hamburg, Jungiusstrasse 9a, 20355 Hamburg, Germany
heinze@physnet.uni-hamburg.de

² IBM Research Division, T. J. Watson Research Center, Yorktown Heights, New York 10598, USA
tersoff@us.ibm.com and avouris@us.ibm.com

Carbon nanotube field-effect transistors (CNFETs) are already competitive in some respects with state-of-the-art silicon transistors, and are promising candidates for future nanoelectronic devices. However, it is difficult to form ohmic contacts to carbon nanotubes, and most of the CNFETs reported to date operate as Schottky barrier transistors rather than conventional FETs. The electrostatics at the contact of a metal to a nanotube leads to device behavior very different from conventional transistors. In this article we discuss the consequences of Schottky barriers in CNFETs with respect to the scaling of transistor performance with reduced device size and the application of CNFETs as optoelectronic devices.

1 Introduction

Aggressive down-scaling of conventional silicon transistors over the past decades has led to characteristic device sizes below 100 nm in today's computer chips. Because of the associated problems, such as the increase of power consumption and device leakage current densities, there is intense interest in finding new materials and alternative devices. Carbon nanotubes are very promising in this respect, because of their exceptional structural, electronic, and optical properties ([1], see also Chap. 13). In particular, they exhibit ballistic transport over length scales of several hundred nanometers. Nanotube devices can be integrated with existing silicon-based structures. And recently, optoelectronic nanotube devices of nanometer dimensions and with tunable optical characteristics have emerged. In this chapter, we focus on the use of single-wall semiconducting carbon nanotubes in electronic devices such as field-effect transistors or in optoelectronic applications such as light-emitting devices.

Since the first demonstration of carbon nanotube field-effect transistors (CNFETs) in 1998 [2,3] intensive research has led to a great improvement of device fabrication techniques and their transport properties. Today, CNFETs are already becoming competitive with state-of-the-art silicon transistors in

several aspects. For example, CNFETs using a top gate led to comparable turn-on voltages and superior transconductance [4], CNFETs with high-k dielectrics showed subthreshold slopes close to the thermal limit [5], and ballistic transport in CNFETs has been demonstrated [6, 7]. Even the first logic gate – a basic building block of a computer chip – has been created from a single carbon nanotube [8].

Despite their similarity to conventional devices, there is now ample evidence that CNFETs generally operate by an entirely different principle [9–13]. This is due to the presence of a Schottky barrier at the metal-nanotube contact, and the very different electrostatics of the quasi-one-dimensional nanotube compared to a planar interface. Important consequences include non-ideal switching behavior [11], unexpected scaling relations of device performance as its size is reduced [14] and new applications such as light emission from a single undoped nanotube (NT) [15].

2 Schottky Barrier Carbon Nanotube Transistors

At most metal-semiconductor contacts there is a Schottky barrier (SB), i.e. an energy barrier for carrier transport, which can be a severe limitation for devices. In semiconductor devices, this problem is generally avoided by replacing metal contacts with heavily doped regions of the semiconductor. However, nanotube devices have generally relied on direct metal-semiconductor contacts. Nonetheless, good device performance can be obtained. The reason is that the Schottky barrier represents a much less severe limitation for CNFETs than for conventional FETs, due to the quasi-one-dimensional (1D) geometry [11].

Another important difference is that in planar metal-semiconductor junctions, the Schottky barrier height is usually a substantial fraction of the bandgap, regardless of the metal used or other details. This is because the Fermi level at the interface is “pinned” deep in the bandgap by “metal-induced gap states” (MIGS)¹ in the semiconductor near the interface [16]. However, because of the very different electrostatics of the quasi-1D geometry, the MIGS are far less effective in pinning the Fermi level at nanotube-metal contacts [17]. The barrier height at NT contacts is therefore strongly affected by the local work functions of the metal and the nanotube. Thus the device properties can be dramatically modified by altering the work function near the contact, e.g. by exposure to oxygen or other gases.

Initially, only p-type transport was observed in CNFETs [2, 3] and led to the assumption that there is a vanishing barrier to the valence band of the

¹MIGS possess a complex wave vector and their wave function decays exponentially in the semiconductor with distance from the interface. They lie in the semiconductor bandgap and are forbidden in the bulk because their wave function rises infinitely in one direction. However, at an interface they can be attached to Bloch states of the metal in this direction and become valid solutions.

NT. Transistor action would then occur due to the modulation of the channel conductance as depicted in Fig. 1(a). At large positive gate voltages, the holes travelling from the drain to the source contact face a high potential barrier in the channel and the current is suppressed. The transistor is in its off-state. As the gate voltage is lowered and turns negative charge accumulates in the channel and the barrier is lowered. A significant current starts to flow and the transistor turns on. If the channel is ballistic the current modulation with gate voltage is governed only by the number of electrons with sufficient thermal energy to overcome the potential barrier. The current thus rises exponentially with gate voltage in the regime between the off- and the on-state (turn-on regime). The ratio between on- and off-current can be several orders of magnitude.

However, the finding of ambipolar conduction in CNFETs [9, 10], the transition from p- to n-type conduction upon gas adsorption [8, 18], and local gating of the CNFET at the contact [19] led to the notion that SBs must play a significant role. Transistor action due to the modulation of a SB has already been proposed for silicon based FETs [20] and has been demonstrated experimentally. In a SB-FET, the conduction of the device results from the modulation of the contact resistance as shown in Fig. 1(b). A SB of height ϕ_B at the nanotube-metal contact represents a potential barrier to charge carriers trying to enter from the source.² At zero gate voltage, only charge carriers thermally excited above the SB can enter the NT, the current is marginal, and the NT transistor is off. Upon a positive gate voltage, the SB to the conduction band is thinned down and thermally assisted tunneling of electrons from the source sets in. This tunneling current becomes significant only if the electric field due to the applied gate voltage can shrink the SB width down to a few nanometers. Analogously, holes can tunnel into the valence band at negative gate voltages. The transistor thus turns on at both negative and positive gate voltages and is in the off-state at intermediate voltages.

The SB assumption qualitatively explains ambipolar conduction, however, the observed output characteristics (I vs. V_d) of CNFETs show a linear slope at low drain voltages typical for a conventional transistor. For a SB transistor in the planar silicon geometry such a linear regime – desirable for many device applications – is unattainable. Thus an adequate model of the SB-CNFET must explicitly take the special properties of the NT such as quasi-1D electrostatics and the NTs electronic structure into account.

Recently, devices with small or vanishing Schottky barrier heights have been reported using Pd or Al contacts [6, 21]. However, relatively large diameter NTs (2 to 3 nm) with correspondingly small bandgaps (0.4 to 0.3 eV) have to be used so far. Due to their small NT bandgaps these devices suffer

²For a single-wall NT in a typical device the bandgap is about 0.6 eV and for a metal Fermi energy located at the middle of the NT gap (at midgap line-up, cf. Fig. 1(b)) the SB is about 0.3 eV.

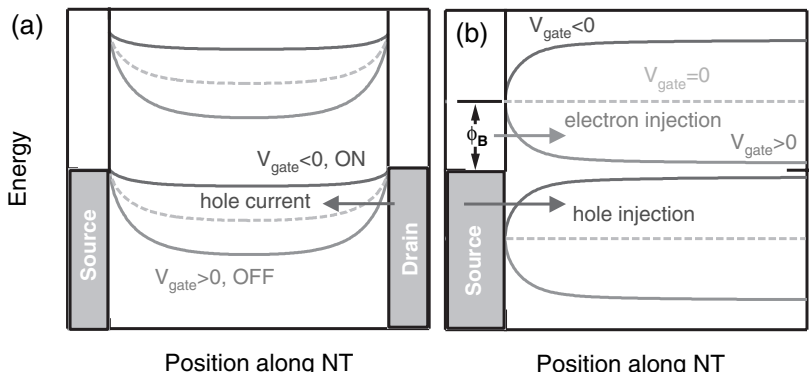


Fig. 1. (Color online) Working principle of (a) a conventional transistor with ohmic contact to the valence band and (b) a Schottky barrier transistor at midgap line-up of the metal Fermi energy with the semiconductor bands. The conventional transistor turns on at negative gate voltages due to the enhanced channel conduction. The SB transistor is ambipolar, i.e. it turns on at both negative and positive gate voltage due to the thinning of the SB width and thermally assisted tunneling

from large off-currents. These leakage currents result from minority carrier injection at the drain contact and will be explained below based on the SB model of a CNFET. Another very promising route to create conventional FETs from a carbon nanotube is to dope both ends of the NT and use these ends as source and drain contacts [22]. This device setup prevents the formation of SBs and leads to transistor action from the modulation of the channel resistance. Subthreshold slopes close to the thermal limit and high on-currents have been observed in such devices [22]. Because of the required extended regions of doped NT it is not clear so far to which size these devices can be scaled down. Very recently, Lin et al. have used a double-gate device geometry to fabricate CNFETs with unipolar n- and p-type bulk switching and excellent performance in the subthreshold regime [23].

Due to the difficulty to achieve ohmic contacts to carbon nanotubes, a good understanding of the consequences and implications of SBs on the transport properties of CNFETs is necessary for further exploration of these promising devices. In addition, new optoelectronic applications are possible due to their existence [15, 24] and can be understood based on the transport model introduced in the following.

2.1 Needle-Like Contact Model

In order to study the operation principle of a SB-CNFET we begin with the idealized model of the CNFET shown in Fig. 2. We assume that the metal electrode is a cylinder with the same diameter as the NT forming a perfectly sharp needle-like contact to the NT. The gate electrode is a metal

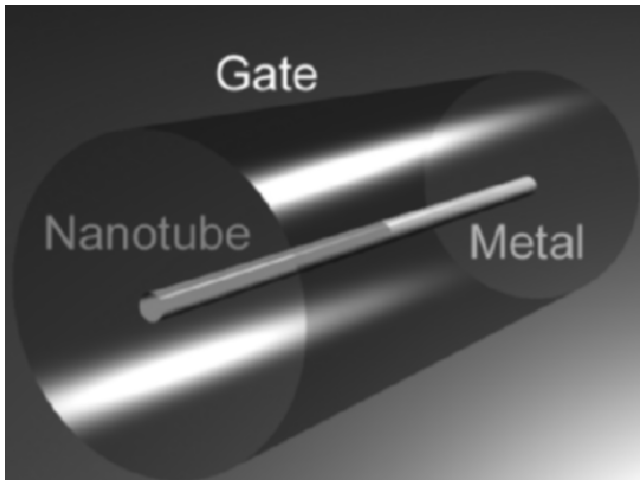


Fig. 2. (*Color online*) Geometry of the needle-like contact model. A cylindrical gate surrounds the nanotube-metal junction. The metal electrode consists of a cylinder of the same diameter as the NT, i.e. on the order of 1 nm

cylinder surrounding the contact. This device geometry is advantageous as the electrostatic kernel $G(z)$ is known analytically [25, 26]. Thus for a given charge distribution $\rho(z)$ on the metal-nanotube junction we can evaluate the electrostatic potential $V(z)$ along the NT:

$$V(z) = V_g + \frac{R_g}{4\pi} \int G(z - z') \rho(z') dz' , \quad (1)$$

where R_g is the gate radius and V_g is the applied gate voltage. We further assume that an electrostatic potential along the NT rigidly shifts the valence and conduction bands of the NT. Thus the local density of states (DOS) of the NT, $D(E)$ [27], is shifted and the charge on the NT can be found by integration over energy:

$$\rho(z) = -\frac{e}{\epsilon} \int_{E_c(z)}^{\infty} F(E) D(E - V(z)) dE + \frac{e}{\epsilon} f , \quad (2)$$

where $F(E)$ is the Fermi distribution and $E_c(z)$ is the local position of the conduction band. We have chosen the case where additional electrons populate the NT conduction band. The case for holes in the valence band is easily obtained as well. The second term on the right hand side is added in order to take uniform doping into account. Hereby, f is the fraction of dopants per atom of the NT and ϵ is the dielectric constant of the surrounding oxide.

Equations (1) and (2) need to be solved self-consistently. Transport over the short length of the NTs used in CNFETs is ballistic [6, 7] and the current through the transistor is calculated from the Landauer-Büttiker formula:

$$I = \frac{4e}{h} \int T(E)[F(E) - F(E + eV_d)]dE , \quad (3)$$

where V_d is the drain voltage (assumed to be small) and $F(E)$ is the Fermi distribution. The transmission $T(E)$ through the SB is calculated within the WKB approximation:

$$\ln T(E) = -\frac{4}{3bV_\pi} \int_{z_i}^{z_f} (\Delta^2 - [E + eV(z)]^2)^{1/2} dz , \quad (4)$$

where $b = 0.144$ nm is the bond length, Δ is half the NT bandgap, and $V_\pi = 2.5$ eV is the tight-binding parameter. The integration is performed along the NT between the classical turning points z_i and z_f . For the calculations we used a NT with a bandgap of 0.6 eV corresponding to a diameter of 1.4 nm. We neglect screening on the NT as it is negligible for a quasi-1D wire [28]. For the dielectric constant ϵ we choose a value of 3.9 as for SiO₂.

For a midgap line-up of the metal Fermi level with the NT bands, the calculated conductance, displayed in Fig. 3, is symmetric with respect to the applied gate voltage V_g . At large gate voltages the SB is thinned down to a few nanometers due to the high electric field at the contact. The barrier then allows a significant electron tunneling current into the NT conduction band at positive gate voltages and hole tunneling into the valence band at negative gate voltages (cf. Fig. 1(b)). The gate voltage required to turn the

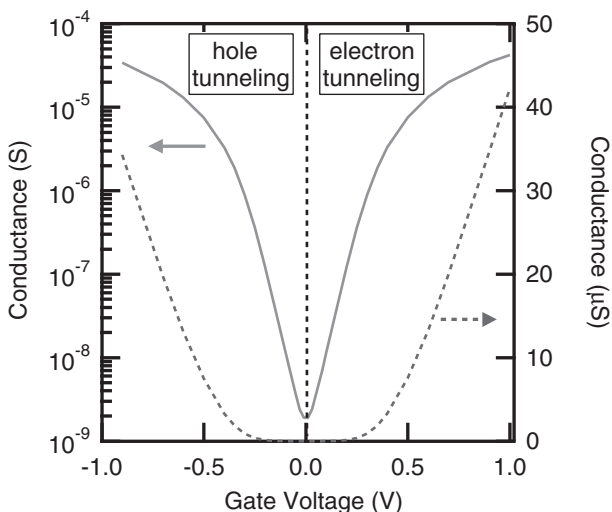


Fig. 3. (Color online) Calculated conductance as a function of the applied gate voltage for the needle-like contact and an oxide thickness of 50 nm. The Fermi energy of the metal is assumed to be at midgap of the NT bands. Solid red (dashed blue) curve is the conductance on a logarithmic (linear) scale

transistor from off ($V_g = 0$, low conductance) to on (high conductance) is about $V_g^{\text{on}} = 0.5$ V which is on the order of the bandgap (0.6 eV). The calculated transfer characteristic (I vs. V_g) is in good qualitative agreement with experimental data [9]. However, the turn-on gate voltage V_g^{on} is much smaller than in the experiment (typical values range from 1 to 20 V). This discrepancy is due to the ideal focusing of the electric field at the needle-like contact. In an actual device, planar gate geometries are used and we need to take this geometry explicitly into account for a realistic model of the transistor.

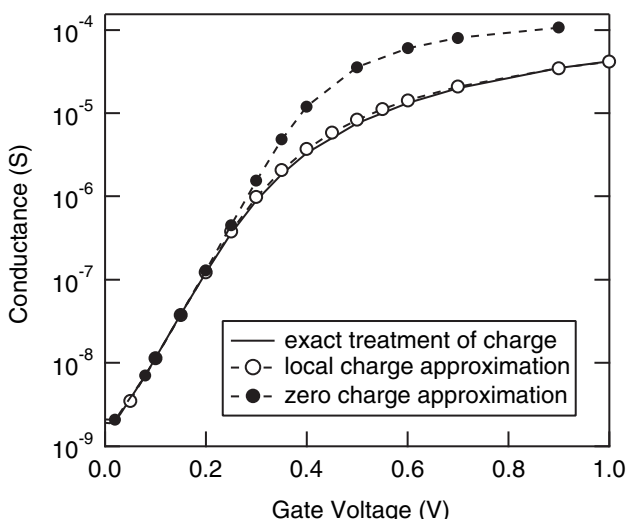


Fig. 4. Comparison of different approximations for the electrostatic potential caused by charge on the NT. All calculations are performed within the needle-like contact model

It is instructive to compare various approximations for the description of the electrostatic potential resulting from charge on the NT. In Fig. 4 the calculated conductance within the needle-like contact model is displayed for the exact treatment and two approximations. In the turn-on regime up to about 0.3 V, charge on the NT can be completely neglected (see the zero-charge approximation in Fig. 4) because the barrier shape which controls the conductance is only weakly affected by charge while the bulk of the NT does not affect the conductance in this voltage regime. However, in the on-state the position of the bulk conduction band limits the current and the zero-charge approximation breaks down. A strictly local approximation, i.e. if we assume that the potential due to charge on the NT is given by $V_{\text{local}}(x) = U\rho(x)$, is valid even far beyond the turn-on regime because the potential in the bulk of the NT is modelled sufficiently accurately.

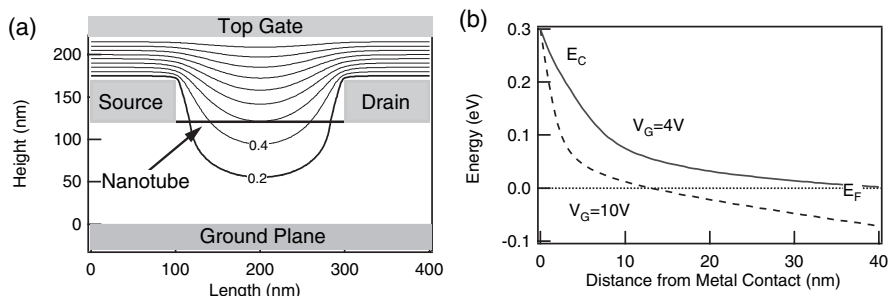


Fig. 5. (a) Cross-section through a carbon nanotube transistor with planar gates. For a top gate device the gate voltage is applied to the top electrode while the bottom electrode is grounded. Potential contour lines in steps of 0.2 V are shown for $V_g = +2$ V. (b) Calculated conduction band along the NT at midgap line-up for $V_g = +4$ V (solid line) and $V_g = +10$ V (dashed line). The resulting conductance is displayed in Fig. 6 ($t_{ox} = 100$ nm)

2.2 Influence of the Contact Geometry

To obtain a better understanding of the experimentally observed transport characteristics the carbon nanotube transistor has to be explored within a planar geometry displayed in Fig. 5(a). The gate voltage is applied to a top gate as in [4] and a grounded bottom electrode has been added for a convenient electrostatic calculation. The source and drain contacts possess a finite thickness in our device. The two-dimensional electrostatic boundary problem can be solved by standard techniques and we treat the potential due to charge on the NT in a local approximation. This is sufficiently accurate even beyond the turn-on regime as we have demonstrated within the needle-like contact model (see Fig. 4). We focus on a midgap line-up. The band bending for two gate voltages is shown in Fig. 5(b). At $V_g = 4$ V there is already considerable charge on the NT, however, the SB at the contact is still about 10 nm wide at 0.1 eV above the Fermi energy. Consequently, the tunneling probability and the current are negligible. With a very large gate voltage of $V_g \geq 10$ V, it is possible to thin down the SB to a few nanometers sufficient for considerable injection of electrons.

In Fig. 6 the conductance is plotted versus gate voltage for several top gate devices with varying oxide thickness and contact geometries. (Due to the symmetric form of the curves only positive gate voltages are considered, i.e. transport due to electron injection.) The shape of the conductance curves is similar to the needle-like contact, however, much larger gate voltages are required to turn on the transistors. As the oxide thickness is reduced a steady increase of the device performance, i.e. turn-on at lower gate voltage, can be observed. The crucial importance of the contact geometry for a SB-CNFET becomes apparent when the thickness of the source and drain contacts is reduced from 50 nm to 5 nm keeping all other parameters, in particular the

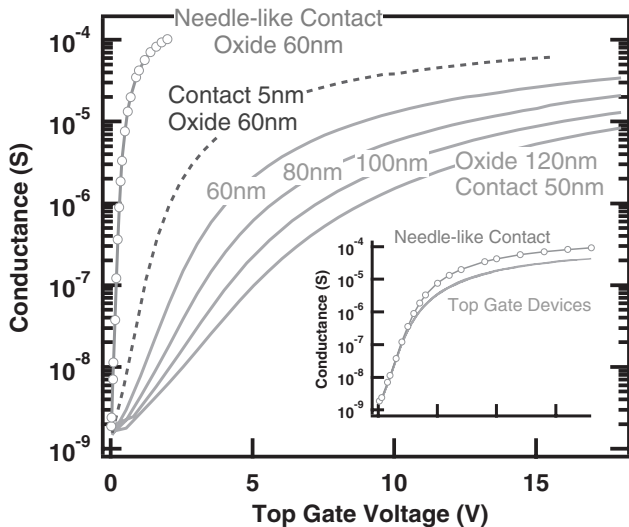


Fig. 6. (Color online) Calculated conductance versus gate voltage for top gate devices (device geometry as in Fig. 5(a)) with various gate oxide thicknesses (i.e. nanotube-top gate distance) and contact thickness of 50 nm (*solid blue lines*) and 5 nm (*dashed blue line*). The needle-like contact model is included for comparison (*solid red line*). The inset shows that the conductance of all top gate devices can be scaled to a single curve

oxide thickness, fixed. Due to the sharper edge of the source contact a larger electric field can be achieved at a given top gate voltage and the device turns on at lower gate voltage. This is in contrast to a conventional transistor which turns on due to the modulation of charge carriers in the channel. For the needle-like contact geometry the improvement due to field focusing at the contact is dramatic as shown in Fig. 6. Thus the contact plays a key role for the transport characteristics of a SB-CNFET. Its precise control is crucial to fabricate devices with excellent and reproducible performance.

The transport curves for top gate devices can be scaled to a single functional form as demonstrated in the inset of Fig. 6. Even the conductance of the needle-like contact CNFET with a very different geometry can be scaled onto the other curves within the turn-on regime. In conclusion, the main effect of a specific contact geometry is to scale the gate voltage range. A quantitative study of scaling issues will be given in Sect. 2.4. Here we note that for problems which require an accurate treatment of the potential from charge on the NT, e.g. to include dopants on the NT or dipoles at the NT-metal contact, the idealized needle-like contact model is more appropriate. A comparison with experiments is obtained by scaling the gate voltage range.

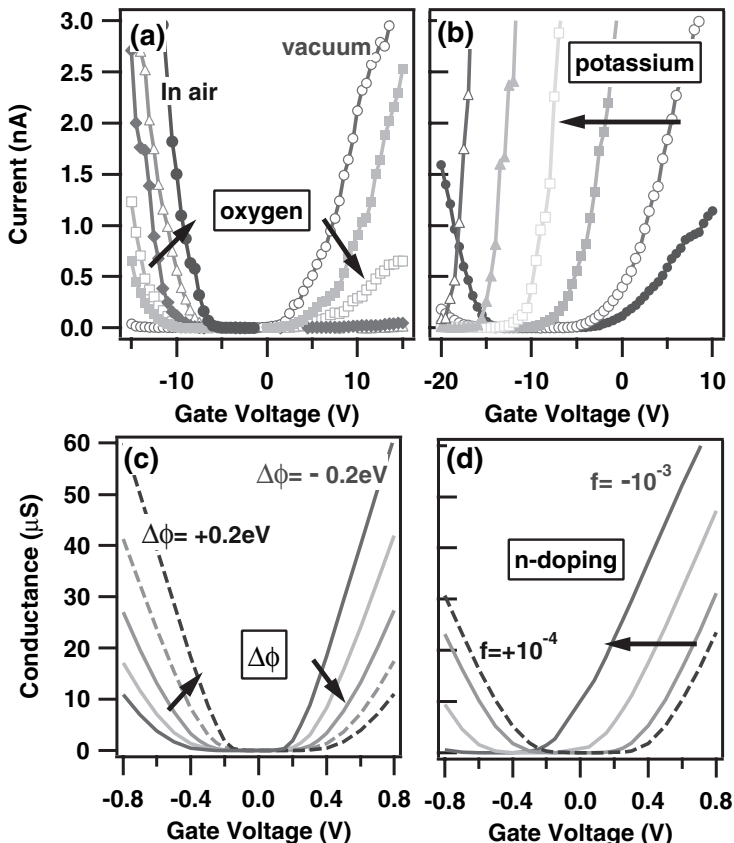


Fig. 7. (Color online) Effect of gas adsorption and doping on a SB-CNFET. (a) and (b) are experimental data and (c) and (d) calculations within the needle-like contact model. In (a) the vacuum annealed (n-type) FET (red, open circles) has been exposed to increasing amounts of oxygen until the ambient is reached (blue, filled circles). In (b) the curves from right to left correspond to increasing deposited amounts of potassium. In (c) the work function difference $\Delta\phi$ between metal and NT is changed from -0.2 eV (solid red line) to $+0.2\text{ eV}$ (dashed blue line) in steps of $+0.1\text{ eV}$. In (d) the doping atomic fraction is from left to right n-type 10^{-3} (red), 5×10^{-4} (orange), and 10^{-4} (green), and p-type 10^{-4} (dashed blue line), respectively. More details can be found in [11] and [18].

2.3 Effect of Gas Adsorption

A longstanding puzzle has been the effect of gas adsorption on the nanotube electronic structure. It has been proposed that e.g. oxygen adsorption leads to doping of the nanotube [29, 30]. However, as shown in Fig. 7(a), the effect of oxygen on the transport properties of a CNFET is a reversible transition from p-type (devices prepared in air) to n-type after annealing the transistor

in vacuum [18]. In contrast, the deposition of an n-type dopant atom such as potassium, Fig. 7(b), shifts the transfer characteristics with respect to the gate voltage. It is known that the work function of a metal surface is altered significantly upon the adsorption of gases due to the formation of interface dipoles. Thus the local work function of the metal electrode can be modified considerably by the adsorption of oxygen at the contacts. If the work function of the metal electrode changes the line-up of the metal Fermi energy with the NT bands will shift [17]. (Note that this is unique for the contact between a metal and a nanotube. In a conventional, planar semiconductor device the position of the Fermi energy is pinned by metal-induced gap states [16].)

Within the needle-like contact model it is straight forward to compare the effect of doping with that of a shift in the line-up, i.e. a reduction of the SB to the conduction band and an increase of the SB to the valence band or vice versa. The results of such calculations are shown in Figs. 7(c) and (d). Apart from the gate voltage scale there is a compelling agreement between the calculation and the experimental data. While n-type doping shifts the transport curves to more negative gate voltages, a change in the work function promotes either the p- or the n-type branch of conduction and reduces the other but the minimum conductance occurs at zero gate voltage for all line-ups.

The characteristic modifications of the conductance in the two cases can be explained based on the band bending at the NT-metal contact. Figure 8(a) shows the diagram for an increased metal work function. In this case, a lower SB forms to the valence band of the NT than to the conduction band. At zero gate voltage, there is a negligibly small current due to thermionic emission

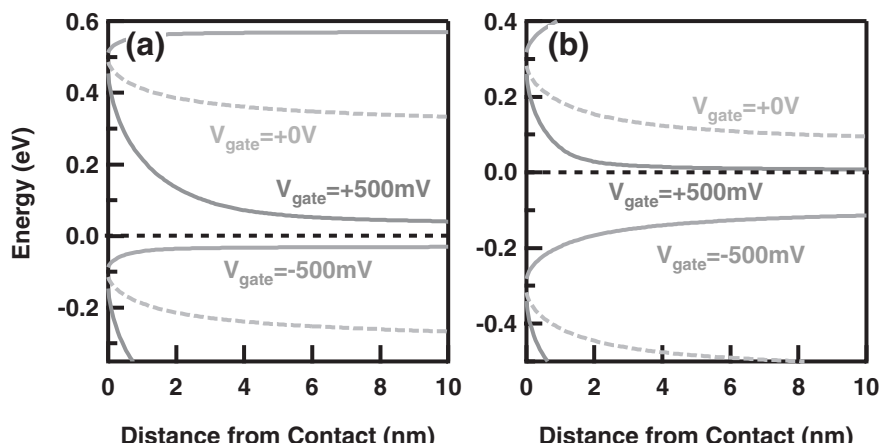


Fig. 8. (Color online) Calculated NT band bending at gate voltages of $V_g = +500$ mV, 0 mV, and -500 mV in the case of (a) a metal work function increase of $\Delta\phi = +0.2$ eV and (b) n-type uniform doping of the NT with a fraction of 5×10^{-4}

into the valence band. Its magnitude is equal to the off-conductance for a midgap line-up as the thermal barrier is still half the NT bandgap, i.e. 0.3 eV in our calculation. Thus there is no change of the conductance at $V_g = 0$ (cf. Fig. 7(c)). When a negative gate voltage is applied the conductance increases exponentially due to a thermal hole current above the reduced barrier to the valence band. At larger negative gate voltages holes can also tunnel into the NT valence band. However, the SB for electrons is much larger in this case than for a midgap line-up which lowers the tunneling probability according to (4). The achievable conductance at positive gate voltages due to electron tunneling is thus reduced (see Fig. 7(c)).

For a uniformly n-type doped NT at midgap line-up, as shown in Fig. 8(b) for comparison, there is a considerable band bending even at zero gate voltage and correspondingly the conductance increases compared to an undoped NT (Fig. 7(d)). Upon a positive gate voltage the SB to the conduction band can be further thinned and electron tunneling is promoted. However, larger negative gate voltages are needed compared to the undoped NT to achieve the same band bending of the valence band and accordingly for the same amount of hole current. Hence the entire conductance curve shifts to the left upon n-type doping and analogously to the right for p-type doping.

The change of the local work function difference between a metal electrode and a carbon nanotube that we have assumed above has been observed directly in experiments by scanning probe methods [31]. Because the work function depends sensitively on the local environment one cannot simply take the metal and nanotube work function from a textbook and compute the band line-up. A microscopic picture of the creation of oxygen dipoles and the charge rearrangement at the interface is crucial for a quantitative understanding [31].

The controlled transition from p- to n-type transistors by gas adsorption and doping has been used to fabricate the first logic gates from single carbon nanotubes [8]. Figure 9(a) shows the device geometry of an inverter created from a single carbon nanotube which lies above three metal contacts. After the first preparation step in air both transistors display p-type transport. The right CNFET was then protected by a photo resist and subsequent potassium doping turned only the unprotected device to an n-type FET. By applying the in-voltage to the common back gate of the two CNFETs and taking the out-voltage at the central metal contact the device operates as a voltage inverter (see Fig. 9(b) for a sketch of the electronic circuit). The measured device characteristic, Fig. 9(c), demonstrates the voltage inversion and the achievement of a voltage gain , i.e. a ratio of output to input voltage larger than one. This is an essential prerequisite to use a logic gate in a real circuit consisting of many gates.

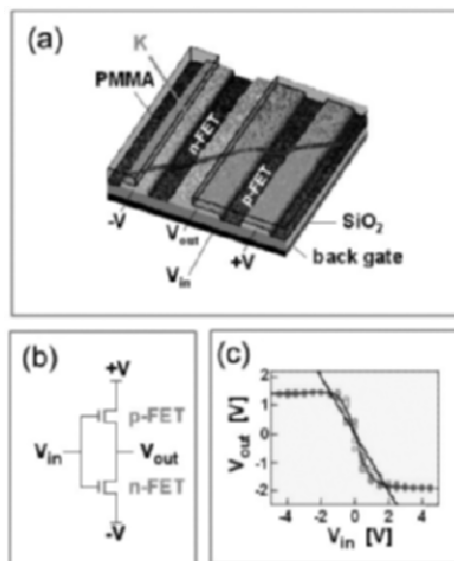


Fig. 9. (*Color online*) Inverter created from a single carbon nanotube [8]. (a) shows a 3D SEM image of the device in which the blue line marks the single-wall carbon nanotube. Three metal electrodes contact the carbon nanotube creating two transistors. The right transistor is protected by a resist (PMMA, shown by transparent blue boxes) from potassium (**K**) doping and remains p-type (as prepared in air) while the left changes to n-type upon doping. The bias voltage is applied to the outer metal contacts while the out-voltage is taken from the central contact. The in-voltage is applied to the back gate. (b) is a schematic plot of the electronic circuit of an inverter created from an n- and p-type FET. In (c) the measured voltage characteristic of the carbon nanotube inverter is displayed

2.4 Scaling of the SB-CNFET Performance

In the last sections, we have demonstrated that the SB model explains transistor action in CNFETs and solves the puzzle of gas adsorption. We concluded that the contact geometry plays a key role for turn-on performance at low bias voltage. In this section we consider the consequences of operation as a SB transistor for device performance, in particular the scaling with reduced device size. An understanding of the scaling relations is a basic ingredient to judge the technological potential of carbon nanotube transistors. The first extrapolation of the performance [13] has been based on CNFETs with fairly thick (bottom) oxides (≥ 20 nm). From that data it seemed that a subthreshold slope, $S = (d \log I/dV_g)^{-1}$ [32], below 100 meV/decade should be possible at ultra-thin oxides between 5 and 2 nm. Surprisingly, the actual devices did not fulfill this prediction. Instead a levelling off of S at low oxide thickness was observed [14].

To study the turn-on performance we need to extend our model to finite drain voltages. At finite bias voltage, a Fermi energy cannot be defined for the NT anymore and a non-equilibrium model such as the Greens function method described in [33] (or in Chaps. 4 to 6) must in principle be applied. Therefore, it may seem surprising at first that an adequate model of the turn-on regime, i.e. as the device is turned from the off-state (low current) to the on-state (high current), can be developed neglecting charge on the NT as shown below. The key observation is that the current is limited by the transmission through the SB and thus by the electrostatic potential in the vicinity of the contact. The main effect of charge on the NT, in contrast, is to change the electrostatic potential within the channel. In the turn-on regime, the channel limits the current only when there is negligible charge on the NT. (In that case the current is due to thermionic emission and not tunneling.) Therefore, we can neglect charge on the NT if we are interested only in the current through the device in the off-state and turn-on regime. However, in the on-state, i.e. as the SB becomes transparent, the non-equilibrium charge on the NT and the capacitance of the gate to NT may become important for the magnitude of the on-current and cannot be neglected [34].

Neglecting charge on the NT simplifies the electrostatics significantly. In particular, we can reduce the problem to solving the Laplace equation in two dimensions fixing the boundary conditions by the given drain and gate voltage [35]. From the electrostatic potential we can calculate the transmission and the current as in the previous sections. The electronic structure of the NT is treated as before.

For the calculation we choose the regime of current saturation , i.e. $V_d = V_g$ shown in Fig. 10, where the barrier at the drain contact vanishes. In this

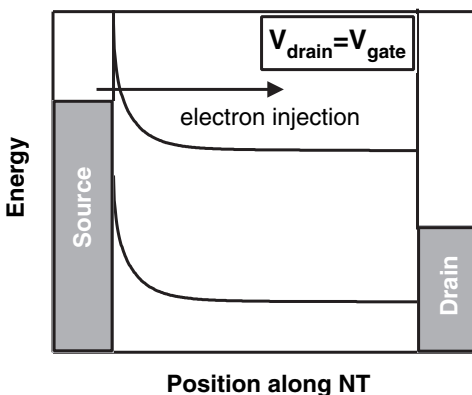


Fig. 10. Band diagram of a SB-CNFET in the regime of current saturation, i.e. if drain and gate voltage are equal (the source is held at zero potential). All electrons injected at the source can be collected at the drain contact where they face no potential barrier

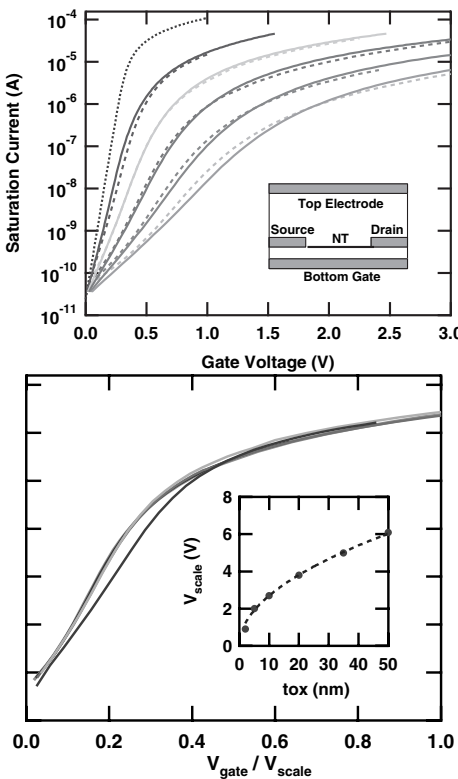


Fig. 11. (Color online) Calculated transfer characteristics for bottom gate SB-CNFETs at midgap with varied oxide thickness. Left panel shows the full calculations (*solid lines*) for $t_{\text{ox}} = 35, 20, 10, 5$ and 2 nm , from right to left and the thermal limit (*dotted black line*). The *dashed lines* are calculations with the analytic model described in the text. The inset displays the bottom gate geometry used in the calculation. The right panel demonstrates the scaling of all curves to a single unique function except for the ultra-thin 2 nm oxide. In the inset the extracted scaling voltage has been plotted versus oxide thickness. A square-root fit is indicated by the dashed line in the inset

case there is only a voltage drop and an electric field at the source contact held at $V_s = 0$. Thus all charge carriers injected at the source are collected at the drain and the current saturates. The scaling relations of the turn-on performance are unaffected by this choice. Experimentally the independence of the subthreshold slope on the applied drain voltage has been confirmed [13, 14]. We use the saturation regime in the following to derive an analytic model and to give explicit scaling relations for the turn-on performance.

The left panel of Fig. 11 displays the results obtained for bottom gate CNFETs with different oxide thicknesses t_{ox} . A continuous improvement of the subthreshold slope with decreasing t_{ox} is observed. However, even for an

ultra-thin oxide of 2 nm and with an ideal sharp corner contact as in our calculation, the thermal limit of a conventional transistor is not reached. In a similar way as in the low bias voltage limit (cf. Fig. 6) we can scale the gate voltage for every device from the left panel of Fig. 11 to find a single functional form of the saturation current, shown in the right panel. Deviations are seen only for $t_{\text{ox}} = 2$ nm. The extracted scaling gate voltages which are a measure of the required turn-on voltage are plotted in the inset of the right panel of Fig. 11 as a function of t_{ox} . A square-root fit (dashed line in the inset) gives an excellent description.

In order to understand whether the square root behavior of the turn-on voltage is of general validity we consider a simple analytic model. Note, that only the electrostatic potential close to the source (metal) contact is needed to evaluate the saturation current. While there is no analytic solution in the bottom gate device geometry, we can solve the electrostatic boundary problem for a device with two planar gates both at a distance t_{ox} from an infinitely thin sheet contact [36]. The potential as a function of distance z from the contact is $V(z) = 2V_g\pi^{-1/2}(z/t_{\text{ox}})^{1/2}$. In the thick oxide limit we can further replace the lower integration boundary, $\Delta - eV_d$, by $-\infty$. We can directly insert the potential into (3) and (4) and solve for the saturation current:

$$I_{\text{sat}} = \frac{4e\Delta}{h} H \left(\frac{V_g}{V_{\text{scale}}^{\text{dg}}} , \frac{\Delta}{kT} \right), \quad (5)$$

where $H(x, y)$ is

$$H(x, y) = \int_{-\infty}^{\infty} \frac{\exp(-h(s)/x^2)}{1 + \exp(sy)} ds \quad (6)$$

and $h(s)$ is

$$h(s) = \int_{\max(0, -1-s)}^{1-s} t [1 - (s+t)^2]^{1/2} dt. \quad (7)$$

The “scaling voltage” for this double-gate device is

$$V_{\text{scale}}^{\text{dg}} = \left(\frac{2\pi\Delta^3}{3be^2V_\pi} \right)^{1/2} t_{\text{ox}}^{1/2}. \quad (8)$$

Since the saturation current depends only on $V_g/V_{\text{scale}}^{\text{dg}}$ a change of t_{ox} leads merely to a scaling of the gate voltage. With a single empirical parameter we can use this idealized model to reproduce the results for the bottom gate devices. If we choose the scaling voltage for the bottom gate geometry as $V_{\text{scale}}^{\text{bg}} = 2.2 V_{\text{scale}}^{\text{dg}}$ the saturation current can be calculated for all t_{ox} as shown in the left panel of Fig. 11 by dashed lines. An excellent agreement is achieved within the whole range of oxide thicknesses. Thus the scaling with t_{ox} of the ideal double gate device applies also for the bottom gate device.

From (8) we conclude that the turn-on voltage scales as the square-root of the oxide thickness which is in agreement with our previous empirical finding. By differentiating the saturation current with respect to the gate voltage we obtain the subthreshold slope:

$$S = \left(\frac{d \log I_{\text{sat}}}{d V_g} \right)^{-1} = V_{\text{scale}} F \left(\frac{V_g}{V_{\text{scale}}^{\text{dg}}} , \frac{\Delta}{kT} \right) \quad (9)$$

where

$$F(x, y) = \ln 10 \frac{H(x, y)}{\partial H(x, y)/\partial x}. \quad (10)$$

The subthreshold slope is evaluated at its minimum value in the turn-on regime, i.e. at a fixed V_g/V_{scale} . Thus the subthreshold slope scales as V_{scale} which is as the square-root of t_{ox} .

In Fig. 12 the inverse subthreshold slope is plotted versus the inverse oxide thickness. For the experimental data a levelling off is seen as the oxide thickness decreases. The performance does not approach the thermal limit of a conventional transistor, a value of about 60 meV/decade. Results for calculated bottom gate devices show a very similar qualitative behavior, however, at lower values of S , i.e. better performance. (The better performance for the calculated devices is probably due to the sharper contact geometry. Experimentally, the contact geometry cannot be characterized accurately on the nanometer scale.) The crucial impact of the contact geometry on device performance is emphasized by a calculation for a planar double gate device with contacts that are only as thick as the NT diameter, i.e. 1.4 nm. The dependence of the subthreshold slope on t_{ox} shows a similar functional form, however, at significantly enhanced performance. For infinitely thin oxides, the subthreshold slope must saturate at the thermal limit. We can thus use a fitting function $S = [\alpha t_{\text{ox}} + (kT \ln 10)^2]^{1/2}$, with α a fitting parameter which depends on the specific contact geometry. Both the experiment and the calculations in the two device geometries can be fitted with this interpolation function as shown in Fig. 12.

From our scaling analysis we conclude that a precise control of the NT-metal contact geometry is essential for SB-CNFETs with high turn-on performance and reproducible properties. The creation of a sharp contact geometry can be much more effective for superior performance than reducing the oxide thickness for a given device design.

For a conventional transistor the subthreshold slope decreases linearly at low temperatures. However, from (9) we find a decrease which levels off to a non-vanishing value at zero temperature as shown in Fig. 13. This unusual low temperature behavior of S has been observed experimentally [13] and provides an experimental way to distinguish a SB-CNFET from a CNFET with ohmic contacts. The evaluation of the temperature dependence of S can also be used to determine the height of the SB in a given device [37].

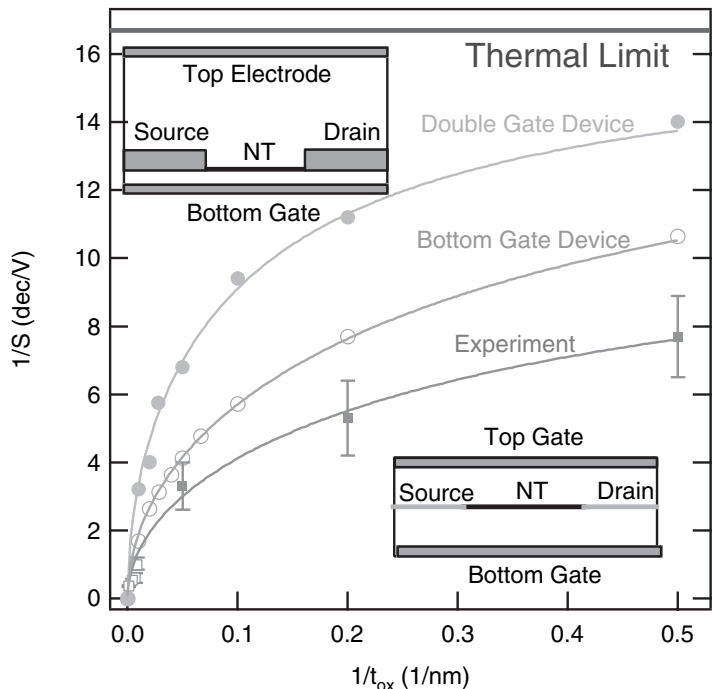


Fig. 12. (Color online) Inverse subthreshold slope S as a function of the inverse oxide thickness t_{ox} . Solid curves are fitted as described in text. Bottom red curve is experiment – open red squares are data from previous work, filled red squares are from our work [14]. Data at $t_{\text{ox}} = 2 \text{ nm}$ and 5 nm represent averages over several devices. For $t_{\text{ox}} = 20 \text{ nm}$ our result agrees with previous reports [4]. Upper two curves are calculated for $V_d = V_g$. The upper left inset shows the bottom gate device geometry (open green circles) while the lower right inset shows the double gate device (filled orange circles)

2.5 Scaling of the Drain Voltage

The scaling relations for the turn-on performance of a SB-CNFET have important consequences for the operation of such devices, especially when ultra-thin gate oxides are used. Because the turn-on voltage decreases as the square-root of t_{ox} it is below 1 V for an oxide thickness of 5 nm. This voltage is comparable to typically applied drain voltages in the operation regime of a transistor. Both the SB at the source and at the drain contact are therefore affected and charge carriers can be injected at both contacts at the same time.

In a typical experiment, the source contact is held at zero potential and the bias (drain) voltage is applied to the drain contact. In this case there is a voltage drop of V_g at the source contact and of $V_g - V_d$ at the drain contact. Figure 14(a) displays the situation of a symmetric potential drop at

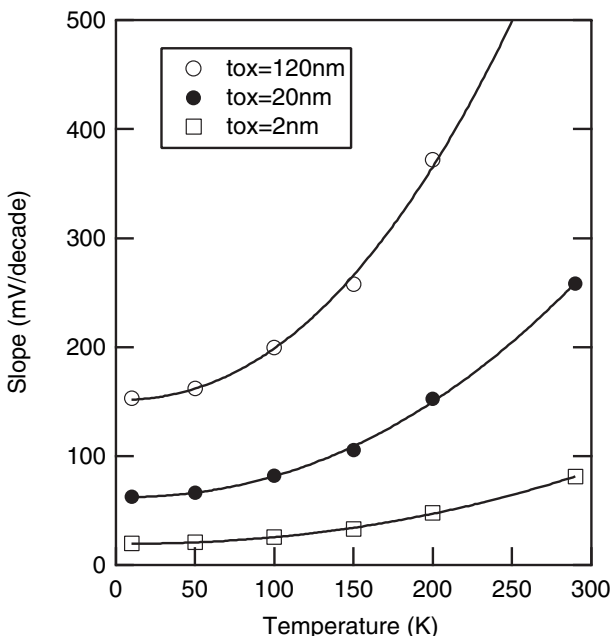


Fig. 13. Calculated temperature dependence of the subthreshold slope versus temperature for bottom gate devices with oxide thicknesses of $t_{\text{ox}} = 2, 20$, and 120 nm. This temperature dependence is in good agreement with experimental data [13]

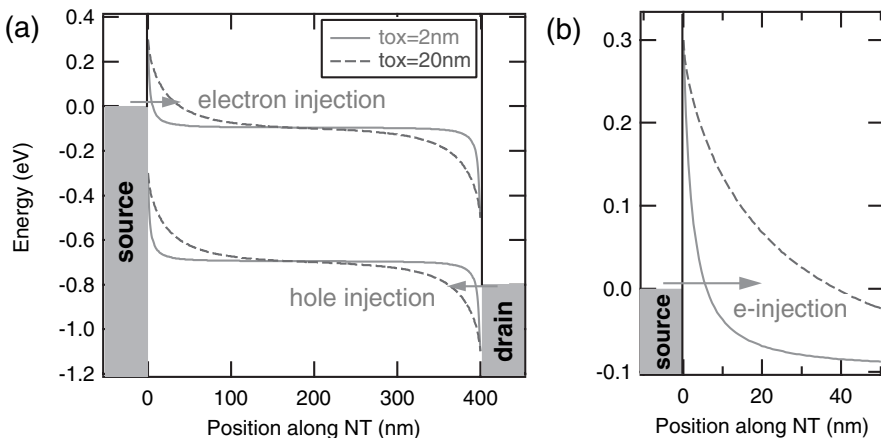


Fig. 14. (Color online) Band diagrams for midgap SB-CNFETs with $t_{\text{ox}} = 2$ nm and 20 nm for a symmetric potential drop at source and drain contacts, i.e. for $V_g = V_d/2 = 0.4$ V (transistor off-state). (a) shows the bands for the full length of the device with arrows indicating tunneling of electrons at the source and tunneling of holes at the drain contact. (b) gives a close-up view at the source contact. Note, that the SB is too wide for the device with $t_{\text{ox}} = 20$ nm to allow a significant tunneling current.

the source and drain contact, i.e. for $V_g = V_d/2$, and for midgap SB-CNFETs with oxide thicknesses of 20 nm and 2 nm. At the source contact, electrons can be injected into the NT conduction band while holes can tunnel into the valence band from the drain contact. For an oxide thickness of 20 nm, however, the barriers are very wide at the contacts and the tunneling current is negligibly small (see Fig. 14(b)). For an ultra-thin oxide of 2 nm, on the other hand, the barriers are only a few nanometers wide and a significant current flows which consists of equal electron and hole contributions injected at the source and drain contact, respectively.

A symmetric potential drop at source and drain contact as in Fig. 14(a) corresponds to the minimum device current (the off-state of the transistor) for a given drain voltage. The full transfer characteristics (I vs. V_g) are shown in Fig. 15(a) to (d) for both devices at positive and negative drain voltages. A midgap line-up has been assumed which leads to symmetric, ambipolar transport curves. The right branch of the transfer characteristics is dominated by electron injection while the left branch results from hole injection. In Fig. 15(a) the electron and hole current have been included explicitly for $V_d = -0.8$ V. At the minimum of the total current there are equal hole and electron contributions. At general gate voltages, either holes or electrons dominate the current and we can consider the other type as minority charge carriers.

In Fig. 15 we observe a shift of the minimum current with V_d according to the relation $V_g^{\min} = V_d/2$. (Thus at negative V_d , (a) and (c), the curves shift to the left with increased $|V_d|$, and at positive V_d , (b) and (d), they shift to the right.) In addition, the off-current increases with V_d . For the CNFET with a moderate oxide thickness of 20 nm, Fig. 15(c) and (d), the change of the transfer curves with V_d is rather small up to $V_d = 0.8$ V and there is only a small increase of the off-current. However, for a device with an ultra-thin oxide ($t_{\text{ox}} = 2$ nm, Fig. 15(a) and (b)) the turn-on voltage is much smaller and thus the increase of the off-current is dramatic. Even at a low drain voltage of $V_d = 0.4$ V the on/off ratio, $I^{\text{on}}/I^{\text{off}}$, is only three orders of magnitude and at larger drain voltages the device becomes inoperable as a transistor due to the decreasing on/off ratio. The calculated transfer characteristics displayed in Fig. 15 are in excellent agreement with experimental data. Both the shift of the transport curves with drain voltage and the exponential increase of the off-current have been confirmed experimentally [38].

We can apply the analytic model introduced in the previous section for the saturation current to calculate the off-current and derive explicit scaling relations with t_{ox} and V_d . From a comparison of the band diagrams in Fig. 14(a) and Fig. 10 we observe that the electron and the hole currents in the off-state correspond to the saturation current at a voltage of $V_g = V_d/2$. The off-current which consists of an equal hole and electron current is then given by:

$$I^{\text{off}}(V_d) = 2 I_{\text{sat}}(V_g = V_d/2) , \quad (11)$$

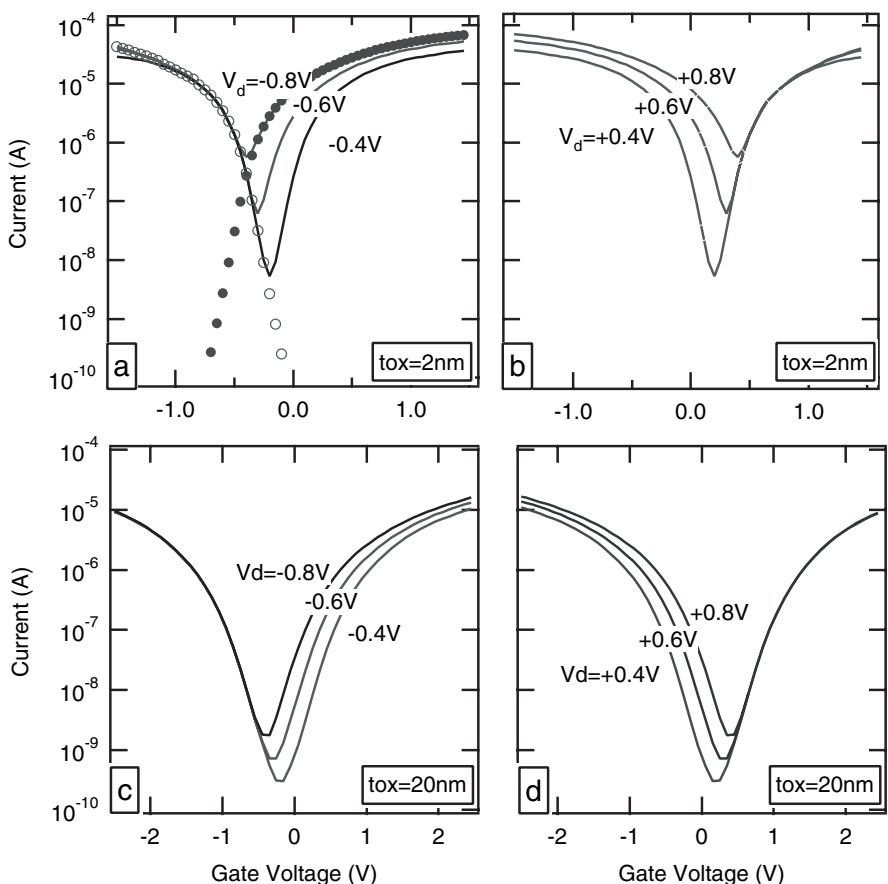


Fig. 15. Calculated transfer characteristics (I vs. V_g) at positive and negative drain voltages. (a) and (b) show the case of a bottom oxide of $t_{ox} = 2$ nm and (c) and (d) the case of $t_{ox} = 20$ nm. In (a) the filled and open circles denote the electron and hole contribution to the current for $V_d = -0.8$ V, respectively

and we can use (5) to analyze the scaling of the off-current. From (11) and Fig. 11(b) it is apparent that the off-current must also increase exponentially with the applied drain voltage.

In Fig. 16 we have plotted the off-current as a function of the applied drain voltage for bottom gate CNFETs with $t_{ox} = 2$ and 20 nm, respectively. If we require a minimum on/off ratio for the transistor we obtain a square-root scaling as t_{ox} for the maximum allowed drain voltage. Numerically, we have determined the maximum drain voltage V_d for an on/off ratio of 10^4 or better and typical NT bandgaps ($0.3\text{ eV} \leq E_g \leq 1.2\text{ eV}$) to $V_d \sim \{(E_g[\text{eV}])^{1.3} - 0.2\} \sqrt{t_{ox}[\text{nm}]} \text{ V}$ for the simulated bottom-gate devices with midgap line-up. For CNFETs with ultra-thin oxides this constraint

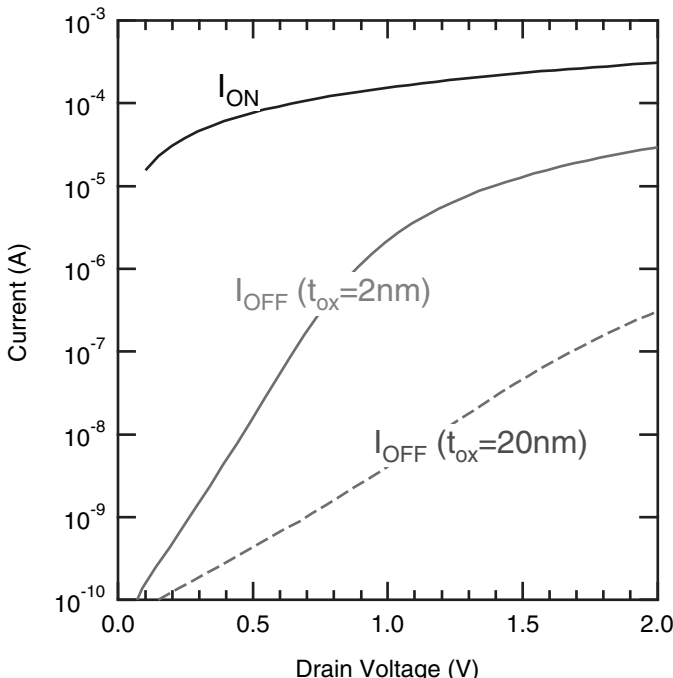


Fig. 16. (Color online) Calculated off-currents ($V_g = V_d/2$) versus drain voltage for oxide thicknesses of 2 nm (solid red curve) and 20 nm (dashed blue curve). The on-current (black line) depends linearly on the drain voltage

limits the achievable on-current as it is proportional to the maximum drain voltage. Using NTs with larger bandgaps, i.e. smaller diameters, is one obvious option to achieve higher drain voltages.

The injection of minority charge carriers limits the device performance. It is important to note that the effect is present even for CNFETs with (nearly) ohmic contacts [6, 39] and can be large if the bandgap of the NT is small, i.e. up to about 0.4 eV. If there is an ohmic contact e.g. to the valence band there will be a SB with a height of the bandgap to the conduction band. Thus for a device with an ultra-thin oxide, which is required for high performance, there will be electron tunneling into the conduction band in the off-state. This limits the off-current in the same way as for a midgap ambipolar CNFET.

A possible way to solve this problem is to fabricate a device with an asymmetric gating of the source and drain contact, e.g. by a variation of the oxide thickness [39, 40]. Such a device geometry allows to suppress the injection of minority charge carriers at the drain contact. Consequently, there is no exponential increase of the off-current with drain voltage. In addition, an asymmetric SB-CNFET can be operated either as an p- or n-type transistor

with the same (excellent) performance which is determined by the source contact geometry [39].

2.6 Light-Emission from a SB-CNFET

While the injection of minority charge carriers at the drain contact can make a CNFET inoperable as a transistor it allows to inject holes and electrons into the NT at the same time. By operating the CNFET in the off-state, i.e. choosing the gate and drain voltages according to $V_g = V_d/2$, we can achieve equal amounts of hole and electron current in the nanotube as shown in Fig. 14(a). If the applied drain voltage is chosen above the turn-on voltage of the transistor high electron and hole currents (exactly half of the off-current shown in Fig. 16) are achieved. Electrons which are injected at the source contact can recombine with holes injected at the drain contact with the emission of a photon. This is illustrated in Fig. 17(a). Experimentally, Misewich et al. have recently demonstrated that biasing a CNFET in the off-state indeed leads to the emission of polarized infra-red light [15].

Within our transport model of a SB-CNFET we can calculate the observed bias and gate voltage dependence of light emission from a NT if we assume an energy independent recombination probability. Figure 18 shows a calculation for a CNFET with an ultra-thin oxide of $t_{\text{ox}} = 2 \text{ nm}$. (The transport characteristics of this device are given in Figs. 15 and 16.) We assume two different models for the recombination of electrons and holes with emission of a photon. The first is efficient recombination, i.e. every electron-hole pair leads to the emission of a photon, and the number of emitted photons is proportional to the minimum of the hole and electron current.

For inefficient recombination, on the other hand, there is only a finite (small) probability of an electron and a hole to recombine under photon emission. In that case the number of photons is proportional to the number of electrons (the electron current) and the number of recombination attempts (given by the number of holes, i.e. the hole current). Thus the number of emitted photons is proportional to the product of hole and electron current.

Both models lead to an exponential increase of the number of emitted photons with applied drain voltage (at the maximum value for $V_g = V_d/2$). This follows naturally from the variation of the off-current because the voltage requirement for maximum light emission is identical to the off-state. Thus the maximum number of photons is proportional to $I^{\text{off}}(V_d)$ or $[I^{\text{off}}(V_d)]^2$ for efficient or inefficient recombination, respectively. Consequently, Fig. 16 can be viewed as the drain voltage dependence of the maximum photon emission from a CNFET. The SB transport model of the CNFET describes the gate and drain voltage dependence of light emission well and can be used to guide the scaling of these optoelectronic devices. However, it cannot be used to determine which mechanism of electron-hole recombination prevails [15].

Recently, the recombination yield per electron-hole pair has been determined to 10^{-6} to 10^{-7} depending on NT length by measurements of the

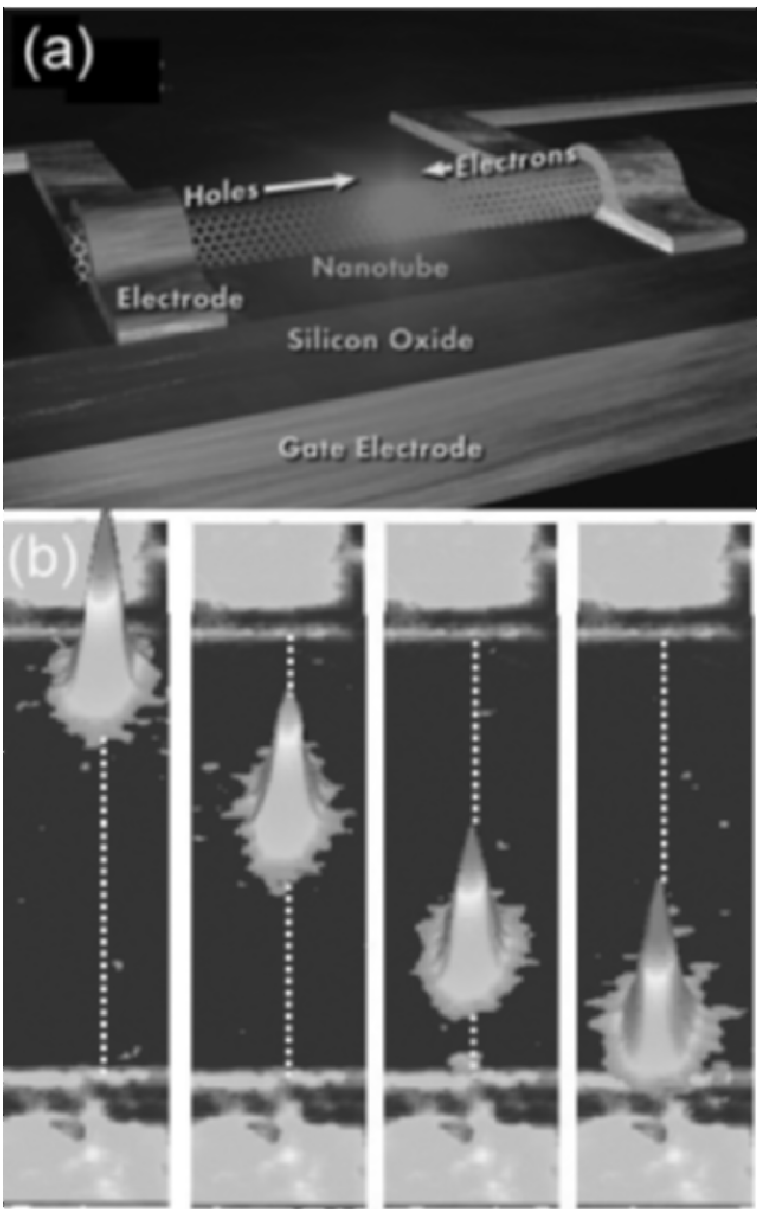


Fig. 17. (Color online) Schematic plot of a light-emitting device from a single carbon nanotube. (a) shows the device geometry and illustrates how electrons and holes are injected from the source and drain contact, respectively. The recombination via exciton intermediate states leads to the emission of infrared light. (b) For a CNFET with a long NT channel (about $50\mu\text{m}$) one can spatially resolve the regime of light emission due to electron-hole recombination [41]. The position of the spot depends on the voltage gating [41]

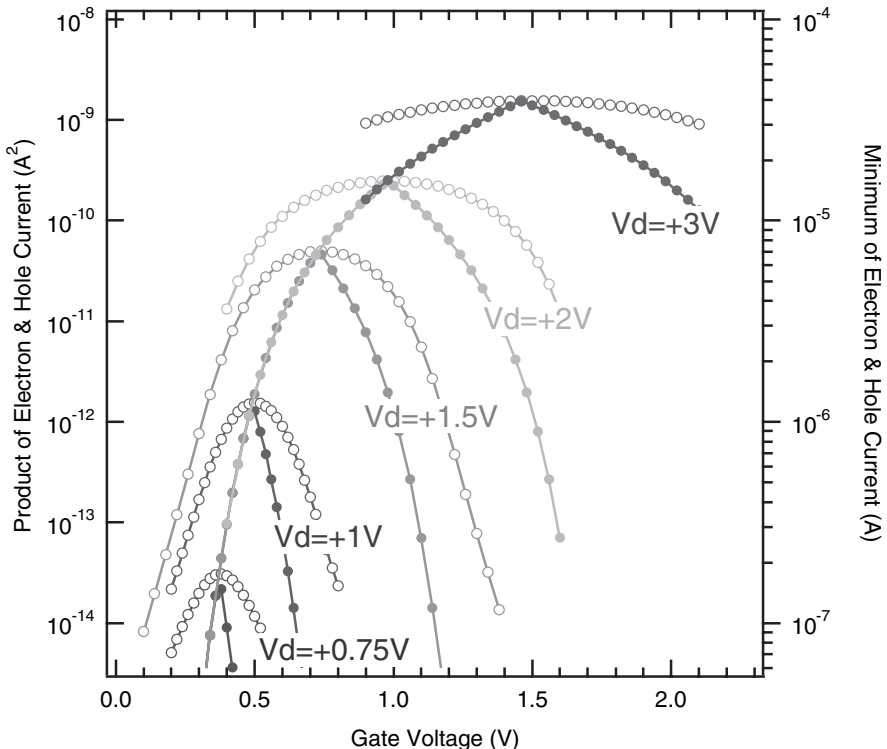


Fig. 18. (*Color online*) Calculated gate voltage dependence of the number of emitted photons from a CNFET with $t_{\text{ox}} = 2 \text{ nm}$ at different drain voltage (compare Fig. 15(a) and (b) for electrical characteristics). Open circles correspond to the inefficient recombination model (product of electron and hole current, left axis) while filled circles denote the efficient recombination model (minimum of electron and hole current, right axis)

spectrum of the light emitted from a CNFET [42]. Due to the confinement of electron-hole pairs on the cylindrical nanotube the Coulomb interaction is very strong resulting in excitons with large binding energies. Perebeinos et al. have used a tight-binding model to derive explicit scaling laws for the exciton binding energies with nanotube radius, effective mass, and dielectric constant of the oxide [43]. Concerning the recombination mechanism, these calculations suggest that the direct interband transition is weakened and the transition via an exciton state dominates light-emission. Thus the measured photon energy is determined by the bandgap reduced by the exciton binding energy which can be up to several 100 meV. Such large binding energies have been confirmed by very accurate but computationally intensive *ab-initio* calculations of excitons performed for selected carbon nanotubes [44, 45].

By spatially resolving the light emission from a long channel device (about 50 μm), Freitag et al. [41] have very recently demonstrated that electron-hole recombination occurs only in a small portion of the NT (see Fig. 17(b)). This novel approach to map the ambipolar domain of a CNFET is very promising for future studies as it gives complementary information to existing transport data. In combination with simulations a more detailed understanding of transistor action in one-dimensional devices may be possible.

3 Conclusions and Outlook

Carbon nanotube electronics remains a very promising route to solve future down-scaling problems of conventional silicon technology. Field-effect transistors with performance that is competitive to state-of-the-art devices [4–6] and even logic gates from single nanotubes [8] have been demonstrated. However, the physics of carbon nanotube electronic devices can be quite different from conventional ones. In particular, carbon nanotubes show ballistic transport over typical device length [6, 7], they have electronic properties linked to their structure [1], and their cylindrical quasi-one-dimensional structure leads to unusual electrostatics e.g. weak screening and no Fermi level pinning [17, 28].

For transistor action in CNFETs Schottky barriers at the metal-nanotube interface play a crucial role [9–13]. Already semiclassical transport models explain key observations of CNFETs such as the effect of gas adsorption [11]. Consequences are the importance of contact geometry for high performance, unusual scaling relations as the device size is reduced [14, 34], and leakage currents due to injection of minority charge carriers at the drain contact [38]. The device physics of CNFETs allows performance control by new parameters e.g. by the material of the metal electrodes which determines the SB height. On the other hand, limitations unknown in conventional transistors occur [34, 38] and require new device designs [39, 40]. To eliminate SBs at the metal-nanotube contacts is a key challenge for future research. For small bandgap nanotubes Javey et al. have recently achieved negligible small barriers by choosing Palladium or Aluminum electrodes [6, 21]. However, the understanding of the favorable contacts is still limited and remains an important issue for further investigations. Controlled doping of the contacts [22] or new device designs [23, 39, 40] may provide a different route to enhanced performance of CNFETs.

Due to their unique optical properties such as equal effective masses of electrons and holes and tunable bandgap carbon nanotubes can be utilized in novel nanoscale optoelectronic devices such as light emitters [15] or photo detectors [24]. We have shown that light emission can be observed from a CNFET by an appropriate choice of gate and drain voltages due to the simultaneous injection of electrons and holes [15]. From the transport models developed for CNFETs we can explain the experimental data and estimate the optimization potential by future down-scaling of the devices. Modelling

of the electron-hole interaction, on the other hand, demonstrates that light emission occurs predominantly via the formation of excitons which can have large binding energies due to the quasi-1D electrostatics [43–45]. Very recent studies have even allowed to spatially resolve the position of light emission for long channel devices [41]. Future research along those lines will provide a wealth of complementary information on transport in 1D devices.

Carbon nanotube electronics still faces a number of serious problems such as the fabrication of large scale arrays of devices before becoming a serious technological alternative to silicon devices. However, considering the short time CNFETs have been investigated the achieved results are very impressive and fuel the hope of powerful carbon nanotube based nanoelectronics. For example, the possibility to use the same carbon nanotube transistor as an electronic or optoelectronic device depending on the applied voltages opens the door to new applications.

Acknowledgements

One of us (S.H.) thanks the Deutsche Forschungsgemeinschaft and the Stifterverband für die Deutsche Wissenschaft for financial support.

References

1. M. S. Dresselhaus, G. Dresselhaus, and Ph. Avouris: *Carbon nanotubes: synthesis, structure, properties, and applications*, Springer-Verlag, Berlin 2001.
2. S. J. Tans, A. Verschueren, C. Dekker: Room-temperature transistor based on a single carbon nanotube, *Nature (London)* **393**, 49 (1998).
3. R. Martel, T. Schmidt, H. R. Shea, T. Hertel, Ph. Avouris: Single- and multi-wall carbon nanotube transistors, *Appl. Phys. Lett.* **73**, 2447 (1998).
4. S. J. Wind, J. Appenzeller, R. Martel, V. Derycke, Ph. Avouris: Fabrication and electrical characterization of top gate single-wall carbon nanotube field-effect transistors, *Appl. Phys. Lett.* **80**, 3817 (2002).
5. A. Javey, H. Kim, M. Brink, Q. Wang, A. Ural, J. Guo, P. McIntyre, P. McEuen, M. Lundstrom, H. Dai: High- κ dielectrics for advanced carbon-nanotube transistors and logic gates, *Nature Materials* **1**, 241 (2002).
6. A. Javey, J. Guo, Q. Wang, M. Lundstrom, H. Dai: Ballistic carbon nanotube field-effect transistors, *Nature* **424**, 654 (2003).
7. S. J. Wind, J. Appenzeller, Ph. Avouris: Lateral Scaling in Carbon-Nanotube Field-Effect Transistors, *Phys. Rev. Lett.* **91**, 058301 (2003).
8. V. Derycke, R. Martel, J. Appenzeller, Ph. Avouris: Carbon Nanotube Inter- and Intramolecular Logic Gates, *Nano Lett.* **1**, 453 (2001).
9. R. Martel, V. Derycke, C. Lavoie, J. Appenzeller, K. K. Chan, J. Tersoff, Ph. Avouris: Ambipolar Electrical Transport in Semiconducting Single-Wall Carbon Nanotubes, *Phys. Rev. Lett.* **87**, 256805-1 (2001).
10. A. Bachtold, P. Hadley, T. Nakanishi, C. Dekker: Logic circuits with carbon nanotube transistors, *Science* **294**, 1317 (2001).

11. S. Heinze, J. Tersoff, R. Martel, V. Derycke, J. Appenzeller, Ph. Avouris: Carbon Nanotubes as Schottky Barrier Transistors, *Phys. Rev. Lett.* **89**, 106801 (2002).
12. T. Nakanishi, A. Bachtold, C. Dekker: Transport through the interface between a semiconducting carbon nanotube and a metal electrode, *Phys. Rev. B* **66**, 073307 (2002).
13. J. Appenzeller, J. Knoch, V. Derycke, R. Martel, S. J. Wind, Ph. Avouris: Field-Modulated Carrier Transport in Carbon Nanotube Transistors, *Phys. Rev. Lett.* **89**, 126801 (2002).
14. S. Heinze, M. Radosavljević, J. Tersoff, Ph. Avouris: Unexpected scaling of the performance of carbon nanotube Schottky-barrier transistors, *Phys. Rev. B* **68**, 235418 (2003).
15. J. Misewich, R. Martel, Ph. Avouris, J. C. Tsang, S. Heinze, J. Tersoff: Electrically induced optical emission from a carbon nanotube FET, *Science* **300**, 783 (2003).
16. J. Tersoff: Schottky Barrier Heights and the Continuum of Gap States, *Phys. Rev. Lett.* **52**, 465 (1984) and Schottky barriers and semiconductor band structures, *Phys. Rev. B* **32**, 6968 (1985).
17. F. Léonard, J. Tersoff: Role of Fermi-Level Pinning in Nanotube Schottky Diodes *Phys. Rev. Lett.* **84**, 4693 (2000).
18. V. Derycke, R. Martel, J. Appenzeller, Ph. Avouris: Controlling doping and carrier injection in carbon nanotube transistors, *Appl. Phys. Lett.* **80**, 2773 (2002).
19. M. Freitag, M. Radosavljević, Y. Zhou, A. T. Johnson, W. F. Smith: Controlled creation of a carbon nanotube diode by a scanned gate, *Appl. Phys. Lett.* **79**, 3326 (2001).
20. J. R. Tucker, C. Wang, P. S. Carney: Silicon field-effect transistor based on quantum tunneling, *Appl. Phys. Lett.* **65**, 618 (1994).
21. A. Javey, Q. Wang, W. Kim, H. Dai: Advancements in Complementary Carbon Nanotube Field-Effect Transistors, *IEDM Tech. Digest.* 741 (2003).
22. A. Javey, J. Guo, D. B. Farmer, Q. Wang, D. Wang, R. G. Gordon, M. Lundstrom, H. Dai: Carbon Nanotube Field-Effect Transistors with Integrated Ohmic Contacts and High-Gate Dielectrics, *Nano Lett.* **4**, 447 (2004).
23. Y.-M. Lin, J. Appenzeller, and Ph. Avouris: Novel Carbon Nanotube FET Design with Tunable Polarity, *IEDM Tech. Digest.* (in press).
24. M. Freitag, Y. Martin, J. Misewich, R. Martel, Ph. Avouris: Photoconductivity of Single Carbon Nanotubes, *Nano Lett.* **3**, 1067 (2003).
25. F. Léonard, J. Tersoff: Novel Length Scales in Nanotube Devices, *Phys. Rev. Lett.* **83**, 5174 (1999).
26. A. A. Odintsov: Schottky Barriers in Carbon Nanotube Heterojunctions, *Phys. Rev. Lett.* **85**, 150 (2000).
27. J. W. Mintmire, C. T. White: Universal Density of States for Carbon Nanotubes, *Phys. Rev. Lett.* **81**, 2506 (1998).
28. F. Léonard, J. Tersoff: Dielectric response of semiconducting carbon nanotubes, *Appl. Phys. Lett.* **81**, 4835 (2002).
29. S.-H. Jhi, S. G. Louie, M. L. Cohen: Electronic Properties of Oxidized Carbon Nanotubes, *Phys. Rev. Lett.* **85**, 1710 (2000).
30. P. G. Collins, K. Bradley, M. Ishigami, A. Zettl: Extreme oxygen sensitivity of electronic properties of carbon nanotubes, *Science* **287**, 1801 (2000).

31. X. Cui, M. Freitag, R. Martel, L. Brus, Ph. Avouris: Controlling Energy-Level Alignments at Carbon Nanotube/Au Contacts, *Nano Lett.* **3**, 783 (2003).
32. S. Sze: *Physics of Semiconductor Devices*, Wiley, New York 1981.
33. S. Datta: *Electronic Transport in Mesoscopic Systems*, Cambridge University Press, Cambridge 1995.
34. J. Guo, S. Datta, M. Lundstrom: Numerical Study of Scaling Issues for Schottky Barrier Carbon Nanotube Transistors, *IEEE Trans. Electron Devices* **51**, 172 (2004).
35. The dielectric properties of the NT are neglected here for simplicity. Within the approximation of neglecting charge on the NT we can take them into the account by appropriate boundary conditions for the electrostatic potential at the NT-oxide interface [14].
36. P. M. Morse and H. Feshbach: *Methods of Theoretical Physics*, McGraw-Hill, New York 1953.
37. J. Appenzeller, M. Radosavljević, J. Knoch, Ph. Avouris: Tunneling Versus Thermionic Emission in One-Dimensional Semiconductors, *Phys. Rev. Lett.* **92**, 048301 (2004).
38. M. Radosavljević, S. Heinze, J. Tersoff, Ph. Avouris: Drain voltage scaling in carbon nanotube transistors, *Appl. Phys. Lett.* **83**, 2435 (2003).
39. S. Heinze, J. Tersoff, Ph. Avouris: Electrostatic engineering of nanotube transistors for improved performance, *Appl. Phys. Lett.* **83**, 5038 (2003).
40. Y.-M. Lin, J. Appenzeller, Ph. Avouris: Ambipolar-to-Unipolar Conversion of Carbon Nanotube Transistors by Gate Structure Engineering, *Nano Lett.* **4**, 947 (2004).
41. M. Freitag, J. Chen, J. Tersoff, J. C. Tsang, Q. Fu, J. Liu, Ph. Avouris: Mobile Ambipolar Domain in Carbon-Nanotube Infrared Emitters, *Phys. Rev. Lett.* **93**, 076803 (2004).
42. M. Freitag, V. Perebeinos, J. Chen, A. Stein, J. C. Tsang, J. A. Misewich, R. Martel, Ph. Avouris: Hot Carrier Electroluminescence from a Single Carbon Nanotube, *Nano Lett.* **4**, 1063 (2004).
43. V. Perebeinos, J. Tersoff, Ph. Avouris: Scaling of Excitons in Carbon Nanotubes, *Phys. Rev. Lett.* **92**, 257402-1 (2004).
44. E. Chang, G. Bussi, A. Ruini, E. Molinari: Excitons in Carbon Nanotubes: An Ab Initio Symmetry-Based Approach, *Phys. Rev. Lett.* **92**, 196401 (2004).
45. C. D. Spataru, S. Ismail-Beigi, L. X. Benedict, S. G. Louie: Excitonic Effects and Optical Spectra of Single-Wall Carbon Nanotubes, *Phys. Rev. Lett.* **92**, 077402 (2004).

Charge Transport in DNA-based Devices

Danny Porath,^{1*} Noa Lapidot¹ and Julio Gomez-Herrero²

¹ Department of Physical Chemistry, The Hebrew University, Jerusalem 91904, Israel
porath@chem.ch.huji.ac.il

² Departamento Física de la Materia Condensada,
Universidad Autónoma de Madrid, Madrid 28049, Spain

Abstract. DNA is probably the molecule that carries the highest possible density of information. Information comes along with structuring and recognition that offer the possibility of using DNA to build self-assembled molecular circuits for nanoelectronics applications. This, however, must be complemented by suitable conductivity, which was tested in a series of experiments on charge migration along DNA molecules. These issues together with reports on possible high rates of charge transfer between donor and acceptor through the DNA, obtained in the last decade from solution chemistry experiments on large numbers of molecules, triggered a series of direct electrical transport measurements through DNA single molecules, bundles and networks. These measurements are reviewed and presented here. From these experiments we conclude that electrical transport is feasible in short DNA molecules, in bundles and networks, but blocked in long single molecules that are attached to surfaces.

Key words: DNA, Molecular Electronics, Bio-Molecular Nanowires, Conductance, Direct Electrical Transport.

1 Introduction

1.1 Devices Go Molecular – the Emergence of Molecular Electronics

The progress of the electronic industry in the past few decades was based on the delivery of smaller and smaller devices and denser integrated circuits, which ensured the attainment of more and more powerful computers. Such a fast growth is, however, compromised by the intrinsic limitations of the conventional technology. Electronic circuits are currently fabricated with complementary-metal-oxide-semiconductor (CMOS) transistors. Higher transistor density on a single chip means faster circuit performance. The trend towards higher integration is restricted by the limitations of the current lithography technologies, by heat dissipation and by capacitive coupling between different components. Moreover, the down-scaling of individual devices to the nanometer range collides with fundamental physical laws. In fact, in conventional silicon-based electronic devices the information is carried by mobile electrons within a band of allowed energies according to the semiconductor

band structure. However, when the dimensions shrink to the nanometer scale, and bands turn into discrete energy levels, then quantum correlation effects induce localization.

In order to pursue the miniaturization of integrated circuits further [1], a novel technology, which would exploit the pure quantum mechanical effects that rule at the nanometer scale, is desired. The search for efficient molecular devices, that would be able to perform operations currently done by silicon transistors, is pursued within this framework. The basic idea of molecular electronics is to use individual molecules as wires, switches, rectifiers and memories [2–6].

Another conceptual idea that is advanced by molecular electronics is the switch from a top-bottom approach, where the devices are extracted from a single large-scale building block, to a bottom-up approach in which the whole system is composed of small basic building blocks with recognition, structuring and self-assembly properties. Different candidates for molecular devices are currently the subject of highly interdisciplinary investigation efforts, including small organic polymers [6–11], large bio-molecules [12–20], nanotubes and fullerenes [21–24]. In the following, we focus on the exploration of DNA bio-molecules as prospective candidates for molecular electronic devices. For the scientists devoted to the investigation of charge mobility in DNA, a no less important motivation than the strong technological drive is that DNA molecules comprise an excellent model system for charge transport in one-dimensional polymers. This well-known polymer enables an endless number of structural manipulations in which charge transport mechanisms like hopping and tunneling may be studied in a controlled way.

The topic of charge transport in DNA and the feasibility of constructing DNA-based devices, though being a relatively young field of research, has kindled a heated debate within the scientific community. Charge transport in DNA has been reviewed by D.P. et al. [25] as well as by Ventra et al. [26] and by Enders et al. [27]. These reviews cover the results obtained by several groups who developed different approaches and techniques to the handling and measurement of charge transport through native and synthetic DNA molecules. These different methods, each with its own unique advantages, difficulties and drawbacks, yielded a wide range of results that fueled a scientific debate over the conduction properties of DNA molecules. We feel, however, that additional works published recently give a better insight into the factors governing the measurements techniques and the handling of DNA molecules and warrant further discussion. Here, we review the important results obtained at the early stage (between 1998 and 2003) and then we emphasize the newer results that were published in late 2003 and 2004 that shed more light on this topic.

1.2 The Unique Advantages of DNA-based Devices – Recognition and Structuring

In the frame of molecular electronics DNA possesses two unique and appealing properties: *recognition* and a special structuring that suggests its use for *self-assembly*. Molecular *recognition* describes the capability of a molecule to form selective bonds with other molecules or with substrates, based on the information stored in the structural features of the interacting partners. Molecular recognition processes may play a key role in molecular devices by: (a) driving the fabrication of devices and integrated circuits from elementary building blocks, (b) incorporating them into supramolecular arrays, (c) allowing for selective operations on given species potentially acting as dopants, and (d) controlling the response to external perturbations represented by interacting partners or applied fields. *Self-assembly*, which is the capability of molecules to spontaneously organize themselves in supramolecular aggregates under suitable experimental conditions [28], may drive the design of well-structured systems. Self-organization may occur both in solution and in the solid state, through hydrogen-bonding, Van der Waals and dipolar interactions, and by metal-ion coordination between the components. By virtue of their recognition and self-assembling properties, DNA molecules seem particularly suitable as the active components for nano-scale electronic devices [29–31]. However, despite the promising development that has been recently achieved in controlling the self-assembly of DNA [32–35] and in coupling molecules to metal contacts [12, 36], there is still a great controversy around the understanding of its electrical behavior and of the mechanisms that might control charge mobility through its structure [37].

The idea that double-stranded DNA may function as a conduit for fast electron transport along the axis of its base-pair stack, was first advanced in 1962 [38]. Later low-temperature experiments indicated, however, that radiation-induced conductivity can be due to highly mobile charge carriers migrating within the frozen water layer surrounding the helix, rather than through the base-pair core [39]. The long lasting interest of the radiation community [40] in the problem of charge migration in DNA was due to its relevance for the mechanisms of DNA oxidative damage, whose main target is the guanine (Gua) base [41]. Recently, the interest in DNA charge mobility has been revived and extended to other interdisciplinary research communities. In particular, the issue of electron and hole migration in DNA has become a hot topic for a number of chemistry scholars [42, 43] following the reports that photoinduced electron transfer occurred with very high and almost distance-independent rates between donor and acceptor intercalators along a DNA helix [44, 45]. This evidence suggested that double-stranded DNA may exhibit a “wire like” behavior [46]. From the large body of experimental studies on the solution chemistry that became available in the last decade and appeared in recent reviews [47, 48], several mechanisms were proposed for DNA-mediated charge migration, depending on the energetics of

the base sequence and on the overall structural aspects of the system under investigation. These mechanisms include single-step superexchange [44], multistep hole hopping [49], phonon-assisted polaron hopping [50] and polaron drift [51]. The above advances drove the interest in DNA molecules also for nanoelectronics. In this field, by virtue of their sequence-specific recognition properties and related self-assembling capabilities, they might be employed to wire the electronic materials in a programmable way [12, 13]. This research path led to a set of direct electrical transport measurements. In the first reported measurement, μm -scale λ -DNA molecules were found to be “practically insulating” [12]. However, the possibility that double-stranded DNA may function as a one-dimensional conductor for molecular electronic devices has been rekindled by other experiments, where e.g. anisotropic conductivity was found in an aligned DNA cast film [52], and ohmic behavior with high conductivity was found also in a 600-nm-long λ -DNA rope [53].

The above measurements, complemented by other experiments which are discussed in Sect. 2, highlight that despite the outstanding results that have been recently achieved in controlling the self-assembly of DNA onto inorganic substrates and electrodes, there is currently nor unanimous understanding neither consensus of its electrical behavior or of the mechanisms that might control charge mobility through its structure. Our purpose in this chapter is to review the main experiments that have been performed to measure directly the conductivity of DNA molecules. The reader may find the theoretical aspects of charge transport through molecular wires and through DNA in the theory parts of this volume (see Chaps. 2,4,8) and in [25–27]. For theory of transport in polymers in general, one may find a nice review by Breads and Street [54].

1.3 Charge Transport in Device Configuration

Conductivity experiments in the solid state are based on several techniques, including imaging, SPM spectroscopy, and electrical transport measurements that reveal the electric current flux through the molecule under an external field. The results pertain to single molecules (or bundles) and can be re-measured many times. In parallel to electron transfer experiments in solution, the roles of the “donor” and the “acceptor” are played either by the metal leads, or by the substrate and a metal tip. In solid state experiments, the “donor” and “acceptor” are referred to as “contacts”. In contrast to the “donor-acceptor” scheme, where the donor is excited and usually a single charge is injected and transferred to the donor, the Fermi level at one of the leads may be elevated and fixed such that a very large number of charge carriers can be injected and transported along the molecule.

The interpretation of the experiments is generally given in terms of *conductivity*, determined by the electronic energy-levels (if the molecular structure supports the existence of localized orbitals and *discrete* energy levels) or band-structure (if the intra-molecular interactions support the formation

of delocalized states described by *continuous* energy levels, i.e. dispersive bands). The metal contacts are reservoirs of charges and this fact allows leaving the charge state along the helix unaltered. It is not specified a-priori if the mobile charges are electrons or holes: this depends on the availability of electron states, on their filling, and on the alignment to the Fermi levels of the reservoirs.

The electronic structure of the investigated molecules is important [55,56] in indirect electrochemical measurements, as well as in the direct transport measurements. It determines the occurrence of direct donor-acceptor tunneling or of thermal hopping of elementary charges or polarons as discussed by Di Felice et al. in this collection [57]. Direct tunneling can occur either “through-space” if the DNA energy levels are not aligned with the initial and final charge sites or reservoirs, or “through-bond” if they are aligned and modulate the height and width of the tunneling barrier. In the case of tunneling, the bridging bases do not offer intermediate residence sites for the moving charges. Contrary to that, in the case of thermal coupling and incoherent hopping, the moving charges physically reside for a finite relaxation time in intermediate sites at base planes between the donor and the acceptor along their path, although this may cost structural reorganization energy. Whether the inherent DNA electronic structure is constituted of dispersive bands or of discrete levels may be revealed only in the solid-state experiments. In fact, for the motion of individual charges injected into free molecules in solution, probed by electrochemistry tools, it is not important whether such charges find in the molecules a continuum of energy levels or discrete levels available to modulate the tunneling barrier. This is because only the modulation of the tunneling barrier or the donor-bridge-acceptor coupling can be detected. Alternatively, in direct electrical transport measurements, where charges are available in reservoirs (the metal electrodes), it makes a difference if there is a continuum of electron states or discrete levels in the molecular bridge that are available for mobile carriers. For the ideal case of ohmic contacts, a continuum in the molecule will be manifested in smoothly rising current-voltage curves, whereas for discrete levels the measured I-V curves will be step-like revealing quantization (for appropriate contacts). This chapter reviews the latter class of experiments.

2 Direct Electrical Transport Measurements in DNA

A series of direct electrical transport measurements *through* DNA molecules that commenced in 1998 was motivated by new technological achievements in the field of electron beam lithography and scanning probe microscopy, as well as by encouraging experimental data suggesting high electron-transfer rates. The latter were based on the interpretation of results of charge-transfer experiments conducted on large numbers of very short DNA molecules in solution, in particular by Barton’s group at Caltech and by other colleagues

[42–50, 58–63]. In perspective it seems now that care should be taken when projecting from those experiments on the electron transport properties of various single DNA molecules in different situations and structures, e.g. long vs. short, on surfaces vs. suspended, in bundles vs. single, in various environmental conditions like dry environment, or in other exotic configurations.

Several works have been published since 1998 describing direct electrical transport measurements conducted on single DNA molecules [12, 14, 36, 53, 64–71, 75, 76, 79]. In such measurements one has to bring (at least) two metal electrodes to a physical contact with a single molecule, apply voltage and measure current (or vice versa). Poor conductivity, which seems to be the case for long DNA attached to surfaces, provides a small measured signal. In such cases the electrode separation should be small, preferably in the range of few to tens of nanometers, yet beyond direct tunneling distance and without any parallel conduction path. Performing good and reliable experiments on single segmented molecules is a demanding task and the interpretation of the experiments on the basis of the current data is even harder. Not only that – each segmented molecule – a polymer – is intrinsically different from the others in the specific details of its structure. Consequently the details of its properties also bear some uniqueness and result in molecule-to-molecule differences. Furthermore, the properties of these molecules are sensitive to the environment and environmental conditions, e.g. humidity, buffer composition etc. Another difficulty that arises in these measurements is that the contacts to a single molecule, as to any other small system, are very important for the transport but difficult to perform and nearly impossible to control microscopically as shown in this collection by Lindsay et al. [80]. For example, the electrical-coupling strength between the molecule and the electrodes will determine whether a Coulomb blockade effect (weak coupling) or a mixing of energy states between the molecule and the electrodes (strong coupling) is measured. In the case of weak coupling, the size and chemical nature of the molecule between the electrodes will determine the relative contributions of Coulomb blockade phenomena and of the intrinsic energy gap of the molecule to the current-voltage spectra. For the outlined reasons, we find a large variety in the results of the reported experiments, most of which done by excellent scientists in leading laboratories.

The question whether DNA is an insulator, a semiconductor or a metal is often raised. This terminology originates from the field of solid-state physics where it refers to the electronic structure of semi-infinite periodic lattices. It has been successfully applied to describe the electrical behavior of one-dimensional wires like carbon nanotubes, where a coherent band-structure is formed. However, it is questionable whether or not this notion describes well, with a similar meaning, the orbital-energetics and the electronic transport through one-dimensional soft polymers, which are formed of a large number of sequential segments. In these polymers the number of junctions and phase-coherent “islands” is large and may determine the electronic structure

and the transport mechanisms along the wire. In some cases it may be those junctions that constitute a bottleneck for the transport. These junctions will then determine the overall electric response of the polymer. In the case of a strong coupling between the islands along the polymer, a complex combination of the molecular electron states and of the coupling strengths at the junctions will determine the electrical response of the wire.

DNA in particular is sometimes said to be an insulator or a semiconductor. In the bulk the difference between a wide band-gap semiconductor and an insulator is mainly quantitative with regard to the resistivity. For DNA and other one-dimensional polymers we may instead introduce the following distinction. If we apply a voltage (even high) across a wide-band-gap polymer and successfully induce charge transport through it *without* changing the polymer structure and its properties *in an irreversible way* then it would be a wide-band-gap semiconductor. However, if the structure is *permanently damaged* or changed upon this voltage application then it is an insulator. This distinction is important with regard to the relevant experiments, where very high fields are present, and to the methods to check whether or not the conduction properties of the molecule are reproducible.

In Sects. 2.1 and 2.2 we will review the direct electrical transport experiments reported on DNA single molecules, bundles, and networks.

2.1 Single Molecules

The first direct electrical transport measurement on a single, 16 μm long λ -DNA, was published in 1998 by Braun et al. [12]. In this fascinating experiment the λ -DNA was stretched on a mica surface and connected to two metal electrodes, 12 μm apart. This was accomplished using the double-strand recognition between a short single-strand (hang-over) in the end of the long λ -DNA and a complementary single-strand that was connected to the metal electrode on each side of the molecule (see Fig. 1). Electrical transport measurements through the single molecule that was placed on the surface yielded no observable current up to 10 V.

Later on in 1999 Fink et al. [53] reported nearly ohmic behavior in λ -DNA molecules with a resistance in the $M\Omega$ range. The molecules were a few hundred nanometers long and were stretched across $\sim 2 \mu\text{m}$ wide holes in a metal-covered transmission electron microscope (TEM) grid, as shown in Fig. 2. This fantastic technical accomplishment was achieved in a high-vacuum chamber where a holographic image was created with a low-energy electron point source (LEEPS) claimed not to radiatively damage the DNA. Note, however, that the bright parts of the DNA in the images may suggest scattering of the beam electrons from the molecule, which may indicate the presence of scattering points along the DNA that could affect the charge transport along the molecule. The actual measurement was performed between a sharp tungsten tip, which was connected to the stretched molecule in the middle of one of the grid holes, and the metal covering the TEM

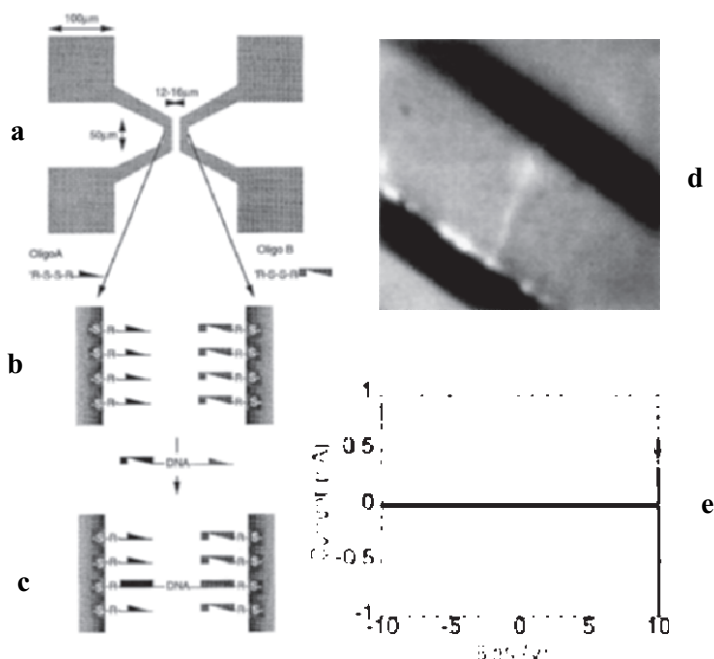


Fig. 1. (a–c) 16 μm long λ -DNA was stretched between two metal electrodes using short hang-over single strands complementary to single-strands that were pre-attached to the metal electrodes. (d) A fluorescent image of the DNA molecule, connecting the metal electrodes. (e) The flat, insulating current-voltage that was measured (from [12], by permission; © 1998 by Nature Macmillan Publishers Ltd)

grid. The tungsten tip was aligned using the holographic image. A nearly ohmic behavior was observed in the current-voltage (I-V) curves, sustained up to 40 mV and then disappeared. The resistance division between two DNA branches appeared consistent with the ohmic behavior. This result seemed very promising. However, while conduction over long distances was observed later in bundles, it was not repeated in further measurements of single DNA molecules with one exception of a superconducting behavior that is discussed later [66]. The resolution of the LEEPS in this measurement did not enable to determine whether it was a single molecule or a bundle that was suspended between the metal tip and the metal grid.

In a further experiment published in 2000 by Porath et al. [14], electrical transport was measured through 10.4-nm-long (30 base-pairs) homogeneous poly(dG)-poly(dC) molecules that were electrostatically trapped [72, 73] between two Pt electrodes (see Fig. 3). The measurements were performed at temperatures ranging from room temperature and down to 4 K. Current was observed beyond a threshold voltage of 0.5–1 V suggesting that the molecules transported charge carriers. At room temperature in ambient atmosphere, the

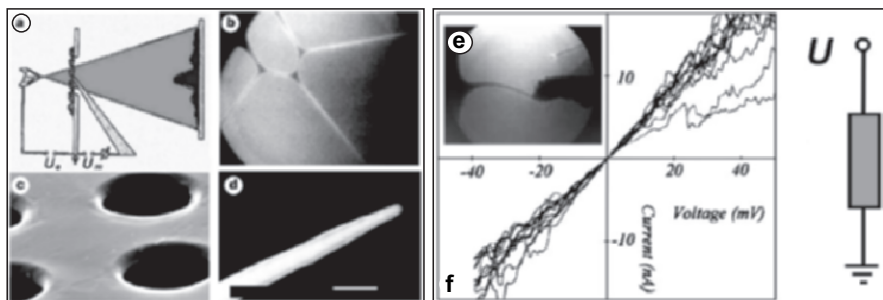


Fig. 2. (a) The LEEPS microscope used to investigate the conductivity of DNA. The atomic-size electron point source is placed close to a sample holder with holes spanned by DNA molecules. Due to the sharpness of the source and its closeness to the sample, a small voltage U_e (20–300 V) is sufficient to create a spherical low-energy electron wave. The projection image created by the low-energy electrons is observed at a distant detector. Between the sample holder and the detector, a manipulation-tip is incorporated. This tip is placed at an electrical potential U_m with respect to the grounded sample holder and is used to mechanically and electrically manipulate the DNA ropes that are stretched over the holes in the sample holder. (b) A projection image of λ -DNA ropes spanning a 2- μm -diameter hole. The kinetic energy of the imaging electrons is 70 eV. (c) SEM image, showing the sample support with its 2- μm -diameter holes. (d) SEM image of the end of a tungsten manipulation-tip used to contact the DNA ropes. Scale bar 200 nm. (e) The metal tip is attached to the λ -DNA molecule. (f) I-V curves taken for a 600-nm-long DNA rope. In the range of $\pm 20\text{ mV}$, the curves are linear; above this voltage, large fluctuations are apparent. A resistance of about $2.5\text{ M}\Omega$ was derived from the linear dependence at low voltage (from [53], by permission; © 1999 by Nature Macmillan Publishers Ltd)

general shape of the current-voltage curves was preserved for tens of samples but the details of the curves varied from curve to curve. The possibility of ionic conduction was ruled out by measurements that were performed in vacuum and at low temperature, where no ionic conduction is possible. High reproducibility of the I-V curves was obtained at low temperature for tens of measurements on an individual sample, followed by a sudden switching to a different curve-shape (see inset of Fig. 4) that was again reproducible (e.g. peak position and height in the dI/dV curves, Fig. 4). This variation of the curves in different samples can originate from the individual structural conformation of each single molecule, or from the different formation of the specific contact. The variation of the curves measured on the same sample may be also due to switching of the exact overlap of the wavefunctions that are localized on the bases. A rather comprehensive set of control experiments helped to verify the results and ensure their validity. The existence of the DNA between the electrodes was verified by incubating the DNA devices with DNase I, an enzyme that specifically cuts DNA (and not any other organic

or inorganic material). Following incubation of the sample with the enzyme the electrical signal was suppressed, indicating that the molecule through which the current was measured before is indeed DNA. The procedure was cross-checked by repeating this control experiment in the absence of Mg ions in the enzyme solution so that the action of the enzyme could not be activated. In this case the signal was not affected by incubation with the enzyme. This procedure ensured that it was indeed the enzyme that did the cut (see Fig. 3b), thus confirming again that it was the DNA between the electrodes. This experiment clearly proves that short DNA molecules with homogeneous structure are capable of transporting charge carriers over a length of at least 10 nm.

In another attempt to resolve the puzzle around the DNA conduction properties, de Pablo et al. [64] applied a different technique to measure single λ -DNA molecules on the surface in ambient. They deposited a large number of DNA molecules on mica, covered some of them partly with gold and using a metal covered AFM tip as a second mobile electrode, measured the conductance along individual molecules. Note that the minimum distance between the macroscopic gold electrode and the AFM tip was 70 nm. (see Fig. 5). No current was observed in these experiments suggesting that charge transport through DNA molecules longer than 70 nm which are attached to surfaces is blocked. Furthermore, they covered \sim 1000 parallel molecules on both ends with metal electrodes (\sim 2 μ m apart) and again no current was observed.

Additional experiments were performed in 2001 by Storm et al. [65], in which DNA molecules (longer than 40 nm) with various lengths and sequence compositions were stretched on different surfaces between planar electrodes in various configurations (see Fig. 6). No current was measured in these experiments, suggesting again that charge transport through DNA molecules, longer than 40 nm and adsorbed on the surface, is blocked.

Yet another negative result published in 2002 was obtained in a similar experiment by Zhang et al. [36] who stretched many single DNA molecules in parallel between metal electrodes, covalently bonded to them with thiols and measured no current upon voltage application. Both results [36,65] were consistent with the de Pablo et al. experiment [64].

In parallel, Kasumov et al. [66] reported ohmic behavior of the resistance of λ -DNA molecules deposited on a mica surface and stretched between rhenium-carbon electrodes (see Fig. 7). This behavior was measured at temperatures ranging from room temperature and down to 1 K. Below 1 K a particularly unexpected result was observed: proximity-induced superconductivity. The resistance was measured directly with a lock-in technique and no current-voltage curves were presented. This surprising proximity-induced superconductivity is in contrast to all the other data published so far, and with theory. No similar result was reported later by this or any other group.

Beautiful and quite detailed measurements with different results on shorter molecules were reported in a series of papers by Watanabe et al.

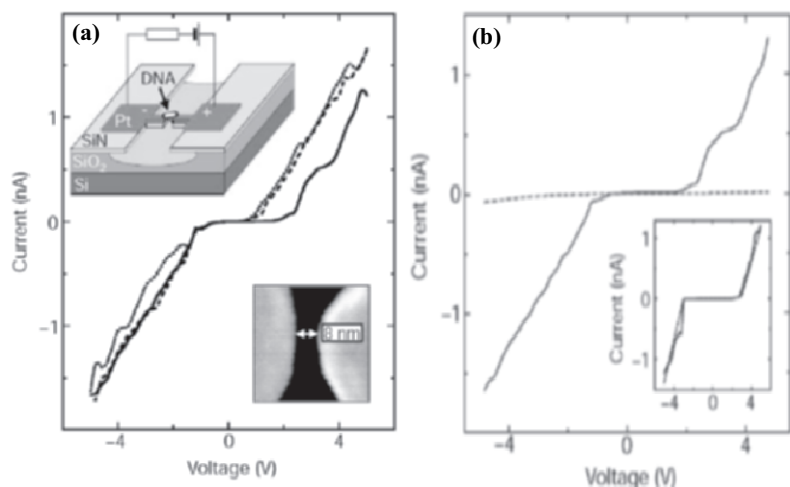


Fig. 3. (a) Current-voltage curves measured at room temperature on a 10.4-nm-long DNA molecule [30 base-pairs, double-stranded poly(dG)-poly(dC)] trapped between two metal nanoelectrodes that are 8 nm apart. Subsequent I-V curves (different curves) show similar behavior but with a variation of the width of the gap. The upper inset shows a schematic of the sample layout. Using electron-beam lithography, a local 30 nm narrow segment in a slit in the SiN layer is created. Underetching the SiO₂ layer leads to two opposite freestanding SiN “fingers” that become the metallic nanoelectrodes after sputtering Pt through a Si mask. The lower inset is a SEM image of the two metal electrodes (light area) and the 8 nm gap between them (dark area). Deposition of a DNA molecule between the electrodes was achieved with electrostatic trapping. A 1 μ l droplet of dilute DNA solution is positioned on top of the sample. Subsequently, a voltage of up to 5 V is applied between the electrodes. The electrostatic field polarizes a nearby molecule, which is then attracted to the gap between the electrodes due to the field gradient. When a DNA molecule is trapped and current starts to flow through it, a large part of the voltage drops across a large ($2 \text{ G}\Omega$) series resistor, which reduces the field between the electrodes and prevents other molecules from being trapped. Trapping of DNA molecules using this method is almost always successful. (b) Current-voltage curves that demonstrate that transport is indeed measured on DNA trapped between the electrodes. The *solid curve* is measured after trapping a DNA molecule as in (a). The *dashed curve* is measured after incubation of the same sample for 1 hour in a solution with 10 mg/ml DNase I enzyme. The clear suppression of the current indicates that the double-stranded DNA was cut by the enzyme. This experiment was carried out for 4 different samples (including the sample of Fig. 4). The inset shows two curves measured in a complementary experiment where the above experiment was repeated but in the absence of the Mg ions that activate the enzyme and in the presence of 10 mM EDTA (ethylenediamine tetraacetic acid) that complexes any residual Mg ions. In this case, the shape of the curve did not change. This observation verifies that the DNA was indeed cut by the enzyme in the original control experiment (from [14], by permission; © 2000 by Nature Macmillan Publishers Ltd)

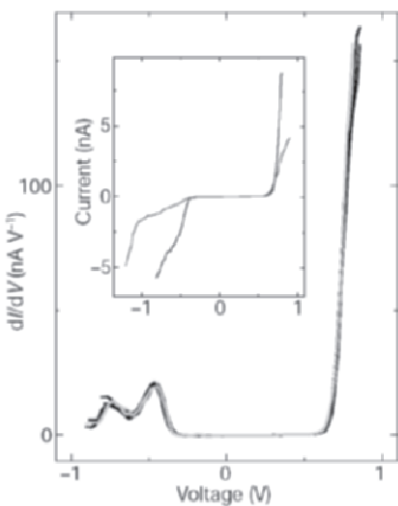


Fig. 4. Differential conductance dI/dV versus applied voltage V at 100 K. The differential conductance manifests a clear peak structure. Good reproducibility can be seen from the six nearly overlapping curves. Peak structures were observed in four samples measured at low temperatures although details were different from sample to sample. Subsequent sets of I-V measurements can show a sudden change, possibly due to conformational changes of the DNA. The inset shows an example of two typical I-V curves that were measured before and after such an abrupt change. Switching between stable and reproducible shapes can occur upon an abrupt switch of the voltage or by high current (from [14], by permission; © 2000 by Nature Macmillan Publishers Ltd)

[67, 69], Shigematsu et al. [68] and Shimotani et al. [70], using a rather sophisticated technique. A short, single DNA molecule was laid on the surface and contacted with a triple probe AFM consisting of 3 conducting CNTs (see Figs. 8a and 8b). Two of them, 20 nm apart, were attached to the DNA (see Fig. 8c). A third carbon nanotube was attached to the AFM tip. In one case voltage was applied between the nanotube on one side of the molecule and the tip-nanotube that contacted the DNA molecule at a certain distance from the side electrode, so that the dependence of the current on the DNA length was measured under a bias voltage of 2 V between the two electrodes. The current dropped from 2 nA at \sim 2 nm to less than 0.1 nA in the length range of 6 to 20 nm. In a second experiment [68], current was measured between the side nanotubes (20 nm apart) under a bias voltage of 2 V while moving the tip-nanotube that served this time as a gate along the DNA molecule. A clear variation of the current due to the effect of the gate electrode, reproducible forwards and backwards, was observed. The current-voltage curves in this experiment are measured through carbon nanotubes. Their conductivity is indeed much higher than that of the DNA molecule and therefore likely to

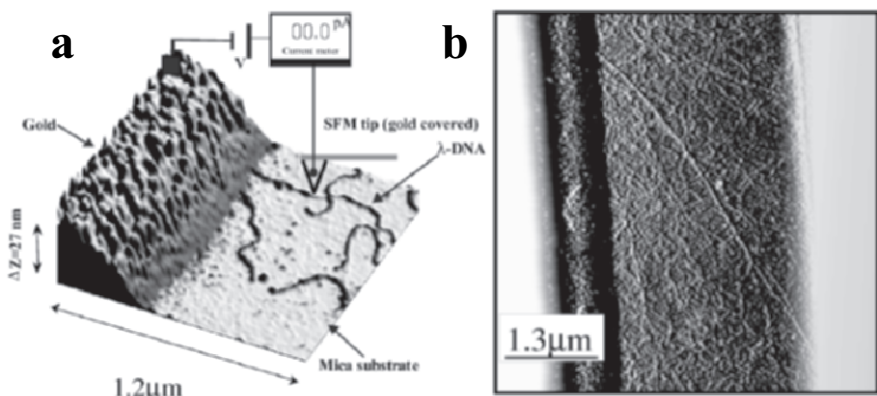


Fig. 5. (a) Three-dimensional SFM image showing two DNA molecules in contact with the gold electrode. The image size is $1.2 \mu\text{m}^2$. A scheme of the electrical circuit used to measure the DNA resistivity is also shown. (b) λ -DNA strands connecting two gold electrodes spanned on a bare mica gap. The image analysis leads to the conclusion that at least 1000 DNA molecules are connecting the electrodes. From the (absence of) current between the electrodes, a lower bound of $10^5 \Omega\text{cm}$ per molecule is obtained for the resistivity of DNA at a bias voltage of 10 V (from [64], by permission; © 2000 by the American Physical Society)

have only a small effect on the I-V's. However, this and the contacts of the nanotubes to the AFM tip and metal electrodes might still have an effect on the measured results.

Watanabe et al. [69] further demonstrated the operation of a single DNA molecule transistor in which three CNT terminals were connected with the DNA molecule, as outlined in Fig. 9 (CNTs used as source, drain and gate). At room temperature, they observed quantum steps in the current measured while scanning the source-drain voltage, when the distance between the source and drain was less than 10 nm.

From the direct electrical transport measurements on single DNA molecules reported so far one can draw some very interesting conclusions. First, it is possible to transport charge carriers through single DNA molecules. This was observed however, only for short molecules in the range of up to 20 nm in the experiments of Porath et al. [14], Watanabe et al. [67, 69] and Shigematsu et al. [68]. All the three experiments demonstrated currents of order 1 nA upon application of voltage of ~ 1 V. The experiments by Fink et al. [53] and Kasumov et al. [66] showed higher currents and lower resistivities over longer molecules (hundreds of nm) but they were never reconfirmed for individual molecules. In all the other experiments, by de Pablo et al. [64], Storm et al. [65] and Zhang et al. [36] that were conducted for molecule length longer than 40 nm on single DNA molecules attached to surfaces, no current was measured.

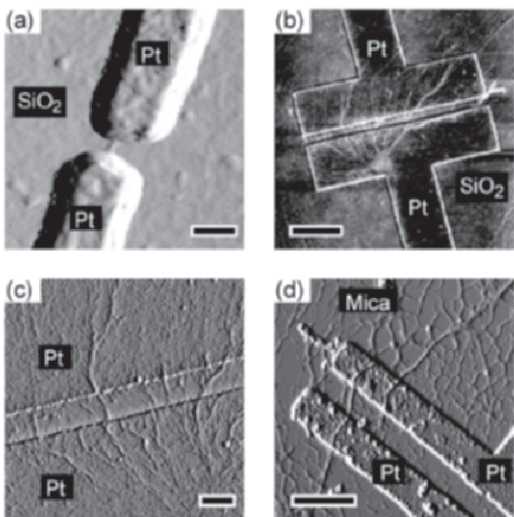


Fig. 6. AFM images of DNA assembled in various devices. (a) Mixed-sequence DNA between platinum electrodes spaced by 40 nm. Scale bar 50 nm. (b) Height image of poly(dG)-poly(dC) DNA bundles on platinum electrodes. The distance between electrodes is 200 nm, and the scale bar is 1 μ m. (c) High magnification image of the device shown in b. Several DNA bundles clearly extend over the two electrodes. Scale bar 200 nm. (d) Poly(dG)-poly(dC) DNA bundles on platinum electrodes fabricated on a mica substrate. Scale bar 500 nm. For all these devices, no conduction was observed (from [65], by permission; © 2001 by the American Institute of Physics)

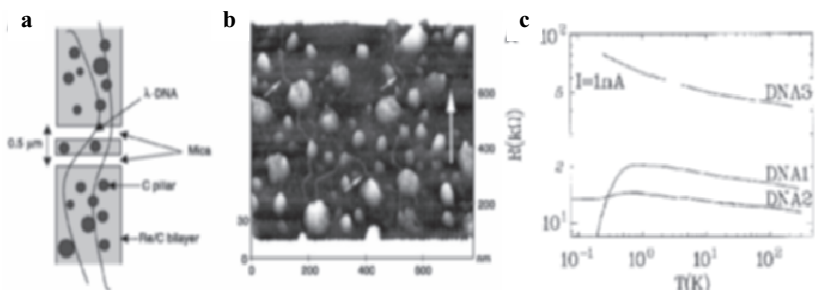


Fig. 7. (a) Schematic drawing of the measured sample, with DNA molecules combed between Re/C electrodes on a mica substrate (b) AFM image showing DNA molecules combed on the Re/C bilayer. The large vertical arrow indicates the direction of the solution flow. The small arrows point towards the combed molecules. Note the forest structure of the corban film. (c) DC resistance as a function of temperature on a large temperature scale for three different samples, showing the power law behavior down to 1 K (form [66], by permission © 2001 by Science)

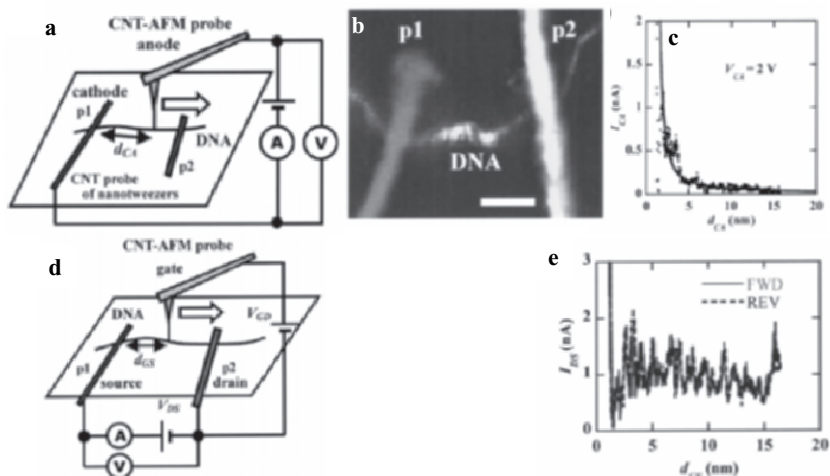


Fig. 8. (a) Schematic of the electric current measurement. Two CNT probes (p1 and p2) of the nanotweezers were set on a DNA. In a two-probe dc measurement, one of the CNT probes (p1) was used as the cathode. A CNT-AFM probe was contacted with the DNA as the anode. The electric current between the source and drain was measured while varying the distance between the anode and cathode d_{CA} . (b) AFM image (scale bar, 10 nm) of a single DNA molecule attached with two CNT probes (p1 and p2) of the nanotweezers, which was obtained by scanning the CNT-AFM probe. (c) d_{CA} -Length dependence, d_{CA} , of the electric current (I_{CA}) between the electrodes, measured with the electrode configuration shown in (a). (d) Schematic of the electric measurement under applied gate bias. Two nanotweezer probes (p1 and p2) and the CNT-AFM probe were used as source, drain, and gate electrodes, respectively. The electric current between the source and drain was measured with varying the distance between source and gate d_{GS} . (e) d_{GS} - dependence of the electric current (I_{DS}) between the source and the drain electrodes measured with the electrode configuration shown in (d). The solid gray line shows the electric current for the CNT-AFM probe moving from the source electrode to the drain electrode. Dashed black line is for the case of the opposite moving direction (from [68], by permission; © 2003 by the American Institute of Physics)

The conclusion of poor conductivity in long single molecules on surfaces is further supported by indirect electrostatic force microscope (EFM) measurements, reported by Bockrath et al. [74] and Gómez-Navarro et al. [75]. In these measurements no attraction was found between a voltage-biased metal-tip and the λ -DNA molecules lying on the surface. This indicates that the electric field at the tip failed to induce long-range polarization in the molecules on the surface, which would in turn indicate charge mobility along the molecule, as was found for carbon nanotubes.

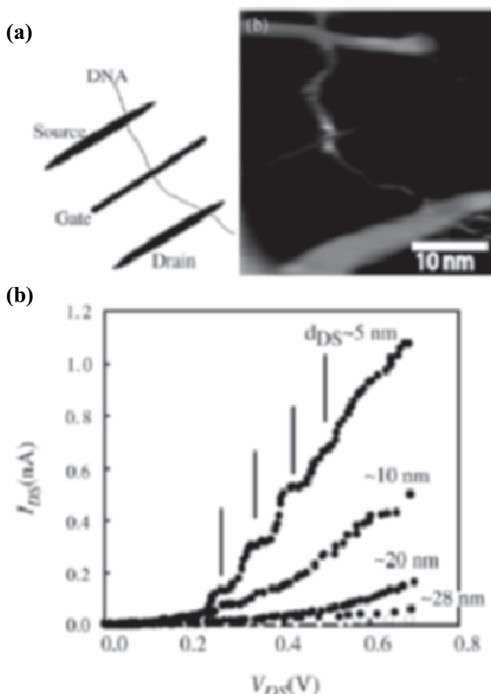


Fig. 9. (a) A schematic of the DNA transistor. A single DNA molecule deposited on SiO₂ (10 nm)/n-Si(100)/Au(20 nm, gate terminal) was connected with source and drain terminals using T-AFM. (b) AFM image of a single molecule DNA transistor. The source-drain distance, dDS, is ~ 20 nm. (c) The IDS-VDS curves of the DNA transistor for several dDS = ~ 5 , ~ 10 , ~ 20 , ~ 28 nm at gate voltage, VG = 2 V. The white circles indicates the leak current plots at dDS = ~ 5 nm. (from [69] by permission; © 2003 by the publisher of thin solid films)

The absence of conductance over the 40 nm length is not too surprising if we recall that DNA is a soft segmented molecule and is therefore likely to have distortions and defects when subjected to the surface force field. This is also manifested in AFM imaging where the measured height of the molecule is different from its “nominal height” [65, 74–76], partly due to the effect of the pushing tip and partly due to the effect of the surface force field. This force field may be the culprit for blocking current transport through DNA strands when attached to surfaces (though there may be other reasons for it as well).

In later experiments to evaluate in depth the conduction properties of DNA, various investigators tried to address specific issues that may have a crucial impact on the measured results. Such issues include the surface force field and its affects on the DNA structure, the influence of humidity and

temperature on the deposited DNA structure and on possible conduction mechanisms as well as the type of contact between the DNA molecules and the electrodes (physical vs. chemical bonding) and its contribution to the overall measurement. The issue of contact to the molecules is widely discussed in Chap. 12 of this book.

Kasumov et al. confirmed that the height of DNA deposited on mica is about half the height that is expected based on DNA crystal structure (about 1 nm vs. about 2.4 respectively), using TEM to image a sample prepared by a shadow evaporation technique [76]. This finding supports numerous reports by various groups who measured the height of DNA deposited directly on solid substrate (i.e. mica or gold) by AFM. Kasumov and his co-workers tried to improve the DNA conductivity by minimizing the surface interaction with the DNA. This was achieved by depositing an intermediate thin, discontinuous layer between the DNA strands and the underlying mica. The layer was formed by glow discharge of pentylamine vapor. The obtained film constitutes mainly of ionized NH_3^+ on which the negatively charged phosphate groups of the DNA backbone get attached. They report that the height of DNA molecules deposited on this film is 2.4 ± 0.5 nm, close to the value expected from X-ray structure of B-form DNA. Over the organic “elevation layer”, Kasumov et al. deposited native DNA to obtain between 1 and 5 molecules that lay between two platinum contacts. They concentrated in their study on charge transport at the very low temperature range between 0.1 and 1 K (ionic conduction can be neglected below ~ 250 K). They report scaling of the conductance obtained under low bias (10^{-5} to 4×10^{-4} V) that is similar to the scaling obtained with CNT, and conclude from that the DNA behaves like a 1D conductor.

Yang et al. [77] tried to evaluated the effects of drying DNA helices on its structure and on the stacking of base pairs, as required for utilization of DNA as molecular wire in electronic devices. For that purpose, they studied the X-ray diffraction of aligned films of DNA complexed within a surfactant, under different conditions: dry, wet and at low temperature. They find that dehydration of pre-hydrated samples causes the base pairs to go from planar to edge stacking and vice versa. The base-pair spacing within the DNA helix are 0.41 nm in dry sample in air at 50% relative humidity, while it is 0.34 nm in aqueous environment at room temperature. At low temperatures, below -16°C , the wet sample becomes dehydrated by crystallization and phase separation of the weakly bound water. This leads to rotation of the bases from planar to edge stacking, which corresponds to poor π -electron overlap. Their findings indicate that the structure of the DNA helix when deposited on dry surfaces may be very different than that found by crystallization of DNA in solution, and may be another reason for the poor conductivity found in a non-aqueous environment.

The issue of type and transmission quality of the contact point between the DNA strands and the metal electrodes was also recognized as a major

factor in performing conductivity measurements in single DNA molecules. Several groups tried to address this issue through chemical bonding of functionalized DNA molecules to the metal surface [36, 71, 79]. This is usually done by attaching a thiol or an S-S end group to the DNA strands, utilizing the well known tendency of sulfur to form a covalent bond with gold surfaces and with gold nanoparticles (GNP) [78]. (See also Chap. 12 in this volume).

Xu et al. [71] used a very elegant method for measuring electrical transport through dsDNA in aqueous solution, where the native form of the DNA is preserved. Their measurement approach enables to accumulate larger statistics than most previous experiments. In addition they vary the DNA sequences by comparing measurements where AT base-pairs replace the GC base-pairs. They studied short sequences of DNA (8, 10, 12 and 14 base-pairs) that are modified at their 3' end with C₃H₆SH. The experimental approach they present addresses the two issues emphasized above: the contact is formed through a chemical bond between the electrode and the DNA molecule, and the DNA molecules are suspended in a buffer solution that maintains their native structure. Their approach presents a powerful investigational tool for short molecules. They allowed thiolated dsDNA to adsorb to a gold electrode in a buffer solution that supports annealing of the two strands and gives preference to the B-form structure of the double helix over other possible structures. In the same buffer solution, they bring into contact a gold STM tip, which is covered with an insulating layer over most of the tip surface except for its end. Once contact is formed – a junction – the tip is pulled backwards and the current is monitored (see Fig. 10). They observe distinct steps in the current when the tip is pulled away, which they interpret as consecutive breaking of junctions (e.g. the number of DNA strands that connect both electrodes is gradually reduced until none remain and the current drops). Xu et al. provide statistics of over 500 individual measurements. They observed some dispersion in the values of the peaks, which is attributed to variations in the microscopic details of the strands. A control experiment is carried out in buffer solution with no DNA, and does not show any current steps. To measure a single molecule, they halt the tip retraction at the position of the last peak (assuming that only one dsDNA connects both electrodes at that position) and measure I-V curves through the molecule. The curves obtained through 3 different single molecules show a rather smooth ohmic profile, coinciding with the average values of conductivity obtained from the pulling experiments.

We note that although STM was used here, no imaging characterization of single molecules or the structure and organization of the molecules on the surface is reported. No similar experiment with ssDNA that can only connect to one side is reported as a control. Such a control could validate the transport of charge through the double stranded helix, and shed light on the role of the chemical contact between the electrode and the measured

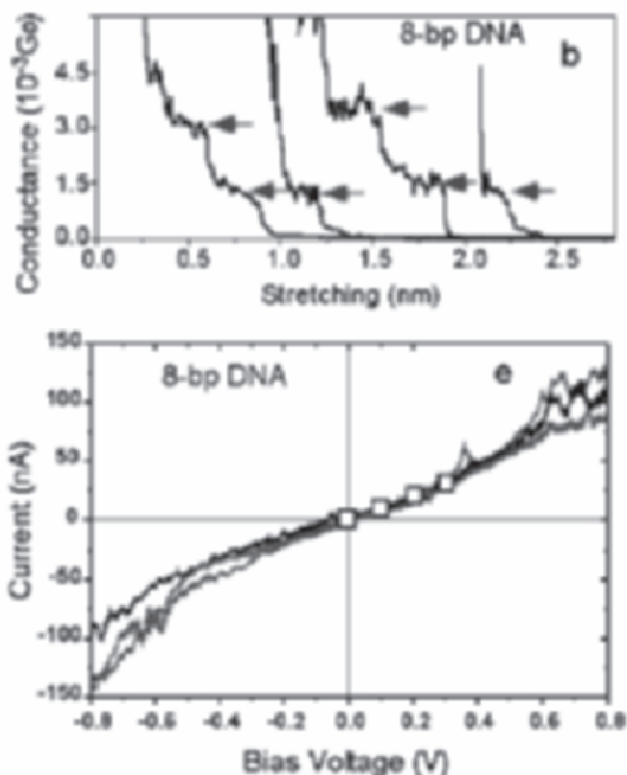


Fig. 10. (a) Schematic illustration of a single DNA conductance measurement. (bp Formation of molecular junctions shown as discrete steps in the conductance (eight-bp DNA duplex). (c) Conductance histogram constructed from more than 500 individual measurements revealing well-defined peaks near integer multiples of a fundamental value, $1.3 \times 10^{-3} G_0$ ($0.1 \mu\text{S}$), which is identified as the conductance of a single eight-bp DNA duplex. (d) Conductance histogram in buffer solution revealing a smooth background. (e) Current-voltage characteristic curves of a single eight-bp DNA. Lines with different colots are obtained by recording current vs. bias voltage for three different DNA junctions. The open squares are from the peak positions of the conductance histograms obtained at different bias voltages (From [71] by permission; © 2003 by the publishers of Nano Letters)

molecule. Nevertheless, we find this report to be one of the most elegant and informative experiments done on electrical transport in DNA so far.

Recently, Nogues et al. [79] published a different experimental approach which is also based on measuring current through dsDNA molecules connecting between a metal substrate and a metal tip. This approach allows measurement of conductivity in a systematic manner through many short DNA molecules and obtaining a large statistics. They form well-characterized monolayers of 5' end thiol-modified 26 bases long ssDNA. The complemen-

tary oligomer, which is also modified with a thiol at its 5' end, is adsorbed onto a GNP of 10 nm in diameter. Hybridization of the two strands affords an insulating ssDNA monolayer in which some of the ssDNA were hybridized with their complementary strands to form dsDNA that can be easily identified by the GNPs connected to them and where a direct contact of the GNP and the metal substrate is prevented. The formed monolayer is scanned with AFM to locate the GNPs indicating the dsDNA. A conductive tip is used to form contact to the GNP, and through this contact the I-V curves are measured through the dsDNA while approaching the tip to the GNP in contact mode. The control over the tip motion and the possible pressing of the GNP towards the surface during the electrical measurement is limited in this way but during the approach, current of a few nA can be measured through the dsDNA. The experimental setup and the measured I-Vs are presented schematically in Fig. 11. It is estimated that up to 10 dsDNA molecules can connect simultaneously between the GNP and the underlying gold surface although it is likely that the number of connecting molecules is smaller. Further investigations and controlled current-voltage measurements are underway in collaboration with us, to utilize this tool for the investigation of various DNA sequences and DNA derivatives.

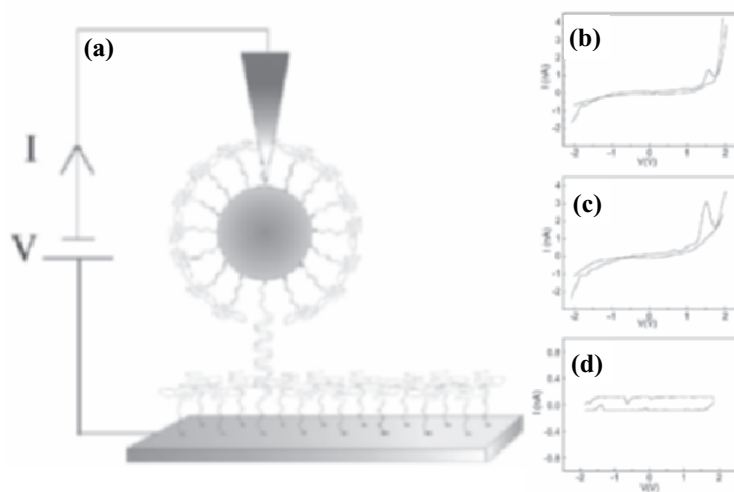


Fig. 11. (a) Schematic of a single-strand DNA monolayer on gold electrode and the double-strand DNA bridge between the gold substrate and the GNP formed through hybridization. (b,c) Consecutive I-V curves characteristic of the Au-DNA-GNP bridge measured by conductive tip AFM. (c) I-V curve measured directly on the single-strand DNA monolayer. Note the expanded scale relative to a, b (from [79] by permission, © 2004 by the publishers of PCCP)

2.2 Bundles and Networks

A few measurements of direct electrical transport were performed also on single bundles. Other measurements were done on networks formed of either double-stranded DNA [80] or alternative poly-nucleotides [81]. All the reported measurements showed current flowing through the bundles. We will show a few examples here.

The most productive group in the “networks field” is the group of Tomoji Kawai from Osaka that published an extended series of experiments on different networks and with various doping methods [82–84] and references therein. In one of their early experiments they measured the conductivity of a single bundle [80]. This was done in a similar way to the de Pablo experiment [64] (see Fig. 7), i.e., covering part of the bundle by a metal (electrode) and attaching a metal-covered AFM tip to the molecules at a various distances from the metal electrode along the molecule (see Fig. 12). The conductivity of a poly(dG)-poly(dC) bundle was measured as a function of length (50–250 nm) and was compared with that of a poly(dA)-poly(dT) bundle. The results showed a very clear length-dependent conductivity that was about an order of magnitude larger for the poly(dG)-poly(dC) bundle.

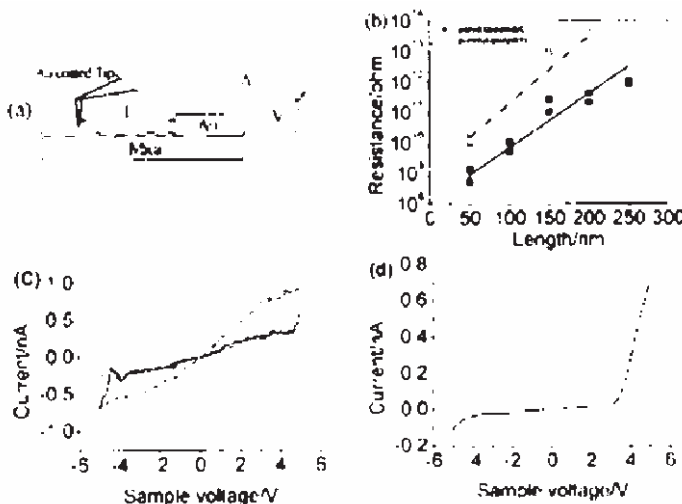


Fig. 12. (a) Schematic illustration of the measurement with a conducting-probe AFM. (b) Relationship between resistance and DNA length for poly(G)-poly(C) (dark marks) and for poly(A)-poly(T) (empty marks). The exponential fitting plots of the data are also shown. (c) Typical I-V curves of poly(dG)-poly(dC), the linear Ohmic behaviors on $L = 100$ nm at the repeat measurement of five samples. (d) Rectifying curves of poly(dG)-poly(dC) at $L = 100$ nm (from [80], by permission; © 2000 by the American Institute of Physics)

More recently [84] Kawai's group investigated the dependence of electrical resistivity of poly(dG)-poly(dC) thin films on humidity. This study was carried out using AC impedance and DC time dependence measurements at various humidity levels (40–80% relative humidity). In these experiments they report strong dependence of the conductivity on the relative humidity, in agreement with the findings of Jo et al. [86]. They also conclude that ionic conduction through the water layers dominates the total resistivity. In another study [85] Kawai's group studied the electrical properties of the contact between a gold-coated AFM tip and networks of 50 bases long oligomers of poly(dA-dT)-poly(dA-dT) and poly(dG-dC)-poly(dG-dC) that form on a highly oriented pyrolytic graphite (HOPG) surface. In this study, the resistance of DNA in air was found to be inversely proportional to the contact area at tip forces between 0 and 50 nN, as seen in Fig. 13. When higher force was applied a direct contact with the HOPG was established. The resistance of the DNA networks at 40 nN was found to be 1 to 5 M Ω . They conclude that in order to utilize DNA in molecular devices, it is necessary to modify the DNA so as to enable improved conductivity at the interface to the metal electrode with a lower potential barrier.

One of the interesting measurements among the "bundle experiments" was done by Rakitin et al. [87]. They compared the conductivity of a λ -DNA bundle to that of an M-DNA bundle [88–90] (DNA that contains an additional metal ion in each base-pair, developed by the group of Jeremy Lee [88–90] from Saskatchewan). The actual measurement was performed over a physical gap between two metal electrodes in vacuum (see Fig. 14). Metallic-like behavior was observed for the M-DNA bundle over 15 μ m, while for the λ -DNA bundle a gap of \sim 0.5 V in the I-V curve was observed followed by a rise of the current.

Another measurement that follows the line of the Porath et al. [14] experiment was performed by Yoo et al. [91]. In this experiment, long poly(dG)-poly(dC) and poly(dA)-poly(dT) molecules were electrostatically trapped between two planar metal electrodes that were 20 nm apart (see Fig. 15) on a SiO₂ surface, such that a bundle, \sim 10 nm wide, was formed. A planar gate electrode added another dimension to this measurement. The current-voltage curves showed a clear current flow through the bundle and both temperature and gate dependencies. The resistivity for the poly(dG)-poly(dC) was calculated to be 0.025 Ω cm.

Very high currents are measured in an experiment reported by Jo et al. [86], who attempted to measure conductivity of λ -DNA versus the conductivity of poly(dG)-poly(dC) and poly(dA)-poly(dT) in vacuum and under controlled humidity conditions. They used electrostatic trapping to attach the molecules to gold electrodes separated by a gap of 150 nm. They present I-V curves obtained immediately after dropping the solution containing the DNA samples, after drying the sample and then putting it in a controlled humidity chamber and in vacuum. S-shaped curves (\sim 1 μ A at 1 V) are reported

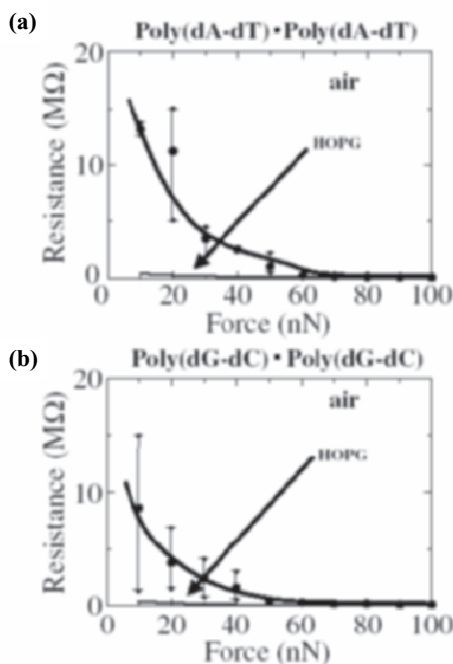


Fig. 13. Relationship between tip force and the resistance of DNA in the vertical direction for: (a) poly(dA-dT)-poly(dA-dT) and (b) poly (dG-dC)-poly (dG-dC). Broken lines show the curve for DNA. The solid line shows the curve for HOPG (from [85] by permission, © 2003 by the publishers of Jpn J Appl Phys)

for all types of DNA at relatively high humidity, which they relate to ionic charge transport by the H^+ ion. Under vacuum the conductivity of poly(dG)-poly(dC) for a given bias (~ 300 nA at 1 V) is found to be three and four orders of magnitudes larger than that of λ -DNA and poly(dA)-poly(dT), respectively, with a rectifying behavior. The authors relate all the changes in the curves to the changes in the humidity conditions. No information is provided regarding the number of molecules that are attached between the electrodes or independent evidence that DNA only is connecting the electrodes. Since the molecules are much larger than the gap between the electrodes, it is likely that bundles are measured in this experiment.

Hwang and co-workers [92] investigated conductivity of thiol-modified poly(dG)-poly(dC) of 60 base pairs. They adsorbed the dsDNA onto gold nanoparticles of 20 nm in diameter. These DNA coated nanoparticles were then dropped onto a 50 nm gap between two gold electrodes, and the I-V of the system was measured. Hwang et al. report currents of about 100 nA for 1 V bias for this system. The curves are generally gapless with some non-linearity. The number of parallel molecules bridging the GNPs and the metal

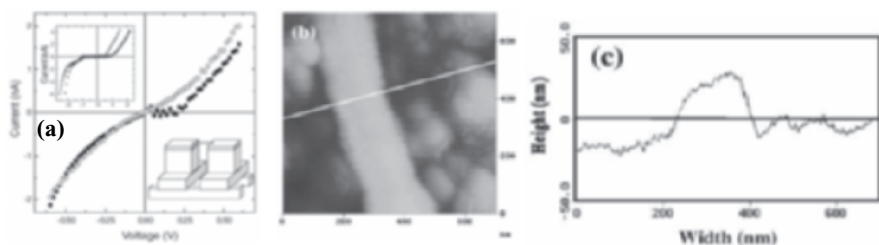


Fig. 14. (a) Current-voltage curves measured in vacuum at room temperature on M-DNA (○) and B-DNA (●) molecules. The DNA fibers are 15 μm long and the inter-electrode spacing is 10 μm. In contrast to the B-DNA behavior, M-DNA exhibits no plateau in the I-V curve. The lower inset shows the schematic experimental layout. The upper inset shows two representative current-voltage curves measured in vacuum at room temperature on samples of Au-oligomer-B-DNA-oligomer-Au in series. (b) AFM Image of a M-DNA bundle on the surface of the gold electrode (scale bar: 1 μm). (c) Cross section made along the white line in (b) using tapping-mode AFM giving a bundle height of 20–30 nm and width of about 100 nm, which implies it consists of ~300 DNA strands (from [87], by permission; © 2001 by the American Physical Society)

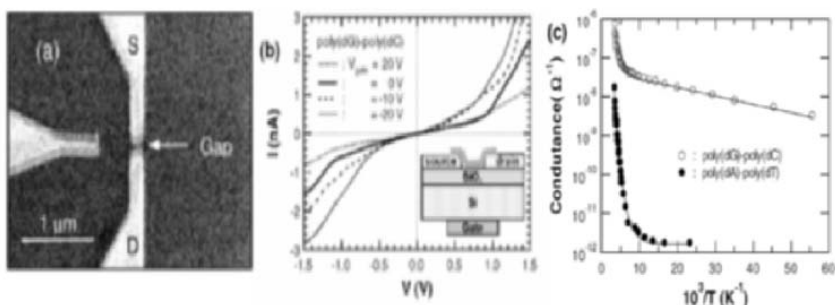


Fig. 15. (a) SEM image of an Au/Ti nanoelectrode with a 20 nm spacing. Three electrodes are shown, S and D stand for source and drain. (b) I-V curves measured at room temperature for various values of the gate voltage (V_{gate}) for poly(dG)-poly(dC). The inset of (b) is the schematic diagram of electrode arrangement for gate dependent transport experiments. (c) Conductance versus inverse temperature for poly(dA)-poly(dT) and poly(dG)-poly(dC), where the conductance at $V = 0$ was numerically calculated from the I-V curve (from [91], by permission; © 2001 by the American Physical Society)

electrodes is, however, not clear but quite large. Therefore, this experiment may reflect a network behavior.

Heim et al. [93] followed the experimental approach of de Pablo [64] as well, to examine conductivity in λ-DNA bundles and ropes, and to study the effects of the underlying solid surface and the electrode contacts on the DNA and its ability to transport charge. They report high resistivity of DNA

bundles, in the range of 10^9 for large bundles ($>\sim 1000$ DNA strands) to 10^{15} for smaller (few hundreds of DNA strands) bundles. This group aimed to reduce the flattening effect that the underlying surface has on the DNA height, by modifying SiO_2/Si substrate with self assembled monolayers of various hydrophobic/hydrophilic character, and with different end-groups. They formed and characterized monolayers of octadecyltrichlorosilane (OTS), oct-70-en-1-trichlorosilane (OETS) and 3-aminopropyltrimethoxysilane (APTMS). They also covered the SiO_2 surface with a spin-casted layer of polystyrene. The height of single DNA molecules that they measured is still about half of the expected crystallographic value of 2.4 nm. For OTS, APTMS and polystyrene the average heights were 1.58, 1.06 and 1.17 respectively. In contrast, Katsunov et al. [76] reported that modification of mica surface with pentylamine resulted in average height of about 2.4 nm. Both pentylamine and APTMS present ammonium groups towards the deposited DNA, and are expected to attract the polyanionic DNA molecules. It is not understood at this stage why the former resulted in height which is similar to that expected from X-ray crystallography, while the latter afforded height which is similar to that obtained on an unmodified surface. In any case, it seems that the underlying surface may play a crucial role by altering the structure and hence on the electrical properties of the DNA molecules.

Lei et al. [94] reported high resistivity of λ -DNA network ($\geq 1 \times 10^7 \Omega\text{cm}$), as measured by EFM using a method similar to that of Gómez-Navarro [75].

An experiment on a DNA-based network embedded in a cast film was done by Okahata et al. already in 1998 [52]. In this pioneering experiment the DNA molecules were embedded (with side groups) in a polymer matrix that was stretched between electrodes (see Fig. 16). It was found that the conductivity parallel to the stretching direction (along the DNA) was ~ 4.5 orders of magnitude larger than the perpendicular conductivity.

Measurements on a different type of DNA-based material were reported by Rinaldi et al. [95–97] (see Fig. 17). In this experiment they deposited a few layers of deoxyguanosine ribbons in the gap between two planar metal electrodes, ~ 100 nm apart. The current-voltage curves showed a gap followed by rise of the current beyond a threshold of a few volts. The curves depended strongly on the concentration of the deoxyguanosine in the solution.

2.3 Conclusions from the Experiments about DNA Conductivity

More and more evidences accumulating from the direct electrical transport measurements show that it is possible to transport charge carriers along short single DNA molecules, in bundles of molecules and in networks, although the conductivity is rather poor. This is consistent with the picture that emerges from the electron-transfer experiments. However, transport through long single DNA molecules (>40 nm) that are attached to the surface is apparently blocked. It may be due to the surface force field that induces many defects in the molecules and blocks the current or any additional reason.

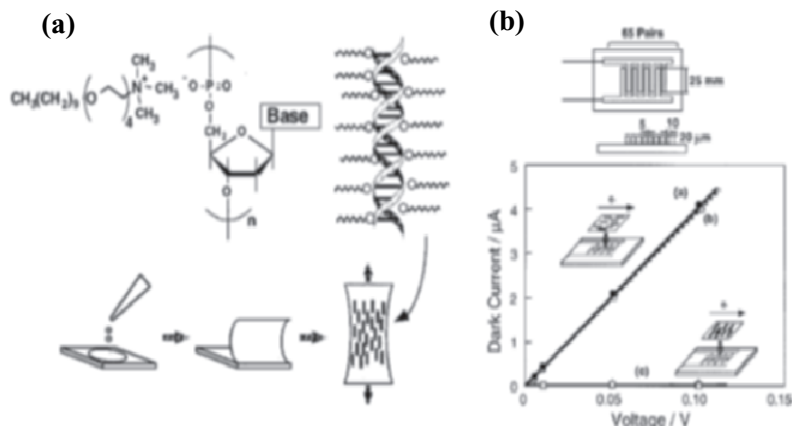


Fig. 16. (a) Schematic illustration of a flexible, aligned DNA film prepared from casting organic-soluble DNA-lipid complexes with subsequent uniaxial stretching. (b). Experimental geometries and measured dark currents for aligned DNA films (20×10 mm, thickness 30 ± 5 μm) on comb-type electrodes at 25°C . In the dark-current plot, the three curves represent different experimental settings and environments: (a) DNA strands in the film placed perpendicular to the two electrodes (scheme in the upper inset) and measured in ambient; (b) the same film as in (a) measured in a vacuum at 0.1 mmHg ; (c) DNA strands in the film placed parallel to the two electrodes, both in a vacuum and in ambient (from [52], by permission; © 1998 by the American Chemical Society)

Therefore, if one indeed wants to use DNA as an electrical molecular wire in nanodevices, or as a model system for studying electrical transport in a single one-dimensional molecular wire, then there are a few possible options. The first is to optimize the contacts by chemical bonding and minimize the surface-molecule interaction by an “elevation layer” (a pre-designed surface layer) that will reduce the surface affinity of the DNA molecules and hence the effect of the surface force field on the attached DNA. In addition it is possible to enhance the intrinsic conductivity of the DNA by doping, e.g., by one of the methods that are described in the literature [82, 87–90] (addition of intercalators, metal ions or O_2 etc.). Yet another way could be to use more exotic structures such as DNA quadruple-helices instead of the double-stranded structure. Such constructions may offer an improved stiffness and electronic overlap that would enhance the conductivity of these molecules.

3 Conclusions and Perspectives

Charge migration along DNA molecules has attracted a considerable scientific interest for over half a century. Results of solution chemistry experiments on large numbers of short DNA molecules indicated high charge-transfer rates

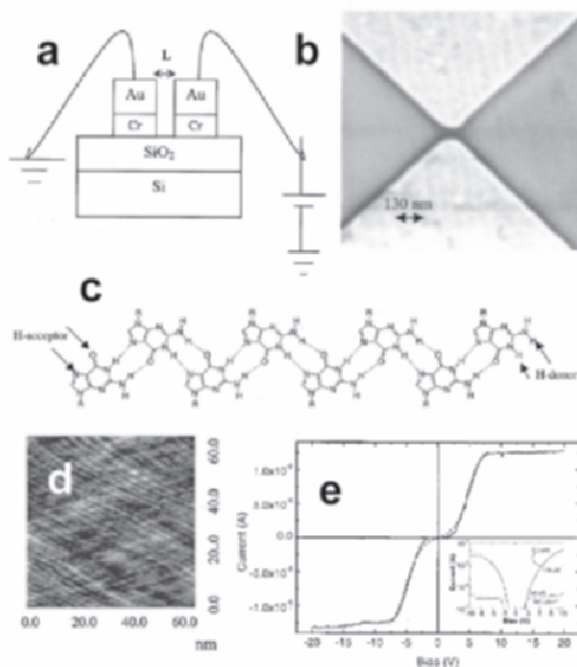


Fig. 17. (a) Schematic of the device used in the experiment. (b) SEM image of the gold nanoelectrodes, fabricated by electron beam lithography and lift-off onto a SiO₂/Si substrate. (c) Schematics of the ribbon-like structure formed by the deoxyguanosine molecules connected through hydrogen-bonds. R is a radical containing the sugar and alkyl chains. (d) AFM micrograph of the ordered deoxyguanosine film obtained after drying the solution in the gap. Regular arrangement of ribbons ranges over a distance of about 100 nm. The ribbon width of about 3 nm is consistent with that determined by X-ray measurements. (e) I-V characteristics of the device (from [95], by permission; © 2001 by the American Institute of Physics)

between a donor and an acceptor located at distant molecular sites. This, together with the extraordinary molecular recognition properties of the double helix and the hope to realize the bottom-up assembly of molecular electronic devices and circuits using DNA molecules, have triggered a series of direct electrical transport measurements through DNA. In this chapter we provided a comprehensive review of these measurements.

After the appearance of some initial controversial reports on the conductance of DNA devices, recent results seem to indicate that native DNA does not possess the electronic features desirable for a good molecular electronic building block, although it can still serve as a template for other conducting materials [12, 13, 98]. Particularly, it is found that short DNA molecules are capable of transporting charge carriers, and so are bundles and DNA-based

networks. However, electrical transport through long single DNA molecules that are attached to surfaces is blocked, possibly due to the attachment to the surface.

In a molecular electronics perspective, however, the fascinating program of further using the “smart” self-assembly capabilities of the DNA to realize complex electronic architectures at the molecular scale remains open for further investigation. To enhance the conductive properties of DNA-based devices there have been already interesting proposals for structural manipulation. These include intrinsic doping by metal-ions incorporated into the double helix (such as M-DNA [87–90, 99, 100], exotic structures like G4-DNA [101, 102], along with the synthesis of other novel helical structures.

A last comment is due on needs for progress in the investigation tools. Further development in the study of potential DNA nanowires requires the advancement of synthesis procedures for the structural modifications, and an extensive effort in X-ray and NMR characterization. Concerning direct conductivity measurements, techniques for deposition of the molecules onto inorganic substrates and between electrodes must be optimized. Moreover, the experimental settings and contacts must be controlled to a high degree of accuracy in order to attain an uncontroversial interpretation and high reproducibility of the data. On the theoretical side, a significant breakthrough might be the combination of mesoscopic theories for the study of quantum conductance and first-principle electronic structure calculations, suitable for applications to the complex molecules and device configurations of interest. Given this background, we believe that there is still plenty of room to shed light onto the appealing issue of charge mobility in DNA, for both the scientific interest in conduction through one-dimensional polymers and the nanotechnological applications. The high interdisciplinary content of such a research manifesto will necessarily imply a crossing of the traditional borders separating solid-state physics, chemistry and biological physics.

Acknowledgements

We thank Rosa Di Felice and Gianaurelio Cuniberti for their assistance. We acknowledge the support of the European grant for Future & Emerging Technologies (IST-2001-38951). D.P. acknowledges the support of The FIRST foundation, The Israeli Academy of Sciences and Humanities and The German Israel Foundation. J.G. acknowledges Funding by MyCT (project MAT2001-0664).

References

1. Luryi S, Xu J, Zaslavsky A (eds) Future Trends in Microelectronics: The Road Ahead. Wiley, New York, USA (1999)

2. Joachim C, Gimzewski JK, Aviram A: Electronics using hybrid-molecular and mono-molecular devices, *Nature* 408, 541 (2000)
3. Aviram A, Ratner MA (eds) *Molecular Electronics Science and Technology: Annals of the New York Academy of Sciences*, vol 852. The New York Academy of Sciences, New York (1998)
4. Aviram A, Ratner MA, Mujica V (eds) *Molecular Electronics II: Annals of the New York Academy of Sciences*, vol 960. The New York Academy of Sciences, New York (2002)
5. Tour JM: Molecular Electronics. Synthesis and Testing of Components, *Acc Chem Res* 33:791(2000)
6. Aviram A, Ratner MA: Molecular rectifiers, *Chem Phys Lett* 29:277 (1974)
7. Metzger RM: Electrical Rectification by a Molecule: The Advent of Unimolecular Electronic Devices, *Acc Chem Res* 9:2027 (1999)
8. Collier CP, Wong EW, Bolohradsky M, Raymo FM, Stoddart JF, Kuekes PJ, Williams RS, Heath JR: Electronically Configurable Molecular-Based Logic Gates, *Science* 285:391 (1999)
9. Reed MA, Zhou C, Muller CJ, Burgin TP, Tour JM: Conductance of a Molecular Junction Science, 278:252 (1997)
10. Collier CP, Mattersteig G, Wong EW, Luo Y, Beverly K, Sampario J, Raymo FM, Stoddart JF, Heath JR: A[2] Catenane-based solid state electronically reconfigurable switch, *Science* 289:1172 (2000)
11. Chen J, Reed MA: Electronic transport of molecular systems, *Chem Phys* 281:127 (2002)
12. Braun E, Eichen Y, Sivan U, Ben-Yoseph G: DNA-templated assembly and electrode attachment of a conducting silver wire, *Nature* 391:775 (1998)
13. Keren K, Krueger M, Gilad R, Ben-Yoseph G, Sivan U, Braun E: Sequence-Specific Molecular Lithography on Single DNA Molecules, *Science* 297:72 (2002)
14. Porath D, Bezryadin A, de Vries S, Dekker C: Direct measurement of electrical transport through DNA molecules, *Nature* 403:635 (2000)
15. Rinaldi R, Biasco A, Maruccio G, Cingolani R, Alliata D, Andolfi L, Facci P, De Rienzo F, Di Felice R, Molinari E: Solid-State Molecular Rectifier Based on Self-Organized Metalloproteins, *Adv Mater* 14:1453 (2002)
16. Rinaldi R, Biasco A, Maruccio G, Arima V, Visconti P, Cingolani R, Facci P, De Rienzo F, Di Felice R, Molinari E, Verbeet MP, Canters GW: Electronic rectification in protein devices, *Appl Phys Lett* 82:472 (2003)
17. Rinaldi R, Branca E, Cingolani R, Di Felice R, Calzolari A, Molinari E, Masiero S, Spada G, Gottarelli G, Garbesi: Biomolecular Electronic Devices Based on Self-Organized Deoxyguanosine Nanocrystals, *Molecular electronics II, Annals of the New York Academy of Sciences* 960:184 (2002)
18. Alberti P, Mergny J-L: DNA duplex-quadruplex exchange as the basis for a nanomolecular machine, *Proc Natl Acad Sci USA* 100:1569 (2003)
19. Benenson Y, Paz-Elizur T, Adar R, Keinan E, Livneh Z, Shapiro E: Programmable and autonomous computing machine made of biomolecules, *Nature* 414:430 (2001)
20. Benenson Y, Adar R, Paz-Elizur T, Livneh Z, Shapiro E: DNA molecule provides a computing machine with both data and fuel, *Proc Natl Acad Sci USA* 100:2191 (2003)
21. Porath D, Millo O: Single electron tunneling and level spectroscopy of isolated C-20 molecules, *J Appl Phys* 81:2241 (1997)

22. Lemay SG, Janssen JW, van den Hout M, Mooji M, Bronikowski MJ, Willis PA, Smalley RE, Kouwenhoven LP, Dekker C: Two-dimensional imaging of electronic wavefunctions in carbon nanotubes, *Nature* 412:617 (2001)
23. Liang W, Shores MP, Bockrath M, Long JR, Park H: Kondo resonance in a single-molecule transistor, *Nature* 417:725 (2002)
24. Thorwart M, Grifoni M, Cuniberti G, Postma HWC, Dekker C: Correlated tunneling in intramolecular carbon nanotube quantum dots, *Phys Rev Lett* 89:196402 (2002)
25. Porath D, Cuniberti G, Di Felice R, in Shuster G (ed.): Charge transport in DNA-based devices, *Topics Curr Chem* 237, (2003) (ISBN: 3-540-20131-9).
26. Ventra M, Di Zwolak M, in Singh Nalwa H (ed.) *Encyclopedia of Nanoscience and Nanotechnology*, American Scientific Publishers, CA. (2003)
27. Enders RG, Cox DL, Singh RRP: The quest for high-conductance DNA, *Rev Mod Phys* 76:195. (2004)
28. Lehn JM: Perspectives in Supramolecular Chemistry – From Molecular Recognition towards Molecular Information Processing and Self-Organization, *Angew Chem Int Ed in English*, 29:1304 (1990)
29. Di Mauro E, Hollenberg CP: DNA technology in chip construction, *Adv Mat* 5:384 (1993)
30. Niemeyer CM: DNA as a material for nanotechnology, *Angew Chem Int Ed in English* 36:585 (1997)
31. Niemeyer CM: Nanoparticles, Proteins, and Nucleic Acids: Biotechnology Meets Materials Science, *Angew Chem Int Ed* 40: 4128 (2001)
32. Chen J, Seeman NC: Synthesis from DNA of a molecule with the connectivity of a cube, *Nature* 350:631 (1991)
33. Zhang Y, Seeman NC: Construction of a DNA truncated octahedron, *J Am Chem Soc* 116:1661 (1994)
34. La Bean T, Yan H, Kopatsch J, Liu F, Winfree E, Reif JH, Seeman NC: Construction, analysis, legation, and self-assembling of DNA triple crossover complexes, *J Am Chem Soc* 122:1848 (2000)
35. Seeman NC: DNA Nicks and Nodes and Nanotechnology, *Nano Lett* 1:22 (2001)
36. Zhang Y, Austin RH, Kraeft J, Cox EC: Insulating behavior of lambda-DNA on the micron scale, *Ong NP Phys Rev Lett* 89:198102 (2002)
37. Dekker C, Ratner MA: Electronic properties of DNA, *Physics World* 14:29 (2001)
38. Eley DD, Spivey DI: Semiconductivity of organic substances. Nucleic acid in the dry state, *Trans Faraday Soc* 12:245 (1962)
39. Warman JM, de Haas MP, Rupprecht A: DNA: a molecular wire, *Chem Phys Lett* 249:319 (1996)
40. O'Neill P, Fielden EM: Primary free radical processes in DNA, *Adv Radiat Biol* 17:53 (1993)
41. Retèl J, Hoebee B, Braun JEF, Lutgerink JT, van den Akker E, Wanamarta AH, Joenje H, Lafleur MVM: Mutational specificity of oxidative DNA damage, *Mutation Res* 299:165 (1993)
42. Turro NJ, Barton JK: Paradigms, supermolecules, electron transfer and chemistry at a distance. What's the problem? The science or the paradigm?, *J Biol Inorg Chem.* 3:201 (1998)

43. Lewis FD, Wu T, Liu X, Letsinger RL, Greenfield SR, Miller SE, Wasielewski MR: Dynamics of photoinduced charge separation and charge recombination in synthetic DNA hairpins with stilbenedicarboxamide, *J Am Chem Soc* 122:2889 (2000)
44. Murphy CJ, Arkin MA, Jenkins Y, Ghatlia ND, Bossman S, Turro NJ, Barton JK: Long-range photoinduced electron transfer through a DNA helix, *Science* 262:1025 (1993)
45. Hall DB, Holmlin RE, Barton JK: Oxidative DNA damage through long-range electron transfer, *Nature* 382:731 (1996)
46. Kelley SO, Jackson NM, Hill MG, Barton JK: Long-range electron transfer through DNA films, *Angew Chem Int Ed* 38:941 (1999)
47. Grinstaff MW: How Do Charges Travel through DNA? – An Update on a Current Debate, *Angew Chem Int Ed* 38:3629 (1999)
48. Barbara PF, Olson EJC: Experimental electron transfer kinetics in a DNA environment, *Adv Chem Phys* 107:647 (1999)
49. Bixon M, Giese B, Wessely S, Langenbacher T, Michel-Beyerle ME, Jortner J: Long-range charge hopping in DNA, *Proc Natl Acad Sci USA* 96:11713 (1999)
50. Schuster GB: Long-range charge transfer in DNA: transient structural distortions control the distance dependence, *Acc Chem Res* 33:253 (2000)
51. Conwell EM, Rakhmanova SV: Polarons in DNA, *Proc Natl Acad Sci USA* 97:4556 (2000)
52. Okahata Y, Kobayashi T, Tanaka K, Shimomura M: Anisotropic electric conductivity in an aligned DNA cast film, *J Am Chem Soc* 120:6165 (1998)
53. Fink HW, Schönenberger C: Electrical conduction through DNA molecules, *Nature* 398:407(1999)
54. Bredas JL, Streat GB: Polarons, bipolarons, and solitons in conducting polymers, *Acc Chem Res* 18:309 (1985)
55. Nitzan A: A relationship between electron-transfer rates and molecular conduction, *J Phys Chem A* 105:2677 (2001)
56. Nitzan A: The Relationship between Electron Transfer Rate and Molecular Conduction. 2. The Sequential Hopping Case, *Isr J Chem* 42:163 (2002)
57. R. Di Felice, A. Calzolari, D. Versano, A. Rubio: Electronic structure calculations for nanomolecular systems, *Lecture Notes in Physics* vvv, xxx (2005); Chap. 3 of this collection.
58. Meggers E, Michel-Beyerle ME, Giese B: Sequence dependent long range hole transport in DNA, *J Am Chem Soc* 120:12950 (1998)
59. Giese B, Amaudrut J, Köhler AK, Spormann M, Wessely S: Direct observation of hole transfer through DNA by hopping between adenine bases and by tunneling, *Nature* 412:318 (2001)
60. Davis WB, Naydenova I, Haselbeger R, Ogorodnik A, Giese B, Michel-Beyerle ME: Dynamics of hole trapping by GG, GG, and GGG in DNA, *Angew Chem Int Ed* 39:3649 (2000)
61. Giese B: Electron transfer in DNA., *Curr Opin Chem Biol* 6:612 (2002)
62. O'Neill MA, Barton JK: Effects of strand and directional asymmetry on base-base coupling and charge transfer in double-helical DNA, *Proc Natl Acad Sci USA* 99:16543, (2002)
63. Henderson PT, Jones D, Hampikian G, Kan Y, Schuster G: Long-distance charge transport in duplex DNA: the phonon-assisted polaron-like hopping mechanism, *Proc Natl Acad Sci USA* 96:8353 (1999)

64. de Pablo PJ, Moreno-Herrero F, Colchero J, Gómez Herrero J, Herrero P, Baró AM, Ordejón P, Soler JM, Artacho E: Absence of dc-conductivity in lambda-DNA, *Phys Rev Lett* 85:4992 (2000)
65. Storm AJ, van Noort J, de Vries S, Dekker C: Insulating behavior for DNA molecules between nanoelectrodes at the 100 nm length scale, *Appl Phys Lett* 79:3881 (2001)
66. Kasumov AY, Kociak M, Guérón S, Reulet B, Volkov VT, Klinov DV, Bouchiat H: Proximity-induced superconductivity in DNA, *Science* 291:280 (2001)
67. Watanabe H, Manabe C, Shigematsu T, Shimotani K, Shimizu M: Dual-probe scanning tunneling microscope: Measuring a carbon nanotube ring transistor, *Appl Phys Lett* 79:2462 (2001)
68. Shigematsu T, Shimotani K, Manabe C, Watanabe H, Shimizu M: Transport properties of carrier-injected DNA, *J Chem Phys* 118:4245 (2003)
69. Watanabe H, Shimotani K, Shigematsu T, Manabe C: Electric measurements of nano-scaled devices, *Thin Solid Films* 438: 462 (2003)
70. Shimotani K, Shigematsu T, Manabe C, Watanabe H, Shimizu M: An advanced electric probing system: Measuring DNA derivatives, *J Chem Phys* 118:8016 (2003)
71. Xu B, Zhang P, Li X, Tao N: Direct conductance measurement of single DNA molecules in aqueous solution, *Nano Lett* 4:1105 (2004)
72. Bezryadin A, Dekker C: Nanofabrication of electrodes with sub-5nm spacing for transport experiments on single molecules and metal clusters, *J Vac Sci Technol B* 15:793 (1997)
73. Bezryadin A, Dekker C, Schmid G: Electrostatic trapping of single conducting nanoparticles between nanoelectrodes, *Appl Phys Lett* 71:1273 (1997)
74. Bockrath M, Markovic N, Shepard A, Tinkham M, Gurevich L, Kouwenhoven LP, Wu MW, Sohn LL: Scanned conductance microscopy of carbon nanotubes and lambda-DNA, *Nano Lett* 2:187 (2002)
75. Gómez-Navarro C, Moreno-Herrero F, de Pablo PJ, Colchero J, Gómez-Herrero J, Baró AM: Contactless experiments on individual DNA molecules show no evidence for molecular wire behavior, *Proc Natl Acad Sci USA* 99:8484 (2002)
76. Kasumov A Yu, Klinov DV, Roche P-E, Gueron S, Bouchiat H: Thickness and low-temperature conductivity of DNA molecules, *Appl Phys Lett* 84:1007 (2004)
77. Yang C, Moses D, Heeger AJ: Base-Pair Stacking in Oriented Films of DNA-Surfactant Complex *Adv Mater* 15:1364 (2003)
78. Salomon A, Cahen D, Lindsay S, Tomfohr J, Engelkes VB, Frisbie CD: Comparison of Electronic Transport Measurements on Organic Molecules, *Adv Mater* 15, 1881 (2003)
79. Nogues C, Cohen SR, Daube SS, Naaman R: Electrical properties of short DNA oligomers characterized by conducting atomic force microscopy, *Phys Chem Chem Phys* 6:4459 (2004)
80. J. Tomfohr, G. Ramachandran, O. F. Sankey, S. M. Lindsay: Making contacts to single molecules: Are we there yet? *Lecture Notes in Physics* vvv, xxx (2005); Chap. 11 of this collection.
81. Cai L, Tabata H, Kawai T: Self-assembled DNA networks and their electrical conductivity, *Appl Phys Lett* 77:3105 (2000)

82. Lee HY, Tanaka H, Otsuka Y, Yoo K-H, Lee J-O, Kawai T: Control of electrical conduction in DNA using oxygen hole doping, *Appl Phys Lett* 80:1670 (2002)
83. Tabata H, Cai LT, Gu J-H, Tanaka S, Otsuka Y, Sacho Y, Taniguchi M, Kawai T: Toward the DNA electronics *Synthetic Metals* 133:469 (2003)
84. Taniguchi M, Lee HY, Tanaka H, Kawai T: Electrical Properties of Poly(dA)-Poly(dT) and Poly(dG)-Poly(dC) DNA Doped with Iodine Molecules *Jpn J Appl Phys* 42:L215 (2003)
85. Taniguchi M, Otsuka Y, Tabata H, Kawai T: Humidity Dependence of Electrical Resistivity in Poly(dG)-Poly(dC) DNA Thin Film, *Jpn J Appl Phys* 42:6629 (2003)
86. Tanaka S, Cai L-T, Tabata H, Kawai T: Electrical Conducting Properties of DNA Molecules in a Metal (tip)/DNA/highly Oriented Pyrolytic Graphite Configuration, *Jpn J Appl Phys* 42:2818 (2003)
87. Jo Y-S, Lee Y, Roh Y: Current-voltage characteristics of lambda and poly-DNA, *Mater Sci Eng* C23:841 (2003)
88. Rakitin A, Aich P, Papadopoulos C, Kobzar Y, Vedeneev AS, Lee JS, Xu JM: Metallic conduction through engineered DNA: DNA nanoelectronics building blocks, *Phys Rev Lett* 86:3670 (2001)
89. Aich P, Labiuk SL, Tari LW, Delbaere LJT, Roesler WJ, Falk KJ, Steer RP, Lee JS: M-DNA: a complex between divalent metal ions and DNA which behaves as a molecular wire, *J Mol Biol* 294:477 (1999)
90. Wettig SD, Wood DO, Lee JS: Thermodynamic investigation of M-DNA: a novel metal ion-DNA complex, *J Inorg Biochem* 94:94 (2003)
91. Li C-Z, Long Y-T, Kraatz H-B, Lee JS: Electrochemical investigations of M-DNA self-assembled monolayers on gold electrodes, *J Phys Chem B* 107:2291 (2003)
92. Yoo K-H, Ha DH, Lee J-O, Park JW, Kim J, Kim JJ, Lee H-Y, Kawai T, Choi HY: Electrical Conduction through Poly (dA)-Poly (dT) and Poly (dG)-Poly (dC) DNA Molecules, *Phys Rev Lett* 87:198102 (2001)
93. Hwang JS, Hwang SW, Ahn D: Superlattices and Microstructures 34:433 (2003)
94. Heim T, Deresmes D, Vuillaume D: Conductivity of DNA probed by conducting-atomic force microscopy: Effects of contact electrode, DNA structure, and surface interactions, *J Appl Phys* 96:2927 (2004)
95. Lei CH, Das A, Elliott M, McDonald JE: Conductivity of macromolecular networks measured by electrostatic force microscopy, (2003) *Appl Phys Lett* 83:482
96. Rinaldi R, Branca E, Cingolani R, Masiero S, Spada GP, Gottarelli G: Phototdetectors fabricated from a self-assembly of a deoxyguanosine derivative, (2001) *Appl Phys Lett* 78:3541
97. Maruccio G, Visconti P, Arima V, D'Amico S, Biasco A, D'Amone E, Cingolani R, Rinaldi R, Masiero S, Giorgi T, Gottarelli G: Field effect transistor based on a modified DNA base, *Nano Lett* 3:479 (2003)
98. Richter J, Mertig M, Pompe W, Mönch I, Schackert HK: Construction of highly conductive nanowires on a DNA template, *Appl Phys Lett* 78:536 (2001)
99. Tanaka K, Yamada Y, Shionoya M: Formation of silver(I)-mediated DNA duplex and triplex through an alternative base pair of pyridine nucleobases, *J Am Chem Soc* 124:8802 (2002)

100. Tanaka K, Tengeiji A, Kato T, Toyama N, Shionoya M: A discrete self-assembled metal array in artificial DNA., *Science* 299:1212 (2003)
101. Calzolari A, Di Felice R, Molinari E, Garbesi A: G-quartet biomolecular nanowires, *Appl Phys Lett* 80:3331 (2002)
102. Phillips K, Dauter Z, Morchie AIH, Lilley DMJ, Luisi B: The crystal structure of a parallel-stranded guanine tetraplex at 0.95 Å resolution, *J Mol Biol* 273:171 (1997)
103. Parkinson GN, Lee MPH, Neidle S: Crystal structure of parallel quadruplexes from human telomeric DNA, *Nature* 417:876 (2002)

CMOL: Devices, Circuits, and Architectures

Konstantin K. Likharev and Dmitri B. Strukov

Stony Brook University, Stony Brook, NY 11794, USA

Abstract. This chapter is a brief review of the recent work on various aspects of the prospective hybrid semiconductor/nanowire/molecular (“CMOL”) integrated circuits. The basic idea of such circuits is to combine the advantages of the currently dominating CMOS technology (including its flexibility and high fabrication yield) with those of molecular devices with nanometer-scale footprint. Two-terminal molecular devices would be self-assembled on a pre-fabricated nanowire crossbar fabric, enabling very high function density at acceptable fabrication costs. Preliminary estimates show that the density of active devices in CMOL circuits may be as high as 10^{12} cm^{-2} and that they may provide an unparalleled information processing performance, up to 10^{20} operations per cm^2 per second, at manageable power consumption. However, CMOL technology imposes substantial requirements (most importantly, that of high defect tolerance) on circuit architectures. In the view of these restrictions, the most straightforward application of CMOL circuits is terabit-scale memories, in which powerful bad-bit-exclusion and error-correction techniques may be used to boost the defect tolerance. The implementation of Boolean logic circuits is more problematic, though our preliminary results for reconfigurable, uniform FPGA-like CMOL circuits look very encouraging. Finally, CMOL technology seems to be uniquely suitable for the implementation of the “CrossNet” family of neuromorphic networks for advanced information processing including, at least, pattern recognition and classification, and quite possibly much more intelligent tasks. We believe that these application prospects justify a large-scale research and development effort focused on the main challenge of the field, the high-yield self-assembly of molecular devices.

1 Introduction

The recent spectacular advances in molecular electronics (for reviews see, e.g., 1–3 and other chapters of this collection), and especially the experimental demonstration of molecular single-electron transistor by several groups [4–8] give hope for the practical introduction, within the next 10 to 20 years, of the first integrated circuits with active single- or few-molecule devices.

This long-expected breakthrough could not have arrived more timely. Indeed, the recent results [9,10] indicate that the current VLSI paradigm, based on a combination of lithographic patterning, CMOS circuits, and Boolean logic, can hardly be extended into a-few-nm region. The main reason is that at gate length below 10 nm, the sensitivity of parameters (most importantly,

the gate voltage threshold) of silicon field-effect transistors (MOSFETs) to inevitable fabrication spreads exponentially. As a result, the gate length should be controlled with a few-angstrom accuracy, far beyond even the long-term projections of the semiconductor industry [11]. Even if such accuracy could be technically implemented using sophisticated patterning technologies, this would send the fabrication facilities costs (growing exponentially even now) skyrocketing, and lead to the end of Moore's Law some time during the next decade.

The main alternative nanodevice concept, single-electronics [10,12], offers some potential advantages over CMOS, including a broader choice of possible materials. Unfortunately, for room-temperature operation the minimum features of these devices (single-electron islands) should be below ~ 1 nm [12]. Since the relative accuracy of their definition has to be between 10 and 20%, the absolute fabrication accuracy should be of the order of 0.1 nm, again far too small for the current and realistically envisioned lithographic techniques.

This is why there is a rapidly growing consensus that the impending crisis of the microelectronics progress may be resolved only by a radical paradigm shift from the lithography-based fabrication to the "bottom-up" approach. In the latter approach, the smallest active devices should be formed in a special way ensuring their fundamental reproducibility. The most straightforward example of such device is a specially designed and chemically synthesized molecule comprising of a few hundreds of atoms, including the functional parts (e.g., acceptor groups working as single-electron islands and short fragments of non-conducting groups as tunnel junctions [4–8]), the groups enabling chemically-directed self-assembly of the molecule on prefabricated electrodes (e.g., thiol or isocyanide groups [1–8]), and very probably some additional groups ensuring sufficient rigidity and stability of the molecule at room temperature.

Unfortunately, integrated circuits consisting of molecular devices alone are hardly viable, because of limited device functionality. For example, the voltage gain of a 1-nm-scale transistor, based on any known physical effect (e.g., the field effect, quantum interference, or single-electron charging), can hardly exceed one, i.e. the level necessary for sustaining the operation of virtually any active analog or digital circuit.¹ This is why we believe that the

¹The very recent suggestion [13] to replace transistors with the so-called Goto pairs of two-terminal latching switches in crossbar circuits runs into several problems, most importantly the relation between the retention time and switching speed. In order to be useful for most electronics applications, the latches should be switched very fast (in a few picoseconds in order to compete with advanced MOSFETs), but retain their internal state for the time necessary to complete the calculation (ideally, for a few years, though several hours may be acceptable in some cases). This means that the change of the applied voltage by the factor of two (the difference between the fully selected and semi-selected crosspoints of a crossbar) should change the switching rate by at least 16 orders of magnitude. However, even the most favorable physical process we are aware of (the quantum-mechanical tunneling through

only plausible way toward high-performance nanoelectronic circuits is to integrate molecular devices, and the connecting nanowires, with CMOS circuits whose (relatively large) field-effect transistors would provide the necessary additional functionality, in particular high voltage gain.

Recently, several specific proposals of such circuits were published and several groups made initial steps toward the experimental implementation of semiconductor-molecular hybrids [15–17]. (Detailed reviews of this, and some other previous work on molecular electronics circuitry may be found in [18, 19]) The goal of this chapter is to review the recent work in one promising direction toward hybrid semiconductor-molecular electronics, the so-called CMOL approach. We will start from a discussion (in Sects. 2 and 3) of the hardware aspects of this concept. The remainder of the chapter is devoted to a discussion of possible architectures and applications of the CMOL circuits. Section 4 describes the results of our recent analysis of their most straightforward application, digital memories. In Sect. 5 we discuss the situation with possible CMOL logic circuits. One more promising direction of CMOL work, toward mixed-signal neuromorphic networks, is reviewed in Sect. 6. Finally, in the Conclusion (Sect. 7) we briefly summarize the results of our discussion.

2 Devices

The first critical issue in the development of semiconductor/molecular hybrids is making a proper choice in the trade-off between molecule simplicity and functionality. On one hand, simple molecules (like the octanedithiols [20]), which may provide nonlinear but monotonic $I - V$ curves with no hysteresis (i.e. no internal memory), are hardly sufficient for highly functional integrated circuits, because a semiconductor memory subsystem would hardly be able to store enough data for processing by more numerous molecular devices. On the other hand, a very complex molecule (like a long DNA strand [21]) may have numerous configurations that can be, as a matter of principle, used for information storage. However, such molecules are typically very “soft”, so that thermal fluctuations at room temperature (that is probably the only option for broad electronics applications) may lead to uncontrollable switches between their internal states, making reliable information storage and usage difficult, if not totally impossible.

This is why we believe that relatively short and rigid molecules (with the number of atoms of the order of one hundred), having two (or a few) metastable internal states, are probably the best choice for the initial development of molecular electronics. Our own best choice is the binary “latching

high-quality dielectric layers like the thermally-grown SiO_2) may only produce, at these conditions, the rate changes below 10 orders of magnitude, even if uncomfortably high voltages of the order of 12 V are used [14].

switch", i.e. a two-terminal, bistable device with $I - V$ curves of the type shown in Fig. 1a.² Such switch may be readily implemented, for example, as a combination of two single-electron devices: a "transistor" and a "trap" (Fig. 1b).³ If the applied drain-to-source voltage $V = V_d - V_s$ is low, the trap island in equilibrium has no extra electrons ($n = 0$), and its net electric charge $Q = -ne$ is zero. As a result, the transistor is in the virtually closed (OFF) state, and source and drain are essentially disconnected. If V is increased beyond a certain threshold value V_+ , its electrostatic effect on the trap island potential (via capacitance C_s) leads to tunneling of an additional electron into the trap island: $n \rightarrow 1$. This change of trap charge affects, through the coupling capacitance C_c , the potential of the transistor island, and suppresses the Coulomb blockade threshold to a value well below V_+ . As a result, the transistor, whose tunnel barriers should be thinner than that of the trap, is turned into ON state in which the device connects the source and drain with a finite resistance R_0 . (Thus, the trap island plays the role similar to that of the floating gate in the usual nonvolatile semiconductor memories [14].) If the applied voltage stays above V_+ , this connected state is sustained indefinitely; however, if V remains low for a long time, the thermal fluctuations will eventually kick the trapped electron out, and the transistor will get closed, disconnecting the electrodes. This ON \rightarrow OFF switching may be forced to happen much faster by making the applied voltage V sufficiently negative, $V \approx V_-$.⁴

Figure 1c shows a possible molecular implementation of the device shown in Fig. 1b. Here two different diimide acceptor groups play the role of single-electron islands, while short oligo-ethynylenephenylene (OPE) chains are used as tunnel barriers. The chains are terminated by isocyanide-group "clamps" ("alligator clips") that should enable self-assembly of the molecule across a gap between two metallic electrodes.

This immediately brings us to possibly the most important challenge faced by the development of VLSI molecular electronics, the reproducible self-assembly of the molecules on prefabricated electrodes. To the best of our knowledge, no group has yet succeeded to achieve acceptable yield of such process even for single devices. Moreover, even successful (conducting) samples differ by the current scale and sometimes the general shape of their $I - V$ curves. This is not entirely surprising, because the used clamp groups (like those shown in Fig. 1c) can hardly ensure a unique position of the molecule

²Multi-terminal devices would be immeasurably more complex for the chemically-directed self-assembly.

³Low-temperature prototypes of this device have been implemented and successfully tested experimentally, with electron trapping times beyond 12 hours [22].

⁴A virtually similar functionality may be achieved using configurational changes of specially selected molecules [13, 23, 24], however, such molecules are rather complex, and their switching may be too slow for most applications.

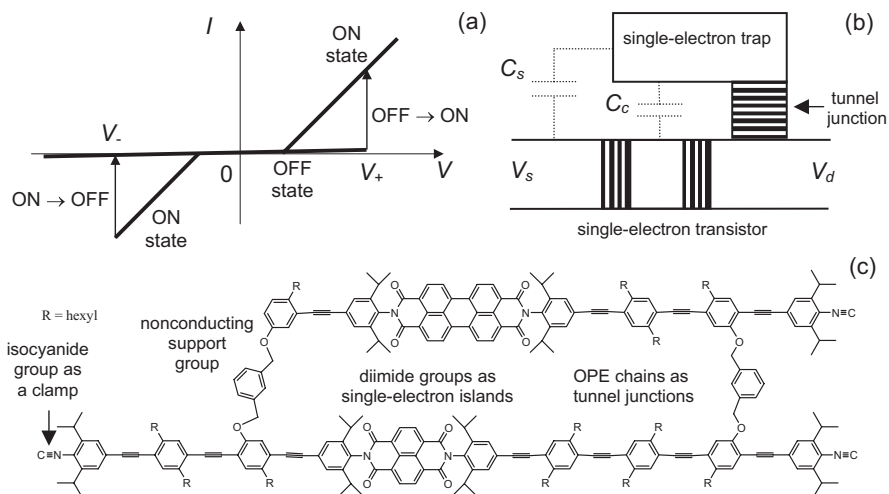


Fig. 1. Two-terminal latching switch: (a) $I - V$ curve (schematically), (b) single-electron device schematics [25], and (c) a possible molecular implementation of the device (courtesy A. Mayr)

relative to the electrodes, and hence a unique structure and transport properties of molecular-to-electrode interfaces.

One possible way toward high self-assembly yield is the chemical synthesis of molecules including relatively large “floating electrodes” (large acceptor groups or metallic clusters – see Fig. 2). If the characteristic internal resistance R_0 of such a molecule is much higher than the range of possible values of molecule/electrode resistances R_i , and the floating electrode capacitances are much higher than those of the internal single-electron islands, then the transport through the system will be determined by R_0 and hence be reproducible.⁵

Another possible way toward high yield is to form a self-assembled monolayer (SAM) on the surface of the lower nanowire level, and only then deposit and pattern the top layer. Such approach has already given rather reproducible results (in the nanopore geometry) for simple, short molecules [20]. The apparent problem here is that each crosspoint would have several parallel devices even if the nanowire width is scaled down to a few nanometers, and

⁵Actually, this approach to interfaces is very much parallel to that accepted de facto in semiconductor electronics. Indeed, despite decades of research, properties of silicon-to-metal interfaces (in particular, the Fermi level pinning due to surface traps) are still neither completely understood nor fully predictable. This is why in most semiconductor circuit technologies, metal-semiconductor junctions are used only as passive Ohmic contacts, while active devices are built around much better explored $p - n$ junctions formed inside the semiconductor.

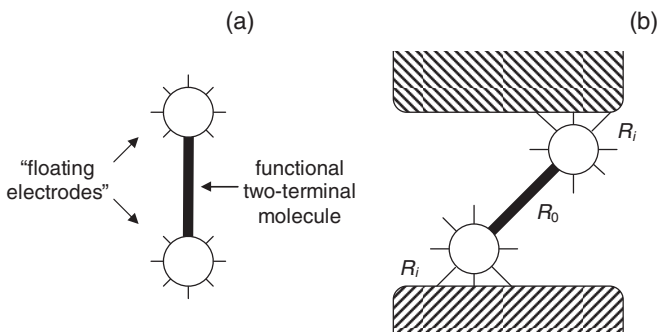


Fig. 2. A molecule with “floating electrodes” (a) before and (b) after its self-assembly on “real electrodes”, e.g., metallic nanowires (schematically)

this number may not be somewhat different from crosspoint to crosspoint. However, all circuits discussed below can function properly even in this case.

The potentially enormous density of molecular devices can hardly be used without individual contacts to each of them. This is why the fabrication of wires with nanometer-scale cross-section is another central problem of molecular microelectronics. The currently available photolithography methods, and even their rationally envisioned extensions, will hardly be able to provide such resolution. Several alternative techniques, like the direct e-beam writing and scanning-probe manipulation can provide a nm-scale resolution, but their throughput is forbiddingly low for VLSI fabrication. Self-growing nanometer-scale-wide structures like carbon nanotubes or semiconductor nanowires can hardly be used to solve the wiring problem, mostly because these structures (in contrast with the specially synthesized molecules that have been discussed above) do not have means for reliable placement on the lower integrated circuit layers with the necessary (a-few-nm) accuracy. Fortunately, there are several new patterning methods, notably nanoimprint [26] and interference lithography [27], which may provide much higher resolution (in future, down to a few nanometers) than the standard photolithography.

3 Circuits

These novel patterning technologies cannot be used, however, for the fabrication of arbitrary integrated circuits, in particular because they lack adequate layer alignment accuracy. This means that the nanowire layers should not require precise alignment with each other and with the CMOS subsystem. While the former requirement may be readily satisfied by using the “crossbar” nanowire structure (i.e., two layers of similar wires perpendicular to those of the other layer), the solution of the latter problem (CMOS-to-nanowire

interface) is much harder. In fact, the interface should enable the CMOS subsystem, with a relatively crude device pitch $2\beta F_{\text{CMOS}}$ (where $\beta \sim 1$ is the ratio of the CMOS cell size to the wiring period), to address each wire separated from the next neighbors by a much smaller distance F_{nano} .

Several solutions to this problem, which had been suggested earlier, seem either unrealistic, or inefficient, or both. In particular, the interface based on statistical formation of semiconductor-nanowire field-effect transistors gated by CMOS wires [28, 29] can only provide a limited (address-decoding-type) connectivity. In addition, the resistivity of semiconductor nanowires would be too high for high-performance hybrid circuits. Even more importantly, the technology of ordering chemically synthesized semiconductor nanowires into highly ordered parallel arrays has not been developed, and the authors of this review are not aware of any promising idea that may allow such assembly.

A more interesting approach was discussed in [30](see also [18]). It is based on cutting the ends of nanowires of a parallel-wire array, along a line that forms a small angle $\alpha = \arctan(F_{\text{nano}}/F_{\text{CMOS}})$ with the wire direction. As a result of the cut, the ends of adjacent nanowires stick out by distances (along the wire direction) differing by $2F_{\text{CMOS}}$, and may be contacted individually by the similarly cut CMOS wires. Unfortunately, the latter (CMOS) cut has to be precisely aligned with the former (nanowire) one, and it is not clear from [30] how exactly such a feat might be accomplished using available patterning techniques.

Figure 3 shows our approach to the interface problem. (We call such circuits CMOL, standing for CMOS/nanowire/MOLecular hybrids.) The difference between the CMOL approach (based on earlier work on the so-called “InBar” networks [31, 32]), and the suggestion discussed above [30] is that in CMOL the CMOS-to-nanowire interface is provided by pins distributed all over the circuit area.⁶ In the generic CMOL circuit (Fig. 3), pins of each type (contacting the bottom and top nanowire levels) are located on a square lattice of period $2\beta F_{\text{CMOS}}$. Relative to these arrays, the nanowire crossbar is turned by a (typically, small) angle α which satisfies two conditions (Fig. 3b):

$$\sin \alpha = F_{\text{nano}}/\beta F_{\text{CMOS}}, \quad (1)$$

$$\cos \alpha = r F_{\text{nano}}/\beta F_{\text{CMOS}}, \quad (2)$$

where r is a (typically, large) integer. Such tilt ensures that a shift by one nanowire (e.g., from the second wire from the left to the third one in Fig. 3c) corresponds to the shift from one interface pin to the next one (in the next row of similar pins), while a shift by r nanowires leads to the next pin in the same row. This trick enables individual addressing of each nanowire even at $F_{\text{nano}} \ll \beta F_{\text{CMOS}}$. For example, the selection of CMOS cells 1 and 2

⁶Such sharp-pointed pins may be fabricated similarly to the tips used in field-emission arrays – see, e.g., [33].

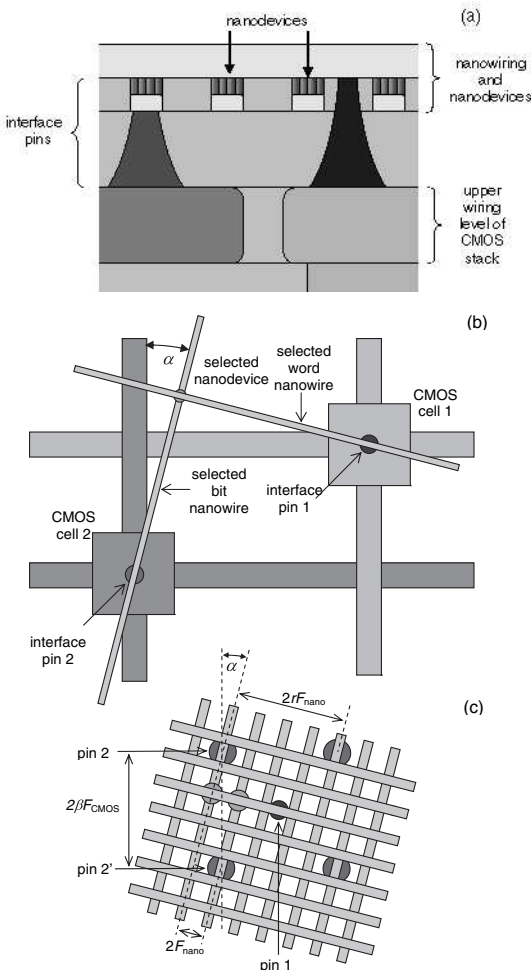


Fig. 3. The generic CMOL circuit: (a) a schematic side view; (b) a schematic top view showing the idea of addressing a particular nanodevice via a pair of CMOS cells and interface pins, and (c) a zoom-in top view on the circuit near several adjacent interface pins. On panel (b), only the activated CMOS lines and nanowires are shown, while panel (c) shows only two devices. (In reality, similar nanodevices are formed at all nanowire crosspoints.) Also disguised on panel (c) are CMOS cells and wiring

(Fig. 3c) enables contacts to the nanowires leading to the left one of the two nanodevices shown on that panel. Now, if we keep selecting cell 1, and instead of cell 2 select cell 2' (using the next CMOS wiring row), we contact the nanowires going to the right nanodevice instead.

It is also clear that if all the nanowires and molecular devices are similar to each other (the assumption that will be accepted in all the following discussion), a shift of the nanowire/molecular subsystem by one nanowiring pitch with respect to the CMOS base does not affect the circuit properties. Moreover, a straightforward analysis of Fig. 3c shows that at an optimal shape of the interface pins, even a complete lack of alignment of these two subsystems leads to a circuit yield loss about 75%. Such loss may be acceptable, taking into account that the cost of the nanosystem fabrication, including the chemically-directed assembly of molecular devices (e.g., from solution [1–3, 34]) may be rather low, especially in the context of an unparalleled density of active devices in CMOL circuits. In fact, the only evident physical limitation of the density is the quantum-mechanical tunneling between parallel nanowires. Simple estimates show that the tunneling current becomes substantial at the distance between the wires $F_{\text{nano}} \approx 1.5 \text{ nm}$. Even by accepting a more conservative value of 3 nm, we get the device density $n = 1/(2F_{\text{nano}})^2$ above 10^{12} cm^{-2} , i.e. at least three orders of magnitude higher than any purely CMOS circuit ever tested.

4 CMOL Memories

The similarity of all molecular devices, that seems necessary for the simplicity of CMOL circuit fabrication, imposes substantial restrictions on architectures and hence possible applications of the circuits. An even more essential restriction comes from the anticipated finite yield of chemically-directed self-assembly of molecular devices, that will hardly ever reach 100%. As a result, all practical CMOL architectures should be substantially defect-tolerant. This tolerance may be most simply implemented in embedded memories and stand-alone memory chips, with their simple matrix structure. In such memories, each molecular device (for example the single-electron latching switch – see Fig. 1) would play the role of a single-bit memory cell, while the CMOS subsystem may be used for coding, decoding, line driving, sensing, and input/output functions.⁷

⁷It may seem that a large problem in such memories is the necessity for the latching switches to combine a sufficient retention time and write/erase speed (see Footnote 1 in the Introduction). However, in memories the speed requirements may be substantially relaxed: a-few-microsecond write/erase time may be acceptable for some, and a-few-nanosecond time, for most applications. Moreover, the periodic memory refresh (similar to that used in the present-day DRAM) may allow to use cells with retention time as low as a few seconds. Hence, the switching speed ratio (at the doubling of applied voltage) should be from about 5 to 9 orders of magnitude. The former requirement may be easy to satisfy, while the latter challenge may possibly be met using single-electron trap barriers with an appropriate structure [35].

We have carried out [36] a detailed analysis of such memories, including the application of two major techniques for increasing their defect tolerance: the memory matrix reconfiguration (the replacement of several rows and columns, with the largest number of bad memory cells, for spare lines), and error correction (based on the Hamming codes). Figure 4 shows the top structure of the CMOL memory, accepted at that analysis. It is essentially a matrix of L memory blocks, each block in turn being a rectangular array of $(n + a) \times (m + b)$ memory cells. Here a and b are the numbers of spare rows and columns, respectively, while $n \times m$ is the final block size after the reconfiguration. (With the account of error correction, the total number of useful bits in the memory is slightly below the product $n \times m \times L$.) A p -bit word addressed at each particular time step is distributed over p blocks. Each of these bits has the same external word and bit addresses in its block,

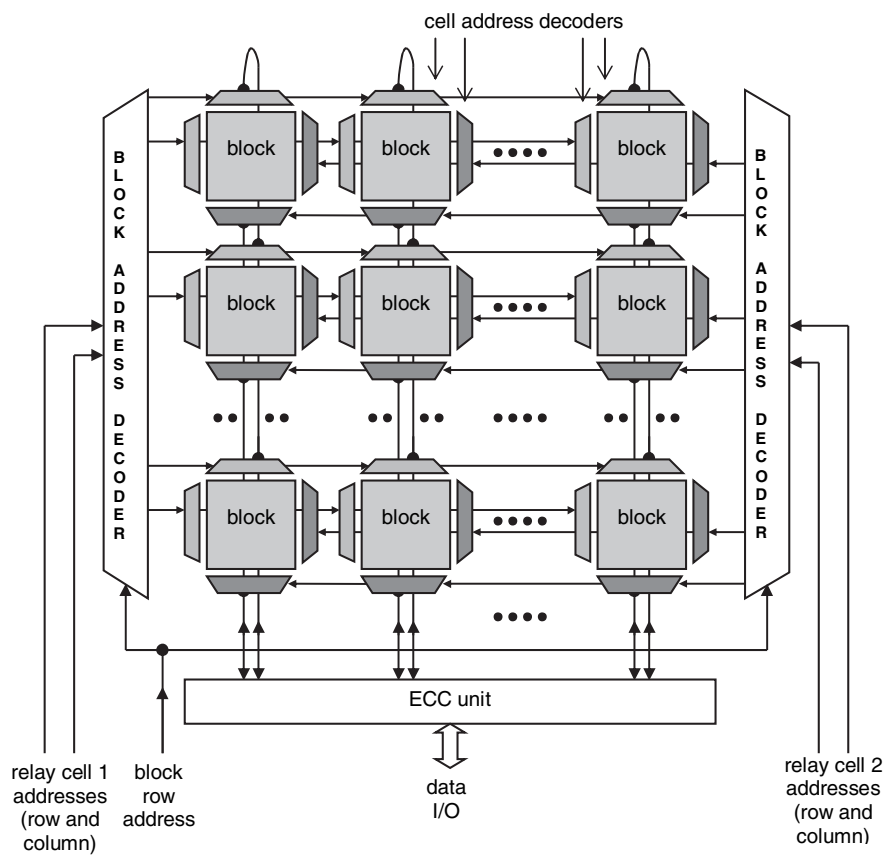


Fig. 4. The top structure of CMOL memory analyzed in [36]. At each instance, block address decoders allow to send the cell row and column addresses to a single row of blocks. The cell addresses are then processed by decoders of each block

though due to the internal line re-routing during the initial reconfiguration process (see below), the real physical location of the used memory cell may be different in each block.

Each block is a CMOL matrix, so that at each elementary operation, the block decoders address two vertical and two horizontal lines implemented in the CMOS layers of the circuit, thus selecting a pair of CMOS cells (Fig. 3b). Each cell has a simple “relay” structure (using either one or two pass transistors [36]) and connects one of CMOS-level wires leading to the cell to the corresponding nanowire. As has been explained in Sect. 3 above, this allows the four cell address decoders of each block to reach each memory cell, even if the cell density is much higher than $1/(F_{\text{CMOS}})^2$.

We have started our analysis with the calculation of the block yield y and the full memory yield Y for several combinations of various reconfiguration techniques with Hamming code error correction (assuming so far only one type of defects: the absence of molecular devices at certain crosspoints, formally equivalent to the “stuck-on-open” faults). Figure 5 shows typical results of such calculation for the following cases:

- (i) no reconfiguration, no error correction;
- (ii) simple “Repair Most” reconfiguration algorithm, in which a worst rows of the array (with the largest number of bad bits) are excluded first, and b worst columns of the remaining matrix next; and
- (iii) upper bound for the best possible, but exponentially complex “Exhaustive Search” reconfiguration.

The figure shows that the array reconfiguration (“repair”) may improve the yield rather dramatically, while the difference between the two repair methods is not too large, especially if the number of redundant lines is not too high – below, or of the order of the final memory size. (The difference is somewhat larger if the array reconfiguration is used together with the error correction.)

Our next step was to use the yield calculation results to evaluate the additional memory area necessary to achieve a certain fixed yield, as a function of the memory parameters, in particular the block size (at fixed total memory size). The area is contributed by spare lines necessary for the array configuration, additional parity bits necessary for the Hamming-code error correction, and CMOS components including the decoders, drivers, sense amplifiers and a relatively small CMOS-based memory storing the reconfiguration results.

Figure 6 shows a typical result for the total chip area (per useful bit) as a function of the linear size n of the block. At small n , the area per bit grows because of the contribution of the peripheral CMOS circuits (mostly, the cell address decoders), while at large n it grows because the necessary number of redundant array lines becomes too large. As a result, there always exist a certain block size (and hence the number of blocks in the full memory) that minimizes the area.

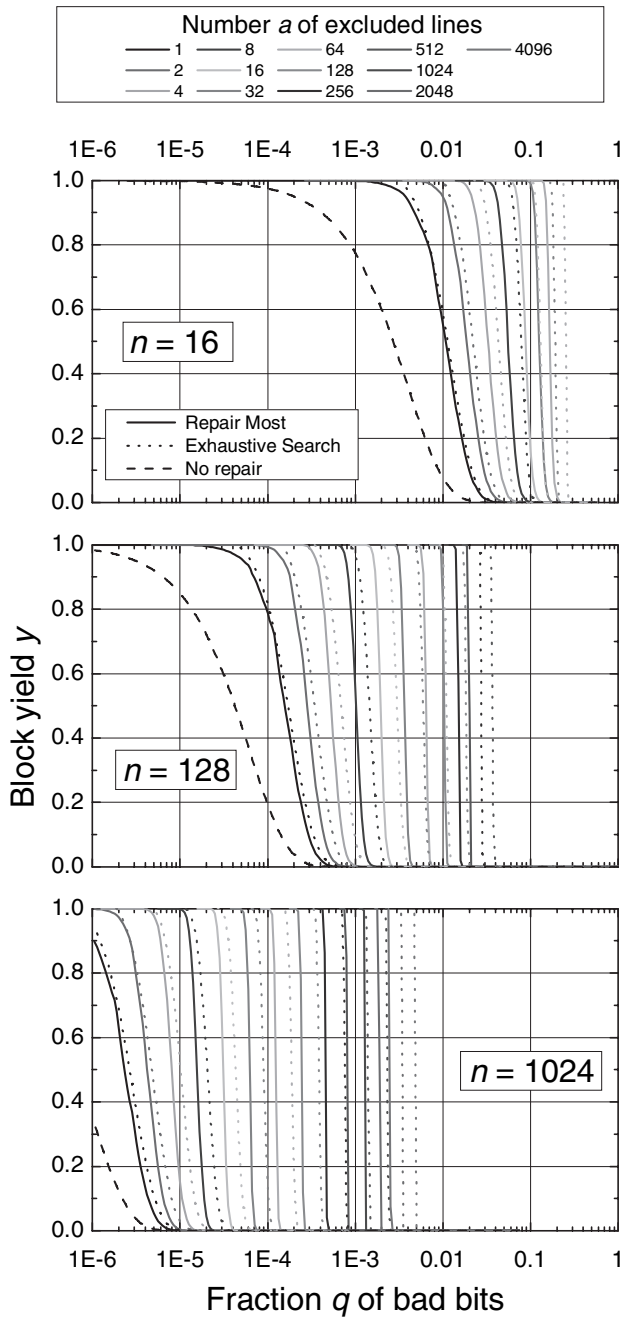


Fig. 5. Comparison of the defect tolerance provided by the two reconfiguration (bad line exclusion) techniques: “Repair Most” (solid lines) and “Exhaustive Search” (dotted lines), without additional error correction, for a square block matrix ($n = m, a = b$). As a reference, dashed lines show the results without the reconfiguration

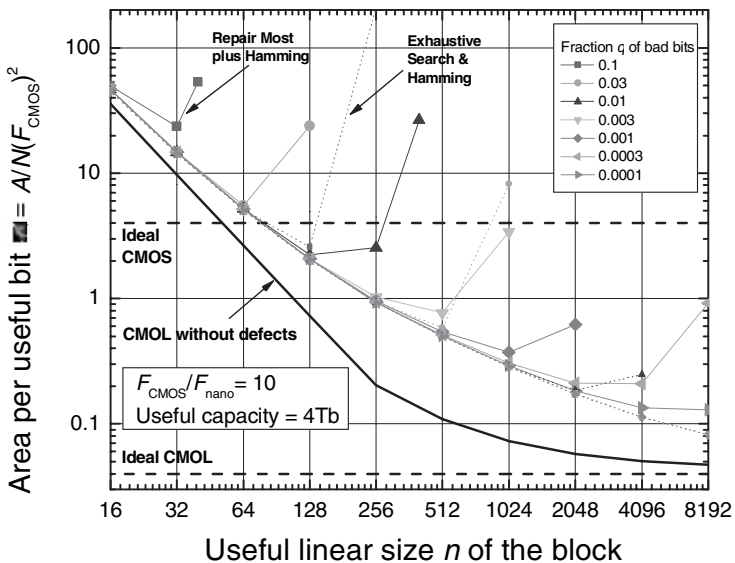


Fig. 6. The reciprocal memory density (area per useful bit) as a function of the block size, for $F_{\text{CMOS}}/F_{\text{nano}} = 10$, and several values of the single device yield. The *dashed lines* show the single bit footprint, i.e., the reciprocal memory density in the ideal case (no bad devices, no peripheral circuits), for CMOS and nanodevice implementations

Figure 7 shows this optimized area per bit as a function of the molecular device yield, for two values of the $F_{\text{CMOS}}/F_{\text{nano}}$ ratio and two defect tolerance boost techniques. (Results for purely CMOS memories are also shown for comparison.) The results show that the array reconfiguration, especially applied in synergy with error correction, can increase the memory defect tolerance very substantially, however, the single bit yield still has to be close to 100%. For example, in a realistic case $F_{\text{CMOS}}/F_{\text{nano}} = 10$, the hybrid memories can overcome a perfect CMOS memory only if the fraction of bad bits is below $\sim 15\%$, even using the Exhaustive Search algorithm of bad bits exclusion, which may require an impractically long time. For the simple and fast Repair Most algorithm, the bad bit fraction should be reduced to $\sim 2\%$. If one wants to obtain an order-of-magnitude density advantage from the transfer to hybrid memories (such a goal seems natural for the introduction of a novel technology), the numbers given above should be reduced to approximately 2% and 0.1%, respectively.

These results for the required single device yield do not look overly optimistic,⁸ but this should not obscure the fact that when this threshold has been achieved, extremely impressive memories will become available. For example,

⁸Our plans are to look for different CMOL memory architectures with a comparable density, but better fault tolerance.

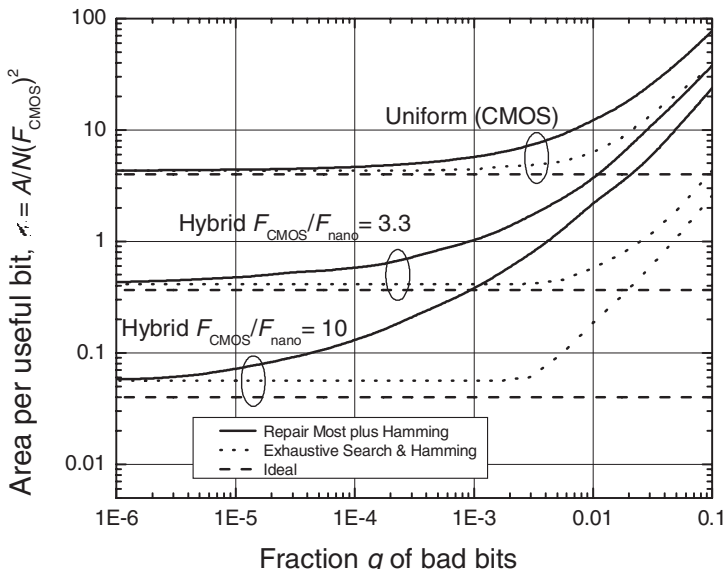


Fig. 7. The area per useful bit after the block size optimization, as a function of single bit yield, for hybrid and purely semiconductor memories

the normalized cell area $a \equiv A/N(F_{\text{CMOS}})^2 = 0.4$ (Fig. 7) at $F_{\text{CMOS}} = 32 \text{ nm}$ means that a memory chip of a reasonable size ($2 \times 2 \text{ cm}^2$) can store about 1 terabit of data – crudely, one hundred Encyclopedia Britannica's.⁹

5 CMOL FPGA: Boolean Logic Circuits

The situation with digital (Boolean) logic is even more complex. In the usual custom logic circuits the location of a defective gate from outside is hardly possible, while spreading around additional logic gates (e.g., providing von Neumann's majority multiplexing [37]) for error detection and correction becomes very inefficient for fairly low fraction q of defective devices. For example, even the recently improved von Neumann's scheme requires a 10-fold redundancy for q as low as $\sim 10^{-5}$ and a 100-fold redundancy for $q \approx 3 \times 10^{-3}$ [38].

This is why the most significant previously published proposals for the implementation of logic circuits using CMOL-like hybrid structures had been based on reconfigurable regular structures like the field-programmable gate arrays (FPGA).¹⁰ Before our recent work, two FPGA varieties had

⁹Comparable densities may be achieved in prospective magnetic and electrostatic data storage systems [10], however, in contrast with random access memories they do not allow a virtually instant (nanosecond-scale) access to every data bit.

¹⁰See [18, 40] for their detailed reviews.

been analyzed, one based on look-up tables (LUT) and another one using programmable-logic arrays (PLA).

In the former case, all possible values of an m -bit Boolean function of n binary operands are kept in m memory arrays, of size $2^n \times 1$ each. (For $m = 1$, and some representative applications the best resource utilization is achieved with n close to 4 [39], while the famous reconfigurable computer Teramac [40] is using LUT blocks with $n = 6$ and $m = 2$.) The main problem with this approach is that the memory arrays of the LUTs based on realistic molecular devices cannot provide address decoding and output signal sensing (recovery). This means that those functions should be implemented in the CMOS subsystem, and the corresponding overhead may be estimated using our results discussed in the previous section. In particular, Fig. 6 shows that for a memory with $2^6 \times 2$ bits, performing the function of a Teramac's LUT block, and for a realistic ratio $F_{\text{CMOS}}/F_{\text{nano}} = 10$ the area overhead would be above four orders of magnitude (!), and would even loose the density (and hence performance) competition to a purely-CMOS circuit performing the same function.¹¹

The PLA approach is based on the fact that an arbitrary Boolean function can be re-written in the canonical form, i.e. in the two-level logical representation. As a result, it may be implemented as a connection of two crossbar arrays, for example one performing the AND, and another the OR function [18]. The first problem with the application of this approach to the CMOS/molecular hybrids is the same as in the case of LUT's: the optimum size of the PLA crossbars is finite, and typically small [42], so that the CMOS overhead is extremely large. Moreover, any PLA logic built with diode-like molecular devices faces an additional problem of high power consumption. In contrast with LUT arrays, where it is possible to have current only through one molecular device at a time, in PLA arrays the fraction of open devices is of the order of one half [18]. Let us estimate the static power dissipated by such an array. The specific capacitance of a wire in an integrated circuit is always of the order of $2 \times 10^{-10} \text{ F/m}$.¹² With $F_{\text{nano}} = 3 \text{ nm}$, this number shows that in order to make the RC time constant of the nanowire below than, or of the order of the logic delay in modern CMOS circuits ($\sim 10^{-10} \text{ s}$), the ON resistance R_0 of a molecular device has to be below $\sim 7 \times 10^7 \text{ ohms}$. For reliable operation of single-electron transistor (and apparently any other active electronic nanodevice) at temperature T , the scale V_0 of voltage $V = V_s - V_d$ across it has to be at least $10 k_B T$ [10]. For room temperature this gives $V_0 > 0.25$

¹¹Increasing the memory array size to the optimum shown in Fig. 6 is not an option, because the LUT performance scales (approximately) only as a log of its capacity [41].

¹²For example, for a simple geometric model of the nanowire crossbar, in which both the width and the thickness of the wire, and both the vertical and the horizontal distances between the nanowires are all equal to F_{nano} , the specific capacitance is close to $C \approx 0.48 \times 10^{-10} \epsilon [\text{F/m}]$, where ϵ is the relative dielectric constant of the insulating environment (3.9 for SiO_2) [36].

Volt, so that static power dissipation per one open device, $P_0 = V_0^2/R_0$ is close to 10 nW. With the open device density of $0.5/(2F_{\text{nano}})^2 \approx 10^{12} \text{ cm}^{-2}$, this creates a power dissipation density of at least 10 kW/cm^2 , much higher than the current and prospective technologies allow to manage [11].

As a matter of principle, power consumption may be reduced by using dynamic logic, but this approach requires more complex nanodevices. For example, [42, 43] describe a dynamic-mode PLA-like structure using several types of molecular-scale devices, most importantly including field-effect transistors formed at crosspoints of two nanowires. In such transistor, one (semiconductor) nanowire would serve as a drain/channel/source structure, while the perpendicular nanowire would play the role of the gate. Unfortunately, such circuits would fail because of the same fundamental physical reason that provides the fundamental limitation the Moore's Law (see the Introduction): any semiconductor MOSFET with a-few-nm-long channel is irreproducible because of exponential dependence of the threshold voltage on the transistor dimensions [45].

Recently, we suggested [46, 47] an alternative approach to Boolean logic circuits based on CMOL concept, that is close to the so-called cell-based FPGA [48]. In this approach (Fig. 8a, b), an elementary CMOS cell includes two pass transistors and an inverter, and is connected to the nanowire/ molecular subsystem via two pins.¹³ During the configuration process the inverters are turned off, and the pass transistors may be used for setting the binary state of each molecular device, just like described above for CMOL memory. Each pin of a CMOS cell can be connected through a nanowire-nanodevice-nanowire link to each of $M \equiv 2r^2 - 2r - 1$ other cells within a square-shaped "connectivity domain" around the pin (painted light-gray in Fig. 8a). Figure 8c shows how such fabric may be configured for the implementation of a fan-in-two NOR gate. This is already sufficient to implement any logic function (see, e.g., Fig. 9), though gates with larger fan-in and fan-out are clearly possible.

Note that during the circuit operation the switching latches should not change their state, working just either as diodes if they are in the ON state or open circuits with some (parasitic) high resistance if they are turned OFF (Fig. 1a). This is why the switching speed to retention time requirement (see Footnote 1) is relaxed even more than in CMOL memories: while the retention time should be long (at least a few hours, better a few years), the programming time as long as a few seconds may be acceptable, because the programming of the whole circuit requires just $\sim M$ sequential steps.

Generally, there may be many different algorithms to reconfigure the CMOL FPGA structure around known defects, including quasi-optimal,

¹³For convenience of signal input and output, the nanowire crossbar is turned by additional 45° in comparison with the generic CMOL (Fig. 3), so that (1), (2) now take the form $\sin \alpha = (r - 1)F_{\text{nano}}/\beta F_{\text{CMOS}}$, $\cos \alpha = rF_{\text{nano}}/\beta F_{\text{CMOS}}$. Also note the breaks in each nanowire in the middle of its contacts with the interface pins.

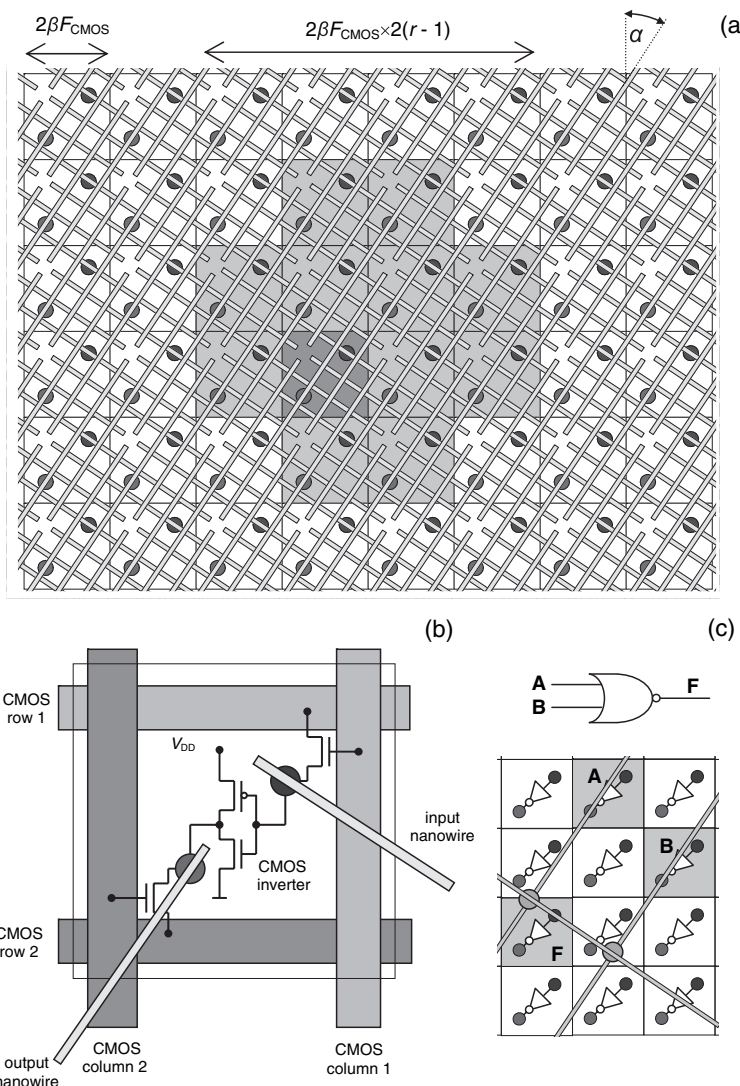


Fig. 8. CMOL FPGA: (a) the general structure of the circuit and (b) a single CMOS cell, and (c) NOR gate implementation. In panel (a), the cells painted light-gray may be connected to the input pin of a specific cell (shown dark-gray). For the sake of clarity, panel (b) shows only two nanowires (that contact the given cell), while panel (c) shows only the three nanowires used inside the NOR gate

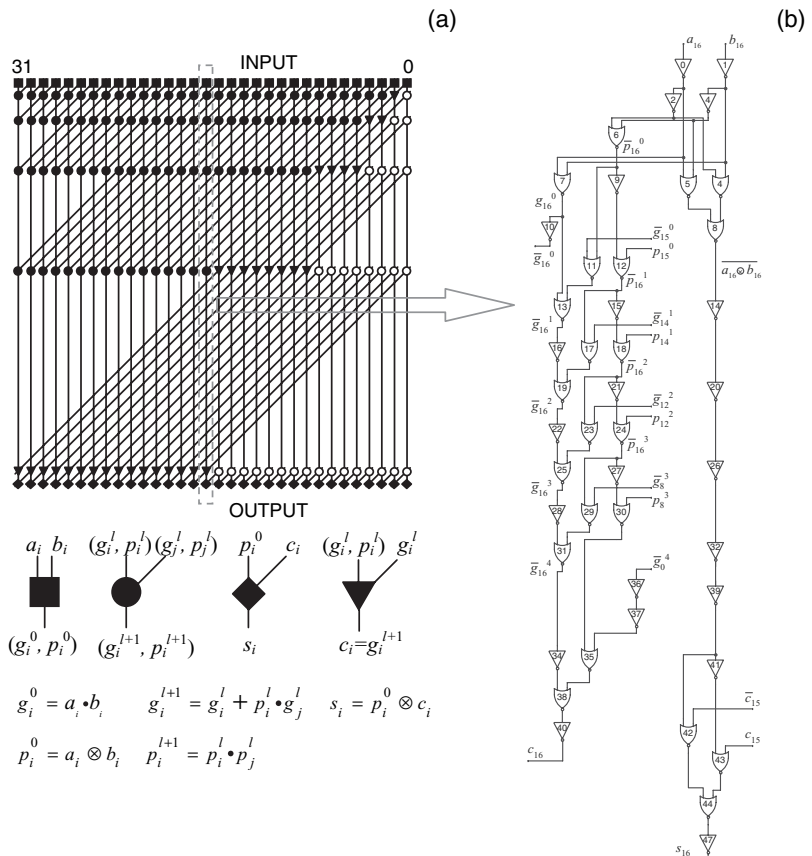


Fig. 9. (a) The 32-bit Kogge-Stone adder and (b) its single (16th) bit slice implemented with NOR gates only

exhaustive-search options which are impracticable, because the resources required for their implementation are exponential in circuit size. We have developed a simple approach, linear in M , in which the CMOL FPGA configuration is carried out in two stages. First, the desired circuit is mapped on the apparently perfect (defect-free) CMOL fabric.¹⁴ At the second stage, the circuit is reconfigured around defective components using a simple algorithm [46, 47].

Our Monte Carlo simulation (again, so far only for the “no-assembly”-type defects) has shown that even this simple configuration procedure may

¹⁴We have found it highly beneficial, from the view of defect tolerance, to confine the cell connections to a smaller square shaped domain of $M' \equiv 2r'^2 - 2r' - 1$ cells, with r' slightly below the maximum connectivity radius r .

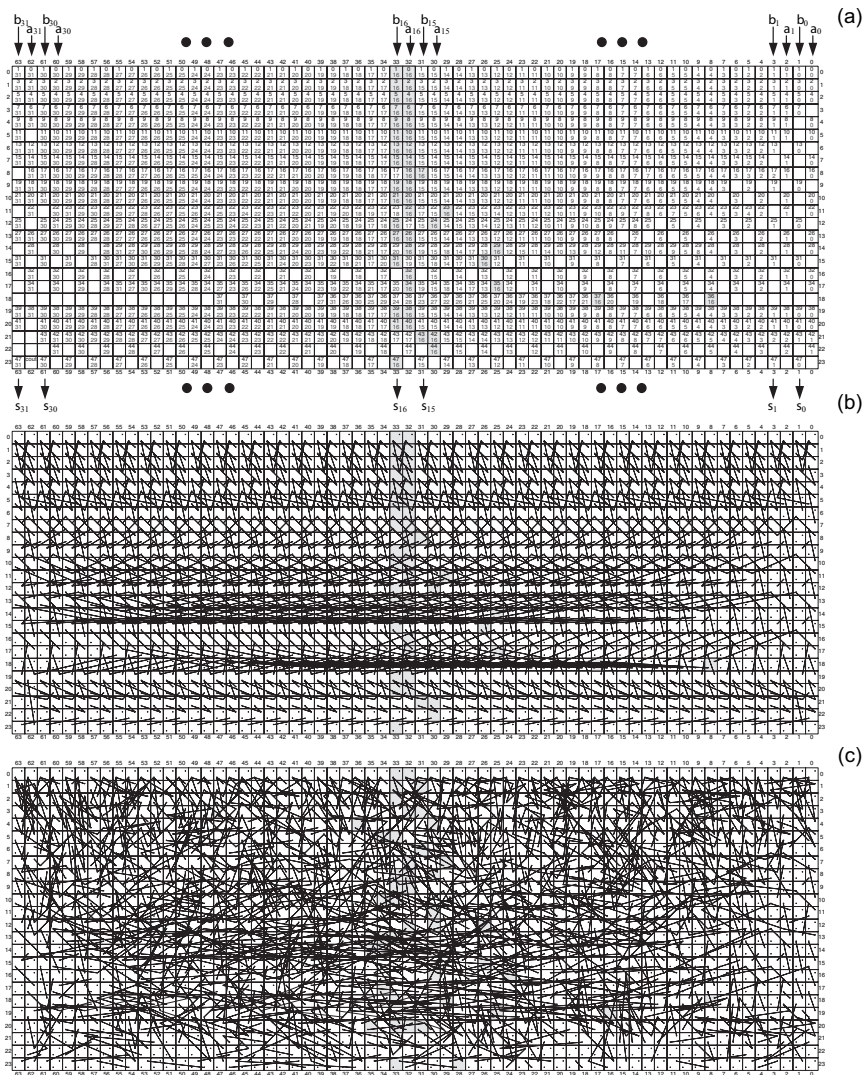


Fig. 10. Mapping of the 32-bit Kogge-Stone adder on CMOL FPGA fabric: (a) the initial cell map, (b) the corresponding initial map of cell connections, and (c) a typical connection map after a successful reconfiguration of the circuit around as many as 50% of randomly located bad nanodevices. Gates of the 16th bit slice (Fig. 9) are painted yellow

ensure very high defect tolerance. For example, Fig. 10c shows that the re-configuration of a simple logic circuit, the 32-bit Kogge-Stone adder [49], mapped on the CMOL fabric with realistic values of parameters $r = 12$ and $r' = 10$, may allow to make fully functional a system with as many as 50% of missing nanodevices. Under a more strict requirement of the 99% circuit yield (sufficient for a 90% yield of properly organized VLSI chips), the defect tolerance of this circuit is about 22%, while that of another key circuit, a fully-connected 64-bit crossbar switch, is about 25%. These impressive results may be explained by the fact that each CMOS cell is served by $M \gg 1$ nanodevices used mostly for reconfiguration.

It is especially important that CMOL FPGA circuits may combine such high defect tolerance with high density and performance, at acceptable power consumption. Indeed, approximate estimates have shown [46, 47] that for the power of 200 W/cm^2 (planned by the ITRS for the long-term CMOS technology nodes [11]), an optimization of the power supply voltage V_{DD} may bring the logic delay of the 32-bit Kogge-Stone adder down to just 1.9 ns, at the total area of $110 \mu\text{m}^2$, i.e. provide an area-delay product of $150 \text{ ns}\cdot\mu\text{m}^2$, for realistic values $F_{\text{CMOS}} = 32 \text{ nm}$ and $F_{\text{nano}} = 8 \text{ nm}$ (Fig. 11c). This result should be compared with the estimated $70,000 \text{ ns}\cdot\mu\text{m}^2$ (with 1.7 ns delay and $39,000 \mu\text{m}^2$ area) for a fully CMOS FPGA implementation of the same circuit (with the same $F_{\text{CMOS}} = 32 \text{ nm}$).

A more detailed evaluation of the CMOL FPGA concept would require the simulation of a substantial number of various functional units and other circuits necessary for digital signal processing and/or general-purpose computing. (This work will probably require, in turn, the development of new, or a modification of existing CAD tools.) Eventually, CMOL FPGA systems should be evaluated on the generally accepted computing benchmarks. However, we believe that even the preliminary estimates described above give a strong evidence that this approach may far outperform CMOS FPGAs in virtually all areas of their application.

The comparison between CMOL FPGA and custom CMOS chips is a more complex issue.¹⁵ Indeed, in the sample circuits explored so far, each CMOS cell is using just a few latching switches for actual operation. As we have seen, this gives a spectacular defect tolerance, but provides only a limited increase in the function density. However, nothing in our CMOL design prevents using gates with much higher fan-in, for which the function density will be substantially improved, hopefully with only a modest sacrifice of the defect tolerance. A quantitative study of this opportunity is one of our immediate goals.

¹⁵If we leave alone the fact that the FPGA approach allows to bypass the current bottleneck of VLSI chip design, i.e. design productivity, which is one of the major problems of microelectronics [11].

6 CMOL CrossNets: Neuromorphic Networks

The requirement of high defect tolerance gives an incentive to consider CMOL implementation of alternative information processing architectures, in particular analog or mixed-signal neuromorphic networks (see, e.g., [50]), because such networks are by their structure deeply parallel and hence inherently defect-tolerant. An additional motivation for using neuromorphic networks comes from the following comparison of the performance of the biological neural systems and present-day Boolean-logic computers in one of the basic advanced information processing tasks: image recognition (more strictly speaking, classification [50]). A mammal's brain recognizes a complex visual image, with high fidelity, in approximately 100 milliseconds. Since the elementary process of neural cell-to-cell communication in the brain takes approximately 10 milliseconds, this means that the recognition is completed in just a few “clock ticks”. In contrast, the fastest modern microprocessors performing digital number crunching at a clock frequency of a few GHz and running the best commercially available code, would require many minutes (i.e., of the order of 10^{12} clock periods) for an inferior classification of a similar image. The contrast is very striking indeed, and serves as a motivation for the whole field of artificial “neural networks”.

Presently, these networks are mostly just a concept for writing software codes that are implemented on usual digital computers. Unfortunately, the high expectations typical for the neural network's “heroic period” (from the late 1980s to the early 1990s) have not fully materialized, in particular because the computer resources limit the number of neural cells to a few hundreds, insufficient for performing really advanced, intelligent information processing tasks. The advent of hybrid CMOL circuits may change the situation.

Recently, our group suggested [31, 32] a new family of neuromorphic network architectures, Distributed Crosspoint Networks (“CrossNets” for short) that map uniquely on the CMOL topology. Each such network consists of the following components:

- (i) Neural cell bodies (“somas”) that are relatively sparse and hence may be implemented in the CMOS subsystem. Most of our results so far have been received within the simplest Firing Rate approach [50], in which somas operate just as differential amplifiers, with a nonlinear saturation (“activation”) function, which are fed by the incoming (dendritic) nanowires and apply their output signal to outgoing (axonic) wires.
- (ii) “Axons” and “dendrites” that are implemented as mutually perpendicular nanowires of the CMOL crossbar.
- (iii) “Synapses” that control coupling between the axons and dendrites (and hence between neural cells) based on the molecular latching switches (see Fig. 1 and its discussion).

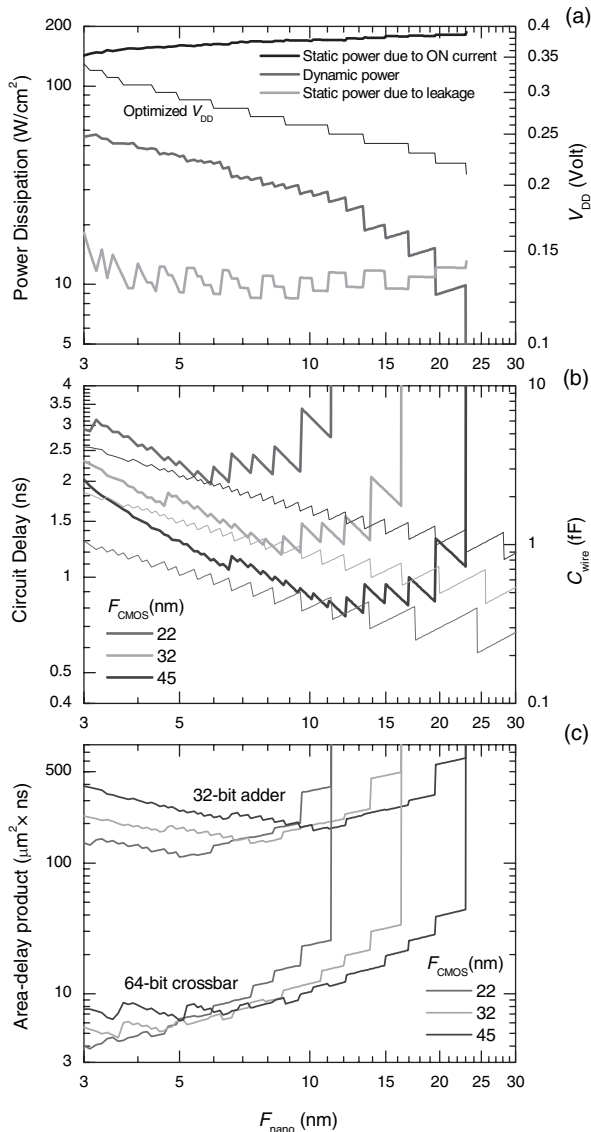


Fig. 11. CMOL FPGA optimization results as functions of nanowire half-pitch: (a) three components of the total power (fixed at 200 W/cm^2), and the optimum value of the power supply voltage V_{DD} , for the 32-bit Kogge-Stone adder with $F_{\text{CMOS}} = 45 \text{ nm}$; (b) nanowire segment capacitance (*thin lines*) and the total logic delay of the circuit (***bold lines***); and (c) area-delay product $A\tau$ of the two CMOL FPGA circuits for three ITRS long-term CMOS technology nodes. The (formal) jump of the $A\tau$ product to infinity at some $(F_{\text{nano}})_{\text{max}}$ reflects the fact that circuit mapping on the CMOL fabric may only be implemented for F_{nano} below this value. The finite sharp jumps of the curves are due to the discrete changes of angle α .

CrossNet species differ by the number and direction of intercell couplings (Fig. 12) and by the location of somatic cells on the axon/dendrite/synapse field (Fig. 13). The cell distribution pattern determines the character of cell coupling. For example, the “FlossBar” (Fig. 13a) has a layered structure typical for the so-called multilayered perceptrons [38], while the “InBar” (in which somas sit on a square lattice inclined by a small angle relatively the axonic/dendritic lattice, Fig. 13b) implements a non-layered “interleaved” network. Also important is the average distance M between the somas, that determines connectivity of the networks, i.e. the average number of other cells coupled directly (i.e., via one synapse) to a given soma. The most remarkable property of CMOL CrossNets is that the connectivity of these (quasi-)2D structures may be very large. This property is very important for advanced information processing, and distinguishes CrossNets favorably from the so-called cellular automata with small (next-neighbor) connectivity which severely limits their functionality.

In contrast to the usual computers, neuromorphic networks do not need an external software code, but need to be “trained” to perform certain tasks. For that, the synaptic connections between the cells should be set to certain values. The neural network science has developed several effective training methods [50]. The application of these methods to CMOL CrossNets faces several hardware-imposed challenges:

- (i) CrossNets use continuous (analog) signals, but the synaptic weights are discrete (binary, if only one latching switch per synapse is used).
- (ii) The only way to reach for any particular synapse in order to turn it on or off is through the voltage V applied to the device through the two corresponding nanowires. Since each of these wires is also connected to many other switches, special caution is necessary to avoid undesirable “disturb” effects.
- (iii) Processes of turning single-electron latches on and off are statistical rather than dynamical [12], so that the applied voltage V can only control probability rates Γ of these random events.

In our recent work [51] we have proved that, despite these limitations, CrossNets can be taught, by at least two different methods, to perform virtually all the major functions demonstrated earlier with usual neural networks, including the corrupted pattern restoration in the recurrent quasi-Hopfield mode (Fig. 14) and pattern classification in the feedforward multilayered perceptron mode [51, 52].¹⁶ Moreover, at least in the former mode the CrossNets can be spectacularly resilient. For example, operating at network capacity at just a half of its maximum, a quasi-Hopfield CrossNet may provide a 99%

¹⁶In order to operate as perceptron-type classifiers, CrossNets require multi-latch synapses. This increase can be achieved by using small (e.g., 4×4) square fragments of CrossNet arrays for each synapse [39]. This increase is taken into account in the density estimates given below.

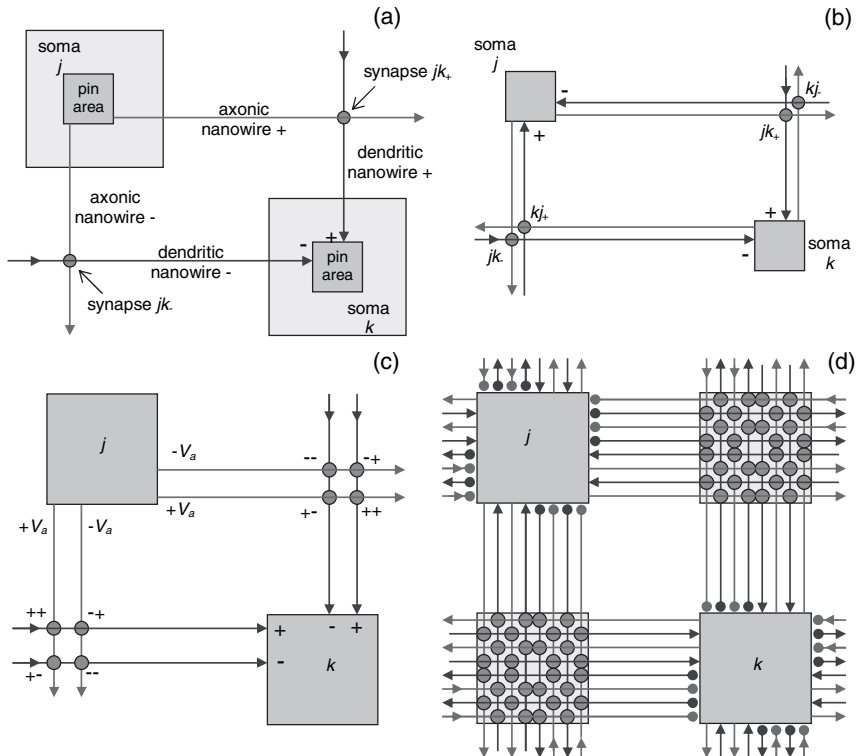


Fig. 12. Schemes of cell connections in CrossNets: (a) simple (non-Hebbian) feed-forward network, (b) simple recurrent network, (c) Hebbian feedforward CrossNet and (d) Hebbian recurrent CrossNet [39]. Red lines show “axonic”, and blue lines “dendritic” nanowires. Dark-gray squares are interfaces between nanowires and CMOS-based cell bodies (somas), while light-gray squares in panel (a) show the somatic cells as a whole. (For the sake of clarity, the latter areas are not shown in the following panels and figures.) Signs show the somatic amplifier input polarities. Green circles denote nanodevices (latching switches) forming elementary synapses. For clarity the panels (a)-(c) show only the synapses and nanowires connecting one couple of cells (j and k). In contrast, panel (d) shows not only those synapses, but also all other functioning synapses located in the same “synaptic plaquettes” (painted light-green) and the corresponding nanowires, even if they connect other cells. (In CMOL circuits, molecular latching switches are also located at all axon/axon and dendrite/dendrite crosspoints; however, they do not affect the network dynamics, resulting only in approximately 50% increase of power dissipation.) The solid dots on panel (d) show open-circuit terminations of synaptic and axonic nanowires, that do not allow direct connections of the somas, in bypass of synapses

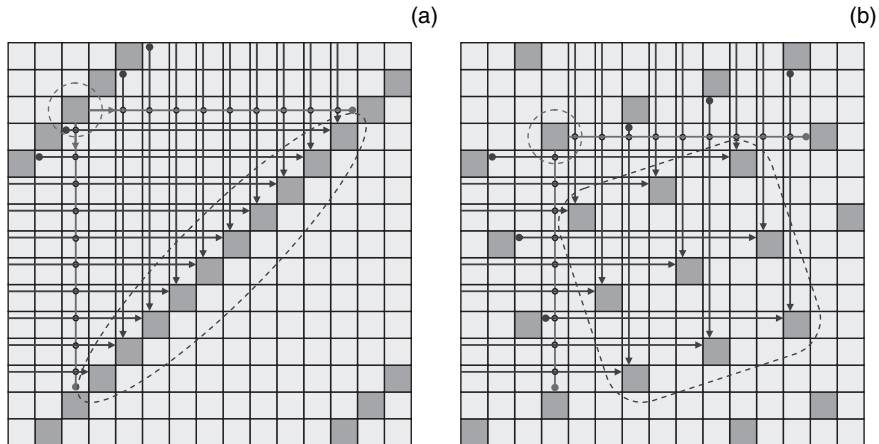


Fig. 13. Two particular CrossNet species: (a) FlossBar and (b) InBar. For clarity, the figures show only the axons, dendrites, and synapses providing connections between one soma (indicated by the dashed red circle) and its recipients (inside the dashed blue lines), for the simple (non-Hebbian) feedforward network

result fidelity with as many as 85% (!) of bad molecular devices – see Fig. 15. This defect tolerance is much higher than that of CMOL memories (see Sect. 4 above) and even that of CMOL FPGA circuits (Sect. 5).

The fact that CrossNets may perform the tasks that had been demonstrated with artificial neural networks earlier may seem not very impressive until the possible performance of this hardware is quantified. Estimates [31, 32, 51] show that for realistic parameters as have been used in Sect. 4 above ($F_{\text{nano}} = 4 \text{ nm}$, $V = 0.25 \text{ Volt}$), and a very respectable connectivity parameter $M \sim 10^3$, the areal density of CrossNets may be at least as high as that of the cerebral cortex (above 10^7 cells per cm^2), while the average cell-to-cell communication delay τ_0 may be as low as $\sim 10 \text{ ns}$ (i.e., about six orders of magnitude lower than in the brain), at power dissipation below 100 W/cm^2 .¹⁷ This implies, for example, that a 1- cm^2 CMOL CrossNet chip would be able to recognize a face in a high-resolution image of a crowd faster than in 100 microseconds [52]. We believe that such applications alone may form not just a narrow market niche, but a substantial market for the hybrid CMOS/molecular electronics.

¹⁷The reason for such a large difference with power estimates for Boolean logic circuits (Sect. 5) is that in neuromorphic networks we can afford to increase the open molecular latch resistance to $\sim 10^9 \text{ ohms}$, and thus increase the logic delay from $\sim 100 \text{ ps}$ to $\sim 10 \text{ ns}$, still providing an extremely high integrated circuit performance ($\sim 10^{12}/10^{-8} \approx 10^{20}$ of a-few-bit operations per cm^2 per second) due to the natural parallelism of the neuromorphic network operation.

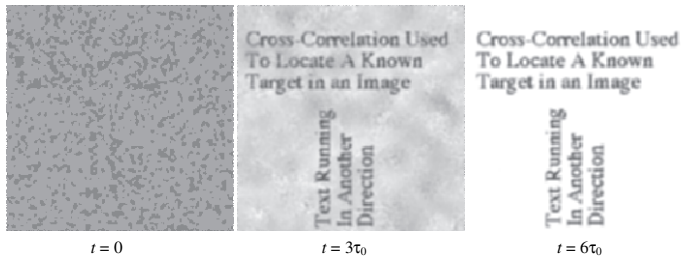


Fig. 14. The recall of one of three trained black-and-white images by a recurrent InBar-type CrossNet with 256×256 neural cells, binary synapses, and connectivity $4M = 64$, operating in the local quasi-Hopfield mode. The initial image (left panel) was obtained from the trained image (identical to the one shown in the right panel) by flipping as many as 40% of randomly selected pixels

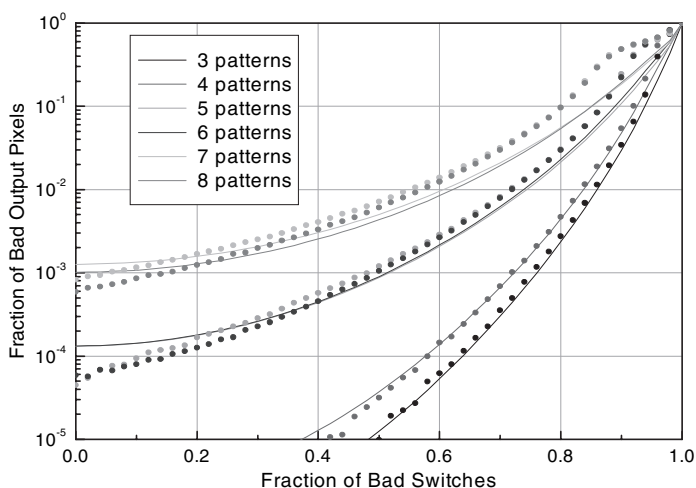


Fig. 15. Defect tolerance of a recurrent InBar with connectivity parameter $M = 25$, operating in the Hopfield mode. Lines show the results of an approximate analytical theory, while dots those of a numerical experiment

Moreover, there is a hope that CrossNets will be able to perform even more complex intelligent tasks if trained using more general methods such as global reinforcement [50, 53]. (A successful result of a very preliminary attempt at such training is presented in Fig. 16.) If these hopes materialize, there will be a chance that such pre-training of a properly organized, hierarchical CrossNet-based system,¹⁸ may help to reach a functionality comparable

¹⁸It is curious that the use of the so-called “X layout”, frequently employed in VLSI circuits, for the CMOS-based subsystem of fast, long-range communications between CrossNet blocks automatically leads to a circuit geometry (Fig. 17) that reminds the mammal brain structure.

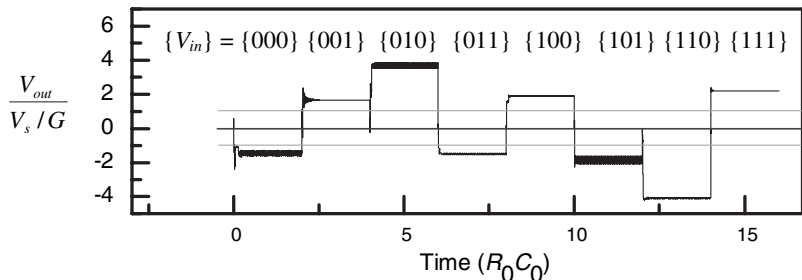


Fig. 16. A result of the global-reinforcement training of a small CrossNet: the dendritic signal of the output stage of a recurrent InBar with quasi-continuous Hebbian synapses, trained to calculate the parity of three binary inputs. All the values of V_{out} above the upper green line correspond to binary 1, while those below the bottom green line, binary 0

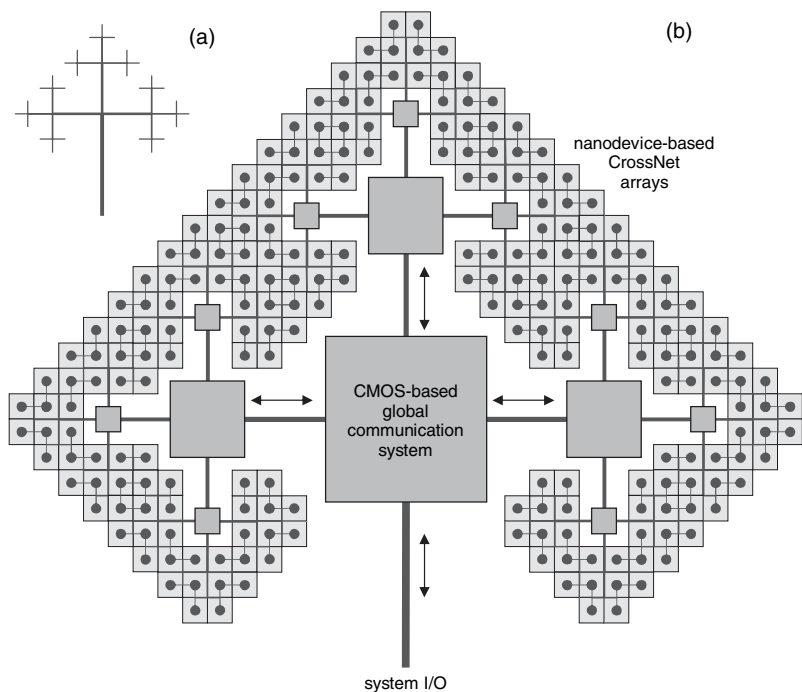


Fig. 17. X layout for the high-speed global communication network: (a) general structure and (b) possible 2D geometry of a hierarchical CMOL CrossNet system using such layout. For the parameters cited above ($F_{nano} = 3\text{ nm}$ and $4M = 10^4$), a $30 \times 30\text{-cm}$ system may have as many neural cells and synapses ($\sim \times 10^{15}$) as the human cerebral cortex, while operating at much higher speed, at manageable power

with that of a newborn child brain, in some sense replacing the DNA-based genetic inheritance. It seems possible that a connection of such pre-trained system to a proper informational environment via a high-speed communication network may trigger a self-development process that may be several orders of magnitude faster than that of the biological cerebral cortex. The reader is invited to imagine possible consequences of such self-development liberated from the dead weight artifacts of the biological evolution.

7 Conclusions

There is a chance for the development, within the next 10 to 20 years, of hybrid “CMOL” integrated circuits that will allow to extend Moore’s Law to the few-nm range. Preliminary estimates show that such circuits could be used for several important applications, notably including terabit-scale memories, reconfigurable digital circuits with multi-teraflops-scale performance, and mixed-signal neuromorphic networks that may, for the first time, compete with biological neural systems in areal density, far exceeding them in speed, at acceptable power dissipation. We believe that these prospects more than justify large-scale research and development efforts in the synthesis of functional molecular devices, their chemically-directed self-assembly, nanowire patterning, and CMOL circuit architectures.

Acknowledgements

Useful discussions of the issues considered in this chapter with P. Adams, J. Barhen, V. Beiu, W. Chen, E. Cimpoiasu, S. Das, J. Ellenbogen, J. H. Lee, X. Liu, J. Lukens, X. Ma, A. Mayr, V. Protopopescu, M. Reed, M. Stan, and Ö. Türel are gratefully acknowledged. Figure 1c is a courtesy by A. Mayr. The work on this topic at Stony Brook was supported in part by AFOSR, NSF, and MARCO via FENA Center.

References

1. J.R. Heath and M.A. Ratner: Molecular electronics, Physics Today **56**, 43 (2003)
2. J. R. Reimers, C. A. Picconatto, J. C. Ellenbogen, and R. Shashidhar (eds.): *Molecular Electronics III*, Ann. New York Acad. Sci. **1006** (2003)
3. J. Tour: *Molecular Electronics* (World Scientific, Singapore 2003)
4. H. Park, J. Park, A. K. L. Lim, E. H. Anderson, A. P. Alivisatos, and P. L. McEuen: Nanomechanical oscillations in a single-C-60 transistor, Nature **407**, 57 (2000)

5. S. P. Gubin, Y. V. Gulyaev, G. B. Khomutov, V. V. Kislov, V. V. Kolesov, E. S. Soldatov, K. S. Sulaimankulov, and A. S. Trifonov: Molecular clusters as building blocks for nanoelectronics: The first demonstration of a cluster single-electron tunnelling transistor at room temperature, *Nanotechnology* **31**, 185 (2002)
6. N. B. Zhitenev, H. Meng, and Z. Bao: Conductance of small molecular junctions, *Phys. Rev. Lett.* **88**, 226801 (2002)
7. J. Park, A. N. Pasupathy, J.I. Goldsmith, C. Chang, Y. Yaish, J.R. Petta, M. Rinkoski, J.P. Sethna, H.D. Abruna, P.L. McEuen, and D. C. Ralph: Coulomb blockade and the Kondo effect in single-atom transistors, *Nature* **417**, 722 (2002)
8. S. Kubatkin, A. Danilov, M. Hjort, J. Cornil, J. L. Bredas, N. Stuhr-Hansen, P. Hedegard, and T. Bjornholm: Single-electron transistor of a single organic molecule with access to several redox states, *Nature* **425**, 698 (2003)
9. D. J. Frank, R. H. Dennard, E. Nowak, P. M. Solomon, Y. Taur, and H. S. P. Wong: Device scaling limits of Si MOSFETs and their application dependencies, *Proc. IEEE* **89**, 259 (2001)
10. K. K. Likharev: Electronics below 10 nm, in *Nano and Giga Challenges in Microelectronics* (Elsevier, Amsterdam 2003), pp. 27-68
11. *International Technology Roadmap for Semiconductors. 2003 Edition, 2004 Update*, available online at <http://public.itrs.net/>
12. K. K. Likharev: Single-electron devices and their applications, *Proc. IEEE* **87**, 606 (1999)
13. P. J. Kuekes, D. R. Stewart, and R. S. Williams: The crossbar latch: Logic value storage, restoration, and inversion in crossbar circuits, *J. Appl. Phys.* **97**, 034301 (2005)
14. W. D. Brown and J. E. Brewer (eds.): *Nonvolatile Semiconductor Memory Technology* (IEEE Press, Piscataway, NJ 1998)
15. Y. Chen, G. Y. Jung, D. A. A. Ohlberg, X. M. Li, D. R. Stewart, J. O. Jeppesen, K. A. Nielsen, J. F. Stoddart, and R. S. Williams: Nanoscale molecular-switch crossbar circuits, *Nanotechnology* **14**, 462 (2003)
16. Z. H. Zhong, D. L. Wang, Y. Cui, M. W. Bockrath, and C. M. Lieber: Nanowire crossbar arrays as address decoders for integrated nanosystems, *Science* **302**, 1377 (2003)
17. C. Li, W. D. Fan, B. Lei, D. H. Zhang, S. Han, T. Tang, X. L. Liu, Z. Q. Liu, S. Asano, M. Meyyappan, J. Han, and C. W. Zhou: Multilevel memory based on molecular devices, *Appl. Phys. Lett.* **84**, 1949 (2004)
18. M. R. Stan, P. D. Franzon, S. C. Goldstein, J. C. Lach, and M. M. Ziegler: Molecular electronics: From devices and interconnect to circuits and architecture, *Proc. IEEE* **91**, 1940 (2003)
19. S. Das, G. Rose, M. M. Ziegler, C. A. Picconatto, and J. C. Ellenbogen: Architectures and simulations for nanoprocessor systems integrated on the molecular scale, Chap. 17 of this collection (2005)
20. W. Wang, T. Lee, and M. Reed: Intrinsic electronic conduction mechanisms in self-assembled monolayers, Chap. 10 of this collection (2005)
21. D. Porath: DNA-based devices, Chap. 15 of this collection (2005)
22. L. Ji, P. D. Dresselhaus, S. Y. Han, K. Lin, W. Zheng, and J. E. Lukens: Fabrication and characterization of single-electron transistors and traps, *J. Vac. Sci. Technol. B* **12**, 3619 (1994)

23. C. P. Collier, E. W. Wong, M. Belohradsky, F. M. Raymo, J. F. Stoddart, P. J. Kuekes, R. S. Williams, and J. R. Heath: Electronically configurable molecular-based logic gates, *Science* **285**, 391 (1999)
24. C. P. Collier, G. Mattersteig, E. W. Wong, Y. Luo, K. Beverly, J. Sampaio, F. M. Raymo, J. F. Stoddart, and J. R. Heath: A [2]catenane-based solid state electronically reconfigurable switch, *Science* **289**, 1172 (2000)
25. S. Fölling, Ö. Türel, and K. K. Likharev: Single-electron latching switches as nanoscale synapses, in *Proceedings of the 2001 International Joint Conference on Neural Networks* (Int. Neural Network Soc., Mount Royal, NY 2001), pp. 216-221
26. S. Zankovich, T. Hoffmann, J. Seekamp, J. U. Bruch, and C. M. S. Torres: Nanoimprint lithography: Challenges and prospects, *Nanotechnology* **12**, 91 (2001)
27. S.R.J. Brueck: There are no fundamental limits to optical lithography, in *International Trends in Applied Optics* (SPIE Press, Bellingham, WA 2002), pp. 85-109
28. P. J. Kuekes and R. S. Williams: Demultiplexer for a molecular wire crossbar network (MWCN DEMUX), US Patent No. 6,256,767 (July 3, 2001)
29. A. DeHon, P. Lincoln, and J. E. Savage: Stochastic assembly of sublithographic nanoscale interfaces, *IEEE Trans. on Nanotechnology* **2**, 165 (2003)
30. M. M. Ziegler and M. R. Stan: CMOS/nano co-design for crossbar-based molecular electronic systems, *IEEE Trans. on Nanotechnology* **2**, 217 (2003)
31. Ö. Türel and K. K. Likharev: CrossNets: Possible neuromorphic networks based on nanoscale components, *Int. J. of Circuit Theory and Appl.* **31**, 37 (2003)
32. K.K. Likharev, A. Mayr, I. Muckra, and O. Türel: CrossNets: High-performance neuromorphic architectures for CMOL circuits, *Ann. New York Acad. Sci.* **1006**, 146 (2003)
33. K. L. Jensen: Field emitter arrays for plasma and microwave source applications, *Physics of Plasmas* **6**, 2241 (1999)
34. J. H. Fendler: Chemical self-assembly for electronic applications, *Chemistry of Materials* **13**, 3196 (2001)
35. K. K. Likharev: Riding the crest of a new wave in memory [NOVORAM], *IEEE Circuits and Devices* **16**, 16 (July 2000)
36. D. B. Strukov and K. K. Likharev: Prospects for terabit-scale nanoelectronic memories, *Nanotechnology* **16**, 137 (2005)
37. J. von Neumann: Probabilistic logics and the synthesis of reliable organisms from unreliable components, in *Automata Studies* (Princeton University Press, Princeton, NJ 1956), pp. 329-78
38. S. Roy and V. Beiu: Multiplexing schemes for cost-effective fault-tolerance, Report at IEEE-NANO'04 (Münich, Germany, Aug. 2004); accepted for publication in *IEEE Trans. on Nanotechnology* (2005)
39. J. Rose, R. J. Francis, D. Lewis, and P. Chow: Architecture of field-programmable gate arrays - the effect of logic block functionality on area efficiency, *IEEE J. of Solid-State Circuits* **25**, 1217 (1990)
40. J. R. Heath, P. J. Kuekes, G. S. Snider, and R. S. Williams: A defect-tolerant computer architecture: Opportunities for nanotechnology, *Science* **280**, 1716 (1998)
41. E. Ahmed and J. Rose: The effect of LUT and cluster size on deep-submicron FPGA performance and density, *IEEE Trans. on VLSI Syst.* **12**, 288 (2004)

42. J. Kouloheris and A. E. Gamal: PLA-based FPGA versus cell granularity, in *Proceedings of the Custom Integrated Circuits Conference* (IEEE Press, Piscataway, NJ 1992), pp. 4.3.1-4
43. A. DeHon: Law of large numbers system design, in *Nano, Quantum and Molecular Computing* (Kluwer Academic Publishers, Boston, MA 2004)
44. A. DeHon and M. J. Wilson: Nanowire-based sublithographic programmable logic arrays, in: *Proc. of FPGA'04* (Monterey, CA 2004), pp. 123-132.
45. V. A. Sverdlov, T. J. Walls, and K. K. Likharev: Nanoscale silicon MOSFETs: A theoretical study, *IEEE Trans. on Electron Devices* **50**, 1926 (2003)
46. D. B. Strukov and K. K. Likharev: A reconfigurable architecture for hybrid CMOS/nanodevice circuits, submitted for presentation at FCCM'05 (Napa Valley, CA, April 2005); preprint available online at <http://rsfq1.physics.sunysb.edu/likharev/nano/FCCM2005.pdf>.
47. D. B. Strukov and K. K. Likharev: CMOL FPGA: A cell-based, reconfigurable architecture for hybrid digital circuits using two-terminal nanodevices, submitted to *Nanotechnology*; preprint available online at <http://rsfq1.physics.sunysb.edu/likharev/nano/FPGA05.pdf>.
48. J. Rabaey, A. Chandrakasan, and B. Nikolic: *Digital Integrated Circuits, A Design Perspective* (Pearson Edication, Singapore 2003)
49. P. M. Kogge, and H. S. Stone: Parallel algorithm for efficient solution of a general class of recurrence equations, *IEEE Trans. on Computers* **22**, 783 (1973)
50. J. Hertz, A. Krogh, and R. G. Palmer: *Introduction to the Theory of Neural Computation* (Perseus, Cambridge, MA 1991)
51. Ö. Türel, J. H. Lee, X. Ma, and K. K. Likharev: Neuromorphic architectures for nanoectronic circuits, *Int. J. of Circuit Theory and Appl.* **32**, 277 (2004)
52. J. H. Lee and K. K. Likharev: CMOL CrossNets as pattern classifiers, submitted for presentation at the 8th Int. Work-Conference on Artificial Neural Networks (Barcelona, Spain, June 2005); preprint available at <http://rsfq1.physics.sunysb.edu/likharev/nano/IWANN05.pdf>
53. R. S. Sutton and A. G. Barto: *Reinforcement Learning* (MIT Press, Cambridge, MA 1998)

Architectures and Simulations for Nanoprocessor Systems Integrated on the Molecular Scale

Shamik Das¹, Garrett Rose¹, Matthew M. Ziegler², Carl A. Picconatto¹,
and James C. Ellenbogen¹

¹ The MITRE Corporation, M/S H619, 7525 Colshire Drive, McLean, VA 22102
`{sdas,grose,picconatto,ellenbgn}@mitre.org`

² IBM T. J. Watson Research Center, 1101 Kitchawan Road, P. O. Box 218,
Yorktown Heights
`zieglerm@us.ibm.com`

Abstract. This chapter concerns the design, development, and simulation of nanoprocessor systems integrated on the molecular scale. It surveys ongoing research and development on nanoprocessor architectures and discusses challenges in the implementation of such systems. System simulation is used to identify some advantages, issues, and trade-offs in potential implementations. Previously, the authors and their collaborators considered in detail the requirements and likely performance of nanomemory systems. This chapter recapitulates the essential aspects of that earlier work and builds upon those efforts to examine the likely architectures and requirements of nanoprocessors. For nanoprocessor systems, simulation, as well as design and fabrication, embodies unique problems beyond those introduced by the large number of densely-packed, novel nanodevices. For example, unlike the largely homogeneous structure of circuitry in nanomemory arrays, a high degree of variety and inhomogeneity must be present in nanoprocessors. Also, issues of clocking, signal restoration, and power become much more significant. Thus, building and operating nanoprocessor systems will present significant new challenges and require additional innovations in the application of molecular-scale devices and circuits, beyond those already achieved for nanomemories. New nanoelectronic devices, circuits, and architectures will be necessary to perform the more complex and specialized functions inherent in processing systems at the nanometer scale. This chapter highlights the fundamental design requirements of such nanoprocessor systems, presents various device and design options, and discusses their potential implications for system performance.

1 Introduction

The excitement that surrounds the field of molecular electronics is premised, to a great extent, upon the prospect that soon we may be able to design, fabricate, and demonstrate an entire, ultra-dense electronic computer that is integrated on the molecular scale. In fact, development of such nanoelectronic

computer systems already is underway. Despite significant challenges, this effort is likely to produce functioning prototype nanomemories and nanoprocessors within a few years [1–9].

Such development is essential to fulfill the promise and the expectations that have been raised by the dramatic recent successes in demonstrating electronic devices and simple circuits on the molecular scale, as is discussed in the foregoing chapters of this book [10–13] and elsewhere [3,14–21]. In this regard, much progress already has been made toward employing molecular-scale devices in building and demonstrating extended nanomemory systems [4, 5, 21]. Pressing on toward much more complex, extended nanosystems, such as nanoprocessors, does not alleviate the need for more research and development on nanodevices. In fact, as we explain below, it places even more stringent demands for understanding, predictability, uniformity, and reliability of performance at the device level.

Nonetheless, the process of developing true nanocomputers does open up an entirely new frontier of systems objectives and issues that require research and development beyond that which presently is being conducted upon isolated nanodevices. It is this new frontier that is the primary topic of the present chapter, which addresses the problem of how to design and simulate an entire nanoprocessor system that is integrated on the molecular scale.

This survey and analysis of nanoprocessor system architectures may be considered as a companion to a recent paper on nanomemories by several of the present authors. In that work, we simulated and analyzed a nanowire-based nanomemory array as a vehicle for considering a range of issues that arises in the development of nanomemory systems [22]. The much more difficult challenges presented by the frontier problem of nanoprocessor design and development are considered here in several ways and at several levels of resolution, as follows:

- In Sect. 2 of this work, we describe how molecular-scale devices fit in and are harnessed within an extended nanowire-based circuit system.
- Section 3 of this work provides a general overview of the nanoprocessor design and architecture problem from a system-level perspective. This review of the issues that must be faced includes a consideration of the problems of migrating conventional microelectronic architectures to the nanoscale, as well as an analysis of the difficulties that might arise with novel nanoelectronic architectures.
- Section 4 contains a brief survey of the various system architecture approaches that have been proposed.
- Then, in Sect. 5, there is detailed consideration of one promising architectural design approach, due to DeHon and Wilson [23–25]. This approach utilizes imprinted or self-assembled nanowires for both the devices and the interconnect structures. It draws from and builds upon well-tested ideas for constructing programmable logic, such as the programmable logic

array (PLA) [26], in formulating the overall architecture. The section begins with a brief description of the structure and function of a PLA. This is followed by a brief survey and perspective on the microscale and nanoscale antecedents of this architectural approach [27]. This survey may be valuable in assisting others toward synthesizing still further design approaches that may be better suited to molecular-scale devices other than those built solely from nanowires.

- We continue in Sect. 6 with a detailed simulation of key nanowire circuits for such a PLA-based nanoarchitecture. This is intended to illustrate in a very specific manner the types of issues that will be encountered in building and operating a nanoprocessor, well before an entire system of this type actually is fabricated and integrated on the molecular scale.

By integration on the molecular scale, we mean that the basic switching devices, as well as the wire widths and the pitch dimensions (i.e., spacing between the centers of neighboring wires), all will measure only a few nanometers – the size of a small molecule – in the computer systems of interest here. Such systems may function using only one or a few molecules within their basic devices [3, 6, 16, 17, 21, 28]. On the other hand, the systems may not use molecules at all, employing instead solid-state quantum dots [29–33], and/or imprinted or self-assembled nanowires [34–36].

From a systems perspective, the very small dimensions of any of these device and interconnect structures open up new design possibilities because of the very high density of function the structures can provide. However, at the same time, the repertoire of structures available to the system designer is limited by the present difficulty of performing precise, flexible, and economical fabrication or assembly at these molecular dimensions for the very large number of conductive components that are required. Especially, the basic structures available and the demonstrated performance of the devices are not yet as diverse or robust as computer-system designers have come to take for granted when developing systems that are integrated only at the microscale. Also, the nanometer-scale switches and interconnects are likely to exhibit a higher degree of structural and functional variability than is common in the much more highly evolved technology for building microelectronics. Thus, the nanoprocessor designer must seek a strategy that takes advantage of and can walk the line between these countervailing facts of life on the nanometer scale – very high densities, but less precision, uniformity, and operational robustness.

One example of this compromise is embodied in the nanowire-based PLAs [25] that are discussed in detail in Sects. 5 and 6 of this work. The fact that the PLA architecture takes advantage of the available density to ameliorate some of the limitations implicit in present-day nanodevice and nanofabrication technologies [24, 37] seems to suggest that this architectural approach can be used successfully to develop a functioning nanoprocessor in the reasonably near term. That is, system simulations indicate that it should not be necessary

to push back very far the thresholds of present limitations on devices and fabrication in order to make progress on the system challenges.

Further, we illustrate here that as the research community attempts to move forward with detailed designs for an entire nanocomputer, system simulation can illuminate the detailed consequences of both the architecture-level design choices and the a priori constraints. Still further, the results of the simulation serve to provide focus for nanodevice and nanofabrication research, showing where it may be necessary to push back on the limits of these technologies, and where such efforts can have the most benefit for the ultimate objective of building a nanocomputer.

2 Starting at the Bottom: Molecular Scale Devices in Device-Driven Architectures for NanoproCESSORS

Whether one considers the design, simulation, or fabrication of an entire processor system, there is a hierarchy of structure and function. In the usual approach of modern electrical engineering, this hierarchy is taken to start at the highest level of abstraction, the architecture level. Then it descends down to the level of its component circuits, and finally, proceeds down to the level of the component switch and interconnect devices [38]. To a great extent, this viewpoint mirrors the “top-down” approach used in the design and fabrication of microprocessors, in which the robust performance of the devices and the ability to tune precisely the structure and performance of those devices – i.e., microelectronic transistors – is somewhat taken for granted. Architectures often are optimized to suit first the high-level, system objectives, such as computational latency and throughput, then the circuits, and finally, the behavior of the devices may be adjusted to suit particular needs of the architecture.

At present, the situation is different when one sets out to design, simulate, or fabricate an entire nanoprocessor system integrated on the molecular scale. The ability to tune the performance of nanodevices still is limited. This is partly because these molecular-scale devices are so new. Thus, the experiments [10–13,39] and the theory [40–47] necessary to understand them, design them, and make them to order still are very much in development, as is evident in the foregoing chapters of this volume. In addition, however, the ability to tune precisely the structure and performance of nanometer-scale devices may be limited inherently by the quantization of those properties, which is ubiquitous on that tiny scale.

Further, designs for nanoelectronic circuits and systems are constrained by the very small size and small total currents associated with molecular-scale switches. This is coupled with the difficulty of making contact with them using structures and materials that are large and conductive enough to provide sufficient current and signal strength to serve an entire nanoprocessor system. This system will be at least tens of square microns, if not tens of

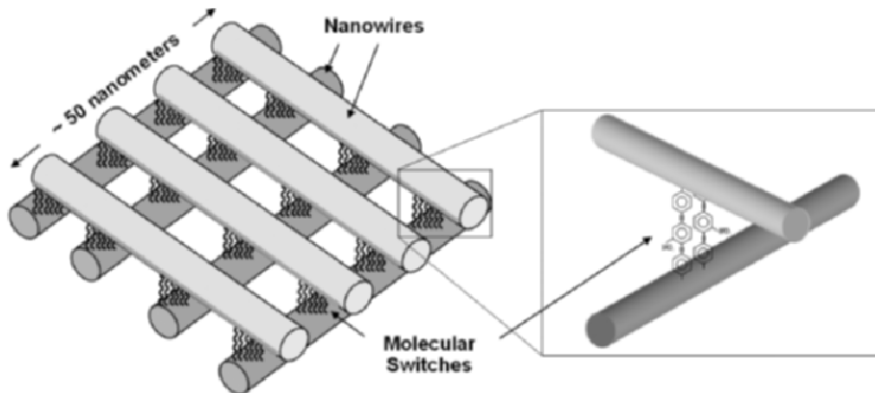


Fig. 1. “Crossbar” array of nanowires with molecular devices at junctions

square millimeters, in extent, which is millions or trillions of times larger than the molecular-scale devices themselves.

Regardless of whether all these limitations are temporary or fundamental, for now they constrain both the circuits and the architectures that are achievable in the relatively near term. Further, these limitations force us to begin consideration of the design and the simulation of nanoprocessor systems at the bottom-most level of the hierarchy, the device level.

As is true in most experiments on the electrical properties of molecules [10, 11, 15, 48, 49], for the purposes of discussing circuits and systems a molecular-scale device consists of a junction between two metal or semiconductor surfaces, with a molecular-scale structure sandwiched between. This molecular-scale structure may be one or a few molecules, as depicted in Fig. 1. Or else, it may be a layer of molecules or atoms only a few nanometers thick, as in the nanowire junction diode depicted in Fig. 2(a). While many electrical properties may be very important (especially capacitance), the electrical behavior of such junction nanodevices is characterized primarily by the current response I to an applied voltage V , a so-called I-V curve, such as is shown in Fig. 2(b).

I-V behaviors of such junctions include: simple resistance at low voltage [6], rectification [13, 22, 50], negative differential resistance (NDR) [18] and hysteresis [6, 22]. A variety of such junction nanodevices have been realized that might be useful for building extended nanoelectronic systems. The hysteretic behavior illustrated in Fig. 2(b) is particularly valuable, as it allows the “programming” of a junction into one of two states. Such bistable switches are essential components of any computing system.

Development of molecular-scale switches with appropriate I-V behaviors is essential to be able to construct functional circuits that can be used to build up processor systems. It is of particular importance to have nanoscale switches that can be used to produce signal restoration and gain, e.g.,

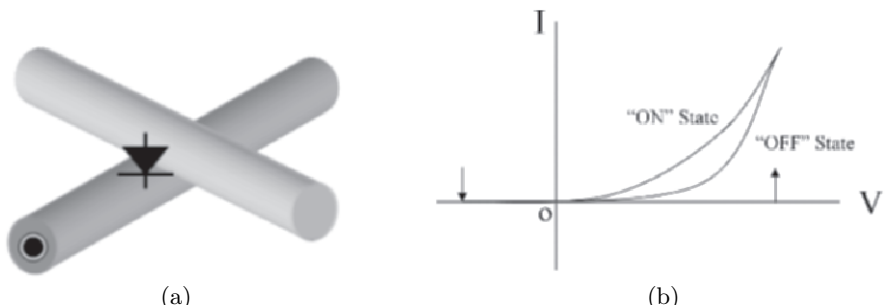


Fig. 2. Illustrations of (a) a rectifying junction switch made of crossed nanowires that sandwich a molecule or layer of molecules or atoms and (b) a representative I-V characteristic for a hysteretic, rectifying device. Hysteresis is indicated by the multiple conductance states. The high-conductance “on” state and low-conductance “off” state are depicted, and the voltage thresholds at which the device switches between states are labeled with arrows. Rectification is indicated by the unequal responses to positive and negative voltages

nanotransistors.¹ These two features are essential to maintaining electrical signals as they move through multiple levels of logic. Nanotransistors have been fabricated using carbon nanotubes (CNTs) [20, 52–54], although it remains very difficult to use them in building extended systems. There also have been some suggestions for fabricating transistors from smaller molecules [13, 55]. A few individual molecular transistors have been demonstrated based on small molecules, but only in very sensitive experiments under cryogenic conditions [56, 57]. On the other hand, robust nanoscale transistors built from crossed nanowires have been demonstrated in a number of experiments at room temperature [19].² A schematic of such a nanowire nanotransistor is displayed alongside models of its I-V curves in Fig. 3. Thus, following architects DeHon and Wilson [25], in the simulations described here, we employ these nanowire transistors in analyzing systems that might be fabricated and operated under realistic conditions in the near term.

In addition to obtaining gain and signal restoration, simpler I-V behaviors, such as strong rectification from two-terminal nanodevices, also are very important. Simulations show that even when using devices that provide good gain, rectification remains important to ensure that signals do not take unintended and undesirable paths through circuits, especially in crossbar arrays.

¹Small circuits, e.g., latches incorporating molecular diodes, also can produce signal restoration [51].

²Note that this transistor is not a junction nanoswitch since, ideally, no current flows between the nanowires. Rather, the top nanowire serves as a gate for the bottom “channel” nanowire, and the two are isolated from each other by a dielectric layer. This is in contrast to the nanowire diode shown in Fig. 2, which is a junction nanoswitch.

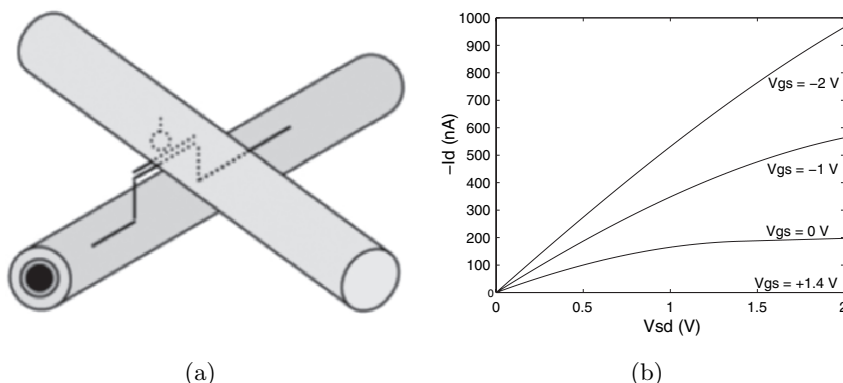


Fig. 3. Illustrations of (a) a crossed-nanowire p-channel field effect transistor (PFET) and (b) a model of the I-V characteristic for this device. The experimental basis for this model was obtained from [19]. For this transistor, the threshold voltage, at which the device produces essentially zero current and turns “off,” is observed to be approximately +1.4 V

A strong rectifier can fulfill this role by permitting current to pass only in one direction in the circuit at the designed operating voltages.

The molecular-scale electronics community is just beginning to succeed in taking the key steps required for actually building and operating an extended nanoprocessor system that integrates two-terminal junction nanodevices, as well as three-terminal nanotransistors. The steps form a hierarchy from the device to the system level, as follows: (a) development of nanofabrication approaches to build large numbers of these devices with precision and regularity, (b) development of interconnect and circuit design approaches that can incorporate such junction structures into extended circuit systems, and (c) determination of architectural approaches that include the aforementioned circuits designs and that can accommodate the limitations of the I-V behaviors available in present-day molecular electronic devices. Challenges exist at each level of this hierarchy.

3 Challenges for Nanoelectronics in Developing Nanoprocessors

3.1 Overview

In order to utilize recent advances in molecular-scale devices and circuits to build extended systems, many challenges must be faced at all levels of design and fabrication. Foremost, the structure and ultra-high density of these novel molecular-scale devices make difficult the use of conventional microprocessor architectures. Such difficulties motivate fundamental departures in

design. This then necessitates the development of new circuits, interconnection strategies, and fabrication methods, each of which, in turn, presents additional challenges. The following sections discuss some of the challenges posed by the use of conventional architectures, as well as the new difficulties that arise in novel architectures.

3.2 Challenges Posed by the Use of Conventional Microprocessor Architectures

The principal challenge of using conventional architectures [58] for the development of nanoprocessor systems is that such architectures have too much heterogeneity and complexity for existing nanofabrication methods. Conventional processor architectures are heterogeneous at every level of the design hierarchy. At the top level, a modern microprocessor consists of logic, cache memory, and an input/output interface. In conventional microscale integration, these three architectural components may be designed using different circuit styles or even different fabrication methods. The logic component itself consists of arithmetic and control subcomponents, both of which require circuits that may be either combinational (e.g., AND, OR, XOR gates) or sequential (i.e., clocked elements such as registers) [58]. Further still, the synthesis of the aforementioned combinational logic gates requires multiple kinds of devices for optimal performance [38]. This differentiation into a wide variety of devices, circuits, and subsystems is an advantageous structural feature provided by present microfabrication. Providing such differentiation is beyond the reach of present nanofabrication techniques. As a result, nanoelectronics research has targeted the development of architectures for nanoprocessors that provide comparable function while avoiding as much as possible the introduction of heterogeneity at the hardware level.

3.3 Challenges in the Development of Novel Nanoprocessing Architectures

Most of the nanoprocessor architectures presently proposed [25, 32, 33, 59–72] are essentially homogeneous at the hardware level and introduce diversification at the programming stage. In this way, they are able to do without the complexity of fabrication characteristic of conventional microprocessors.

Many of these nanoprocessor architectures inherit their design characteristics from microscale programmable logic [27], especially field-programmable gate arrays (FPGAs) [73] and PLAs [26]. As described in detail in Sect. 5, FPGAs and PLAs are regular arrays of logic gates whose inter-gate wiring can be reconfigured. Software is used to configure FPGAs and PLAs to compute particular logic functions. In contrast, the logic functions in conventional microprocessors are hard wired during construction. Thus, in FPGAs and PLAs, the use of software to “complete” the hardware construction allows the hardware design to be simplified to a homogeneous form.

Although these physically homogeneous architectures simplify fabrication, they do introduce a new set of challenges. For nanoprocessing, these challenges may be illustrated by considering the example of a nanoscale crossbar switch array. This is a homogeneous approach that combines a high degree of scalability with some of the smallest circuit structures demonstrated to date [3, 21]. The basic crossbar architecture consists of the combination of planes of parallel wires that are laid out in orthogonal directions, such as is shown in Figs. 1 and 4. Computation and communication rely on molecular-scale junction switches formed at the crosspoints of the wires as the fundamental devices.

These ultra-dense arrays are fabricated using specialized techniques such as nanoimprinting [3, 74] or flow-based alignment [34]. Prototype nanoelectronic circuits and reasonably large memory arrays already have been constructed using these techniques [7, 19, 21, 75, 76]. Moreover, a number of architectural proposals have been put forth that involve the tiling of crossbar subarrays to form programmable fabrics, including the design shown in Fig. 4 [7, 23, 25, 66].

Among the reasons that these regular crossbar structures are attractive is because it is possible to assemble them using presently available nanofabrication techniques. However, the structural regularity can increase the complexity of realizing logic at nearly every other level of the design hierarchy. One pays a penalty in the use of area and time in order to program topologically-irregular logic circuits into a physically homogeneous crossbar architecture. For example, programmable microscale circuits such as FPGAs incur approximately a 20 to 50-fold area penalty [77] and a 15-fold delay penalty [78] when compared to heterogeneous, custom-designed solutions. Thus, one significant challenge for nanoprocessing lies in developing programming algorithms that can produce area- and time-efficient realizations of heterogeneous logic using regular structures.

Furthermore, microscale PLAs and FPGAs are “mostly” regular, but some irregularity often is introduced at the lowest levels of the hardware hierarchy in order to promote more efficient utilization of physical resources [73]. Likewise, the ability to provide even a limited amount of irregularity with future nanofabrication methods might have a large, beneficial impact on the overall density and performance of a nanoprocessor.

In addition to the challenges enumerated above, the task of designing and developing novel nanoprocessor architectures must confront further difficulties in the circuit and device domains. Some of these challenges also are faced in the development of nanomemories, as described and illustrated in previous work [22]. For nanoprocessing, such issues are compounded. For example, in nanomemories, the use of two-terminal devices without gain imposes system-level constraints due to requirements for signal restoration. In nanoprocessors, requirements for signal restoration are more stringent, because the signals may need to traverse larger portions of nanoscale circuitry

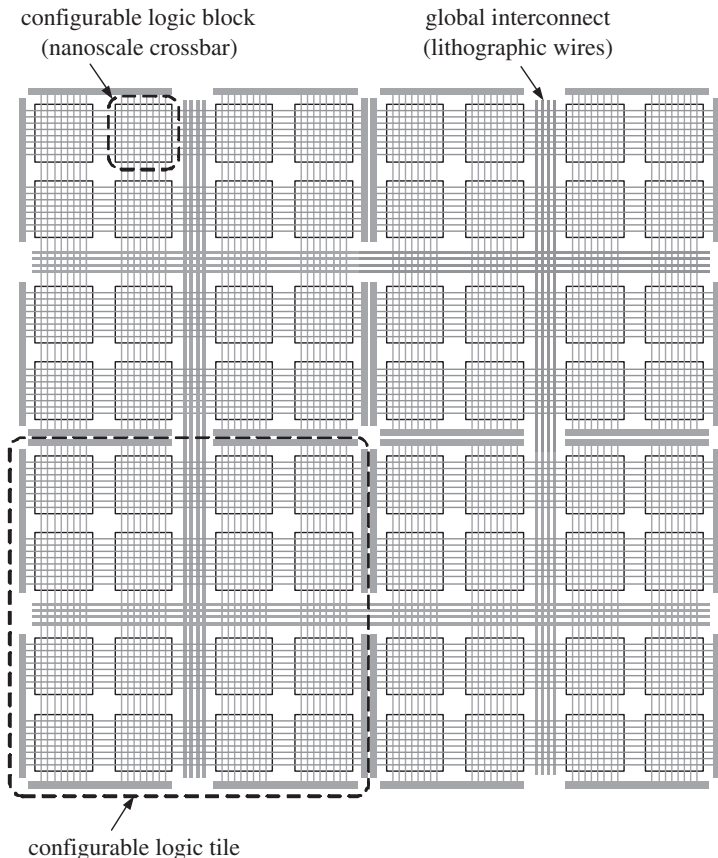


Fig. 4. A programmable fabric incorporates molecular-scale devices into the cross-bar structures shown in Fig. 1. The fabric builds from them an extended structure of molecules or molecular devices, crossed nanowires, and microwires, such as is shown above. This can provide a platform for realizing a nanoprocessor [23]

without the aid of the microscale amplifier circuits proposed for use with nanomemories [79]. Also, wires and the signals they carry must fan out in order to construct the complex logic required for processing, such as arithmetic functions. Still further, as in nanomemories, there are issues of signal integrity due to the signal coupling that arises when devices and interconnects are as densely packed as is proposed for nanoprocessors. The high density of devices also will make difficult the task of maintaining a low enough power density so that system temperature can be controlled [80].

A challenge for nanoprocessing that does not arise in nanomemories is that sequential (clocked) elements will be required. Such elements can be inefficient to realize using the combinational logic that is most readily available using

crossbars that incorporate molecular-scale resistors and rectifiers. Specialized nanocircuits have been proposed to serve as sequential elements [68, 81–84]. These circuits operate using Goto pairs [85] in implementations that were used previously in solid-state nanoelectronic circuit designs [86, 87]. In crossbars, these circuits may be built by incorporating NDR molecules [18].

One virtue of using Goto-pair-based circuits for nanoelectronic systems is that they can provide restoration using only two-terminal devices. In effect, these circuits can provide some of the gain required to restore logic signals, thus reducing the gain requirements for the other circuits in the system. Such circuits might be able to limit, and possibly even eliminate, the need for nanotransistors. However, a potential drawback is that, unlike transistor-based circuits, Goto-pair circuits may require additional components in order to provide electrical isolation between logic stages. Such isolation might be provided by distinct nanodevices such as rectifiers. However, with or without such additional devices for isolation, localized insertion and placement of Goto-pair-based clocked elements into a crossbar array probably would require introducing a degree of heterogeneity into an otherwise regular nanofabric.

A recent development that has the potential to alleviate some of these difficulties is the crossbar latch designed by the Hewlett-Packard Corporation [51, 88]. This latch has been demonstrated to produce signal restoration and inversion using only molecular two-terminal devices. It is a clocked element that is designed to be fabricated using junction molecular devices within the same homogeneous crossed-nanowire molecular-scale circuit systems (see Fig. 4) that have been used to fabricate nanomemories [4, 6, 21, 89]. Such latches could be introduced into nanoprocessor systems based on crossbars, without requiring a heterogeneous set of devices. Furthermore, as with the Goto-pair circuits, the use of these crossbar latches in a nanoelectronic system might reduce gain requirements for other circuits in the system, even to the point where nanotransistors may not be required. Nanoprocessor system architectures based on these latches still are under development [90].

For all approaches to nanoprocessor system design based upon molecular switches, it is well understood that many device-level challenges also must be addressed [2, 59]. Impedance matching between bulk solid contacts and molecular-scale devices, precise characterization of device behaviors, variability, and yield of devices are among the chief examples. These challenges will be discussed further in connection with the nanoprocessor simulations described in Sect. 6. These issues must be managed either by improving fabrication capabilities or by introducing defect and variation tolerance into system architectures.

4 A Brief Survey of Nanoprocessor System Architectures

4.1 Overview

The previous section discussed some of the challenges facing the design and fabrication of future nanoprocessors based on novel nanodevices and new nanofabrication techniques. In this section, we survey the major architectural approaches that have been proposed to address these challenges. Some of these approaches rely on new architectural paradigms that are very different from those applied in conventional microprocessors. Others borrow heavily from these microprocessor architectures. However, all of these nanoscale approaches attempt to harness molecules or molecular-scale structures to build up electronic circuits and systems. These approaches and the nanoelectronic systems that will be developed in accordance with them have the potential to utilize effectively the much higher device densities that are possible at the nanoscale. Further, because they take advantage of potentially inexpensive, novel nanofabrication techniques, it may be possible to address the issue of exponentially rising costs that presently plagues the microelectronics industry [91, 92].

Substantial progress also continues to be made in the scaling of complementary metal-oxide-semiconductor (CMOS)-based conventional microprocessors. Thus, some nanocomputer architects propose to leverage the substantial knowledge and infrastructure available in CMOS technology. Rather than devise new or modified architectures to accommodate the properties of novel nanodevices, these architects attempt to use them simply to augment the CMOS devices employed in conventional microprocessors. For the most part, such efforts retain conventional microprocessor architectural designs.

In the following sections, both the scaling of conventional architectures and the development of novel approaches are discussed. First, in Sect. 4.2, the aggressive miniaturization of conventional architectures to the molecular scale is described. Second, in Sect. 4.3, alternatives to conventional architectures are described for cases in which recent nanodevice and nanofabrication developments have made such architectures especially relevant.

4.2 Migration of Conventional Processor Architectures to the Molecular Scale

Virtually all conventional microprocessor architectures use CMOS to implement a basic architectural design originally due to von Neumann, Mauchly, and Eckert [93–95]. First described in the 1940’s, this architecture divides a computer into four main “organs:” arithmetic, control, memory, and input/output. Present examples of such CMOS-based processors include the well-known Intel Pentium® 4 and the AMD Opteron™ chips. As Fig. 5 shows for the AMD Opteron,™ the organ structure still is evident.

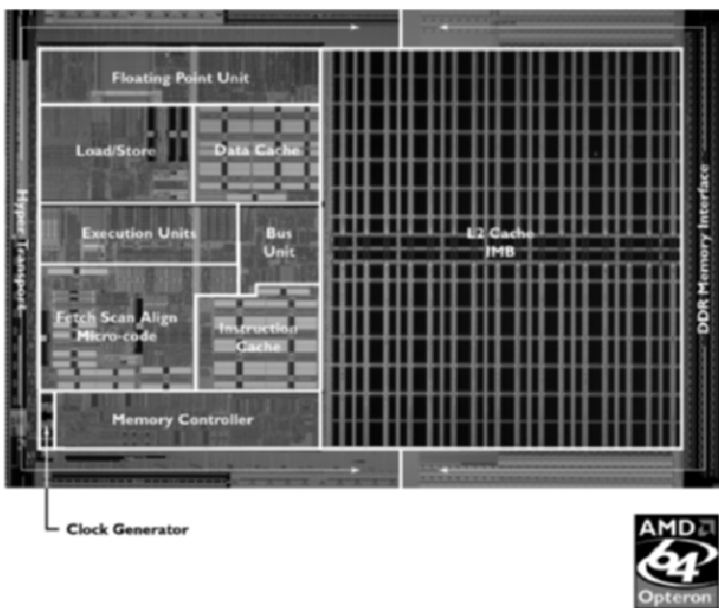


Fig. 5. AMD OpteronTM die photo with annotated block structure [96]

Because of its long-term investment, industry places a high premium on maintaining these architectures as it seeks to achieve ultra-dense integration on the nanometer scale. The primary industry approach today to building nanoprocessors is the aggressive scaling of CMOS technology to nanometer dimensions.³ However, for a number of years, industry investigators and others have examined the likely limits of CMOS technology [98–100, 102, 103] and the possibility that it might not be cost-effective to use it to build commercial systems with devices scaled down to a few tens of nanometers. This is one of the reasons that new architectural ideas inspired by nanotechnology and molecular-scale electronics are so compelling.

An alternative to the straightforward, two-dimensional, aggressive scaling of CMOS is to expand silicon technology into a third dimension [102]. Three-dimensional integration, or 3-D CMOS [104, 105], refers to any of several methods that take conventional, “flat” CMOS wafers and stack them together with an inter-wafer interconnect [106–111]. For microprocessors, it has been shown that 3-D integration allows for a substantial improvement in performance, and, furthermore, that this improvement increases as device and interconnect dimensions decrease [112]. Therefore, 3-D architectures may

³This topic has been reviewed and discussed extensively elsewhere [97–101]. We include a brief discussion of it here both for completeness and to provide a reference point for the other, more novel approaches we discuss.

have particular utility in combination with novel molecular-scale devices, such as might be implemented using a 3-D crossbar array.

So-called “hybrid” approaches that incorporate novel nanostructures into CMOS devices constitute a third avenue by which conventional processor architectures may be migrated toward the molecular scale. Major industrial research laboratories have begun to explore how nanowires and CNTs might be employed to enhance CMOS and CMOS-like structures. For example, some of the Intel Corporation’s designs for future transistors call for the incorporation of silicon nanowire channels to increase current density and to control short-channel effects [113]. Similarly, work at IBM has examined the increased current that results from the insertion of CNTs into CMOS field-effect transistor (FET) channels [114].

Another hybrid approach involves the use of self-assembled monolayers of redox-active molecules to enhance the function of traditional silicon devices. Thresholds and conductances of the underlying silicon substrate can be altered by the incorporation of these monolayers. In addition, new and novel devices might be enabled; for example, the redox states of the molecules in the SAMs may be used to form multi-level bits (i.e., n-ary digits) [115, 116]. Such so-called molecular FETs, or MoleFETs, which employ NDR molecules or charge-storage porphyrin molecules on silicon, might be used to implement multi-level memories or logic. It appears that molecules and molecular layers can be inserted into CMOS production processes for this purpose. For example, the porphyrin molecules proposed for some of these hybrid devices have been shown to be able to survive the 400°C processing temperature used for conventional CMOS components [117]. Also, Nantero Corporation is succeeding in introducing novel carbon nanotube-based devices and circuits into a CMOS production line [118].

Hybridization also may be employed at the architectural level. An example of such a hybrid design is the CMOL architecture. As is depicted in the previous chapter of this volume [69], CMOL circuits combine CMOS with crossed nanowires and molecular devices (see also Fig. 1 and Sect. 3.3 of the present chapter). Specifically, CMOL circuits are to be fabricated in two layers, with one layer consisting of CMOS blocks, or “cells,” and the other layer containing an array of crossed nanowires employed as interconnects between the CMOS cells. As with many other crossbar architectures, the nanowire crosspoints are designed to contain programmable molecular devices. These devices should permit reconfiguration of the nanowire-based connections between the CMOS cells. Therefore, if physical experiments confirm the designers’ preliminary analyses [69, 70], it is likely that CMOL may be used to implement any architecture based upon programmable interconnects. Thus far, quantitative analyses of the CMOL designs seem promising, but no fabrication experiments have been undertaken to build and test CMOL circuits.

Two types of CMOL circuit architectures have been proposed, neural networks and FPGAs [69, 70]. The salient features of these architectures

serve here to illustrate the potential advantages and challenges of hybrid CMOS/nano designs in general. For example, like microscale neural networks, the CMOL neural-network architecture exploits parallelism in order to reduce operating speed and thereby save power. However, the designers assert that, unlike microscale neural networks, CMOL may be able to achieve the density of cells and interconnects required in order to emulate advanced neural networks, such as organic brains. As another example, CMOL FPGAs may be able to improve performance significantly, relative to conventional CMOS FPGAs, by utilizing nanoscale interconnects. This is because conventional FPGA circuit performance is limited predominantly by interconnect performance [119]. In both examples, CMOL is designed to build upon conventional CMOS circuitry, yet circumvent its limitations by exploiting the ultra-high density of devices available at the nanoscale.

In general, hybridizing at device, circuit, or architectural levels may allow the semiconductor industry to leverage the best features of both conventional CMOS and novel nanostructures. However, this combination does introduce additional challenges. One potential difficulty lies in designing the interface between CMOS and nanoscale components. For systems built solely from nanodevices, such an interface is required only at a relatively small number of points at the periphery of the nanoelectronic circuit system. In contrast, hybrid architectures necessitate tighter and denser integration of the many, many individual CMOS components and nanostructures *within* the circuit system.

For example, the CMOL approach proposes novel interface pins to accomplish this task [69]. However, such pins must be manufactured to tight, sublithographic tolerances. Also, to contact these pins, precise linear and angular alignment of the nanowire array is likely to be required. In addition, because of the high bandwidth of communication proposed between CMOS and nanoscale components, impedance matching between these components is a potential source of difficulty. Experimental measurement of the impedances of proposed interface pins must be undertaken in order to determine the suitability of such pins for hybrid approaches.

A more fundamental difficulty introduced by combining CMOS with nanostructures is that overall scalability may be limited by the scalability of CMOS technology. Such technology is almost certain to hit physical barriers to further scaling. Thus, new processor architectures must be devised that can operate solely with novel nanodevices. Proposals for such architectures are reviewed in the following section.

4.3 Overview of Novel Architectures for Nanoelectronics

A set of clever, yet profound architectural concepts underlies the prototype nanomemory and nanoprocessor circuit systems that just now are emerging [23,25,32,59,61,63,65]. These architectural innovations seek to take advantage

of the strengths of novel nanodevices (especially, high device density and non-volatile, low-power operation), as well as to ameliorate some of the limitations discussed in Sect. 3 in the techniques presently available for fabrication and assembly at the nanoscale (e.g., the inability to place nanostructures precisely or to make them readily with arbitrary shape or complexity). At the highest level, one may view these architectural innovations as falling into two classes, as discussed in the subsections immediately below.

Radical Departures from Microelectronic Architectures

One broad class of architectures has been devised strictly by taking demonstrated nanodevices and considering how to combine them into circuits or circuit-like structures that may then be fashioned into complex systems. This bottom-up style of nanoprocessor design has resulted in a number of architectural approaches that differ drastically from conventional architectures. These novel approaches, which are considered in detail elsewhere, include quantum cellular automata (QCA) [32, 33, 60–62], nanoscale neural networks [63, 69], nanocells [28, 64, 65], and biologically inspired electronic system structures such as the virus nanoblock (VNB) [120, 121]. Each of these encompasses important ideas and has virtues either in ease of fabrication or in ultra-low power consumption.

The QCA approach seeks to use electric fields, rather than currents, to set bits and propagate signals by moving the charge distributions in arrays of multi-quantum-dot structures termed quantum-dot cells. The primary virtue of this approach is that it is predicted to have ultra-low power dissipation, which is highly desirable in a very dense array of nanostructures. Also, the very small size of molecular quantum dots may permit this scheme to operate at room temperature, in contrast to solid-state QCA approaches that require cryogenic operation. However, a circuit employing a molecular QCA approach has not yet been demonstrated.

The nanocell architecture employs an array of nanoparticles randomly distributed and randomly connected by self-assembled molecules that typically exhibit negative differential resistance and voltage-dependent switching. No attempt is made to control the placement of the molecules that make up the individual interconnects; rather, the designer takes advantage of the molecules' switching characteristics to program the nanocell after it has been assembled. Input and output connections are fabricated on the lithographic scale using conventional techniques. This permits relative ease in manufacturing nanocells, as well as in connecting them to form higher-order circuits. As such, high-level designs may be possible that are similar to today's Very Large Scale Integrated (VLSI) circuits [64].

The nanocell architecture avoids potential difficulties in precise nanoscale fabrication. Instead, the desired connectivity is established by intensive post-fabrication testing and programming. Because of its random assembly and

post-fabrication programming, the nanocell approach is inherently defect and fault tolerant [64]. Experimental nanocell memories recently have been fabricated [28] and logic gates have been simulated, but not yet demonstrated.

These architectures, which depart significantly in their operational and organizational principles from those of present-day computers, may make important contributions over the long term. However, their differences from almost all industry architectures mean that they cannot harness easily the significant infrastructure developed by the existing electronics industry. Thus, at the moment, they have more hurdles to overcome and appear to be further from being applied to build extended nanoprocessing systems than the regular array structures discussed below.

Regular Array Architectures Derived from Microelectronics

This second class of novel nanoelectronic architectures is derived via the adaptation and ultra-miniaturization of microelectronic FPGAs and PLAs so that they can be implemented with novel nanodevices and new nanofabrication techniques. For the purposes of achieving some near-term successes in developing and operating prototype nanoprocessors, these regular arrays occupy an important middle ground between the radical departures discussed above and the very inhomogeneous architectures used in conventional microprocessors. Nanoarray architectures have an appealing structural simplicity that takes advantage of a number of the strengths of novel nanodevices and nanofabrication techniques. Thus, physical prototypes of extended nanoarray processors are approaching realization based upon much systematic effort [3, 5–7, 21, 25, 75], including the detailed simulations described in Sect. 6.

There have been criticisms of the use of PLAs to develop nanoprocessors [69]. Some of these criticisms are premised on the assumption that nanoPLAs will not incorporate gain-producing or restoration-producing nanodevices. However, this is not necessarily the case. For example, the nanoPLA architecture due to DeHon and Wilson [25] does incorporate gain-producing nanowire-based nanotransistors, as is described in detail below. Other criticisms focus on the issue of heat dissipation. This is a valid concern, due to the high density of current-based devices. However, circuit techniques, such as the use of dynamic instead of static logic, may alleviate this problem [25].

Thus, because the path to the realization of these novel nanoelectronic architectures seems clearer and nearer at hand, the rest of this chapter will focus on a discussion of the operational principles, advantages, and trade-offs of FPGA- and PLA-type nanoarray processor architectures.

5 Principles of Nanoprocessor Architectures Based on FPGAs and PLAs

5.1 Overview

Having provided a brief survey above of various architectural approaches for nanoprocessors, we now focus our attention exclusively on regular arrays such as FPGAs and PLAs. Until recently, the use of such regular arrays in general-purpose, microscale computation has been disfavored relative to the use of conventional, heterogeneous architectures. Thus, to understand how regular arrays may be leveraged for nanoprocessing, it is important to review their use in conventional processing systems and to illustrate the benefits and challenges. Following this brief review, a specific regular architecture for a nanoprocessor will be explored, the DeHon-Wilson PLA.

5.2 Description of Regular Arrays, FPGAs, and PLAs: Advantages and Challenges

A regular array is a homogeneous two- or three-dimensional grid of configurable logic elements (such as four-input logic tables) interconnected by wires with embedded programmable switches (i.e., “programmable wires”) [73]. The array is configured by programming the individual logic elements and switches to define a hardware implementation of a desired logic function. Thus, regular arrays attempt to eliminate heterogeneity at the hardware level, introducing it at the software level instead. Present fabrication methods for nanoelectronics, which rely on bottom-up, self-assembly approaches, produce such homogeneous systems of nanostructures relatively easily [3, 5, 75].

In conventional microelectronics, regular structures are employed for special-purpose applications in the form of circuits such as FPGAs and PLAs. A schematic diagram of a PLA is given in Fig. 6(a). Figure 6(b) shows an extended system architecture based on PLAs. This system structure is similar to that used for FPGAs. (See Sect. 3.3 for a brief description of FPGAs.)

Because of the underlying homogeneity of such structures, thus far they have been outperformed by classical microprocessor architectures at carrying out general-purpose computation. For a given application, an FPGA may be programmed to outperform a general-purpose microprocessor. However, a key capability of general-purpose microprocessors is their ability to switch rapidly between various applications. If the FPGA is configured to provide an equal amount of so-called “context switching” capability, the FPGA implementation usually lags in performance [77].

This is because the general class of functions that can be computed by a conventional processor is quite large, and the best way to compute the whole class of functions on an FPGA has been to program the FPGA as a conventional processor. This is inefficient. However, this inefficiency is not believed to be fundamental. It may be the case that migration to the nanoscale will

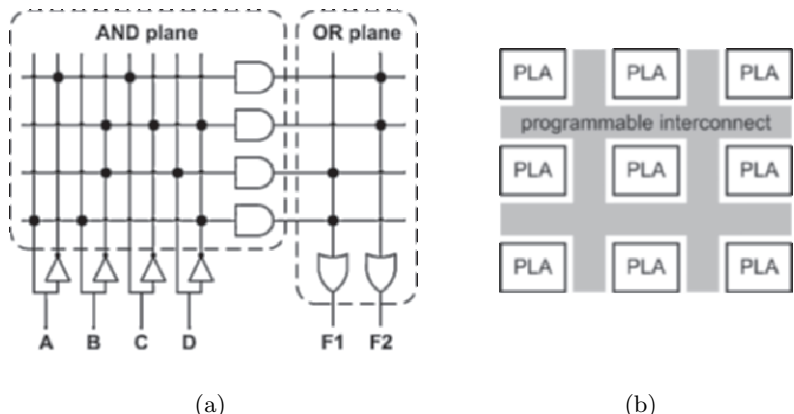


Fig. 6. Schematic illustrations of (a) a single PLA and (b) an extended system architecture based on an array of PLAs. A single PLA consists of a plane of AND gates followed by a plane of OR gates. The interconnections between these gates are reconfigurable after fabrication. In this example, output F_1 is programmed to compute $(A \text{ AND } B \text{ AND } (\text{NOT } D)) \text{ OR } ((\text{NOT } B) \text{ AND } D)$, based on the configured connections shown by the *black dots*. More complex, hierarchical logic can be constructed using an array of PLAs, such as is shown in part (b). Here, outputs such as F_1 and F_2 can be used as inputs to other PLAs in the array

address this problem. At the nanoscale, it is conceivable to operate with many trillions of devices per processor. With so many devices, it may be possible to implement simultaneously all the required functions that make up a given set of programs [122]. Similarly, the existence of programmable nanoscale interconnects may improve the efficiency of array-based implementations, since the area overhead of each switch can be reduced.

Thus, due to the large number of available devices and the inherent regularity produced by several nanofabrication methods, array architectures have become prominent in nanocomputation research. In the next section, we will describe one such promising architecture, due to DeHon and Wilson [25].

5.3 The DeHon-Wilson PLA Architecture

A very thoroughly thought-out example of a nanoarray architecture that utilizes nanowires in readily realizable crossbar structures is the DeHon-Wilson PLA architecture [23–25, 37]. A high-level diagram of this architecture is shown in Figs. 4 and 6 (b), while Fig. 7(a) provides a detailed view of the low-level implementation. As with microelectronic PLA-based designs [26], the large-scale architecture of this nanoprocessor combines a number of PLAs into still larger arrays.

In general, a PLA consists of a programmable AND plane (with a number of AND gates in parallel) followed by a programmable OR plane (with

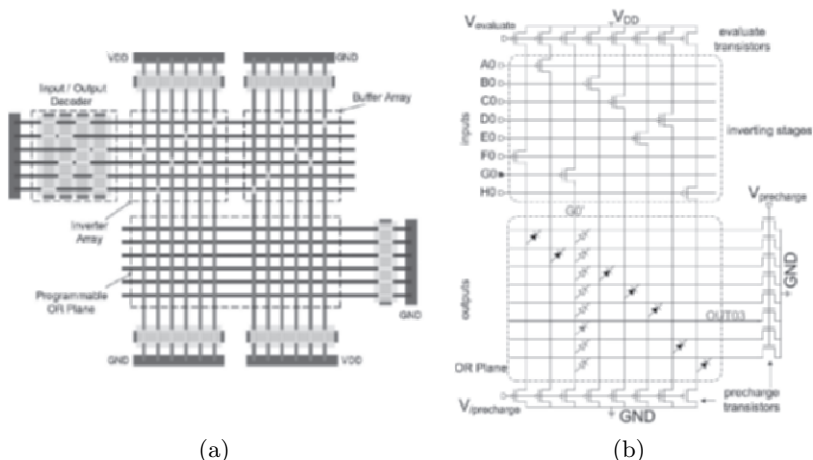


Fig. 7. Illustrations of (a) the DeHon-Wilson PLA Architecture and (b) an 8×8 inverting block. The eight vertical wires shown in part (b) correspond approximately to the vertical wires in the left-hand side of the subarray in part (a)

a number of OR gates in parallel), as shown in Fig. 6(a). Inverters also are available for all inputs. Since any combinational logic function can be written as the OR of some number of AND terms, any such function can be synthesized using a PLA, assuming the PLA is large enough to contain all the logic terms [38].

In the DeHon-Wilson design, a crossbar subarray is used to provide the logical equivalents of the AND and OR planes of the PLA, as shown in Fig. 7(a). The system is extended by tiling crossbar subarrays, as illustrated in Fig. 4. Figure 7(a) shows the four major subsystems of the DeHon-Wilson PLA implementation: an array of crossed-nanowire diodes used as a programmable OR plane, one inverting subarray of crossed nanowire transistors, a similar buffering subarray, plus an input/output decoder. The inverting and buffering subarrays each are used to regenerate signals and maintain their strengths.

In this PLA scheme, the AND planes are replaced by logically-equivalent pairs of inverting subarrays and OR planes. Figure 7(b) shows a more detailed circuit-level characterization of the left-hand side of the system in Fig. 7(a). In the bottom half of the subarray shown in Fig. 7(b), all the crossed-wire junctions are taken to contain switchable or “programmable” diodes. By programmable, we mean that the diode can be set to either a high (“on”) or low (“off”) conductance state in the conductive direction. Where the diodes are not shown, they are taken to be always off, so that the block depicted produces the desired function. Where the solid diodes are shown explicitly, they are taken to be always on. The hollow diodes are turned on or off within a simulation in order to test fan-out in the system. In addition to the transistors

and diodes shown, the representation in a simulation can incorporate parasitic resistances and capacitances that have been omitted for visual clarity.

The DeHon-Wilson architecture is notable because it is designed explicitly to tolerate shortcomings in present-day nanofabrication. Within the crossbars of the DeHon-Wilson architecture, redundant wires are used to overcome potential failures due to misalignment or physical defects. A stochastic scheme is used to connect to and thereby address specific wires so that unique addressing can be nearly guaranteed without the need to pick and place individual wires [24]. Also, the inverter and buffer arrays can function in two modes, static and dynamic [25]. In dynamic mode, static power consumption is reduced [38]. This ameliorates the potential problem [69] of heat dissipation in ultra-dense, current-based designs.

Efforts are underway to implement the DeHon-Wilson architecture. Prior to its actual fabrication, there are parameters that remain to be tuned and assumptions that remain to be verified. The most cost-effective method for doing this is the use of nanoprocessor system simulation, as has been demonstrated convincingly in the development of conventional microprocessors [123] and as is discussed further below.

6 Sample Simulation of a Circuit Architecture for a Nanowire-Based Programmable Logic Array

System simulation can produce an integrated, multi-level view of candidate nanocomputer architectural performance. This view considers optimization at the device level simultaneously with the problems of designing the system at the circuit and architecture levels. At this early stage of nanocomputer development, it is possible to provide useful insights and guidance to device developers, as well as system architects, by simulating even small component circuits and subsystems. In the following subsections, we describe a simulation and analysis of the DeHon-Wilson PLA [25].

6.1 Methodology for the Simulation and Analysis of Nanoprocessors

The details of our nanoelectronic system simulation methodology have been described previously [22]. Thus, only a brief overview is presented here.

The simulation methodology consists of three parts. First, empirical I-V behavior models are developed for the fundamental component nanodevices and small prototype circuits that have been demonstrated experimentally. Second, these device models are incorporated into schematic descriptions of the nanoprocessor system, as well as extended subsystems, based on the architectural design. Finally, system simulations are carried out using representative inputs. The simulations have the effect of extrapolating from the

experimentally known device behaviors and the planned circuit designs to obtain a projection of the behavior of an entire nanoprocessor system. From these results, the tuning of device, circuit, and architectural design parameters may be investigated for its effect on the overall system performance. Significantly, this may be done in advance of time-consuming, costly, and difficult trial-and-error experiments.

The primary simulation software that has been used in the work described here is the DFII integrated-circuit computer-aided design package available from Cadence Design Systems of San Jose, California [124]. This commercial off-the-shelf software tool was chosen for the substantial time savings and reliability associated with the use of readily available, well-tested software. The Cadence package also incorporates particularly useful features, such as a graphical interface and modeling languages, that have been developed over many years specifically for the flexible modeling of custom circuits and devices. This enabled the authors to adapt the simulation tools particularly for the novel nanoelectronic devices and circuit structures described here. Individual device models were developed from empirical fits of experimental data, either from published literature or provided by the developers, using the hardware description language (HDL) Verilog-A. These empirical models then were incorporated into the component Spectre circuit simulator, which supports co-simulation of both novel components modeled in Verilog-A and conventional devices modeled using SPICE.

6.2 Device Models for System Simulation of the DeHon-Wilson NanoPLA

Construction of a nanoprocessor according to the DeHon-Wilson nanowire-based PLA architecture requires four distinct nanodevices, each of which requires a distinct I-V behavior model within the system simulation. All four of these devices are represented, for example, in the schematic in Fig. 7(b). Three of these devices are the nonvolatile nanowire (NVNW) diode, the microwire top-gated FET (TG-FET), and the nanowire interconnects. A diagram of the nanowire diode is depicted in Fig. 2(a). It is made from two crossed, bandgap-engineered nanowires. The microwire TG-FET resembles the crossed-nanowire FET shown in Fig. 3(a), except that for the TG-FET, the top wire is a much larger microwire. Detailed descriptions of the I-V behavior models derived for all three of these devices are published in prior work [22].

The fourth device and device model required for the nanoPLA is the crossed-nanowire FET (cNWFET) [5, 34–36], which acts as the input transistor for the restoration blocks. The cNWFETs are constructed by crossing a nanowire over another nanowire that is coated with silicon dioxide, as depicted in Fig. 3(a) [34]. The oxide isolates the coated nanowire and allows it to act as the channel of a field-effect transistor, while the uncoated nanowire serves as the gate. Figure 3(b) shows an I-V behavior model that has been

developed for this device and incorporated into the simulations. This model reproduces published experimental I-V characteristics [19], although some extrapolation beyond the measured voltages was necessary.

One important observation from the I-V characteristics of the cNWFETs is that the experimentally-observed threshold voltage (V_T) of the p-channel FETs (PFETs) ranges into positive values. In contrast, conventional micro-electronic circuits employ PFETs that have a negative threshold [38]. Some circuits, including the ones we explore here, can be made to function correctly using PFETs with positive thresholds. However, such operation is disadvantageous. In static mode, these circuits consume a great deal of power and usually are not capable of providing adequate signal restoration. Thus, dynamic-mode operation would be preferable. However, for the dynamic operation of the circuits we examine, the PFET V_T threshold must be negative.

Recent experimental results suggest that nanowire p-channel transistors can be fabricated with the desired negative thresholds [35] and that the value of this threshold can be controlled [36]. Based on these experimental results, we have extrapolated a cNWFET model with a reasonable negative value for the PFET threshold voltage. Use of this model permits simulation of these circuits in dynamic mode.

With the device models developed for all required devices, as described above, system simulations were conducted in accordance with the proposed architecture shown in Fig. 7. Parasitic behaviors of the nanowire arrays, such as coupling capacitance, also were incorporated.

6.3 Simulations and Analyses of the NanoPLA

The simulations described here consider primarily the performance of a 64-bit PLA. This is represented by an 8×8 OR plane driven by eight inverting stages, as shown in Fig. 7(b). The PLA is programmed with the pattern of diodes depicted there and described in Sect. 5.3. The input vectors to the PLA are given in Table 1.

The generally accepted method for determining the viability of a circuit system is to assess its operation under the least favorable circumstances. Thus, analysis is performed here by examining the worst-case high and low output voltages. The signal OUT_{03} , which is labeled in Fig. 7(b) and is the inversion of the G_0 input, is likely to produce the worst-case measurements. This is because, given the switch configuration shown, the length of wire traversed for this output is greatest, which results in the largest parasitic resistance and capacitances.

Functionality of the circuit can be determined by providing a specific input waveform and programmed function, then simulating the output waveform to determine if the function is realized. Such a simulation is illustrated in Fig. 8, which shows an output waveform for OUT_{03} when the circuit in Fig. 7(b) is programmed to implement the inversion of G_0 . Also shown is the clocking scheme (i.e., the precharge and evaluate signals) for operating the inverting

Table 1. PLA Input Vectors

A_0	B_0	C_0	D_0	E_0	F_0	G_0	H_0	
1	1	1	1	1	1	0	1	High Output
0	0	0	0	0	0	1	0	Low Output

block in dynamic mode. To understand this scheme, it is first necessary to appreciate that the circuit operates in dynamic mode by storing charge on the wires and the terminals of the devices. Thus, the precharge signals serve to set the charge state of all these elements (e.g., to a charge state that produces a low voltage equivalent to logic “0”). Then, the evaluate signal is used to change the charge state appropriately on some of the wires and terminals (e.g., those for which the correct logic value would be “1”).

The dynamic precharge-evaluate cycle first begins when the precharge signal goes high. This has the effect of switching on the n-channel FETs at the right of Fig. 7(b), to discharge the outputs of the inverting block to a low voltage. After the precharge is completed, the evaluate signal transitions to a low voltage, which turns on the evaluate PFETs at the top of Fig. 7(b) in order to produce the desired output signal on OUT_{03} . As can be seen in Fig. 8, the OUT_{03} waveform will continue to be pulled to a high voltage until the evaluate signal is turned back high. After the evaluate transistors turn off, the signal begins to drop, due primarily to leakage through the transistors.

Analyses based upon simulations of this type allow the determination of system behavior and limits. For example, by setting a priori the levels for the minimum logic “1” voltage and maximum logic “0” voltage, a minimum operating frequency may be calculated from the signal decay data shown in the bottom graph of Fig. 8. Thus, these simulations can help characterize how transistor leakage impacts the performance of the system.

Alternative simulations can examine still other effects. For example, diode loading can affect system operation. Simulations suggest that there is a limit to the number of diodes that may be turned on and permitted to load a single input column of the inverting stage. For one such simulation, Fig. 9 shows the output-voltage dependence of the number of diodes programmed in the “on” state along the G'_0 column (see Fig. 7(b)), which drives the OUT_{03} output row. The high output voltage, and thus the voltage swing, is reduced as more diodes are programmed “on” and load the driving column. This is a result of current being divided among multiple outputs.

From another simulation for which results are plotted in the bottom curve of Fig. 9, it is seen that the low or “0” output voltage signal remains relatively constant as the number of “on” diodes is increased. This is because the input vector in Table 1 used in this simulation for the low output drives all the row wires in Fig. 7(b) except OUT_{03} to logic “1.” This has the effect of

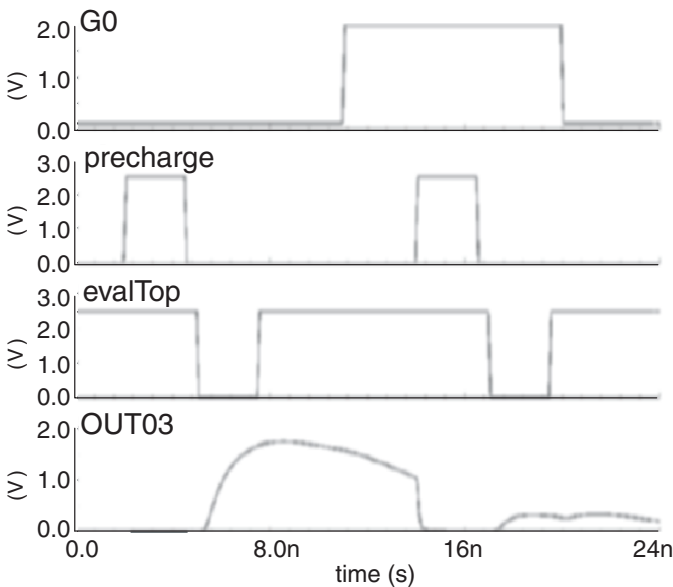


Fig. 8. Waveforms describing how the circuit in Fig. 7(b) inverts input signal G_0 to produce output signal OUT_{03} . See discussion in text

reverse-biasing all the diodes on the G'_0 column that connect to rows other than OUT_{03} . Thus, little current will flow through the diodes into those rows.

While these results show that the circuits can function correctly, they also suggest a limit to the number of “on” diodes that can load the restoring columns. The simulations suggest the maximum number of diodes that can load each column is approximately five. Otherwise, it is found that the voltages representing “1” and “0” get so close together that they cannot be distinguished by the gates in the downstream logic stages. Thus, there is a limit on the number of functions that may use the same input.

There are a number of ways to increase this limit. One way would be to reduce leakage through the nanowire transistors. This requires that difficult experiments be carried out in order to alter device performance appropriately. Another way to increase the limit would be to increase the capacitance at each output. However, this increased capacitance, which takes longer to discharge, also takes longer to charge. This reduces the maximum operating speed of the system. Still a third way would be to introduce duplicate columns, where the input transistors are driven by the same row nanowire.

Also, the restoration-producing portions of the nanoPLA array are likely to be particularly sensitive to variability in the nanodevices. In simulations we have performed on the buffering subarrays, it is seen that a buffer can fail to restore signals adequately if the control signals that would derive from

Output Voltage and Diode Loading

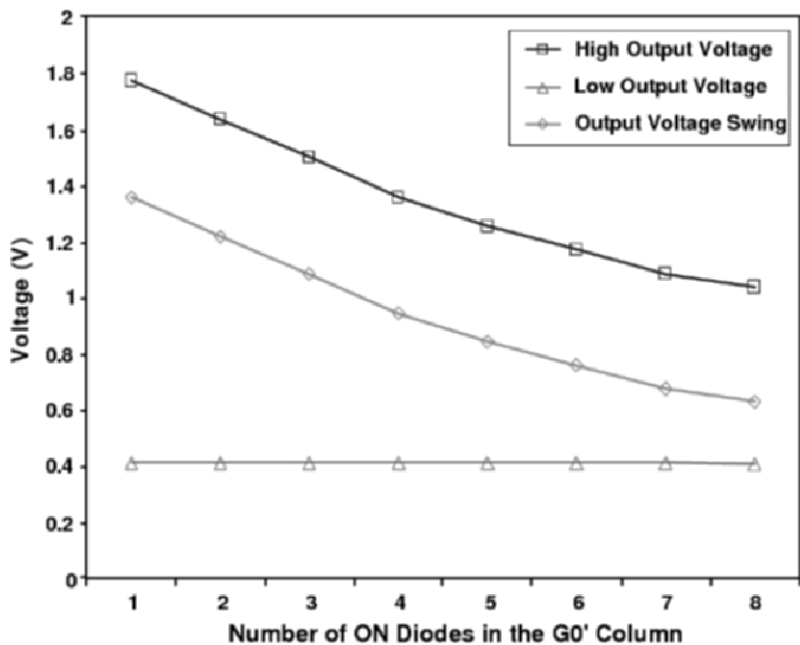


Fig. 9. High and low output voltages and output voltage swing plotted against the number of diodes programmed ON in the G'_0 column

other logic subsystems vary outside of a small acceptable range. A likely source of control signal variation is variation in the structures of devices.

Specific results and design guidance, such as are described in the examples above, illustrate that system simulation is an effective way to extrapolate from device experiments to consider and improve various nanoelectronic system design options.

6.4 Further Implications and Issues for System Simulations

Although the results shown above are derived from simulations of a particular nanoprocessor system, the implications are significant for a wide variety of potential designs and architectures. Any system based on electronic currents flowing through densely-packed circuits must consider issues such as signal integrity, power density, fan-in, fan-out, and gain. For example, we have shown explicitly in Sect. 6.3 how the design of such systems must consider fan-out, which in the DeHon-Wilson architecture is the number of diode-connected rows a single inverting column can drive. Fan-out is an important issue to the design of any nanoscale architecture, in that greater fan-out capability aids in reducing the number of logic levels and the area required when imple-

menting complex functions. Several of the nanoscale architectures proposed to date are based on PLAs, much as is envisioned in the DeHon-Wilson architecture [23, 25, 59, 66, 67]. As such architectures move toward realization, it will be up to device and circuit designers to find ways to address issues like fan-out for the purpose of optimizing system robustness.

It is important to note that the simulations presented here represent only the first steps toward detailed, extensive simulations of complete nanocomputer architectures. There are further issues that must be explored for the DeHon-Wilson architecture and other architectures. These issues include system impacts of crosstalk, transistor leakage, and power density. Crosstalk, the loss of signal through coupling capacitances between neighboring wires, can impair significantly the performance of any system consisting of closely-packed wires. Understanding the extent of crosstalk, and devising means for controlling it, can provide design flexibility to improve signal integrity, while possibly reducing power density. Leakage current is another factor that contributes to increased power consumption and to signal degradation. Preliminary experimental data suggest that leakage currents can be relatively large for many of the devices used in this architecture. This would result in increased static power consumption and decreased output voltage-level stability. While it probably will be feasible to reduce the leakage, this will require further careful experimentation.

Well in advance of such time-consuming experiments, system simulations can indicate the extent to which such enhancements in devices might improve system performance. If such improvements are significant, then it becomes worthwhile for experimentalists to invest in enhancing designs and techniques for fabricating nanodevices.

7 Conclusion

In this chapter, we have surveyed a range of possible architectural approaches to the development of electronic nanoprocessors. Following this survey, we have focused upon architectures that occupy an important middle ground between conventional microelectronic architectures and a set of more radical nanoelectronic architectures. To explore this middle ground, we have adapted the simulation tools and techniques used by the microelectronics industry. In so doing, we are attempting to bridge the gap between the present realm of pure research in nanoelectronics and the application of the resultant innovations in functional, manufacturable systems.

Using the detailed simulations of the subsystems embodied in one such middle-ground nanoprocessor architecture, the DeHon-Wilson PLA, we have examined some of the trade-offs that affect such a system based upon molecular-scale devices. Many of these trade-offs apply to almost any nanoprocessor architecture that might be adopted to harness molecules or molecular-scale devices in ultra-dense electronic computing structures. Thus,

we believe that the simulations described here should assist experimentalists to understand better the path they must follow if they are to take steps toward applying their structures and devices.

Work of the type described above translates the hard-won results of difficult experiments upon nanodevices and small circuits into insights that illuminate the new frontier of nanoprocessor systems development. Thus, by simulations such as we have described, coupled closely with device and system experiments, it may be possible both to speed the realization and optimize the performance of ultra-dense electronic computers integrated on the molecular scale.

References

1. K. S. Kwok, J. C. Ellenbogen: Moletronics: future electronics, *Materials Today* **5**, 28–37 (2002).
2. J. R. Heath: Wires, switches, and wiring. A route toward a chemically assembled electronic nanocomputer, *Pure Appl. Chem.* **72**, 11–20 (2000).
3. N. A. Melosh, A. Boukai, F. Diana, B. Gerardot, A. Badolato, P. M. Petroff, J. R. Heath: Ultrahigh-density nanowire lattices and circuits, *Science* **300**, 112–115 (2003).
4. P. J. Kuekes, J. R. Heath, R. S. Williams: Molecular wire crossbar memory, United States Patent 6,128,214 (2000).
5. D. Whang, S. Jin, Y. Wu, C. M. Lieber: Large-scale hierarchical organization of nanowire arrays for integrated nanosystems, *Nano Lett.* **3**, 1255–1259 (2003).
6. Y. Chen, G. Jung, D. A. A. Ohlberg, X. Li, D. R. Stewart, J. O. Jeppesen, K. A. Nielsen, J. F. Stoddart, R. S. Williams: Nanoscale molecular-switch crossbar circuits, *Nanotechnology* **14**, 462–468 (2003).
7. G. Snider, P. Kuekes, R. S. Williams: CMOS-like logic in defective, nanoscale crossbars, *Nanotechnology* **15** (2004).
8. Overview of the DARPA Moletronics Program at <http://www.darpa.mil/MTO/mole/>.
9. Overview of the DARPA MoleApps Program at <http://www.darpa.mil/dso/thrust/matdev/moleapps.htm>.
10. J. Tomfohr, G. Ramachandran, O. F. Sankey, S. M. Lindsay: Making contacts to single molecules: Are we there yet?, *Lect. Notes Phys.: Intro. Mol. Elect.* (2005).
11. W. Wang, T. Lee, M. Reed: Intrinsic electronic conduction mechanisms in self-assembled monolayers, *Lect. Notes Phys.: Intro. Mol. Elect.* (2005).
12. J. van Ruitenbeek, E. Scheer, H. B. Weber: Contacting individual molecules using mechanically controllable break junctions, *Lect. Notes Phys.: Intro. Mol. Elect.* (2005).
13. R. M. Metzger: Six unimolecular rectifiers and what lies ahead, *Lect. Notes Phys.: Intro. Mol. Elect.* (2005).
14. J. C. Ellenbogen, J. C. Love: Architectures for molecular electronic computers: 1. logic structures and an adder designed from molecular electronic diodes, *Proc. IEEE* **88**, 386–426 (2000).

15. M. A. Reed, C. Zhou, C. J. Muller, T. P. Burgin, J. M. Tour: Conductance of a molecular junction, *Science* **278**, 252–254 (1997).
16. C. P. Collier, E. W. Wong, M. Belohradsky, F. M. Raymo, J. F. Stoddart, P. J. Kuekes, R. S. Williams, J. R. Heath: Electronically configurable molecular-based logic gates, *Science* **285**, 391–394 (1999).
17. C. P. Collier, G. Mattersteig, E. W. Wong, Y. Luo, K. Beverly, J. Sampaio, F. M. Raymo, J. F. Stoddart, J. R. Heath: A [2]catenane-based solid state electronically reconfigurable switch, *Science* **289**, 1172–1175 (2000).
18. J. Chen, M. A. Reed, A. M. Rawlett, J. M. Tour: Large on-off ratios and negative differential resistance in a molecular electronic device, *Science* **286**, 1550–1552 (1999).
19. Y. Huang, X. Duan, Y. Cui, L. J. Lauhon, K. H. Kim, C. M. Lieber: Logic gates and computation from assembled nanowire building blocks, *Science* **294**, 1313–1317 (2001).
20. A. Bachtold, P. Hadley, T. Nakanishi, C. Dekker: Logic circuits with carbon nanotube transistors, *Science* **294**, 1317–1320 (2001).
21. Y. Luo, C. P. Collier, J. O. Jeppesen, K. A. Nielson, E. Delonno, G. Ho, J. Perkins, H. Tseng, T. Yamamoto, J. F. Stoddart, J. R. Heath: Two-dimensional molecular electronics circuits, *ChemPhysChem* **3**, 519–525 (2002).
22. M. M. Ziegler, C. A. Picconatto, J. C. Ellenbogen, A. DeHon, D. Wang, Z. H. Zhong, C. M. Lieber: Scalability simulations for nanomemory systems integrated on the molecular scale, in *Molecular Electronics III* (2003), Vol. 1006 of Ann. N.Y. Acad. Sci., pp. 312–330.
23. A. DeHon: Array-based architecture for FET-based, nanoscale electronics, *IEEE TNANO* **2**, 23–32 (2003).
24. A. DeHon, P. Lincoln, J. E. Savage: Stochastic assembly of sublithographic nanoscale interfaces, *IEEE TNANO* **2**, 165–174 (2003).
25. A. DeHon, M. J. Wilson: Nanowire-based sublithographic programmable logic arrays, in *Proc. ACM/SIGDA FPGA* (ACM Press, Monterey, CA, 2004), pp. 123–132.
26. B. Zeidman: *Designing with FPGAs and CPLDs* (CMP Books, Lawrence, KS, 2002).
27. M. Barr: Programmable logic: What's it to ya?, *Embedded Systems Programming* pp. 75–84 (1999). Also available online at <http://www.embedded.com/1999/9906/9906sr.htm>.
28. J. M. Tour, L. Cheng, D. P. Nackashi, Y. X. Yao, A. K. Flatt, S. K. S. Angelo, T. E. Mallouk, P. D. Franzon: Nanocell electronic memories, *J. Am. Chem. Soc.* **125**, 13 279–13 283 (2003).
29. A. Fijany, B. N. Toomarian: New design for quantum dots cellular automata to obtain fault tolerant logic gates, *J. Nanop. Res.* **3**, 27–37 (2001).
30. C. S. Lent, B. Isaksen: Clocked molecular quantum-dot cellular automata, *IEEE Trans. Elect. Dev* **50**, 1890–1896 (2003).
31. C. S. Lent, B. Isaksen, M. Lieberman: Molecular quantum-dot cellular automata, *J. Am. Chem. Soc.* **125**, 1056–1063 (2003).
32. C. S. Lent, P. D. Tougaw: Device architecture for computing with quantum dots, *Proc. IEEE* **85**, 541–557 (1997).
33. W. Porod, C. S. Lent, G. H. Bernstein, A. O. Orlov, I. Amlani, G. L. Snider, J. L. Merz: Quantum-dot cellular automata: computing with coupled quantum dots, *Intl. J. Elect.* **86**, 549–590 (1999).

34. Y. Huang, X. Duan, Q. Wei, C. M. Lieber: Directed assembly of one-dimensional nanostructures into functional networks, *Science* **291**, 630–633 (2001).
35. A. B. Greytak, L. J. Lauhon, M. S. Gudiksen, C. M. Lieber: Growth and transport properties of complementary germanium nanowire field-effect transistors, *Appl. Phys. Lett.* **84**, 4176–4178 (2004).
36. Y. Cui, Z. Zhong, D. Wang, W. U. Wang, C. M. Lieber: High performance silicon nanowire field effect transistors, *Nano Lett.* **3**, 149–152 (2003).
37. H. Naeimi, A. DeHon: A greedy algorithm for tolerating defective crosspoints in nano PLA design, in *Proc. IEEE Intl. Conf. Field Prog. Tech.* (2004).
38. J. M. Rabaey, A. P. Chandrakasan, B. Nikolic: *Digital Integrated Circuits*, 2nd edn. (Prentice-Hall, Inc., Englewood Cliffs, NJ, 2002).
39. E. Thune, C. Strunk: Quantum transport in carbon nanotubes, *Lect. Notes Phys.: Intro. Mol. Elect.* (2005).
40. J. Jortner, A. Nitzan, M. A. Ratner: Foundation of molecular electronics – charge transport in molecular conduction junctions, *Lect. Notes Phys.: Intro. Mol. Elect.* (2005).
41. P. Hanggi, S. Kohler, J. Lehmann, M. Strass: AC-driven transport through molecular wires, *Lect. Notes Phys.: Intro. Mol. Elect.* (2005).
42. R. DiFelice, A. Calzolari, D. Versano, A. Rubio: Electronic structure calculations for nanomolecular systems, *Lect. Notes Phys.: Intro. Mol. Elect.* (2005).
43. K. Stokbro, J. Taylor, M. Brandbyge, H. Guo: Ab-initio based nonequilibrium Green's function formalism for calculating electron transport in molecular devices, *Lect. Notes Phys.: Intro. Mol. Elect.* (2005).
44. A. DiCarlo, A. Pecchia, L. Latessa, T. Frauenheim, G. Seifert: Tight-binding DFT for molecular electronics (gDFTB), *Lect. Notes Phys.: Intro. Mol. Elect.* (2005).
45. N. Bushong, M. DiVentra: Current-induced effects in nanoscale conductors, *Lect. Notes Phys.: Intro. Mol. Elect.* (2005).
46. M. Wegewijs, M. H. Hettler, J. Konig, A. Thielmann, C. Romeike, K. Nowack: Single electron tunneling in small molecules, *Lect. Notes Phys.: Intro. Mol. Elect.* (2005).
47. M. Thorwart, M. Grifoni, R. Egger: Transport through intrinsic quantum dots in interacting carbon nanotubes, *Lect. Notes Phys.: Intro. Mol. Elect.* (2005).
48. L. A. Bumm, J. J. Arnold, M. T. Cygan, T. D. Dunbar, T. P. Burgin, L. Jones, D. L. Allara, J. M. Tour, P. S. Weiss: Are single molecular wires conducting?, *Science* **271**, 1705–1707 (1996).
49. Y. Selzer, M. A. Cabassi, T. S. Mayer, D. L. Allara: Temperature effects on conduction through a molecular junction, *Nanotechnology* **15**, S483–S488 (2004).
50. R. M. Metzger: All about (*N*-hexadecylquinolin-4-iun-1-yl) methylidenetrcyanoquinodimethane, a unimolecular rectifier of electrical current, *J. Mater. Chem.* **10**, 55–62 (2000).
51. P. J. Kuekes, D. R. Stewart, R. S. Williams: The crossbar latch: Logic value storage, restoration, and inversion in crossbar circuits, *J. Appl. Phys.* **97** (2005).
52. S. J. Tans, A. R. M. Verschueren, C. Dekker: Room-temperature transistor based on a single carbon nanotube, *Nature* **393**, 49–52 (1998).
53. H. W. C. Postma, T. Teepen, Z. Yao, M. Grifoni, C. Dekker: Carbon nanotube single-electron transistors at room temperature, *Science* **293**, 76–79 (2001).

54. S. Heinze, J. Tersoff, P. Avouris: Carbon nanotube electronics and optoelectronics, *Lect. Notes Phys.: Intro. Mol. Elect.* (2005).
55. J. C. Ellenbogen: Monomolecular electronic device, United States Patent 6,339,227, issued to the MITRE Corporation (2002).
56. J. Park, A. N. Pasupathy, J. I. Goldsmith, C. Chang, Y. Yaish, J. R. Petta, M. Rinkoski, J. P. Sethna, H. D. Abruna, P. L. McEuen, D. C. Ralph: Coulomb blockade and the Kondo effect in single-atom transistors, *Nature* **417**, 722–725 (2002).
57. W. Liang, M. P. Shores, M. Bockrath, J. R. Long, H. Park: Kondo resonance in a single-molecule transistor, *Nature* **417**, 725–729 (2002).
58. J. L. Hennessy, D. A. Patterson: *Computer Architecture: A Quantitative Approach*, 3rd edn. (Morgan Kaufmann, San Mateo, CA, 2002).
59. J. R. Heath, P. J. Kuekes, G. S. Snider, R. S. Williams: A defect-tolerant computer architecture: Opportunities for nanotechnology, *Science* **280**, 1716–1721 (1998).
60. G. L. Snider, A. O. Orlov, I. Amlani, G. H. Bernstein, C. S. Lent, J. L. Merz, W. Porod: Quantum-dot cellular automata: Line and majority logic gate, *Japanese J. Appl. Phys. Part 1* **38**, 7227–7229 (1999).
61. V. P. Roychowdhury, D. B. Janes, S. Bandyopadhyay: Nanoelectronic architecture for Boolean logic, *Proc. IEEE* **85**, 574–588 (1997).
62. G. Toth, C. S. Lent, P. D. Tougaw, Y. Brazhnik, W. W. Weng, W. Porod, R. W. Liu, Y. F. Huang: Quantum cellular neural networks, *Superlattices and Microstructures* **20**, 473–478 (1996).
63. O. Turel, J. H. Lee, X. Ma, K. K. Likharev: Neuromorphic architectures for nanoelectronic circuits, *Int. J. Circ. Theor. Appl.* **32**, 277–302 (2004).
64. C. P. Husband, S. M. Husband, J. S. Daniels, J. M. Tour: Logic and memory with nanocell circuits, *IEEE Trans. Elect. Dev.* **50**, 1865–1875 (2003).
65. J. M. Tour, W. L. van Zandt, C. P. Husband, S. M. Husband, L. S. Wilson, P. D. Franzon, D. P. Nackashi: Nanocell logic gates for molecular computing, *IEEE TNANO* **1**, 100–109 (2002).
66. S. C. Goldstein, M. Budiu: Nanofabrics: Spatial computing using molecular electronics, in *Proc. Intl. Symp. Comp. Arch.* (2001).
67. M. R. Stan, P. D. Franzon, S. C. Goldstein, J. C. Lach, M. M. Ziegler: Molecular electronics: From devices and interconnect to circuits and architecture, *Proc. IEEE* **91**, 1940–1957 (2003).
68. G. S. Rose, M. R. Stan: (2005), Programmable logic using molecular devices in a three-dimensional architecture, presentation at the Engr. Intl. Conf. on Mol. Elect., San Diego, CA (unpublished).
69. K. K. Likharev, D. B. Strukov: CMOL: Devices, circuits, and architectures, *Lect. Notes Phys.: Intro. Mol. Elect.* (2005).
70. D. B. Strukov, K. K. Likharev: CMOL FPGA: A reconfigurable architecture for hybrid digital circuits with two-terminal devices, submitted for publication (2005).
71. J. Han: Fault-tolerant architectures for nanoelectronic and quantum devices, Ph.D. thesis, Delft University of Technology, Delft, The Netherlands (2004).
72. V. Beiu: A novel highly reliable low-power nano architecture when von Neumann augments Kolmogorov, in *Proc. IEEE Intl. Conf. on App. Spec. Sys., Arch. and Proc. (ASAP)* (2004).
73. S. Trimberger (Ed.): *Field Programmable Gate Array Technology* (Kluwer Academic Publishers, Boston, 1994).

74. M. D. Austin, H. Ge, W. Wu, M. Li, Z. Yu, D. Wasserman, S. A. Lyon, S. Y. Chou: Fabrication of 5 nm linewidth and 14 nm pitch features by nanoimprint lithography, *Appl. Phys. Lett.* **84**, 5299–5301 (2004).
75. G. Y. Jung, S. Ganapathiappan, D. A. A. Ohlberg, D. L. Olynick, Y. Chen, W. M. Tong, R. S. Williams: Fabrication of a 34×34 crossbar structure at 50 nm half-pitch by UV-based nanoimprint lithography, *Nano Lett.* **4**, 1225–1229 (2004).
76. Z. Zhong, D. Wang, Y. Cui, M. W. Bockrath, C. M. Lieber: Nanowire crossbar arrays as address decoders for integrated nanosystems, *Science* **302**, 1377–1379 (2003).
77. A. DeHon: Reconfigurable architectures for general-purpose computing, Technical Report AIRTR-1586, Massachusetts Institute of Technology (1996).
78. P. S. Zuchowski, C. B. Reynolds, R. J. Grupp, S. G. Davis, B. Cremen, B. Troxel: A hybrid ASIC and FPGA architecture, in *Proc. Intl. Conf. Comp. Aid. Des.* pp. 187–194, (2002).
79. M. M. Ziegler, M. R. Stan: CMOS/nano co-design for crossbar-based molecular electronic systems, *IEEE TNANO* (2003).
80. M. Forshaw, R. Stadler, D. Crawley, K. Nikolic: A short review of nanoelectronic architectures, *Nanotechnology* **15**, S220–S223 (2004).
81. R. P. McConnell: Diode-based power gain for molecular-scale electronic digital computers, report MP 00W0000310, The MITRE Corporation, McLean, VA (2000).
82. R. P. McConnell, J. C. Ellenbogen, T. S. Mayer, T. E. Mallouk, S. P. Goldstein: Requirements and designs for molecular computer architectures that incorporate gain-producing elements, presentation at the Engr. Found. Conf. on Mol. Elect., Kona, HI (unpublished) (2000).
83. S. C. Goldstein, D. Rosewater: Digital logic using molecular electronics, in *Proc. Intl. Sol. St. Circ. Conf.* (2002).
84. G. S. Rose, M. R. Stan: Memory arrays based on molecular RTD devices, in *Proc. IEEE-NANO* pp. 453–456, (2003).
85. E. Goto, K. Murata, K. Nakazawa, K. Nakagawa, T. Moto-Oka, Y. Matsuoka, Y. Ishibashi, T. Soma, , E. Wada: Esaki diode high speed logical circuits, *IRE Trans. Elect. Comp.* pp. 25–29 (1960).
86. H. C. Liu, T. C. L. G. Sollner: High-frequency resonant-tunneling devices, in *Semiconductors and Semimetals*, ed. by R. A. Kiehl, T. C. L. G. Sollner, Vol. 41 (Academic Press, Boston, 1994), pp. 359–418.
87. R. H. Mathews, J. P. Sage, T. C. L. G. Sollner, S. D. Calawa, C.-L. Chen, L. J. Mahoney, P. A. Maki, K. M. Molvar: A new RTD-FET logic family, *Proc. IEEE* **87**, 596–605 (1999).
88. P. J. Kuekes: Molecular crossbar latch, United States Patent 6,586,965 (2003).
89. Y. Chen, D. A. A. Ohlberg, X. Li, D. R. Stewart, J. O. Jeppesen, K. A. Nielsen, J. F. Stoddart, D. L. Olynick, E. Anderson: Nanoscale molecular-switch devices fabricated by imprint lithography, *Appl. Phys. Lett.* **82**, 1610–1612 (2003).
90. P. J. Kuekes, R. S. Williams: in press.
91. M. van den Brink: Litho roadmap shows difficult terrain – part 2 – technology information, *Electronic News*, Jan. 17, 2000.
92. Semi industry to reach \$360 billion by 2010, says report, *Silicon Strategies*, Dec. 2, 2003.

93. A. W. Burks, H. H. Goldstine, J. von Neumann: Preliminary discussion of the logical design of an electronic computing instrument, in *John von Neumann Collected Works*, ed. by A. H. Taub, Vol. V (The Macmillan Co., New York, 1963), pp. 34–79.
94. H. H. Goldstine, J. von Neumann: On the principles of large scale computing machines, in *John von Neumann Collected Works*, ed. by A. H. Taub, Vol. V (The Macmillan Co., New York, 1963), pp. 1–32.
95. J. von Neumann: First draft of a report on the EDVAC, in *From ENIAC to Univac: An Appraisal of the Eckert-Mauchly Computers*, ed. by N. Stern (Digital Press, Bedford, MA, 1981).
96. Reprinted from the AMD Virtual Pressroom at <http://www.amd.com>.
97. Semiconductor Industry Association: International technology roadmap for semiconductors: 2003 edition, Technical report, SEMATECH (2003).
98. J. D. Meindl, Q. Chen, J. A. Davis: Limits on silicon nanoelectronics for terascale integration, *Science* **293**, 2044–2049 (2001).
99. V. V. Zhirnov, R. K. Cavin, J. A. Hutchby, G. I. Bourianoff: Limits to binary logic switch scaling – a gedanken model, *Proc. IEEE* **91**, 1934–1939 (2003).
100. D. J. Frank, R. H. Dennard, E. Nowak, P. M. Solomon, Y. Taur, H. S. P. Wong: Device scaling limits of Si MOSFETs and their application dependencies, *Proc. IEEE* **89**, 259–288 (2001). This article is one of several that appeared in a Special Issue on Limits of Semiconductor Technology.
101. M. T. Bohr: Nanotechnology goals and challenges for electronic applications, *IEEE TNANO* **1**, 56–62 (2002).
102. J. A. Davis, R. Venkatesan, A. Kaloyerous, M. Beylansky, S. J. Souris, K. Banerjee, K. C. Saraswat, A. Rahman, R. Reif, J. D. Meindl: Interconnect limits on gigascale integration (GSI) in the 21st century, *Proc. IEEE* **89**, 305–324 (2001). This article is one of several that appeared in a Special Issue on Limits of Semiconductor Technology.
103. M. Ieong, B. Doris, J. Kedzierski, K. Rim, M. Yang: Silicon device scaling to the sub-10-nm regime, *Science* **306**, 2057–2060 (2004).
104. A. Rahman: System-level performance evaluation of three-dimensional integrated circuits, Ph.D. thesis, Massachusetts Institute of Technology, Cambridge, MA (2001).
105. R. Reif, A. Fan, K.-N. Chen, S. Das: Fabrication technologies for three-dimensional integrated circuits, in *Proc. Intl. Symp. Qual. Elect. Des.* pp. 33–37, (2002).
106. S. F. Al-Sarawi, D. Abbott, P. D. Franzon: A review of 3-D packaging technology, *IEEE Trans. CPMT B* **21**, 2–14 (1998).
107. A. Fan, A. Rahman, R. Reif: Copper wafer bonding, *Elect. Sol. St. Lett.* **2**, 534–536 (1999).
108. J. A. Burns, C. Keast, K. Warner, P. Wyatt, D. Yost: Fabrication of 3-dimensional integrated circuits by layer transfer of fully depleted SOI circuits, in *Proc. Mat. Res. Soc. Symp. G* Vol. 768 (2003).
109. Y. Kwon, A. Jindal, J. J. McMahon, J.-Q. Lu, R. J. Gutmann, T. S. Cale: Dielectric glue wafer bonding for 3-D ICs, in *Proc. Mat. Res. Soc.* (Spring 2003).
110. L. Xue, C. C. Liu, H. S. Kim, S. Kim, S. Tiwari: Three-dimensional integration: Technology, use, and issues for mixed-signal applications, *IEEE Trans. Elect. Dev.* **50**, 601–609 (2003).

111. V. Subramanian, P. Dankoski, L. Degertekin, B. T. Khuri-Yakub, K. C. Saraswat: Controlled two-step solid-phase crystallization for high-performance polysilicon TFT's, *IEEE Elect. Dev. Lett.* **18**, 378–381 (1997).
112. S. Das: Design automation and analysis of three-dimensional integrated circuits, Ph.D. thesis, Massachusetts Institute of Technology, Cambridge, MA (2004).
113. R. Chau, B. Boyanov, B. Doyle, M. Doczy, S. Datta, S. Hareland, D. Jin, J. Kavalieros, M. Metz: Silicon nanotransistors for logic applications, *Physica E: Low-dimensional Systems and nanostructures* **19**, 1–5 (2003).
114. S. J. Wind, J. Appenzeller, R. Martel, V. Derycke, P. Avouris: Vertical scaling of carbon nanotube field-effect transistors using top gate electrodes, *Appl. Phys. Lett.* **80**, 3817–3819 (2002).
115. Z. M. Liu, A. A. Yasser, J. S. Lindsey, D. F. Bocian: Molecular memories that survive silicon device processing and real-world operation, *Science* **302**, 1543–1545 (2003).
116. C. Li, W. Fan, B. Lei, D. Zhang, S. Han, T. Tang, X. Liu, Z. Liu, S. Asano, M. Meyyappan, J. Han, C. Zhou: Multilevel memory based on molecular devices, *Appl. Phys. Lett.* **84**, 1949–1951 (2004).
117. Q. L. Li, S. Surthi, G. Mathur, S. Gowda, Q. Zhao, T. A. Sorenson, R. C. Tenent, K. Muthukumaran, J. S. Lindsey, V. Misra: Multiple-bit storage properties of porphyrin monolayers on SiO₂, *Appl. Phys. Lett.* **85**, 1829–1831 (2004).
118. B. J. Feder: Nanotech memory chips might soon be a reality, *New York Times*, June 7, 2004.
119. E. Kusse: Analysis and circuit design for low power programmable logic modules, M.S. thesis, Univ. of California, Berkeley, CA (1997).
120. A. S. Blum, C. M. Soto, C. D. Wilson, J. D. Cole, M. Kim, B. Gnade, A. Chatterji, W. F. Ochoa, T. W. Lin, J. E. Johnson, B. R. Ratna: Cowpea mosaic virus as a scaffold for 3-D patterning of gold nanoparticles, *Nano Lett.* **4**, 867–870 (2004).
121. J. Y. Fang, C. M. Soto, T. W. Lin, J. E. Johnson, B. Ratna: Complex pattern formation by cowpea mosaic virus nanoparticles, *Langmuir* **18**, 308–310 (2002).
122. P. Beckett, A. Jennings: Towards nanocomputer architecture, in *Proc. ACS Conf. Res. Prac. Inf. Tech.* Vol. 6 pp. 141–150, (2002).
123. N. Weste, K. Eshraghian: *Principles of CMOS VLSI Design*, 2nd edn. (Addison-Wesley Publishing Company, Reading, MA, 1994).
124. Cadence Design Framework II, Version IC 5.0.33, Cadence Design Systems, Inc., San Jose, CA, 2004.

Index

- ab-initio 83, 94, 97, 103, 104
acetylene 257, 263
addition energy 369, 370
Aharonov-Bohm effect 365
ambipolar conduction 383
architecture *see* nanoprocessor
armchair 354, 355, 359, 360
asymmetric gating 402
Atomic forces 165
Aviram-Ratner model 1
- ballistic transport 381
band structure 358, 359, 361
bandstructure 83, 86, 97
benzene 213
benzenedithiol 266
Boolean logic 447, 460, 471
Bosonization 233
break junction 253, 258, 271
- C₆₀ 258, 263–265
carbon monoxide 257, 263
carbon nanotube 381
doping 390
light emission 403
ohmic contact 384
oxygen adsorption 390
carbon nanotube (CNT) 5
charge transfer 83, 84
chemical potential 130
chiral vector 354, 355, 359
CMOL circuits 447, 452
CMOL technology 447, 449, 452
CMOS technology 447
Coherent current 164
coherent transport 118
Conductance
Line shape 234
Linear conductance 234
conductance 254, 259–261, 263–270
inelastic 200
conductance channels 263
conductance fluctuations 261, 263,
265, 271
conductance histogram 259, 260, 263
conductance histograms 263
conductance plateau 265, 266
conducting atomic force microscopy
301
contact geometry 388, 397
contacting molecules 301
Contour integration 162
cooling 199
Coulomb blockade 209, 229, 303
coulomb blockade 369–372
Coulomb interaction 231
Finite range 236
Zero range 236
crossbar 483, 487, 489, 492, 497, 498
CrossNet 447, 467
crystal momentum 122
current
peak 221
through a nanoscale junction 185
Current operator 163
current spectroscopy 209
current-induced effects 185
current-induced forces 188
current-voltage characteristic 259,
267–270
- defect tolerance 447, 459, 464, 466,
471, 472
density functional based tight binding
(DFTB) 5
Density Functional Theory 117

- density functional theory 261, 263
 density functional theory (DFT) 4
 density matrix 130
 device models *see* simulation
 DFT 79, 117
 DFTB 155
 Diagrams 157
 differential conductance 259, 261, 264,
 268
 direct force 189
 DNA 83, 84, 95
 DTB 126
- Ehrenfest's theorem 188
 electromigration 142
 electromigration breaking 254, 255,
 264
 electron interference 363
 electron transfer 1
 electron transport 117
 electron-electron interaction 372, 373
 electron-hole recombination 404
 Electron-phonon scattering 169
 electronic devices 381
 electrostatics
 quasi-one-dimensional 382
 exchange interaction 371, 372
 excited state 88, 89
 exciton 405
- fabrication yield 447, 451, 455, 459,
 466
- Fabry-Perot regime 243
 Fano factor 58, 71, 193
 oscillation with wire length 193
- Fermi level
 pinning 382
- FET *see* transistor
- field-effect transistor 381, *see*
 transistor
- field-programmable gate array 496
 field-programmable gate array 486,
 487, 493, 495, 496
- floating electrodes 451
 floating gate 450
 Floquet approach 59
 Floquet equation 64
 force
 current-induced forces 188
- FPGA *see* field-programmable gate
 array
- Franck-Condon factor 220
 fullerene 258, 263, 265
- gate electrode 264, 266, 271
 gate voltage 207
 gold 253, 258, 264–267, 269, 270
 gold nanoparticles 302
 graphene 351, 352, 354–360, 363
 Green's function 117
 grid molecule 215
 group velocity 133
- Hartree potential 131
 heating 194
 Hellman-Feynman theorem 188
 hierarchy
 of architecture 486
 of design 482, 485, 487
- hydrogen 257, 260–263
 hysteresis 483
- Incoherent current 164
 inelastic conductance 200
 inelastic electron spectroscopy 261
 interface 452
 inverter 393
 isocyanide groups 448, 450
 isotope substitution 261, 262
- junction switch *see* nanoswitch
- Keldysh 160
 Kondo effect 371, 372
- Landauer 102
 Landauer-Büttiker formula 385
 Landauer-Büttiger 117
 Landauer-Büttiker formulation 188
 latch 484, 489
 latching switch 448, 450, 455, 462, 466,
 467, 469, 470
- light emission 403
 local heating 194
 logic gate 392
- Markovian master equation 236
 master equation 66

- MCBJ 253–259, 265–268, 270
 McDAL 134
 memories 447, 455, 474
 metal-induced gap states 382
 Modes 174
 molecular spintronics 8
 Molecular Wires 135
 Moore's Law 448, 462, 474
 Moore's law 2
 MOSFET 448, 462
 multi-wall 351–353, 357, 362–365,
 368–370, 372, 373

 Nagaoka effect 217
 nanocomputer 479
 architecture *see* nanoprocessor
 design challenges 485
 nanomemory 479, 480, 493
 nanoprocessor 479
 architecture 479, 481, 482, 485, 490,
 493
 array 483, 487, 492, 495–497, 499
 design challenges 485, 488
 hybrid CMOS/nano 492
 organ structure 490
 nanoscale junction 185
 nanoswitch 483, 487, 489, 494
 bistable 483
 nanotransistor 483, 489, 492, 495, 501
 hybrid 492
 leakage 502, 503, 505
 nanotube-metal contact 382
 nanotubes 80, 82, 100, 105
 nanowire crossbar 447, 452, 453, 461,
 462, 467
 negative differential conductance 210
 NEGF 117
 neuromorphic networks 447, 467, 474
 noise
 shot noise 190
 noise power 63
 noise spectroscopy 222
 Non-equilibrium forces 141

 octanethiol 301
 off-current 400
 ohmic contact 384
 OPE chains 450
 optical properties 91, 94, 95

 optoelectronic devices 381
 organic light emitting diodes 8
 overlap population 142

 pattern classification 447, 469
 pattern recognition 447, 469
 phase coherence length 366, 367
 phonons 194
 photochromic molecule 270
 photon absorption/emission 60
 photon-assisted transport 70
 PLA *see* programmable logic array
 plane wave basis set 187
 platinum 253, 257, 260–263
 Poisson equation 164
 Poisson limit 193
 Poisson's equation 131
 polarization 93, 97, 99, 100
 population inversion 218
 power consumption 447, 461, 466, 471
 Power dissipation 178
 programmable logic array 496
 programmable logic array 481
 programmable logic array 486,
 495–497, 500, 501
 protein 94

 quantum conductance 84, 98, 104, 105
 Quantum dot 229
 Quantum Monte Carlo 242
 quantum ratchet 55

 radiative relaxation 214
 rectification 483, 489
 importance of 485
 retention time 448, 455, 462

 scanning probe microscopy (SPM) 7
 scanning probe technique 253, 254
 scanning probe techniques 254
 scattering states 122
 Schottky barrier 382
 height 383
 Schottky barrier transistors 381
 Schottky's value for the Poisson limit
 193
 Schrödinger equation 119
 screening approximation 122
 self-assembly 447, 448, 450, 455, 474

- Self-energy 160, 172
 shot noise
 Poisson limit 193
 shot noise 190
 peak 224
 simulation 479, 481, 483, 499
 device models 484, 499, 500
 single molecule 253, 263, 269, 301
 single-electron transistor 447, 450, 461
 single-electron trap 450, 455
 single-electron tunneling 211
 single-electronics 448, 450
 single-wall 352, 353, 357, 362, 363, 368,
 369, 372
 Single-wall carbon nanotubes 229
 Spanish initiative for electronic simulations with thousands of atoms
 (SIESTA) 5
 spin blockade 217
 subthreshold slope 393
 super-poissonian noise 210, 224
 switch *see* nanoswitch
 switching speed 448, 455, 462
 symmetry 254, 257, 267–269
- TDDFT 88, 89, 92, 93
 thiol group 253, 258, 266, 267, 269, 270
 time-dependent current 62
 Tomonaga-Luttinger 373
 Tomonaga-Luttinger liquid 229
 TLL parameter 233
 transfer characteristics 400
 TranSIESTA 134
 transistor 383, *see* nanotransistor
 current saturation 394
 off-state 383
 on-state 383
 performance scaling 393
 scaling 401
 thermal limit 397
 turn-on performance 394
 turn-on regime 383
 transmission coefficients 134
 transport 84, 87, 97, 102
 transport channels
 competing 208
 Tunneling
 Coherent resonant tunneling 235
 Correlated sequential tunneling 229
 Uncorrelated sequential tunneling
 229
 tunneling 383, 386, 448, 450, 455
 two-terminal devices 447, 448, 450
- universal conductance fluctuations
 365–367
- van Hove singularities 360–362
 vibration 219
 vibrational relaxation 220
 Vibrations 169
 Virtual contact 163
 Virtual NanoLab 134
 voltage gain 392, 448, 449
- Wannier functions 97, 99, 105
 weak localization 365–367
 weak-coupling approximation 65
 Weisskopf-Wigner approximation 239
 wind force 189
- zero-bias gap 303
 zigzag 354, 355, 359, 360

Lecture Notes in Physics

For information about earlier volumes
please contact your bookseller or Springer
LNP Online archive: springerlink.com

Vol.633: H.-T. Elze (Ed.), Decoherence and Entropy in Complex Systems, Based on Selected Lectures from DICE 2002

Vol.634: R. Haberlandt, D. Michel, A. Pöppel, R. Stannarius (Eds.), Molecules in Interaction with Surfaces and Interfaces

Vol.635: D. Alloin, W. Gieren (Eds.), Stellar Candles for the Extragalactic Distance Scale

Vol.636: R. Livi, A. Vulpiani (Eds.), The Kolmogorov Legacy in Physics, A Century of Turbulence and Complexity

Vol.637: I. Müller, P. Strehlow, Rubber and Rubber Balloons, Paradigms of Thermodynamics

Vol.638: Y. Kosmann-Schwarzbach, B. Grammaticos, K. M. Tamizhmani (Eds.), Integrability of Nonlinear Systems

Vol.639: G. Ripka, Dual Superconductor Models of Color Confinement

Vol.640: M. Karttunen, I. Vattulainen, A. Lukkarinen (Eds.), Novel Methods in Soft Matter Simulations

Vol.641: A. Lalazissis, P. Ring, D. Vretenar (Eds.), Extended Density Functionals in Nuclear Structure Physics

Vol.642: W. Hergert, A. Ernst, M. Däne (Eds.), Computational Materials Science

Vol.643: F. Strocchi, Symmetry Breaking

Vol.644: B. Grammaticos, Y. Kosmann-Schwarzbach, T. Tamizhmani (Eds.) Discrete Integrable Systems

Vol.645: U. Schollwöck, J. Richter, D. J. J. Farnell, R. F. Bishop (Eds.), Quantum Magnetism

Vol.646: N. Bretón, J. L. Cervantes-Cota, M. Salgado (Eds.), The Early Universe and Observational Cosmology

Vol.647: D. Blaschke, M. A. Ivanov, T. Mannel (Eds.), Heavy Quark Physics

Vol.648: S. G. Karshenboim, E. Peik (Eds.), Astrophysics, Clocks and Fundamental Constants

Vol.649: M. Paris, J. Rehacek (Eds.), Quantum State Estimation

Vol.650: E. Ben-Naim, H. Frauenfelder, Z. Toroczkai (Eds.), Complex Networks

Vol.651: J. S. Al-Khalili, E. Roeckl (Eds.), The Euroschool Lectures of Physics with Exotic Beams, Vol.I

Vol.652: J. Arias, M. Lozano (Eds.), Exotic Nuclear Physics

Vol.653: E. Papantonopoulos (Ed.), The Physics of the Early Universe

Vol.654: G. Cassinelli, A. Levriero, E. de Vito, P. J. Lahti (Eds.), Theory and Application to the Galileo Group

Vol.655: M. Shillor, M. Sofonea, J. J. Telega, Models and Analysis of Quasistatic Contact

Vol.656: K. Scherer, H. Fichtner, B. Heber, U. Mall (Eds.), Space Weather

Vol.657: J. Gemmer, M. Michel, G. Mahler (Eds.), Quantum Thermodynamics

Vol.658: K. Busch, A. Powell, C. Röthig, G. Schön, J. Weissmüller (Eds.), Functional Nanostructures

Vol.659: E. Bick, F. D. Steffen (Eds.), Topology and Geometry in Physics

Vol.660: A. N. Gorban, I. V. Karlin, Invariant Manifolds for Physical and Chemical Kinetics

Vol.661: N. Akhmediev, A. Ankiewicz (Eds.) Dissipative Solitons

Vol.662: U. Carow-Watamura, Y. Maeda, S. Watamura (Eds.), Quantum Field Theory and Noncommutative Geometry

Vol.663: A. Kalloniatis, D. Leinweber, A. Williams (Eds.), Lattice Hadron Physics

Vol.664: R. Wielebinski, R. Beck (Eds.), Cosmic Magnetic Fields

Vol.665: V. Martinez (Ed.), Data Analysis in Cosmology

Vol.666: D. Britz, Digital Simulation in Electrochemistry

Vol.667: W. D. Heiss (Ed.), Quantum Dots: a Doorway to Nanoscale Physics

Vol.668: H. Ocampo, S. Paycha, A. Vargas (Eds.), Geometric and Topological Methods for Quantum Field Theory

Vol.669: G. Amelino-Camelia, J. Kowalski-Glikman (Eds.), Planck Scale Effects in Astrophysics and Cosmology

Vol.670: A. Dinklage, G. Marx, T. Klänger, L. Schweikhard (Eds.), Plasma Physics

Vol.671: J.-R. Chazottes, B. Fernandez (Eds.), Dynamics of Coupled Map Lattices and of Related Spatially Extended Systems

Vol.672: R. Kh. Zeytounian, Topics in Hypersonic Flow Theory

Vol.673: C. Bona, C. Palenzuela-Luque, Elements of Numerical Relativity

Vol.674: A. G. Hunt, Percolation Theory for Flow in Porous Media

Vol.675: M. Kröger, Models for Polymeric and Anisotropic Liquids

Vol.676: I. Galanakis, P. H. Dederichs (Eds.), Half-metallic Alloys

Vol.678: M. Donath, W. Nolting (Eds.), Local-Moment Ferromagnets

Vol.679: A. Das, B. K. Chakrabarti (Eds.), Quantum Annealing and Other Optimization Methods

Vol.680: G. Cuniberti, G. Fagas, R. Klaus (Eds.), Introducing Molecular Electronics